An Integrated Modelling Approach to Inform Package Design for Optimal Cooling of Horticultural Produce

A thesis presented in partial fulfilment of the requirements for the degree of

Doctor of Philosophy

in

Food Technology

at Massey University, Palmerston North, New Zealand

Jamal Rimkeit Olatunji

2018

Abstract

Forced-air cooling is a widely used pre-cooling process that enables the New Zealand horticultural industry, valued at over NZD $8B in 2016, to maintain the quality of perishable exports. In the typical systems used in New Zealand's horticultural industry, forced-air cooling involves stacking fruit boxes into pallets, which are stacked together in a refrigerated room, and a fan is used to create a pressure drop through the pallets. This forces cold air through the packaging ventilation and over the fruit, facilitating heat transfer and rapidly cooling the product from the field heat (~20 °C) to the storage temperature (0-2 °C), thus prolonging shelf life and preserving fruit quality.

Package design is linked with cooling performance, as the specifics of the ventilation (i.e. placement and size of vents in the boxes) results in different airflow patterns. Unfortunately, it is not well understood how to predict the performance of a hypothetical design, which is partly why in industry and academia there has been a focus on package design testing – where through experimental or computational means, the performance of a given design is thoroughly tested. Trial-and-error experimental work represents a steep materials cost, and construction and validation of detailed mathematical models can be a highly arduous and specialised task. It would therefore be beneficial to the New Zealand horticulture industry and academia to have a suite of methodologies that can simply and rapidly predict performance of a hypothetical package design. It was proposed that such methods are based upon mathematical modelling, with a focus on flexibility, computational efficiency, and automation. The goal is that such a model can be used to rapidly develop mathematical descriptions of a wide variety of products and cooling scenarios, and if integrated with optimisation routines, will allow swift iteration toward an optimised design.

To meet this goal a new interpretation of the zonal modelling approach was developed and validated at the single box scale for the forced-air cooling of modular bulk packages of polylined kiwifruit – kiwifruit representing the largest horticultural crop in New Zealand (worth NZD $1.7B in 2016). The model focused on developing a simplified heat transfer model, with airflow considerations being a separate research project. The model is fast – with heat transfer solution times on the order of 1-2

seconds; flexible – as the model will solve for any input geometry; and automated – as the model was capable of algorithmically generating the zonal network, requiring no manual input beyond initial configuration settings.

A random stacking model was also developed to complement the heat transfer model. This is capable of automatically generating a realistic bulk fruit geometry inside of any package size or shape in only 150 seconds, relying on only a shape equation for kiwifruit and a weight distribution index as inputs. The stacking model can also simulate the presence of a polyliner wrapping, which is used in many horticultural packaging systems, including for many kiwifruit systems. The model was validated against empirically measured bulk fruit shapes, collected via CT scanning. The random stacking model increased the flexibility of the methodology and opened up the design space considerably for building models of a wide variety of package designs and products, without requiring physical prototypes or requiring "idealised" packaging configurations. The stacking model has an added functionality of predicting the volumetric efficiency of different package types.

Cooling uniformity was identified as a key performance metric for the forced-air cooling process. The airflow pattern imposes a range of rates of cooling for different fruit positions throughout the same pallet. This can have large impacts on the quality and shelf-life of individual fruit, which causes significant logistical problems for pack-house/product managers. A new quantitative heterogeneity index was developed, capable of condensing total process heterogeneity into one dimensionless number, the Overall Heterogeneity Index, or OHI.

This suite of tools can be used for a variety of tasks. Although the modelling work was only applied to the forced-air cooling of polylined kiwifruit inside of modular bulk packages, building models for other crops, package designs and cooling scenarios is trivial to implement. The speed of the zonal heat transfer model makes it ideal for integration with an iterative optimisation routine, so that many hundreds or thousands of designs can be investigated in a short period of time. The heat transfer model could also be combined with a machine learning algorithm (such as a genetic algorithm) to iteratively approach an optimised design. However, such an implementation requires an equally fast and flexible pallet scale airflow model, which remains a task for further work.

Acknowledgements

Thanks to my supervisors Dr. Richard Love (chief supervisor), Prof. Andrew East (co-supervisor) and Dr. Young-Min Shim (co-supervisor) for their technical, moral and professional help during my years of study. Thanks to Prof. John Bronlund, who saw potential in me as an undergraduate and convinced me to pursue my doctorate; and Dr. Maria Ferrua who co-supervised at the beginning of the project.

A huge thank you to industrial partners OJI Fibre Solutions and Zespri International who provided vital material and financial support.

Thanks to students Alicia Tan, Lyall McDonald, Julia Zhou, Angela Yang and Tim Cook for their help collecting experimental data. The volume of information collected would not have been possible without your assistance. Integral experimental equipment that made the pallet scale experiments possible were inherited from work done by Dr. Justin O'Sullivan, so a great deal of thanks to him too.

Also thanks to Nicki Moffat for allowing us to use your departments CT scanning equipment.

This PhD was the result of funding from the New Zealand Ministry of Business, Innovation and Employment (Fibreboard Packaging Design Project, MAUX1302).

This thesis is dedicated to my parents and their incredible journey.

Table of Contents

List of Tables

List of Figures

Nomenclature

English Symbols

A – area, m^2

a – translational acceleration (m·s^{-2})

a, b, c – empirical constants

B_X, B_Y, B_Z – planar cut positions for zones

C – specific heat capacity, J·kg^{-1}·°C^{-1}

c – index

C_{ij} – Connectivity Matrix

CP – cumulative proximity

CT_{Number} – CT number

C_{XYZ} – Coordinate Matrix

d_s – equivalent mean particle diameter, m

D – permeance, m·s^{-1}

d – diameter, m

d_c – characteristic distance, m

$\overline{d_{min}}$ – average voxel distance, m

$d_{\overrightarrow{nm}}$ – distance between a voxel and a surface voxel, m

D_X, D_Y, L_k – dimensions of a kiwifruit, m

dX, dY, dZ – dimensions of zones

dx, dy, dz – dimensions of voxels, m

e – coefficient of restitution

e – experiment index

E_{total} – residual between experiment and model, °C·h

F – force, kg·m·s^{-2}

F – Forchheimer coefficient, m^{-1}

F – volume force, N·m^{-3}

$F_{N.C.}$ – natural convection correction factor

G – gravity force, kg·m·s^{-2}

g – acceleration due to gravity, m·s^{-2}

Gr – Grashof number, dimensionless

H – moment of force, kg·m^{2}·s^{-2}

h - heat transfer coefficient, W·m^{-2}·°C^{-1}

H_1, H_2, H_3 – height of package ventilation, m

HI – heterogeneity index, °C or K

I – identity matrix

I – inertia, kg

I – number of elliptical disks

K_ε – intrinsic permeability, m^{2}

K – permeability, m^{2}·s^{-1}

L_{vap} – latent heat of vaporisation, 2260 kJ·kg^{-1}

L – characteristic length, m

L_1, L_2, L_3 – length of package ventilation, m

$\dot{m}$ – moisture flux, kg water·s^{-1}

M – mass, kg

m – index

n – index

$\boldsymbol{n}$ **–** normal vector

N_S – number of kiwifruit in a box

N_{total} – number of zones

Nu – Nusselt number, dimensionless

N_X, N_Y, N_Z – number of zones in the X, Y and Z directions

o – index

OHI – overall heterogeneity index, dimensionless

p_c – contact point

P – pressure, Pa

p – position index

P_1, P_2, P_3 – position of package ventilation, m

Pr – Prandtl number, dimensionless

P_X, P_Y, P_Z – polyliner dimensions, m

$\dot{Q}$ – volumetric flowrate, m^3·s^{-1}

r – random number

R – resistance, m^2·°C·W^{-1}

Ra – Rayleigh number, dimensionless

R_{CO_2} – rate of CO_2 production, mol·kg^{-1}·s^{-1}

Re – Reynolds number, dimensionless

S – fruit shoulder coefficient

Sc – Schmidt number, dimensionless

Sh – Sherwood number, dimensionless

T – temperature, °C

t – time, h

TKE – turbulent kinetic energy, m^2·s^{-2}

T_{Owen} – Owen's T function

Tu – turbulence intensity, dimensionless

u - velocity, m·s^{-1}

V – volume, m^3

W – weight, kg

X, Y, Z – Cartesian coordinates, m

Y – Fractional Unaccomplished Temperature Change, dimensionless

Greek Symbols

α – rotational acceleration (rad·s^{-2})

α – shape factor

β – thermal expansion coefficient, K^{-1}

δ – collision margin, m

ε – porosity, $m^3 \cdot m^{-3}$

θ_{fruit} – pixel/voxel threshold

θ_{search} – search radius

θ – angle, °

κ – thermal diffusivity, $m^2 \cdot s^{-1}$

λ_b – effective thermal conductivity of the packed bed, $W \cdot m^{-1} \cdot °C^{-1}$

λ – thermal conductivity, $W \cdot m^{-1} \cdot °C^{-1}$

$\mu_{Material}$ – X-ray absorption coefficient for the material

μ_{surf} – coefficient of friction

μ_{water} – X-ray absorption coefficient for water

μ – fluid viscosity, Pa·s

ξ – location factor

ρ – density, $kg \cdot m^{-3}$

σ_{rad} – Stefan–Boltzmann constant (5.67×10^{-8} $W \cdot m^{-2} \cdot K^{-4}$

σ – standard deviation

τ – characteristic index of process progression, $s \cdot s^{-1}$

υ – kinematic viscosity, $m^2 \cdot s^{-1}$

ω – scale factor

ϵ – emissivity, dimensionless

ϕ – heat flux, W or $J \cdot s^{-1}$

Miscellaneous Symbols

$\leftarrow, \rightarrow, \uparrow, \downarrow, \otimes, \odot$ – zonal adjacency

$\mathbb{B}_C$ – height of chute, m

$\mathbb{B}_X, \mathbb{B}_Y, \mathbb{B}_Z$ – inner dimensions of a package, m

$\mathbb{K}$ – kiwifruit

$\mathcal{P}_X, \mathcal{P}_Y, \mathcal{P}_Z$ – polyliner dimensions, m

$\mathbb{P}$ - zonal properties

$\mathbb{p}$ – pixel

$\mathbb{v}$ – voxel

Subscripts

A	A – air phase
cond	$cond$ – conduction
conv	$conv$ – convection
diff	$diff$ – diffusion
eff	eff – effective
evap	$evap$ – evaporation
Exp	Exp – experimental
ext	ext – external
f	f – final
i	i – initial
i	i – zone i, index

ii ii – intra-zonal

ij ij – inter-zonal

int int – internal

j j – zone j, index

Mod Mod – Model

O O – bulk air phase

P P – packaging phase

p p – product (fruit)

rad rad – radiation

ref ref – refrigerated fluid (in context, air)

S S – solid, or fruit, phase

surf $surf$ – surface

t t – time

tot tot – total

Z Z – phase

Za Z_α – primary phase

Zb Z_β – secondary phase

Mathematical Operators

Φ_s – standard normal cumulative distribution

ϕ_s – standard normal distribution

Δ - difference

∇ - partial derivative with respect to all directions in Cartesian space

d – total derivative

Ω – surface (robin boundary conditions)

∂ – partial derivative

Abbreviations

AVDC – Average Voxel Distance Calculator

CFD – Computational Fluid Dynamics

CPRR – Centre for Postharvest and Refrigeration Research

CT – Computed Tomography

DEM – Discrete Element Modelling

DNS – Direct Numerical Simulation

FUTC – Fractional Unaccomplished Temperature Change

HCT – Half-Cooling Time, h

OECT – One Eighths Cooling Time, h

SECT – Seven Eighths Cooling Time, h

SN – Skew-Normal

VSD – Variable Speed Drive

Chapter 1

Introduction and Literature Review

1.1: Background and Context

The value of the New Zealand horticultural sector exceeded NZ $8B in 2016, with over 60% coming from exports to foreign markets (Aitken and Hewett, 2016). Considering that fresh horticultural products are perishable, these volumes are particularly impressive as New Zealand is an island nation, thousands of kilometres from the nearest international port, a distance representing weeks or months of travel time by sea. Despite the obstacles, New Zealand maintains a reputation for exporting some of the highest quality fresh produce in the world (Coriolis and New Zealand Ministry of Business, Innovation and Employment, 2017), which is accomplished through advances and innovations in packaging and refrigeration technology (Han, 2014; Carson and East, 2017). A key process that allows the quality of horticultural products to be maintained as it moves through the supply chain is pre-cooling. This is a specialised cooling operation designed to quickly and efficiently remove the field heat from a product immediately after harvest, which can have significant shelf-life and quality benefits over longer time cooling processes (ASHRAE, 2010; Boyette *et al.*, 1989; Boyette *et al.*, 1990; Fraser, 1998). The most common pre-cooling process is forced-air cooling, where fans are used to create a pressure drop through a stacked pallet of produce, forcing refrigerated air through the packaging structure to exchange heat with the product inside (de Castro *et al.*, 2004; Zou *et al.*, 2006a). There is a synergy between the package design and the performance of a forced-air cooling process. Package ventilation can change the airflow pattern through the pallet, impacting the cooling rate and level of temperature uniformity. For the New Zealand horticultural industry to continue to grow, the performance of the forced-air cooling process must be optimised through package optimisation.

In industry and academia there has been a focus on package design testing. Either through experimental or computational means, the performance of a given package design is thoroughly tested (for example, Ferrua and Singh, 2009a). Innovative designs can be imagined and tested, but each new design is an isolated invention. In other words, most packaging design testing is focussed around evaluating the performance of a package and it is difficult to draw conclusions that can be usefully used to design the next package. This is because there is currently a lack of detailed understanding of how the various design elements of package design (package size, package shape, vent size, vent number, vent shape and vent position) combine to cool the product inside the stacked containers. This trial-and-error approach to package design is restrictive to innovation – fabricating newly imagined packages and filling them with fruit for experimental cooling trials can represent a large material cost, and the time during which experiments can be performed is limited to when the fruit is in season (Redding *et al.,* 2016). A detailed mathematical model can also take several years to fully develop and validate, but as noted have so far been largely 'case specific' with little cross applicability to other products or package designs (Zou *et al.,* 2006a). Intensive computational resources and a considerable amount of computational time is also often required to solve the model (Ferrua and Singh, 2009c; Defraeye *et al.,* 2014). Thus, there is little practical, systematic capability to design a package for a specific function; or to use the performance of one package design to inform the design of the next. It would therefore be beneficial to the New Zealand horticulture industry and academia to have a methodology or suite of methodologies that would inform the performance of a particular package design system. It is proposed that these methods are based upon mathematical modelling, with a focus on flexibility – so that many different types of packages and products can be investigated – and computational efficiency – so that the model can be integrated into an optimisation procedure. This will allow rapid iteration toward an optimised design that satisfies a particular function. It is the goal of this thesis to develop such a model.

While the goal is to develop a flexible modelling methodology that can be applied to any horticultural product in a wide variety of palletised packaging systems, the primary context of this thesis project is the New Zealand kiwifruit industry. Kiwifruit represents the largest New Zealand fresh horticultural export at NZD $1.7B in 2016 (Aitken and Hewett, 2016), with an intention to grow to NZD $4.5B by 2025 (Zespri® International, 2017). This project therefore is focused on the forced-air cooling of count 36 Hayward Green kiwifruit (*Actinidia deliciosa*) – count 36 is a weight based grading category –

packaged into 'modular bulk' packages containing approximately 102 kiwifruits, totalling 10.3 kg per box. The fruit within the box is wrapped in a polyliner, a thin plastic bag designed to retain saleable moisture weight and prevent shrivelling. The model should be developed so that it can be applied to other systems with minimal additions. Other systems include static cooling and cooling without a polyliner, and variations in fruit size, shape, and other properties. However, the model may not be validated or developed in detail outside of the primary context.

This project was funded by the New Zealand Ministry of Business, Innovation and Employment (MBIE) with important stakeholder industrial partners including Zespri® International and OJI Fibre Solutions (Fibreboard Packaging Design Project (MAUX1302)). This project is part of a bigger, multi-PhD project at Massey University, with multiple researchers investigating both the mechanical strength properties and cooling implications of fibreboard package design.

1.2: Literature Review

1.2.1: New Zealand Export Industry

New Zealand is dependent on international markets as a major source of commerce and trade. Total exports in the year 2016 (ending in March) were over NZD $70B, an increase of over 450% since 1990 (Statistics NZ, 2017a). Perishable food products represented a large proportion of the total export earnings, with NZD $11.2B in dairy, NZD $5B in horticultural produce and NZD $6.6B in meat exports (Statistics NZ, 2017a). The magnitude of wealth generated from the New Zealand agricultural sector would not be possible without advances in packaging and mechanised refrigeration technologies that preserve the quality of perishables as they are transported incredible distances to foreign consumers (Han, 2014) – see Figure 1.1 for a breakdown of export destinations by value. It has even been suggested that without these innovations, New Zealand may have become part of Australia (Carson and East, 2017). For the New Zealand export market to continue to grow, it must continue to innovate in the areas of package design and refrigeration.

The term 'supply chain' is used when describing a transport system that moves a product from the supplier to the customer (Fahimnia *et al.*, 2015). Easily perishable products, such as fresh horticultural produce, require a more sophisticated system to ensure quality is preserved while in transit. Placing a strong emphasis on the prevention of damage to the product, steps are taken to mitigate mechanical damage through the use of packaging, as well as biological damage through the use of refrigeration (Restuccia *et al.,* 2010). When a supply chain incorporates temperature control it is instead known as the 'cold chain'. The cold chain implies a supply chain that consists of a series of unbroken storage and transportation stages that all maintain the same low temperature and atmospheric conditions (Hundy *et al*., 2008). An estimated 60% of all New Zealand food exports are shipped in a refrigerated state (Carson and East, 2017).

In general, the horticultural export cold-chain can be summarised as the following series of processing and handling stages: Farm → Harvest → Pre-Cooling → Export → Consumer (Carson and East, 2017; Bachmann and Earles, 2000). The fruits and vegetables produced during the Farm stage are picked, sorted and packaged in the Harvest stage (Mitchell, 1987; Pathare and Opara, 2014). The Pre-Cooling stage is the first 'cold' stage of the horticultural cold chain, and is where the product temperature is rapidly reduced, in bulk, from the field temperature (in New Zealand, usually around 20-30°C, depending on local conditions) to the storage temperature (or near to; usually between 0-5°C, depending on the specific product; Fraser, 1998).

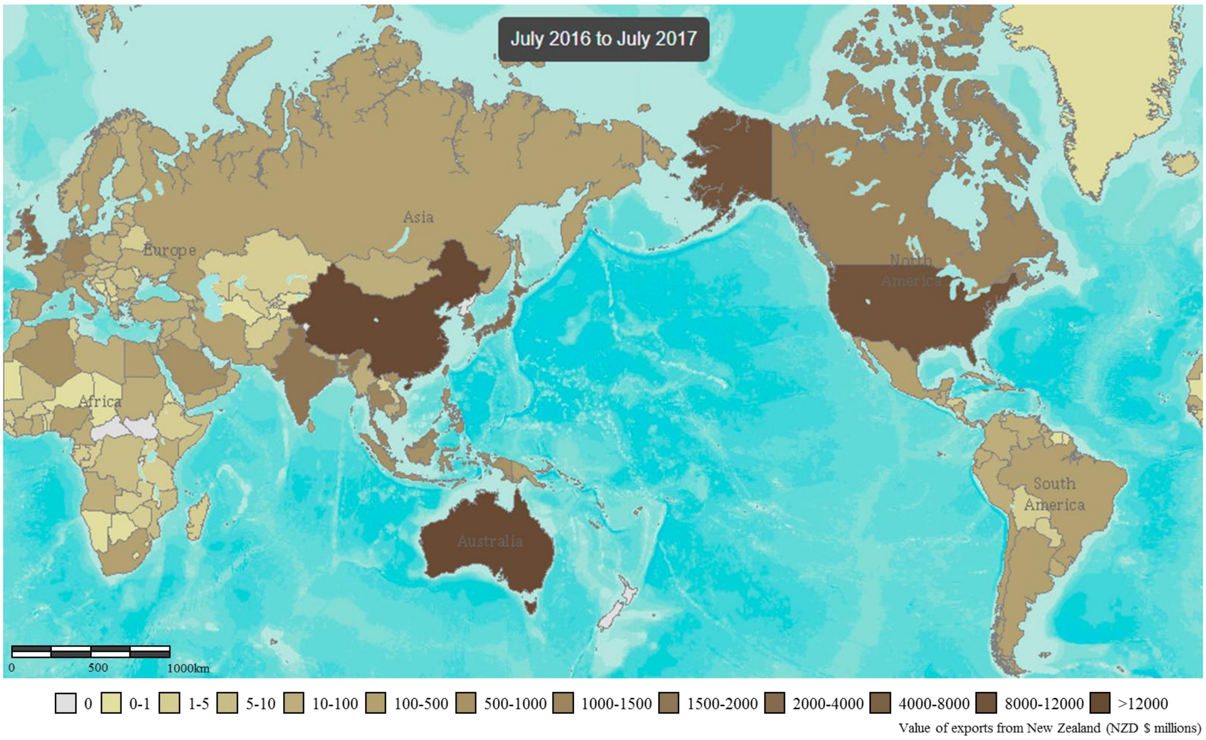

Figure 1.1: Exports from New Zealand to international markets over 2016-2017. Colours represent export values in NZD $ millions. This work is based on/includes Statistics NZ (2017b) data, which are licensed by Statistics NZ for re-use under the Creative Commons Attribution 4.0 International licence.

If the cold chain is properly designed and operated, the product will then remain at the storage temperature for the remainder of its journey, with the Export stage including all storage and transport stages that deliver product from New Zealand to foreign shelves – this may include long-term refrigerated storage (weeks or months), refrigerated transport within New Zealand to port or staging areas, refrigerated shipment via sea-faring vessels (reefer or container ships) or refrigerated air freight, foreign refrigerated distribution centres and associated refrigerated transport (trucks or vans or rail), with the product ultimately delivered to a retail outlet and the Consumer (based on Carson and East, 2017). Once at a foreign supermarket, the Consumer is able to purchase the New Zealand product, which has retained much of its original quality despite thousands of kilometres and weeks of transit time (see Figure 1.1).

Horticultural products are living organisms with ongoing metabolic processes and begin to deteriorate after they have been harvested through the senescence process (Sargent *et al*., 2007). Although it is impossible to halt senescence entirely, it can be significantly decelerated by removing the field heat, the heat energy stored in the product at the time of harvest (Boyette *et al*., 1989). For example, apples degrade twice as fast at 4°C as at 0°C, and six times as fast at 15°C (Boyette *et al*., 1989). Minimizing senescence maintains the quality of the product during transport, and improves the shelf life significantly. In apples, a one-hour delay in the removal of the field heat can reportedly reduce the shelf life by one day (Fraser, 1998). It is therefore vital to reduce the temperature of the perishable product to its storage temperature as soon as possible after it is harvested.

The portable refrigeration systems on vehicles during the export stage – such as shipping containers and trucks – are not large enough to lower the temperature of their cargo; instead, they are only sufficient for temperature maintenance (Tassou *et al.,* 2009). Similarly, long term refrigerated storage centres would need to have much larger and more expensive refrigeration units if product were entering this stage significantly above the storage temperature (Boyette *et al.*, 1989). By incorporating a dedicated unit operation specifically designed for rapid temperature reduction, the remainder of the cold chain can be significantly reduced in size and energy usage (Boyette *et al.*, 1989). Concentrating capital and operational expenses into this single stage means that small improvements in pre-cooling performance has a large benefit to the cold chain as a whole: reductions in cooling time mean a higher overall throughput; and reductions in fan-power and refrigeration energy usage can translate into large savings in operational expenses as pre-cooling is the most energy intensive stage of the cold chain (James and James, 2010).

1.2.2: Pre-Cooling Operations

Available precooling methods include room cooling, forced-air cooling, vacuum cooling and hydro-cooling (Pathare *et al.*, 2012):

1.2.2.1: Room Cooling

The simplest pre-cooling set up is room or static cooling. Pallets of ambient temperature produce are placed into a refrigerated room, and ceiling fans next to the evaporator circulate cold air throughout the space, facilitating convective energy transfer from the surface of each pallet (Figure 1.2). Ambient temperatures during the New Zealand picking season are approximately 20-30 ºC depending on location, and the refrigeration temperature is approximately 0-2 ºC (ASHRAE, 2010).

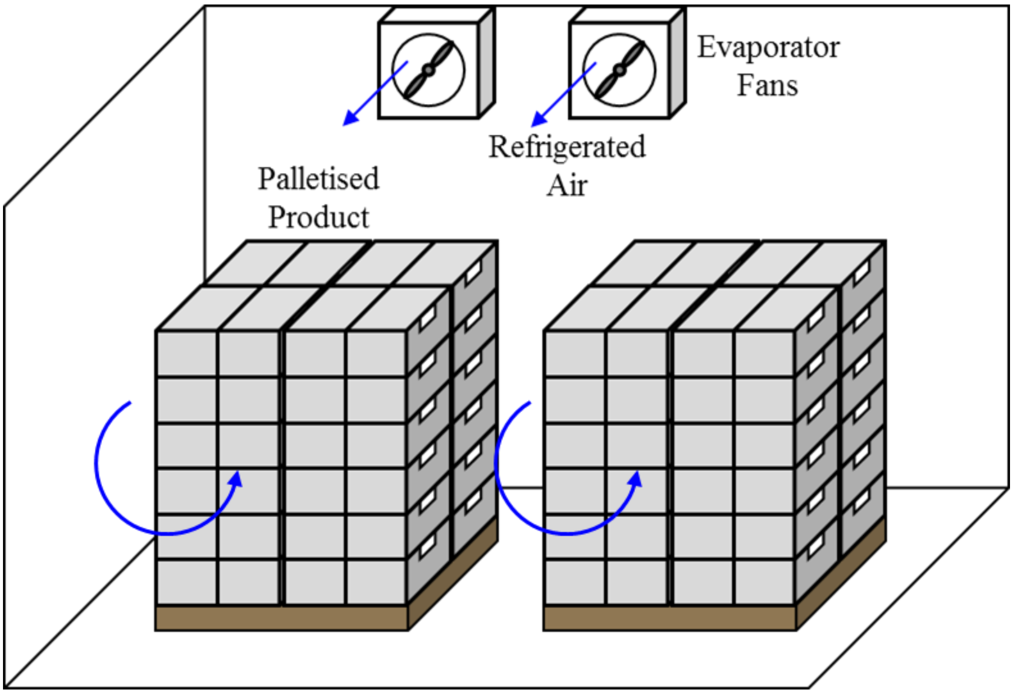

Figure 1.2: Static or room cooler for horticultural produce. Evaporator fans circulate refrigerated air around the room.

Room cooling pre-coolers are nearly identical to a cold storage room, however they have a larger refrigeration unit as the energy requirement of removing heat is much greater than temperature maintenance (Boyette *et al.*, 1989). Sometimes storage rooms are used as room pre-coolers. This means that the refrigeration plant must be designed for the much larger heat flows during pre-cooling, and may run very inefficiently during the long storage periods. In room cooling, pallets should be properly spaced to allow maximum air circulation (Fraser, 1998). Although this method requires the minimum amount of handling, labour and electrical cost, it is also the slowest pre-cooling method, taking days or weeks for product to reach the refrigeration storage temperature. This is because of the slow, limiting rate of heat transfer via conduction from the fruit in the centre of the pallet. The long-time translates into a higher degree of fruit degradation, shortened shelf-life and reduced throughput (therefore a larger physical facility size to accommodate a high throughput). Room cooling is too slow for many horticultural products, and is best suited for products with low respirations rates such as potatoes, cured sweet potatoes and dried onions (Sargent *et al.*, 2007).

1.2.2.2: Forced-Air Cooling

The most common pre-cooling process is forced-air cooling (de Castro *et al.*, 2004, Zou *et al.*, 2006a). A forced-air cooling operation induces a pressure drop across a pallet of produce, pulling cold air from the refrigerated room through the package ventilation and directly over the product (Fraser, 1998). A common forced-air cooling set up is a tunnel cooler (Figure 1.3), where two rows of palletised product are sealed using a tarpaulin, and a fan is used to pull air from the recess, dropping the pressure on one side of each pallet (Boyette *et al.*, 1989). Another system usually used for relatively low volume products has individual pallets placed in small refrigeration chambers where cold air is directly blown through the pallet.

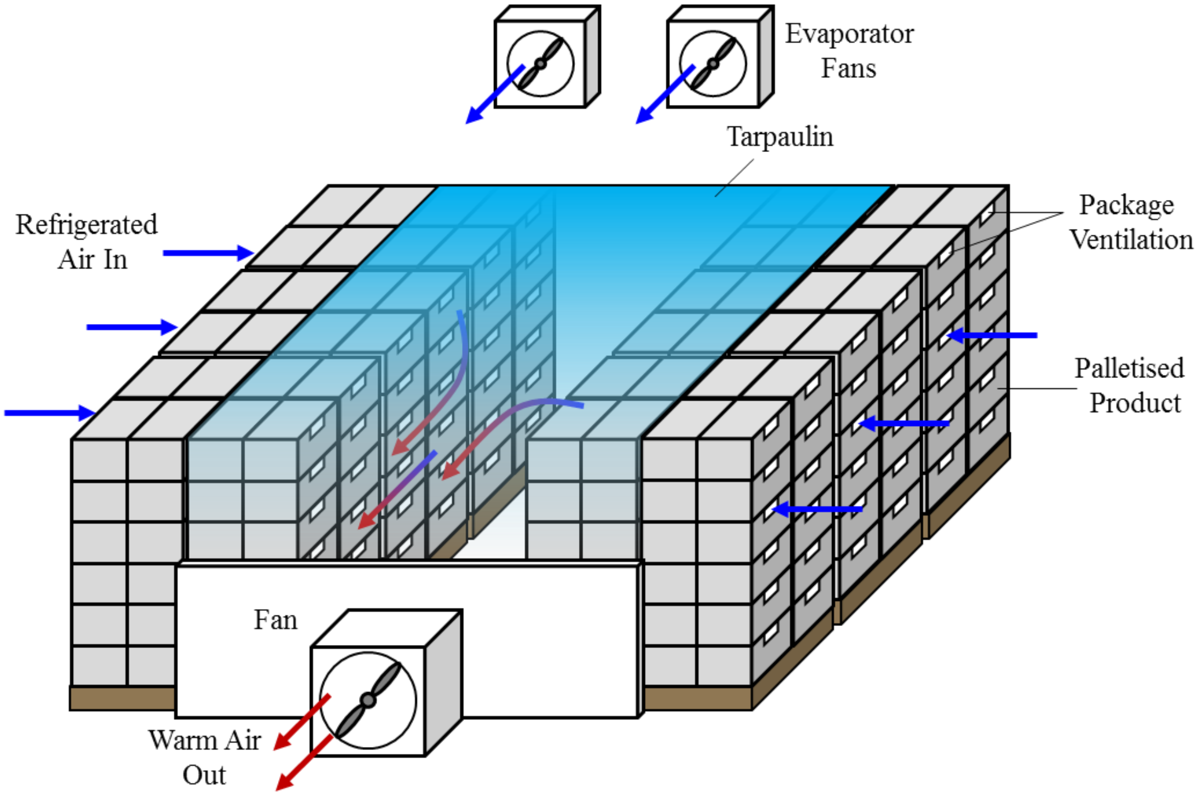

Figure 1.3: A tunnel cooler, a common forced-air cooling device. Pallets of horticultural produce are stacked into two rows and covered with a tarpaulin, where a fan is used to create a vacuum in the cavity to draw refrigerated air through the ventilation in the palletised produce, facilitating cooling. Pallet length is illustrative – real systems are typically 10 or more pallets long.

Forcing air through the pallet structure accelerates the airflow rates and facilitates the penetration of cold air into the centre of the pallet – this means the cooling rate is accelerated and more uniform when compared with room cooling (Pathare *et al.*, 2012). Volumetric air flowrates are suggested to be in the range of 0.5–1.5 $L \cdot kg\ product^{-1} \cdot s^{-1}$ (Fraser, 1998). The convective heat transfer coefficient is much larger than in room cooling because of the higher airflow speeds and the higher surface area available for heat transfer because refrigerated air flows directly over the fruit. Bennett *et al.* (1996) calculated a surface heat transfer coefficient of 62 $W \cdot m^{-2} \cdot K^{-1}$ for Hamlin oranges at a 1.7 $m \cdot s^{-1}$ superficial velocity, compared with just 8.5 $W \cdot m^{-2} \cdot K^{-1}$ for room cooling (Baird and Gaffney, 1976).

Boyette *et al.* (1995) stated that forced-air cooling process, when compared to the room cooling, is advantageous in the following ways: it decreases the time produce remains at elevated temperatures, thereby reducing deterioration and improving shelf life; shorter cooling times mean a more efficient use of the cooling facility; it is capable of effectively cooling a variety of container types without wetting the packaging or product, or subjecting it to excessive handling; it is often more energy efficient than room cooling when large volumes of product must be cooled; and an available room cooling or refrigerated storage room can be converted into a forced-air cooling operation with only a relatively small investment in fans (if the refrigeration capacity of the room is high enough). Incorporating a forced-air cooling process into an operation can reduce the cold storage facility size by one-quarter to one-third because of the significantly shorter cooling times (ASHRAE, 2010).

Forced-air cooling can result in a higher rate of mass transfer (i.e. moisture) away from the product than room cooling (Becker *et al.*, 1996). Loss of moisture can result in wilting and accelerated deterioration (Watada *et al.*, 1996), may cause shrivelling which makes the product unappealing to consumers (Burdon *et al.*, 2014), and can reduce the saleable weight of the product (Singh and Heldman, 2009). However, due to the short-times spent in the forced-air cooler the total amount of moisture loss is usually slight (even if the rate was high). Actions to reduce moisture loss are therefore more important during long-term storage (the low rate, but long time, accumulates to a large total moisture loss). During long term storage humidity control is an important method for preventing moisture loss, where the refrigerated room is held at a high humidity of 80-95% to lower the concentration gradient between the product and the air (Crisosto *et al.*, 2012; Hundy *et al.*, 2008). However, the capital cost of a storage room designed to maintain high humidity can be expensive, so an alternative option is to wrap the product in an impermeable barrier to prevent moisture from escaping the package, by maintaining a high local relative humidity. In the case of kiwifruit in New Zealand, kiwifruit is commonly wrapped in a polyliner (O'Sullivan *et al.,* 2016). However, the presence of the polyliner changes the airflow pattern significantly and prevents direct interaction with the fruit. Therefore, if the polyliner (added to reduce moisture loss during long-term storage) is present during the pre-cooling process it will reduce the cooling rate and levels of temperature uniformity.

1.2.2.3: Other Pre-Cooling Operations

A less common pre-cooling operation is hydro-cooling. This process involves either submerging or spraying the product with chilled water (Bachmann and Earles, 2000; Sargent *et al.,* 2007; Boyette *et al*, 1990). Outside the horticulture industry this is sometimes known as immersion cooling and cold brines, or cryogenic fluids (liquid N_2, for example) can be used instead of chilled water. Hydro-cooling brings product to storage temperature more rapidly than forced-air cooling because the heat transfer coefficient into water is much greater than for air. The external rate of heat transfer being very large, the main factor impacting the performance of hydro-cooling is the size of the fruit: Stewart and Lipton (1960) showed cooling times were 20 and 10 minutes for size 36 and 45 melons, respectively. Hydro-cooling also prevents moisture loss, and in some cases can even rehydrate a slightly shrivelled product (Hardenburg *et al.,* 1990). Packaging must be either wood or plastic, or wax-dipped fibreboard, to ensure the package survives submersion in water (Hardenburg *et al.,* 1990). Products that are easily susceptible to chilling injury cannot be hydro-cooled, as well as products that cannot tolerate total submersion (Bachmann and Earles, 2000), some products may also be more susceptible to rots following hydro-cooling. Hydro-cooling can be expensive if the chilled water is not recirculated; and if recirculation is employed, the water must be treated with anti-bacterial chemicals to prevent pathogens from spreading. The rapid cooling rates and spread of pathogens makes hydro-cooling unsuitable for kiwifruit, as they are particularly susceptible to chilling injury (Zhao *et al.,* 2014).

Another pre-cooling operation is vacuum cooling. Vacuum cooling operates by placing a batch of produce within an air tight chamber which is then evacuated to lower the pressure to near vacuum. This decreases the evaporation temperature of the free water within the product, which in turn then evaporates. This phase change requires energy, which is taken from the heat energy contained in the fruit (McDonald and Sun, 2000, Everington, 1993). Vacuum cooling is ideal for products that have a high surface area to mass ratio, and have a robust internal structure so that the inevitable moisture loss does not result in wilting. The extreme moisture loss rules out many products – including kiwifruit, which are so sensitive to shrivelling that they are exported in a polyliner bag (O'Sullivan *et al.*, 2016) – beyond leafy vegetables, such as lettuce, or mushrooms (McDonald and Sun, 2000).

1.2.3: Package Design

Research on fibreboard packaging is focused primarily on its mechanical properties (Ferrua and Singh, 2009a). While package strength is vital to the proper functioning of the cold chain – protecting fruit from mechanical damage from the external environment and allowing large scale transportation of product through stable palletisation (Sargent *et al.*, 2007) – this focus neglects the airflow and cooling considerations that package ventilation has on the performance of a forced-air cooling operation. Proper ventilation is needed to allow a sufficient amount of cooling air to penetrate the packaging to remove heat from the product; and size of vents, vent shape, vent number and the orientation of individual packages in the pallet combine to form a unique airflow pattern that can significantly affect the rate of cooling or the uniformity of cooling (Defraeye *et al.*, 2013; Pathare *et al.*, 2012; Dehghannya *et al.*, 2011).

1.2.3.1: Definition of Cooling Performance

The average cooling rate is an important metric for determining the performance of a pre-cooling process. Cooling trials may be conducted at a variety of locations and times, and at a variety of refrigeration conditions. For two or more packaging systems to be compared fairly, the cooling rate must be given in a form that is independent of such variation. The Fractional Unaccomplished Temperature Change Y, or FUTC, is an appropriate dimensionless temperature:

$$Y_t = \frac{T_t - T_{ref}}{T_i - T_{ref}} \tag{1.1}$$

Where T is the temperature of the product at time t; T_{ref} is the refrigeration temperature; and T_i is the initial temperature (field temperature) of the product (Brosnan and Sun, 2001). At $t = 0, T = T_i$ so that $Y = 1$. As $t \rightarrow \infty$, the product will begin to approach the storage temperature: $T = T_{ref}$ so that $Y = 0$. Therefore Y is a fractional value between 1 and 0. Using the FUTC allows the cooling rate of different package designs or operational settings to be compared. For example, the average half-cooling time or seven-eighths cooling time occurs when $Y = 0.5$ and $Y = 0.125$, respectively.

In addition to the average cooling rate, the performance of a pre-cooling process is also determined by the uniformity of cooling. Due to the complex air-flow patterns throughout the pallet, the cooling rate varies spatially. This is an important consideration because different cooling rates means fruit from the same box or pallet will experience different degrees of degradation through senescence or chilling injury, and therefore will have different shelf lives and qualities at the end of the cold chain (Alvarez and Flick, 1999a; Alvarez and Flick, 1999b). Dehghannya *et al.* (2011) reports Eq. 1.2 as a heterogeneity index:

$$HI = \frac{\sqrt{\left(T_p - \overline{T_p}\right)^2}}{\overline{T_p}} \times 100 \tag{1.2}$$

Where T_p is the instantaneous temperature of an individual product; and $\overline{T_p}$ is the average temperature of all recorded product temperatures. However, this heterogeneity index has some significant shortcomings which make it unsuitable for use in some important scenarios: such as being unable to describe the heterogeneity of the entire system (it is only point specific); eliminating information concerning whether a temperature position is hotter or colder than the average; is not mathematically robust to changes in temperature units (such as using Kelvin rather than degrees Celsius gives a different value of HI); and is not applicable to systems where the refrigeration temperature is near 0°C (typical in horticultural product cooling), as the average temperature of the product also approaches 0°C and the heterogeneity index approaches infinity. It would be beneficial for a new heterogeneity index to be developed that addresses these significant shortcomings.

1.2.3.2: Vent Size

Vents must be sufficiently large to allow enough cold air into the packaging structure. However, as a ‘vent’ is essentially a hole in the packaging, larger vents mean less packaging material to bear the load, weakening the box. Therefore, the mechanical strength considerations of a package design are in direct conflict with the ventilation considerations (de Castro *et al.*, 2005). Optimising a package with only strength considerations in mind would result in a package with no vents; and optimising considering only cooling would result in a box with no packaging. Fortunately, a trade-off between the two can be reached: many studies have shown that the relationship between vent size and the cooling rate is diminishing, and that after a critical total opening area (TOA) there is no improvement from a cooling perspective ventilation (Ferrua and Singh, 2009c; de Castro *et al.,* 2005; Figure 1.4).

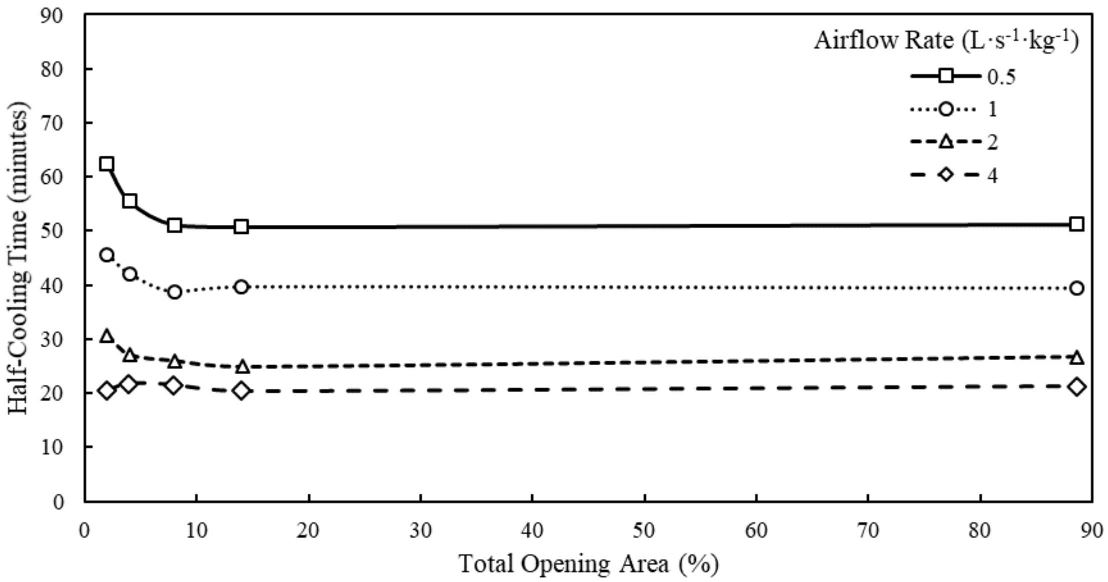

Figure 1.4: Half-cooling time vs opening vent ratio. As the vent ratio increases the half-cooling time improves at a diminishing rate. Figure based on de Castro et al., 2005.

The precise mechanisms for why there is an upper limit are not well understood, but the following explanations have been given: although a larger amount of air passes through the system at higher vent openings, a high percentage bypasses the product and does not contribute to the cooling performance (Ferrua and Singh, 2009c; de Castro *et al.,* 2005). Another possible explanation is the maintenance of the temperature gradient. With larger vent area openings, the air that does *not* bypass is warmed as it exchanges heat with the fruit. Warmer air then interacts with fruit at the back of the box or pallet, maintaining the same or similar temperature gradient between the air and fruit, so there is no increased rate of energy transfer (Ferrua and Singh, 2009 c).

Package designers should identify the critical TOA and ensure the vent opening is below this number, otherwise the package strength will be needlessly compromised by excess vents. There is no consensus for what the critical TOA is: de Castro *et al.* (2005; Figure 1.4) showed a maximum TOA of ~9%, however Pathare *et al.* (2012) compiled a list of recommended opening areas from a variety of published studies and found TOA suggestions ranging from 2.5% for peaches to 27% for Shamouti Oranges. It would seem that the maximum TOA is case specific and may change for different products, product geometry, package types and packaging features. Having a flexible model that is easily amended to new systems could be a useful tool for quickly determining the critical TOA.

1.2.3.3: Vent Number

In addition to the size of vents, the number of vents also plays a significant role in the performance of pre-cooling. Spreading the total opening area across several holes may result in a more evenly distributed airflow pattern, which could result in a more uniform cooling profile. de Castro *et al.* (2004) investigated a wide variety of vent sizes and numbers, using a ball matrix as a produce simulator. It was found that the number of vents in the X direction (and interestingly, *not* the Y direction) had a significant impact on the cooling rate and profile; with Stepwise Forward-Backward Regression being used to determine that X direction vent number explains 1.5% of the HCT variation (compared to <0.1% for Y direction vent number). Dehghannya *et al.* (2011) simulated the effects of different vent numbers on a 2-D ball matrix, reporting an HI of 0.62 for one vent, compared to just 0.06 (i.e. less variation) for 5 vents, at 180 minutes of cooling (Eq. 1.2)

These studies show that the vent number plays a significant role in pre-cooling performance. However, it is important to note that in these studies, more vent holes also represented a higher total opening area – for example, in Dehghannya *et al.* (2011) one vent represented 2.4% TOA, while 5 vents represented

12.1% TOA. Because vent number and total opening area have not been de-coupled in these studies, it cannot be confidently concluded that the improvement in cooling rate and uniformity is due to the increase in vent number or the increase in total vent area. To truly investigate vent number as an optimisation parameter, the performance must be determined using the same total opening area spread over a different number of vents.

1.2.3.4: Vent Shape

Martines-Hermosilla *et al*. (2016) showed that vents of the same TOA but had different shapes had an impact on the compression strength of a package, however the effect of vent shape from a cooling perspective has so far been largely ignored (Pathare *et al*., 2012). As shown in studies of orifice plates, the shape of the exit opening can significantly affect the airflow pattern, and therefore distribution of air (El-Hassan *et al*., 2011; Mangate and Chaudhari, 2015). Defraeye *et al.* (2014) changed the vent shape from circular to semi-circular, which showed a significant effect on the performance of the CFD model developed. However, in this study, the total number of vents was increased from 2 to 6; and was moved from having two vents at the centre of the package to 3 vents at the top and 3 vents on the bottom. The changes observed could be due to vent number and position change, and total vent opening area, rather than the new shape. Delele *et al*. (2013) investigated a number of vent shapes using CFD, reporting that vent shape in CFD predictions has a minimal effect on cooling performance.

1.2.3.5: Package Orientation

In the majority of practical scenarios, pre-cooling is carried out on the pallet scale, where individual packages are stacked next to and on top of each other to form a larger structure. The performance of the system will depend on the way that the pallet is constructed; namely, the orientation of individual packages and how vent position and package shape interacts between individual packages. When the pre-cooler consists of multiple stacked pallets, how the pallets are stacked next to each other may also have a large impact on the air flow. Improperly designed packaging and poorly stacked pallets can lead to air short-circuiting, where the cooling air passes through the system without interacting with the product (Ferrua and Singh, 2009c). Packages are designed to be flush with each other when combined into a pallet so that the void space for bypass air is minimised (Fraser, 1998).

Although individual packages have the same dimensions, there is a multitude of ways that they can be combined to form a pallet. For example, Zespri® Modular Bulk and Modular Loose kiwifruit pallets can be assembled in two orientations, shown in Figure 1.5. The performance of orientation Figure 1.5b versus Figure 1.5c is dependent on where vents are positioned. Sargent *et al.* (2007) suggested a vent configuration of Figure 1.6 that connects vents between packages in a maximum number of ways. This could promote a more even airflow distribution and may promote faster and more uniform cooling. Alternatively, the pallets could be cooled from a different direction, as was done by O'Sullivan *et al.* (2013). O'Sullivan reported a significant increase in the cooling rate when airflow entered the 1.2 m side, compared with the 1.0 m side.

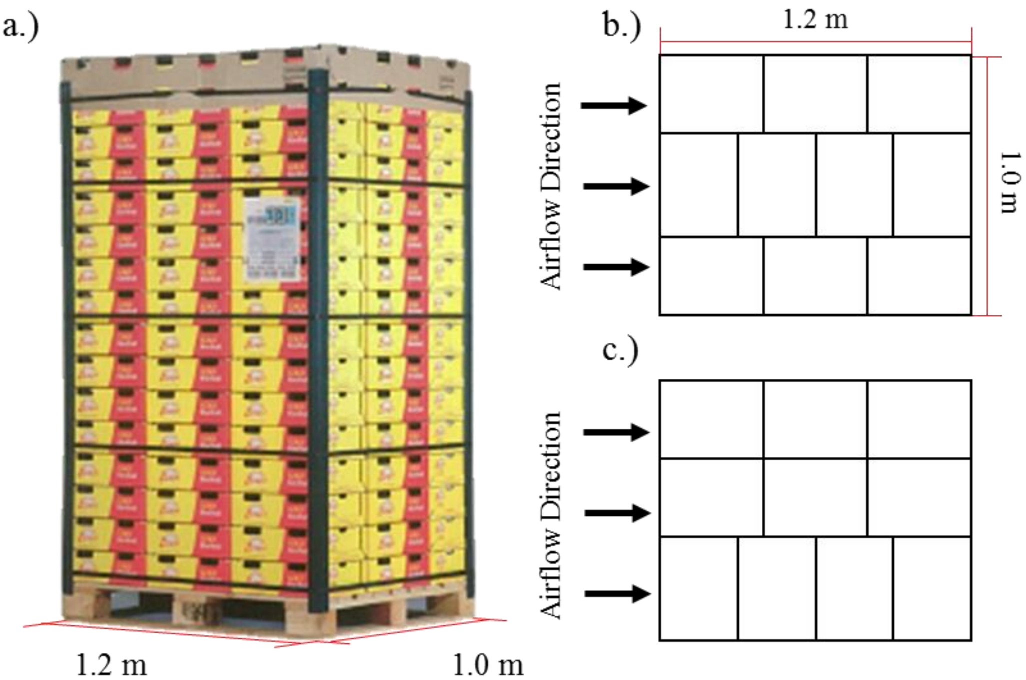

Figure 1.5: Zespri® Modular Loose pallet configurations for international export: 10 packages per layer with a pallet base of 1.2m × 1m, orientated with a 4 box row and two 3 box rows, with either a.) the 4 box row to the side or b.) in the middle.

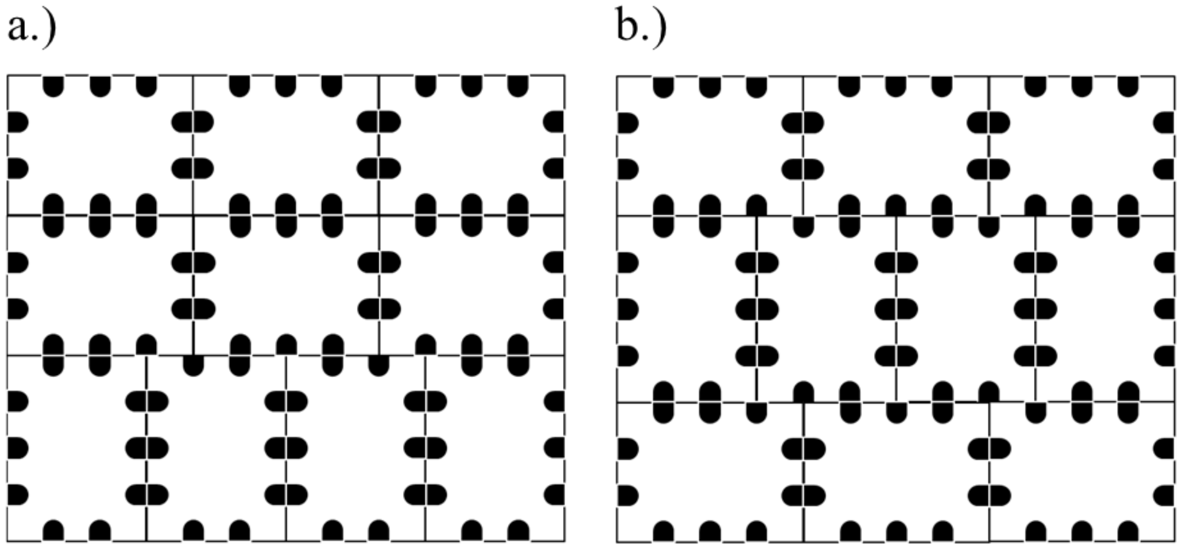

Figure 1.6: An example based on Sargent et al. (2007) of improved vent placement. This vent and pallet orientation allows for the maximum number of interactions between individual packages as air flows through the pallet structure as a whole.

1.2.4: Heat and Mass Transfer Mechanisms

Modelling and optimising the forced-air cooling process will require an understanding of the heat, mass and momentum transfer mechanisms involved, as well as their relative significance to the overall performance of the process.

Four mechanisms have been identified from the literature as important (Holman 2010; Tanner *et al.*, 2002b):

- Conduction;
- Convection;
- Radiation, and;
- Evaporation.

1.2.4.1: Conduction Heat Transfer

Conduction is the transfer of thermal energy from a high temperature region to a low temperature region via molecular motion. Conduction occurs with no physical movement of the object, and as a consequence, heat transfer via conduction can only occur within a material, or between two objects that are in direct contact with each other (Holman, 2010). Fourier's equation for conductive heat transfer is:

$$\phi_{cond} = \lambda \cdot A \cdot \frac{\Delta T}{x} \tag{1.3}$$

Where ϕ_{cond} is the rate of conductive heat transfer (W), λ is the thermal conductivity of the material ($W \cdot m^{-1} \cdot K^{-1}$), A is the heat transfer surface area (m^2), ΔT is the temperature gradient (ºC) and x is the distance (m). Conduction will play a very important role in the overall heat transfer model that is to be developed, because it is the common mode of heat transfer within opaque solids, such as food (Singh and Heldman, 2009). The heat transferred to the surface from inside the product will primarily be due to conduction. It can also contribute to the external rate of heat transfer between two touching products, or if the product is touching the packaging wall.

1.2.4.2: Convection Heat Transfer

Heat transfer via convection involves the exchange of heat between the surface of an object and a moving fluid (air in this case). The fluid will be in motion because of natural convection – pressure gradients created by temperature differences in the fluid – or because of forced convection, caused by an artificially induced pressure drop. Ideally, during the forced-air cooling process, forced-convection will be dominant over natural convection, and in some cases natural convection can be ignored (Norton and Sun, 2006). However, with systems that have a polyliner and no direct contact between fruit and air, this may not be the case (O'Sullivan *et al.,* 2013).

The magnitude of the rate of heat convection from a surface depends on the physical properties of the air, the velocity of the air, and the geometry of the surface. These considerations can be collated into a more practical proportionality constant, the convective heat transfer coefficient, h ($W \cdot m^{-2} \cdot K^{-1}$). Newton's equation for convective heat transfer is:

$$\phi_{conv} = h \cdot A \cdot \Delta T \tag{1.4}$$

Where ϕ_{conv} is the rate of convective heat transfer (W). The heat transfer coefficient is correlated to the fluid velocity and geometry through the use of dimensionless correlations. For example, a typical correlation is that of Pohlhausen (Kakaç *et al.*, 2014):

$$\mathrm{Nu} = a \cdot \mathrm{Pr}^{b} \cdot \mathrm{Re}^{c} \tag{1.5}$$

Where Nu is the Nusselt number:

$$\mathrm{Nu} = \frac{h \cdot L}{\lambda_A} \tag{1.6}$$

Where h is the convective heat transfer coefficient ($\mathrm{W \cdot m^{-2} \cdot K^{-1}}$); L is the characteristic length of the system (m); and λ_A is the thermal conductivity of the fluid ($\mathrm{W \cdot m^{-1} \cdot K^{-1}}$). Pr is the Prandlt number:

$$Pr = \frac{\upsilon}{\kappa} \tag{1.7}$$

Where υ is the kinematic viscosity ($\mathrm{m^2 \cdot s^{-1}}$); and κ is the thermal diffusivity of the fluid ($\mathrm{m^2 \cdot s^{-1}}$). Re is the Reynolds number:

$$\mathrm{Re} = \frac{\rho_A \cdot v \cdot L}{\mu} \tag{1.8}$$

Where ρ_A is the density of the fluid ($\mathrm{kg \cdot m^{-3}}$), v is the velocity of the fluid ($\mathrm{m \cdot s^{-1}}$), L is the characteristic dimension (m); and μ is the viscosity of the fluid (Pa·s). a b and c are empirical constants that apply to a particular system.

Convection is reported to be the most significant mode of heat transfer for the forced-air cooling process (Defraeye *et al.*, 2014; Ferrua and Singh, 2009c; O'Sullivan *et al.*, 2016) and is highly dependent on the airflow distribution, which in turn is impacted by package ventilation (Dehghannya *et al.*, 2011).

1.2.4.3: Mass Transfer and Evaporative Heat Transfer

Perishable products have a high water content, therefore when undergoing pre-cooling or transport, can lose water to atmosphere. This can cause the product to shrivel, promotes degradation, and ultimately means less product to sell at the end of the supply chain (Watada *et al*., 1996). Mass transfer is analogous to heat transfer in the sense that there are internal and external modes, but is instead driven by concentration gradients, rather than gradients in temperature (Singh and Heldman, 2009). Because of the analogy, many of the equations pertaining to heat transfer apply to mass transfer. For example, the Schmidt number, Sc, is the mass transfer equivalent to the Prandtl number:

$$\mathrm{Sc} = \frac{\mu}{\rho_a K} \tag{1.9}$$

Where K is the permeability ($m^2 \cdot s^{-1}$). The Sherwood number, Sh, is the mass transfer analogy to the Nusselt number:

$$\mathrm{Sh} = \frac{D \cdot L}{K} \tag{1.10}$$

Where D is the permeance ($m \cdot s^{-1}$).

Like convection, they are related to each other through the Reynolds number, such as in the case of convective mass transfer from a bulk of spherical fruits or vegetables (Becker and Frike, 1996):

$$\mathrm{Sh} = 2.0 + 0.552 \cdot \mathrm{Re}^{0.53} \cdot \mathrm{Sc}^{0.33} \tag{1.11}$$

Heat is also lost when mass transfer occurs because the water changes phase:

$$\phi_{evap} = \dot{m} \cdot L_{vap} \tag{1.12}$$

Where ϕ_{evap} is the rate of evaporative heat transfer (W), L_{vap} is the latent heat of vaporisation, $kJ \cdot kg^{-1}$, and $\dot{m}$ is the mass transfer rate of water ($kg \cdot s^{-1}$). The latent heat of vaporisation for water at atmospheric pressure is 2260 $kJ \cdot kg^{-1}$ (data from Serway and Jewett, 2013).

1.2.4.4: Radiation Heat Transfer

All objects above absolute zero spontaneously emit electromagnetic waves and absorb electromagnetic radiation emitted by other objects, representing an exchange of energy. The rate of emission depends on the absolute temperature difference of the objects, meaning that two spatially separated surfaces can exchange energy though the emission and absorption of infrared light. Radiation does not require a physical medium.

The net rate of thermal emission between two surfaces depends on the temperature difference ΔT to the fourth power, given by Stefan's Law (taken from Serway and Jewett, 2013):

$$\phi_{rad} = \sigma_{rad} \cdot \epsilon \cdot A \cdot \Delta T^4 \tag{1.13}$$

Thermal radiation is expected to be the least important mode of heat transfer. Alvarez *et al.* (2003) contributed a 2.8% error when excluding it from the modelling process. Tanner *et al.* (2002b) combined radiation with convection to give a 'pseudo-convection', which is a common approach (ASHRAE 2013).

1.2.5: Mathematical Modelling Considerations

Mathematical modelling will play a vital role in optimising the forced-air cooling process. As shown by Pathare *et al*. (2012), there is currently no consensus on the optimal vent size or configuration. Determining the optimal package design for a new product or package type in a wholly experimental setting will involve a large amount of trial and error, with each iteration representing a time and money investment that may investigate parameters that do not necessarily increase the cooling efficiency. With an accurate mathematical model, finding a real world solution could be achieved with much less effort by iterating in the mathematical space (Figure 1.7). Through understanding the physical mechanisms that occur, the system is described mathematically through the 'model formulation' process, transforming the real-world problem into a mathematical problem. The iterative process is now on the right-hand side of Figure 1.7, where materials are free and a large number of variables can be investigated in a short amount of time, given that the model is also computationally efficient. Through 'model interpretation', the mathematical solution can be applied to the real-world problem, forming a real-world solution that has cost less money and taken a shorter amount of time to identify (Olatunji, 2012).

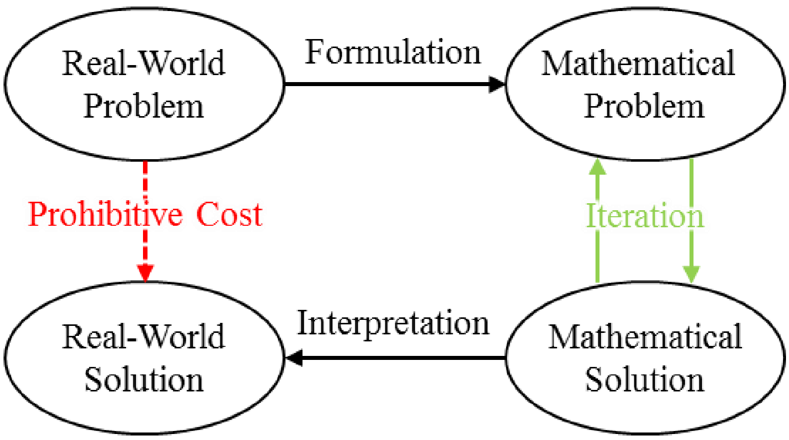

Figure 1.7: The mathematical modelling process. Image based on Cheng, 2001

Formulating a model requires observation – the identification and mathematical expression of physical mechanisms that combine into experimentally observed phenomena – and simplification – the identification and removal of insignificant processes or the inclusion of relevant assumptions (Giordano *et al*., 2013). This section outlines the modelling approaches that have been used to study forced-air cooling systems in the past, with an emphasis of reviewing the flexibility, speed and core assumptions of each method so as to assess its relevance to this project.

1.2.5.1: Important Model Variables

Figure 1.8 presents a cause and effect diagram (Ishikawa, 1982), assembled from literature sources (Boyette *et al.*, 1989; Fraser, 1998; Alvarez and Flick, 1999a; Bachmann and Earles, 2000; Tanner *et al.*, 2002a; Tanner *et al.*, 2002b; Ferrua and Singh, 2009a; Pathare *et al.*, 2012; Defraeye *et al.*, 2014; O'Sullivan *et al.*, 2016), summarising the physical mechanisms and variables that must be accounted for in the model to be developed in order to correctly predict the cooling rate and level of cooling uniformity.

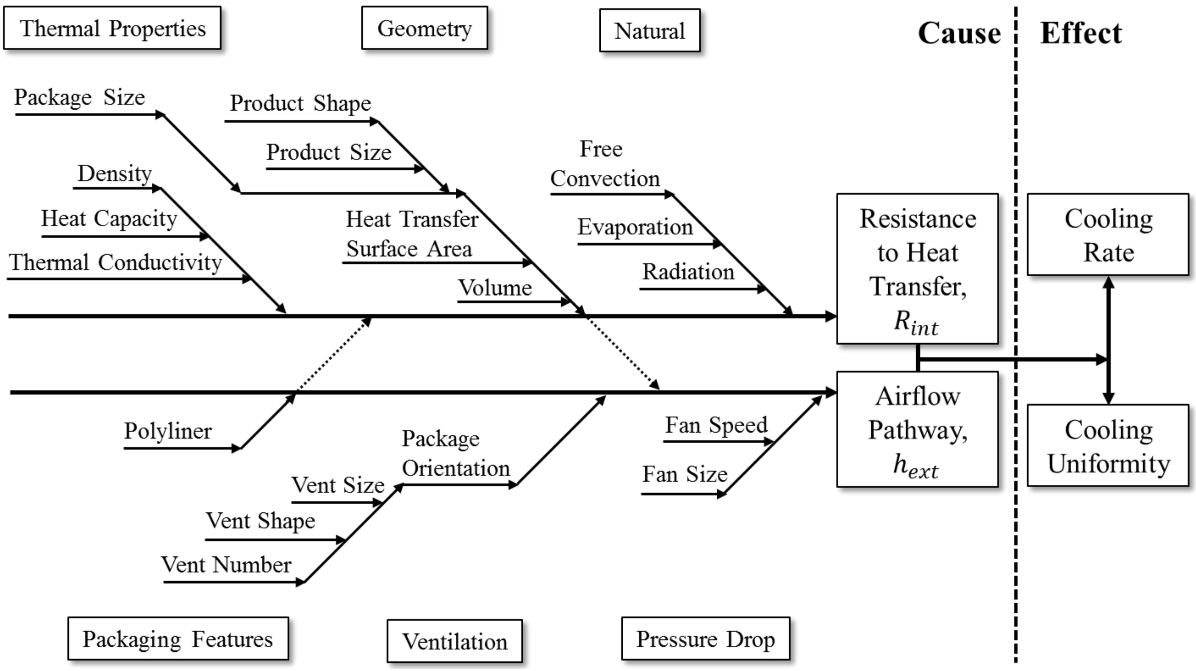

Figure 1.8: Cause and effect diagram (Ishikawa, 1982) for the forced-air cooling of polylined, palletised kiwifruit.

The problem was divided into two categories: the mechanisms and variables that combine to form a particular airflow pathway through the package, which gives a certain level of external heat transfer, h_{ext}; and the mechanisms and variables that combine to give a certain degree of internal resistance to heat transfer, R_{int}. These can be considered separately because Ferrua and Singh (2009c) showed that airflow and heat transfer can be decoupled – in other words, the airflow pattern is constant over time and is not affected by temperature gradients through the fluid, as the maximum temperature difference over the cooling period is typically just 20 ºC. The implication is that separate models can be developed independently and combined at a later time: one that focuses on predicting an airflow pattern; and another focusing on describing the fruit and packaging geometry and its internal resistance to external heat transfer.

Producing a successful heat transfer model must incorporate variables such as the thermal properties of the fruit and packaging, the geometry of the fruit and natural heat transfer mechanisms. The thermal properties contribute significantly to the internal resistance and rate of cooling, defining how much ambient heat energy is stored in the fruit per kilogram and how quickly heat can be transferred to the surface of the product via conduction. They are intrinsically linked to the chemical composition of the fruit and should be measured, or they can be estimated via methodologies such as ASHRAE (2010). The size and shape of the product has a significant impact on the rate of observed cooling for the same flowrate of cooling air per kilogram of product (Thompson *et al.*, 2008); not just individually, but as a bulk of stacked fruit inside of the package. Touching fruits conductively transfer heat, which can be a major source of heat removal for locations where airflow is sparse, so that different levels of contact area from different stacking patterns can potentially impact the internal resistance. While fruits such as oranges and apples have been modelled successfully as spheres (Defraeye *et al.*, 2014; Han *et al.*, 2015), an ideal model would include methods to describe more complex fruit shapes such as pears or kiwifruit (Rogge *et al.*, 2015; O'Sullivan *et al.*, 2016). Additional heat transfer mechanisms can lower the internal resistance, with free convection, evaporative cooling and thermal radiation potentially occurring independent of forced airflow, contributing to the rate of cooling.

A successful airflow model must produce an accurate airflow pattern as a function of the pressure drop induced across the system and the nature of the packaging. Larger or faster fans generate greater pressure drops, which can increase the volumetric flowrate and airflow velocity. At higher velocities, turbulence may produce an altered airflow pattern (Alvarez *et al.*, 2003). How the air is distributed throughout a box or pallet is dependent largely on the package ventilation – vent number, vent shape and vent size – and the package orientation, or how the vents align between boxes on the pallet scale (Sargent *et al.,* 2007).

Cross-over between the two aspects of the problem are: the fruit geometry, as how the fruit are stacked in the box can have a profound impact on the airflow pattern, seeing as air is forced through the packaging and over the bulk of stacked fruit; and packaging features like the presence of a polyliner, which not only changes the airflow pattern significantly but can also alter the internal resistance by restricting the surface area of direct contact between fruit and airflow and trapping a large quantity of stagnant air, a known insulator, inside of the polyliner bag.

1.2.5.2: Direct Numerical Simulation

Direct Numerical Simulation (or DNS) is a high resolution finite element modelling strategy for solving the continuum problem (i.e. heat, mass and momentum transfer, Pathare *et al.,* 2012). DNS divides the system under study into finite elemental volumes and solves the appropriate set of partial differential equations – which in this case are momentum, mass and heat transfer PDEs – with little to no simplification. Sometimes this method is also called the finite element approach (Becker *et al.,* 1996). This method allows for the flow fields – the instantaneous velocity and pressure of the fluid across all locations – to be determined, making it a form of computational fluid dynamics, or CFD (Löhner, 2008). Due to the complexity of the approach, it has only been in recent times, with the steady advance of affordable computational power, that DNS has become a viable approach for modelling the forced-air cooling process (Dehghannya *et al.*, 2010). DNS models sometimes do not make simplifications pertaining to model geometry, such as Ferrua and Singh (2009a) who re-created the exact 3D shape of a collection of strawberries stacked inside of a clamshell package, however, often very complex geometries *are* simplified to reduce solution times.

DNS is capable of computing the time-dependent solution of the Navier-Stokes equations, even when the air domain is complex due to the packaging, package ventilation and irregularly shaped channels created by the spaces between fruits (Dehghannya *et al.,* 2010). The fidelity of the modelling approach is unparalleled, allowing for the investigation of effects such as percentage of bypass air, turbulence as a function of pressure drop and location, and the temperature gradient within individual fruits (Ferrua and Singh, 2009b).

A variety of similarly detailed DNS models have been published in recent years, such as: forced-air cooling of oranges in bulk packages on the single box (Verboven *et al.*, 2006) and pallet scale (Delele *et al.*, 2013, Defraeye *et al.*, 2013); oranges cooled in bags (Defraeye *et al.*, 2014); apples in bulk packages at the single box scale (Berry *et al.*, 2017, Han *et al.*, 2015); and kiwifruit in bulk packages and wrapped in a polyliner (O'Sullivan *et al.*, 2016).

DNS models require a significant time and effort investment to correctly construct and validate, where typically DNS model development and validation are PhD topics and hence take 3-4 years and ~$200,000 to develop (Ferrua, 2007; O'Sullivan, 2016; Berry, 2017). The method relies on a complex body-fitted mesh generation strategy to correctly model the complicated geometries inside of the package, a daunting task for many model users (Frei, 2013; Zou *et al.*, 2006a). Meshes are highly detailed and can be prohibitively large – Ferrua and Singh (2009a) reported 2.9 million finite elements. The extensive number of finite elements and small time steps result in a modelling methodology that is computationally intensive and inefficient, with solution times commonly in the 24 hour to 1-week range (Ferrua and Singh, 2009b; Defraeye *et al.*, 2014; Delele *et al.*, 2013). A fully integrated DNS model is therefore not viable for the purposes of this project as it is a rigid, highly manual and slow approach.

Simplified uses of DNS could be useful for this project, however. Rather than developing a fully integrated DNS model, reduced DNS models have been developed to investigate the effects of random stacking on the pressure drop through a package (Delele *et al.*, 2008) or the heterogeneity of cooling as a function of vent number (Dehghannya *et al.*, 2011). In Delele *et al*. (2008), no heat transfer was included in the model, significantly reducing the complexity. It was found that the size distribution and random stacking patterns of spheres did not have a significant effect on the overall pressure drop. In Dehghannya *et al*. (2011), a 2-D model was constructed, where the internal package geometry was described as an ordered stack of circles, rather than spheres. This allowed a massive reduction in the mesh size – just 150,000 elements – to derive important conclusions concerning the uniformity of temperatures when vent number and position are changed. It may be appropriate to use DNS in a limited sense, for example to produce a detailed airflow solution through the packaging headspace – which has a much simpler geometry than the rest of the package and could be considered as a channel – or as a comparative tool to directly compare the accuracy, flexibility and solution time trade-offs of using a less detailed modelling methodology.

1.2.5.3: Porous Media Approach

A porous medium is a material that consists of a solid interconnected matrix, with voids that are filled with at least one fluid phase (Nield and Bejan, 2006). On a small scale, the behaviour of the moving fluid is irregular and difficult to predict. However, it has been experimentally determined that measuring the fluid flow characteristics over areas that encompass many pores allows for the simplification of the system. Porous mediums have been used to describe the product-in-package geometry for many mathematical modelling studies, as the inside of the package contains a matrix of solids (the product) with a fluid flowing through the void spaces (the cooling air) (Xu and Burfoot, 1999; Zou *et al.,* 2006a; Zou *et al.,* 2006b; van der Sman, 2002; Gowda *et al.,* 1997; Datta and Dhall, 2011). Using this approach allows the complex geometry inside of the package to be collapsed into a single term: the porosity, the ratio between the solids volume and the total volume.

Using this approach, the finite elements become 'space averaged' and the airflow fields and heat transport phenomena can be predicted with lower computational resources (Zou *et al.,* 2006a; Zou *et al.,* 2006b). However, the accuracy of this approach is product subjective. As a requirement of the porous medium approach to be valid, any sample volume taken must contain both a solid and a liquid phase. For cases where the package-to-product equivalent diameter ratio is below 10, the porous medium approach cannot be applied because of the high probability of having a space averaged element that is entirely solid or air (Verboven *et al.*, 2006; Eisfeld and Schnitzlein 2001).

The porous medium approach is a combination of empirical observation and finite element modelling when used with forced-air cooling. The relevant coefficients must be empirically determined, through either experiment or the use of an empirical relationship that has already been validated. The important empirical relationships that relate to the porous medium approach are: the intrinsic permeability through a bed of packed spheres, K_ε (m^2); and the inertial coefficient known as the Forchheimer coefficient, F (Ergun, 1952; Zou *et al.*, 2006a).

$$K_\varepsilon = \frac{{d_s}^2 \varepsilon^3}{a(1-\varepsilon)^2} \tag{1.14}$$

$$F = \frac{b}{\sqrt{a\varepsilon^3}} \tag{1.15}$$

Where a and b are empirical constants, ε is the porosity of the medium ($m^3_{product}/m^3_{total}$), and d_s is the equivalent mean diameter of spherical solid phase particles (m). K_ε and F are used to compute the volume-average velocity of fluid in the porous medium (see Zou *et al*, 2006a). Heat transfer between solid and liquid is driven by h, the heat transfer coefficient ($W \cdot m^{-2} \cdot K^{-1}$). This is estimated by using an empirical correlation, such as one given by Geankoplis (1993) for a packed spherical bed:

$$\varepsilon \frac{\mathrm{Nu}_\varepsilon}{\mathrm{Re}_\varepsilon \cdot \mathrm{Pr}} \mathrm{Pr}^{0.66} = \frac{2.876}{\mathrm{Re}} + \frac{0.3023}{\mathrm{Re}^{0.35}} \tag{1.16}$$

Where the dimensionless numbers Nusselt, Nu; and Reynolds, Re; are calculated in their space averaged forms. Incropera and DeWitt (1981) suggested that the right hand side of Eq. 1.16 can be multiplied by a linear correction factor to account for non-spherical shapes.

Zou *et al.* (2006a) and Zou *et al.* (2006b) presented a model that predicted the performance of tray-packaged apples undergoing the forced-air cooling process using the porous medium approach. It was assumed that the space in-between layers of apples could be modelled as a porous medium, allowing for a coarse mesh to be generated that had good prediction capabilities and high computational efficiency. Air flow patterns, pressure maps and temperature profiles were predicted throughout a layer of apples as it underwent forced-air cooling.

If a fully integrated porous medium model were to be developed for this project, it would immediately rule out a large number of products that must be packaged into small containers – including the scenario that is being investigated directly; 102 count 36 Hayward kiwifruit in a modular bulk package has a package-to-product ratio of approximately 6. Another downside of the porous medium approach is that it is a semi-empirical approach, so there is a risk of having to re-measure all of the empirical constants necessary for the approach to work when the product or package design is changed.

1.2.5.4: Zonal Approach

The zonal modelling approach solves a heat, mass and energy balance over a small number of space averaged elements, called zones. Each zone is driven by a sub-model, and these sub-models combine to predict changes to the system as a whole. A zonal model has three kinds of sub-models: (A), a sub-model describing energy, mass or momentum within a zone; (B), a sub-model describing the transport of energy, mass or momentum within a zone; and (C), a sub-model describing the transport of energy, mass or momentum between adjacent zones (Figure 1.9).

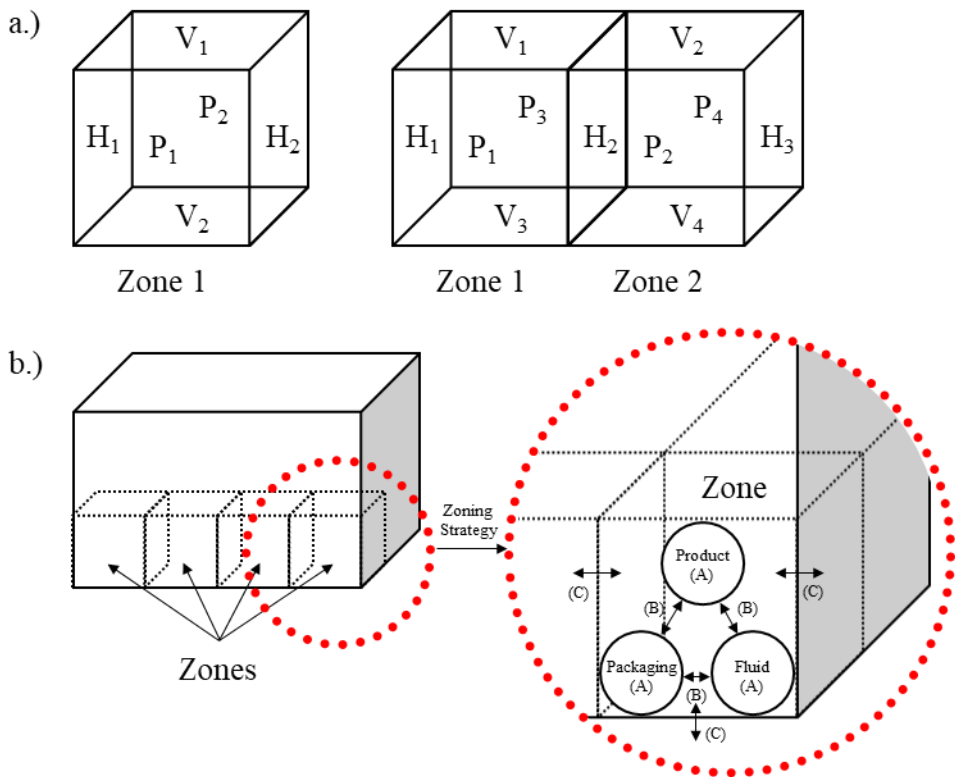

Figure 1.9: The zonal approach, with examples of the zone and zone boundary numbering and coding system. Based on Tanner et al., 2002a.

Tanner *et al.* (2002a), Tanner *et al.* (2002b) and Tanner *et al.* (2002c) presented a zonal based model of the forced-air cooling process of apples in a three-part publication. The heat, mass and momentum balances were combined into just two overall equations that took into account all of the modes of transfer between all of the different zones. The energy balance equation was:

$$(M_p C_p)\ \frac{dT_p}{dt} = \phi_{p-a} + \sum_{i=1}^{n}\sum_{j=1}^{m} \phi_{i,j} + \phi_{resp} \tag{1.17}$$

Where M_p is the product mass (kg), C_p is the product specific heat capacity (J·kg^{-1}·K^{-1}), $\frac{dT_p}{dt}$ is the change in product temperature over time (°C·s^{-1}), n is the number of boundaries, m is the number of transfer processes, i and j correspond to specific boundaries and transfer processes, ϕ_{p-a} is the heat transfer between the product and the cooling air (W), $\phi_{i,j}$ is the heat transfer between zones (W), and ϕ_{resp} is the rate of heat generated by the product (W).

The mass transfer equation was:

$$\frac{dM_p}{dt} = \dot{m}_{p-a} + \sum_{x=1}^{X} \dot{m}_{x-p} \sum_{i=1}^{n}\sum_{j=1}^{m} \dot{m}_{i,j} \tag{1.18}$$

Where $\frac{dM_p}{dt}$ is the change in moisture over time (kg water·s^{-1}), $\dot{m}_{p-a}$ is the rate of mass transfer of water between the product and the air (kg water·s^{-1}), $\dot{m}_{i,j}$ is the rate of mass transfer between zones (kg water·s^{-1}), and $\dot{m}_{x-p}$ is the mass transfer of water between the product and the various packaging materials, where x corresponds to a specific packaging material, up to a maximum of X (kg water·s^{-1}).

The zonal approach could prove to be the most appropriate modelling methodology for accomplishing this thesis' goal of developing a flexible heat transfer model. The relatively small set of space averaged zones significantly reduces the number of ODEs required to predict the bulk cooling rate and temperature uniformity, suggesting very fast solution times. However, a zonal model requires a zonal network with properties that are representative of the reality of the system to produce an accurate solution. If these properties must be manually determined, then the approach is not flexible to product or package changes. Additionally, there is no method for predicting airflow through a zonal model, and Tanner *et al.* (2002b) used empirical airflow measurements as an input. Again, this makes the approach insensitive to changes in package ventilation. Mitigating these problems would represent a great advancement in the zonal modelling approach.

1.2.6: Literature Summary

Pre-cooling is an important industrial process that facilitates the large scale export of high quality fresh product to international markets, and forced-air cooling is the most commonly used commercial pre-cooling operation. Improving the performance of this process by developing packaging that improves the overall cooling rate or uniformity of temperatures throughout the pallet represents a significant economic benefit to New Zealand.

Mathematical modelling can be a useful tool to test the performance of a given package design before it is put into mass production. In the past there has been a focus on package design testing; that is to say, given a specific package design, what is the performance? While an accurate strategy, this approach represents a significant time and money investment. From the perspective of the industrial package designer, it would be more useful to have a mathematical model that can be used as a design tool to rapidly identify an optimised design, sacrificing some accuracy for flexibility and computational efficiency.

There are three primary modelling methodologies employed in the literature to predict the performance of a forced-air cooling process: direct numerical simulation (DNS); the porous media approach; and the zonal approach. DNS is the most detailed and potentially most accurate, but is also the most manual and computationally expensive technique, making it largely unsuitable for this project. However, DNS could be useful in limited applications such as airflow predictions without heat transfer, or as a comparison tool for determining the accuracy, flexibility and solution time trade-offs of other modelling approaches. The porous media approach was successful in predicting airflow behaviour and the cooling rate for a variety of products in a computationally efficient manner; however, it is not suitable for this project as the package-to-product ratio of Hayward kiwifruit is below the threshold of 10. The zonal modelling approach appears to be the best suited approach for this project. It offers fast solution times;

however, it is currently rigid as model construction is still a manual process and airflow cannot be predicted. Addressing these shortcomings will advance the zonal modelling approach significantly.

Airflow and heat transfer can be decoupled, the implication being that two separate models can be developed independently and combined at a later time: one for heat transfer prediction and the other for predicting the airflow pattern.

Chapter 2

Research Objectives

This project aims to develop a fast, flexible and automated heat transfer model for horticultural products undergoing the forced-air cooling process, to be used as an iterative tool to rapidly identify the optimal package design. Although the goal is to produce a universally applicable model, the primary context is kiwifruit and kiwifruit packaging. As heat transfer can be decoupled from airflow, this project will focus on the development of a heat transfer model; within the larger project structure, an independent airflow model will be developed separately and the two halves will be integrated at a later date. The zonal modelling approach was chosen as it was the most likely to satisfy the conditions of speed and flexibility; however, new techniques must be developed to make the approach automated. Without an airflow model it was decided that the scope of this thesis be simplified to a single box scale. If a single box heat transfer model can be developed and validated, then the model can be easily upgraded to the pallet scale when it is integrated with a pallet scale airflow model.

The primary objectives of this project were as follows:

---

1. Build a data library of experimental data for a variety of package designs and cooling scenarios to empirically investigate the impact of package design features;
2. Identify or develop new quantitative metrics to assess system performance, measured (1) or predicted (4);
3. Develop methods to measure and/or generate the 3D bulk fruit and polyliner shape inside of a package in a way that is suitable for an input to the heat transfer model;
4. Develop a flexible, computationally efficient and automated heat transfer prediction model, using the zonal modelling approach and (3) as an input;
5. Validate the model developed in (4) against the data library collected in (1).

Chapter 3*

Empirical Forced-Air Cooling Performance

3.1: Introduction

To model a system, it is first important to assess how it behaves in reality, not only for validation purposes but also to provide an indication for the relative magnitude of operations settings such as pressure drop or vent size on the system performance. The efficiency of a forced-air cooling process is not just defined by the cooling rate but also the cooling heterogeneity. If individual products experience a diversity of cooling rates, this can result in variable levels of quality and shelf life from the same batch at the end of the cold chain. Therefore, there is also a need for a robust heterogeneity metric to quantify the variability in a cooling profile so that this can be compared or optimised. In section 3.2, a new quantitative metric for total process heterogeneity is developed. Section 3.3 explores a systematic approach to experimental package design testing; and section 3.4 collects cooling data for single boxes with well-defined boundary conditions for model validation purposes.

3.2: Development of a New Temperature Heterogeneity Index

3.2.1: Introduction

Iterative optimization routines require cost functions to minimise or maximise. These cost functions should be continuous descriptors of system performance, so that for example, the advantage (or disadvantage) of increasing the pressure drop across a pallet can be quantified as X% better (or worse), where X is any continuous number. This would allow a more rigorous approach to evaluating innovations.

Chilling operations are typically compared by reporting the average cooling rate with metrics such as the half-cooling time (HCT) or seven-eighths cooling time (SECT). While this 'average rate of cooling'

* This chapter contains material published in the paper:
Olatunji, J.R., Love, R.J., Shim, Y.M., Ferrua, M.J., East, A.R. (2016). *Quantifying and visualising variation in batch operations: A new heterogeneity index.* Journal of Food Engineering, 196, 81-93

is important, when reported in isolation it ignores other factors that impact performance – notably, the cooling heterogeneity. Heterogeneity is a leading cause of losses within the food manufacturing industry – for example, in chilling operations, products that cool much faster than the average cooling rate may be more vulnerable to chilling injury, of which kiwifruit is known to be particularly susceptible (Zhao *et al*., 2014). Additionally, any temperature variation at the process end time (typically the SECT) will persist for a long period of time as the pallet sits in long-term refrigerated storage, which may impart significant quality differences to different fruit within the same batch.

As that heterogeneity is such an important factor, a mathematical description of heterogeneity is required. Previously (Dehghannya *et al.*, 2011; Han *et al.*, 2015; Defraeye *et al.*, 2015; Lu *et al.*, 2014; Barbin *et al.*, 2012), the relative standard deviation was used as a metric for heterogeneity (Eq. 3.1):

$$HI = \frac{1}{\bar{\bar{T}}}\sqrt{\frac{1}{m-1}\sum_{n=1}^{m}(T_n - \bar{T})^2} \tag{3.1}$$

Where T_n is the temperature of product n of a total m number of products, and $\bar{T}$ is the average temperature.

Unfortunately, this metric has significant shortcomings. It:

- Only evaluates the heterogeneity at a single point of time, whereas the history may also be significant for product quality. Although a time series of HI values can be plotted to indicate changes in heterogeneity over time, it may be preferable to have a single value that concisely represents total process heterogeneity over the entire processing time;
- Eliminates information concerning whether a product is hotter or colder than the average temperature (only the absolute difference is considered), and does not provide information pertaining to the shape of the temperature distribution, or how the shape of the distribution changes over time. Retaining this information would identify whether different cooling processes promote operations that are dominated by colder than average temperatures (more products susceptible to chilling injury) or that favour warmer than average temperatures (higher rates of senescence).

Therefore, it would be preferable to have a new heterogeneity index that includes tools to compare the shape of temperature profiles;

- Becomes mathematically unstable when the refrigeration temperature approaches zero, or is less than zero. As $\bar{T}$ is the denominator in Eq. 3.1, and many cooling operations are conducted near or below 0°C, the HI approaches infinity or becomes negative. As suggested by Defraeye *et al.* (2015), this problem can be addressed by using an appropriate offset, namely the Kelvin temperature scale (K). Although this solves one issue, others then arise: $T_n - \bar{T}$ remains the same when using °C or K, but $\bar{T}$ is much larger when using K, resulting in disparate HI values from the same set of data, where only the units of temperature have been changed. It would be preferable to have a new heterogeneity index that is dimensionless so that a wide number of systems can be fairly compared.

Therefore, there was a need for a new, robust heterogeneity index that addressed these issues.

3.2.2: Dimensionless Units

Collected temperature and time data must be non-dimensionalised so that different systems can be fairly compared (Brosnan and Sun, 2001).

3.2.2.1: Dimensionless Temperature Change

The Fractional Unaccomplished Temperature Change – or FUTC – is a commonly used dimensionless temperature parameter (Brosnan and Sun, 2001). It represents how much cooling remains to shift the product temperature to a reference temperature (i.e. the refrigerated air) given an initial and instantaneous product temperature. This has been used throughout this thesis:

$$Y_{t,n} = \frac{T_{t,n} - T_{ref}}{T_{i,n} - T_{ref}} \tag{3.2}$$

Where Y is the FUTC and T is temperature. Subscripts t is time; n is an individual product out of a total number of recorded products, m; and i is the initial temperature.

3.2.2.2: Characteristic Index of Process Progression

Comparing the distribution of dimensionless temperatures at absolute times – such as seconds, minutes or hours, etc – is not correct, as it is biased by the rate of cooling. At the beginning of a cooling process there is ideally no heterogeneity, as all of the product is equilibrated at the same initial temperature (practically, especially industrially, there may be small differences depending upon the conditions in which the pallets are staged). As cooling progresses, there is a separation in temperatures as different products experience different cooling rates; this increased until roughly HCT, when a system is expected to have its maximum level of temperature variability (confirmed experimentally in Figure 3.21). The level of heterogeneity then drops as the individual products begin to tend toward the refrigeration temperature, so that at the process end time (typically the SECT), heterogeneity has decreased considerably. Han *et al.* (2015) reported that a new package for apples had an improved HCT of approximately 150 minutes, compared with a HCT of approximately 300 minutes for the original package design. They then concluded that the new package was also more uniform by reporting the relative standard deviation (Eq. 3.1) for both packages at 300 minutes of cooling – 0.275 for the new package, compared with 0.31 for the original. This comparison at 300 minutes is not robust as it pits the original package at the HCT – when heterogeneity is at its maximum – with the new package when it's nearer to the SECT – when its heterogeneity is expected to be much lower. The consequence of comparing heterogeneity at absolute times is that the faster system will almost always appear to be more uniform, a clear bias that is an artefact of the cooling rate. Heterogeneity should instead be compared at the same *characteristic* times, such as the HCT of each operation (150 and 300 minutes for each box in the Han *et al.* (2015) example), or the SECT. This can be achieved by creating a dimensionless time scale, or a characteristic index of process progression.

The average fractional unaccomplished temperature change is one option to accomplish this:

$$\bar{Y}_{X,t} = \sum_{n=1}^{m} Y_{X,t,n}/m \tag{3.3}$$

Using $\bar{Y}$ ensures each system is continuously compared at the same average cooling state. Every system will begin at $\bar{Y} = 1$, and as cooling progresses, $\bar{Y}$ will tend towards 0. For a chilling process, the HCT occurs at $\bar{Y}$ = 0.5; and the SECT at $\bar{Y}$ = 0.125.

While it is recommended that $\bar{Y}$ is used wherever possible, there may be scenarios where it's not appropriate. For example, short operational changes are often made to batch chilling processes, such as ceasing cooling momentarily to rotate the pallet and change the direction of airflow (Ferrua and Singh, 2009b); or an intermediary warming period. These would cause a discontinuity or a reversal on the progress (or dimensionless time) scale. This interferes with further analysis and is confusing when presented. An alternative is to use the fractional unaccomplished cooling completion time, τ:

$$\tau_{X,t} = 1 - {}^{t}/_{t_f} \tag{3.4}$$

Calculating τ requires a consistent definition of t_f, the time at which the process ends. For example ceasing pre-cooling operations at the SECT is often recommended; therefore t_f would be the SECT for each system under study. In this scenario, each system will begin at τ = 1, and will cease at τ = 0. For a chilling process, the HCT occurs at $\tau \approx$ 0.667; and the SECT at τ = 0.

It should be stressed that a system analysed using $\bar{Y}$ *cannot* be compared to a system analysed using τ; comparisons can only be made between systems analysed using the same methodology. Also, if τ is used, comparisons can only be made between systems analysed using the same definition of t_f. Both process progression indexes are discussed further in section 3.2.3.2.1.

3.2.3: Heterogeneity

Heterogeneity, or temperature variability, can be analysed at specific times, or can be inspected across the entire cooling process. Describing and quantifying variability in both cases are important to assess the performance of a pre-cooling system.

3.2.3.1: Heterogeneity at Single Points in Time

A majority of products cool near to the average rate, with a proportion of other products that cool quickly, and others that cool slowly, giving rise to hot and cold spots. The number and magnitude of these positions is expressed by the dimensionless temperature difference, ΔY:

$$\Delta Y_{X,t,n} = Y_{X,t,n} - \bar{Y}_{X,t} \tag{3.5}$$

When ΔY is plotted as a histogram, the distribution of temperatures at a given point in time will form a bell curve (Figure 3.1a), although potentially skewed in either direction. By definition, the mean value of the ΔY bell curve is 0. Positive numbers represent products warmer than average and hence cooling slowly (hot spots); while negative numbers represent products colder than average, and hence cooling faster (cold spots). For a low variation in temperatures, the ΔY bell curve is tall and narrow; while short and wide bell curve indicates high levels of variability. Temperature variability at specific time points can therefore be modelled as a population bell curve with a mean of zero, and a standard deviation representing the standard deviation of ΔY. This can be described with a simple Gaussian function (Terrell and Fomby, 2006):

$$f_N(\Delta Y) = \frac{1}{\sigma\sqrt{2\pi}} \cdot exp\left(-\frac{(\Delta Y - \overline{\Delta Y})^2}{2\sigma^2}\right) \tag{3.6}$$

Where $f_N(\Delta Y)$ is the frequency of a given value of ΔY, $\overline{\Delta Y}$ is the mean of ΔY ($\overline{\Delta Y} = 0$), and σ is the standard deviation of ΔY.

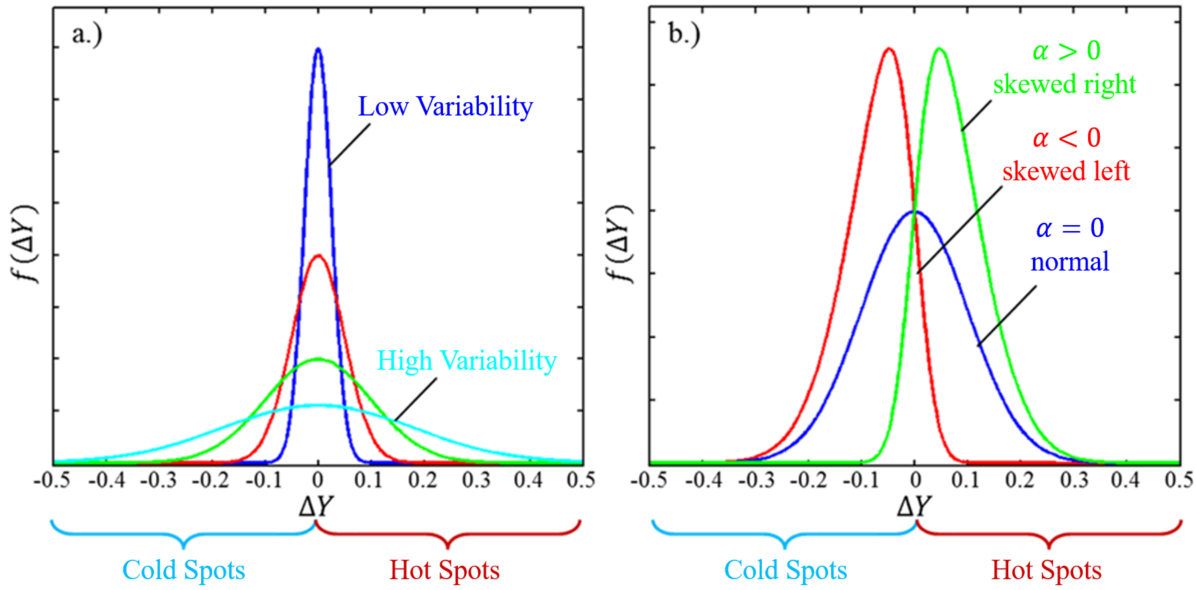

Figure 3.1: a.) Potential heterogeneity at a single instant in time, using a Gaussian distribution; b.) potential heterogeneity at a single instant in time modelled using a Skew-Normal distribution, to account for non-normal distributions of ΔY.

Eq. 3.6 and Figure 3.1a assumes a normally distributed ΔY bell curve. However, there are many reasons for a non-normal distribution. Products in preferential locations with respect to the cold airflow may cool disproportionately quickly compared to the average rate, while other products may be shielded from the refrigerated air and cool disproportionately slowly. Differences in product size, thermal properties, a poor selection of sample temperature positions, or equipment error could also contribute to a skewed temperature distribution. Regardless of cause, these effects need to be accounted for mathematically for the heterogeneity index to be robust. The skew-normal (SN) distribution (O'Hagan and Leonard, 1976; Terrell and Fomby, 2006) extends the normal Gaussian distribution (Eq. 3.6) to incorporate skewness through the use of α, a shape factor. When $\alpha = 0$, skewness vanishes and the distribution reverts back to normality. When $\alpha > 0$, the distribution is skewed to the right, representing a temperature profile that has a higher proportion of warmer temperatures; and when $\alpha < 0$ the distribution is skewed to the left, a temperature profile with a higher magnitude of colder temperatures (Figure 3.1b). The SN density function is (Terrell and Fomby, 2006):

$$f_{SN}(\Delta Y) = 2\phi_s\left(\frac{\Delta Y - \xi}{\omega}\right)\Phi_s\left(\alpha\frac{\Delta Y - \xi}{\omega}\right) \tag{3.7}$$

Where ϕ_s is the standard normal distribution and Φ_s is the standard normal cumulative distribution. The two additional terms: ξ, defined as location; and ω, defined as scale; are the SN analogues to the mean ($\overline{\Delta Y}$) and standard deviation (σ), respectively. The SN cumulative density function is (Terrell and Fomby, 2006):

$$F_{SN}(\Delta Y) = \Phi_s\left(\frac{\Delta Y - \xi}{\omega}\right) - 2T_{Owen}\left(\frac{\Delta Y - \xi}{\omega}, \alpha\right) \tag{3.8}$$

Where T_{Owen} is Owen's T function (Owen, 1956). Hence, a temperature distribution at a given point in time can be summarised quantitatively using just three parameters: α, ξ and ω.

3.2.3.2: Heterogeneity over Time

3.2.3.2.1: Visualising Heterogeneity over Time

Plotting ΔY (Y-axis) against $\bar{Y}$ or τ (X-axis) produces a variability over time plot that's dimensionless in terms of temperature and time. Named the heterogeneity plot, it provides engineers and technologists with a useful visual tool to compare the variability of two or more systems over the entire processing time. To better illustrate the value of the heterogeneity plot, theoretical heterogeneity plots are presented in Figure 3.2 and Figure 3.3. These plots represent hypothetical chilling operations with temperature uniformity at the beginning of the process, maximum heterogeneity at the HCT, and temperature uniformity again when $t \to \infty$ and all products are at the storage temperature. Each was constructed to illustrate how the heterogeneity plot is interpreted and how to visually identify differences between systems. Each line of the 11 lines on each figure represents an individual product temperature time series. These represent the temperature at representative locations. A larger proportion of products have ΔY close to 0 at all times, as they are cooling similarly to the average cooling rate. Hence, lines on the heterogeneity plot are closer together near $\Delta Y = 0$. The proportion of products hotter and colder than the average diminishes away from $\Delta Y = 0$, so that the lines of the heterogeneity plot separate toward highly positive or negative values of ΔY. This gives all heterogeneity plots a characteristic 'eye' shape, where it is tapered at both ends, as heterogeneity is low at the beginning and end of a cooling process; and a bulge at approximately the HCT, where variability is highest.

Hypothetical cooling operations are illustrated. System A (Figure 3.2a and Figure 3.3a) shows a system with a normal distribution of hot and cold spots, with a high level of total process heterogeneity. System B (Figure 3.2b and Figure 3.3b) is again normally distributed, but represents a system with low total process heterogeneity. System C (Figure 3.2c and Figure 3.3c) shows a system that has skewness over time behaviour. System D (Figure 3.2d and Figure 3.3d) shows a process with a short intermediary warming period. Visually comparing system A to B, it is apparent that system B has a lower spread of temperatures over time; thus system B would be considered superior in terms of homogeneity. Comparing system B to C makes the presence of skewness visually evident; System C clearly showing a higher proportion of cold spots at the beginning of the chilling process, and a higher proportion of hot spots toward the end. System D illustrates a scenario where $\bar{Y}$ is an inappropriate process progression index. Because of the short warming period, $\bar{Y}$ increases for a short period, causing the line on the heterogeneity plot to reverse on the X-axis. This inconsistency is solved by using τ (Figure 3.3d) instead of $\bar{Y}$ (Figure 3.2d).

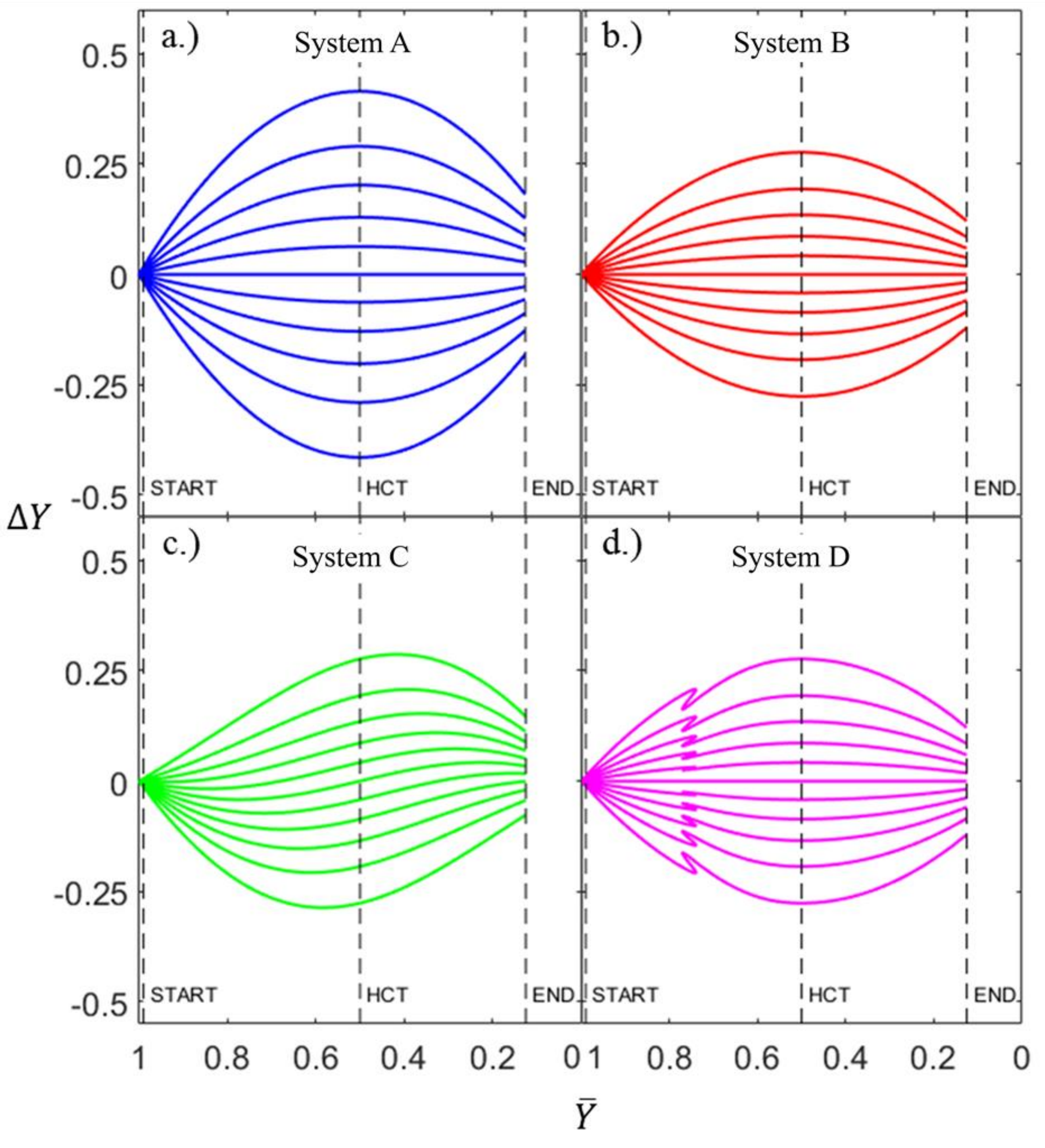

Figure 3.2: Idealised heterogeneity plots, plotting ΔY for each individual product against $\bar{Y}$, for four theoretical systems: a.) System A, with a normal distribution of hot and cold spots, and a high level of heterogeneity; b.) System B, with a normal distribution of hot and cold spots, and a lower level of heterogeneity; c.) System C, with skewness-over-time behaviour, and; d.) System D with a short intermediary warming period, making $\bar{Y}$ an inappropriate process progression index.

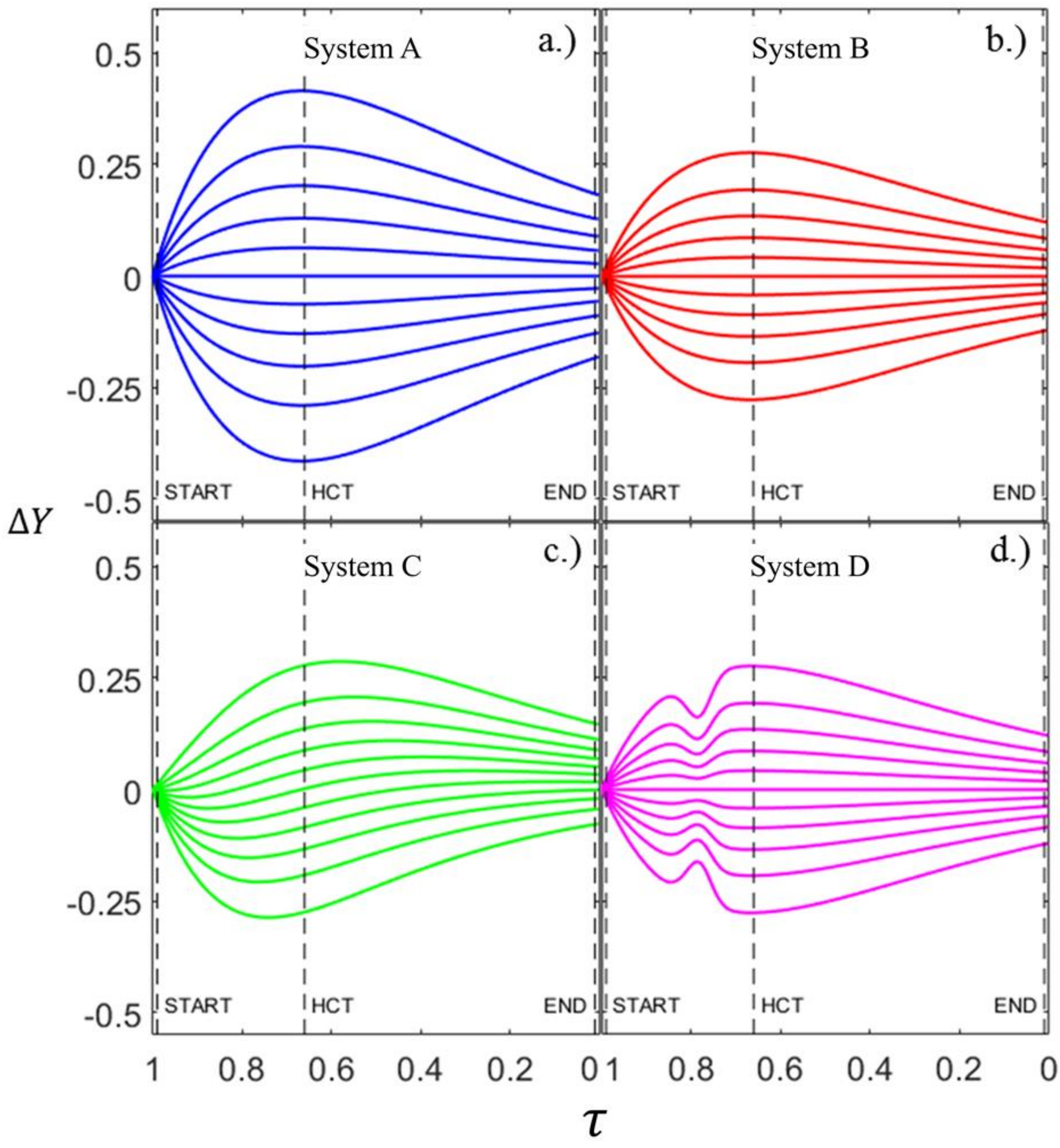

Figure 3.3: Idealised heterogeneity plots, plotting ΔY for each individual product against τ for four theoretical systems: a.) System A, with a normal distribution of hot and cold spots, and a high level of heterogeneity; b.) System B, with a normal distribution of hot and cold spots, and a low level of heterogeneity; c.) System C, with skewness-over-time behaviour, and; d). System D, with a short intermediary warming period, making τ the appropriate process progression index.

3.2.3.2.2: Quantifying Heterogeneity over Time

A quantitative metric for heterogeneity over time is also required. The heterogeneity map was developed for this purpose, shown for hypothetical systems in Figure 3.4. It is a 3D plot with the dimensionless temperature difference (ΔY) on the Z-axis, the chosen process progression index – $\bar{Y}$ or τ – on the X-axis, and the cumulative distribution of ΔY on the Y-axis ($F(\Delta Y)$) (Figure 3.4a and c). Alternatively, for a 2D heterogeneity map that is perhaps easier to interpret, the Z-axis can be replaced by contours or a colour spectrum across the ΔY range (Figure 3.4b and d).

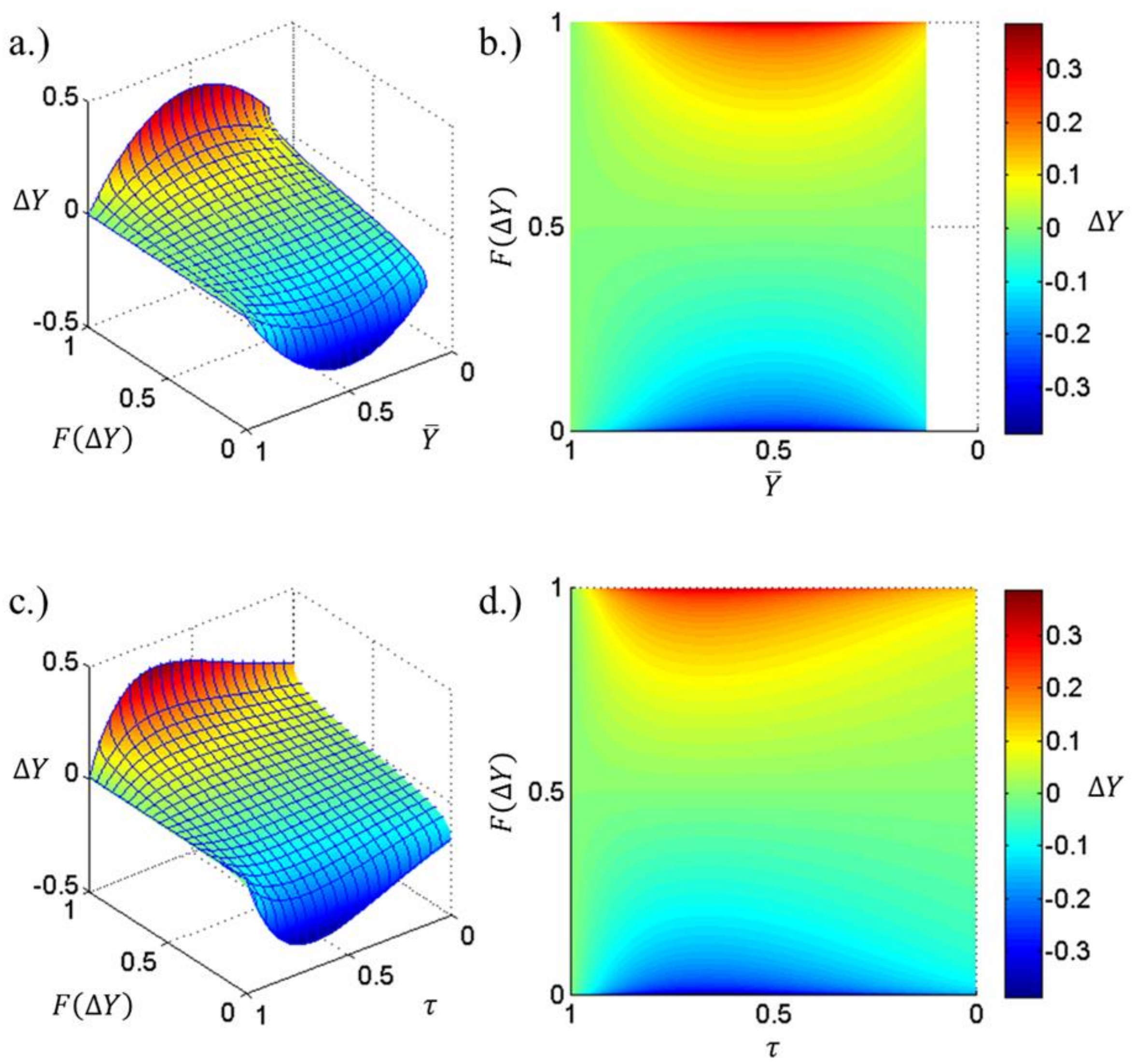

Figure 3.4: Idealised heterogeneity maps. 3D heterogeneity maps (a and c) plot ΔY on the Z-axis, while the 2D heterogeneity maps (b and d) displays ΔY as a colour spectrum. a and b use $\bar{\mathrm{Y}}$ as the process progression index, while c and d use τ.

From this data plot, the Overall Heterogeneity Index (OHI) is derived: a single, continuous and quantitative metric for total process heterogeneity that is dimensionless in terms of temperature and time. The theoretical best case scenario in terms of temperature uniformity is represented by a heterogeneity map with a perfectly flat plane at $\Delta Y = 0$ (Figure 3.5a). This scenario has an OHI = 0, as it is not possible to have a more homogenous system. Systems with some level of heterogeneity will have curvature: products that cool faster than the average rate will drop below, and products that cool slower than the average rate will rise above the plane of the Z-axis origin. Any deviation from the best case scenario will have an $OHI > 0$; and by extension, the higher the OHI, the higher the total process heterogeneity. Individual products that are at or near to the average temperature contribute minimally to the OHI, while products that are significantly hotter or colder than the average temperature contribute greatly to the OHI.

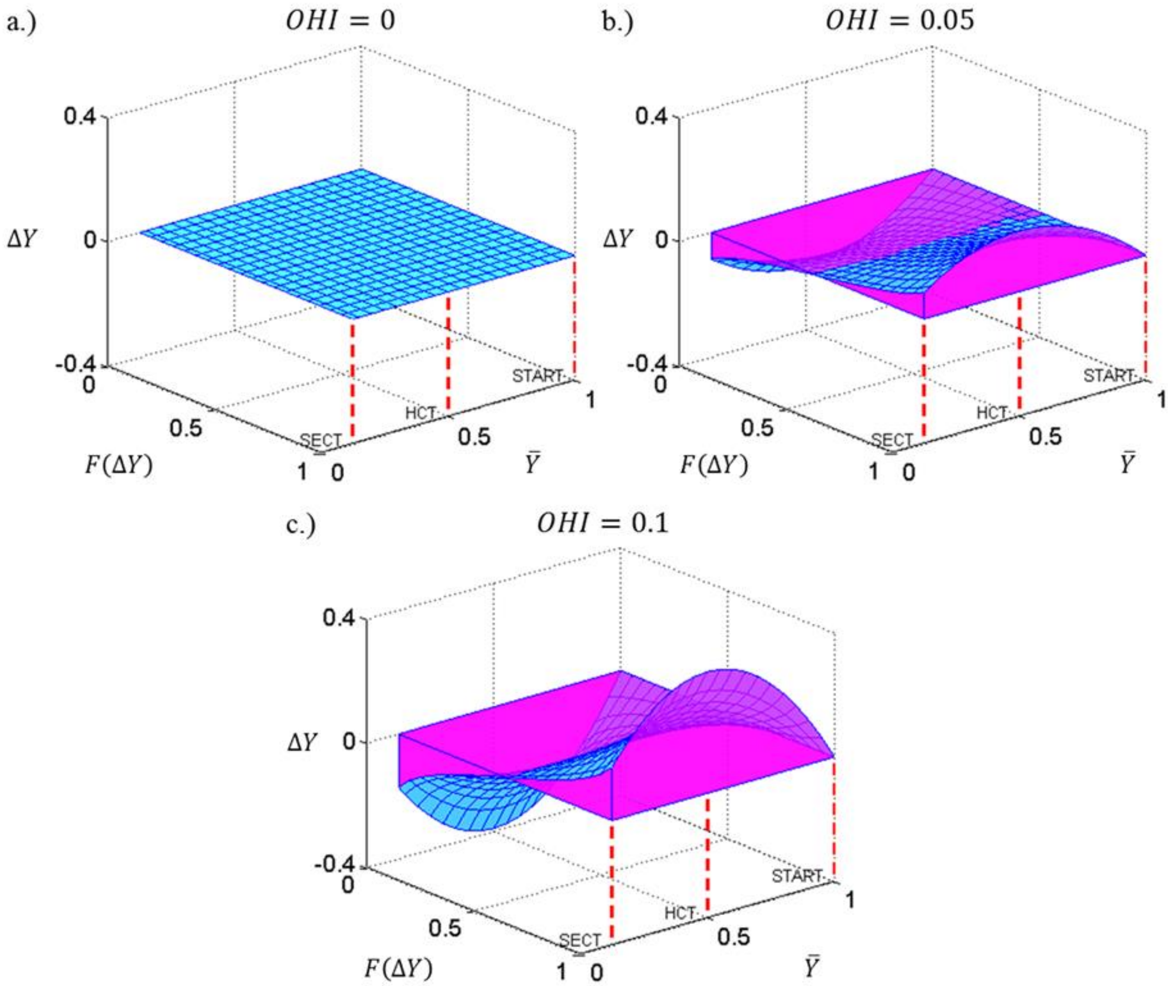

Figure 3.5: Idealised heterogeneity maps of three hypothetical systems with varying levels of process heterogeneity: a.) a system with perfect temperature uniformity ($\mathrm{OHI} = 0$*); b.) a system with a low level of heterogeneity (*$\mathrm{OHI} = 0.05$*); a system with a high level of heterogeneity (*$\mathrm{OHI} = 0.1$*).*

Therefore the OHI is equal to the volume that the surface of the heterogeneity map encompasses above and below the Z-axis origin – as represented by the magenta coloured volume in Figure 3.5b and c. This volume (the OHI) can be determined by:

$$OHI = \int_0^1 \int_{\mathcal{T}_{\text{END}}}^{\mathcal{T}_{\text{START}}} |\Delta Y| \; d\mathcal{T} \; dF(\Delta Y) \tag{3.9}$$

Where OHI is the Overall Heterogeneity Index, $|\Delta Y|$ is the absolute dimensionless temperature difference for all temperature positions and times, $\int_0^1 dF(\Delta Y)$ is the integral along the Y-axis, and $\int_{\mathcal{T}_{END}}^{\mathcal{T}_{START}} d\mathcal{T}$ is the integral along the process progression index, X-axis (either $\bar{Y}$ or τ) of the heterogeneity map.

When using $\bar{Y}$, $\mathcal{T}_{START}$ = 1 and $\mathcal{T}_{END}$ = 0.125:

$$OHI_{\bar{Y}} = \int_0^1 \int_{0.125}^1 |\Delta Y| \, d\bar{Y} \, dF(\Delta Y) \tag{3.10}$$

When using τ, $\mathcal{T}_{START}$ = 1 and $\mathcal{T}_{END}$ = 0:

$$OHI_{\tau} = \int_0^1 \int_0^1 |\Delta Y| \, d\tau \, dF(\Delta Y) \tag{3.11}$$

The OHI is robust to comparisons between systems where a different number of temperature positions are used, as the integral along the Y-axis is consistently 0 → 1 in all cases, so that the OHI scales appropriately. The OHI is also not overly sensitive to measurement error, such as thermocouple failure (elimination of a temperature position) or rogue data points; as the OHI incorporates the ΔY of each individual product, a few outliers has a minimal impact on the overall value, if there is a reasonably high overall sample size.

Again it should be emphasised that an OHI derived using $\bar{Y}$ is not comparable to an OHI derived using τ. A shortcoming of the OHI is that in isolation it does not indicate the extent to which a process is dominated by products hotter or colder over time. However, as $F(\Delta Y)$ in Eq. 3.11 can be modelled as a SN distribution (Eq. 3.8), representative α, ξ and ω can be assigned at various process times and reported in conjunction with the OHI to give a total description of process heterogeneity over time (section 3.3.4.3.2).

3.3: Performance Impact on Operational Changes During Pre-Cooling

3.3.1: Introduction

A large body literature investigates the link between operational conditions and the performance of the forced-air cooling process (see section 1.2). The majority of such studies are case specific – as evidenced by the wide variety of recommended vent opening areas by Pathare *et al*. (2012) – and there was a lack of any systematic approach to package design. For example, Han *et al.* (2015) added 2 additional vents to an apple carton and reported an improvement in cooling performance and cooling uniformity. However, there was not a detailed discussion pertaining to the location of vent placement, vent size, or vent number, beyond a packaging strength justification. How to use their findings to replicate performance gains for the kiwifruit modular bulk package is therefore uncertain. Berry *et al.* (2017) tested 4 new apple packages, the rationale for these designs being "aimed at better distributing airflow to all fruit layers within a carton when trays are present", but did not discuss how the new designs accomplished this goal. The impact on cooling heterogeneity has also never been examined in detail. In most cases the sole performance metric is the cooling rate, or the relative standard deviation is used, which is unsuitable and mathematically unstable (sections 3.2.2.1 and section 3.3.4.3.1).

To address these issues and to begin the formulation of a systematic, repeatable experimental approach to package design, a new set of experiments were designed. This involved the forced-air cooling of 9 pallets of Hayward kiwifruit, each in a different configuration. This represented the most extensive look at the empirical performance of a pre-cooling system with large products wrapped in polyliners to date. Rather than designing radically new packages, each experimental iteration represented a change in exactly one parameter, all others being held constant. A desired outcome was quantitative statements about system performance, such as: "an increase (or decrease) in vent size by X% resulted in an increase (or decrease) of Y% in cooling rate and Z% in cooling heterogeneity". In addition to improving future experimental work, this has the potential to guide the development of the mathematical model by highlighting which operational changes have the largest impact on system performance; parameters that are key can be iteratively optimised, while less important parameters can be ignored and held at a constant within an optimization loop. It also provided an opportunity to use the newly developed heterogeneity index (section 3.2) in a comprehensive way, demonstrating its data analysis capabilities.

3.3.2: Objectives

The primary goal was to quantitatively assess the performance impact (cooling rate and cooling heterogeneity) of operational changes on the forced-air cooling of pallets of polylined Hayward kiwifruit. Exactly one change was investigated at a time: increases to pressure drop through the pallet, increases to vent size, decreases to vent size and changes in vent number. Package designs and pressure drops were selected carefully to maximise the number of direct comparisons. This was to establish a systematic experimental framework for investigating the link between system performance and operational settings.

3.3.3: Materials and Methods

3.3.3.1: Laboratory Scale Pre-Cooler

This apparatus was designed and used by previous PhD student Justin O'Sullivan (O'Sullivan, 2016; Figure 3.6). The pre-cooler was situated inside of a large refrigerated room, where the temperature and humidity could be tightly controlled. Essentially, the pre-cooler consisted of three parts:

- A wind tunnel, where the fruit boxes sit, with the same inner dimensions as a standard international shipping pallet (1000×1200mm). The front and back were open, while the sides were solid polycarbonate walls, so that a pressure drop imposed over the wind tunnel would force refrigerated air through the stacked boxes, simulating an industrial pre-cooling process. The wind tunnel was tall enough to allow 5 layers of modular bulk packages – approximately half the size of a standard kiwifruit industry pallet, where 10-12 layers are standard, depending on the type of shipping container. Polystyrene and aluminium foil insulation was attached to the top and sides of each pallet to prevent conductive heat transfer through the sides and top and therefore restrict the predominant mode of heat transfer to forced convection with the refrigerated air forced through the wind tunnel.

- An airflow screen consisting of two metal meshes strung tightly across a metal frame. The purpose of this screen was to better promote a uniform inlet of air into the wind tunnel, so that a similar velocity and refrigerated air temperature is experienced across the front face of the stacked boxes of fruit.
- The variable speed drive (VSD) fan consisting of a funnel at the front, which lined up with the wind tunnel section, so that all three parts could be attached to become air-tight in the direction of the airflow. At the rear was the VSD (AP0502AA5/16, Fantech, Wellington, New Zealand), capable of speeds ranging from 0 – 50 RPS in increments of 0.1 RPS. Pressure drops created by a particular fan speed were measured across the pallet (using a Honeywell SSCDRRN005ND2AA5, USA barometer), and the flowrate through the entire system measured by relating the pressure drop measured across an orifice plate situated just before the fan, to the previously measured system curve (see O'Sullivan, 2016).

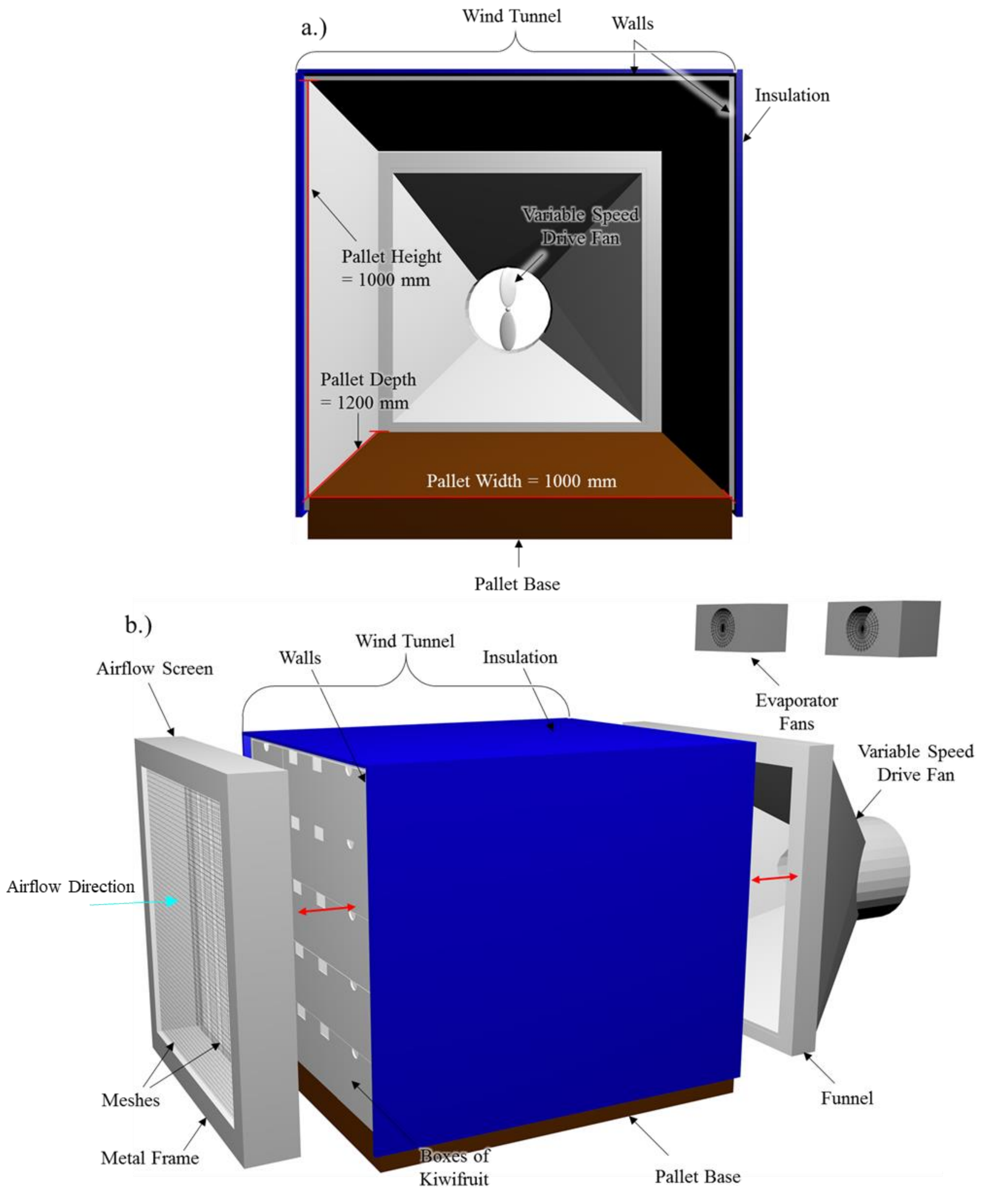

Figure 3.6:The laboratory forced-air cooling tunnel, consisting of an airflow screen, wind tunnel and variable speed drive fan.

3.3.3.2: Temperature Measurement

Pallets of count 36 Hayward kiwifruit were delivered to Massey University by Zespri® International and stored in refrigerated rooms at 0 °C until immediately prior to experimentation. Each trial required 500 kg (50 boxes) of fruit. The fruit was removed from cold storage and packed into the wind tunnel (Figure 3.6). The refrigerated room where the pre-cooler was situated was initially set to 20°C, and the VSD was turned on to force warm air through the pallet to impose a uniform starting temperature on the fruit, and to simulate the field heat. This incubation period lasted for 24 h.

After incubation, the pallet was deconstructed so that temperature logging equipment could be inserted into the pallet to measure cooling. Within the wind tunnel were 5 layers of 10 kiwifruit boxes; these were labelled alphabetically from A-E, from bottom to top (Figure 3.7).

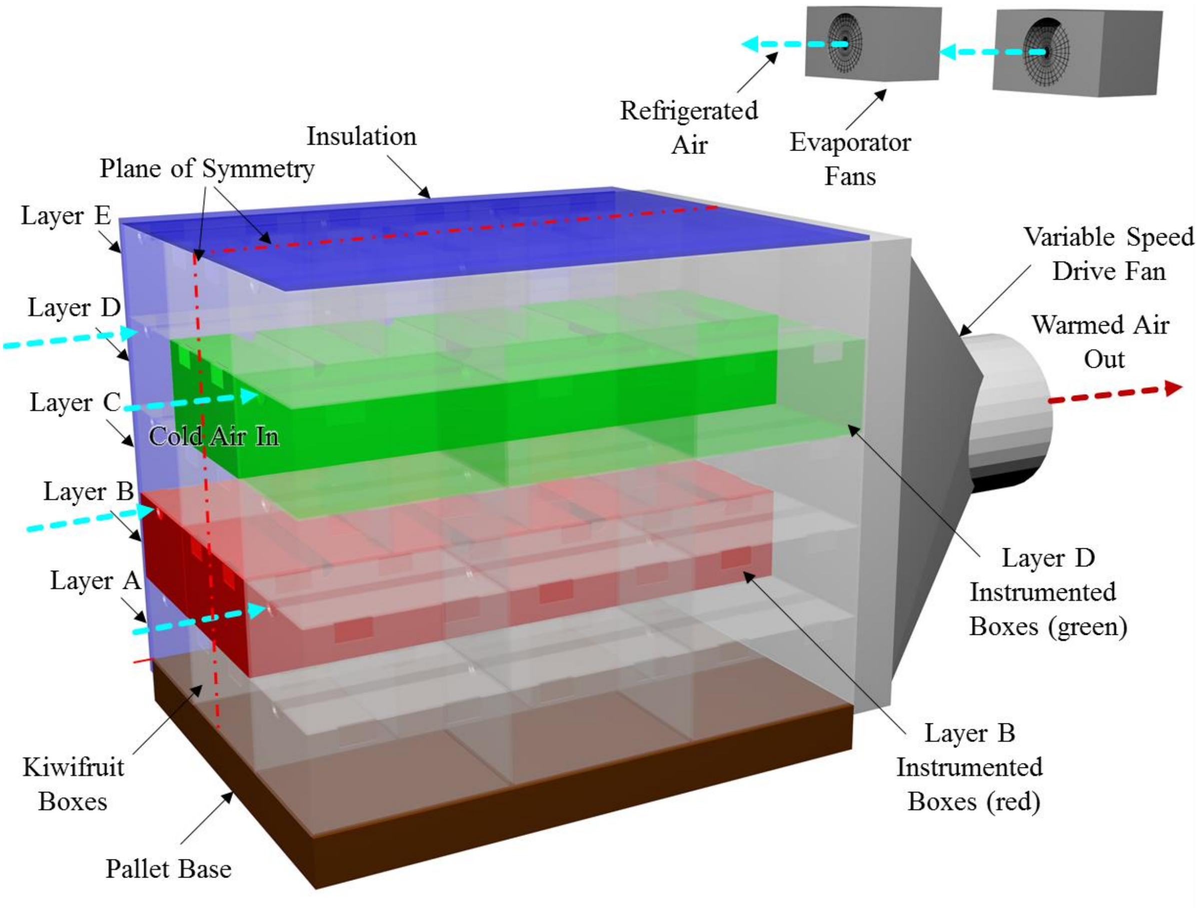

Figure 3.7: Laboratory forced-air cooling tunnel set-up: 50 boxes of kiwifruit stacked into a pallet, connected to a VSD fan. 14 boxes were instrumented: 7 in layer B (highlighted in red) and 7 in layer D (highlighted in green).

Due to the airflow screen, the uniform inlet of refrigerated air and the box stacking pattern, a plane of symmetry was assumed (Figure 3.7). Thus only half of a pallet layer was measured. The highlighted 14 boxes were selected for instrumentation: 7 in row B (Figure 3.7, red), including all 4 boxes in the centre of the pallet and three of the side row boxes on the left, relative to the direction of the inlet airflow; and 7 boxes in row D (Figure 3.7, green), with the middle row and the side row to the right. Layers B and D were selected because they were more representative of the conditions experienced by the majority of boxes within a pallet: the bottom and top layers (layers A and E) have different boundary conditions, such as the bottom of layer A conducting heat to the pallet base, and the top of layer E being insulated.

Kiwifruits were manually stacked into a repeatable pattern, to ensure that a repeatable sample of temperature positions could be recorded in addition to restricting the impact on the cooling rate and heterogeneity to changes in operational settings, rather than an artefact of different random stacking patterns (Figure 3.8).

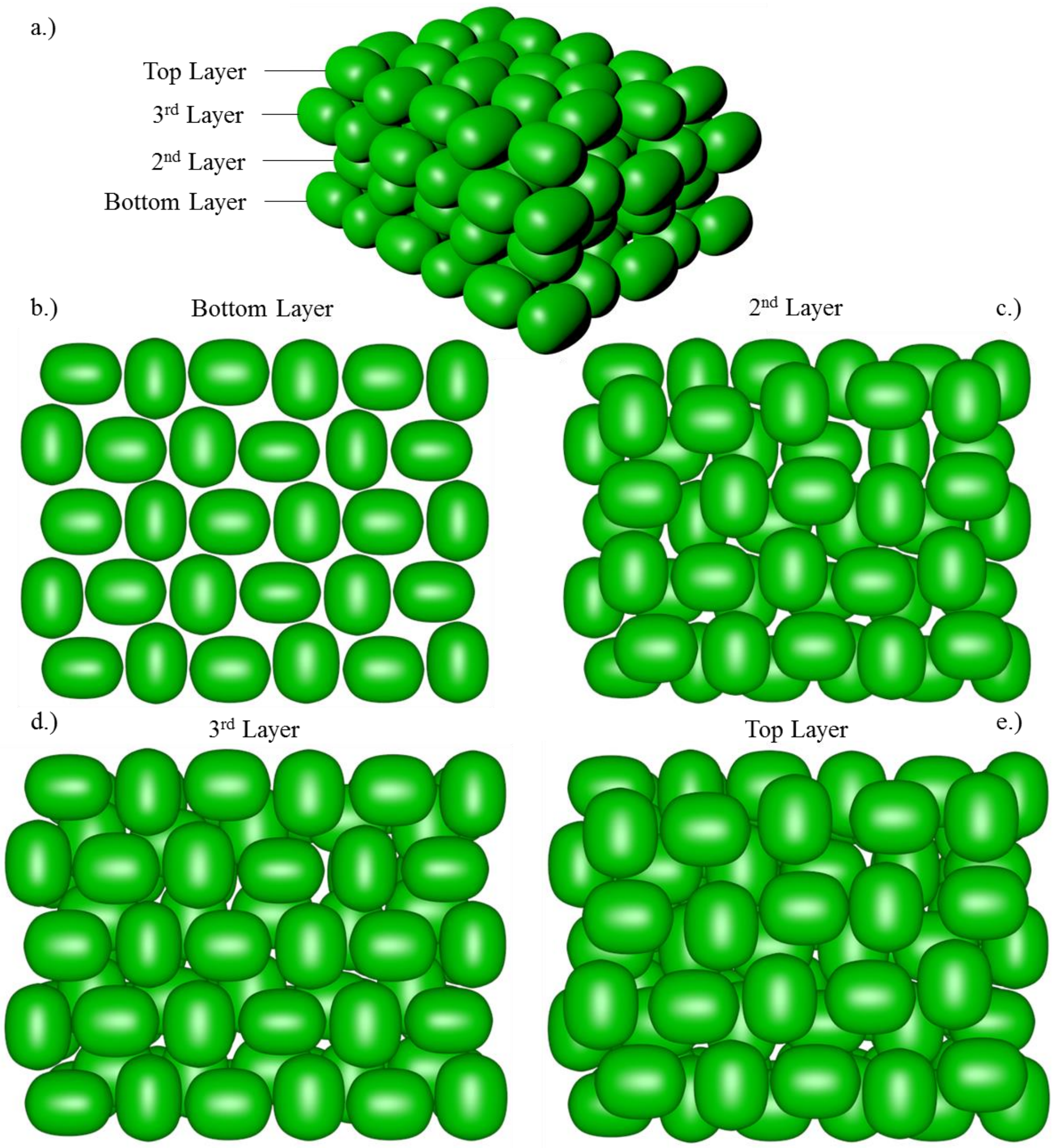

Figure 3.8: Kiwifruit stacked into a repeatable pattern, consisting of 4 distinct layers of fruit, used during all experiments.

The bottom layer (Figure 3.8b) had 30 fruit, stacked in a pattern 5 fruit deep and 6 across, alternating between a portrait and landscape orientation. The next layer had 20 fruit (Figure 3.8c), stacked in a similar pattern but only 4 fruit deep, 5 across, in the recesses formed by the bottom layer. The third layer had 30 fruit again, and mimicked the pattern of the bottom layer (Figure 3.8d). The top layer again mimicked the 2nd layer with 20 fruit, in the recesses of the 3rd layer (Figure 3.8e). This meant that every instrumented box had 100 kiwifruits, 2 less than the standard industry target of 102.

The temperature of fruit within the 14 selected boxes were measured by inserting Type-T thermocouples into the centre of select kiwifruit (Figure 3.9). Thermocouples and thermocouple loggers were tested in an ice bath prior to experimentation, where an acceptable maximum of 0.5 ºC error was observed. A thin metal rod was used to puncture the kiwifruit to the centre of the fruit, after which the thermocouple was inserted. These thermocouples were connected to 64-channel data loggers (1000 Series Squirrel Meter/Logger, Eltek Ltd. Cambridge, UK).

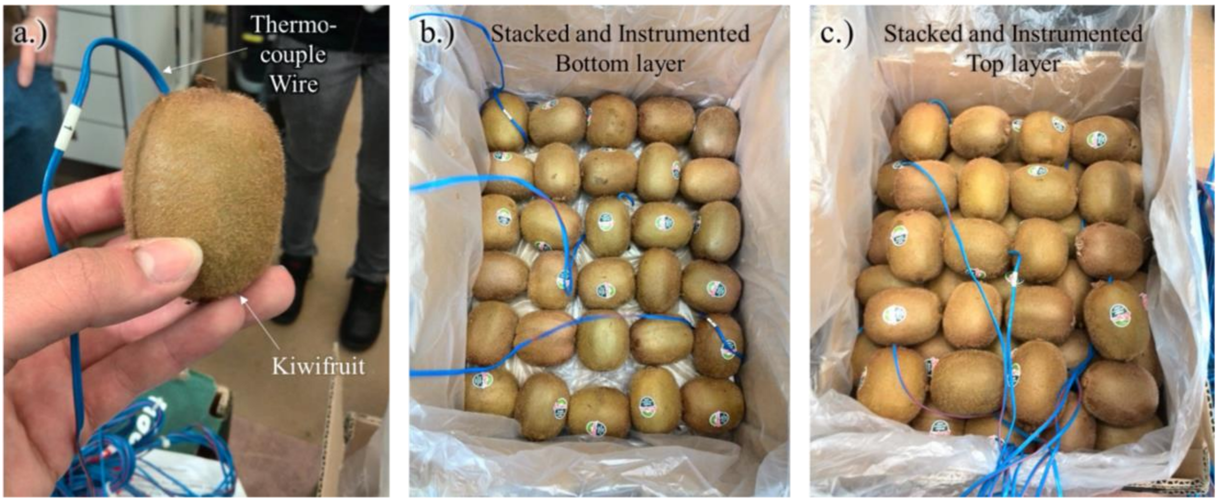

Figure 3.9: Experimental kiwifruit instrumentation: a.) Type-T thermocouples were inserted into the centre of a select number of kiwifruit; b and c.) fruit were stacked into a repeatable pattern to ensure thermocouples were placed in the same position for each trial.

As the objective was to collect information pertaining to both the average rate of cooling as well as the heterogeneity of cooling, a wide spatial sample of fruit were instrumented. Two sampling patterns were selected: a 12% sample size (Figure 3.10a) and a 16% sample size (Figure 3.10b). Each sampling pattern had the same number of instrumented fruit per layer (3 per layer in the 12% sample size, 4 per layer in the 16% sample size). The same sampling pattern was used consistently throughout the pallet of a given experiment, so that a pallet was either wired entirely with a 12% sample size or a 16% sample size.

The refrigerated room was then re-equilibrated from 20°C to 0°C and 80% RH, to simulate the atmospheric conditions of an industrial pre-cooler. The pallet was then reassembled in the wind tunnel, and the wind tunnel was attached to the VSD and airflow screen, the VSD fan turned on. The fan speed was adjusted until the desired pressure drop across the pallet was achieved to simulate a specific fan size in an industrial pre-cooler (see section 3.3.3.3 and 3.3.3.4). Although a typical forced-air cooling process is halted at the SECT (for a kiwifruit pallet, ~12 hours, O'Sullivan *et al*., 2016), each pallet was cooled for a minimum of 20 hours to ensure cooling had reached completion. All temperatures were recorded at one minute intervals.

Refrigeration air temperatures were measured by attaching thermocouples to the inlet vents of each front facing box.

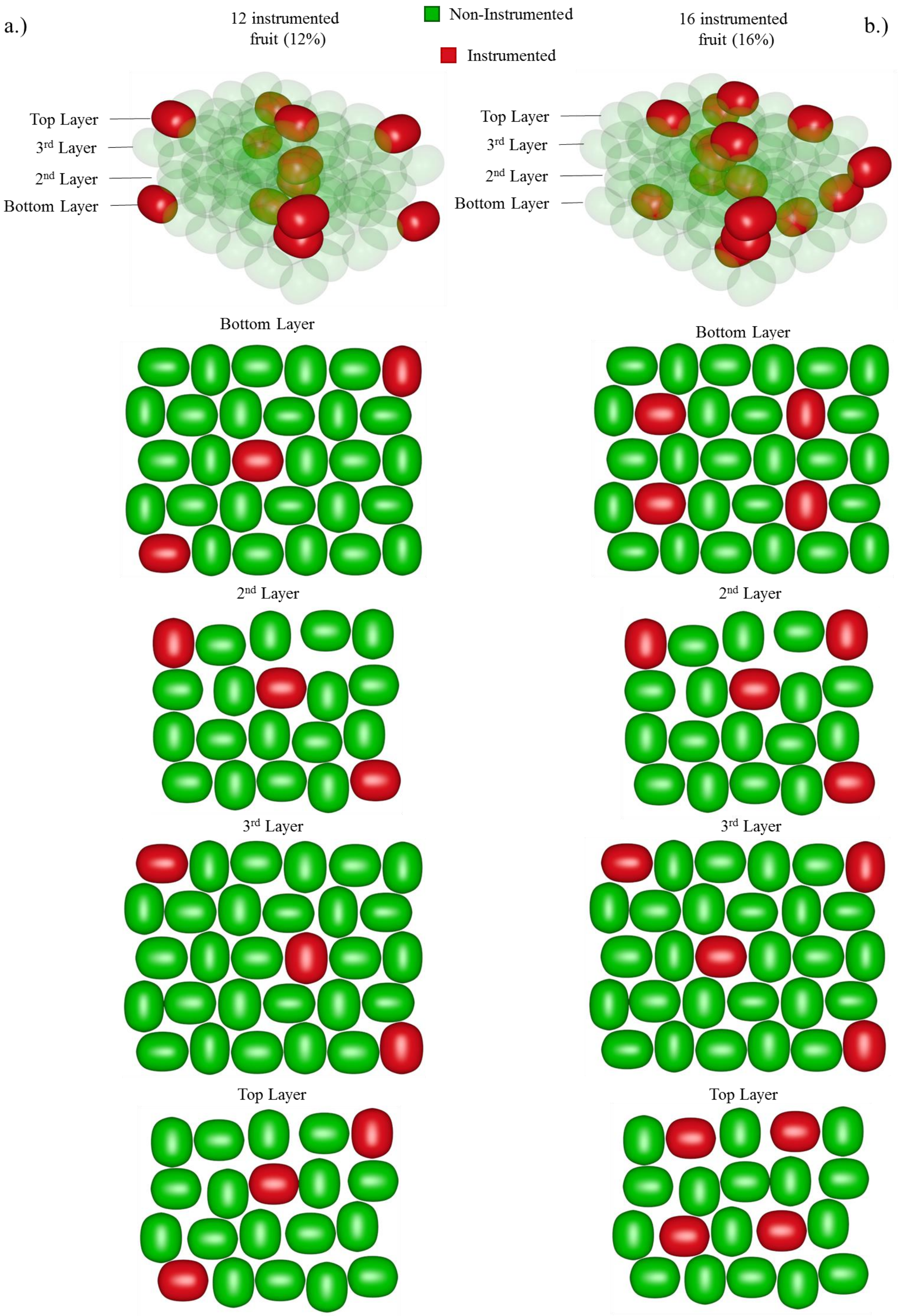

Figure 3.10: Two sample sizes: a.) 12% sample size, and; b.) 16% sample size. Kiwifruit highlighted in red were instrumented with a type-T thermocouple.

Figure 3.11: Photos of experimental equipment: a.) the wind tunnel with kiwifruit boxes half-way through instrumentation; b.) a fully instrumented wind tunnel; c.) the airflow screen being attached to the wind tunnel; d.) the wind tunnel being attached to the VSD.

3.3.3.3: Pressure Measurement

The pressure drop induced by the VSD fan was measured using a barometer (Honeywell SSCDRRN005ND2AA5, USA). There were several locations along the connected pre-cooling simulator where the barometer could be attached with tubing to measure the pressure differential; these are marked in Figure 3.12.

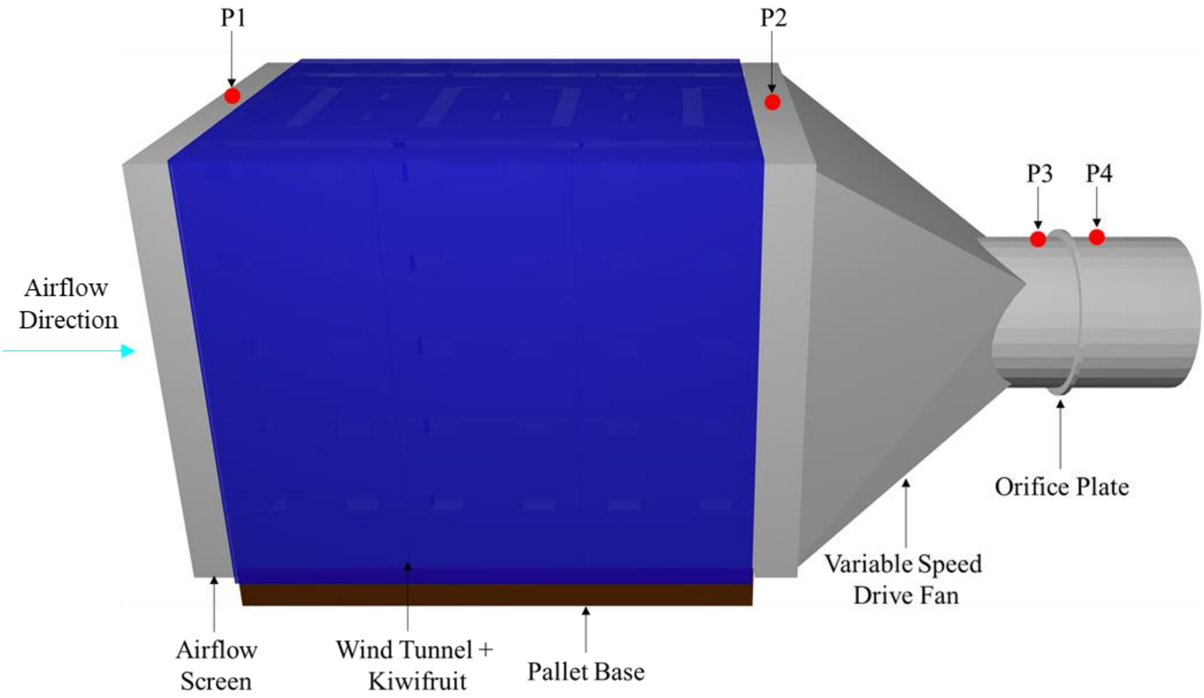

Figure 3.12: Pressure measurement positions in the laboratory tunnel pre-cooler.

The pressure drop across the pallet of fruit was measured by attaching the barometer to P1 and P2: $\Delta P_{pallet} = P2 - P1$. The volumetric flow rate was determined by measuring the pressure drop across the orifice plate, attaching the barometer to P3 and P4: $\Delta P_{orifice} = P4 - P3$. The system curve is measured in O'Sullivan, 2016.

3.3.3.4: Changes in Key Variables Affecting Performance

The cooling rate and cooling uniformity performance impact of three key variables are explored in this study: the pressure drop, and hence the volumetric airflow rate; the opening area of package ventilation (both increases and decreases); and the number of vents.

New box designs were sent to our commercial packaging partner for fabrication. In total, 6 new package designs were drafted, 60 of each delivered to Massey University. Additionally, 180 standard modular bulk packages were fabricated and delivered, enough for three half-pallets to investigate changes in pressure drop with no package design changes. The designs of the new packages, with the dimensions and positions of vents, are shown in Figure 3.13:

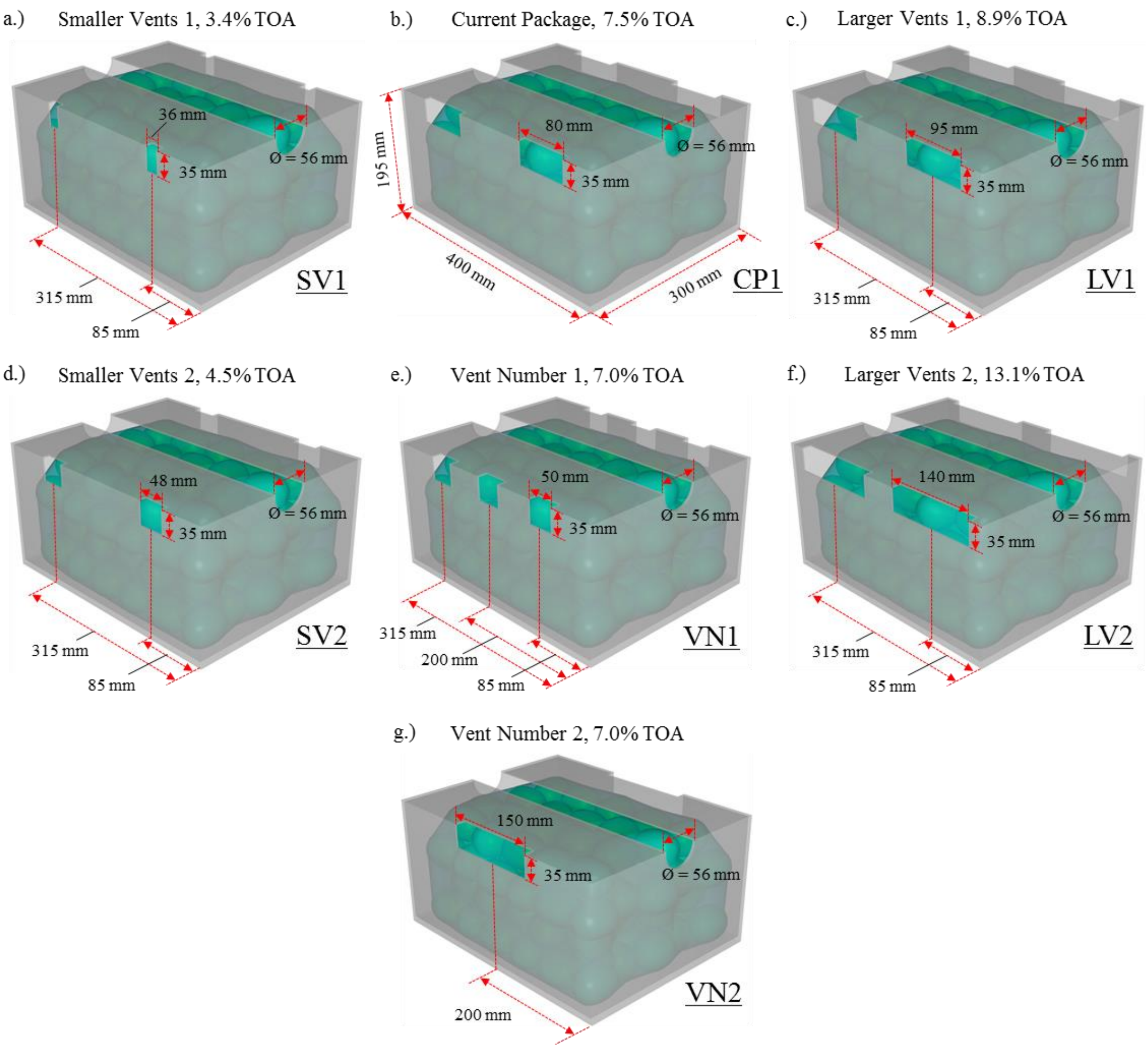

Figure 3.13: Package and ventilation dimensions of the 7 package designs fabricated and tested during this experiment.

The current packaging, a modular bulk package with 2 vents at 7.5% total opening area (TOA) and 130 Pa pressure drop was defined as a 'baseline'. New cooling regimes were an incremental change of exactly one of the investigated variables, producing a total of 9 cooling regimes (Figure 3.14).

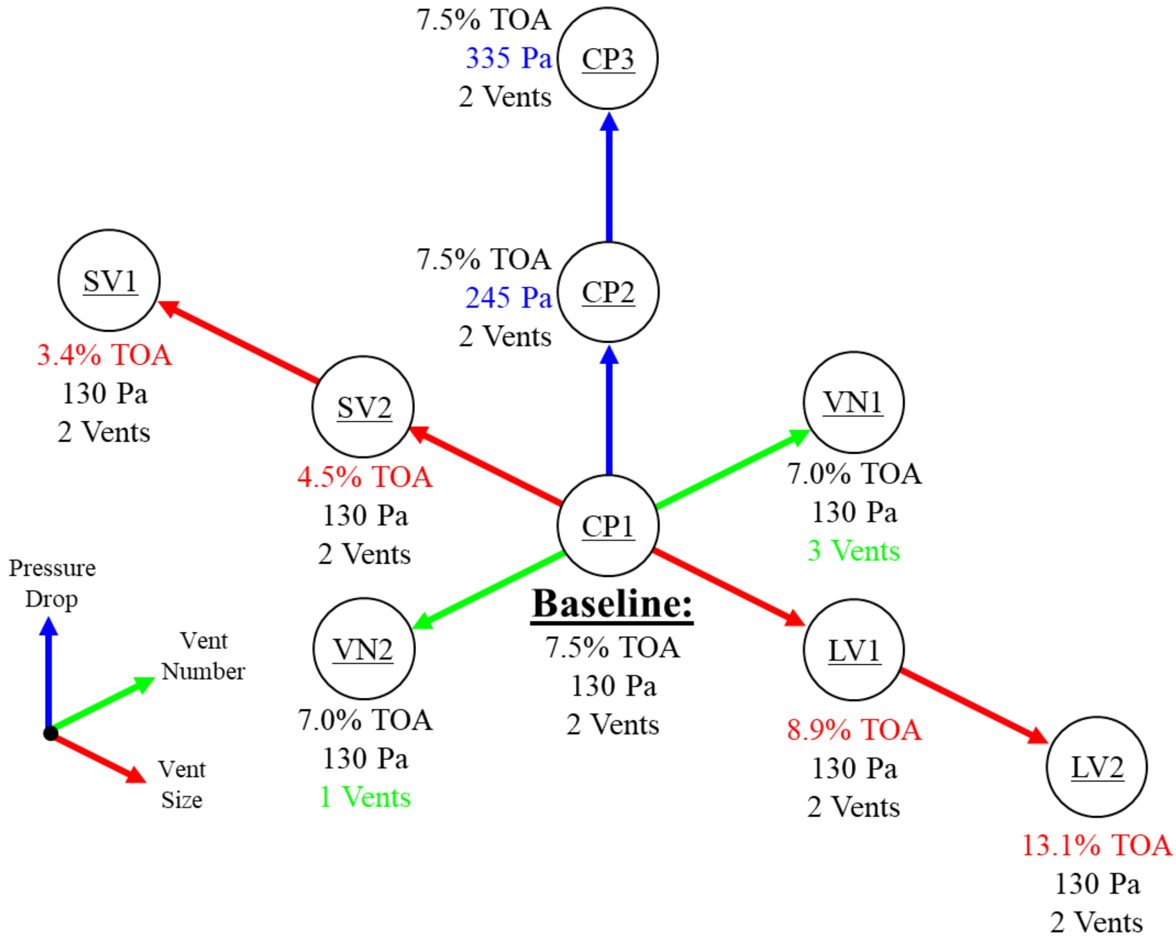

Figure 3.14: The 9 unique operational conditions tested, compared with the baseline package CP1 (7.5% TOA distributed over 2 vents, 130 Pa pressure drop).

The baseline package (Figure 3.13b) was given the label CP1. Changes were restricted to the front-facing vents, so that the side vents had a consistent 2% TOA and were centred on the side face of each box. The alternative packages maintained the height of ventilation, 35mm in all cases, and the central position of both front-facing vents were also maintained. The TOA was therefore altered through amendments to the width of the vents. Two packages had smaller vents (Figure 3.13a and d), labelled SV1 and SV2, with a 3.4% and 4.5% TOA, respectively. Two packages had larger vents (Figure 3.13c and f), labelled LV1 and LV2, with 8.9% and 13.1% TOA, respectively. The two remaining packages were fabricated to investigate the effect of different vent numbers: VN1 and VN2

(Figure 3.13e and g) were designed to have a similar TOA as the seed package, but the opening area was re-distributed to 3 or 1 vent, respectively. The baseline (CP1) had a low pressure drop of 130 Pa. Pallets with elevated pressure drops, 245 Pa and 335 Pa, labelled CP2 and CP3 respectively, were pre-cooled using the same standard modular bulk package as CP1. Subsequently, changes to the package design similarly required that the pressure drop of the baseline experiment be maintained; so for LV1, LV2, SV1, SV2, VN1 and VN2, a 130 Pa pressure drop was imposed.

The specific packages and pressure drops were chosen to allow for a number of direct comparisons. For example, CP1 and LV2 is a doubling of vent size, while CP1 and SV1 is a halving of vent size. Furthermore, VN1 and SV2 have the same vent size but VN1 has 1 additional vent, and LV2 and VN2 has the same vent size with 1 less vent. The remaining comparisons are shown in Figure 3.15. Note: some comparisons stated in Figure 3.15 are not exact, such as CP1 and LV2 being slightly less than double (7.5% versus 13.1%). This is due to the industrial parter being constrained in their manufacturing capability to produce a die with 160 mm wide vents, 140 mm being the nearest acceptable width. This is similar to VN1 and SV2, with a 2 mm difference in vent size and other cases. Exact dimensions are given in Figure 3.13 and Figure 3.14.

Pallets CP1, CP2 and CP3 used a 12% sample size, with 168 temperature positions (Figure 3.10a); while pallets LV1, LV2, SV1, SV2, VN1 and VN2 used a 16% sample size, with 224 temperature positions (Figure 3.10b).

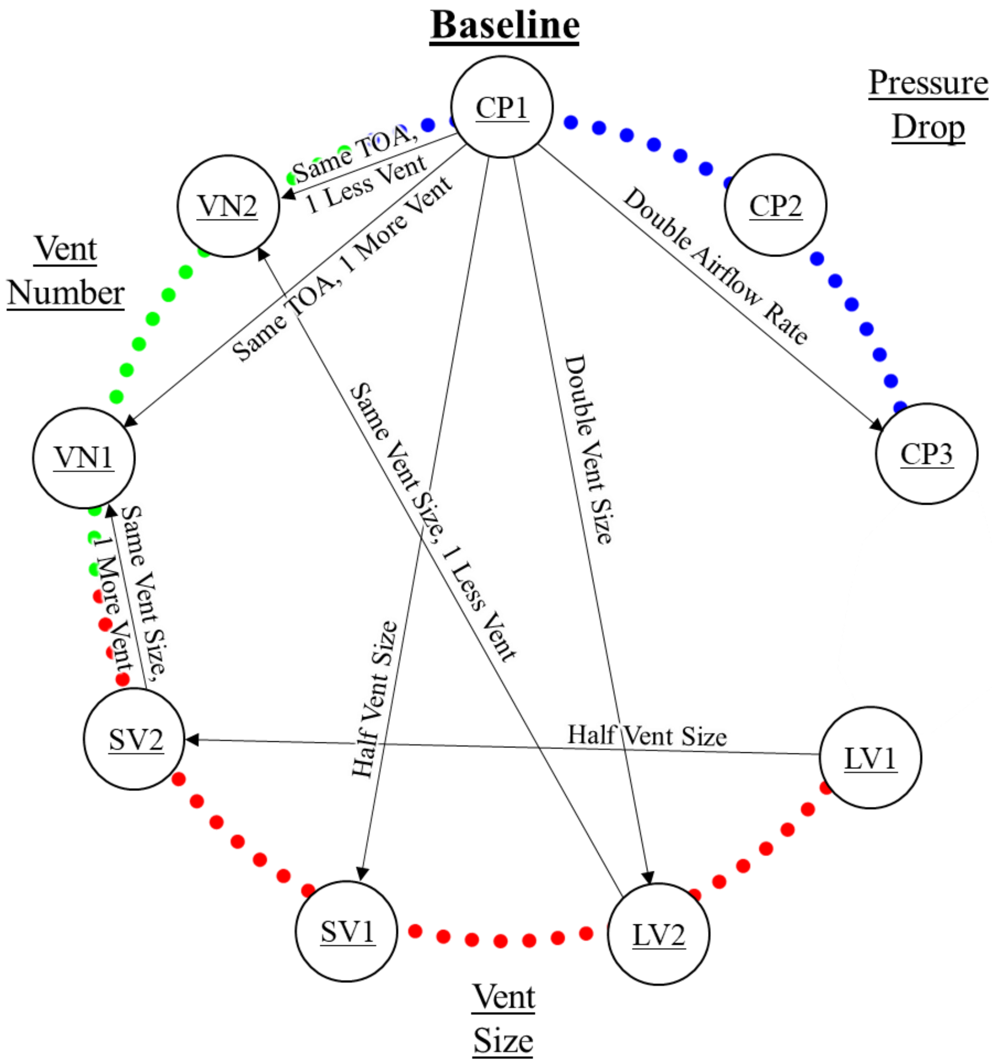

Figure 3.15: A comparison chart, illustrating the direct comparisons between the 9 unique operational conditions.

3.3.4: Results and Discussion

3.3.4.1: Experimental Results

Pallet layers were considered independent so that each pre-cooling trial had two replicates – layer B and layer D (see Figure 3.7). The experimental cooling results for CP1 (see Figure 3.14b) is shown in Figure 3.16. Individual fruit temperatures were plotted over the entire cooling process, displayed as solid yellow, orange and red lines (different colours of solids lines are merely used to better distinguish individual fruit cooling profiles and do not have a physical meaning). The average fruit temperature of the pallet layer (blue dashed line) and refrigerated air temperature (solid light blue line) were overlaid. Important average temperature milestones – the 1/8th cooling time (OECT), $\overline{Y}$ = 0.875; half-cooling time (HCT), $\overline{Y}$ = 0.5; and 7/8th cooling time (SECT), $\overline{Y}$ = 0.125, as calculated from the FUTC using the average air temperature – were marked as dotted lines also. Results from the remaining packages are in appendix A.2.

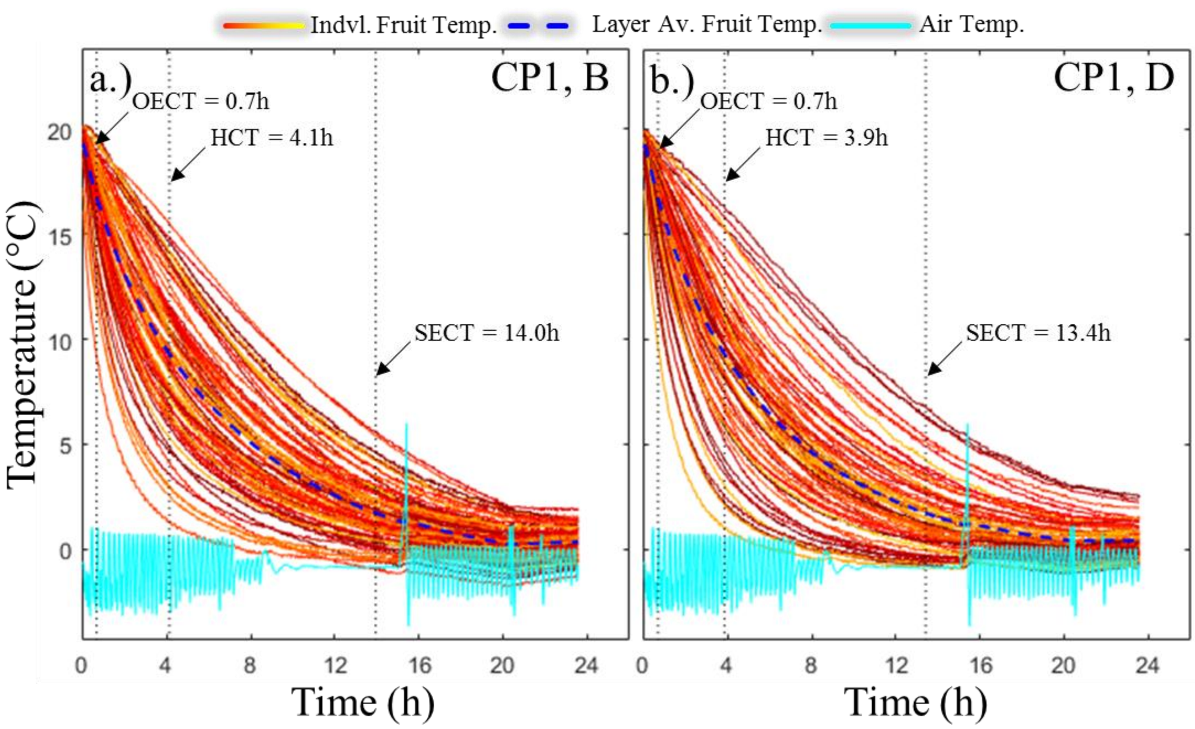

Figure 3.16: Empirical cooling curve for pallet CP1: 2 vents, 7.5% TOA, 130 Pa pressure drop. a.) Layer B, and b.) Layer D.

Overall, these experiments were successful at capturing not only the overall cooling rate of the pallet, but also the temperature variability that occurs during pre-cooling. These cooling curves make it obvious that the pre-cooling of polylined kiwifruit is a highly variable process. In all scenarios there was a small percentage of fruit that reached the refrigeration temperature after only a few hours, while in the same pallet, there is a select few fruit in the 5-10°C range at the pallet average SECT, when the cooling process should be halted. While there were some clear differences between the different operational settings – for example, the cooling profile of CP3 is clearly accelerated compared with CP1 (see appendix A.2) – there were other trends that were less conspicuous, such as the comparative temperature heterogeneity and differences in the shape of the temperature distribution. Minutiae such as these are determined quantitatively later with the tools developed with the new heterogeneity index.

However, before results are discussed, it's important to first comment briefly on some faults that occurred, not atypical for these large scale, large data point trials. Firstly, every experiment experienced at least some data loss, where one or more thermocouples did not record the fruit temperature over the entire cooling duration. Broken wires were repaired after being identified for use in the next experiment, but the problem continued to persist regardless. However, because of the large number of fruit temperature positions recorded (168 or 224 positions, Figure 3.10), individual thermocouple losses did not contribute significantly to error. Additionally, the thermocouple logging equipment appears to have failed in pallet SV1 (see appendix A.2). Numerous instrumented fruit behaved in a non-realistic fashion, with temperatures continuing to decrease, even below the refrigeration temperature. These anomalous fruit were all concentrated in layer B, so that the average cooling rate of SV1B appears to be faster than SV1D – accelerating the SECT by over 4 hours. It is speculated that this was the result of a faulty logger, and a different logger was used for subsequent trials and the error no longer appears. Although SV1B is included in the analysis of cooling rate and heterogeneity, it is marked clearly as an error, and SV1D is instead considered representative of the entire pallet. Another fault to highlight was the cooling of pallet VN2: the cooling process for this pallet was halted at 20 hours, which was not long enough for the entire pallet to reach the SECT. In hindsight, the pallet should have been cooled for 24 hours. This impacted how results are reported later, such as comparisons of SECT and the calculation of the OHI. Due to the fruit and time requirements for each trial, it was not possible to repeat the anomalous trials.

3.3.4.2: Impact on Cooling Rate

All temperatures were converted into their dimensionless equivalent, the fractional unaccomplished temperature change (FUTC, Eq. 3.2). The average FUTC of each pallet layer was then computed (Eq. 3.3) and plotted over time (Figure 3.17). CP1 being the 'seed' experiment can be compared in 4 ways: increased pressure drop (Figure 3.17a), decreased vent size (Figure 3.17b), increased vent size (Figure 3.17c) and the same TOA but distributed over a different number of vents (Figure 3.17d). In the case of VN2, both pallet layers did not reach the SECT, so the SECT is HCT×3; theoretically, the SECT should be 3 times the HCT if there is a perfectly exponentially decaying cooling profile, however in the other cooling scenarios the true SECT is slightly longer than HCT×3, so the estimates for pallet VN2 are likely to be underestimates. Also SV1B should be ignored due to equipment error artificially increasing the cooling rate, per the previous discussion. These special cases are marked with asterisks.

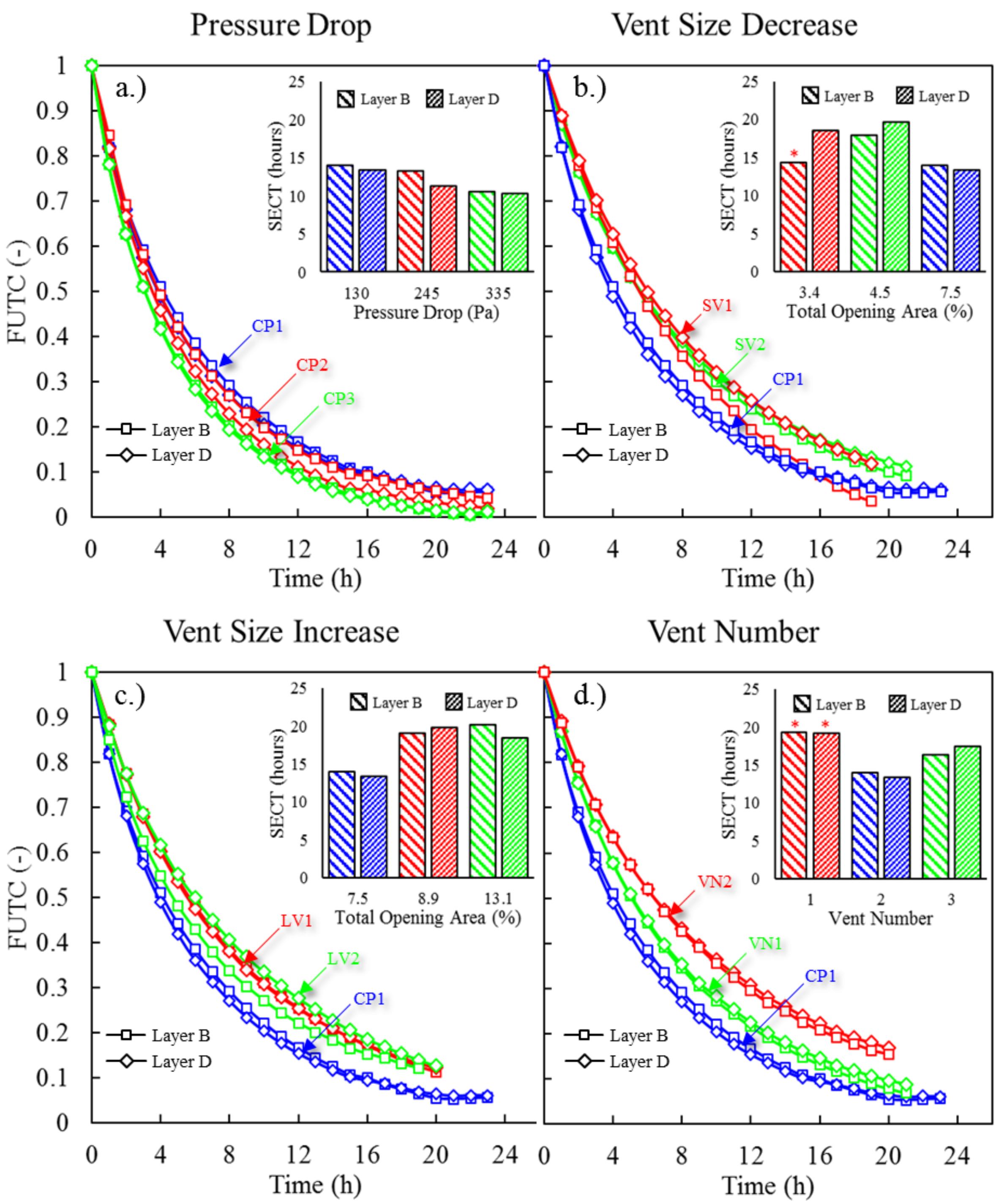

Figure 3.17: Impact on the average pallet cooling rates when: a.) increasing pressure drop; b.) decreasing vent size; c.) increasing vent size, and; d.) redistributing the TOA over a different number of vents. Special cases marked with asterisks; see section 3.3.4.1.

<u>3.3.4.2.1: Cooling Rate Impact of Pressure Drop</u>

Pressure drop appears to have a significant positive impact on the cooling rate. The SECT of CP1 averaged 13.7 h, and using the same package design with an increase in pressure drop by 89% (245 Pa) improved the SECT by 11% on average. Further increasing the pressure drop – an approximate doubling of the volumetric airflow rate from 0.38 $m^3 \cdot s^{-1}$ at 130 Pa to 0.77 $m^3 \cdot s^{-1}$ at 335 Pa – improved the SECT by 27% on average.

Incorporating economic factors such as fan power costs and the number of pallets cooled per unit time offers an opportunity for optimization. According to standard fan relationships (Capehart *et al.,* 2003), the power consumption of a fan increases by 8 times when doubling the velocity; thus CP3 consumes 8.3 times more fan power compared with CP1. Although there is an increase in operational costs, the throughput of pallets per day is improved: CP1 can cool 1.75 pallets per 24-hour period, compared with 2.30 for CP3. It may be beneficial to lower the pressure drop, sacrificing some throughput for a saving in electricity costs. By cooling at the rate of pallet CP2, throughput would drop by only 0.35 fewer pallets per day (1.95 pallets/day or 15% fewer pallets than CP3), while using 42% less fan power than CP3.

3.3.4.2.2: Cooling Rate Impact of Decreasing Vent Size

Decreasing the vent size had a negative impact on the cooling rate. When the TOA was approximately halved, from 7.5% (CP1) to 3.4% (SV1), the SECT worsened to 18.5h, a -38% decline in cooling performance on average. At 4.5% TOA (SV2), there was a performance decline of -37% on average. This provides clear evidence that there must be sufficient ventilation for forced-air cooling to be effective. CP1, SV1 and SV2 would all have consumed the same fan power but the latter cases would harshly penalise throughput.

3.3.4.2.3: Cooling Rate Impact of Increasing Vent Size

Surprisingly, and perhaps counter intuitively, increasing vent size also had a negative impact on the cooling rate, to a similar magnitude as decreases in vent size. An approximate doubling of the TOA, 7.5% (CP1) to 13.1% (LV2) worsened cooling performance by -41% on average. A smaller increase of 8.9% TOA (LV1) performed similarly poorly, an average -42% decline in performance compared with CP1. Both de Castro *et al.* (2004) and Delele *et al.* (2013) suggests that a maximum TOA, after which there are no gains in cooling performance, of approximately 9% TOA. This result would appear to contradict this conclusion, showing that increases to vent size are not merely non-beneficial, but can be detrimental. Upon further inspection, it is speculated that the poor cooling of LV1 and LV2 was an indirect result of poor packaging strength.

This is because the large vents in LV1 and LV2 weakened the front face of the packaging, inducing package bowing (Figure 3.18). A resulting gap can be clearly seen between box layers; the lack of packaging strength creating new and unexpected airflow pathways between the top of one box and the bottom of the next through which air was able to bypass the pallet with little interaction with the fruit, culminating in a slower overall cooling rate. Though packaging strength was not considered in this thesis (section 1.1), this result shows that there is a possible link between strength and cooling performance beyond the obvious need to balance vent design to maximise airflow and minimise loss of strength. A sturdy, rigid package not only protects the fruit from mechanical and vibrational damage, but also presents an impermeable barrier to the incoming airflow, forcing refrigerated air through the package ventilation and over the fruit, preventing alternative pathways.

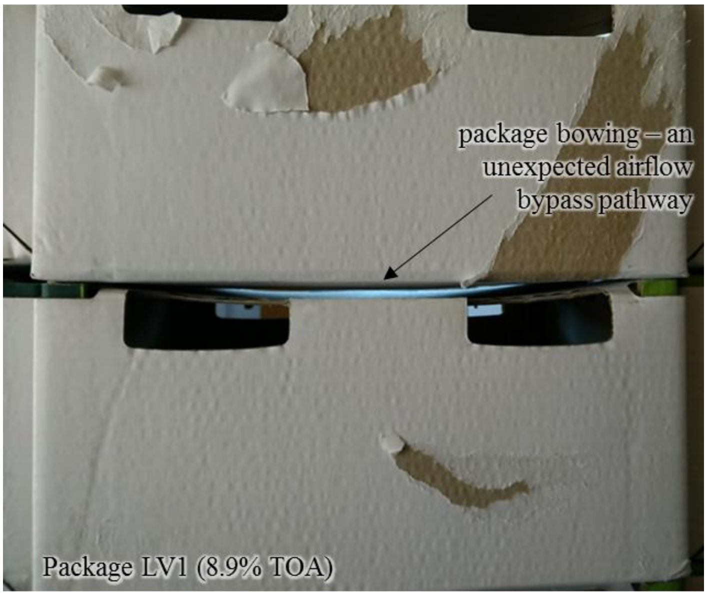

Figure 3.18: Package bowing as a result of weakened packaging, due to increased vent sizes. This created an unexpected airflow bypass pathway. Note that the tears on the packages are just superficial damage to the surface as a result of handling and thermocouple attachment. This does not represent structural damage.

3.3.4.2.4: Cooling Rate Impact of Changing Vent Number

Redistributing the same (or similar) TOA over a different number of vents had a negative impact on the cooling rate; however, the decline in performance was greater for a single vent, with an average drop of -41% (comparing VN2 with CP1); while three vents only penalized performance by -23% on average (comparing VN1 with CP1). This suggests there is more to cooling performance than just the total opening area, and that the number of vents can also play a role.

VN1 (Figure 3.13e) had the same individual vent size as SV2 (Figure 3.13d), but with an additional vent in the centre of the package. The airflow restriction that occurred in pallet SV2 (Figure 3.17; section 3.3.4.2.2) appears to also occur in pallet VN1, but with the additional vent, the penalty for such a restriction is somewhat mitigated. VN2 (Figure 3.13g) was the worst performing design of the entire set, even though it has the same or similar TOA as CP1 and VN1; and had a similar individual vent size as LV2 (13.1% TOA, 2 vents).

This indicates that multiple openings are preferred for a well-designed box, where two or three vents encourage airflow mixing and improves the interaction between fruit and the refrigerated airflow.

3.3.4.3: Impact on Heterogeneity

3.3.4.3.1: Shortcomings of the Relative Standard Deviation

To justify the need for the new heterogeneity index (section 3.2), the shortcomings of the previously used heterogeneity metric is first demonstrated by applying the relative standard deviation (Eq. 3.1) to pallets CP1 and CP3 (Figure 3.19). The general heterogeneity trends discussed previously in section 3.2.2.2 and section 3.2.3.2.1 are not reflected when using the relative standard deviation with °C as the temperature unit (Figure 3.19a). Instead, heterogeneity is calculated to increase constantly over time, contrary to what occurs in reality, and in fact becomes mathematically unstable toward the end of the cooling process. This is due to the average fruit temperature approaching the refrigeration temperature of 0 ºC, which artificially inflates the heterogeneity metric toward infinity – vertical bands appear on Figure 3.19a because $\bar{T}$ fluctuates between positive and negative numbers very close to zero near the process end time.

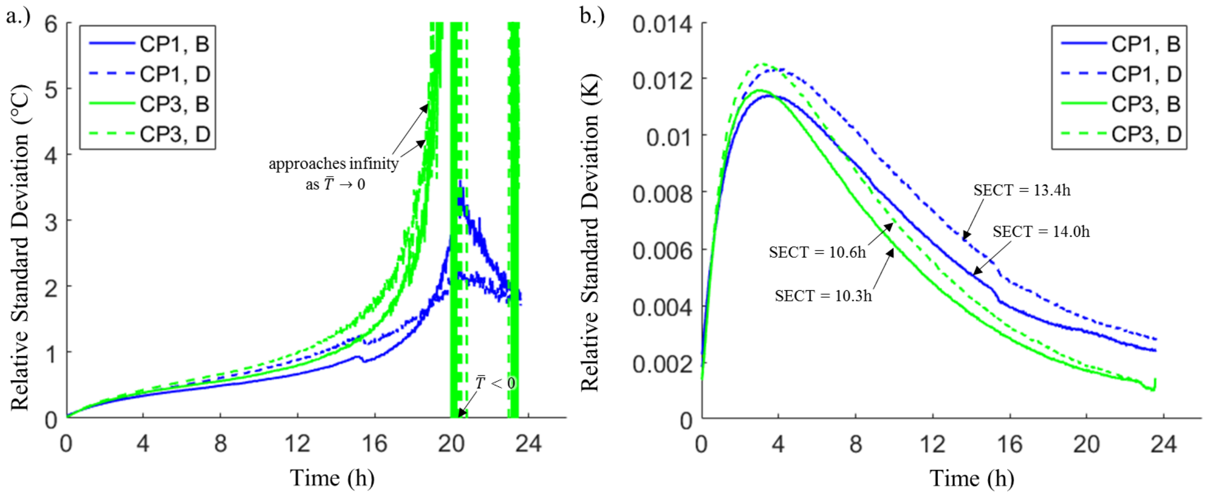

Figure 3.19: Heterogeneity analysis of pallets CP1 (green) and CP3 (blue) using the relative standard deviation, the previously used heterogeneity metric. The heterogeneity trends are not accurate due to mathematical instability in the case of a.) °C, and artefacts of the difference in overall pallet cooling rate in case of b.) K.

This problem is solvable by using Kelvin (K) instead of Celsius (ºC) as the temperature unit, as shown in Figure 3.19b. The expected trends with respect to the initial and final heterogeneity appear in this case, but a new potential problem arises if systems are compared at absolute times (section 3.2.2.2): in Figure 3.19b CP3 appears to be cooling in a more uniform manner. In reality, this is an artefact of the accelerated cooling rate, showcasing the need to compare different cooling operations using a characteristic index of process progression ($\bar{Y}$ or τ) in order to compare different processes that have achieved the same amount of cooling.

Furthermore, the relative standard deviation masks any differences there may be in the shape of the distribution of temperatures. This is demonstrated by plotting histograms of FUTC values of pallet CP1 and CP3 (data from both layers were combined for this example) at key cooling progression stages (Figure 3.20):

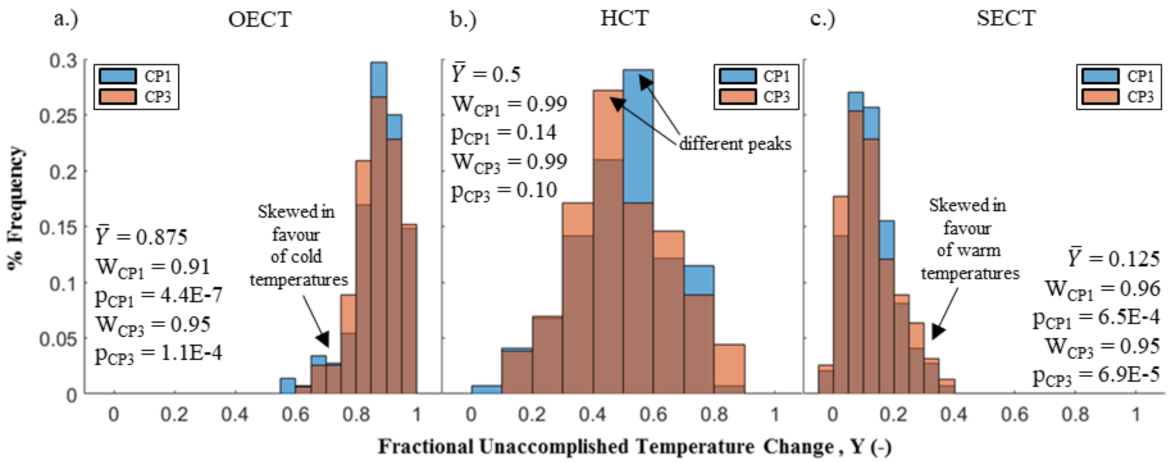

Figure 3.20: Temperature distributions from pallet CP1 (orange bars) and CP3 (blue bars) at a.) $\bar{Y}$ = 0.875; b.) $\bar{Y}$ = 0.5 and c.) $\bar{Y}$ = 0.125. W = Shapiro-Wilks test statistic, p = p-value.

These histograms reveal that at the OECT (Figure 3.20a), the temperature distribution is skewed heavily, as a proportion of fruit have cooled disproportionately faster than the average rate from being in preferential locations with respect to the incoming cold airflow. These fruit that are cooling disproportionately quickly will be potentially more likely to develop chilling injury, and a pallet with a larger degree of negative skewness at the beginning of the cooling process is more likely to have a greater number of fruit develop the condition. The level of skewness appears to have decreased at the HCT (Figure 3.20b), so that there is a more equitable spread of hot and cold spots throughout the pallet. At the SECT (Figure 3.20c), skewness had returned but in the opposite direction, there being a proportion of fruit that had lagged behind the average cooling rate due to being shielded from the flow of refrigerated air, such as fruit stacked into the centre of the box. As this is the stage at which the cooling process is halted and the pallets are moved into cold storage, any warm spots are expected to persist for an extended period of time as the cooling rate in a room cooling situation is significantly slower (Boyette *et al.*, 1989). Thus, pallets with a greater degree of positive skewness at the end of the cooling process is more likely to have fruit losses from senescence.

These observations were further supported with Shapiro-Wilks tests (Shapiro and Wilk, 1965), where only the temperature distribution at the HCT can be considered normally distributed. These plots also reveal that even at the same average temperature there are differences between temperature distributions. Though the mean is identical at the HCT (Figure 3.20b), the *mode*, or peak in the distribution, is disparate, with CP3 having a peak shifted toward colder temperatures. Additionally, at the SECT, pallet CP3 has a higher percentage of fruit that are warmer than average (Figure 3.20c). These minute details are lost when using the relative standard deviation, but can be accounted for quantitatively with the new heterogeneity index by fitting SN distributions to these empirical distributions and reporting and comparing the shape (α), scale (ω) and location (ξ) values at certain cooling stages for each pallet.

3.3.4.3.2: Application of the New Heterogeneity Index

$\bar{Y}$ was deemed an appropriate process progression index as there were no discontinuities in cooling (section 3.2.2.2). Heterogeneity plots, qualitative charts that show temperature variability that are dimensionless in terms of time and temperature (see section 3.2.3.2.1) are shown for CP1, CP2 and CP3 (Figure 3.21). Heterogeneity plots for the remaining pallets are in appendix A.3. These empirical heterogeneity plots correctly reflect the expected heterogeneity behaviour over time from the theoretical plots described in section 3.2.3.2.1 (Figure 3.2). The characteristic ‘eye’ shape is clearly reflected and the skewness over time behaviour is apparent by the absence of longitudinal symmetry – similar to the hypothetical system C (Figure 3.2c), where there is a higher proportion of cold temperatures at the beginning of a cooling process and then a higher proportion of hotter temperatures near the end. Despite the large increases in pressure drop from CP1 to CP3 (Figure 3.21a - b versus Figure 3.21e - f), the levels of heterogeneity are largely similar. These visual trends are quantified later in this section.

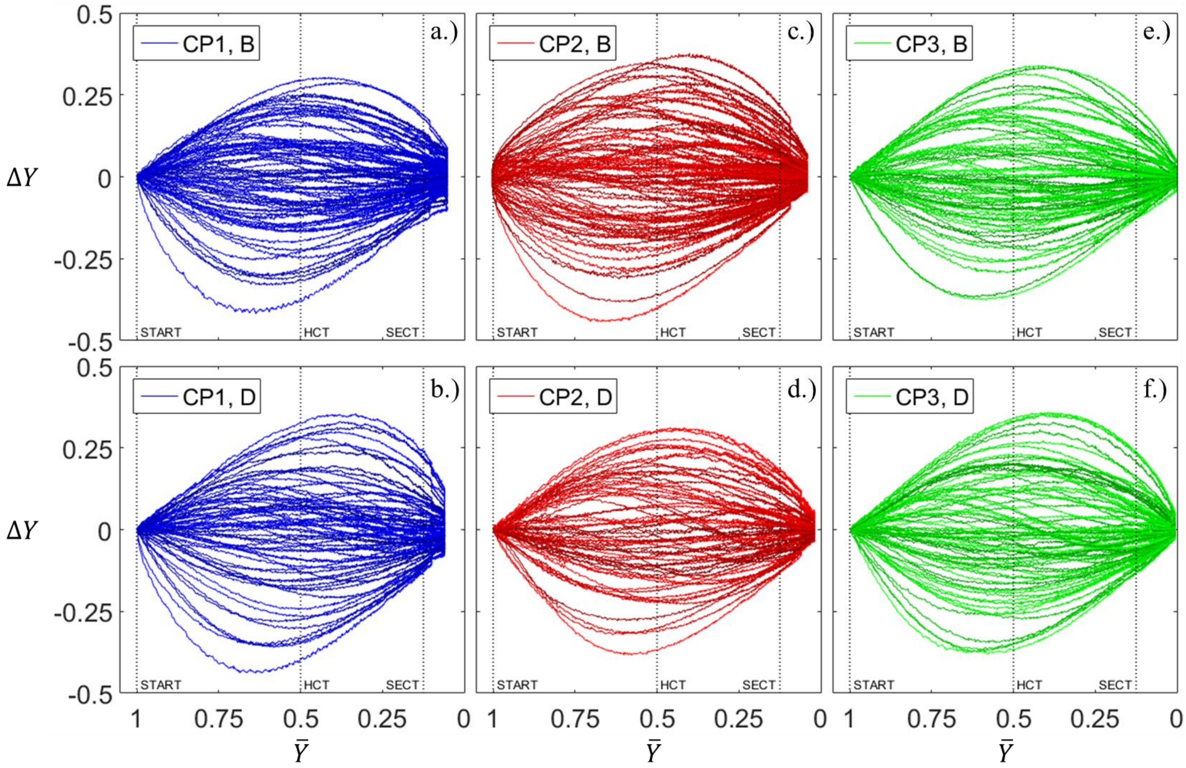

Figure 3.21: Experimental heterogeneity plots for pallets a.) and b.) CP1; c.) and d.) CP2 and e.) and f.) CP3.

The heterogeneity of the entire cooling process is represented by the overall heterogeneity index, OHI (Eq. 3.10). The OHI for each pallet layer are presented in Figure 3.22.* Heterogeneity maps for each pallet and pallet layer (see section 3.2.3.2.2) from which OHI is derived can be seen in appendix A.4.

The OHI does not have information pertaining to the *shape* of the temperature distribution, nor how it changes over time. Therefore, a representative SN distribution was fitted to the empirical temperature distribution for every pallet layer at 8 cooling stages ($\bar{Y}$ = 1, 0.875, 0.75, 0.625, 0.5, 0.375, 0.25 and 0.125) to obtain the shape (α), scale (ω) and location (ξ) values of each representative distribution (Figure 3.23 – Figure 3.26). Distributions were fitted using least-squared non-linear regression and validated with Kolmogorov-Smirnov tests (Pons, 2014), where $p \gg 0.05$ in all cases (see appendix A.5). The end of the cooling process is an especially important cooling stage, as the temperature distribution

* The OHI value for SV1B should be ignored as there was equipment error during this trial. Also, VN2 did not reach the SECT before the experiment was halted, which Eq. (3.10 relies on to compute a fair OHI. VN2B was ceased at $\bar{Y}$ = 0.1674, and VN2D at $\bar{Y}$ = 0.1553; a special OHI was computed for these cases using these end values. Error bars of 5.1% and 3.6% were added to approximate the true OHI if the pallet had been allowed to cool until $\bar{Y}$ = 0.125. These special cases are marked with asterisks.

at that time will likely persist for a long period of time when the pallet is moved into cold storage (Table 3.1).

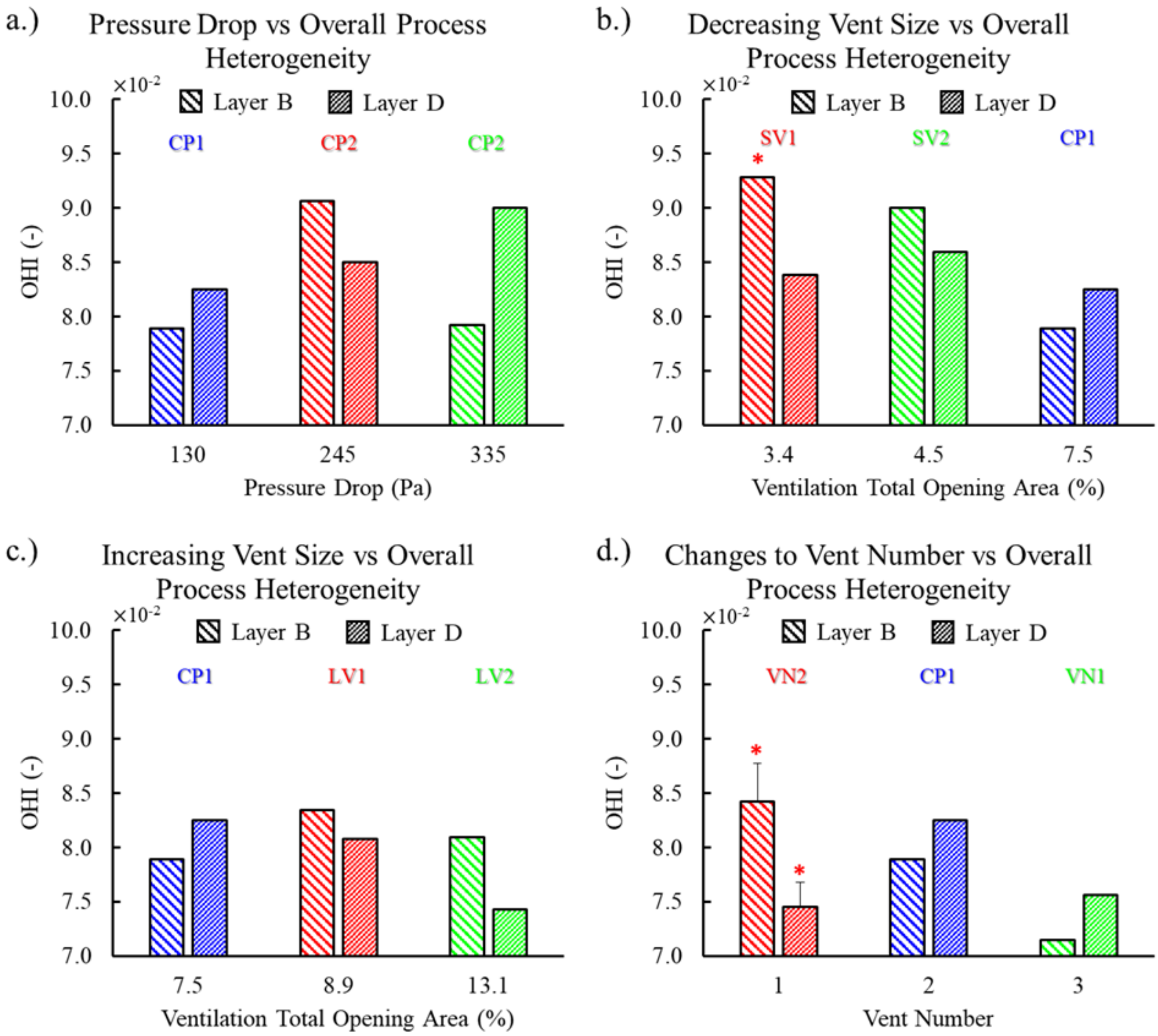

Figure 3.22: Total process heterogeneities, represented by the overall heterogeneity index (OHI), comparing a.) changes in pressure drop; b.) decreases to vent size; c.) increases to vent size, and; d.) the same TOA distributed over a different number of vents.

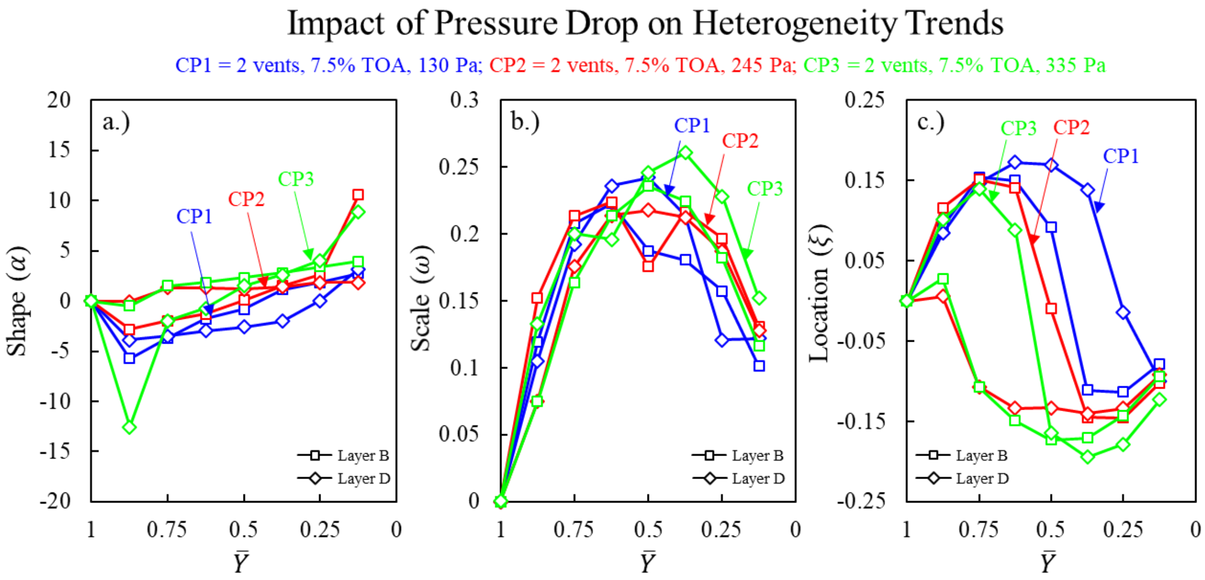

Figure 3.23: Differences in the distribution of temperatures, expressed by representative shape (α), scale (ω) and location (ξ) values, when the pressure drop is increased: pallets CP1, CP2 and CP3.

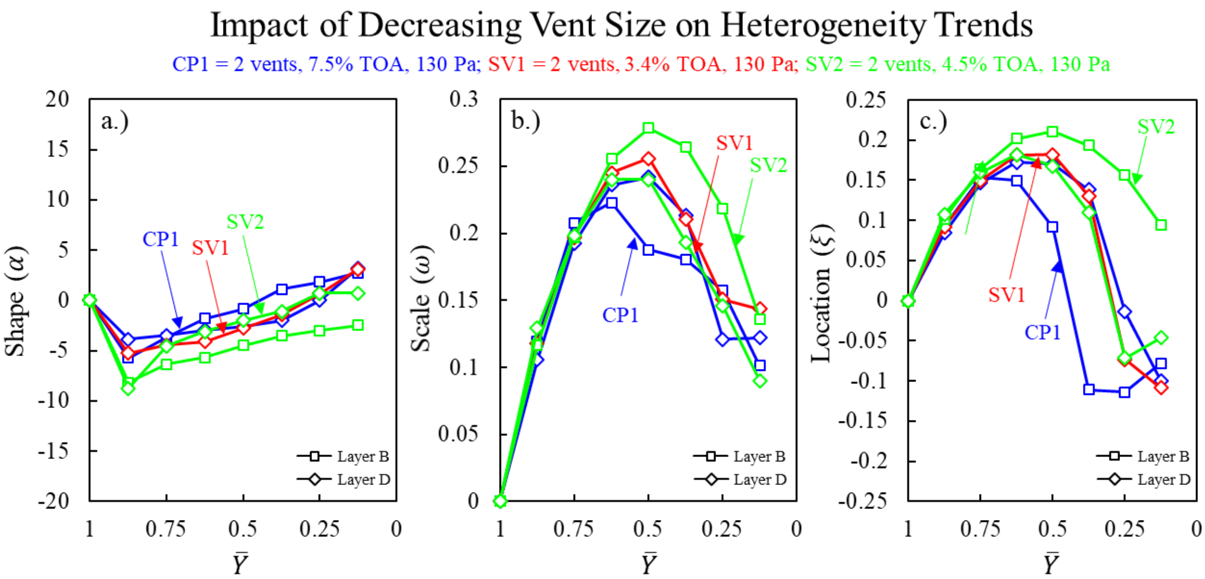

Figure 3.24: Differences in the distribution of temperatures, as expressed by representative shape (α), scale (ω) and location (ξ) values, when the size of vents was decreased: pallets CP1, SV1 and SV2.

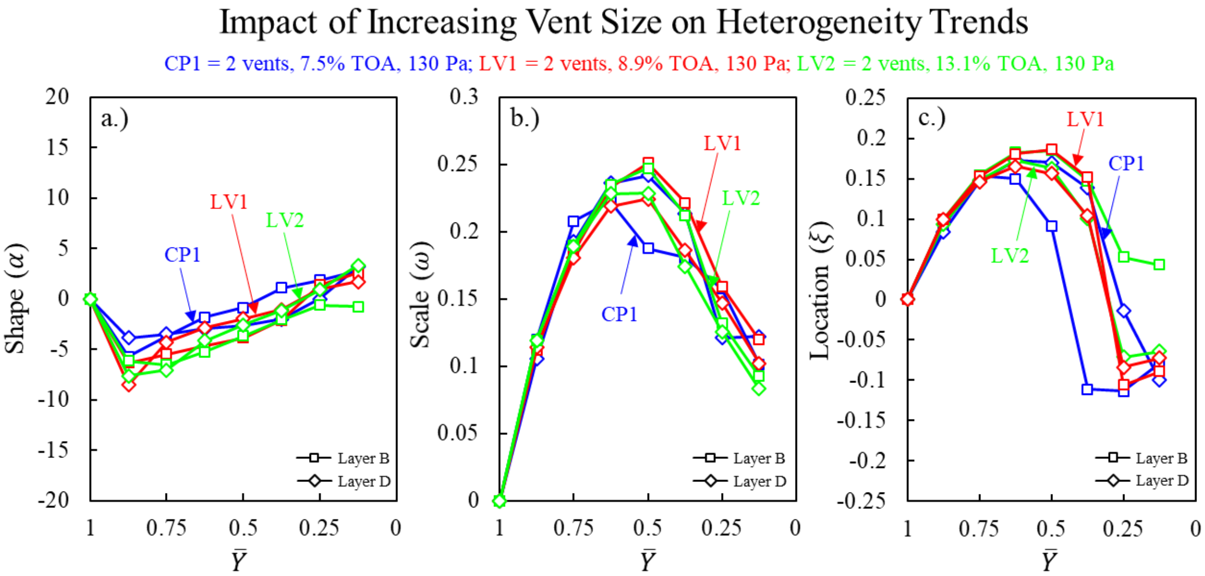

Figure 3.25: Differences in the distribution of temperatures, as expressed by representative shape (α), scale (ω) and location (ξ) values, when the size of vents was increased: pallets CP1, LV1 and LV2.

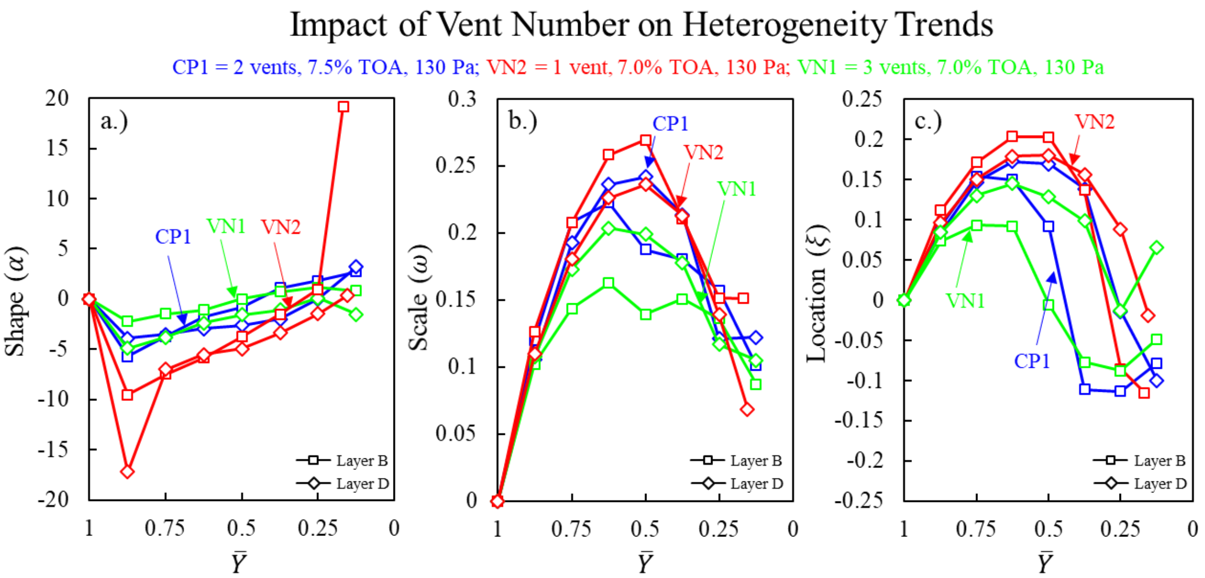

Figure 3.26: Differences in the distribution of temperatures, as expressed by representative shape (α), scale (ω) and location (ξ) values, when the same TOA is distributed over a different number of vents: pallets CP1, VN1 and VN2.

		SN Distribution at SECT		
Pallet	**Pallet Layer**	**Shape (α)**	**Scale (ω)**	**Location (ξ)**
CP1	B	2.74	0.101	-0.078
	D	3.19	0.122	-0.100
CP2	B	10.58	0.131	-0.102
	D	1.85	0.128	-0.092
CP3	B	3.96	0.116	-0.094
	D	8.90	0.152	-0.123
VN1	B	0.85	0.087	-0.048
	D	-1.52	0.105	0.066
VN2	B*	19.17	0.151	-0.115
	D**	0.33	0.068	-0.019
SV1	B	0.91	0.163	-0.090
	D	3.13	0.144	-0.109
SV2	B	-2.50	0.136	0.095
	D	0.74	0.090	-0.046
LV1	B	2.59	0.120	-0.089
	D	1.73	0.102	-0.072
LV2	B	-0.76	0.092	0.043
	D	3.33	0.083	-0.064

Table 3.1: Shape of the temperature distribution at the end of the cooling process (SECT), as representative shape (α), scale (ω) and location (ξ) values.

3.3.4.3.3: Heterogeneity Impact of Pressure Drop

The 'baseline' pallet, CP1, with a pressure drop of 130 Pa, had an average OHI of 0.0807 (Figure 3.22a).

Increasing the pressure drop had a negative impact on the cooling heterogeneity: an increase of 89% in

* $\bar{Y}$ = 0.1674
** $\bar{Y}$ = 0.1553

the pressure drop for pallet CP2 worsened the OHI by -9%. Increasing the pressure drop to double the volumetric flowrate of pallet CP1, pallet CP3 also resulted in more heterogeneity, but to a lesser degree: -4.7% on average.

More is revealed when observing how the shape of the temperature distribution changes over the cooling process (Figure 3.23). All pallets followed a general trend of being skewed negatively near the beginning of the process and positively at the end; however CP3D showed extremes of this behaviour, with a shape value of α = -12.5 at the OECT and α = 10.58 at the SECT (Figure 3.23a). This pallet is therefore likely to be more susceptible to chilling injury with a large proportion of fruit cooling very rapidly at the start of the process, and a higher degree of fruit softening from senescence as the pallet ends cooling with a larger proportion of warm fruit. The scale values (ω) – analogous to the standard deviation – are also generally higher at the SECT for accelerated airflow rates (Table 3.1), indicating a greater degree of temperature variability at the process end time.

Overall, increasing the pressure drop is detrimental to system performance, from a heterogeneity perspective. Optimization could come from lowering the pressure drop, sacrificing throughput (less pallets per day) to achieve a more uniform cooling profile, which could be beneficial from a product losses stand-point (more $ per pallet); also note that in a facility total throughput could be maintained by increasing the number of pre-coolers in operation. To establish such an optimization, the link between heterogeneity metrics such as the OHI, scale, shape and location values and the degree of product losses from chilling injury and/or senescence should be investigated further, though it is not in this thesis.

3.3.4.3.4: Heterogeneity Impact of Decreasing Vent Size

Decreasing vent size appears to have a negative impact on heterogeneity. Halving the vent size to 3.4% TOA worsened the OHI by -1.5% (Figure 3.22b), whereas total heterogeneity worsened at 4.5% TOA (SV2) by -9% on average compared to the baseline CP1. Both pallets SV1 and SV2 showed negative skewness over time behaviour that was greater than CP1 (Figure 3.24a), so that there may be more fruit with chilling injury from these pallets. Negative skewness persisted even to the process end time, where

SV2B had a shape value of α = -2.50 at the SECT (Table 3.1). This indicates a plurality of *colder* temperatures when the pallet is moved into cold storage, potentially reducing the degree of degradation due to senescence.

Reducing vent size is not recommended for Hayward kiwifruit – it has a negative impact on both the cooling rate (section 3.3.4.2.2) and the heterogeneity, and may promote chilling injury. For an alternative crop that is resilient to chilling injury and more susceptible to senescence, it may be beneficial to reduce vent size.

3.3.4.3.5: Heterogeneity Impact of Increasing Vent Size

Increasing vent size had an indeterminate impact on heterogeneity – better in some cases, worse in others. Increasing TOA to 8.9% (LV1) worsened the OHI by -2% on average compared to the baseline package (CP1); while increasing vent size further to 13.1% TOA improved heterogeneity by +4.5% on average compared to CP1 (Figure 3.22c).

Both larger vent designs showed a more negatively skewed temperature distribution (Figure 3.25a), indicating there may be slightly more chilling injury in these pallets. LV2 ended up with slight improvements to the scale value at the SECT (Figure 3.25b; Table 3.1), indicating the pallets are better suited for long-term cold storage. Generally, increasing vent size had a trivial impact on the heterogeneity. This may be due in part to the package strength failure issue discussed previously (section 3.3.4.2.3).

3.3.4.3.6: Heterogeneity Impact of Changing Vent Number

Ceasing cooling at 20 hours meant that VN2 did not reach the SECT, so that a fair OHI cannot be computed. However, estimates of 0.0885 and 0.0772 were computed using $\bar{Y}$ = 0.1674 and 0.1553 as the end point, and with 5.1% and 3.6% added to estimate the missing information (Figure 3.22d)

VN2, with 7.0% TOA but only a single vent, saw a small average decline of -3% in heterogeneity performance compared with CP1. This same 7.0% TOA but distributed over three vents (VN1) saw a marked improvement in heterogeneity of +8.5% on average compared with CP1.

Looking at heterogeneity trends, VN2 showed extreme skewness over time behaviour (Figure 3.26a) with a sharp decline into negative shape values at the OECT and then later a sharp increase into positive shape values as cooling progressed toward the SECT. The pallet may therefore promote more chilling injury *and* senescence degradation in cold storage, both contributing factors towards product losses. Conversely, VN1 showed very minor skewness over time behaviour, with less negative shape values at the OECT and near 0 or negative shape values at the SECT, beneficial for the minimisation of both chilling injury and senescence (Figure 3.26a; Table 3.1).

More vents are therefore clearly superior to less vents at the same TOA, showing improved heterogeneity and mitigation of skewness over time behaviour that can negatively impact product quality. This coupled with the superior cooling rate of VN1 over VN2 (section 3.3.4.2.4) further supports that it is preferable to have more ventilation openings. This aligns with the findings of Dehghannya *et al.,* 2011.

3.3.5: Conclusions

This section sought to develop a systematic experimental approach to package design for the forced-air cooling process, where four key operational settings were studied in isolation: increases to pressure drop through the pallet, increases to vent size, decreases to vent size and changes in vent number. Performance between pallets was compared in terms of cooling rate via the pallet average SECT (hours); and in terms of cooling heterogeneity, the OHI. An overall summary is given in Figure 3.27. No new design or operational condition was categorically better than the baseline package CP1, as evidenced in Figure 3.27b having an empty upper-right-hand quadrant. In general, increasing the pressure drop (CP2 and CP3) accelerated the cooling rate, which also increased cooling heterogeneity. Decreasing vent size (SV1 and SV2) was very detrimental to the cooling rate *and* uniformity, showing that poorly ventilated horticultural packaging restricts access of refrigerated air throughout the package. Interestingly, increasing vent size (LV1 and LV2) worsened the cooling rate at levels as severe as decreasing vent size, with an indeterminate impact on cooling uniformity. This revealed a new link between package strength and the cooling efficiency, where the large vent holes weakened the package enough to create small gaps between boxes, creating new bypass airflow pathways.

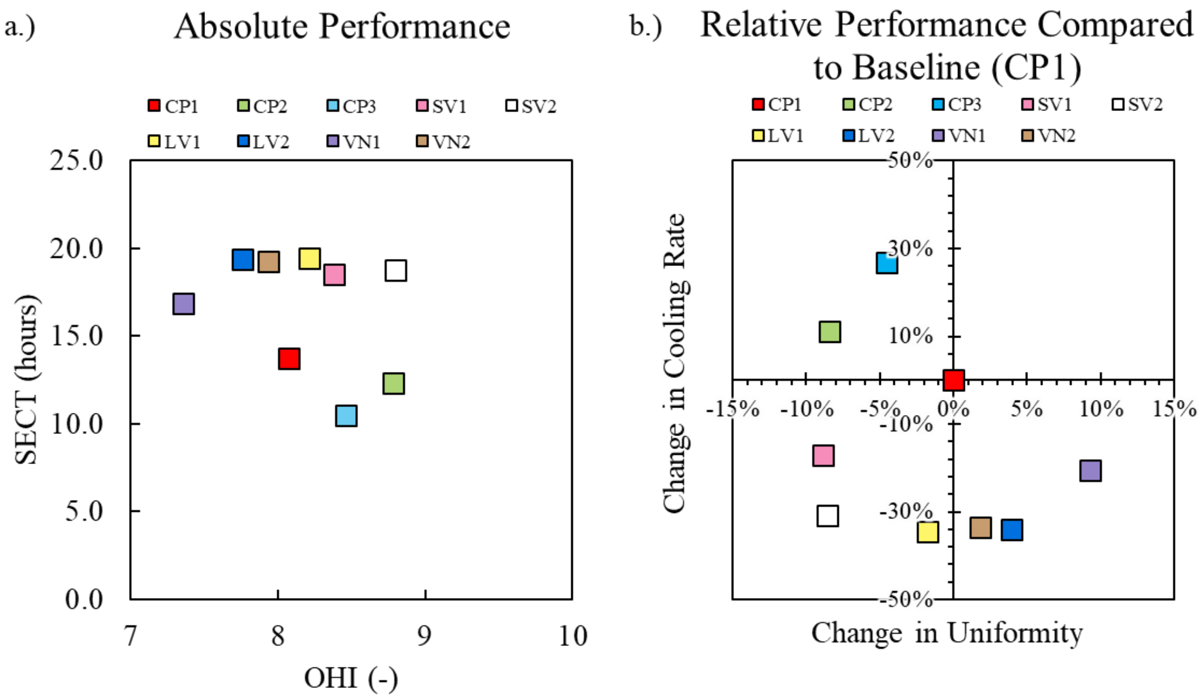

Figure 3.27: Performance of each package design, reported by the average cooling rate (SECT, hours) and cooling uniformity (OHI). a.) absolute performance; b.) performance relative to the baseline package, CP1.

Redistributing the same TOA into a different number of vents (VN1 and VN2) favoured the package with more vents, with the largest improvement to cooling uniformity and only a modest decline in the cooling rate relative to the baseline (CP1).

3.4: Single Box Cooling Validation Data

3.4.1: Introduction

Section 5.5 and section 6.2 later outlines that the heat transfer model to be developed was a single box scale model, for which there is a need for validation data. It was originally intended that the first box to receive inlet refrigerated air in the pallet scale experiments be used for validation, but this information had boundary conditions that were not easily described without modelling the whole pallet – the front of the box was exposed to cooling air, but the back and sides of the box conduct heat to the packages it's in contact with, the temperature of which is not constant and changes at a different rate over time according to the airflow pattern created by the packaging ventilation. As such, a new experiment was designed to collect single box cooling validation data with well-defined boundary conditions.

3.4.2: Materials and Methods

The intention of this experiment was to design a forced-air cooling set-up with well-defined boundary conditions for a single package. The wind tunnel used for pallet scale experiments in section 3.3 was modified to produce a slimmer tunnel inside of which a stack of single boxes could sit flush with the tunnel walls, by placing thick slabs of polystyrene insulation on either side of the tunnel (Figure 3.28).

Stacking a single layer of boxes in the new wind tunnel reproduces the boundary conditions of a pallet of kiwifruit (O'Sullivan *et al.,* 2016) but at the single box scale: the sides of each box are insulated by the polystyrene insulation, the front and backs of each box are directly exposed to high velocity refrigerated air, and if only the packages in the centre of the stack are instrumented, each box has a high velocity of air flowing through the package ventilation and over the top of the polyliner, which also acts as a significant mode of heat transfer by convection of heat conducted through the bottom of the box above it.

As highlighted in red in Figure 3.28, there were three instrumented boxes per trial. Boxes were instrumented in an identical fashion to section 3.3.3.2, with the fruit in each box stacked into a repeatable pattern (Figure 3.8) with a 12% sample size (Figure 3.10a).

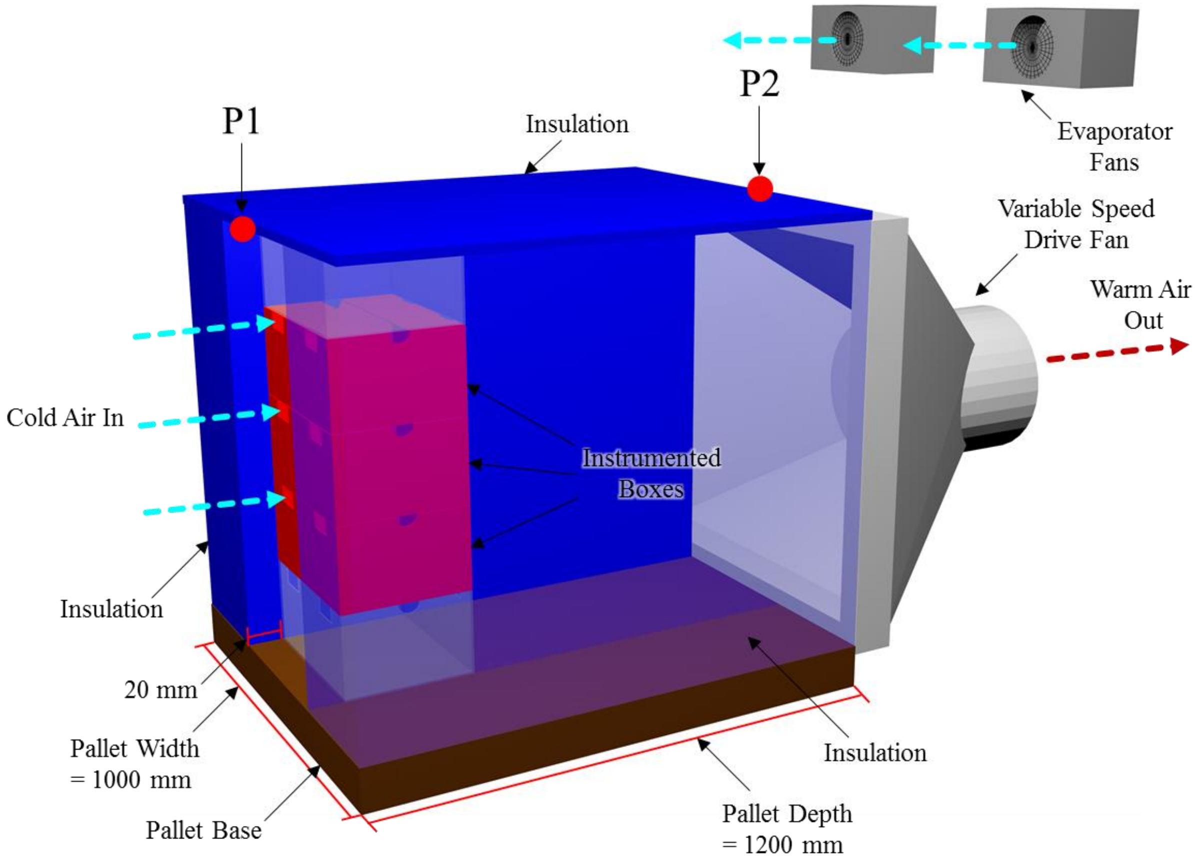

Figure 3.28: Laboratory forced-air cooling tunnel set-up for single box cooling: 5 boxes of kiwifruit stacked into a column in the wind tunnel, connected to a VSD fan. 3 boxes were instrumented, highlighted as red.

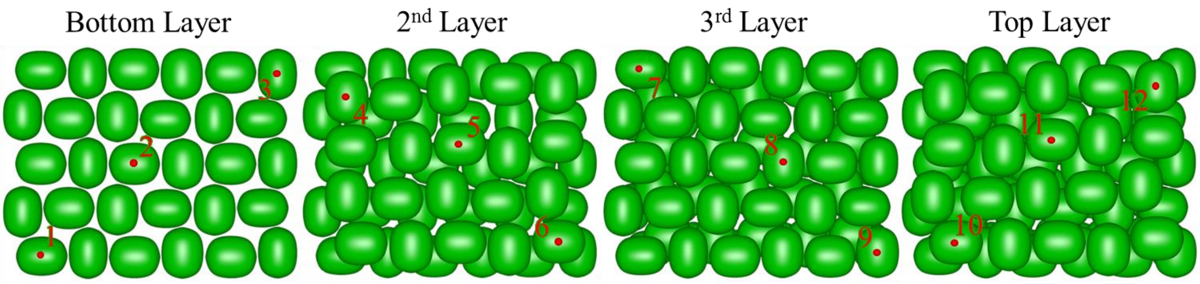

Figure 3.29: Fruit temperature positions.

Fruit were incubated to ~20 ºC and cooled for a 24-hour period in a refrigerated room set to 0ºC, with a one-minute logging interval. Four airflow rates were investigated by changing the variable speed drive to produce four across-pallet pressure drops (measured as the pressure difference between points P1 and P2 – Figure 3.28 – see section 3.3.3.3) of approximately 15, 30, 60 and 120 Pa.

3.4.3: Results and Discussion

Temperature profiles at each recorded temperature position (Figure 3.29) for each pressure drop is presented in Figure 3.30, Figure 3.31, Figure 3.32 and Figure 3.33; and the box average fruit temperature profiles are presented in Figure 3.34:

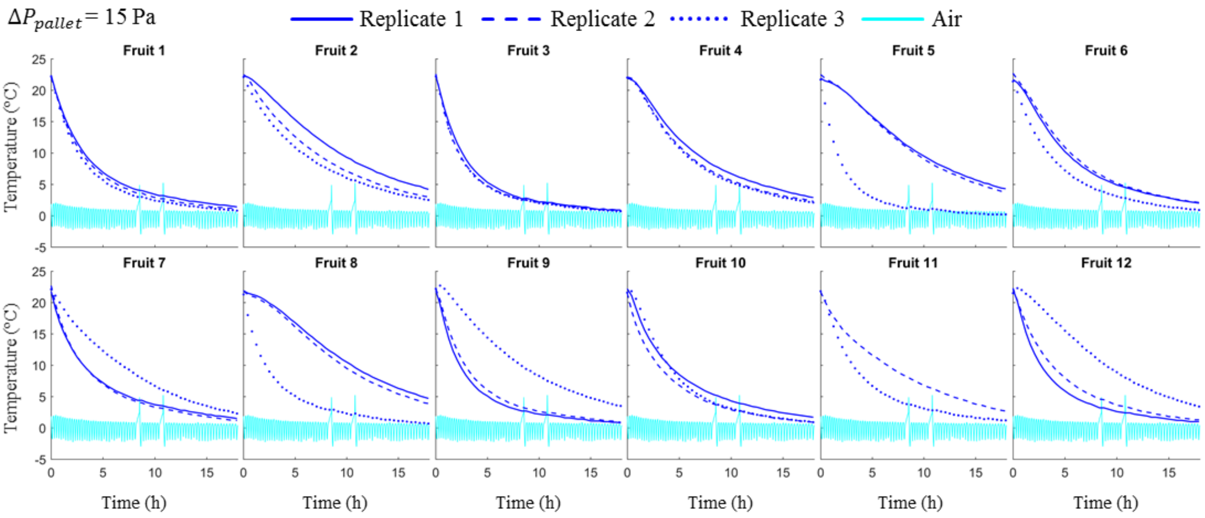

Figure 3.30: Individual temperature position cooling profiles, ΔP_{pallet} *= 15 Pa.*

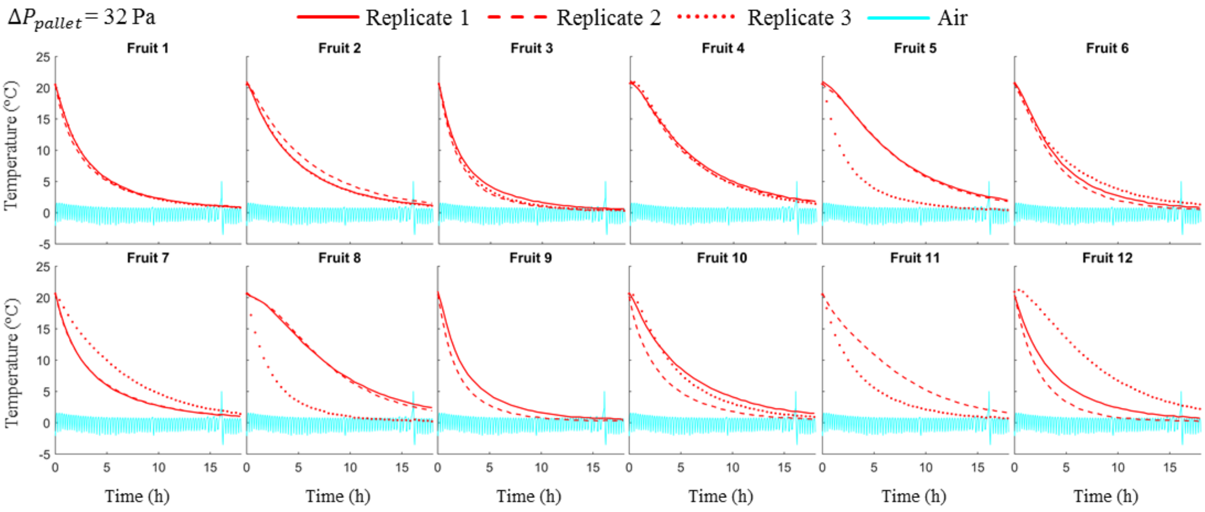

Figure 3.31: Individual temperature position cooling profiles, ΔP_{pallet} *= 32 Pa*

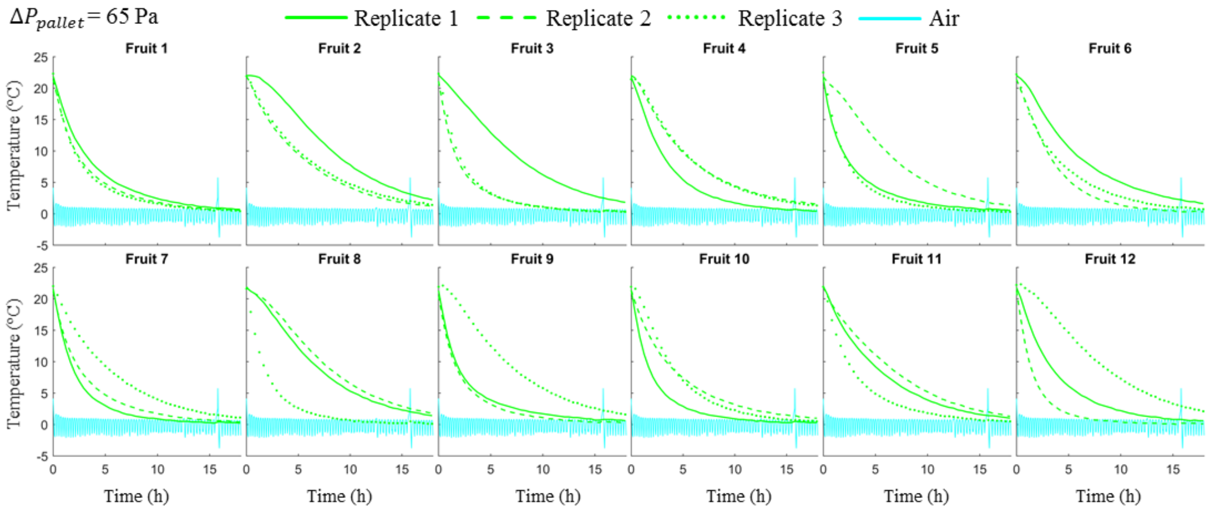

Figure 3.32: Individual temperature position cooling profiles, $\Delta P_{\mathrm{pallet}}$ *= 65 Pa*

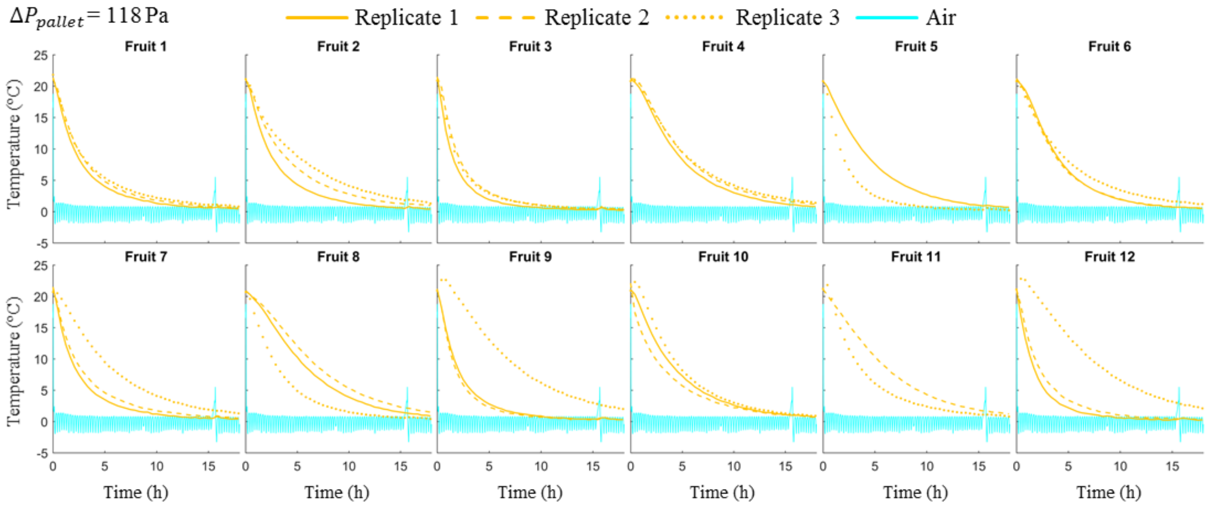

Figure 3.33: Individual temperature position cooling profiles, $\Delta P_{\mathrm{pallet}}$ *= 118 Pa*

Some locations show a high degree of variability, while others are more uniform. Fruits 1, 2 and 3 generally show closeness across replicates; these being the fruit on the bottom of the package, they primarily exchange heat via conduction through the fibreboard they are pressed up against. Differences in contact area and placement would therefore be relatively small. Other locations, such as fruits 10, 11 and 12, show a larger separation in cooling rates between replicates. These fruits, at the top of the box, primarily cool through convection with the refrigerated airflow.

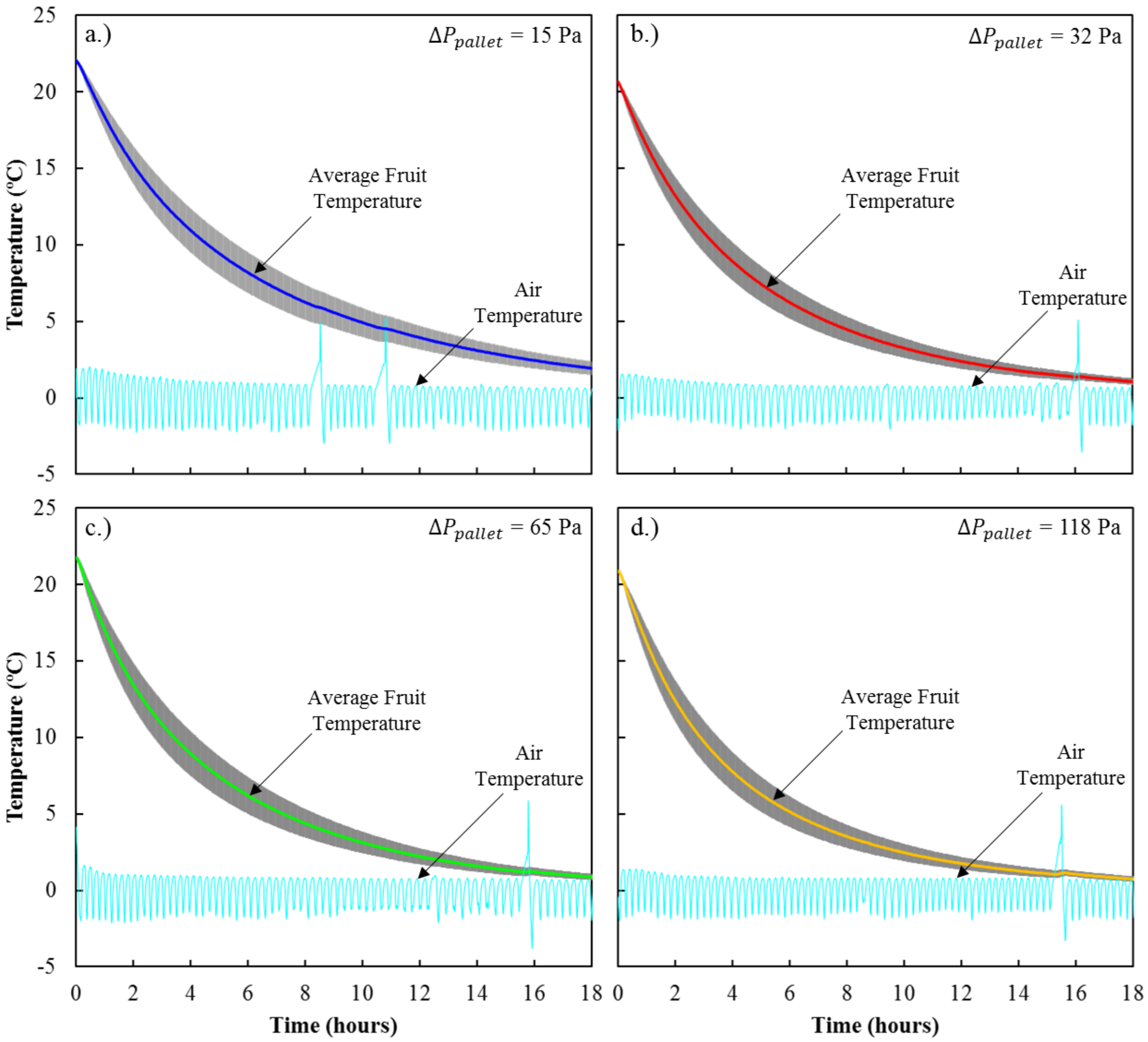

Figure 3.34: Box average temperature profiles. Error bars are the 95% confidence interval.

The shape of the polyliner in the headspace is potentially complicated and inconstant, where small deviations in how the bag is wrapped around the fruit and secured could mean the polyliner is pressed tightly against the top fruits, or there is a small air gap – this is confirmed later in section 5.3.3. Minute differences in the stacking pattern and individual fruit sizes/shapes can also impact the airflow pattern formed during cooling, contributing to the observed variances.

Chapter 4

Bulk Fruit Geometry

4.1: Introduction

This thesis is predicated on a philosophy of flexibility and automation. One of the major obstacles to model flexibility is the construction of accurate 3D bulk fruit geometry. When a collection of horticultural products is packed into a box, the shape of the individual fruits or vegetables combine to form a convoluted shape that may have a significant impact on the airflow pathway and hence the rate of cooling via convection; and the magnitude through which touching fruits exchange heat via conduction could be dependent on the random stacking pattern. While some horticultural products can be simplified as a stack of spheres – such as apples or oranges (Tanner *et al*, 2002b; Defraeye *et al*, 2014) – kiwifruit are proto-ellipsoids and simplification in this manner may introduce an unacceptable level of error. It would be beneficial to have a methodology that informs the model user of the geometry inside of a given package; such a procedure would greatly open the design space, increasing the size and scope of systems which can be modelled.

A bulk fruit geometry generation tool is developed in this chapter. In section 4.2 the internal geometry of fruit packages are empirically studied via X-ray tomography (CT scanning); in section 4.3, a shape equation for kiwifruit is developed so that digital fruit analogues can be rapidly generated in CAD software; and section 4.4 describes the development of a random stacking model, simulating gravity and friction forces on a collection of fruit to fill any enclosure.

4.2: X-Ray Tomography of Bulk Fruit Shape

4.2.1: Introduction to X-ray tomography

Tomography is a powerful tool that is used predominantly for medical applications, allowing the cross-sectional shape of an object – usually a person or animal – to be determined in a non-invasive manner (Robb, 1985; Larsen and Jacobi, 1986). The same techniques for imaging used in medicine can be used as a non-destructive method to determine the internal structure of a material or collection of materials (Cartz, 1999), such as a modular bulk package filled with horticultural products. Several tomography techniques exist that can provide the relevant information concerning the internal geometry of a package. Emission Computed Tomography – which includes Photon and Positron Emission Tomography – is not useful for the primary focus of this thesis, as it requires the administration of a radioactive isotope into the object under study, adding prohibitive cost and risk to the experimental design (Kak and Slaney, 1988). X-Ray Computed Tomography (CT scanning), Ultrasound and Magnetic Resonance Imaging (MRI scanning) on the other hand are all viable methods; these emit a source of energy – light, sound or magnetism – into the target material and measure its absorption or reflection at a specified point (Robb, 1985; Zeng, 2010). X-ray tomography was viable in this scenario as X-ray absorption is proportional to the density of the material, which is distinct between the principle phases – namely air, $\rho_A \approx 1.205$ kg.m^{-3}; kiwifruit, $\rho_S = 1037$ kg.m^{-3}; and packaging $\rho_P = 200$ kg.m^{-3} (section 5.4). The Massey University Veterinary Hospital had a suitable CT scanning machine available for hire (Model: Phillips Optimus Diagnost Ceiling System; Stockin *et al*., 2008), so CT scanning was used for this project. It had a circular field-of-view, with a diameter of 0.5m; large enough for small animals (dogs, cats or sheep) to have full body scans, or for large animals (horses, cows) to have parts of their anatomy scanned, with the assistance of a winch. The modular bulk packages of kiwifruit that were scanned had a maximum outer dimension of 0.4 m, so that full boxes of kiwifruit could be scanned as is, without the need for miniaturisation or modification to the scanner or packaging system. A schematic of the scanner is given in Figure 4.1a.

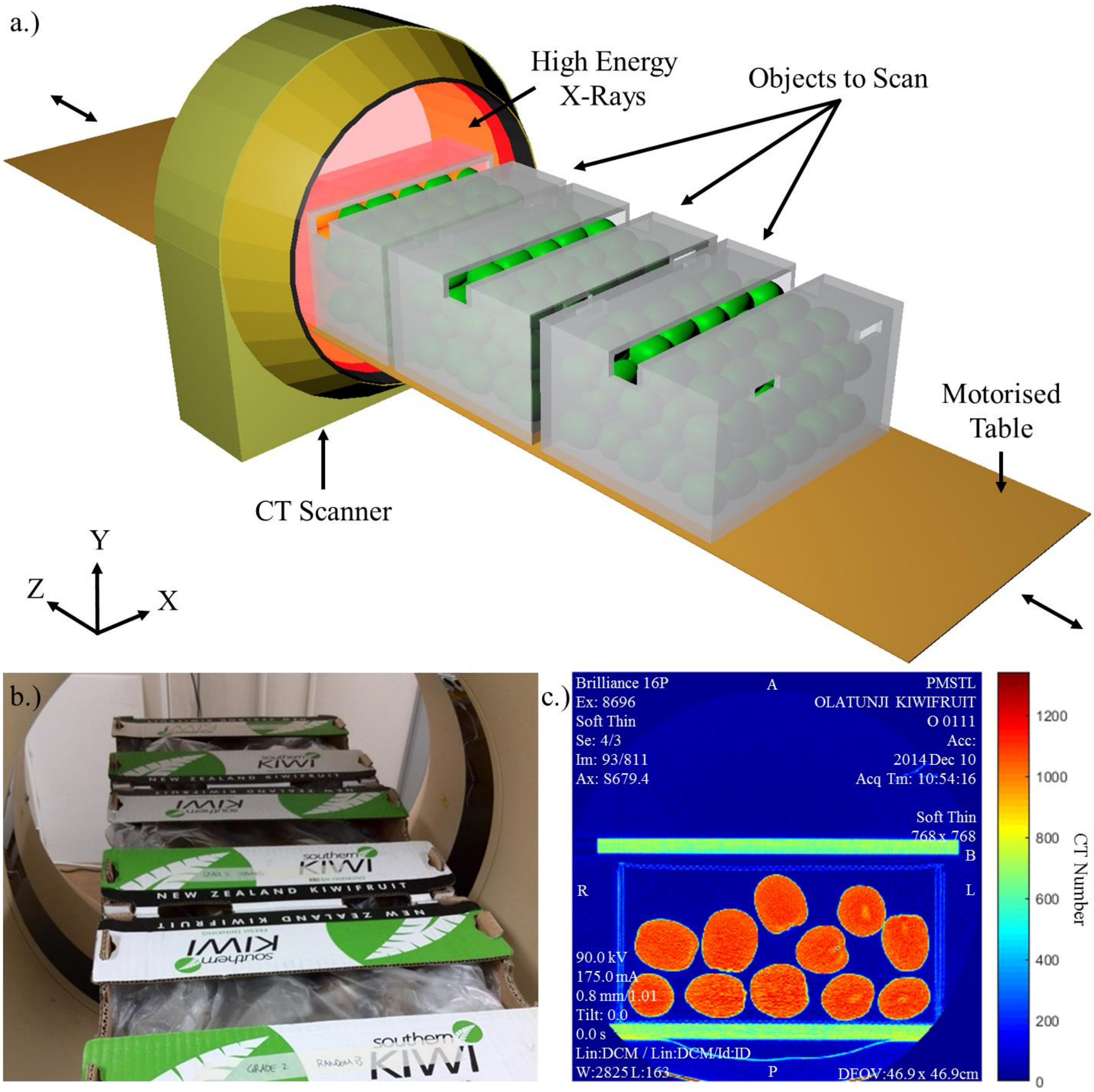

Figure 4.1: a.) Illustration of the CT scanner and its major components; b.) Photograph of kiwifruit boxes inside the Massey University Veterinary Hospital CT scanner; c.) a single CT scan image from the CT scanner, showing the cross-section of a box of kiwifruit, colour representing the CT number (level of X-ray absorption).

CT scanning is becoming a popular technology in the field of agrifood research, with the technique being utilised to investigate the internal and external structure of horticultural products and processed foods: for example, Rogge *et al.* (2015) used a CT scanner to measure the external shape of individual apples and pears, which was then used as an input to develop a 3D contour based geometrical model generator. This enabled a virtual investigation into the optimum controlled atmosphere settings, where a 2kPa partial pressure of O_2 gave the lowest chance of storage browning (Ho and Rogge *et al.*, 2016); and Alvarez *et al.* (2015) used X-ray micro-CT (µCT) – with a voxel size of 5µm – to investigate the internal structure of ice cream, where histogram and watershed segmentation was applied to the CT scan information to determine the fraction of air bubbles, ice crystals and fat globules within a $1mm^3$ cubic sample. These recent works show that CT scanning has potential to be useful in the current application – deriving the bulk shape of kiwifruit stacked in a modular bulk package.

The specifics of X-ray tomography – such as how a set of raw transmission and reflection signal data is processed into a cross-sectional image – are not given here, but can be found in Kak and Slaney (1988) and Robb (1985). In practice, it is only important to know that a CT scanner outputs a series of Digital Imaging and Communications in Medicine, or DICOM files (.dcm). Contained within each .dcm file is a 2D map of the X-ray absorption of each position, given in CT numbers (computed tomography numbers; Bryant *et al.*, 2012):

$$CT_{Number} = \frac{\mu_{Material} - \mu_{water}}{\mu_{water}} 1000 \qquad (4.1)$$

Where CT_{Number} is the CT number, $\mu_{Material}$ is the X-ray absorption coefficient for the material, and μ_{water} is the X-ray absorption coefficient for water. An example 2D cross section DICOM image – derived from the scanning of a box of kiwifruit – is provided in Figure 4.1c, where the colour scale represents CT number.

4.2.2: Raw CT Data Collection

Grade 1 export quality count 36 hayward kiwifruit were delivered to the CPRR from Zespri® International (the same batch of fruit used for cooling experiments, section 3.3) and stored in a refrigerated room. Immediately prior to scanning, three boxes of kiwifruit were removed from cold storage and placed into fresh modular bulk packages. The boxes were transported a short distance from the CPRR Postharvest Laboratory to the Massey University Veterinary Hospital for scanning. Two packages were placed into the CT scanner to collect two replicates of the empirical bulk shape of randomly stacked fruit. A third package was opened and the fruit were rearranged into the same orderly stacking pattern used throughout the forced-air cooling experiments (section 3.3; Figure 3.8). Boxes were scanned at the maximum possible resolution of 0.8 mm slices.

4.2.3: CT Scan Data Processing

The MATLAB function ‘dicomread’ was used to import the .dcm files into memory. A given CT scan slice resembles a typical pixel set, (Figure 4.2a; Cohen-Or and Kaufman, 1995). Pixels were given the notation of $\mathbb{p}$, where an individual pixel is denoted as $\mathbb{p}_n = x$, which is interpreted thusly: the subscript n is used to identify the location of the pixel being referred to, and x is the value of the referred pixel. x can be a continuous number, an integer or a Boolean, depending on the nature of the image processing technique being applied to the slice. For example, x can be a continuous number like the CT number; it can also be an integer where each number corresponds to a specific phase, such as air = 1, packaging = 2 and fruit = 3; or it can be a Boolean, where x = 1 represents that a pixel is ‘on’, and x = 0 represents the pixel is ‘off’. The size of a given pixel, dx and dy, depends on the depth of view, information stored in each .dcm file and can be accessed with the MATLAB function ‘dicominfo’ to provide the exact pixel spacing.

A collection of CT scan slices can be combined in the 3rd dimension to form a voxel set (Figure 4.2b; Cohen-Or and Kaufman, 1995). Like the pixel set, the voxel set is a regular 3-dimensional grid with many of the same mathematical properties. The voxel is denoted as $\mathbb{v}$, and an individual voxel as $\mathbb{v}_n = x$, with the same conventions as previously. The size of a voxel is given by the pixel spacing (dx and dy) as well as the thickness of the CT scan slice (dz), which was the smallest possible value for the CT scanning machine, 0.8 mm.

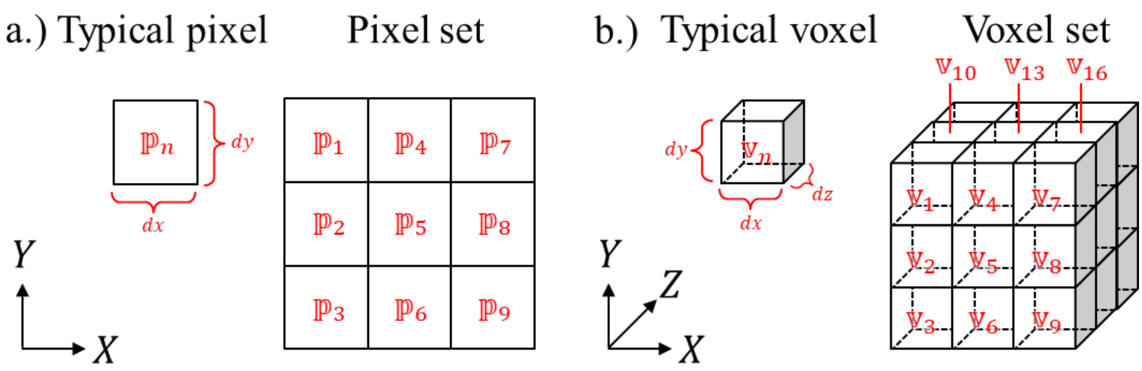

Figure 4.2: a.) a typical 2D pixel set, a regular 2D grid, with individual pixels defined by $\mathbb{p}_\mathrm{n}$ *of size* dx *and* dy*; b.) a typical voxel set, a regular 3D grid, individual voxels defined by* $\mathbb{v}_\mathrm{n}$ *of size* dx, dy *and* dz.

Identifying which voxels belong to which phase was an important consideration for building useful 3D geometries from raw CT scan data. The procedure developed for phase separation is demonstrated in this section on a single CT scan slice to make the process easier to understand – however this resulted in a number of error that do not occur when applied to the full 3D voxel set.

Figure 4.3 shows a raw CT scan slice. Colour represents the CT number of each pixel – dark blue areas being spare material, dark red being dense material. Below the box is the cross-section of the table it is resting on. The kiwifruit inside of the boxes were wrapped in a polyliner when they were scanned, however it would appear that the thin plastic film does not appear in the scans. The first step was to execute a simple crop, to eliminate as much superfluous information (such as the table) as possible. Pixels outside the specified range were set to $\mathbb{p}_n = 0$ (Figure 4.3b).

The X-ray absorption of a pixel is closely related to the density of the material in that position, and the three phases within the system have disparate densities: fruit with $\rho_S \approx 1037$ kg.m^{-3}, packaging $\rho_P \approx 200$ kg.m^{-3} and air $\rho_A \approx 1.205$ kg.m^{-3} (see section 5.4). Therefore, clearly separate non-overlapping ranges of CT numbers can be identified that correspond to each of the three phases, which in turn can be used to discretize the pixel set from continuous CT numbers to quantized integers that correspond to each of the three phases. For example, these ranges could be defined manually by inspecting Figure 4.3 and selecting appropriate values: fruit were visually conspicuous as dark red objects with higher CT numbers than the rest of the pixel set, so perhaps pixels with $\mathbb{p}_n \gtrsim 900$ could be considered fruit pixels, where fruit pixels are denoted as $\mathbb{p}_n = 3$; packaging appeared as light blue lines with intermediate CT numbers, so that perhaps $200 \lesssim \mathbb{p}_n \lesssim 900$ could be considered packaging pixels, converting them into $\mathbb{p}_n = 2$; and air appeared as dark blue with very low CT numbers, so $\mathbb{p}_n \lesssim 200$ could be considered air pixels, $\mathbb{p}_n = 1$. However, manually selecting the ranges for discretization is neither flexible nor automated, so there needed to be a computational method that could analyse a CT pixel or voxel set and output the best ranges for image discretization. Otsu's method was employed to achieve this (Otsu, 1979) via MATLABs 'multithresh' function.

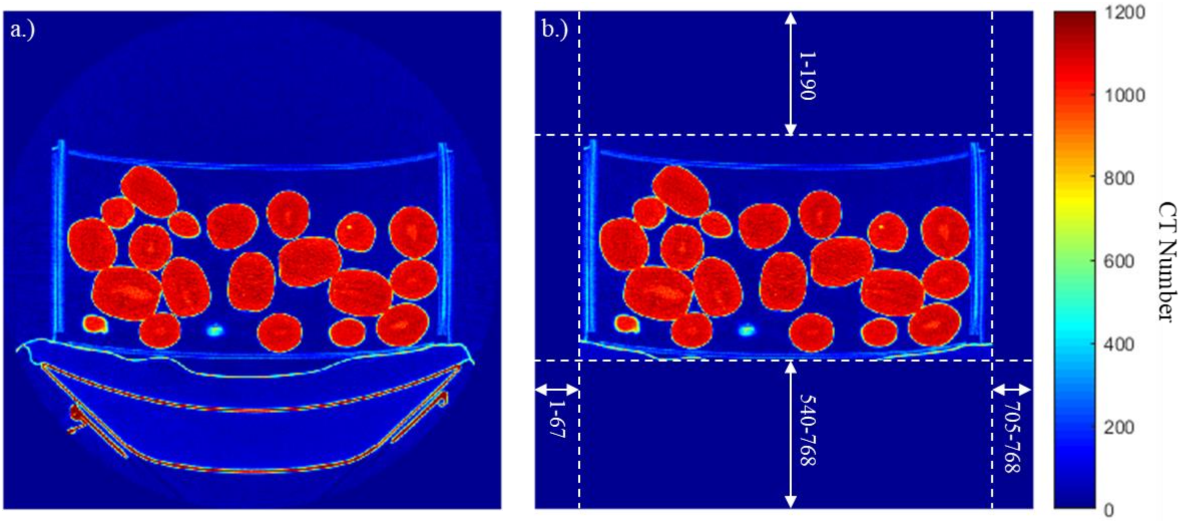

Figure 4.3: A raw CT scan slice of fruit inside of a modular bulk package. Colours represent CT number. a.) raw CT scan slice; b.) raw CT scan slice with superfluous information cropped out.

The function requires two inputs: the image to be discretized, and the number of discretization levels. The function then outputs the best ranges for discretization. This is demonstrated in Figure 4.4 where 2 to 7 discretization levels were applied to Figure 4.3. At two levels of discretization (Figure 4.4a), Otsu's method recognised two phases within the system, assigning solids (packaging and fruit) as any pixel with $\mathbb{p}_n > 212$; and air as any pixel ≤ 212. At three levels (Figure 4.4b) – the same number as the number of phases within the system – Ostu's method recognised fruit as $\mathbb{p}_n > 665$ (yellow), packaging as $141 \leq \mathbb{p}_n \leq 665$ (cyan) and air as $\mathbb{p}_n < 141$ (blue). While this discretization was mostly successful in identifying which pixel belonged with which phase, there was still a large degree of mischaracterisation – seen most predominantly within the kiwifruit epidermis (skin), these pixels have been falsely identified as packaging as they share a similar radio-absorption as the fibreboard. These mischaracterisations need to be corrected – details of this process is explained later in this section.

As long as there is a relatively large difference in X-ray absorption between fruit, packaging and air, this method of assigning pixels to a particular phase is expected to remain applicable when dealing with other horticultural products packed into boxes. Fruits and vegetables have a high water content which is responsible for most of their radiation absorption properties. According to Zespri® International (2011), green Hayward kiwifruit has a water content of 83.5%; while other popular New Zealand horticultural exports (Aitken and Hewett, 2016) apples, pears and avocados have water contents of 84%, 84%, and 74%, respectively (ASHRAE, 2010); thus the average CT number of these products is expected to be similar to the current kiwifruit situation. If the packaging material does not exhibit an intermediary CT number range as it was in the case of the kiwifruit box, then it is suggested that a custom package is created for use with the CT scanner, made of sparse material (such as fibreboard) but retaining the shape of the original package.

To further illustrate Otsu's method of discretization, higher orders of discretization are shown in Figure 4.4c - f, where the function was used to identify 4-7 discrete levels. As the level of discretization increased, Otsu's method began to detect the internal physiological structure of the kiwifruit as separate phases, highlighting the differences between the inner pericarp (core), outer pericarp (flesh) and epidermis (skin). These features have potential to be useful in an alternative application, such as a horticultural product that requires modelling as a multi-phase, anisotropic object – such as an avocado, which has a leathery skin, soft flesh and a large hard stone. Increasing Ostu's method to identify 5 phases (skin, flesh, stone, packaging and air) would accommodate for this. However, this added level of complexity isn't necessary for the situation at hand (kiwifruit); there is no evidence to suggest that modelling, for example, the inner pericarp and outer pericarp as separate phases adds accuracy compared to a lumped approach, where individual kiwifruits are modelled as a single solid phase with effective thermal properties (Datta and Dhall, 2011). Therefore, Otsu's method with three discretization levels was taken (Figure 4.4b) and carried forward.

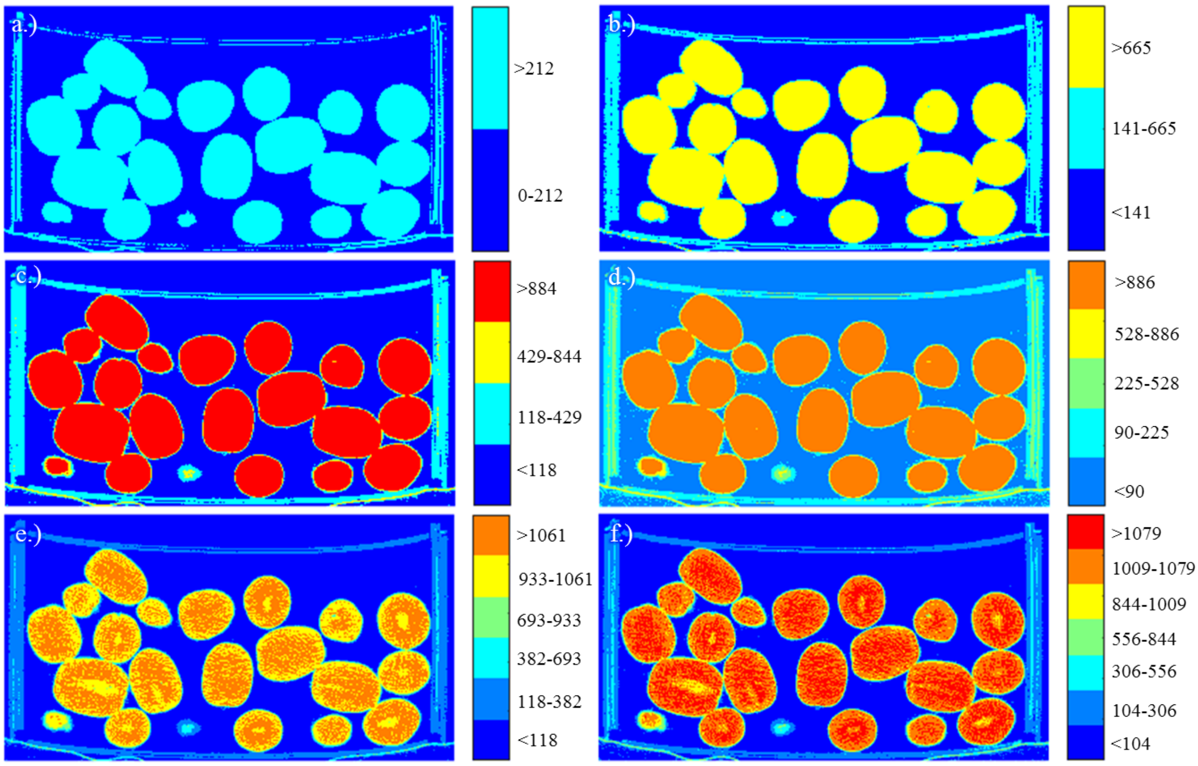

Figure 4.4: CT scan slice subjected to the 'multithresh' function (Otsu, 1979), with an increasing amount of discretization levels: a.) 2 levels; b.) 3 levels; c.) 4 levels; d.) 5 levels; e.) 6 levels; f.) 7 levels.

Figure 4.5 shows Figure 4.4b in more detail, where the degree of mischaracterisation is more apparent. Otsu's method misinterpreted many pixels, such as there being packaging 'wrapped' around the fruit, as the epidermis region of the fruit shared a similar X-ray absorption as fibreboard ($141 \leq \mathbb{p}_n \leq 665$). Additionally, some pixels within the table on which the box sits were mischaracterised as fruit, as it is composed of similarly dense material ($\mathbb{p}_n > 665$). Finally, there is a small region within the fruit that has been mischaracterised as packaging. Although this 'hole' in the fruit only occurred once in this demonstration, these areas of unusually low X-ray absorption within the flesh of the fruit is very common throughout the remainder of the slices, and is caused by fruit damage such as bruising, chilling injury and rotting. X-ray absorption may be a useful method for non-destructively identifying such pathology during grading, but was not useful for this application. Methods for correcting each of these mischaracterisations were therefore developed and explained further in this section.

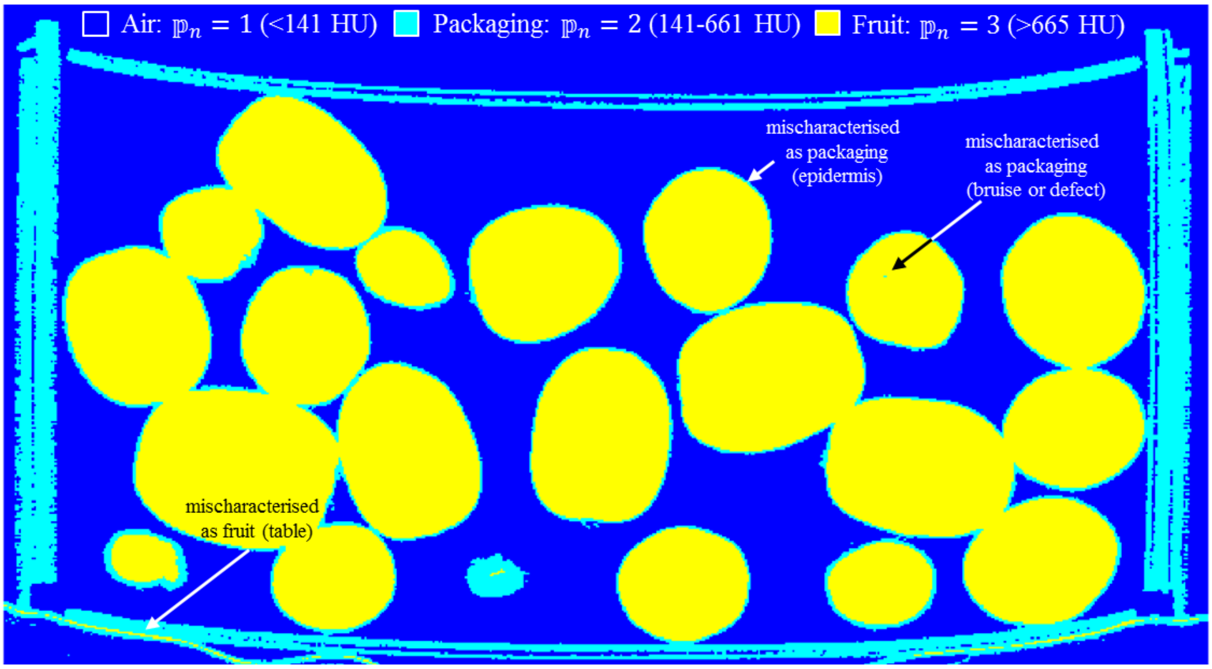

Figure 4.5: Enlarged result of applying Otsu's method (Otsu, 1979) with 3 discretization levels to the raw CT scan slice, with mischaracterised pixels (fruit injuries, epidermis pixels and pixels in the table the box is resting on).

First, the mischaracterised fruit pixels within the table were addressed. The packaging pixels (any pixel with a value of 2) were temporarily removed, and the remaining information converted to binary (air pixels = 0; fruit pixels = 1; Figure 4.6a). The MATLAB function 'regionprops' was used to divide the binary image into identifiable connected regions, shown in Figure 4.6b. The output of the 'regionprops' function was the number of pixels and the position of each pixel within a given connected region. As fruit are considerably larger than the mischaracterised regions in the table, regions below a certain threshold, θ_{fruit}, were deemed to be mischaracterisations and were eliminated; in this case, a threshold of θ_{fruit} = 100 pixels was used. This meant that pixels within regions 1-7, 10-18, 20-21, 21 and 30-40 were set to 0 (see Figure 4.6b). An error occurs during this step as a result of this demonstration being applied to a single 2D slice, rather than the entire 3D voxel set: a legitimate fruit region was deleted, region 24. As this region represents the top of a fruit that is more predominantly features in further CT scan slices, it had a pixel size of only 11 pixels, underneath the θ_{fruit} = 100 threshold. When applying this process to the 3D voxel set, small regions like region 24 are considered connected to a much larger region through the Z direction, so that this error does not occur normally.

Next, the mischaracterisations within the flesh of the fruit were investigated. The pixel data was inverted so that air pixels = 1 and fruit pixels = 0 (Figure 4.6c). 'regionprops' was applied again to identify regions within the binary image. The first and largest region (region 1, 143124 pixels) is the air outside of the surface of the fruit (see Figure 4.6d). Any additional regions are those caused by internal injuries inside of the fruit (region 2, 2 pixels). All regions except for the largest one were therefore eliminated. In this 2D demonstration there is a possibility of there being a pocket of air 'trapped' between several fruit, disconnected from the bulk of air inside of the package. This routine would also recognise this region as a fruit defect and falsely delete it. However, this risk is an artefact of the 2D nature of this demonstration; there is not the possibility of there being a disconnected air region trapped between fruit in the 3D case, as these regions are connected to the bulk air via the Z (out of page) direction.

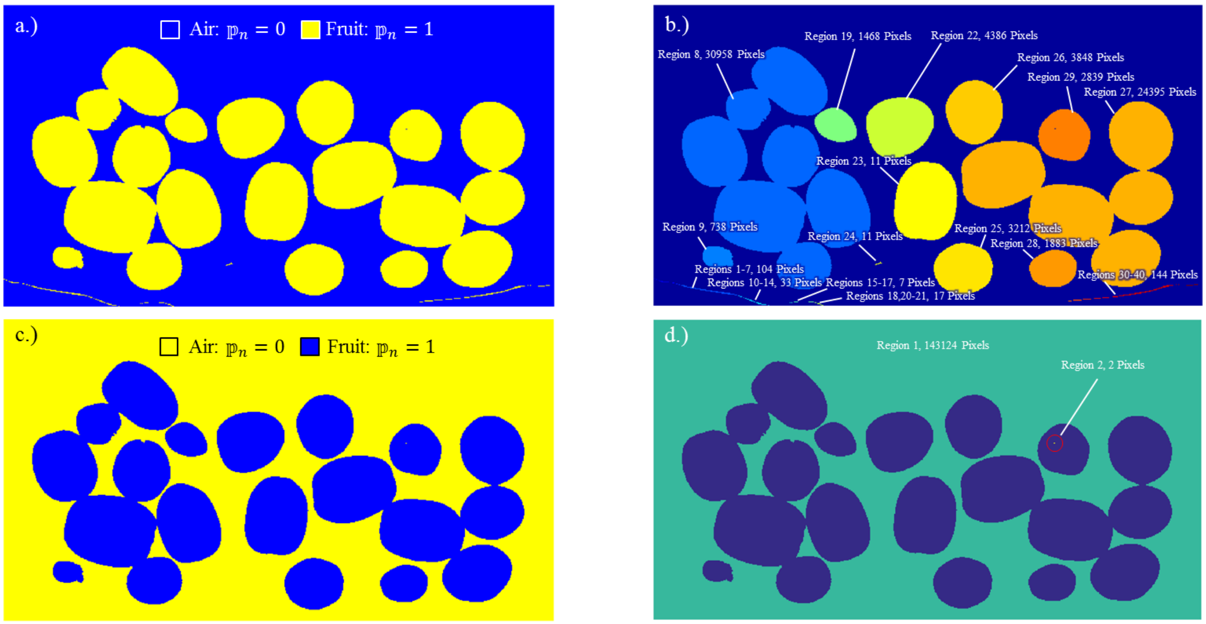

Figure 4.6: Illustrations of processes undertaken to compensate for mischaracterised pixels: a.) packaging pixels removed, then the remaining pixels were converted to binary; b.) 'regionprops' MATLAB function was applied to find the number of connected regions and their pixel size; c.) all regions under $\theta_{\text{fruit}} = 100$ *threshold removed, and the binary image was then inverted; d.) 'regionprops' applied again, and all regions except for the largest was eliminated.*

Although there was only one small defect in the 110th slice of the CT scan data, this process was a necessary inclusion as there were many more defects within the fruit in subsequent slices.

The packaging pixels temporarily removed in a previous step (Figure 4.6a) were then examined. This data contained a large number of pixels within the fruit epidermis mischaracterised as packaging. A routine was developed to reassign as many mischaracterised pixels as possible, while simultaneously leaving correctly identified packaging pixels alone. This was done by examining the positional data of every packaging pixel in the pixel set: pixels in close proximity to fruit pixels ($\mathbb{p}_n = 3$) were more likely to be mischaracterised epidermis pixels, while pixels in close proximity to other packaging pixels were more likely to be correctly characterised packaging pixels. A square search radius of a specified size, θ_{search}, was implemented around each packaging pixel, and the number of fruit pixels were added to, and the number of packaging pixels subtracted from, the cumulative proximity, CP (Eq. 4.2); Figure 4.7):

$$CP_n = \left(\sum \mathbb{p}_{\theta_{search}} = 3\right) - \left(\sum \mathbb{p}_{\theta_{search}} = 2\right) \tag{4.2}$$

Where CP_n is the cumulative proximity of packaging pixel n, and $\mathbb{p}_{\theta_{search}}$ are all pixels inside of the search radius θ_{search}.

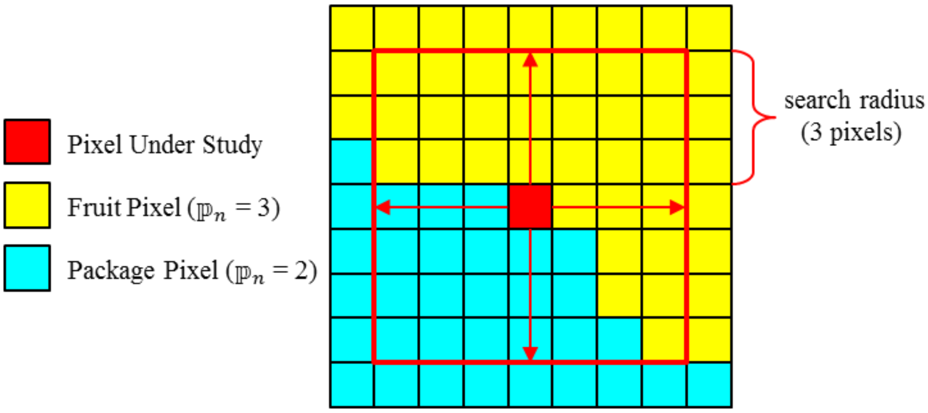

Figure 4.7: Visualisation of the cumulative proximity routine developed to assess whether a pixel within the fruit epidermis has been mischaracterised as a packaging pixel.

Positive CP values correspond to mischaracterised fruit pixels as they are in close proximity to other fruit pixels, and so were switched from packaging to fruit ($\mathbb{p}_n = 2 \rightarrow 3$). Negative CP values correspond to correctly characterised packaging pixels and were left alone. Results of this routine are shown in Figure 4.8a – green representing positive CP, and red negative CP, where a θ_{search} = 5 pixel search radius was used. The routine was largely successful at correcting the mischaracterisations, especially for regions where the fruit was touching the packaging – there was a risk that some packaging pixels that had been identified correctly as packaging were accidentally switched to fruit, but the routine appears to have avoided overcompensation. There was one error – marked in Figure 4.8 – where fruit epidermis pixels were not correctly identified as mischaracterisations. This error is a result of the fruit pixels from region 24 being eliminated, so that there were no fruit pixels within the search radius. This is again an artefact of this 2D demonstration: these pixels are not eliminated in the more relevant 3D voxel scenario, and therefore this small error does not occur when all of the CT scan slices are taken into account. Results from the cumulative proximity routine were applied, flipping positive CP values from $\mathbb{p}_n = 2 \rightarrow 3$ and negative CP values to $\mathbb{p}_n = 2 \rightarrow 2$. The result is Figure 4.9. This reveals that there was still a slight amount of epidermis pixels that remained as packaging; however the routine was successful in 95% of the cases (6331 flipped out of a total 6649, not including the error highlighted in Figure 4.8), more than acceptable considering the computational efficiency of the routine. Therefore, the pixel set was subjected to the same elimination process of Figure 4.6b, where small regions of packaging were identified and removed under a threshold of $\theta_{packaging}$ = 100. This entire process – starting with the raw image, applying Otsu's method, filling holes within the fruit and compensating for the mischaracterised epidermis pixels – was coded into a MATLAB script, the final result shown in Figure 4.9b. The computational efficiency of the entire process was excellent, taking only 3.8 seconds of computation time (Intel® i7-4770 with 16GB of RAM).

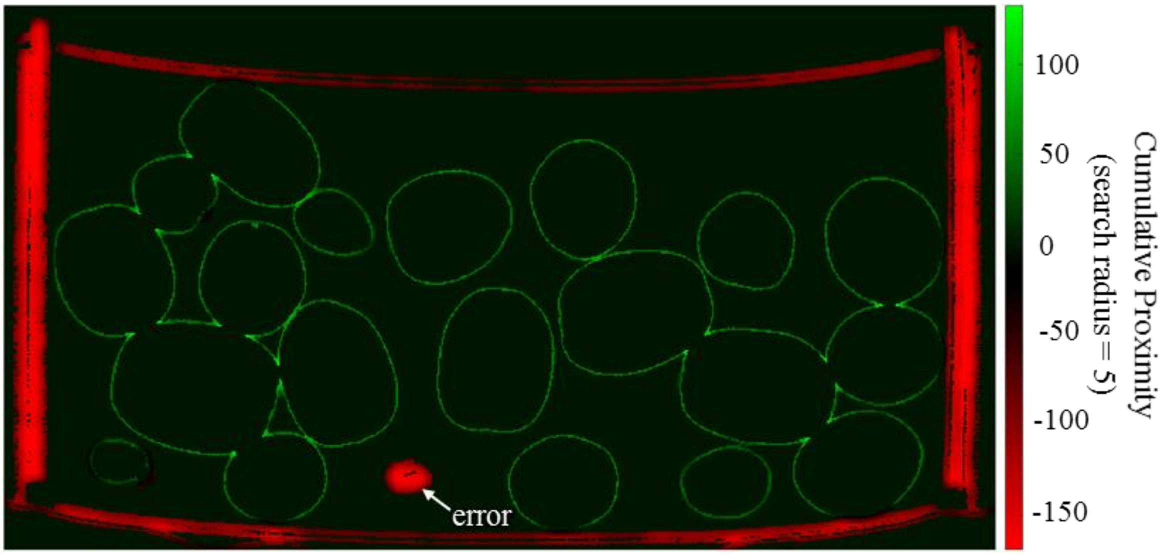

Figure 4.8: Results of the cumulative proximity routine applied to all pixels recognised as packaging ($\mathbb{p}_{\mathrm{n}}$ = 2); green having positive CP *and were flipped ($\mathbb{p}_{\mathrm{n}}$ = 2→3), red having negative* CP *and were not flipped ($\mathbb{p}_{\mathrm{n}}$ = 2→2).*

These processes were expanded to the full voxel set to create useful 3D geometries of the empirical bulk fruit shape. After all CT scan slices were imported into MATLAB, superfluous information was cropped out (such as the table) and Otsu's method was applied to divide the raw data into 3 phases, results shown in Figure 4.10a. As selection of the discretisation bands included the entire voxel set, the discretisation levels were slightly different than the 2D case (Figure 4.5): for air, $\mathbb{v}_n$ < 167; packaging, $\mathbb{v}_n$ = 167-674; and fruit, $\mathbb{v}_n$ > 674. Mischaracterised voxels – most from the epidermis, but also some from internal fruit injury which cannot be seen in this 3D case as the external surface of the fruit is obstructing the view – were cleaned using the cumulative proximity method (Figure 4.7) with a search radius of θ_{search} = 5 to give Figure 4.10b; and Figure 4.10c has transparent packaging voxels so that the bulk fruit shape is more easily observed.

The phase separation process was more computationally intensive than the 2D demonstration but was still sufficiently rapid – under 5 minutes (298 seconds with an Intel® i7-4770 and 16GB of RAM) – to be a useful piece of software that was used repeatedly on CT scan experiments.

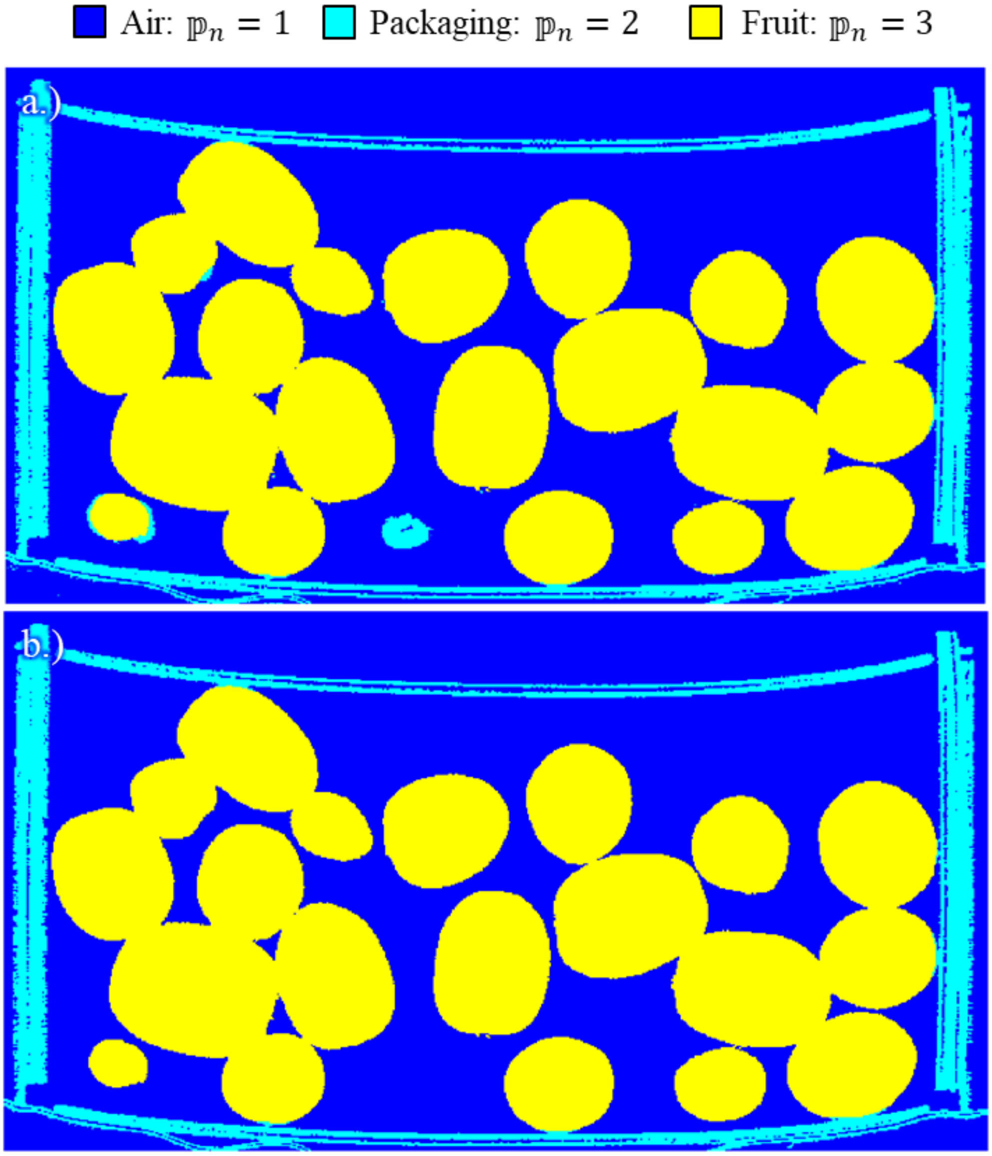

Figure 4.9: a.) application of the cumulative proximity routine to compensate for mischaracterised packaging pixels in the fruit epidermis; b.) final phase separated image, with mischaracterised pixels compensated for or removed.

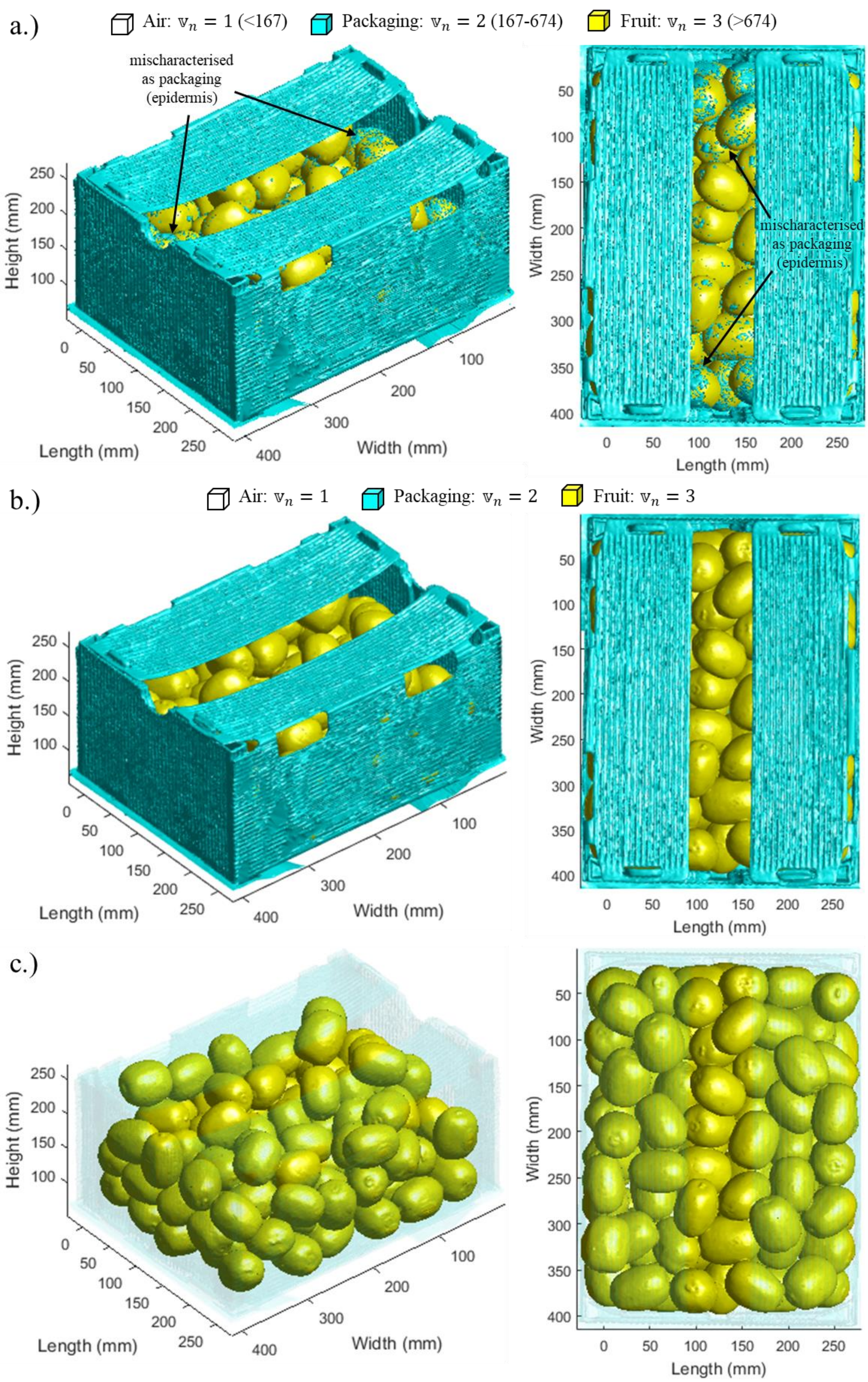

Figure 4.10: a.) CT scan slices combined and separated into phases (discretization levels: air, $\mathbb{v}_n$ < 167; packaging, $\mathbb{v}_n$ = 167-674; fruit, $\mathbb{v}_n$ > 674); b.) mischaracterised voxels compensated for and cleaned; c.) packaging voxels transparent to better show the fruit geometry.

4.2.4: CT Scanning Results

The phase separation process (section 4.2.3) was applied to the raw CT scan data for the three scanned boxes. Results are shown in Figure 4.11 with packaging is excluded so that only fruit is examined.

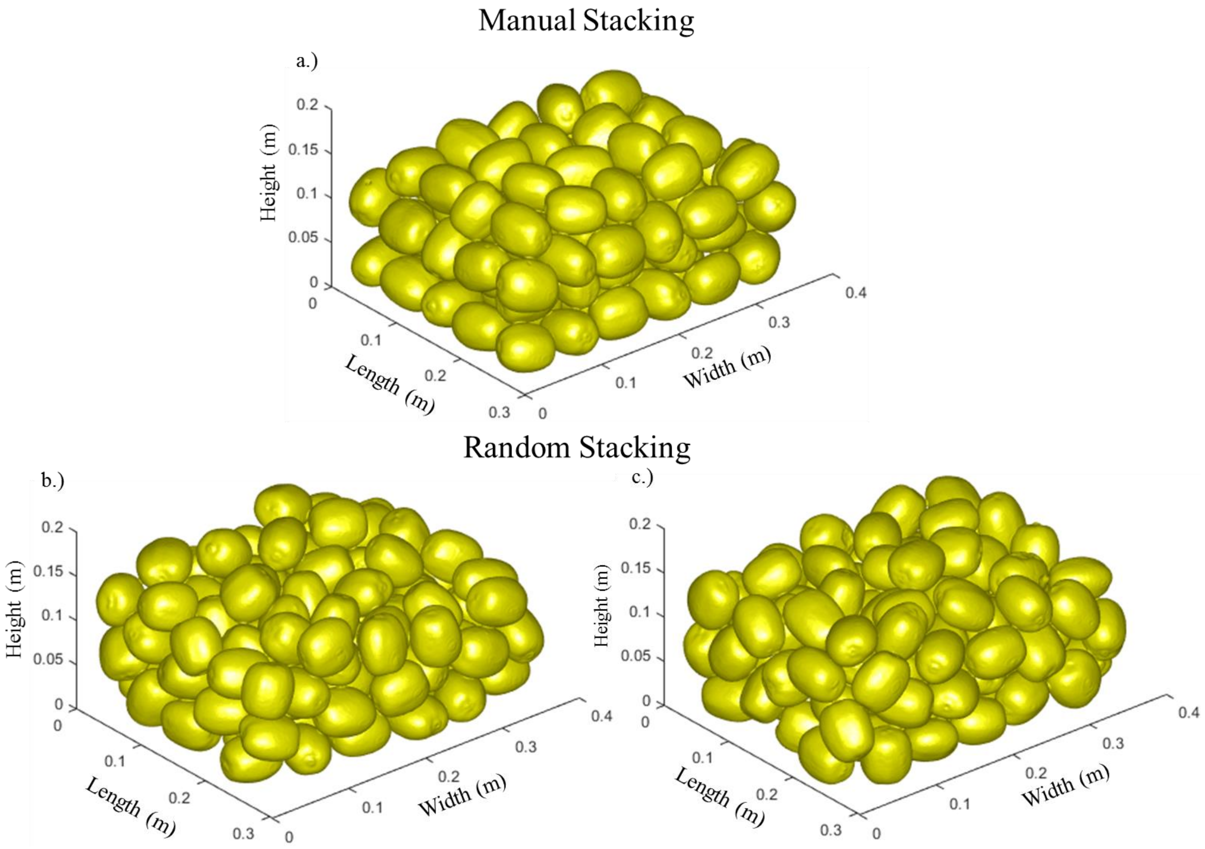

Figure 4.11: CT scans of count size 36 Hayward kiwifruit in multiple stacking configurations: a.) a manually stacked box (according to section 3.3); b and c.) randomly (naturally) stacked boxes of kiwifruit.

The visual differences between the manually stacked box (Figure 4.11a) and randomly stacked boxes (Figure 4.11b and c) is apparent – the manually stacked geometry shows an intentionally imposed 4 layers of fruit, while the naturally stacked boxes were amorphous and lacked a regular structure. The contrast between the different stacking regimes is discussed in further detail later (section 4.5).

4.3: Kiwifruit Shape Equation

It was initially the intention to integrate X-ray tomography as a vital component of the model, as it is a relatively quick technique for appropriating the internal bulk fruit geometry of a given package. However, it is not necessarily a flexible approach. If the model relied entirely upon input CT scan data, problems will quickly arise when attempting to build models outside of the studied scenario. Changes to the package size and shape will result in a different randomly stacked geometry, requiring new scans for each package iteration.

Section 4.4 outlines an alternative approach, a random stacking model designed to add more flexibility to the model construction process; but this first required a method for drawing 3D kiwifruit shapes of any specified size. A shape equation for kiwifruit is developed in section 4.3.1, and its application demonstrated in section 4.3.2. As there is a natural distribution of kiwifruit sizes (and weights) within a given count size range, a shape index is developed in section 4.3.3 to generate fruit that follows a certain input weight distribution.

4.3.1: Development of Kiwifruit Shape Equation

The geometry inside of a modular bulk package consists of approximately 100 individual kiwifruits. Determining the aggregate shape requires a method of drawing 3D shapes that are anatomically comparable to individual real world Hayward kiwifruit. A typical Hayward kiwifruit is shown in Figure 4.12. The major geometrical attributes of a singular fruit are: the length (distance from the largest axial cross section to the apex), L; major axis (maximum distance at the largest axial cross section), D_X; and minor axis (minimum distance at largest axial cross section), D_Y. Superficially, a kiwifruit appears to be an ellipsoid. However, Lorestani and Tabatabaeefar (2006) modelled several hundred kiwifruit as true ellipsoids with the same semi-axis dimensions as the L, D_X and D_Y, and found this approach consistently underestimated the true volume and surface area of the measured fruit (by up to 30%), and so 'fudge factor' coefficients were needed to make up the difference. Rashidi and Gholami (2008) used an image processing technique, combined with the disk method (Riddle, 1974), whereby photographs of Hayward kiwifruit were taken and the interior of the resulting 2D image was filled with 3D elliptical disks. The volume of the modelled shapes was compared to real kiwifruit, measured using the water-displacement method. The differences between the predicted and measured volumes were not found to be statistically significant ($p>0.05$), but using an ellipsoid to approximate the kiwifruit also consistently under predicted the empirically determined volume. The approach of Rashidi and Gholami (2008) also still relies on the availability of source images of kiwifruit. Rogge *et al.* (2015) used a Fourier series to describe the profile of fruits (pears and apples), where natural shape variability could be modelled by altering the values of the harmonics. Though a powerful technique, and adaptable to many different horticultural products, the approach was mathematically complex and required empirical 3D fruit geometry input data to function, supplied in their case by X-ray tomography.

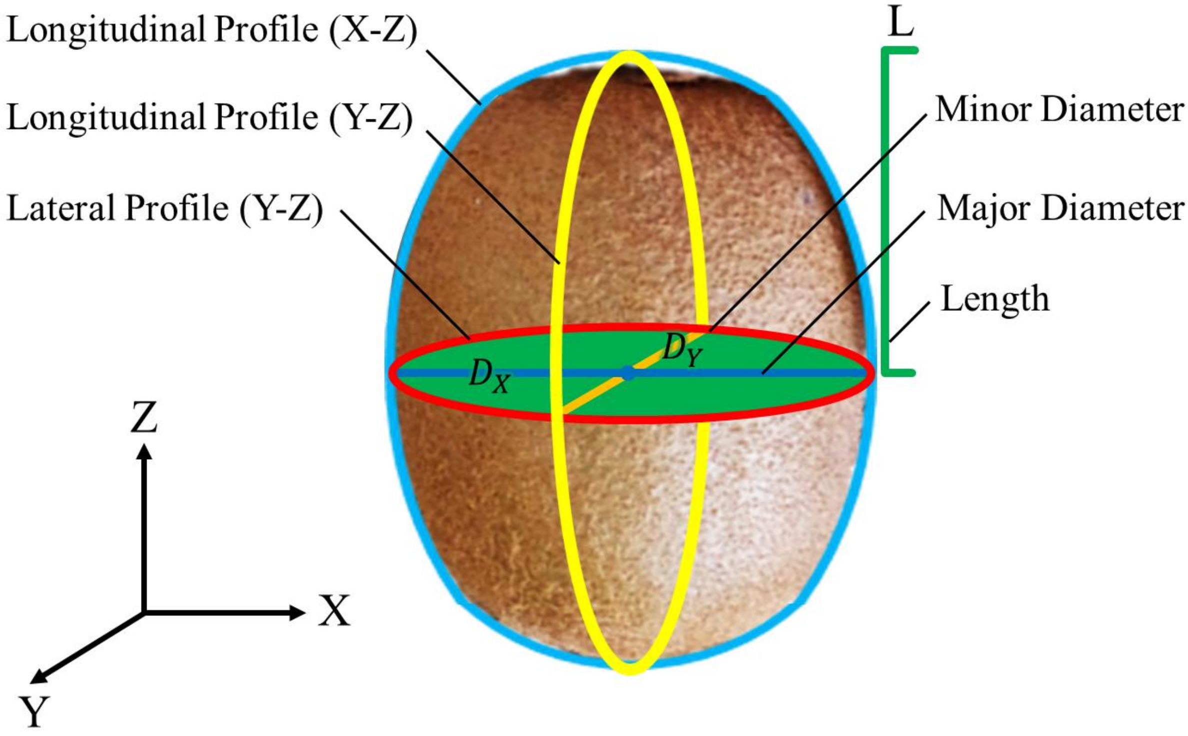

Figure 4.12: A generic 'Hayward' kiwifruit with the major geometrical attributes highlighted: D_X = *major diameter;* D_Y = *minor diameter;* L = *length.*

O'Sullivan *et al.*, (2016) took kiwifruit shape profiles, provided from industry sourced grading data by Anonymous (1997) to manually plot vertexes in 3D space, knitting them together into surfaces and then solid objects in ANSYS FLUENT. Though anatomically correct, in O'Sullivan *et al.*, (2016) approach, each fruit is the same size and shape, and as the modelled fruit are created manually it is time-consuming to apply to other horticultural products (or even to other kiwifruit grade categories).

To develop a new methodology for modelling a Hayward kiwifruit a primary concern was that the approach: 1.) was independent of shape input data (such as Rogge *et al.*, 2015; Rashidi and Gholami, 2008; and O'Sullivan *et al.*, 2016), 2.) performed better than the ellipsoid approximation, 3.) was sufficiently simple to implement as a few short lines of code, executed natively in modelling software (such as COMSOL or Blender), and 4.) can be used to draw an accurate 3D kiwifruit of any shape or size with little to no modification of the original equation(s). The best method to meet these criteria is an algebraic function that follows the longitudinal profiles of a Hayward kiwifruit, and can be scaled/sized to different grades by the setting the value of several scale factors.

The shape of a kiwifruit generally has three profiles (as shown in Figure 4.12): the lateral X-Y profile (red line), a function of D_X and D_Y; the longitudinal X-Z profile (blue line), a function of D_X and L; and the longitudinal Y-Z profile (yellow line), a function of D_Y and L. Anonymous (1997), an industrial partner, provided shape data of count 36 Hayward kiwifruit (based on measurements of 117 fruit; Figure 4.13), which could be used for validation.

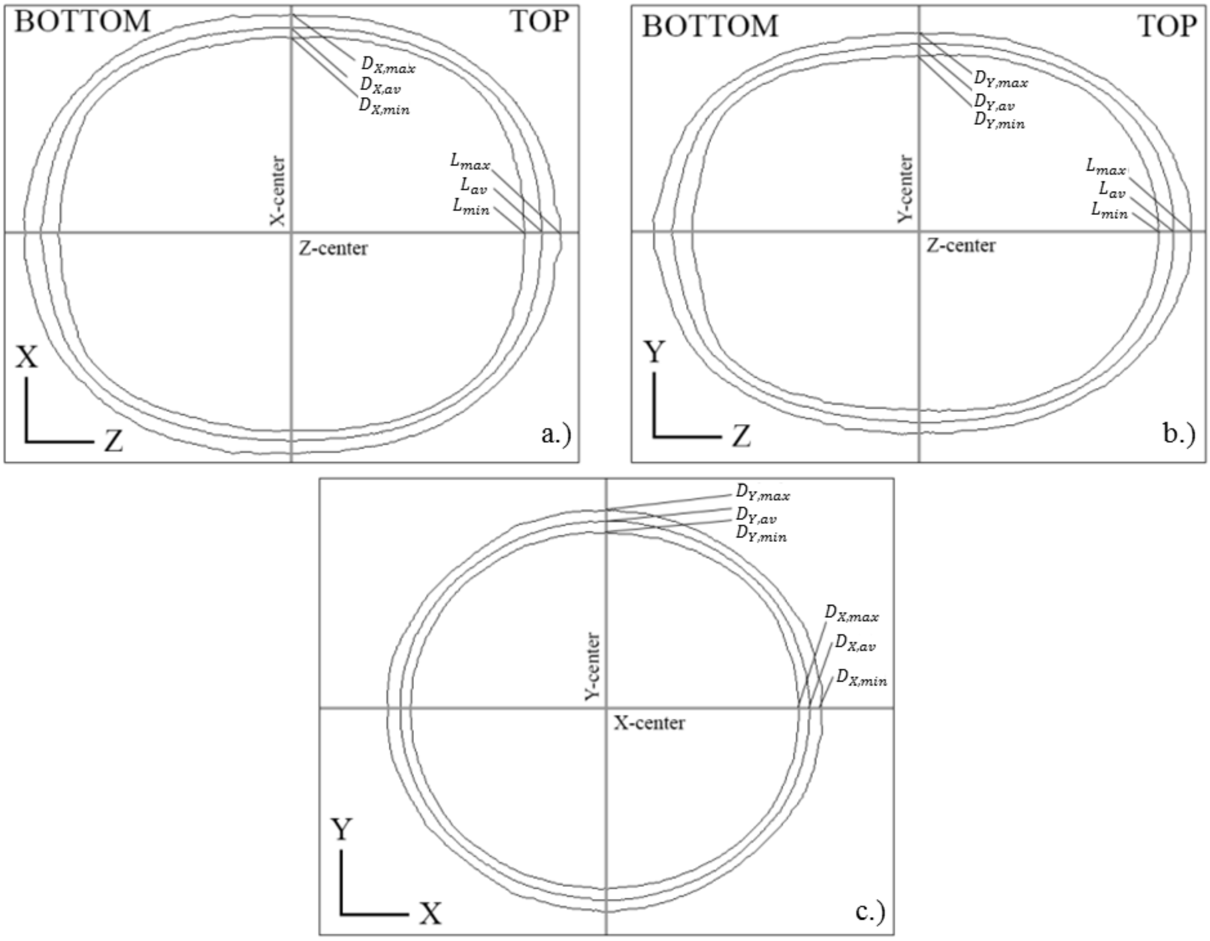

Figure 4.13: Empirical shape profiles in the a.) X-Z, b.) Y-Z and c.) X-Y directions for count 36 Hayward kiwifruit. Minimum, average and maximum profiles are the result of tracing the shape of 117 fruit (Anonymous, 1997). Images not to scale; scale omitted to preserve data confidentiality.

The shape data was provided as images of the empirically determined lateral and longitudinal profiles (X-Z (Figure 4.13a), Y-Z (Figure 4.13b) and X-Y (Figure 4.13c)) for the maximum, minimum and average fruit size within each weight grade of exportable Zespri® Hayward kiwifruit. The average shape derived from this sample of fruit is represented by the middle lines (subscript: av); and the maximum and minimum shape profiles are represented by the outer and inner lines, respectively (subscripts: max and min, respectively). As this information is commercially sensitive, Figure 4.13 is not to scale, and the scale has been omitted. Subsequent analysis and discussion of the kiwifruit profiles uses dimensionless forms.

4.3.1.1: Lateral Profile

A description of the lateral profile was developed which represents the cross-section of kiwifruit in the Y-X direction.

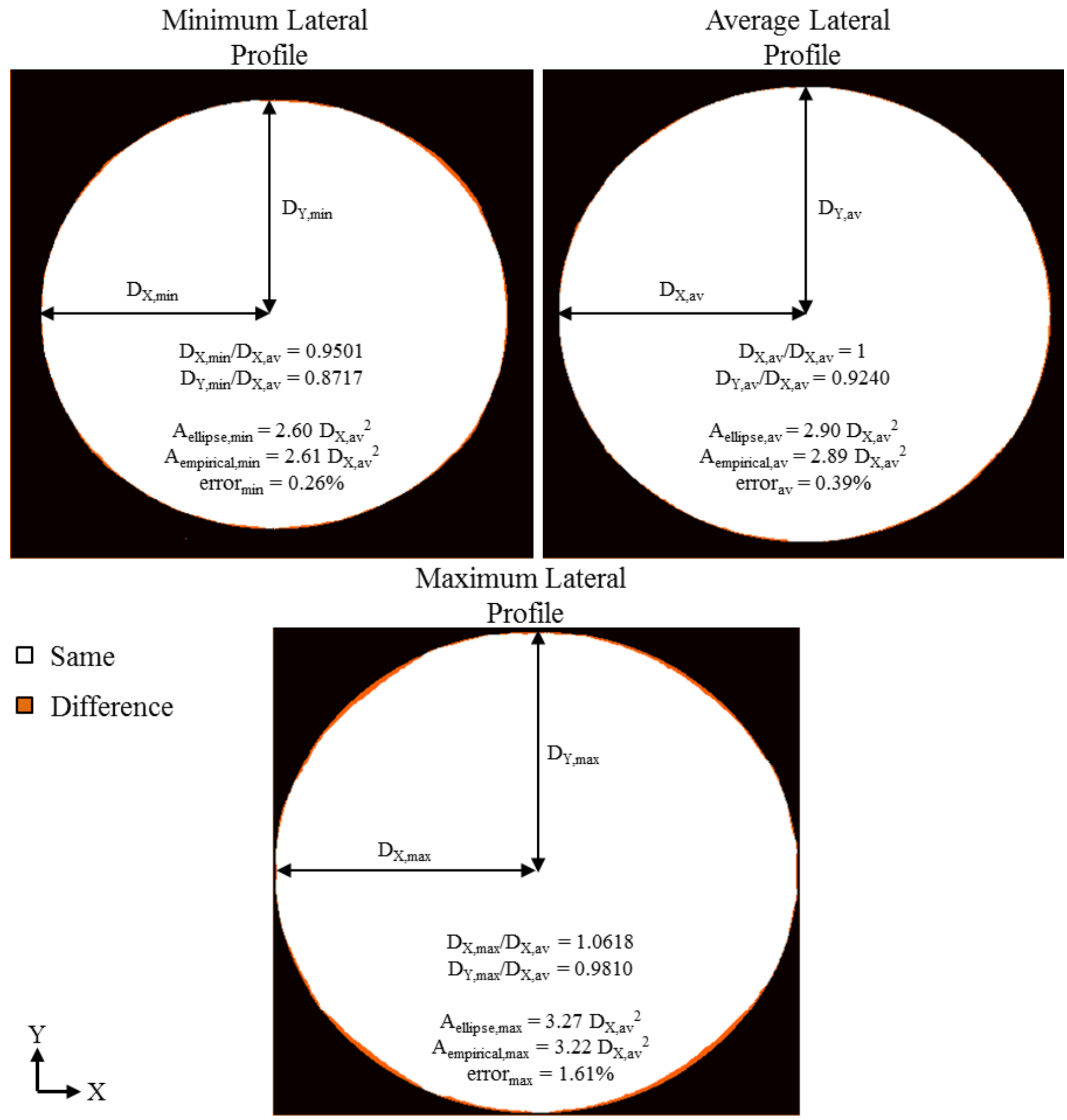

Figure 4.14: Comparison between empirical a.) minimum, b.) average and c.) maximum lateral profiles with an ellipse of the same D_X *and* D_Y.

Although the entire volume of the kiwifruit is not an ellipsoid (Lorestani and Tabatabaeefar, 2006), the fruit cross-section in the X-Y direction is nearly elliptical. When the differences between the empirical shape data, and ellipses with the same major and minor axes as D_X and D_Y are compared (orange highlights in Figure 4.14) small inconsistencies can be seen, but are minimal – with the largest error being a 1.6% difference for the case of the maximum profile; this is well below the natural variability within the count 36 size range (which can vary by up to 20%), and demonstrates that an ellipse can accurately describe the lateral profile of a Hayward kiwifruit.

4.3.1.2: Longitudinal Profiles

Lorestani and Tabatabaeefar (2006) showed that using an ellipsoid for both the lateral and longitudinal profiles under-predicts the true shape, and hence volume and surface area (by up to 30%). This is because kiwifruits are relatively flat near the centre of the fruit, and then curve sharply at the apices to form a shoulder (see Figure 4.13 a and b); a shape distinctively different from a smooth ellipse. A new longitudinal profile function (LPF) is therefore needed to better describe the kiwifruit.

The generalised form of the LPF is:

$$d_{j,k} = f_1(D_j, L_k, Z) \qquad (4.3)$$

Where f_1 is the LPF; a function of the diameter of the fruit (D), the length of the fruit (L) and the distance from the centre of the fruit (largest axial cross section) to the apices (Z). As there are two longitudinal profiles, there are two LPFs – one each for the X-Z and Y-Z directions; indicated by subscript j, where $j = X$ or Y. The origin of the Z-axis (where $Z = 0$) is the largest axial cross section, marked as the X-centre and Y-centre on Figure 4.13. Separate LPFs are considered for the top (calyx) and bottom (stem) halves of the fruit. This is indicated by subscript k, where $k = calyx$ or $stem$. The LPF (f_1) gives d, the distance from the Z-centre line to the outer edge of the fruit along the X- or Y-axis, at any point along the Z-axis. It is assumed there is symmetry along the Z-centre line. This will usually be true in the context of this thesis, as the fruit is graded to eliminate significant morphological deformities prior to packaging (Anonymous, 1997).

At the centre of the fruit ($Z = 0$), the output of the function must be $d_X = D_X$ or $d_Y = D_Y$; and at the apex of the fruit ($Z = L_k$), the output must be zero, $d_j = 0$. Within the limits of $0 \leq Z \leq L_k$, this behaviour is given by:

$$f_1 = \frac{L_k - f_2(L_k, Z)}{L_k} \times D_j \qquad (4.4)$$

f_2, (Eq. 4.4) defines the rate that d changes with respect to Z. f_2 also has limits where at $Z = 0$, $f_2 = 0$; and at $Z = L_k$, $f_2 = L_k$. The form of f_2 influences the rate at which d diminishes to 0: if there is a linear relationship between d and Z (Eq (4.5), the profile of the fruit is a straight line (Figure 4.15a, blue):

$$f_2 = Z \tag{4.5}$$

For a fruit profile matching an ellipse, f_2 is (Eq. 4. 6; Figure 4.15a, red):

$$f_2 = L_k - \sqrt{{L_k}^2 - Z^2} \tag{4. 6}$$

So that the LPF for an ellipsoid is (4.7):

$$d_{j,k} = \frac{\sqrt{{L_k}^2 - Z^2}}{L_k} \times D_j \tag{4.7}$$

As a kiwifruit is relatively flat in the middle and forms a sharp shoulder near the stem or calyx, f_2 needs to be a function that diminishes slowly at low to medium Z values; and then quickly diminishes to 0 as Z approaches L_k. This is achieved by using an exponential function (Eq (4.8):

$$f_2 = \exp(Z) - 1 \tag{4.8}$$

However, (4.8 violates the limits imposed for f_2 ($Z = 0$, $f_2 = 0$; and $Z = L_k$, $f_2 = L_k$) so the following additions are required (Eq (4.9; Figure 4.15a, green):

$$f_2 = \frac{L_k}{\exp(S) - 1} \times \left[\exp\left({}^{S \cdot Z}/_{L_k}\right) - 1\right] \tag{4.9}$$

S is the ‘shoulder coefficient’, where different values of S impact the steepness or flatness of the curve (Figure 4.15b). Substituting the final form of f_2 into f_1 gives the LPF for kiwifruit (Eq (4.10):

$$d_{j,k} = \frac{L_k - \left(\frac{L_k}{\exp(S) - 1} \times \left(\exp\left({}^{S \cdot Z}/_{L_k}\right) - 1\right)\right)}{L_k} \times D_j \tag{4.10}$$

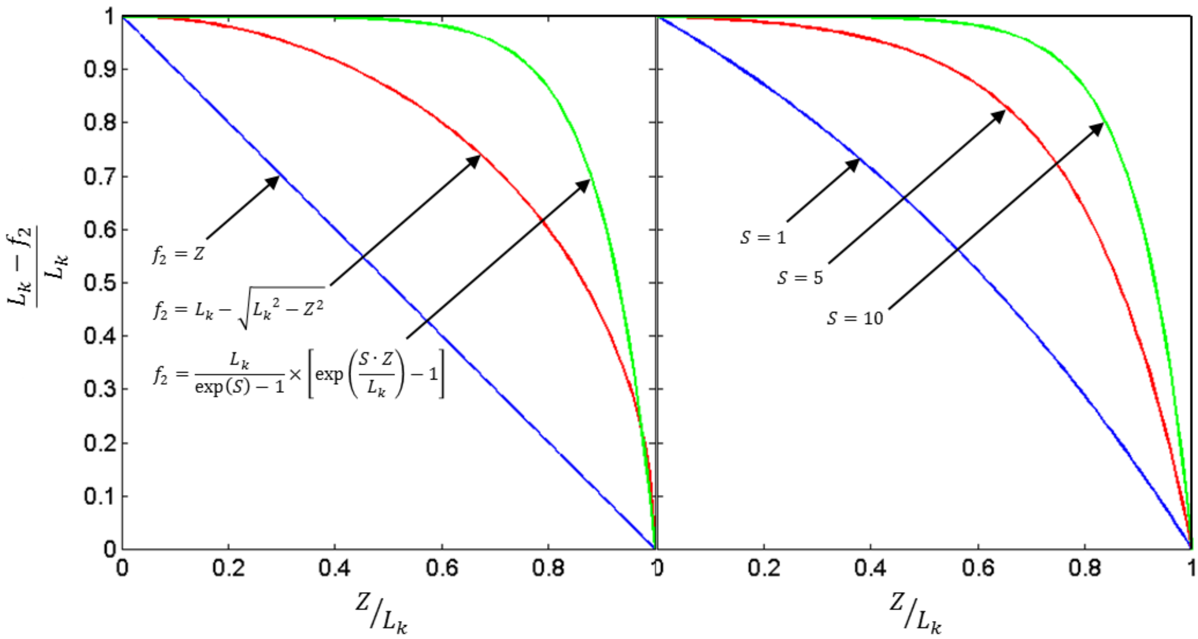

Figure 4.15: a.) How different f_2 *functions change the shape of the LPF; b.) How the shape of the exponential LPF changes with different values of* S*, the shoulder coefficient.*

The performance of the newly developed LPF was assessed using the shape data provided by Anonymous (1997), comparing (4.10 with the X-Z and Y-Z profile in both the stem and calyx directions. Eq. 4.7, the LPF for an ellipsoid, is also compared to illustrate why an ellipsoid is an inappropriate model for a kiwifruit. Results are shown in Figure 4.16. The average profile is presented in solid red, with the maximum and minimum bounds of variability within the count 36 weight range presented as dashed red lines. D_X, D_Y, L_{calyx} and L_{stem} were taken from the average profile from Anonymous (1997; Figure 4.13). All measurements were transformed to non-dimensional forms. The ellipsoid LPF (Eq. 4.7) is shown in cyan; and the new LPF for kiwifruit (Eq. 4.10) in blue. Non-linear least squared regression was used (MATLABs 'lsqnonlin' function) for each of the 4 profiles to determine the optimum value of S – the shoulder coefficient that impacts the curvature of the LPF – to best fit the average profile.

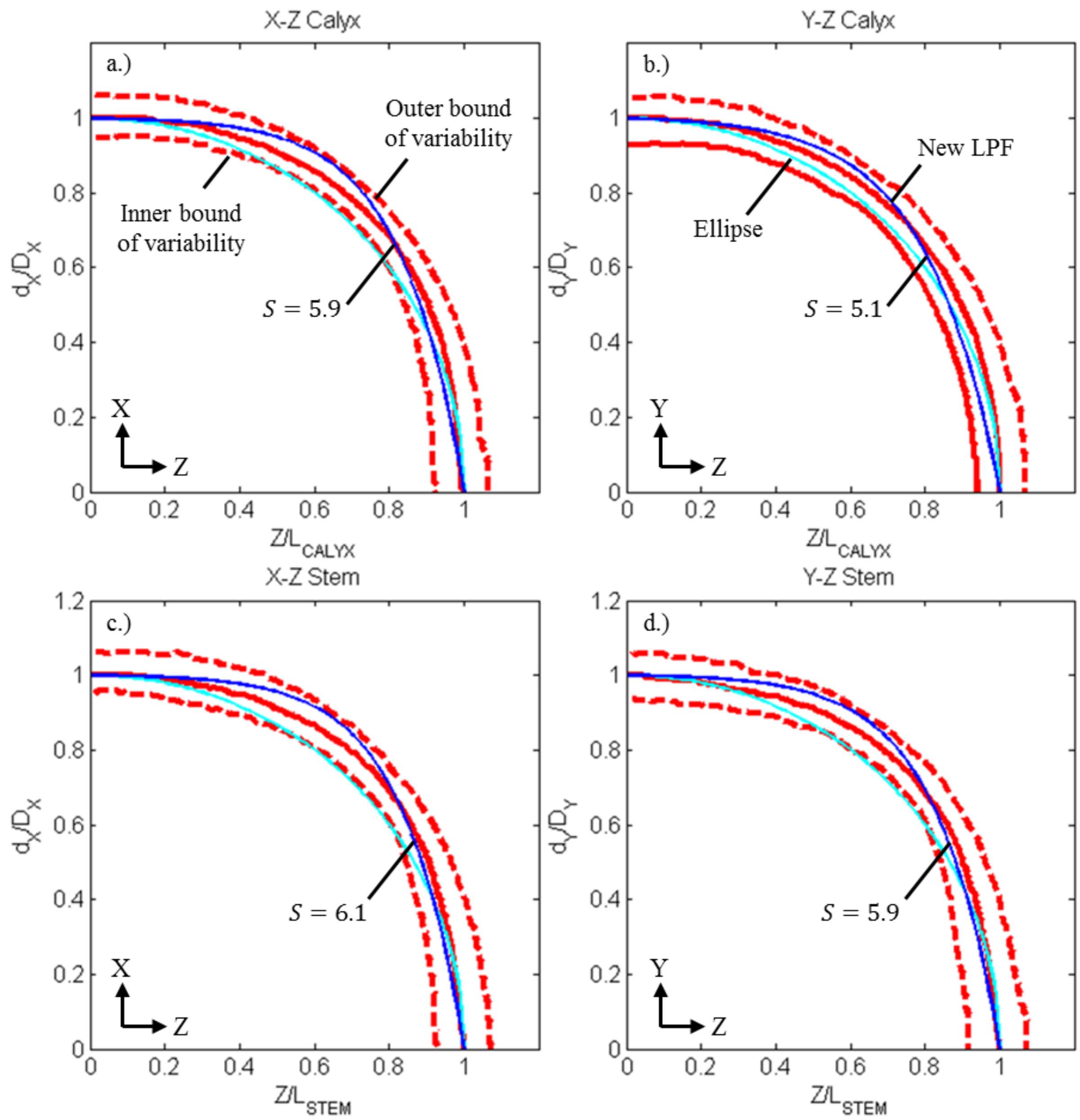

Figure 4.16: Non-Dimensional empirical minimum, average and maximum shape profiles for count 36 Hayward kiwifruit (red) compared with an ellipsoid (cyan, Eq. 4.5) and the new exponential LPF (blue, Eq. 4.8).

The new LPF shows much closer agreement to the average empirically determined profiles than an ellipsoid profile, which routinely under predicted the true shape of the kiwifruit. The new LPF over predicts near the middle of the fruit, and under predicts near the apices of the fruit; however, the error is within the bounds of variability in all locations along the Z-axis, unlike the ellipsoid that went beyond the bounds of variability in 3 out of 4 comparisons (Figure 4.16a, c and d).

Although the new LPF shows a closer agreement to the *average* empirical profile, the magnitude of over and under prediction near the middle and apex of the kiwifruit, respectively, is still problematic. The profiles provided by Anonymous (1997) include the minimum and maximum sizes for this weight range, and ideally the shape equation should produce an accurate fruit shape of any size within this range. Using Eq. 4.10 alone is limited just to an average-sized fruit. The ellipsoid LPF lacks the relative flatness near the middle of the fruit; however, it has a softer curve near the apices. Conversely, the LPF curves too sharply toward the apices, but is flatter near the middle. Therefore, the two profiles are complementary and can be combined to help mitigate the deficiencies of the other. Combining the ellipsoid (Eq. 4.7) and new LPF (Eq. 4.10) gives:

$$d_{j,k} = \left(\left[\frac{L_k - \left(\frac{L_k}{\exp(S) - 1} \times \left(\exp\left(S \cdot Z / L_k\right) - 1\right)\right)}{2 \cdot L_k}\right] + \left[\frac{\sqrt{{L_k}^2 - Z^2}}{2 \cdot L_k}\right]\right) \times D_j \qquad (4.11)$$

The performance of the updated LPF (Eq. 4.11) was assessed again by comparing predicted profiles with the industry supplied shape data; however, rather than deriving individual S values for a given profile (as in Figure 4.16), a universal value of S was calculated. This allows a single equation to accurately predict not only the average shape, but the shape across the weight range of count 36 Hayward kiwifruit. S was found by minimising the sum of the error across all comparisons (12 comparisons in total: the minimum, maximum and average profiles for the Z-X, Z-Y, stem and calyx directions; see Table 4.1), where the error was the percentage difference between the empirical and predicted area under the curve. S values were constrained to lie between 1 to 15 and the optimum S = 7.0 was found (Figure 4.17). As expected, Eq. 4.11 is much more accurate than Eq. 4.10 at predicting the average profile (maximum error of 0.55%) and is also accurate across all 12 possible comparisons, with a maximum error of just 3.09% in the case of the minimum Y-Z stem profile (Figure 4.17d).

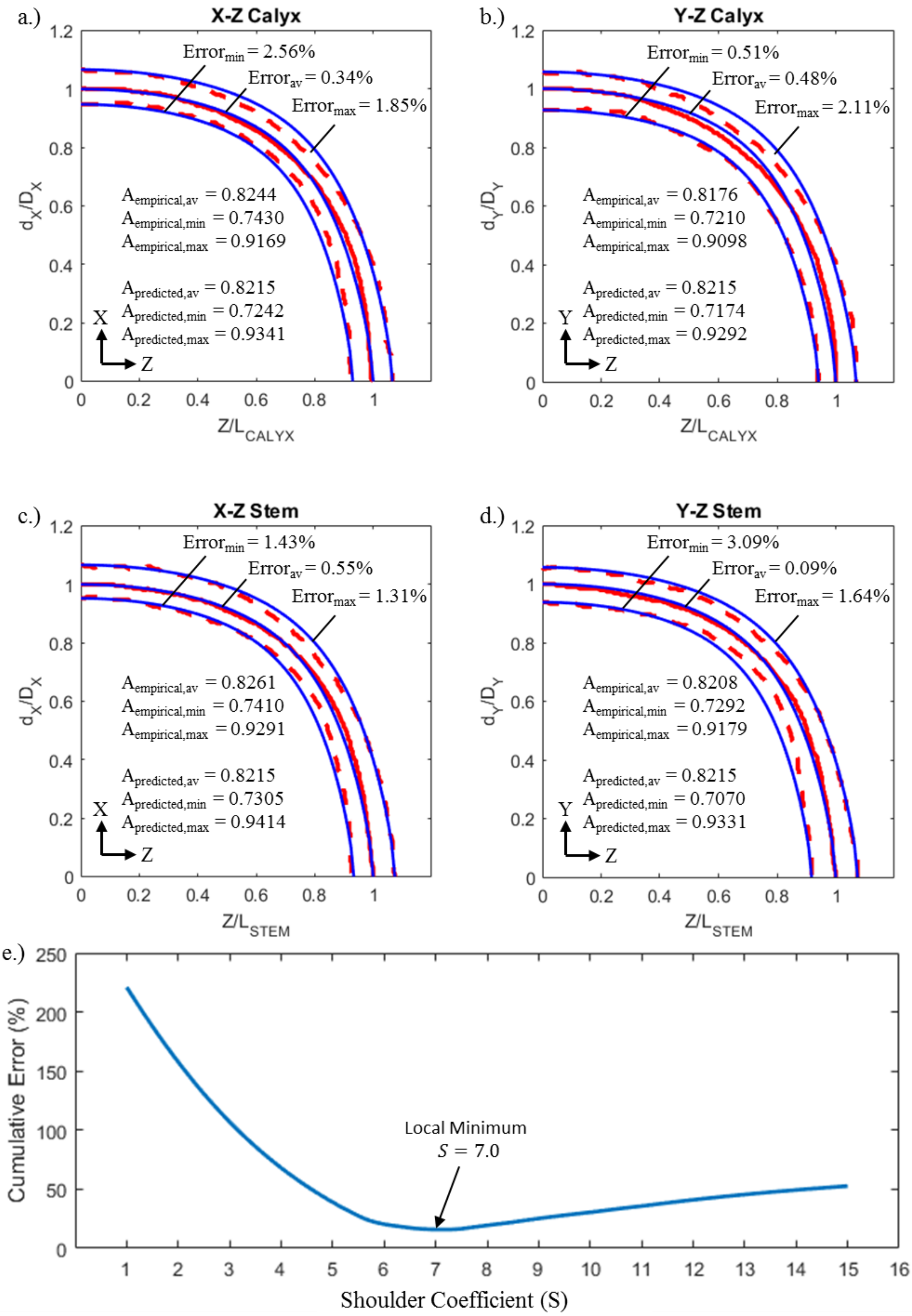

Figure 4.17: a, b c and d.) Dimensionless empirical minimum, average and maximum shape profiles for count 36 Hayward kiwifruit (red) compared with the updated LPF where S = 7.0 (blue, Eq. 4.9); and e.) Cumulative error across all 12 comparisons as a function of S, the shoulder coefficient.

Eq. 4.11 is a single equation that requires only 3 input parameters, the measurable major geometric attributes of a kiwifruit (D_X, D_Y and L); and one constant (S = 7.0) and can accurately describe both the X-Z and Y-Z longitudinal profiles, for any fruit size within the count 36 weight range. Eq. 4.11 can also be implemented in a single line of code and can be easily utilized to estimate geometrical attributes – such as volume and surface area – or combined with other methods to draw 3D fruit shapes – such as the utilisation of a parametric surface. These are demonstrated later (section 4.3.2). Similar steps can be used to create new LPFs to model other horticultural products.

4.3.2: Application of Shape Equation

With methods that accurately describe the longitudinal and lateral profiles of kiwifruit, the next consideration was how to utilise these profiles to generate fruit shapes suitable for modelling, and how to derive the characteristic geometrical attributes that are important for modelling.

4.3.2.1: Volume and Surface Area

As shown in section 4.3.1.1, the X-Y lateral profile (the cross-section) of a kiwifruit can be modelled accurately as an ellipse. Therefore, the disk method (Riddle, 1974) was used to numerically estimate the volume of a kiwifruit with a given set of D_X, D_Y and L values (Olatunji *et al*, 2015):

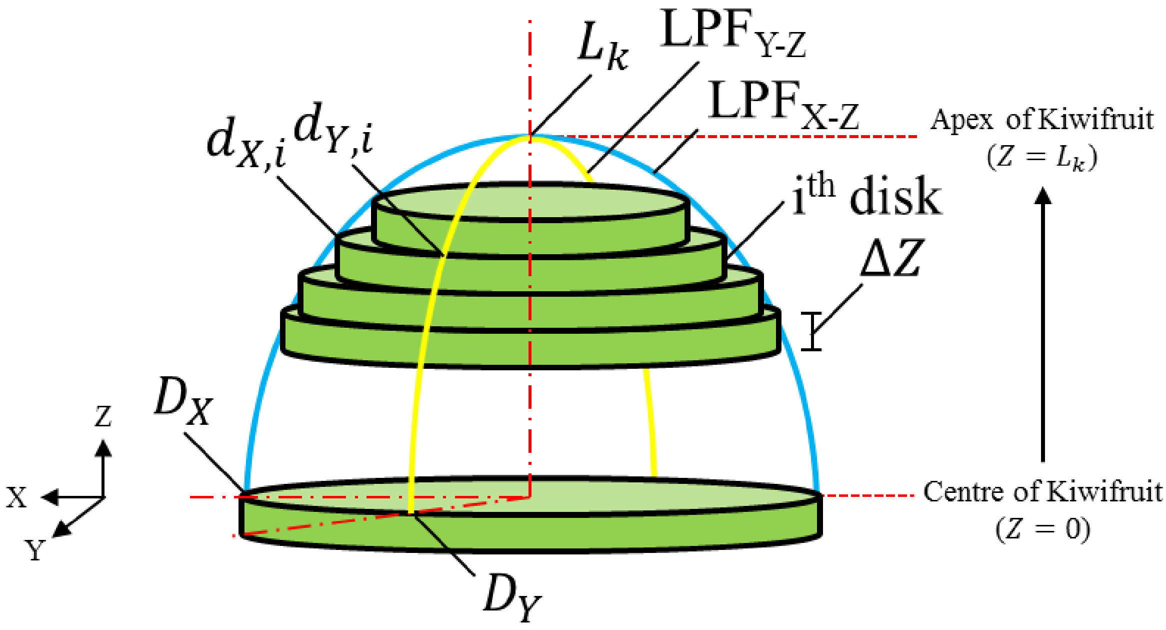

Figure 4.18: Calculation technique for numerically approximating fruit volume using the disk technique (Riddle, 1974) with the newly developed LPF for kiwifruit. Image based on Olatunji et al., 2015.

The elliptical disk at the centre of the fruit (Z = 0) has the same major and minor diameter as D_X and D_Y. The size of subsequent disks along the Z-axis are defined by the shape equation for kiwifruit (Eq. 4.11), where the thickness of each disk is dependent on the number of disks used:

$$\Delta Z = \frac{L_k}{I} \tag{4.12}$$

Where I is the total number of elliptical disks; L_k is the length from the centre of the fruit to the stem or calyx; and ΔZ is the thickness of each disk. An individual disk is given the subscript i, where the volume of a given disk is:

$$V_i = \pi d_{X,i} d_{Y,i} \Delta Z \tag{4.13}$$

So that the total volume of the fruit is numerically approximated as the sum of all disks:

$$V_{num} = \sum_{i=1}^{I} \pi d_{X,i} d_{Y,i} \Delta Z \tag{4.14}$$

The accuracy of Eq. 4.14 was validated by varying the resolution of the discretization process. For a hypothetical fruit, sized $D_X = D_Y = L_k = 1$ (also assuming $L_{stem} = L_{calyx}$), the predicted volume was investigated for I values ranging from 5 to 500, with results in Figure 4.19. At low discretization resolution ($I = 5$), the predicted volume was high – 1.4 m^3. Increasing discretization resolution showed that the numerical predictions began to converge quickly towards 1.238 m^3 at I = 500.

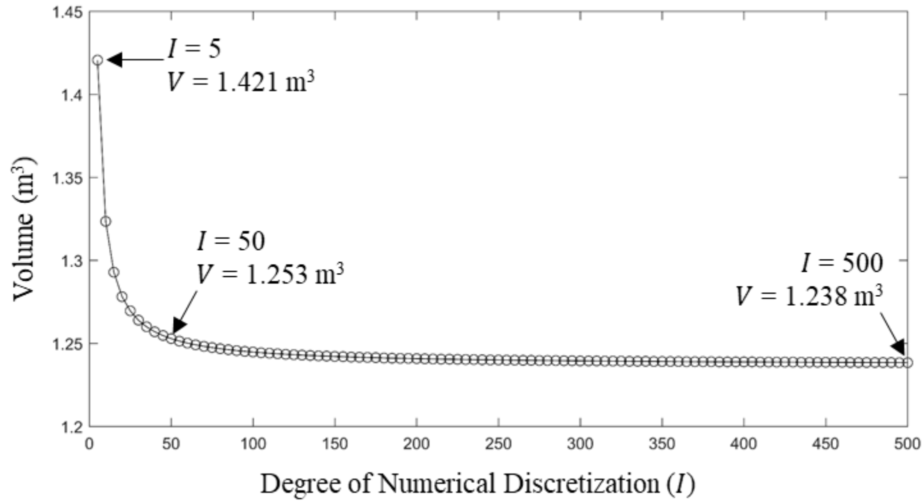

Figure 4.19: Efficacy of using the disk method to numerically approximate the volume (blue line) and surface area (orange line) of a kiwifruit shape as a function of degree of numerical discretization resolution.

4.3.2.2: CAD Software

The disk method (Riddle, 1974) was used extensively in the code-based environment of MATLAB and is demonstrated later in this thesis for the development of a fruit shape index (see section 4.3.3). However, a separate methodology was necessary for use in CAD software, such as Blender and COMSOL Multiphysics®. A feature in many CAD programs is the parametric surface, so that if the kiwifruit shape equation (Eq. 4.11) can be converted into a parametric surface it can be used natively in these software packages. Parametric surfaces are generally described as Eq. 4.15:

$$r(u, v) = f_X(u, v) + f_Y(u, v) + f_Z(u, v) \tag{4.15}$$

The three functions, f_X, f_Y and f_Z, each specify the shape of the surface in the x, y and z dimensions, respectively. The u variable is the radial coordinate direction, so that $0 \leq u \leq 2\pi$; and v is the coordinate in the vertical direction, so that $f_Z = v$ and $0 \leq v \leq L_k$. f_X and f_Y are the shape equations for kiwifruit (Eq. 4.11) in the x and y directions, respectively, but D_X and D_Y are replaced with $D_X \cdot \cos(u)$ and $D_Y \cdot \sin(u)$, respectively, to transform into the radial coordinate direction, u. Z is simply transformed to be v as these coordinate directions are both equivalent (for more details on surfaces, see Faux and Pratt, 1979). These transformations give Eq. 4.16:

$$
\begin{gathered}
r(u,v) = \left(\left[\frac{L_k - \left(\frac{L_k}{\exp(S)-1} \times \left(\exp\left({S \cdot v}/{L_k}\right) - 1\right)\right)}{2 \cdot L_k}\right] + \left[\frac{\sqrt{{L_k}^2 - v^2}}{2 \cdot L_k}\right]\right) \\
\times D_X \cdot \cos(u) + \\
\left(\left[\frac{L_k - \left(\frac{L_k}{\exp(S)-1} \times \left(\exp\left({S \cdot v}/{L_k}\right) - 1\right)\right)}{2 \cdot L_k}\right] + \left[\frac{\sqrt{{L_k}^2 - v^2}}{2 \cdot L_k}\right]\right) \\
\times D_Y \cdot \sin(u) + v
\end{gathered}
\tag{4.16}
$$

The use of the shape equation in COMSOL is summarised in Figure 4.20. It was decided that the fruit should be divided into 8 faces, similar to how COMSOL creates spheres and ellipses. Therefore, 8 separate parametric surfaces were created to describe the kiwifruit. The first 4 were for the top half of the fruit, with each parametric surface describing ¼ of the total radial direction; so that parametric surface 1 has $0 \leq u \leq 0.5\pi$, parametric surface 2 has $0.5\pi \leq u \leq \pi$, etc. The final four parametric surfaces were duplicates of the first four, but for the bottom half of the fruit as there is a plane of symmetry through the fruit centre at $v = 0$, so that $-L_k \leq v \leq 0$. After the 8 Parametric Surfaces were created, they were converted into a solid entity using the ‘Convert to Solid’ function.

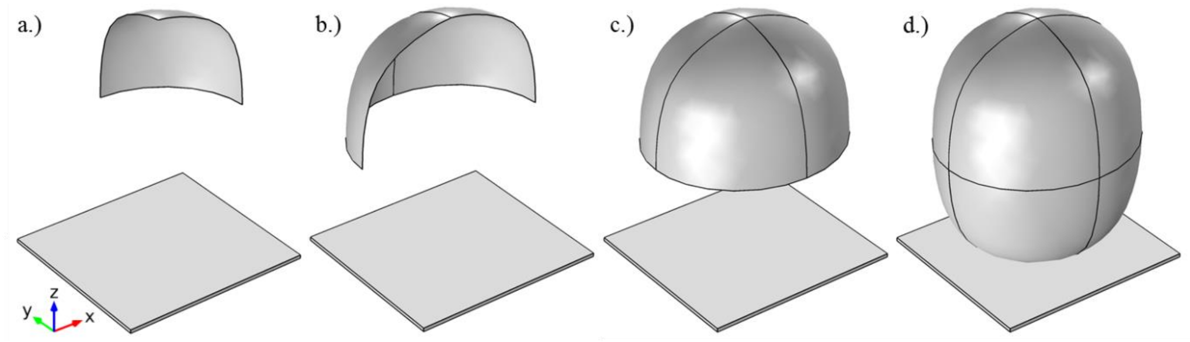

Figure 4.20: Creating a kiwifruit in COMSOL as 8 parametric surfaces; a.) 1 parametric surface, b.) 2 parametric surfaces, c.) 4 parametric surfaces (top half of fruit), d.) whole fruit.

In Blender, kiwifruits were created in a similar fashion, using the XYZ Math Surface Function. The equation to describe the parametric surface – f_X, f_Y and f_Z (Eq. 4.16) – can then be added. In this case, only two surfaces were created: one for the top, another for the bottom of the fruit (Figure 4.21). Creating fruit in this fashion, using only the Graphical User Interface (GUI) of Blender, would require that the shape equation be manually inserted every time – a menial, time consuming task, especially in the case of creating many hundreds of fruit, with different D_X, D_Y and L values (see section 4.3.3). Fortunately, Blender has a competent command line back-end; any and all functionality of the GUI has a code equivalent, allowing the software to be driven entirely by a Python script (see van Rossum, 1995). This allowed this fruit creation process to be automated. The script was computationally efficient, only 0.5 seconds to generate a kiwifruit of any specified size with an Intel® i7-4770 and 16GB of RAM), so that many fruit models can be created in a short period of time. This is used later in section 4.4.

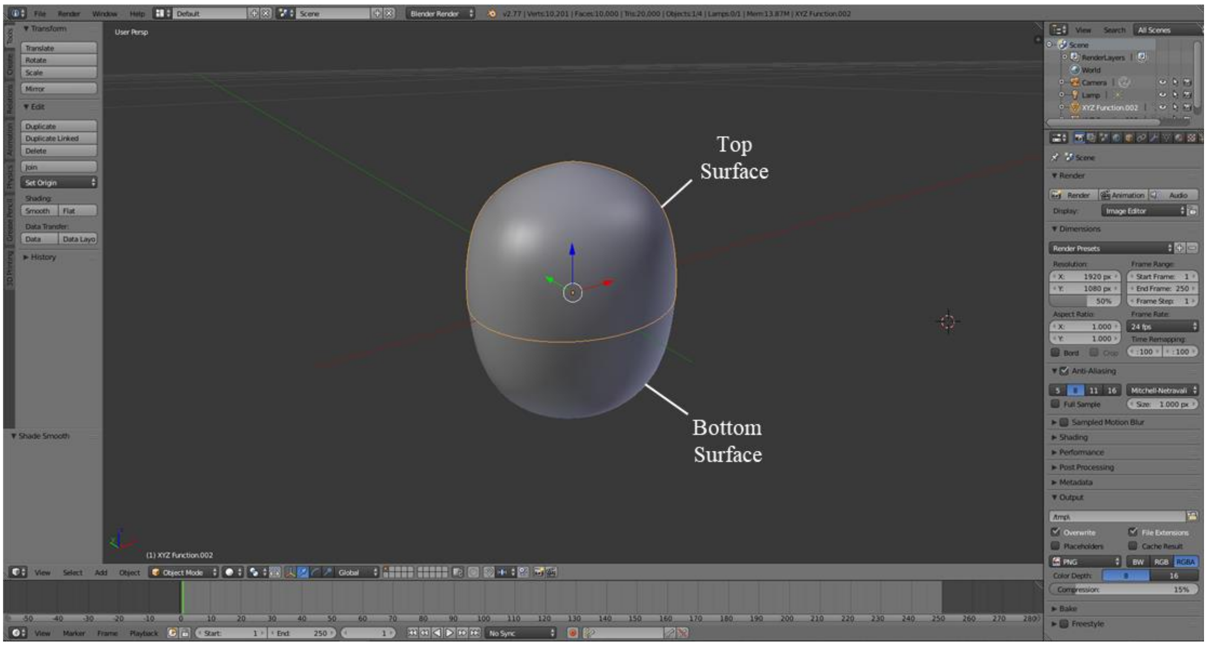

Figure 4.21: Creating a kiwifruit in Blender as two parametric surfaces (XYZ Math Surface).

4.3.3: Natural Size Variability

Fruits and vegetables are known for their wide variability in shapes and sizes, even within a given cultivar; Hayward kiwifruit being no exception. Genetic, environmental and nutritional differences result in each fruit having a unique size, weight and shape (Ho and Rogge *et al.*, 2016; Arendse *et al.*, 2016; Moreda *et al.*, 2012; Alcobendas *et al.*, 2013). Taking this variability into account is a key obstacle to engineering efficient processes in the horticultural industry, with larger design tolerances being required to operate competently compared with other industries, driving up costs (Baudrit *et al.*, 2009). Though some of these variances are controlled at the pack-house in the New Zealand kiwifruit industry – where kiwifruit is sorted electronically into weight ranges and graded according to morphological defects (Anonymous, 1997; Rashidi and Seyfi, 2007) – there is still a large discrepancy in sizes within a given weight range. As demonstrated in Thompson *et al.* (2008), the size of the product has a significant impact on the rate of cooling for the same flowrate of cooling air per kilogram of product. Therefore, while section 4.3.1 and 4.3.2 outlined a simple and repeatable method for generating accurate kiwifruit shapes, there was an additional need for a shape index, a controlled list of D_X, D_Y and L values to randomly sample from that results in a distribution of weights that is the same as an observed or desired distribution. This weight distribution not only has potential to impact the cooling rate, but also the stacking pattern and the volumetric efficiency of a given package design.

4.3.3.1: Empirical Weight Distribution

A large database of kiwifruit weights was made available by Zespri® International. The database was compiled by contractors sampling random kiwifruits from 46 orchards across a wide geographical area within New Zealand, a total sample size of 89941 fruit collected between the 9th of February and the 5th of July, 2016. The database contained weight information from 5 different varieties of export grade kiwifruit, but because this thesis is focused on Hayward green kiwifruit, the other varieties were excluded, giving a revised sample size of 22786 fruit from 16 growers. The distribution of weights from the revised database is shown for each grower line in Figure 4.22; and the entire database in Figure 4.23.

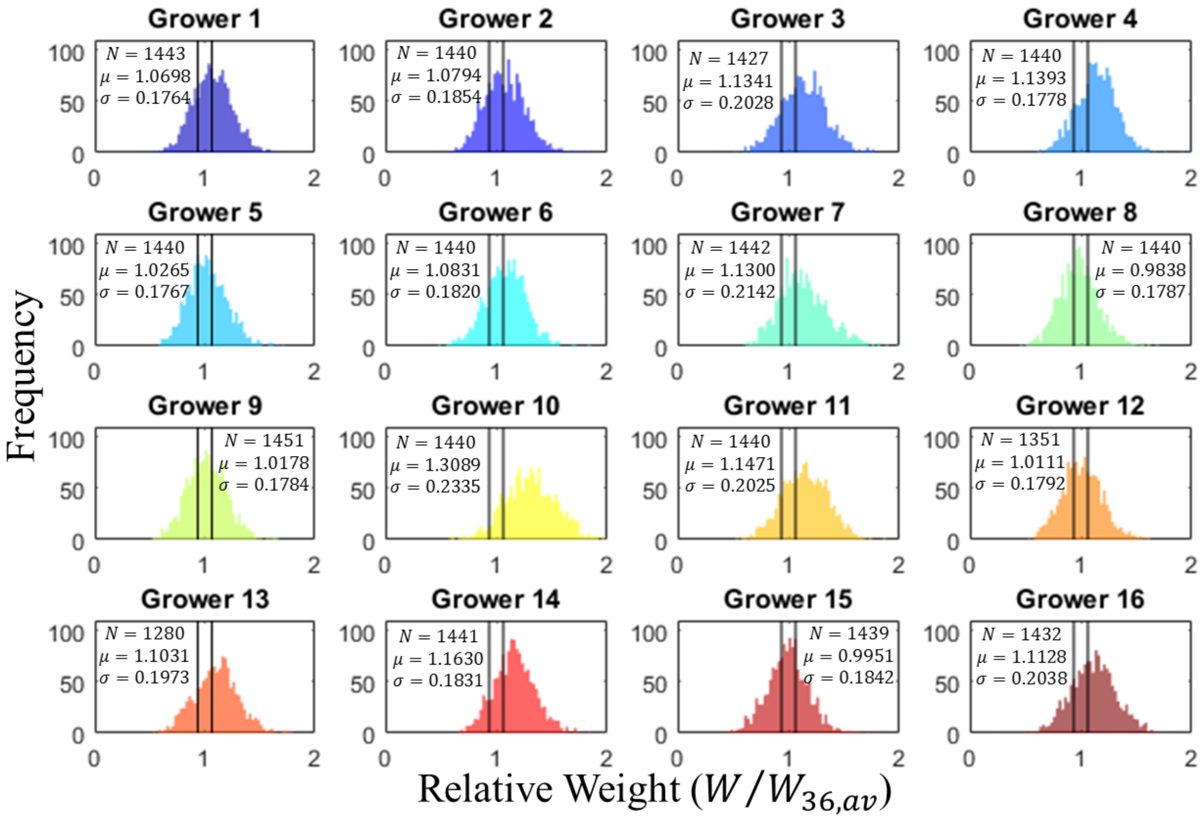

Figure 4.22: Weight distributions of picked Hayward kiwifruit from 16 growers across the New Zealand 2016 season. Weight is given as a fraction relative to the average weight of count 36 fruit.

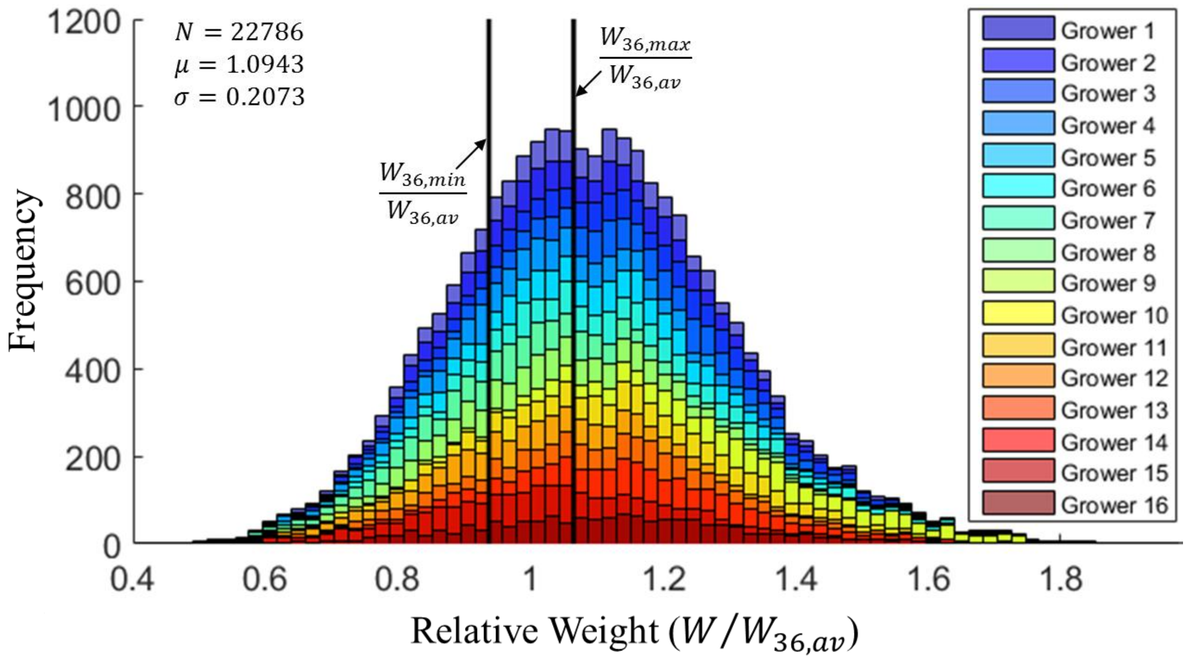

Figure 4.23: Combined weight distribution of picked Hayward kiwifruit from all 16 growers across the New Zealand 2016 season. Weight is given as a fraction relative to the average weight of count 36 fruit.

These distributions are potentially commercially sensitive information, therefore, the weight scale was made dimensionless. The database of weights was divided by $W_{36,av}$, the weight of what Anonymous (1997) considers to be an 'average' sized count 36 kiwifruit (Figure 4.13). Generally, it would seem that the weight distribution from each grower (Figure 4.22) was normally distributed – however, there was some evidence of alternative distributions. Many could be considered a 'combed' distribution, with singular peaks appearing in places other than the crest of the bell curve – though these appear frequently throughout the data set, the most notable examples are grower 2 and grower 7. Skewness appeared in many cases: growers 6, 13 and 16 showed some evidence for negative (left) skewness, favouring heavier fruit; and grower 7 positive (right) skewness, signifying a preference for smaller fruit. Some grower distributions could also be considered bimodal, with two distinct crests in the bell curve distribution – notable examples include growers 1 and 3. The two black vertical bands imposed over each grower line represents the weight range for 'count 36'; thus, the distribution within these two bands is the distribution of interest. This 'of interest' weight distribution can be quite different between growers, for example: grower 8 had the lowest average fruit weight, at just 0.98 $W/W_{36,av}$; this put the distribution peak near to the lower weight limit, $W_{36,min}$, so that fruit from this grower had a greater proportion of lighter, smaller fruit within the 'count 36' weight range. Filling many boxes with fruit from this grower may fit more fruit per box on average, compared with another grower. Conversely, grower 10 had the heaviest overall fruit – 1.31 $W/W_{36,av}$ – with a peak well outside of the 'count 36' band. The weight distribution inside of the 'count 36' band was therefore functionally square, an equitable population of fruit weights across the range of interest.

Combining the distributions of all 16 grower lines gave Figure 4.23. Though there was enough evidence to conclude that a simple Gaussian (normal) model is likely an insufficient statistical model for all of the individual growers, it does appear that the combined weight distribution across the entire industry is normal. A normal Gaussian distribution was used to model the system, using the distribution mean of 1.09 $W/W_{36,av}$ – so that the average sized Hayward kiwifruit was approximately 9% heavier than $W_{36,av}$ – and standard deviation of 0.21 $W/W_{36,av}$ as model parameters (Eq. 4.17):

$$f\left(\frac{W}{W_{36,av}}\right) = \frac{1}{\sqrt{2 \times 0.21^2 \pi}} e^{-\frac{\left(\frac{W}{W_{36,av}} - 1.09\right)^2}{2 \times 0.21^2}} \tag{4.17}$$

Performance of the statistical model across the entire kiwifruit industry is shown in Figure 4.24a and b. There was close agreement between the empirical distribution (blue bars; blue solid line) and the chosen statistical model (Eq. 4.17; dashed red line). Observing the distribution within just the count 36 size range, the model also performed well (Figure 4.24c and d. Because the crest of the combined distribution lies to the right of $W_{36,max}$, the shape of the weight distribution within the band of interest slopes upward. This non-uniform distribution of weights within the targeted weight range intimates a higher proportion of heavier, larger fruit. 53.44% of fruit within the target range is above the weight of $W_{36,av}$, so that stacking many boxes with fruit that come from this distribution would on average fit *less* fruit into a given package, compared with boxes stacked with fruit all of the same average size.

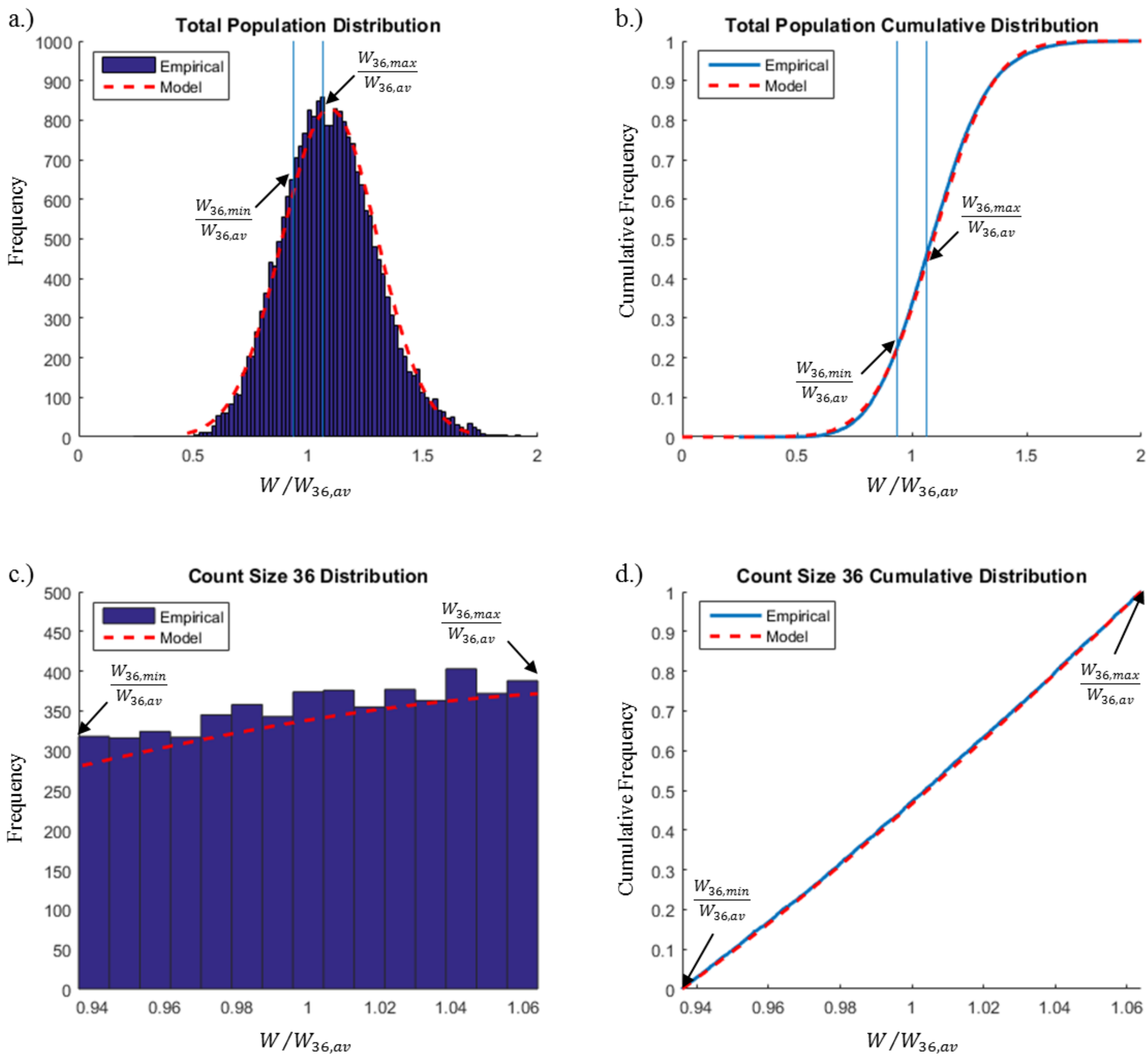

Figure 4.24:Comparison of the empirical weight distribution (blue bars and solid blue lines) of picked Hayward kiwifruit over the New Zealand 2016 season with the statistical model (dashed red line): a and b.) over the entire weight distribution; c and d.) within the count 36 weight range.

4.3.3.2: Shape Index

With knowledge of the empirical weight distribution, the next step was to develop a methodology that can incorporate either an empirical or model distribution into the randomised creation of kiwifruit. Named a 'shape index', this was envisioned as a large list of D_X, D_Y and L values that when randomly sampled from, produces digital fruit with a pre-specified weight distribution.

Initially, a simple routine for creating kiwifruit shapes was explored. This straightforward approach was a Monte-Carlo routine that created a large list of D_X, D_Y and L values, chosen at random. This routine, in flowchart form, is shown in Figure 4.25:

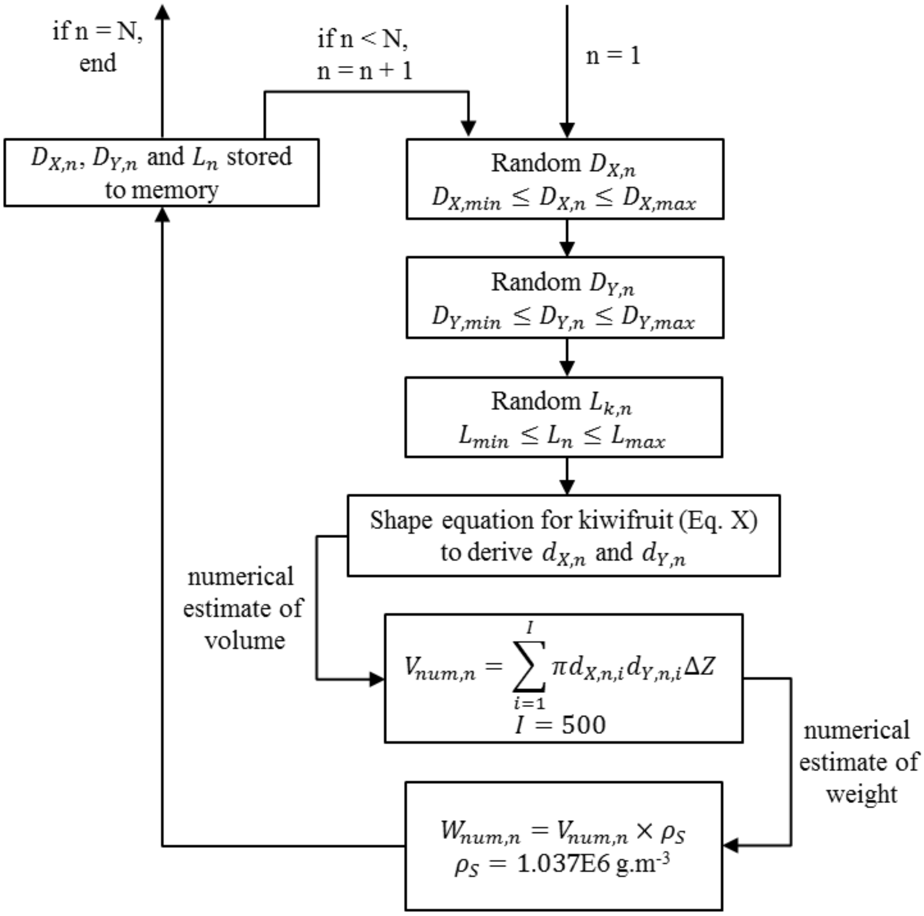

Figure 4.25: Flowchart outlining the Monte-Carlo routine, used initially to build a shape index comprised on randomly selected fruit dimensions.

Restrictions were placed on the allowable dimensions of the fruit, as defined by Anonymous (1997), and given in Table 4.1, where $D_{X,min} \le D_X \le D_{X,max}$, $D_{Y,min} \le D_Y \le D_{Y.max}$ and $L_{min} \le L \le L_{max}$:

Dimension	$\frac{D_{X,min}}{D_{X,av}}$	$\frac{D_{X,av}}{D_{X,av}}$	$\frac{D_{X,max}}{D_{X,av}}$	$\frac{D_{Y,min}}{D_{X,av}}$	$\frac{D_{Y,av}}{D_{X,av}}$	$\frac{D_{Y,max}}{D_{X,av}}$	$\frac{L_{min}}{D_{X,av}}$	$\frac{L_{av}}{D_{X,av}}$	$\frac{L_{max}}{D_{X,av}}$
Relative Length (m/m)	0.950	1.000	1.062	0.872	0.921	0.981	1.138	1.221	1.349

Table 4.1: Minimum, average and maximum dimensions of count 36 Hayward kiwifruit, according to Anonymous (1997) and Figure 4.13.

There was an equal chance of selecting any continuous value within these limits (MATLABs 'rand' function). For a particular trio of dimensions, the weight of the fruit was predicted by multiplying the numerically estimated volume, using the disk method (Riddle, 1974; Eq. 4.14; I = 1000) with the density of kiwifruit, ρ_S = 1037 kg.m^{-3} (see section 5.4).

The original supposition was that square distributions of fruit dimensions would also result in a square weight distribution. As the empirical weight distribution within the count 36 weight range was near to a square distribution, but sloped upward to favour heavier fruit, it was naively thought that modifying the random number generator to slightly favour larger D_X, D_Y and L dimensions and would then transform the index weight distribution to match the empirical distribution. However, the first assumption – that square distributions of fruit dimensions would result in a square distribution of weights – was proven false (Figure 4.26):

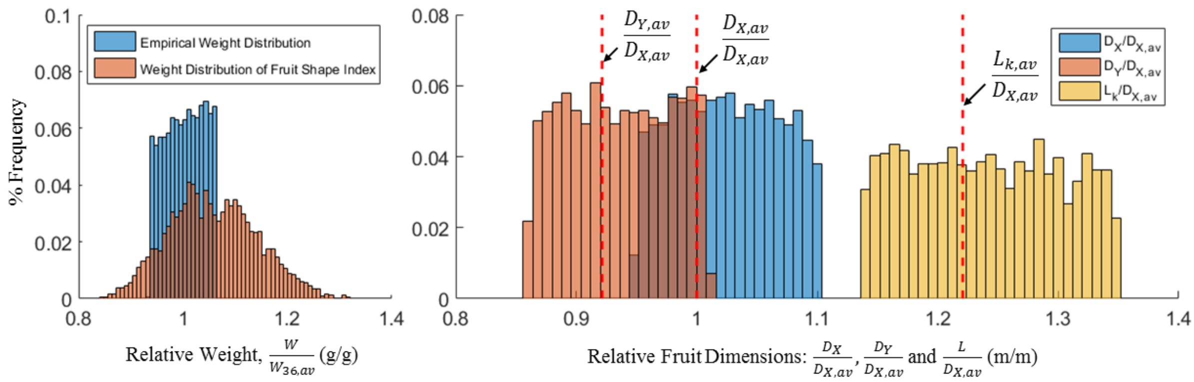

Figure 4.26: Results from building the unconstrained shape index, demonstrating that square distributions of randomly selected fruit dimensions did not result in a square weight distribution due to the non-linear relationship between the fruit dimensions and weight.

After creating N = 3000 fruit according to the basic routine (Figure 4.25), the resulting weight distribution formed a bell-curve that extended well above and below the allowable weights within the count 36 grading category, even though the dimensions of fruit were restricted to those allowed by Anonymous (1997) which represents the empirically determined size range of count 36. This was due to the non-linear relationship between fruit dimensions and the weight; for example, a low value of L (near to L_{min}) will create a disproportionately light fruit, even if large D_X and D_Y values are randomly chosen. It was therefore necessary to reverse the approach – rather than deriving a weight distribution from fruit dimensions, it was required that indexes of fruit dimensions be derived from a given input weight distribution.

The updated approach is shown in Figure 4.27 in flowchart form. As an input is the weight distribution, either from a statistical model (Eq. 4.17), or an empirical distribution. A 'weight target list', W_{target}, was derived from this information by taking the inverse cumulative distribution. N in length, this list contains weight values that continuously increase from $W_{36,min}$ to $W_{36,max}$, following the input weight distribution. A fruit with random dimensions was then created, with dimensions within the ranges specified above (Table 4.1). The weight of the created fruit is predicted numerically in the same fashion as previously (Eq. 4.14; $I = 1000$; ρ_S = 1037 kg.m^{-3}). The weight of this fruit, $W_{num,n}$, is compared to the current target weight, $W_{target,n}$. There must be a very small difference between the randomly created fruit weight and the target weight for the shape to be accepted. As there are an infinite number of combinations of D_X, D_Y and L to give a specific fruit weight, perfect agreement between $W_{num,n}$ and $W_{target,n}$ cannot be achieved; rather a very small threshold was introduced – in this case θ_{weight} = 0.05%, corresponding to approximately 0.05 grams' difference. Another criteria was added, that $D_Y/D_X >$ 0.8; according to Anonymous (1997), fruit with $D_Y/D_X <$ 0.8 are considered too morphologically defective to be included in the 'grade 1' category, and are sorted out prior to packaging. If these two criteria are not satisfied then the fruit is rejected, another is created and the comparison process beginning anew. The algorithm continues to cycle through random fruit shapes until it arrives at an acceptable triplet of D_X, D_Y and L values, which are stored to memory. The routine then moves onto $n = n + 1$, where it searches for a fruit shape that satisfies the new value of $W_{target,n+1}$. This continues until $n = N$, after which the full shape index has been constructed.

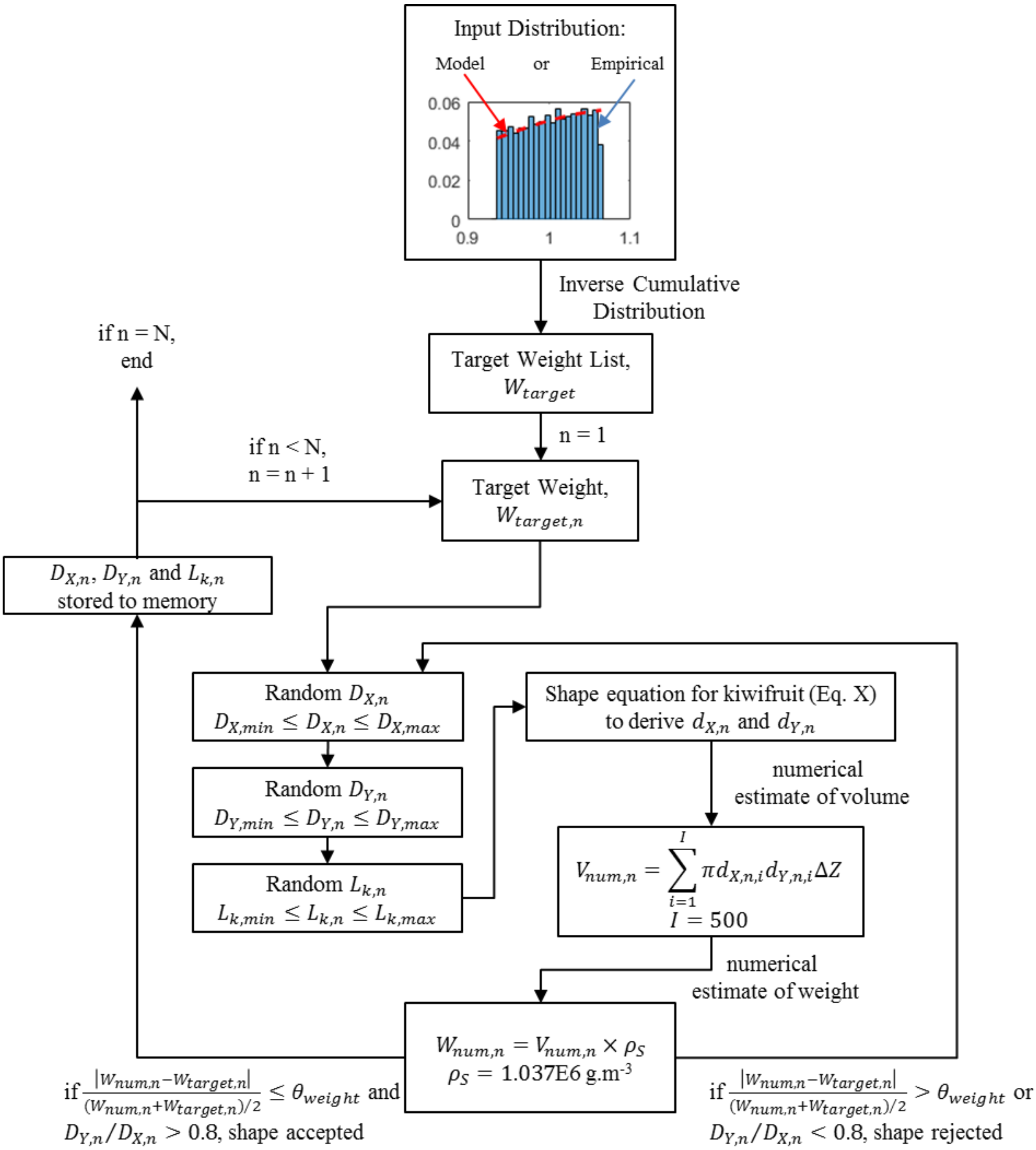

Figure 4.27: Flowchart outlining the updated Monte-Carlo routine, where an empirical or model distribution is used as an input to reject randomly sized fruit that lie significantly beyond a specified weight target.

Results for the updated approach are shown in Figure 4.28. As the algorithm relied heavily on repetition and randomization, 3 separate indexes of $N = 3000$ were computed to determine if subsequent applications of the routine resulted in significant changes between different indexes derived from the same input distribution. The weight distribution in all three indexes (orange bars) showed a very close agreement to the empirical weight distribution (blue bars), as well as the model (Eq. 4.17); red dashed line), granting credibility to the new approach. Small differences between the weight distribution of the created indexes and the empirical distribution arose from using a threshold value of θ_{weight} = 0.05%, where there was a maximum of 0.05 grams difference between weight comparisons.

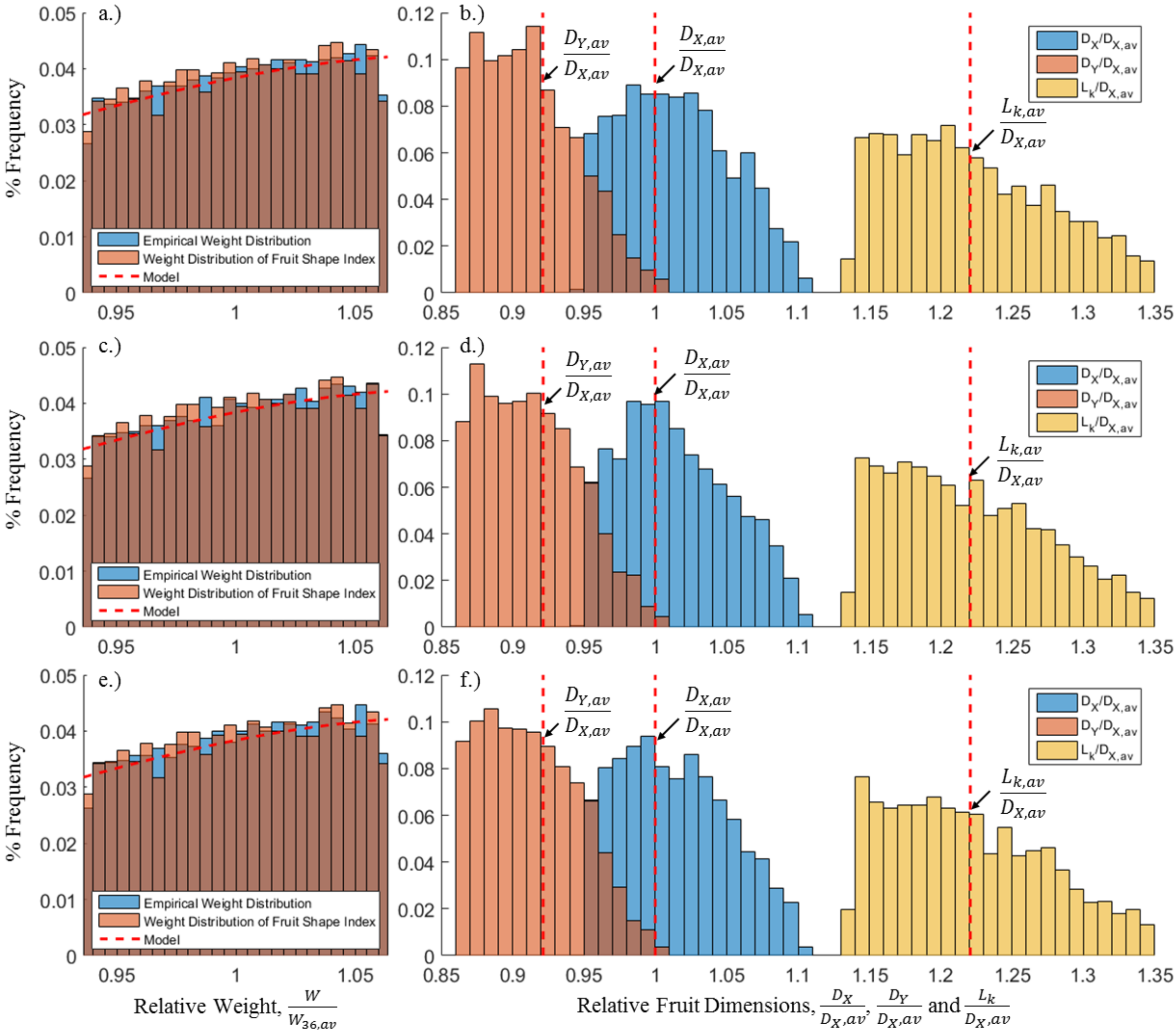

Figure 4.28: Results from building the shape index with the updated, empirically constrained method (Figure 4.27). To demonstrate that a comparable shape index can be built from the same input distribution despite the high degree of randomisation and repetition, the shape index is build 3 times.

A closer agreement could have been achieved by using a lower threshold value; however, as the approach relied upon large amounts of randomisation and repetition, doing so increases the number of fruit shapes that are rejected before an acceptable fruit shape is found, increasing the computational time required to build an index. At 0.05%, the differences were acceptably small and there was good computational efficiency – just 1-2 minutes to build an index of N = 3000 – so that a lower threshold value was not necessary. The differences between the distribution of fruit dimensions derived from the input weight distribution were similarly small between indexes: slight differences were observed, as the algorithm was free to selected any triplet of D_X (blue bars), D_Y (orange bars) and L (yellow bars) values to satisfy a particular target weight; however, the overall shape of each distribution was very much alike, granting robustness to the fruit shape index creation algorithm, and that although it relied on randomization, comparable shape indexes are derived from the same input.

Though the shape index built in this case was specifically for kiwifruit within the count 36 size range, and used the industry average (combination of all 16 grower lines for the 2016 season, Figure 4.23) as the input empirical weight distribution, a similar process could be used to create a shape index for a future or past season of harvest, a different count size, an index that represents only a single grower, or an index for a different horticultural product. Constructing an alternative shape index for different grower lines is as simple as using their specific weight distribution (see Figure 4.22) as the input to the index creation script. It is possible that this could assist industry in understanding the differences in packing efficiencies and pre-cooling completion times from a given orchard. Upgrading the approach for a larger or smaller range of weights would first require that the shape index for kiwifruit (Eq. 4.11) is compared with the empirical shape profiles of fruit within these ranges. If comparable, then the input weight distribution will need to be shifted to the new weight range, and the range of acceptable D_X, D_Y and L values updated.

Use of this method with different horticultural products should require no significant amendment: with a shape equation and empirical weight distribution, the method summarised in Figure 4.27 remains applicable.

4.4: Random Stacking Model

It would be beneficial to this project to have a rapid computational process that can automatically generate the bulk fruit geometry, regardless of the package shape, or shape of individual fruits. Methods developed in section 4.3 to generate a population of 3D kiwifruit analogues that follow a specific weight and size distribution are used here to accomplish this goal, through development of a random stacking model. The digitally created kiwifruits are modelled as bodies subjected to a gravity force and also allowed to bounce and roll off each other and the walls of the box. Thus settling into the packaging in a natural way. This generates a bulk fruit geometry that can be used as a model input for heat transfer modelling.

It was decided that a stacking model was the best solution to achieve automated geometry construction because it mimics parts of the industrial packing process: this process begins at the orchard, where fruit are picked manually from vines and placed into large bins (Figure 4.29a). The fruit are then individually graded (Figure 4.29b), the primary goal to sort fruit into their appropriate weight ranges. Fruit within the count 36 size range are automatically deposited in batches of 102 from the grader, where this collection of fruit falls and stacks into a waiting modular bulk package (Figure 4.29c). A line operator closes the polyliner and lid of the box, and adds the filled box to a stack of previously filled boxes until a full pallet is formed (Figure 4.29d). This pallet is then taken quickly to a pre-cooler, where the forced-air cooling process brings the fruit down to seven-eighths of the storage temperature. However, modelling the stacking process that occurs in Figure 4.29c was not the only incentive for taking this route: another major incentive was that it was easier to develop an automated geometry construction method that was agnostic to fruit shape by pursuing a random stacking regime. Other mathematical routines could have been exploited to fill a certain space with objects, such as in Jodrey and Tory (1985), where the position of spheres were randomly generated inside of a digital space, and any overlaps were corrected iteratively by moving spheres away from each other's centre of mass until no collisions were detected. Such a process may have been useable in this scenario had products such as apples or oranges been the focus, which have been modelled successfully as spheres (Tanner *et al.,* 2002b; Defraeye, *et al.,* 2014; Zou, *et al.,* 2006a); however kiwifruits were proto-ellipsoids with randomised dimensions, so that it was not suitable in this case; and furthermore, in the pursuit of keeping the model as flexible as possible, there should not be a limit on the size, shape, or variability of sizes and shapes between individual products that can interfere with the methods ability to generate the internal bulk geometry. For these reasons, the Discrete Element Method (DEM) physics engine integrated with Blender was exploited to achieve the previously stated goals. Instead of making assumptions about the shape or size of the dynamic objects included in the model, Blender calculates and applies translational and rotational time integration on the faces and vertexes that comprise the object, and performs collision detection based on conjunctions in the surface topographies of separate objects. So long as there is a method that can generate a shape made of a manifold surface, comprised of a mesh of faces and vertexes, this same DEM model can be used to generate the bulk geometry inside of a package for fruit of any shape.

The use of Blender as the vehicle to solve DEM problems is also becoming more frequent (Izadi and Bezuijen, 2015; Kretz *et al.*, 2016), as results can be analysed and visually rendered in high definition within the same free and open source software package. Furthermore, a Python script can be used to drive Blender, so that any models developed can be condensed into a deliverable to be handed over to industry partners. In the immediate context of horticultural packaging, the work is scarce. Delele *et al.* (2008) used the DEM approach to investigate the effects of random stacking of spheres on the pressure drop through a package (a DEM-CFD combination). However, this study did not investigate the heat transfer consequences. Recently, Gruyters *et al.* (2016) used this combined DEM-CFD method to determine the difference between a randomly stacked package of spheres, compared with a randomly stacked package of apple shape simulators. To the author's knowledge, there has not been an investigation that combines DEM, heat transfer, and the existence of a polyliner to a forced-air cooling scenario.

The following modules of the random stacking model are all performed automatically within the Python script written for the random stacking model.

Figure 4.29: The processes involved with filling modular bulk boxes with kiwifruit: a.) fruit are picked and placed into large bins, then delivered by truck to a packing house; b.) fruit are sorted automatically by a grader, which sorts fruit into their various weight categories, including count 36; c.) fruit within the count 36 size range are automatically deposited from the grading line and into a modular bulk box; d.) after boxes are filled, they are stacked into pallets and taken to a forced-air pre-cooler.

4.4.1: Chute Creation

The first consideration in the development of this stacking model was the creation of the rigid barriers inside of which the fruit were to stack, simulating the stiff fibreboard packaging of the box. These were created in Blender as planes, flat objects without thickness but with a specified length and width that can be programmed to prohibit other objects (fruit) from passing through them.

As work began on this stacking model, several problems arose: first, there was an issue concerning the top layer of fruit when stacking a box with 102 count 36 fruit – the standard amount according to industry. It was a frequent occurrence that fruit would stack inequitably into one side or corner of the box (a result of random processes described later in section 4.4.2 and section 4.4.3), so that either there were several fruit above the top of the box – so that the lid of these particular boxes of fruit wouldn't be able to close – and in some more extreme cases, fruit would stack high enough to fall out of the package. In these events there was the coupled issue of an absence of fruit on the opposite side of the box. These problems also occur in industry, but these 'rogue' fruit are redistributed manually by an operator on the packing lines – boxes are either shaken to even the top surface, or one or two fruit are simply moved by hand into the recesses on the other side of the box. Though Blender was a competent enough tool to potentially create an alternative Python script that identified these rebel fruits and relocated them to gaps in the top of the package – automating the manual processes done in industry – a much more elegant and straightforward solution was to overfill the box with more fruit than the nominal target of 102 fruit and then identify and remove fruit that do not fit (until the correct number of fruit remain and all remaining fruit fit); a process described in section 4.4.4.

This overfilling strategy had the additional benefit of predicting the volumetric efficiency of alternative package designs. The number of fruit packed into the box can impact the cooling time, as it is proportional to the initial thermal mass. Although the industry standard packing efficiency for the modular bulk package with count 36 fruit is 102 (~10.3 kg), this information changes when the box is shrunken or enlarged even slightly. Developing a flexible cooling model that is applicable to alternative package designs therefore requires the capability to construct the internal geometry in such a way that the maximum – or at the very least, near maximum – number of fruit are packed within the confined space (see section 4.4.4).

With this overfilling principle in mind, the box geometry was constructed thusly: 4 'Wall Planes' to represent the vertical part of the box, and one 'Floor Plane' to represent the box bottom. These planes created a square recess for the fruit to fall into that had the same footprint as the internal geometry of the box in terms of length ($\mathbb{B}_X$) and width ($\mathbb{B}_Y$); however the height of this digital space was well above the ordinary height of the box ($\mathbb{B}_Z$) so that a 'chute' was created, the height of which was $\mathbb{B}_C$. Above the chute, 4 more 'Funnel Planes' were created, intended to channel falling fruit down and into the chute. These were created with an angle of ¼π radians (45°), though their creation was coded in a way that any angle could be chosen – a slighter angle makes the funnel larger, which may be useful in other applications but is not considered here (Figure 4.30).

The Python script creates the chute geometry automatically based upon the input parameters of $\mathbb{B}_X$, $\mathbb{B}_Y$ and $\mathbb{B}_C$ (Figure 4.30). Although these were $\mathbb{B}_X$ = 372 mm and $\mathbb{B}_Y$ = 292 mm for a modular bulk package, the same code can be executed with no changes (other than the input parameters) to investigate smaller and larger packages.

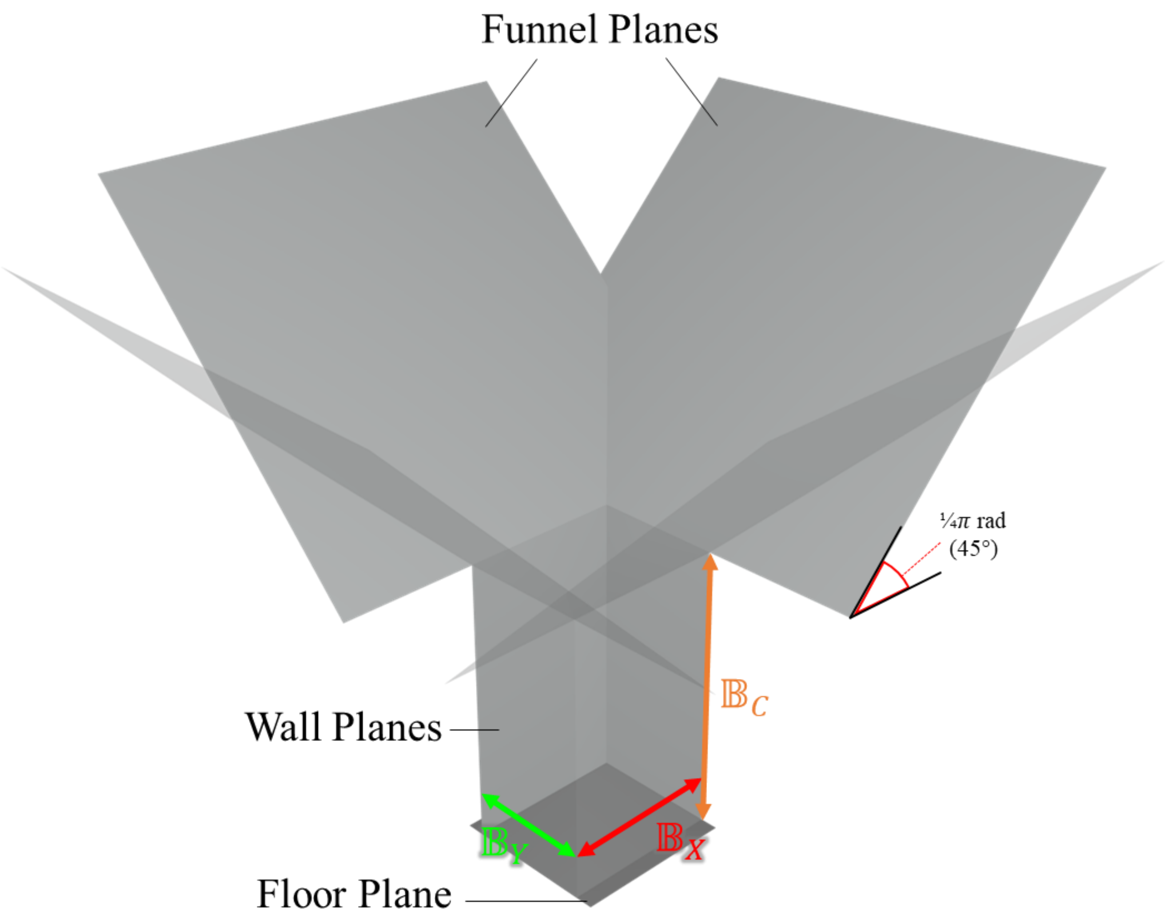

Figure 4.30: Model geometry of the chute, created with the same footprint as the inner dimensions of the box under study, inside of which a multitude of digital kiwifruit are to stack.

4.4.2: Fruit Creation

The next consideration was how to give the model the capability to automatically create a user-defined number (N) of kiwifruits to stack into the chute. The important aspects of developing this capability were how to properly utilize loops and randomisation to draw fruit of disparate shape and size, but which also followed a pre-specified weight distribution; and that each time a computational stack is executed, a unique bulk shape of kiwifruit is generated. An individual kiwifruit is denoted as:

$$\mathbb{K}_{n,X,Y,Z,\theta_X,\theta_Y,\theta_Z,D_X,D_Y,L}$$

Where $\mathbb{K}_n$ represents the digital kiwifruit n, out of a total number N; X, Y and Z is the location in 3D space where the fruit is created and corresponds to its centre of gravity; θ_X, θ_Y and θ_Z is the angle of rotation along each of the X, Y and Z axes at the fruit genesis, again calculated from the centre of gravity; and D_X, D_Y and L is the major diameter, minor diameter and length of the fruit created. Fruit were created in Blender using the process outlined in section 4.3.2.2. A loop was coded with N number of iterations, after which a new kiwifruit was created in Blender. At the beginning of each iteration, unique values of size (D_X, D_Y, L), location (X, Y, Z) and angle values ($\theta_X, \theta_Y, \theta_Z$) were chosen either sequentially or randomly.

First, the dimensions of $\mathbb{K}_n$ were randomly chosen. This relied upon there being a fruit shape index, created in section 4.3.3, which came in the form of a very large list of D_X, D_Y and L values that followed a specific weight distribution (Figure 4.28). A random integer was then chosen between 1 and 3000, which defined the row from which D_X, D_Y and L were extracted from the shape index to create a fruit.

The location of the fruit at the moment of creation was at the origin (0,0,0). The next step was to move the fruit into position above the chute. The XYZ coordinates of each fruit were defined sequentially by*:

$$X = \left[\left(\left\lfloor\frac{n-1}{3}\right\rfloor \mathbf{mod}\ 3\right) - 1\right] \times \frac{B_X}{2} \tag{4.18}$$

$$Y = [(n\ \mathbf{mod}\ 3) - 1] \times \frac{B_Y}{2} \tag{4.19}$$

$$Z = \lceil n/9 \rceil \times 0.15 + B_C \tag{4.20}$$

Eq. 4.18, Eq. 4.19 and Eq. 4.20 automatically group the fruit neatly into aisles of 9 above the chute, in a way that scales infinitely so any value of N kiwifruit can be chosen (Figure 4.31):

* For clarity: $\lfloor x \rfloor$ is the floor function, greatest integer less than or equal than x; $\lceil x \rceil$ is the ceiling function, the smallest integer greater or equal to x; and $\mathbf{mod}$ is the modulus, remainder after division

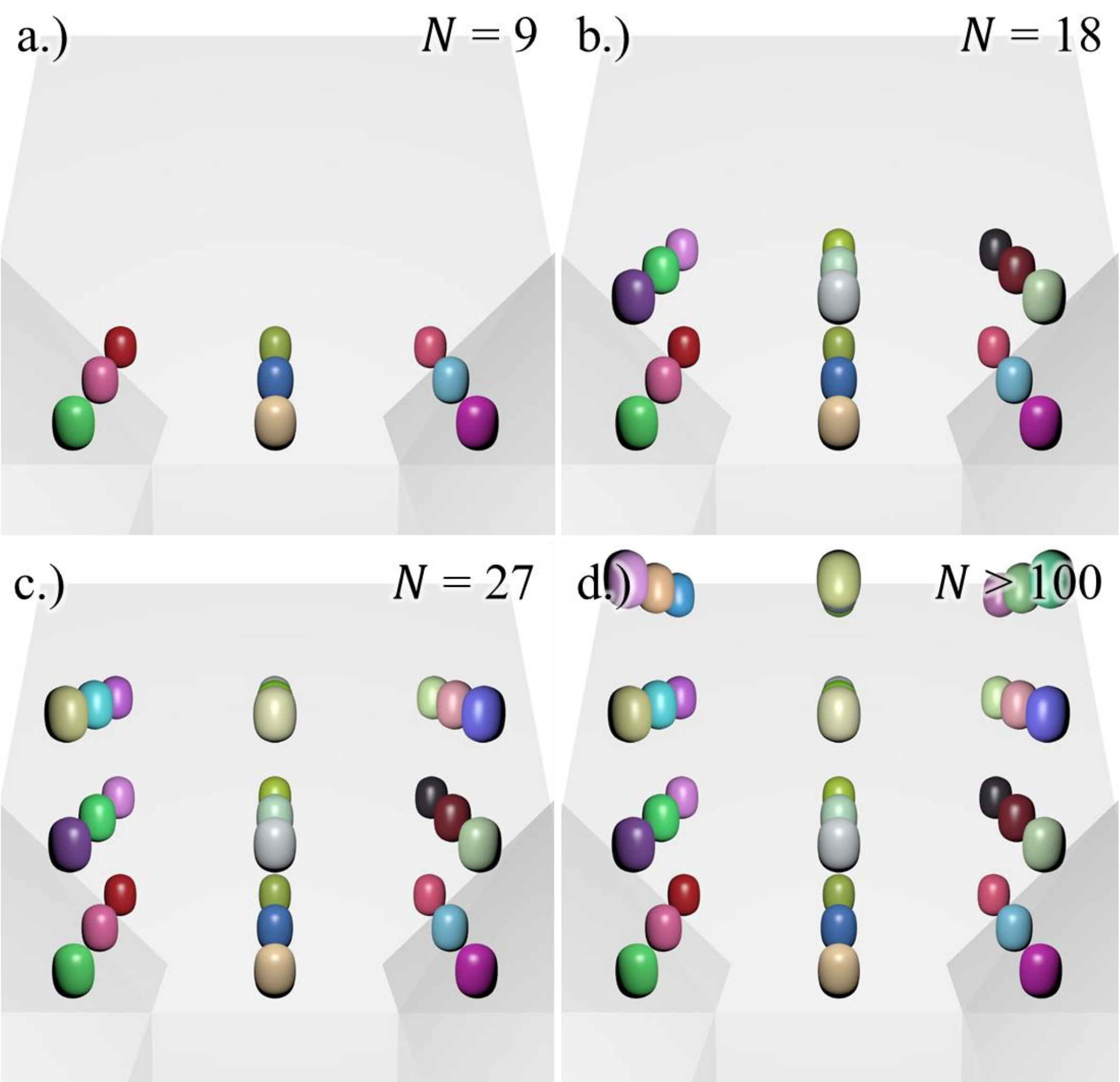

Figure 4.31: Demonstration of the sequential placement process of digital kiwifruit above the chute, where according to Eqs. (4.18), (4.19) and (4.20), fruit are automatically grouped into aisles of 9. Note: for illustrative purposes, shape variation has been removed. Colours were randomly chosen to better distinguish individual fruits and did not have a physical meaning.

The angle of rotation for each of the fruit (θ_X, θ_Y and θ_Z) created initially (Figure 4.31) was (0,0,0). It was necessary to randomise these values to ensure that the fruit formed a unique bulk shape every time the script was executed:

$$\theta_X = r \times 2\pi \tag{4.21}$$

$$\theta_Y = r \times 2\pi \tag{4.22}$$

$$\theta_Z = r \times 2\pi \tag{4.23}$$

Where the angles are in radians. In conjunction with randomization of the angle, some more randomness was further incorporated into the X and Y location of $\mathbb{K}_n$:

$$X = \left(\left[\left(\left\lfloor\frac{n-1}{3}\right\rfloor \mathbf{mod}\ 3\right) - 1\right] + \left[(r - 0.5) \times \frac{B_X}{4}\right]\right) \times \frac{B_X}{2} \tag{4.24}$$

$$Y = \left([(n\ \mathbf{mod}\ 3) - 1] + \left[(r - 0.5) \times \frac{B_Y}{4}\right]\right) \times \frac{B_Y}{2} \tag{4.25}$$

Where r is a random number uniformly distributed between 0 and 1. Figure 4.32 shows the resulting geometry at the end of the fruit creation loop.

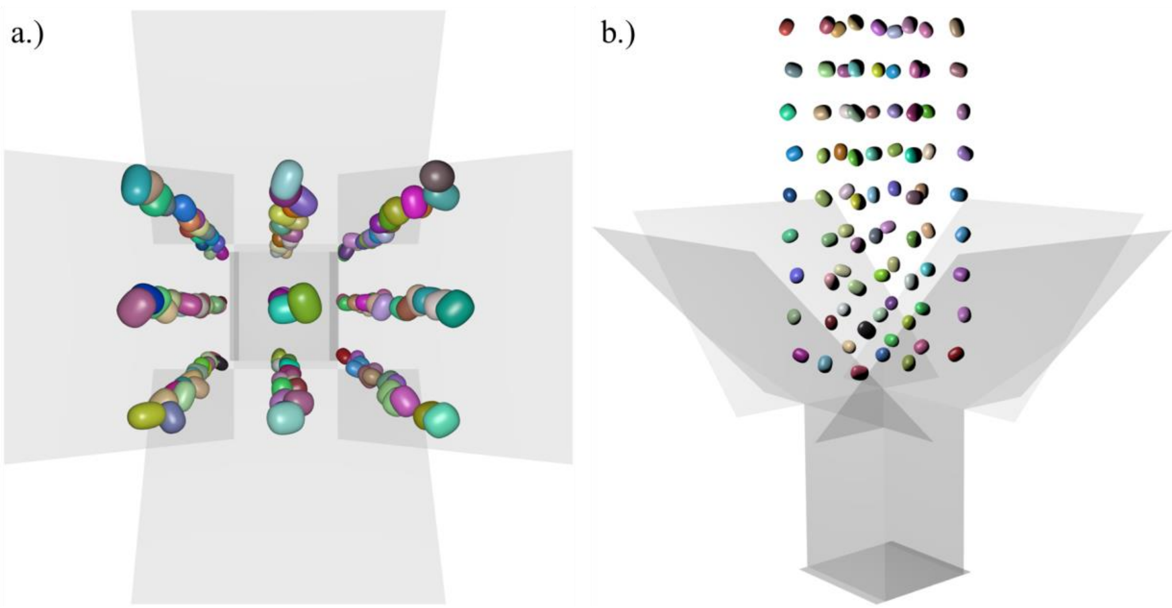

Figure 4.32: Result of creating N = *150 digital kiwifruit with randomised shape, creation location and creation angle: a.) birds-eye view and b.) perspective view.*

Fruits have a variety of sizes and shapes – some long and skinny, some short and squat, with a distribution of shapes intermediary to these extremes. The fruit are lined up into 9 aisles as before (Figure 4.31), but with less uniformity due to the small randomised shift forward or back, left or right;

and the randomised angle of each fruit was unique. These random processes are important, as they ensure a unique set of initial conditions each time the model is executed so that the result at the end of the stacking simulation is unique (see section 4.4.3).

4.4.3: Gravity and Rigid Body Dynamics Simulation

Bullet Physics (Coumans, 2012) is an open source physics engine capable of performing collision detection, soft body and rigid body dynamics, which has been integrated with Blender so that stacking modelling, rendering and analysis of results can be performed on one platform (Izadi and Bezuijen, 2015). DEM is a technique used to model an assembly of particles, interacting with each other through simulated gravity and collisions (Tijskens *et al*, 2003). In this application of DEM, the digitally created kiwifruit act as the particles colliding with each other and with the walls of the chute.

It was decided that this system would be modelled as a rigid body problem, rather than a soft body problem. Rigid body problems are where the particles aren't permitted to overlap, nor can the surface topography be deformed from external forces; where as in a more realistic sense, most particles are deformable – a soft-body problem – where object deformation and elasticity are taken into account computationally by allowing particles to overlap (Tijskens *et al*, 2003; Marczewska *et al.,* 2016). Modelling this system as a soft-body problem increases the complexity, as the elastic properties of kiwifruit would need to be measured precisely via pendulum and dropping experiments (Dintwa *et al.*, 2008); and a texture analyser to determine the degree of deformation as a function of external forces to resolve all of the necessary model parameters. Such a model could be necessary to answer questions surrounding the handling of kiwifruit as it moves through the supply chain, such as formulation of alternative stacking methods that minimise bruising, where on a fruit is bruising most likely to occur, or the extent of vibrational damage inside of boxes or pallets of fruit as they are transported through specific stages of the cold chain (Van Zeebroeck *et al.,* 2006; Van Zeebroeck *et al.,* 2008; Dintwa *et al.,* 2008). However, solving handling problems clearly lie outside the scope of this thesis. As the goal of this project was a fast and flexible cooling model, the primary motivation for creating this stacking model was to have a tool that can generate the internal geometry inside of a package in a short amount of computational time, is easily adaptable to changes in package size and shape, could be equally applicable to alternative (non-kiwifruit) horticultural products, and can then be exported from Blender into modelling software such as COMSOL or MATLAB. Therefore, it was of much less concern to accurately predict the journey the fruit takes as it falls into the box. Rather, the end product, the bulk geometry formed after all kiwifruit have been allowed to settle, was of much greater importance. Predicated on these modelling priorities, the considerably simpler and computationally efficient rigid-body approach was taken. Furthermore, the assumption that a rigid-body problem can be applied to kiwifruit falling into a box can be made with confidence, considering that Hayward kiwifruit are picked very early into ripening and are particularly rigid – New Zealand kiwifruit are picked with a firmness of 7-8 kgf, where ethylene is used later in the cold-chain to ripen and soften the fruit to a consumer ready and palatable 0.5-1 kgf (Jabbar *et al.*, 2014). As only freshly picked fruit end up in the pack house, these stiff fruits must be subjected to 8kg of force to induce stress-load failure. Considering the largest fruit in the count 36 size range is approximately 0.1 kg, the forces exerted on the kiwifruit by collisions from other fruit causes negligible deformation, and can therefore be ignored. This also lends credence to simulating the box geometry as a vertical chute; though it would be more accurate to model the system as fruit moving horizontally along a conveyor belt and then ejected into the box (Figure 4.29: c), the primary objective was the determination of the settled state of the fruit, so it was appropriate to model the box geometry as a vertical chute; even if the two different approaches to modelling the box geometry would result in different trajectories for the fruit to take into the box.

The rigid body dynamics engine integrated with Blender executes a simulation loop consisting of collision detection, collision resolution and time integration segments (Coumans, 2012; Izadi and Bezuijen, 2015; Coutinho, 2013; Figure 4.33).

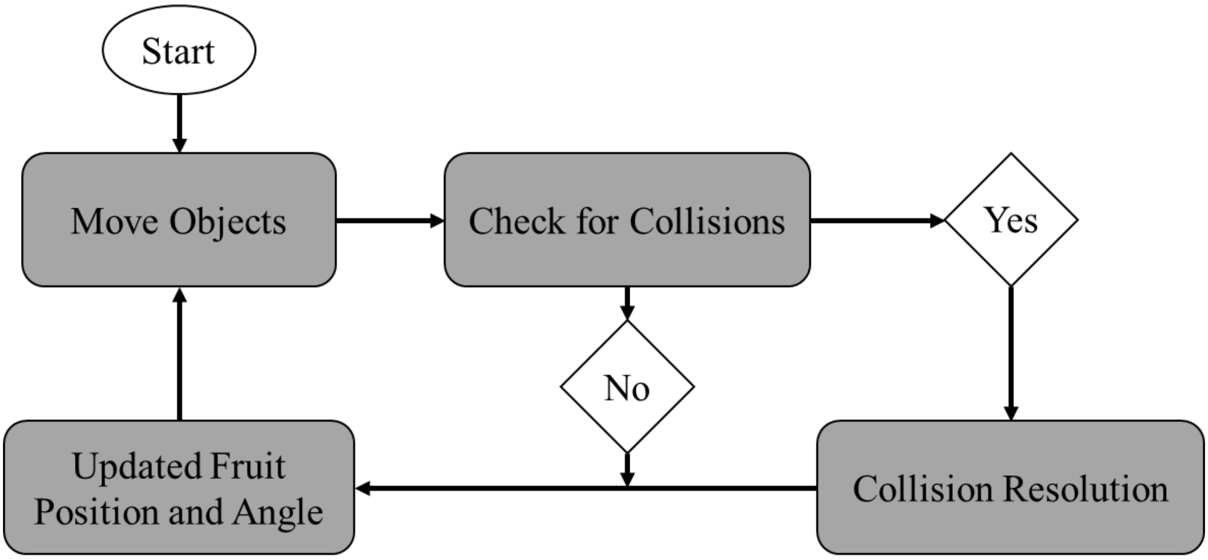

Figure 4.33: Rigid body dynamics simulation loop, consisting of collision detection, collision resolution and time integration segments. Figure based on Coutinho, 2013.

The simulation loop begins at some time t_0, where the engine advances time by some small interval, Δt, to reach a new dynamic state, $t_1 = t_0 + \Delta t$. The engine advances all $\mathbb{K}_n$ from the beginning to the end of the time step, according to the velocity, acceleration and torque calculated in the previous time step, ignoring all collisions and following Newton's laws of motion:

$$M_n a_n = G_n + \sum_c F_{cn} \qquad (4.26)$$

$$G_n = \begin{bmatrix} 0 \\ 0 \\ -M_n g \end{bmatrix} \qquad (4.27)$$

$$I_n \alpha_n = H_n + \sum_c p_{cn} \times F_{cn} \qquad (4.28)$$

$$H_n = \begin{bmatrix} 0 \\ 0 \\ 0 \end{bmatrix} \qquad (4.29)$$

Where M_n and a_n are the mass (g) and translational acceleration (m·s^{-2}) of kiwifruit $\mathbb{K}_n$, respectively; G_n is the gravity force acting on $\mathbb{K}_n$, g being the gravitational acceleration constant, 9.81 m.s^{-2}; I_n and α_n are the inertia (g) and rotational acceleration (rad·s^{-2}), respectively; and H_n the moment acting on $\mathbb{K}_n$; $\sum_c F_{cn}$ is the sum of all contact forces acting on $\mathbb{K}_n$, the number of contacts being the subscript c; and p_{cn} is the position vector of a contact point (p_c) and the centre of mass (p_n) of kiwifruit $\mathbb{K}_n$. After the engine has calculated new locations and angles for all $\mathbb{K}_n$ at t_1, the engine checks for collisions.

This is performed by checking for conjunctions of surface topographies (Coumans, 2012). If no collision is detected – such as in the case at the model inception, when fruit are spatially separated so that there are no collision forces, only gravity forces (Figure 4.34a) – then the model advances each $\mathbb{K}_n$ downward at g = 9.81 m.s^{-2} and the simulation loop continues to the next time integration step. When one or more collisions are detected, then the collision resolution step is required to resolve the collision forces at play. Two types of collisions can occur: between a fruit and a wall (Figure 4.34b), or between a fruit and another fruit (Figure 4.34c).

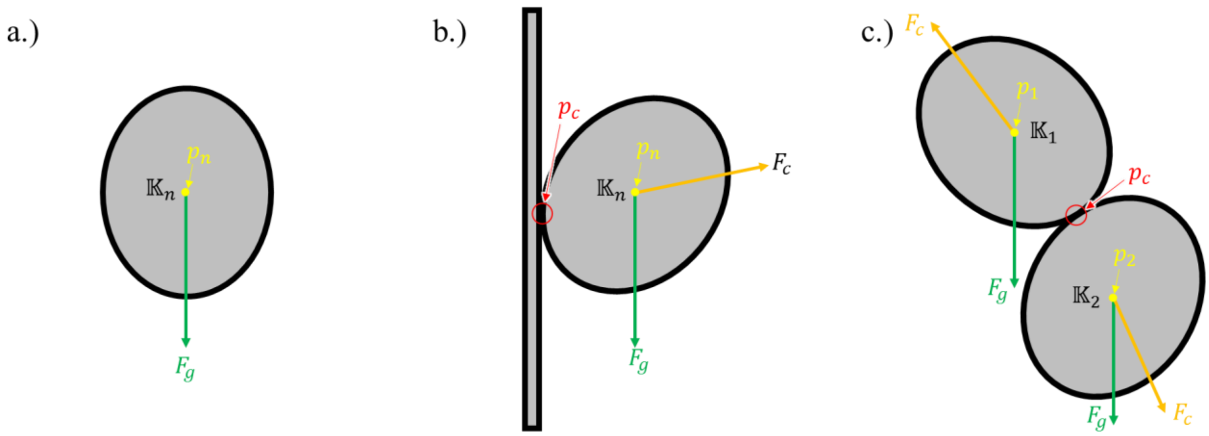

Figure 4.34: Body forces acting on $\mathbb{K}_\mathrm{n}$ during stacking: a.) gravity force; b.) gravity and collision force with the walls; c.) gravity and collision forces between fruits. Figure based on Coutinho, 2013.

To resolve the collision, the engine moves the colliding objects backwards through time using linear interpolation, to estimate the time and position within $t_0 \leq t \leq t_1$ just before the objects intersect, t_c, allowing the collision point, p_c, and collision normal (direction of collision force) to be calculated (Figure 4.34). The force exerted on each $\mathbb{K}_n$ due to collisions are calculated using the force-contact model of the rigid body dynamics engine (Coumans, 2012) – these forces are dependent on p_{cn}, the direction and distance between the centre of mass and the point of contact; the coefficient of surface friction, μ_{surf}, defined as the objects resistance to movement; and the coefficient of restitution (or 'bounciness'), e, defined as the tendency for objects to bounce after colliding (Kuwabara and Kono, 1987). The physical constants μ_{surf} and $e_{\mathbb{K}}$ are estimated from literature sources later in this section. The ODEs for motion are again applied to each $\mathbb{K}_n$, taking into account the new acceleration and torque values introduced by collision forces, but over a much smaller time step, Δt_c (see Figure 4.35). Another important aspect of collision detection is the use of collision margins, δ_o. A collision margin is a length

≥ 0 that defines the offset from an objects visual surface where a collision is still detected: δ being the length of the margin, and because any object can have a separate collision margin (for example, fruit may have a separate collision margin than the walls of the chute), the subscript o is used to denote which object has the specified margin. This increases the apparent size of objects without impacting their original shape or mass, and increases the stability of the simulation. It also can be used to ensure an overlap between surface topographies of objects does not occur, which can be utilised to impose the 'near miss' principle on a stack of fruit (for more on the 'near miss' principle, see section 5.2) where a 2 mm gap between fruits could be imposed on the simulation by giving δ_{fruit} = 0.001m.

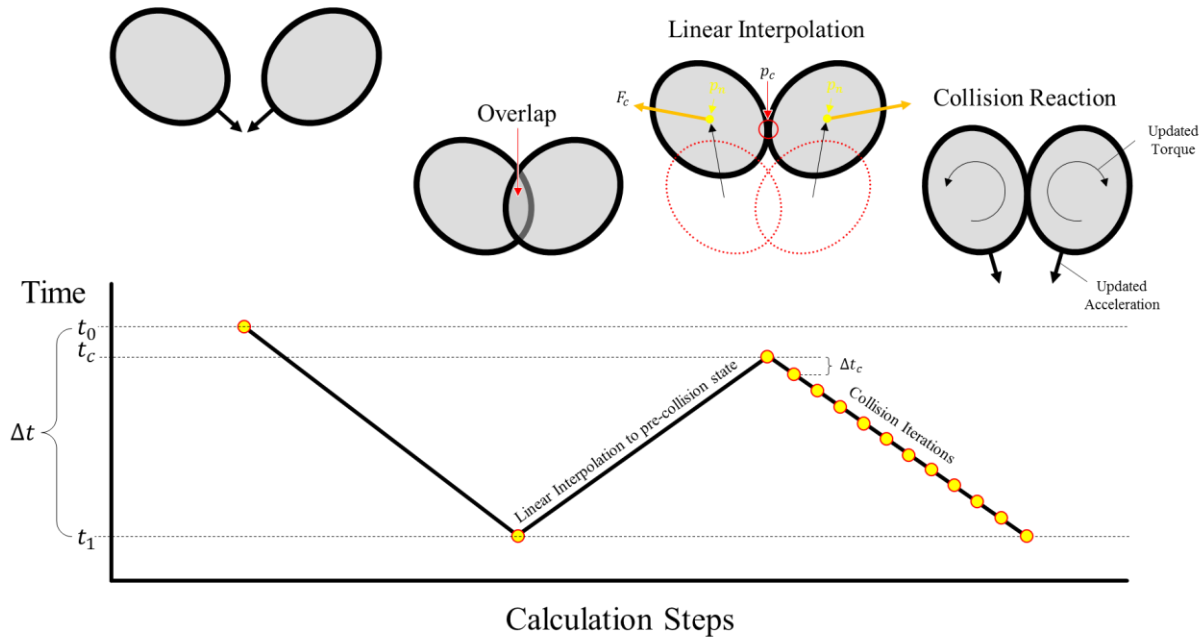

Figure 4.35: Diagram of how collision detection and collision resolutions are solved in the DEM engine. Figure based on Coutinho, 2013.

Δt and Δt_c are very important model parameters. As with many numerical integration problems, these values being small increases accuracy and stability, but at the cost of computational efficiency. Δt must be sufficiently low for the collision detection algorithm to function correctly; for example, if Δt were large, and the velocity of two fruit were also high, there is an elevated chance that the fruit are translated through each other over the time step, so that no collision is detected. The default value in Blender was Δt = 1/60, however this value was increased to Δt = 1/80 as there were problems with collision detection when the first of the fruit fell into the chute – occasionally, the fruit velocity was high enough to translate through the Floor Plane without a collision being detected. Similarly, Δt_c was important in ensuring that fruit were correctly separated during the simulation. High values of Δt_c promoted object overlap as there weren't enough iterations to properly model the motion of a collision, which unfairly increased the volumetric packing efficiency, as well as caused major meshing problems later when the fruit geometry was to be exported into COMSOL or MATLAB. The default setting in Blender was $\Delta t_c = \frac{t_1 - t_c}{10}$, however Tijskens *et al*. (2003) recommends $\Delta t_c = \frac{t_1 - t_c}{20}$, while Shäfer *et al.* (1996) recommends $\Delta t_c = \frac{t_1 - t_c}{100}$. As the model involved potentially hundreds of objects colliding with each other, it was appropriate to use the smaller recommendation, so that $\Delta t_c = \frac{t_1 - t_c}{100}$ was used.

The coefficient of friction (μ_{surf}) of Hayward kiwifruit was measured by Razavi and Bahram-Parvar (2007), where depending on the surface the fruit was colliding with, gave friction coefficients between 0.34 on glass to 0.49 against plywood. In the pursuit of simplicity, the mid-point value of μ_{surf} = 0.4 was applied to every $\mathbb{K}_n$. To the authors knowledge, the coefficient of restitution for kiwifruit was not published in the literature at the time of writing. A restitution coefficient of 0 means that the object absorbs 100% of the energy of a collision, and a coefficient of 1 means that the object translates 100% of the collision energy; therefore, the value of 0.8 was taken so that the fruit lost momentum over time as they settled into the package (Kuwabara and Kono, 1987).

The stacking simulation was put into motion based on the aforementioned discussion of rigid body dynamics. The entire process – chute creation, kiwifruit creation and stacking simulation – was automated with a Python script. The model parameters used are summarised in Table 4.2. $\mathbb{K}_n$ were created randomly using the shape index derived from the weight distribution of the overall 2016 picking season (Figure 4.28a). The model was integrated over 250 seconds of simulated stacking time.

Simulation Parameter	Symbol	Value	Unit
Number of Kiwifruit	N	150	-
Size of Chute, X direction	$\mathbb{B}_X$	372	m
Size of Chute, Y direction	$\mathbb{B}_Y$	292	m
Size of Chute, Z direction	$\mathbb{B}_C$	325	m
Time Integration	Δt	1/80	s
Collision Integration	Δt_c	$\frac{t_1 - t_c}{100}$	s
Collision Margin Fruit	δ_{fruit}	0.0005	m
Collision Margin Walls	δ_{walls}	0.001	m
Coefficient of Friction	μ_{surf}	0.4	-
Coefficient of Restitution	e	0.8	-

Table 4.2: Stacking simulation parameters

Results of the stacking simulation are shown in Figure 4.36 at two angles: a perspective view (Figure 4.36a - d) and front view (Figure 4.36e - h); and at four times: at the simulation start time (Figure 4.36a and e), 10 seconds (Figure 4.36b and f), 40 seconds (Figure 4.36c and g) and the end time (250 second, Figure 4.36d and h). This showed that the DEM approach was successful in generating the internal geometry inside of a package, with simulated gravity and collisions between fruits and the walls of the chute combining to successfully channel the fruit down into the chute to form a realistic bulk shape. In addition to this entire process being automated by the Python script (Figure 4.36 can be generated with a single push of a button), the computational efficiency of the entire process was excellent: 0.005 s to create the chute geometry; 85.0 s to generate 150 randomly sized fruit from the kiwifruit shape index; and only 65.3 s to compute 250 seconds of simulated stacking time, making the stacking model faster than real-time.

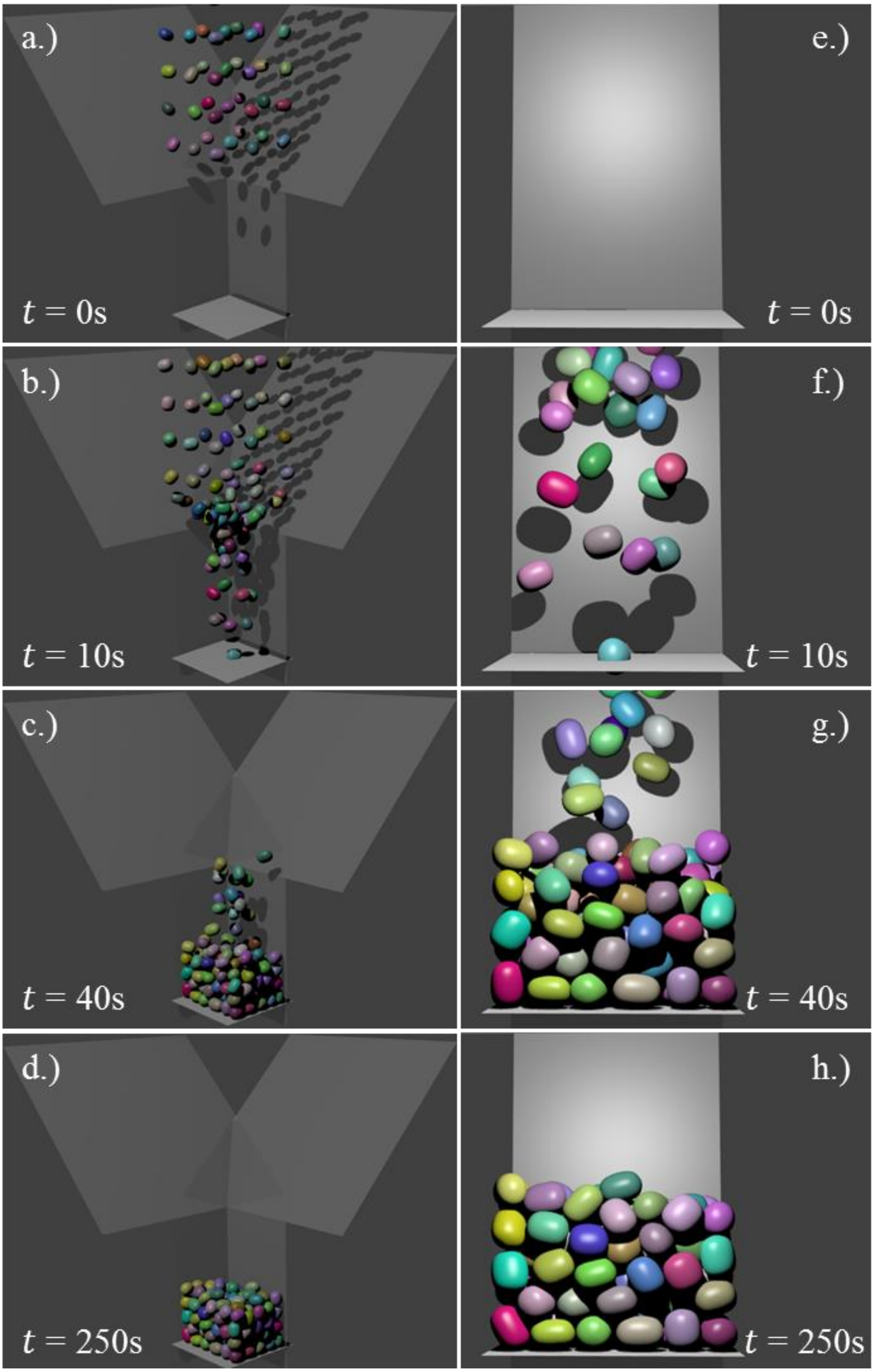

Figure 4.36: Results of DEM simulation, where N = 150 digital kiwifruit were stacked into a box over 250 seconds of simulated time. a - d.) perspective view; e - h). front view.

In total this represents only 150 seconds of computation time to generate the geometry inside of a package in a fully automated fashion. This adheres to the flexibility and computational philosophies of this thesis: the input model parameters can be easily changed in the Python script that drives the stacking model, so that a model geometry can be generated for any alternative package size in only a couple of minutes. Additionally, the stacking model is agnostic to the shape of the objects modelled as rigid bodies – using a different shape equation or method to draw different fruit other than kiwifruit can easily be incorporated into the stacking model to have the bulk shape computationally generated in the same fashion, without sacrificing computational efficiency. To illustrate, three alternative packing scenarios were briefly explored in Figure 4.37:

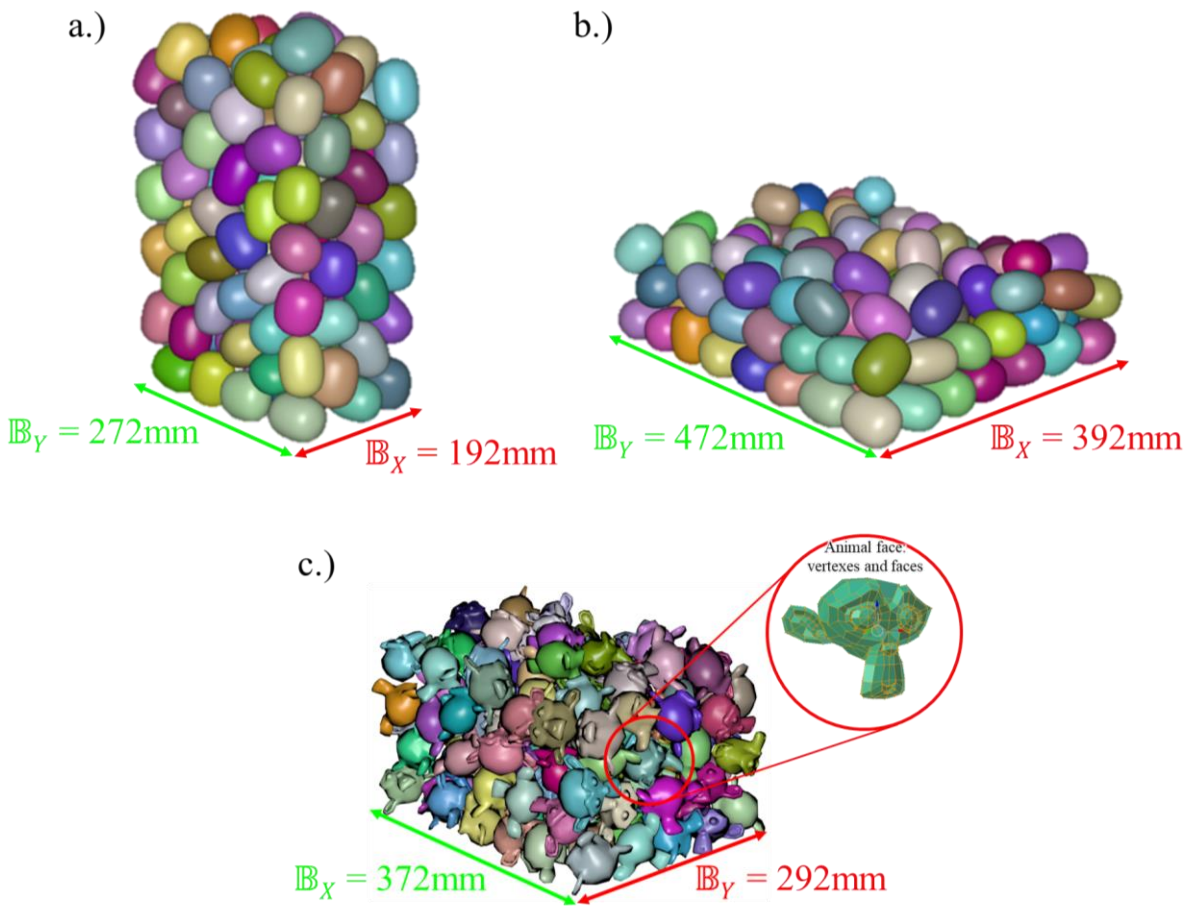

Figure 4.37: Exploration of the stacking model to alternative packing scenarios: a.) a smaller package, with a footprint of 272×192mm; b.) a larger package, with a footprint of 472×392mm; c.) a standard modular bulk package (372×292mm), filled with N = *150 complex shapes (animal faces) to demonstrate the applicability of the model to alternative shapes.*

Each scenario in Figure 4.37 packaged 150 objects. In Figure 4.37a, kiwifruit were packed into a smaller box than the current package (272×192mm). As the X and Y inner dimensions of this new package was smaller than the previous example (Figure 4.36), the height of the stack was much larger*. Figure 4.37b shows a larger package (472×392mm). With a larger footprint, the height of the stack is lower. Figure 4.37c shows 150 more complex, non-kiwifruit objects packed into a standard modular bulk package (372×292mm). The objects were animal faces with protruding eyes, ears and mouths, a shape built into Blender. Despite the shape being much more complex and with sharp edges, both the animal faces and the kiwifruit are made up of essentially the same thing: a surface topography of vertexes and faces. Thus, the rigid body dynamics engine can be applied equally to the complex shape; and by extension, any other object, horticultural or otherwise.

4.4.4: Elimination of Overfill

As explained previously, it was deemed necessary to construct the model in such a way as to incorporate overfilling. It is recommended that approx. 50% more fruit were stacked into the box – so in the current scenario, rather than stacking 102 fruit, 150 were computationally stacked. This was to solve the problem of there being an uneven top surface, as well as allowing for the packing efficiency to be explored. Therefore, there was a need for an additional step of correcting overfill.

Ordinarily, the height of the box, $\mathbb{B}_Z$, is not considered in the chute geometry. Following the completion of the stacking model (Figure 4.38a and e), this important parameter is reintroduced into the model as a horizontal plane that is B_Z above the Floor Plane (Figure 4.38b and f). This plane represents the closed lid of the box, and is therefore considered the Lid Plane. Any fruit that is either above or intersecting this plane will impede the proper closing of the box, and therefore should be eliminated. Marking fruit for elimination was done by comparing the height (Z value) of every vertex of every fruit with the height of the Lid Plane. If any fruit contained even a single vertex that was $\geq B_Z$ then that is considered to be impinging on the closing of the lid, and was therefore marked for removal (Figure 4.38c and g). After eliminating the overfilled fruit, the remaining fruit represented the finalised geometry to be

* Both Figure 4.36 and Figure 4.37a require an additional processing step that eliminates the overfilled fruit, which is discussed later in section 4.4.4.

exported into modelling software, such as COMSOL or MATLAB. This process was computationally efficient, taking only 1.23 seconds to detect and eliminate overfilled fruit.

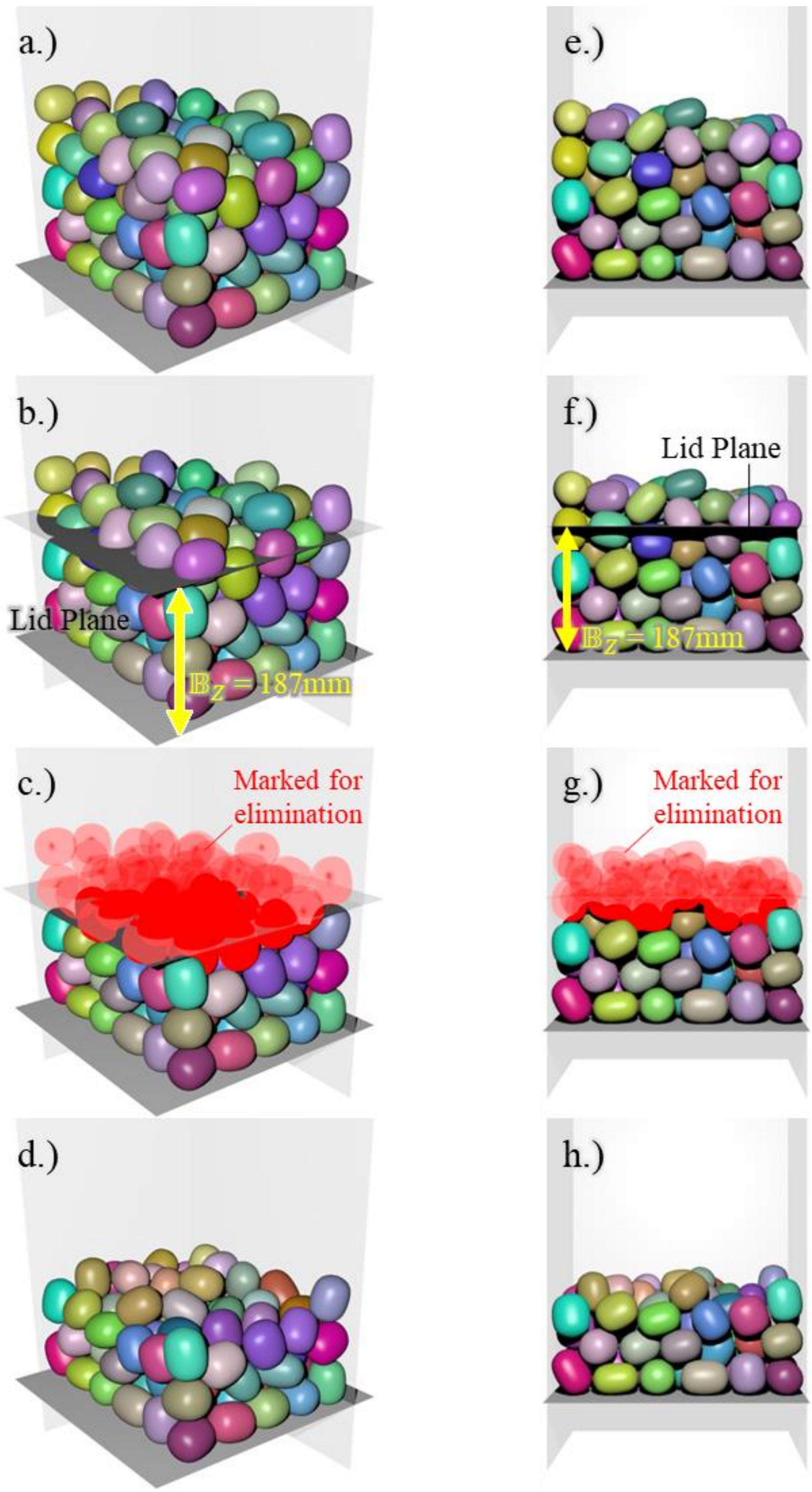

Figure 4.38: Identification and elimination of overfilling: any fruit with even a single vertex above the inner height of the box ($\mathbb{B}_Z$ = 187mm) is marked for elimination (red fruits in c and g).

4.4.5: Polyliner Creation

A major component of the kiwifruit pre-cooling system is the existence of the polyliner, a thin plastic material wrapped around the bulk of the fruit in every box. This packaging feature has a profound impact on the airflow mechanisms at play, which in turn has a significant impact on the rate of heat transfer and the uniformity of cooling: as the polyliner prevents direct airflow through the bulk of the fruit, the preeminent mode of heat transfer, forced convection, is limited to the polyliner surface; additionally, the polyliner acts as a moisture barrier, artificially promoting a local high humidity environment, preventing evaporative cooling.

Modelling the geometry of the polyliner in a realistic manner represented a major obstacle. The polyliner is a flexible and thin object, and it clings tightly to the fruit bulk it is wrapped around. It is speculated that the difficulty in properly describing the polyliner geometry has prevented modelling work into polylined pre-cooling systems, despite the increased popularity of using such a packaging feature. Delele *et al.* (2012) modelled a polyliner system of grapes, but considered the fruit-air system as a porous media, an approach that is not always applicable due to the package-particle ratio, and is not applicable in the kiwifruit system. To this author's knowledge, only O'Sullivan (2016) has explicitly modelled a polylined pre-cooling system, but in that case the polyliner was constructed manually so that it was applicable only in the case of kiwifruit stacked in an orderly pattern; and was a non-realistic, blocky shape which may have impacted the airflow pattern through the box. In the interests of satisfying the flexibility philosophy of this thesis, there is a need for a method that can take the bulk shape of fruit as the input, and as an output generate a realistic geometry that represents the polyliner, in a way that is automated, rapid, and agnostic to the shape of the bulk fruit.

This method was again developed inside of Blender, and was automated through the use of a Python script. The method took advantage of a series of object modifiers, operations that distort the surface topography of the selected object. Specifically, the 'Subdivision Surface', 'Shrinkwrap' and 'Smooth' modifiers were used – each is described below, but for more detail see Blender Foundation (2017).

The first step in the polyliner creation process was to create the object that would eventually become the polyliner. At this initial stage this object was a simple cuboid. As shown in Figure 4.39, the cuboid was given the same size as the internal geometry of the box, but slightly larger:

$$\mathcal{P}_X = \mathbb{B}_X + (\mathbb{B}_X * 0.1) \tag{4.30}$$

$$\mathcal{P}_Y = \mathbb{B}_Y + (\mathbb{B}_Y * 0.1) \tag{4.31}$$

$$\mathcal{P}_Z = \mathbb{B}_Z + (\mathbb{B}_Z * 0.1) \tag{4.32}$$

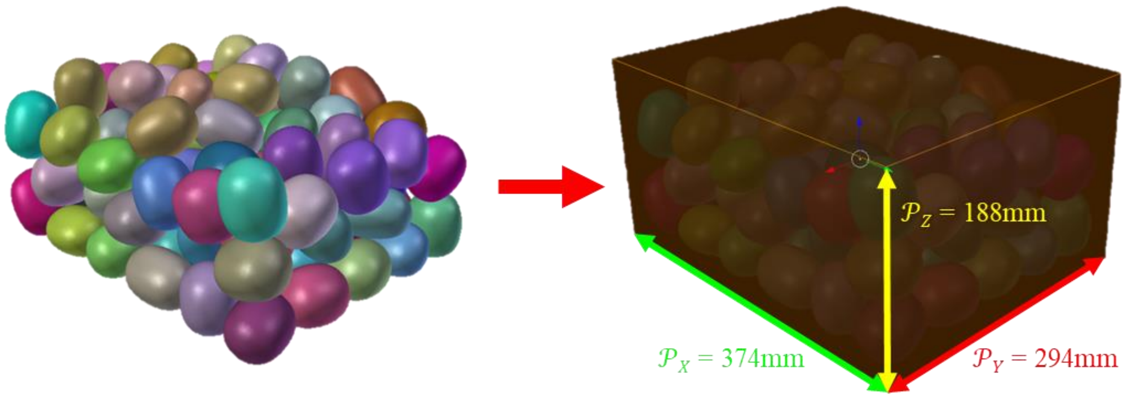

Figure 4.39: Inception of the polyliner geometry: a cuboid with 10% larger dimensions as the inner dimensions of the box.

This 10% increase in size compared with the internal box geometry was implemented to ensure that the polyliner encompasses the entirety of the bulk of fruit. The object modifier ‘Subdivision Surface’ is applied to the cuboid to split the face of the mesh into a larger number of faces, while maintaining the shape of the original mesh, to make it capable of being flexible (Figure 4.40).

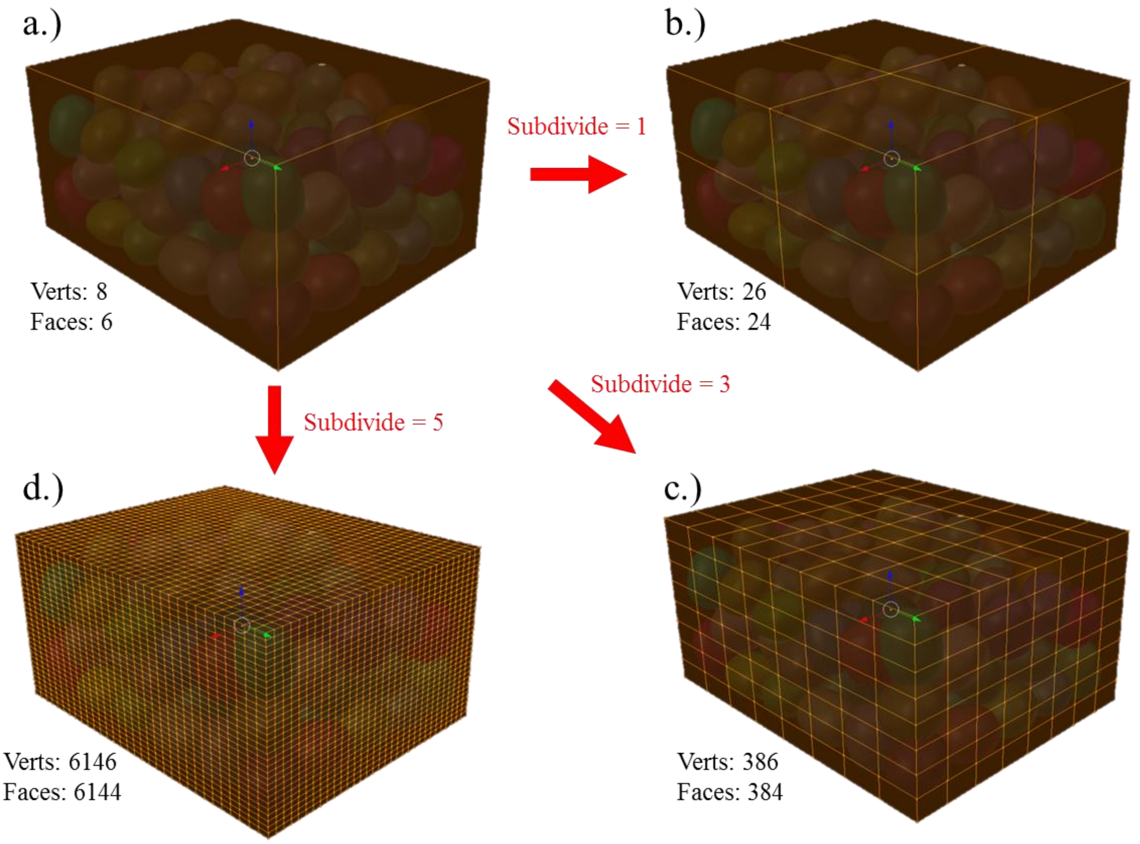

Figure 4.40: Application of the 'Subdivide Surface' object modifier, which divides the surface mesh into a larger number of smaller faces.

The tuning variable in this modifier was the number of subdivisions. Increasing the number of subdivisions creates more faces and vertexes, making the polyliner more malleable, so that it can bend and flex around objects with more degrees of freedom.

Having prepared the polyliner object for deformation, the next step was the application of the 'Shrinkwrap' object modifier. This modifier moves vertexes from the polyliner geometry to the nearest vertex on the target object, in this case the bulk fruit geometry, while maintaining a minimum angle between adjacent faces. This process is shown in Figure 4.41, which also explores the interaction between the malleability of the polyliner (degree of subdivision) and the efficacy of the 'Shrinkwrap' object modifier. When the 'Shrinkwrap' modifier is applied at a low number of subdivisions, the flexibility isn't sufficient enough to properly account for the curves in the bulk shape of the kiwifruit. As shown in Figure 4.41a and b, not all of the fruit was contained within the polyliner shape, with a high degree of fruit protruding through the surface topography of the polyliner. Though a certain degree of overlap between the fruit and polyliner can be desirable, as this represents a small portion of the fruit surface having direct contact with the bulk external airflow, the magnitude of this should be carefully controlled. This is discussed in further detail later (section 5.3.3). In the case of Figure 4.41a and b the fruit protrusion through the polyliner was unintentional and caused by the lack of flexibility in the polyliner surface mesh. Only when at least 5 subdivision levels were applied (Figure 4.41c) did the polyliner correctly wrap around the entire fruit bulk geometry.

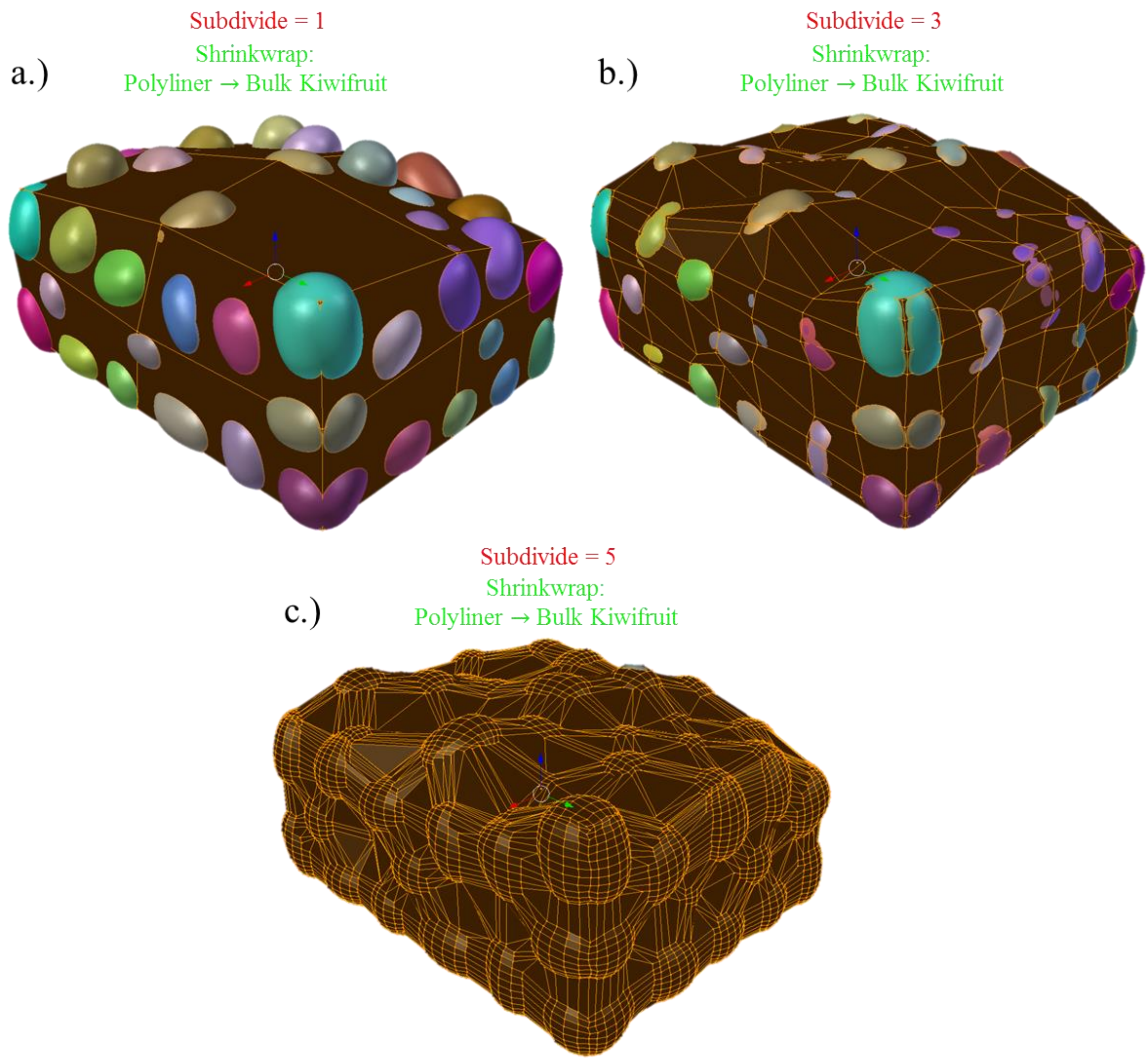

Figure 4.41: Application of the 'Shrinkwrap' object modifier, which brings the vertexes of one object (polyliner) to the nearest vertex of a target object (bulk kiwifruit shape).

The surface topography following the application of the 'Shrinkwrap' modifier with a sufficient amount of subdivision (Figure 4.41c) had an imbalanced distribution of vertexes, bunching at the surface of the fruit and being scarce over fruit voids. This is problematic for export and import into other modelling software such as COMSOL or MATLAB, as skewness in the surface topography increases the chance that the import process will fail. To ease the import process, the ‘Smooth’ object modifier was applied. This modifier functions by changing vertexes to the average position of surrounding vertices. The smoothing process is applied iteratively, the number of iterations a tuning variable. As shown in Figure 4.42, increasing iterations of the ‘Smooth’ modifier improves the uniformity of vertexes while largely maintaining the general shape of the object. However, this modifier also has the consequence of shrinking the overall shape – each iteration of the ‘Smooth’ modifier moved the polyliner ~0.2 mm inward toward the geometric centre. This is why as the number of smoothing iterations increases from 1 to 10 (Figure 4.42b and d), the degree of fruit protruding through the polyliner surface increases.

Controlling the exact degree of fruit protrusion is vital to the development of a successful heat transfer model. As discussed later in section 5.3.3, a small degree of direct fruit-polyliner contact was necessary to validate the cooling model. Allowing the polyliner to pass through the fruit at a slight depth is *not* intended to represent the polyliner literally penetrating through solid kiwifruit, but rather areas where the polyliner is in perfect contact with the fruit.

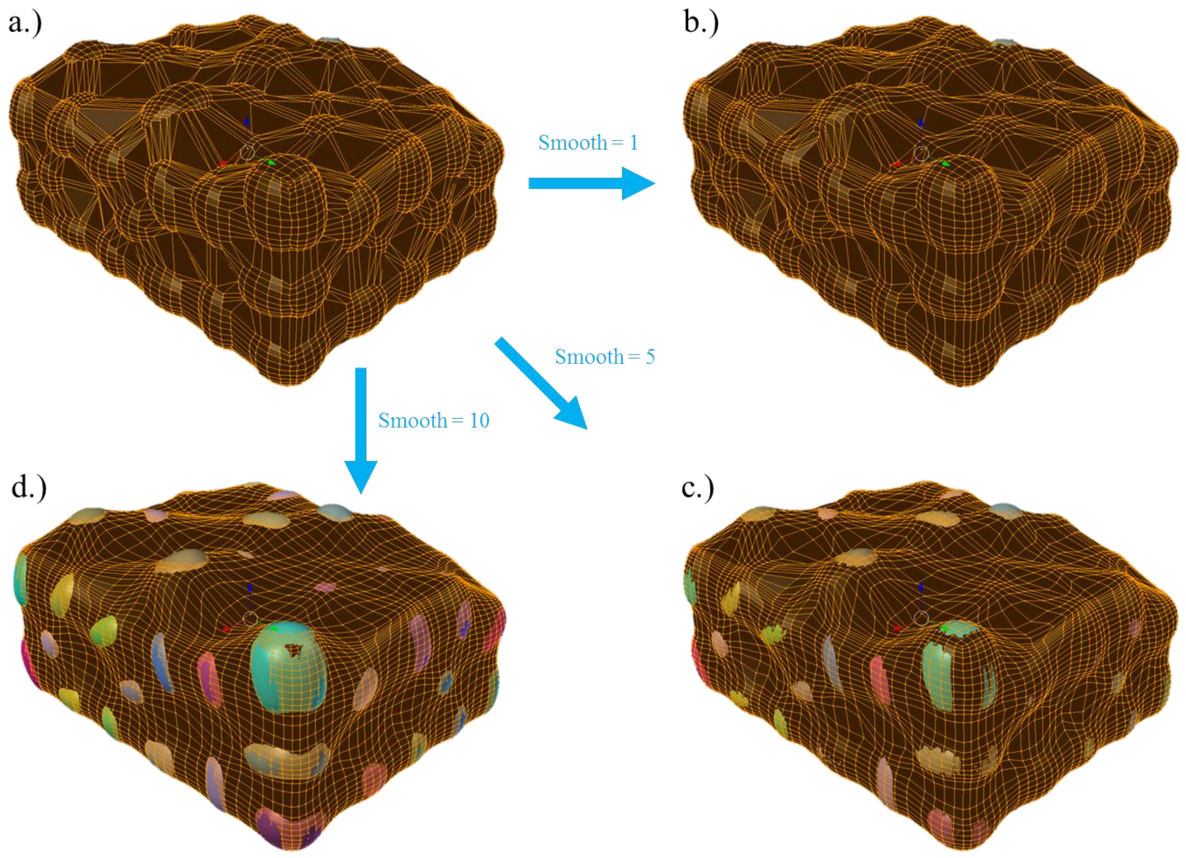

Figure 4.42: Application of the 'Smooth' operator, which creates a more uniform distribution of vertexes

The alternative scenario may also be desirable, where there is a slight gap between the fruit and the polyliner. Such a model would be significantly easier to implement into a finite element modelling scheme, as there is no direct contact between objects. This is most likely not suitable for modelling pre-cooling processes but it could be useful in modelling other parts of the cold chain, such as room cooling, long term cold storage, or refrigerated transport, where conduction plays a more significant role in temperature maintenance. Thus, to keep the model flexible to a range of modelling situations, it was imperative that both of these scenarios be incorporated into the creation of a polyliner shape, and the depth of penetration or gap between the product and the polyliner should be a user-controllable parameter. This was accomplished by utilising the 'offset' parameter in the 'Shrinkwrap' modifier: rather than bringing polyliner vertexes right to the surface of the nearest fruit vector, a distance can be imposed between vertex pairs. This offset distance can be positive (gaps) or negative (protrusion). Remembering that the 'Smooth' modifier introduces a penetration of 0.2 mm per iteration, the desired magnitude of gap or penetration must take this into account. This is demonstrated in Figure 4.43.

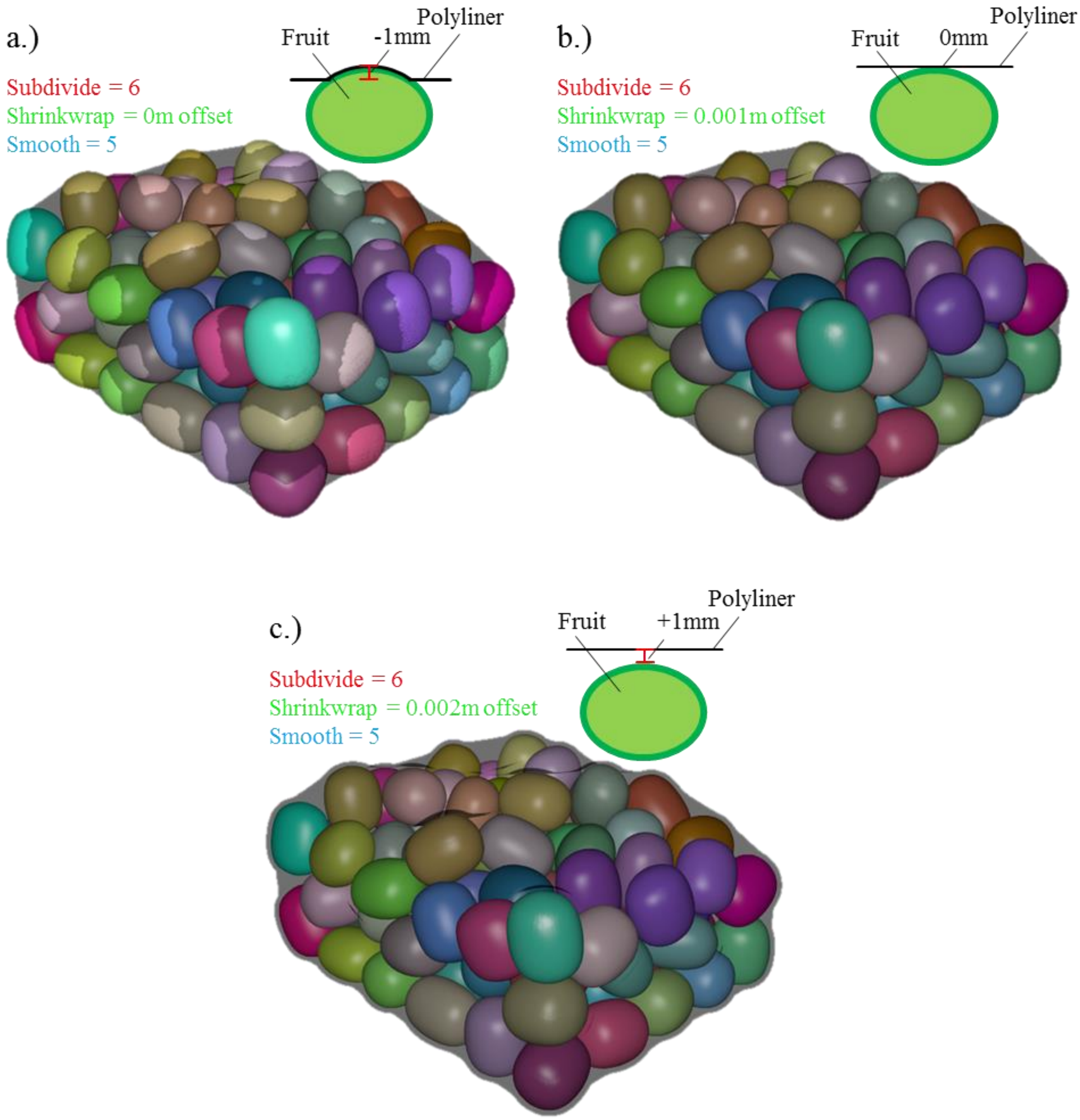

Figure 4.43: Impact of the Shrinkwrap Modifier offset, affecting the degree of direct fruit contact with the bulk motion of the airflow: a.) a 1mm penetration depth; b.) no gap, and; c.) a 1 mm gap.

Figure 4.43a shows the polyliner-fruit geometry with a 1mm penetration depth. To create the 1mm penetration, the ‘Shrinkwrap’ modifier was given an offset of 0m, and then 5 smoothing iterations were applied. At 0.2 mm per iteration, this resulted in a net 1mm penetration depth. This introduces some clear regions of direct fruit-polyliner contact. Figure 4.43b shows a polyliner that is flush with the fruit geometry. The ‘Shrinkwrap’ modifier was given an offset of 1mm, which was then erased by the 5 smoothing iterations. Finally, Figure 4.43c shows the poyliner-fruit geometry with a 1mm gap, with a 2 mm ‘Shrinkwrap’ offset, which was reduced to 1mm by the smoothing iterations.

This polyliner creation process was flexible and agnostic to both the shape of the individual fruits, as well as the generated bulk fruit shape. To demonstrate the flexible capability of this method, the same Python script was applied to 4 separate stacks of objects: shown in Figure 4.44, each was of a modular bulk package (372×292×187 mm) filled with either different objects, or an alternative stacking pattern. For added clarity, the polyliner surface mesh is displayed in red. Figure 4.44a is a random stack of kiwifruit, generated in the same fashion as described in section 4.4.3; Figure 4.44b is a stack of kiwifruit with an imposed, ordered stacking pattern, the same pattern as that imposed during cooling experiments (see section 3.3); Figure 4.44c is a random stack of cubes (cubes had an edge length of 0.04 m); and Figure 4.44d was a random stack of animal faces (faces had a 'radius' of 0.03 m). In each scenario, the same polyliner creation variables were used: Subdivide = 6, Shrinkwrap = 0.0015 offset, and Smooth = 5.

The agnosticism and flexibility of the polyliner creation method is successfully demonstrated in Figure 4.44. Despite the obvious dissimilarities of the bulk shape formed in each of these cases, the same method and code was successful in creating a realistic, form fitting polyliner geometry. This routine was computationally efficient, taking only 0.3 seconds to complete.

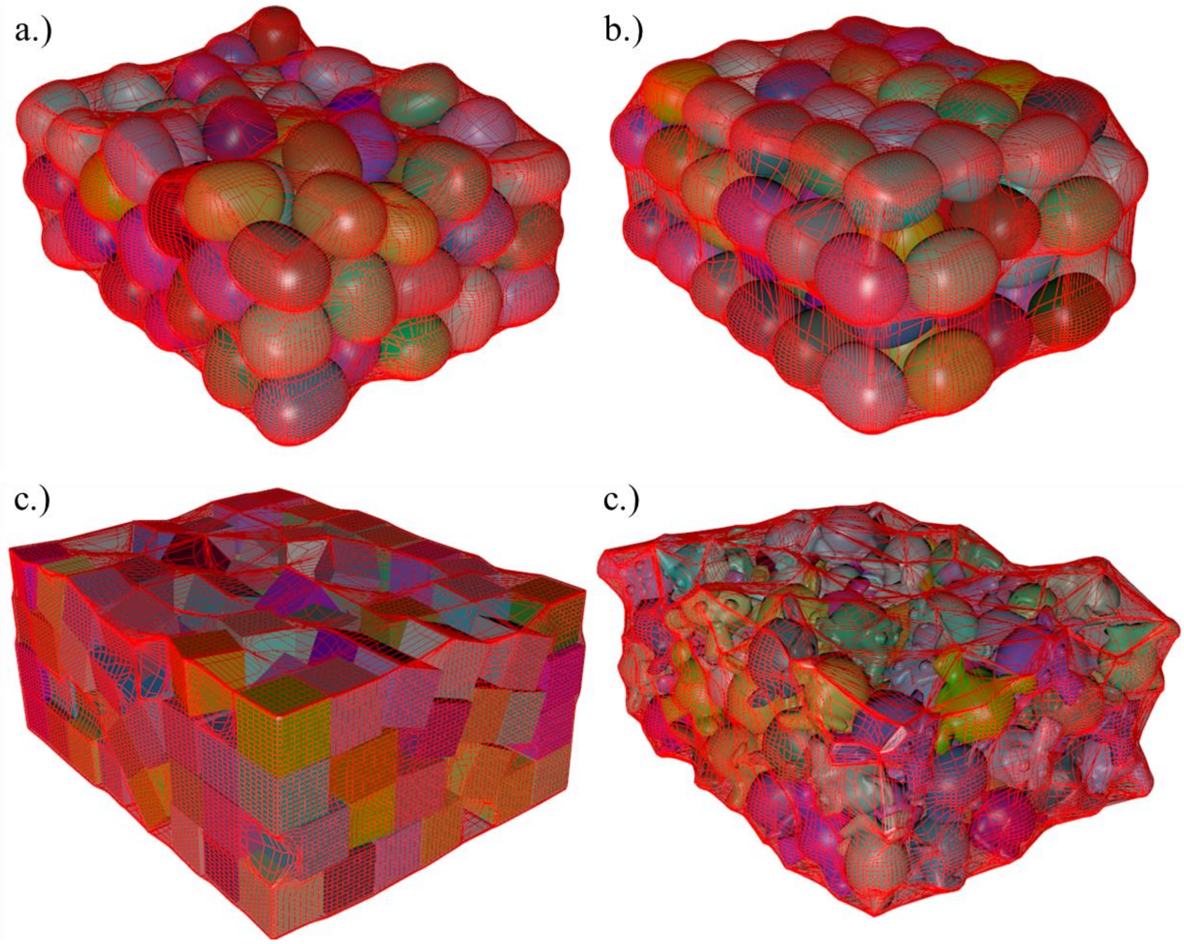

Figure 4.44: Demonstration of the flexibility of the polyliner creation process. The same code was executed on a.) a randomly stacked box of fruit; b.) a manually stacked, ordered stack of fruit; c.) a random stack of cubes (edge length of 0.04m), and; d.) a random stack of animal faces (radius of 0.03m).

4.5: Validation of Random Stacking Model

The random stacking model of section 4.4, being capable of producing the bulk internal fruit geometry expeditiously and automatically, is validated in this section through comparisons between the computationally generated stacks and the empirically measured stacks via CT scanning in section 4.2.

4.5.1: Position of Individual Fruits

Comparing the empirical bulk shape data with the computationally generated stacks requires that the position of individual fruits be known. The CT scanner resolution was not high enough to resolve individual fruits – or the space between touching fruits as separate, with a maximum resolution of 0.8mm slices – meaning that the bulk fruit shape is considered to be a single connected object in MATLAB. Thus, additional image processing was necessary to ascertain the X, Y and Z position of individual fruits.

After the raw CT scan data was processed into phases (section 4.2.2; Figure 4.45a), the Euclidean Distance transform was computed (the MATLAB function 'bwdist'), and the corresponding values were non-dimensionalised (Figure 4.45b). Values below 0.5 – corresponding to voxels near to the surface of the fruit – were eliminated. This essentially peeled away the outer layer of fruit, creating a collection of smaller objects that retained the general shape of the individual fruits they were derived from, positioned in the centre of each individual fruit. Shown in red in Figure 4.45c, these new smaller fruit shapes are spatially separated, so they can be identified as isolated regions. Properties of these regions can be derived with MATLABs 'regionprops' function, the most important in this application being the centroid – the centre of mass. The centroid of the red shapes in Figure 4.45c are assumed to be approximately equal to the centroid of the real kiwifruit, as they are derived from the shape of the individual fruits and are positioned in their centre. Thus, the number of fruit in the box and their position in XYZ space can be determined (Figure 4.45d).

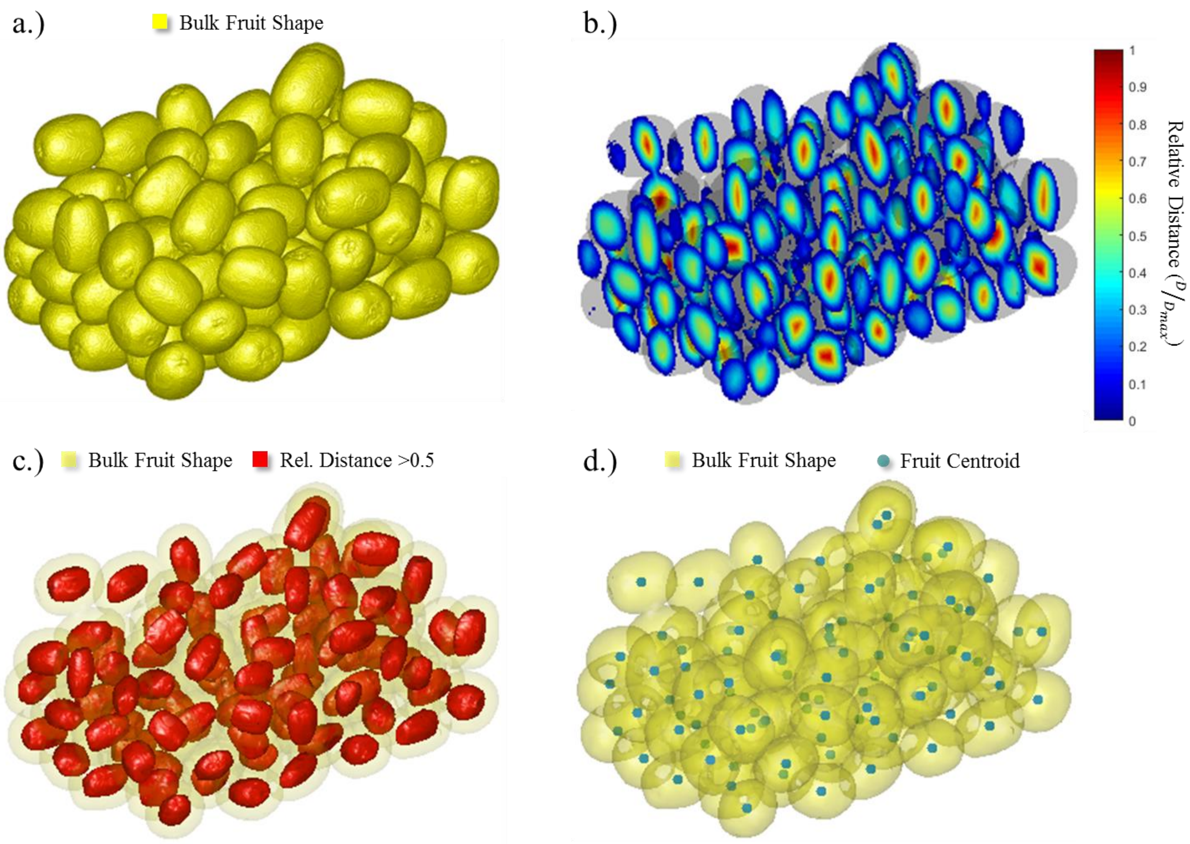

Figure 4.45: Illustration of procedure developed to measure the centroid position of individual fruits from CT scan information: a.) CT scan of kiwifruit stacked in a box; b.) application of the non-dimensionalised Euclidean Distance transform to the CT scan information; c.) temporary elimination of all fruit voxels with a relative distance <0.5: original CT scan information in transparent yellow; new objects in opaque red; d.) centroid position of individual fruits, marked as blue dots, derived as the centre of mass of the new opaque red objects.

The 0.5 threshold for eliminating voxels was chosen as the best trade-off between centroid accuracy and error in correctly identifying the number of fruit inside the box. A lower value would mean a shallower depth of fruit is peeled away, so that the resulting shapes are closer to the true shape of the kiwifruit, hence the centroid position is closer to the 'true' centroid. However, this also increases the risk of these being 'voxel bridges', where not enough of the outer layer has been removed so that two or more fruit are still connected by a small amount of voxels where the fruit are touching (Figure 4.46a). These two or more connected fruit would be recognised as a single fruit – not only calculating the number of individual fruit incorrectly, but also the centroid position. A higher threshold value lowers the risk of there being connection bridges, but also increases the amount of voxels removed. The centroid of these shapes may be disparate to the 'true' centroid as they contain little of the original information – and there is also a risk of completely eliminating all voxels from the smallest fruit (Figure

4.46b). Thus not only would the centroid position be inaccurate, but the number of fruit identified inside of the box would be less than in reality.

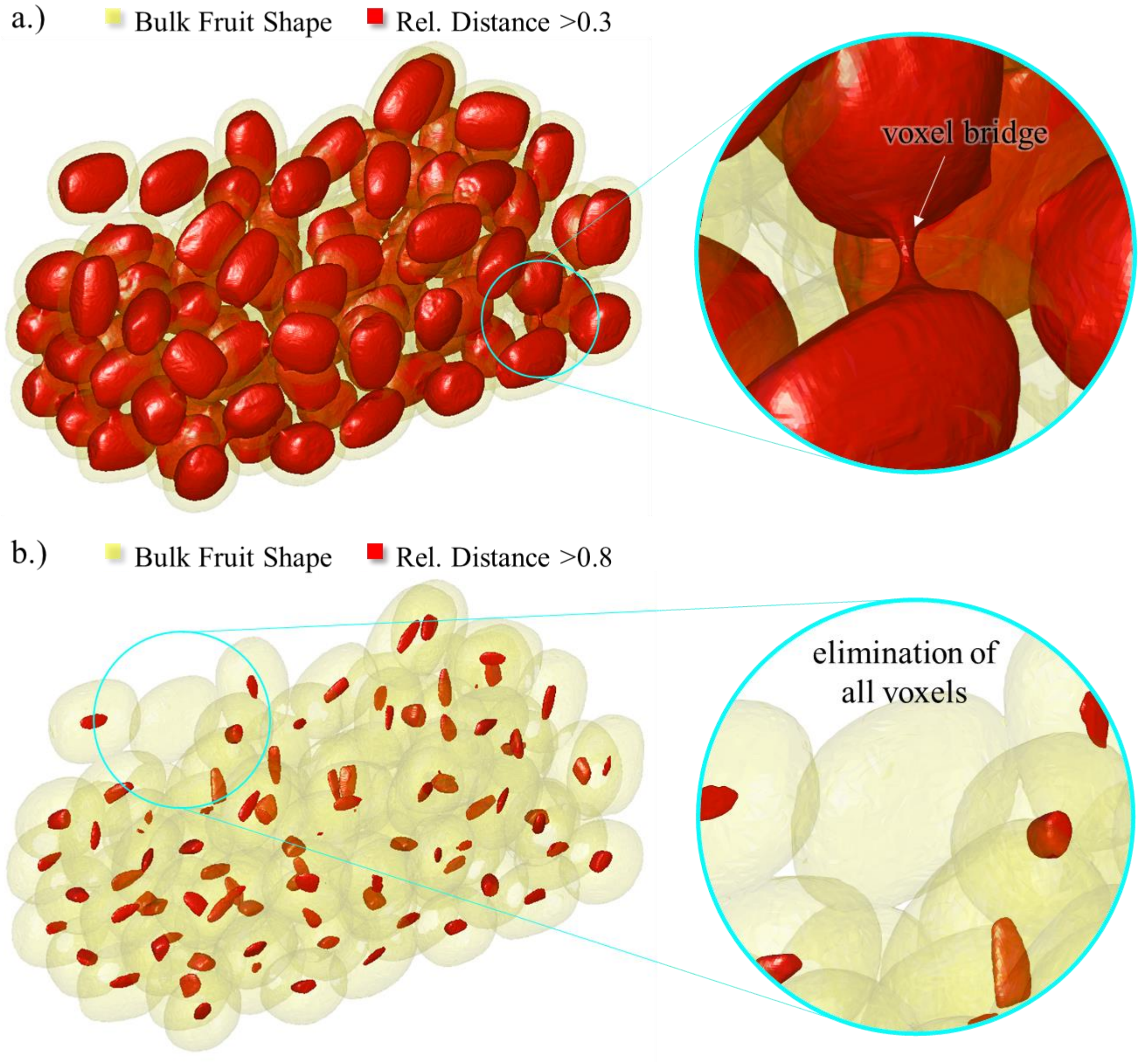

Figure 4.46: Demonstration of different relative distance thresholds: a.) example of the threshold being too low (0.3), failing to completely separate individual fruits, forming a 'voxel bridge' in many scenarios; b.) example of the threshold being too high (0.8), completely eliminating all voxels from individual fruits in some cases.

4.5.2: Manually Stacked Package

The first comparison was between manually stacked packages, the stacking pattern imposed upon all cooling experiments (section 3.3). The pattern was created by physically placing 100 count 36 Hayward kiwifruit into 4 distinct layers: 30 fruit on the bottom layer, 20 fruit on the 2nd layer, 30 fruit on the 3rd layer and 20 on the top layer. During modelling work later in this thesis, this same stacking pattern was constructed manually in Blender (see section 5.2) and is compared with the empirical stack measured via CT scanning in this section.

The purpose of this first comparison was to test and refine comparison techniques. As both the CT scanned geometry and Blender constructed geometry were made manually by hand, and the fruit were placed in a well-defined repeatable pattern, the differences between the two should be small – in a visual, qualitative sense, 3D or flattened images of both should be comparable; and in a quantitative sense, the positional distribution of individual fruits should be largely similar.

For a visual comparison, the 3D volume of both the CT scanned box and the Blender constructed geometry was compared (Figure 4.47a and b, respectively). Because fruit in the centre and at the back of the box are obscured by fruit at the front, a flattened 2D relative density map was also created (Figure 4.47c and d) to provide an alternative view of the geometry inside the box. For the empirical data, this density map was created by first separating voxels into phases (section 4.2.2), so that voxels identified as fruit had a value of 1, air and package voxels a value of 0. Voxels were then summed along the Y-axis (width), adding each X-Z slice to the next slice, flattening the 3D volume into a 2D density map. The values of the subsequent pixel set created after the flattening process corresponds to the frequency at which a fruit voxel exists at that position on the X-Z axis. These values were made relative by dividing by the global maximum, to give a relative density map. The same process was done for the computational Blender geometry; however, it was first necessary to discretize the 3D surface into voxels. This was done using the voxelisation technique outlined in section 5.5.4.

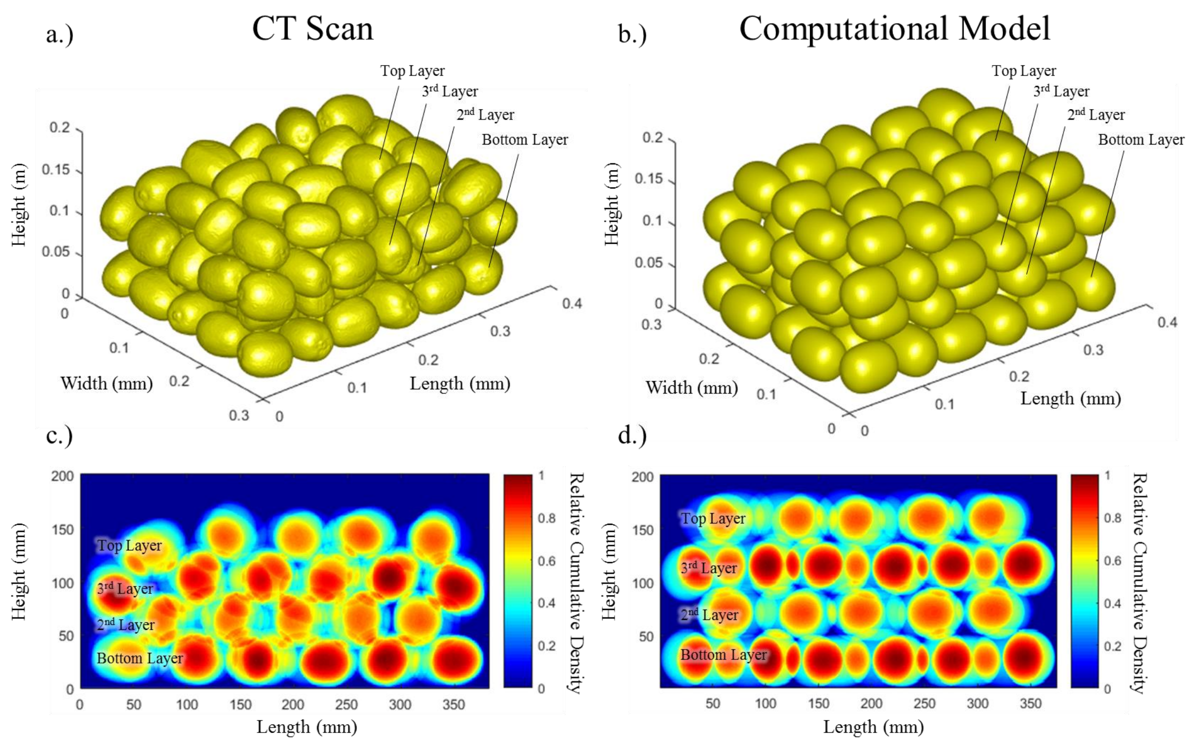

Figure 4.47: Comparing ordered stacks of kiwifruit: a.) empirically determined (through CT scanning) 3D render of manually stacked box; b.) 3D render of manually constructed computational model of an ordered stack; c and d.) flattened 2D relative density maps of the 3D renders.

Next, techniques for comparing the two geometries quantitatively were explored. Comparisons using bulk metrics such as the volume or surface area were not as powerful as comparing the positional distribution of individual fruits inside the box. The former two compares geometries using only a single value, masking information as to *how* fruit are stacked inside the box; while the latter allows a comparison at 100 points or more. Taking the front left corner of the box as the origin (0,0,0), the X (length), Y (width) and Z (height) position of the centroid of each individual fruit was extracted from the CT scan using the process described in section 4.5.1. The next concern was how to summarise the positional distribution in a way that was easy to interpret, gave a succinct outline of the distribution inside the package, and allowed similarities and differences between stacks to be plainly identified. In this endeavour, the cumulative height distribution satisfied these criteria, shown in Figure 4.48. The distribution of the X and Y positions does not provide detailed information about the stacking pattern, as fruit are more or less evenly distributed across the box foot print. The same cannot be said of the Z positions (height), as fruit form distinct layers as they stack on top of each other. Therefore, the cumulative height distribution plot was used as a quantitative comparison tool, and was interpreted thusly: fruit on the left-most side of the plot represents fruit at the bottom of the box, while fruit on the right represents fruit at the top. Moving from left to right, regions of horizontality represent a well-defined layer of fruit, the length of the region corresponding to the number of fruit within that layer. Curvature in the distribution corresponds to a less well-defined, more amorphous layer of fruit. Sharp changes in the distribution correspond to the end of one layer and the beginning of the next layer – therefore, identifying how many fruit layers exist within the box and how many fruit lie within each layer can be identified by also plotting ΔH – the first derivative of the cumulative height – and examining where peaks form.

Visually comparing the manually stacked CT scan geometry (Figure 4.47a) with the Blender geometry (Figure 4.47b), the imperfection of the real-world scenario is apparent. Fruit have rougher surfaces compared to the smooth and perfect fruit created in Blender, and many fruit have been dislodged from their intended position, twisting and rotating to rest under the natural force of gravity at angles in-between the recesses caused by the layers of fruit above and below. As the Blender geometry was constructed manually and gravity forces were not applied, fruit were fixed to the position they were assigned, and in fact were able to 'float', where a slight separation between fruit was preferable due to the 'near miss' principle (O'Sullivan *et al.,* 2016; Defraeye *et al.,* 2014; Berry *et al.,* 2017; section 5.2). Inspecting the density maps (Figure 4.47c - d), four layers of fruit are visually conspicuous in both cases; however, they were less well defined in the CT scan geometry, especially the 2nd and 3rd layer which showed more spatial variation per row of fruit than the Blender geometry. It was also clear that the CT scan geometry was packed tighter, the top of the entire stack being lower than the Blender geometry. This again was due to the fruit being allowed to settle under gravity.

Differences between the CT scan (red circles) and Blender geometry (solid black line) were investigated quantitatively with the cumulative height distribution (Figure 4.48). Four distinct regions can be seen in both cases, corresponding to the four layers of fruit imposed on the geometry, the location of the formation of a new layer and the number of fruit within each layer confirmed by the peaks that formed in the ΔH plot (dashed lines) at 30, 50 and 80% - so that the bottom layer contained 30% of the fruit, 2nd layer 20%, 3rd layer 30% and top layer 20%, which was precisely the number of fruit placed into each layer. The horizontality of the height distribution – representing a well-defined fruit layer – is much more pronounced in all four layers of the Blender geometry. The CT scan shows a well-defined bottom and 2nd layer, but a less orderly 3rd and top layer. The fruit on the lower layers were supported by the bottom of the package, a flat and rigid object perpendicular to the floor, lending toward there being a higher degree of order. Higher layers relied on the support of the lower layers of fruit, and as these were irregular and nebulous surfaces, showed a greater height distribution across the layer. Additionally, in the 3rd layer, fruit near the sides of the box relied on the packaging to remain at the same height as fruit near the middle of the box – and upon inspection of the density map (Figure 4.47c), fruit instead tended to fall into the gap created between layers 2 and 3. With the exception of the bottom layer, each subsequent layer of the fruit from the CT scan is consistently lower in height than the Blender geometry. As discussed previously, the real world fruit geometry was subject to the natural force of gravity, which has created an overall much more compacted, shorter stack compared with the Blender geometry.

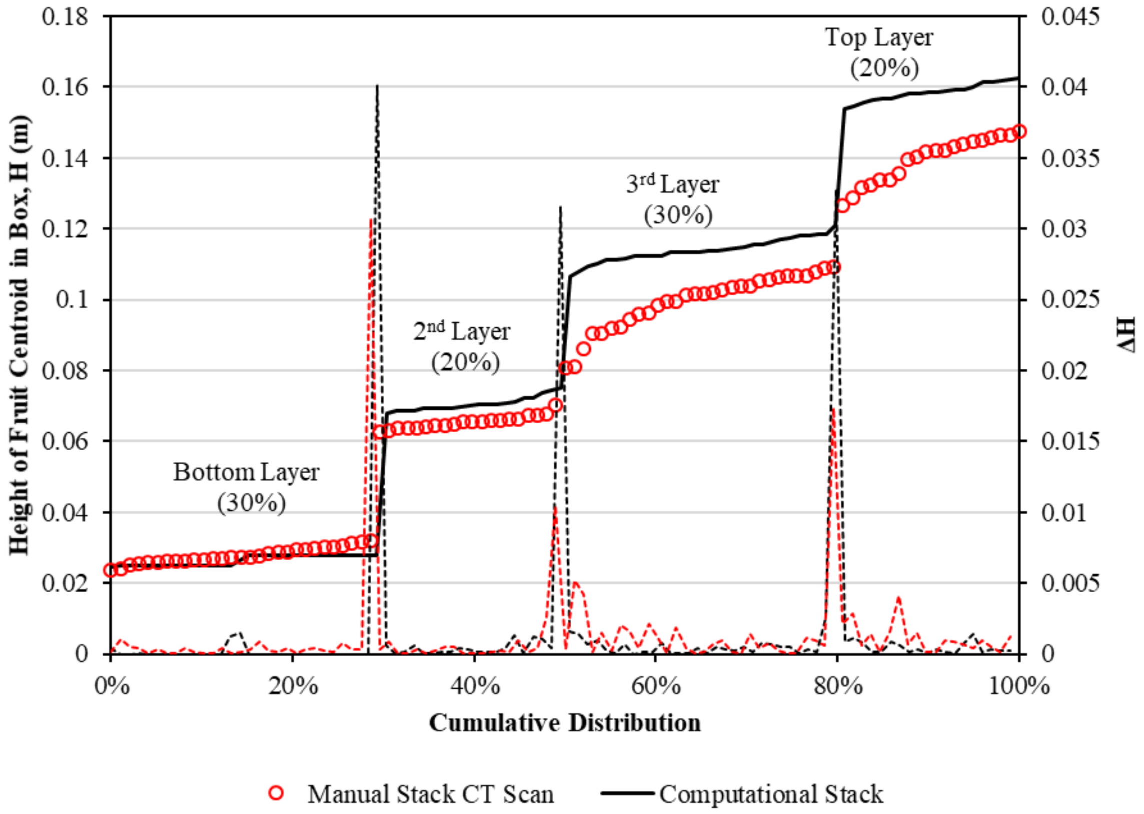

Figure 4.48: Cumulative distributions of the height of the geometrical centre of individual kiwifruits for: a CT scanned box (red circles), and the manually created computational geometry (solid black line). Dashed lines represent the first derivative of the cumulative height curve, ΔH*, peaks indicating the position of a new layer of fruit: red dashed line = CT scanned box, black dashed line = computational geometry.*

4.5.3: Randomly Stacked Package

The comparison techniques developed in the previous section (section 4.5.2) were used to assess the accuracy of the random stacking model.

2 separate boxes of 102 count 36 Hayward kiwifruit, wrapped in a polyliner, were scanned. Centroid positions of individual fruits were determined using the technique in section 4.5.1. To compare, 5 stacks of fruit were created computationally using the random stacking model (section 4.4). Model parameters for each stack were the same as Table 4.2. Each stack was generated in just 150 seconds of computational time. 3D renders of the two CT scanned boxes are shown in Figure 4.49a and b. 3D renders of the five computationally generated randomly stacked boxes are shown in Figure 4.49c - g. For a more detailed visual comparison, the first CT scan and the first computational stack are shown in closer detail in Figure 4.50: a and b being 3D renders and c and d flattened 2D density maps. Quantitative comparisons using the cumulative height distribution are shown in Figure 4.51. Identification of the location of layers and the number of fruit within each layer via plots of the ΔH is shown in Figure 4.52.

Examining the full set of geometries from Figure 4.49, the imperfections of the empirical CT scans are, again, apparent. Real kiwifruit displayed rougher, bumpier surfaces, with additional features such as the picking wound and some bruises, causing cavities in the surface topography; features which were not present in the stacking model geometries. However, the differences between the CT scan and model geometries were not as visibly pronounced as the previously compared manual stacks: as a strict stacking pattern was imposed in the preceding case, deviations such as fruit becoming dislodged or resting at an angle were much more obvious in the empirical CT scan; while in the present case, both CT scans and model generated geometries showed the same gravity inspired randomness, so that in an overall sense the reality and the simulations were more comparable. Although each stack appeared to be superficially unique – the size distribution across the count 36 weight range combining with the random chaotic nature of settling under gravity creating a distinct geometry in each instance – trends were observed when examining the full set as a whole. Each stack contained a well-defined bottom layer, as these fruit were supported by the rigid and flat floor of the packaging; then there was an amorphous, less well defined second layer; followed by a better defined top layer again. Thus, stacking a box naturally creates three layers of fruit rather than the four imposed inside the package manually.

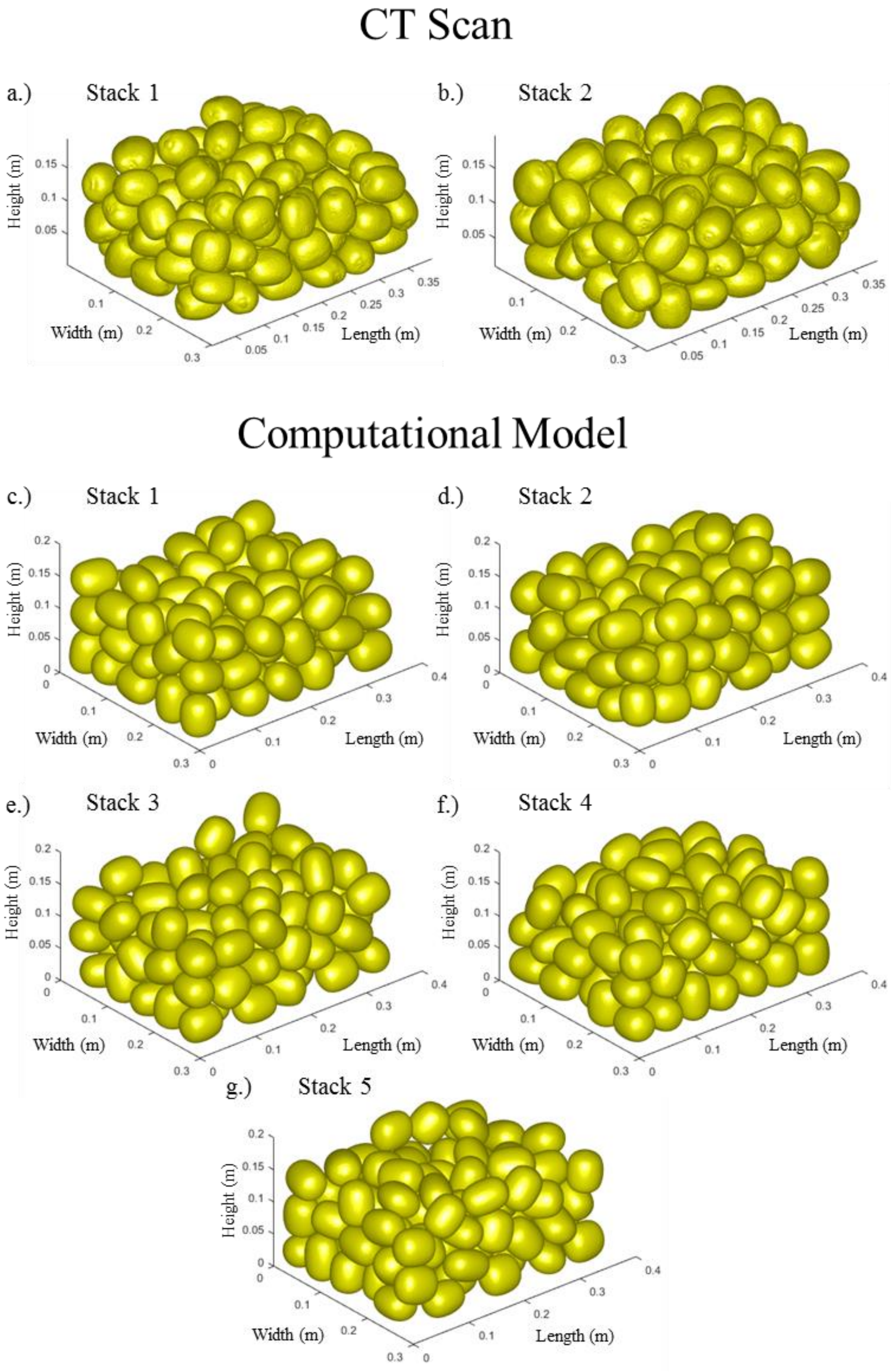

Figure 4.49: Comparing random stacks of kiwifruit: a. and b.) empirically determined (through CT scanning) 3D renders of real boxes of fruit; e. – g.) 3D renders of computationally generated random stacks of fruit through DEM.

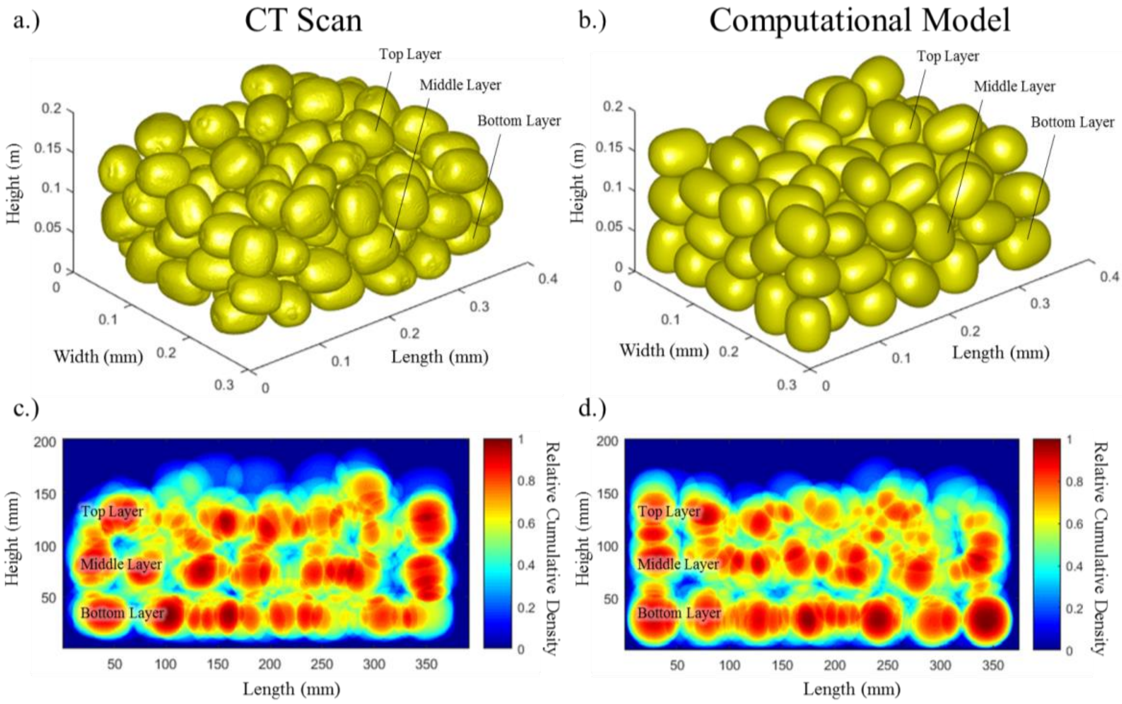

Figure 4.50: Comparing select random stacks of kiwifruit: a.) empirically determined (through CT scanning) 3D render of a real box of fruit; b.) 3D render of a computationally generated random stack of fruit. c. and d.) flattened 2D relative density maps of the 3D renders.

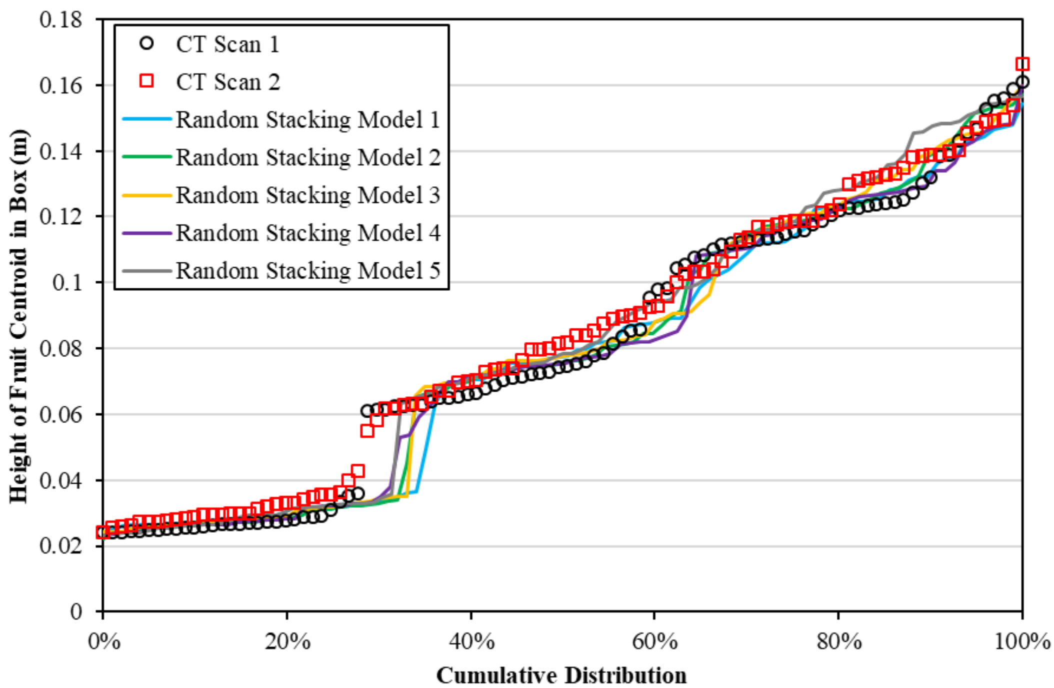

Figure 4.51: Cumulative distributions of the height of the geometrical centre of individual kiwifruits for: the CT scanned boxes (red squares and black circles); and the 5 computationally generated random stacks (solid lines of varying colours).

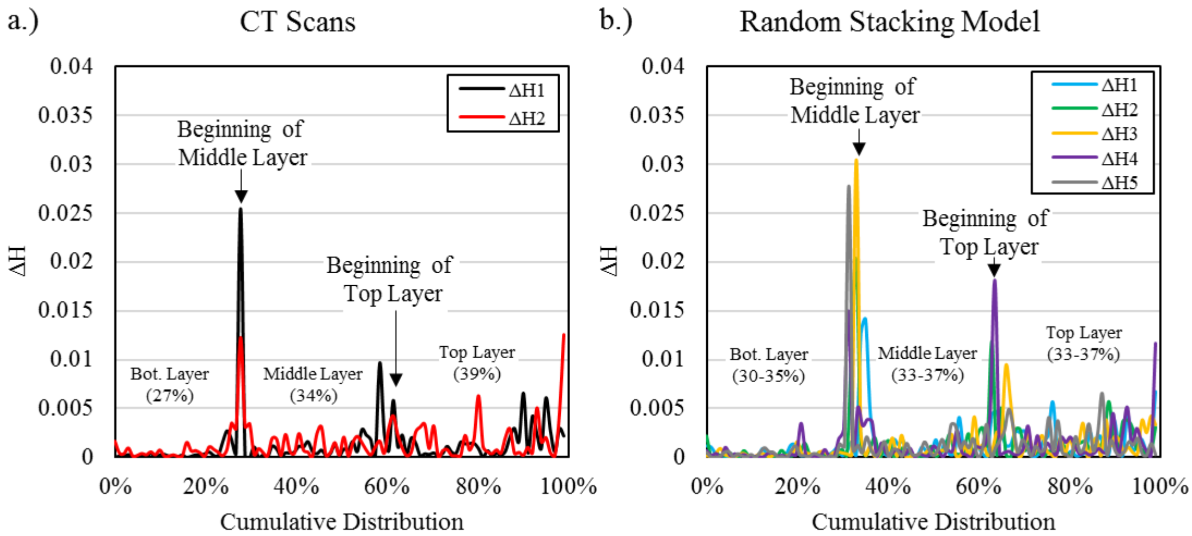

Figure 4.52: First derivative of the cumulative height curves, ΔH, *peaks indicating the position of a new layer of fruit: a.)* ΔH *for the CT scanned boxes; b.)* ΔH *for the computationally generated randomly stacked boxes.*

The 3D renders of the geometries obscured fruit in the middle and back of the package, so 2D flattened density maps were used to further investigate the first CT scan (Figure 4.49a) and the first simulated stack (Figure 4.49c) in Figure 4.50. The three layers intimated from the 3D renders are more clearly seen: there was a fairly equitable distribution of fruit across the bottom of the box to form the distinct bottom layer in both the empirical and simulated cases, with another two layers perceived above – a middle layer and a top layer, marked on Figure 4.50; however, they were much more nebulous as fruit rested upon the layers below. A major difference between the empirical and simulated stacks can be seen in the corners at the bottom of the box: in the simulated case it was favoured for a fruit to be pushed into each of the 4 corners of the box, showing a high density in these positions; while empirically there was a preference for there to be an absence of fruit at these same positions, so that the density at the bottom corners is noticeably lower – this can also be seen clearly in the 3D render of Figure 4.50a. The cause of this difference is discussed below.

The difference between reality and the stacking simulation was investigated quantitatively with the cumulative height distribution (Figure 4.51) and their accompanying ΔH plots (Figure 4.52a and b). The empirical height distributions (red squares, black circles) showed a well-defined bottom layer intimated through the horizontality of the distribution in that region, which – according to Figure 4.52a – contained 27% of the fruit. Comparing this to the simulated stacks (solid lines), the model also predicted a well-defined bottom layer in all 5 cases, however the number of fruit deposited into this layer was 30-35%, an over prediction of 3-8%. As mentioned previously, there was a tendency for the random stacking model to push fruit all the way into the corners of the packaging, while in reality fruit tended to be absent from these positions. This difference of 4 fruit in the corners explains about half of the discrepancy. A major contribution to this difference is the existence of the polyliner in the real-world package: this packaging feature, which encompasses the entirety of the fruit bulk, is pulled tight and securely shut to ensure that there are minimal leaks with the outside environment. The tautness of the polyliner creates small slopes at the corners of the packaging, preventing fruit from populating those areas. The polyliner is added digitally (section 4.4.5) only after the fruit geometry has been created in the case of the stacking model, so these polyliner created slopes do not exist and the fruit is free to populate the entire volume of the box. The remainder of the discrepancy is possibly due to how the stacking algorithm functioned, as boxes were overfilled by approximately 50% (150 fruit were stacked instead of the recommended 102) and after being allowed to settle under simulated gravity, the overfilled fruit (fruit existing above the 187mm height threshold) were eliminated. This meant that as the fruit were being allowed to settle there was additional weight above the bottom layer of fruit that would not normally be there. This may force the additional 2 or 3 fruit into the bottom layer. Beyond this divergence at the bottom layer, the cumulative height distribution of the 5 simulated stacks follows the empirical height distribution for in the empirical boxes very closely for the remainder of the box.

4.6: Conclusions

In conclusion, a new method for rapidly appropriating an accurate bulk fruit geometry was developed in this chapter. The methodology was a result of several pieces of work, including a shape equation for kiwifruit, which was able to generate accurate computational kiwifruit analogues of any size within the count 36 size range expeditiously; a shape index, which allowed kiwifruit to be randomly generated according to a specific weight distribution; and a DEM stacking model, which simulated gravity and friction forces on a collection of generated kiwifruit to naturally fall and stack into a box. This computational stacking process took only 150 seconds, and the similarity of the generated stack was validated against empirical bulk fruit shape data collected via CT scanning. The stacking model can now be used to rapidly accelerate heat transfer model development, as the bulk fruit shape can be used as an input geometry. It would be trivial to use the stacking model for other horticultural products, expanding the scope of problems which can be investigated via modelling – provided there is a shape equation for the new crop. It also has potential to be used to investigate the volumetric efficiency of new package designs.

Chapter 5

Model Development

5.1: Introduction

Methods were developed to automatically generate the geometry inside of a box of kiwifruit in chapter 4, and an indication of the experimental cooling rate under a series of cooling conditions were measured in chapter 3. The next pertinent matter was the development of a modelling methodology that satisfied this thesis' goal of being fast, flexible and automated. In section 5.2 and section 5.3, Direct Numerical Simulation (DNS) is used to investigate which heat and mass transfer mechanisms are important, to decide which should be included or excluded from future modelling work. Section 5.4 discusses the derivation of the relevant thermophysical properties; and section 5.5 covers the rationale for basing the model on the zonal modelling approach, covering the formulation of an array of automated computational operations called 'geometric procedures' that allows a zonal network to self-form using the geometry information supplied by chapter 4.

5.2: Direct Numerical Simulation

The use of Direct Numerical Simulation (DNS), which includes finite element and computational fluid dynamics models, is a powerful, high fidelity technique that has been widely used to solve heat and mass transfer problems in the pre-cooling of horticultural produce (Ferrua and Singh, 2009a; Defraeye *et al.,* 2014; Delele *et al.,* 2013). However, its exclusive use is not suitable for accomplishing the goals of this thesis – to develop a modelling methodology that is automated, flexible and fast. In fact, the deficiencies of DNS were the primary motivator for the establishment of this project, and the development of a zonal model.

Nonetheless, there was still some validity in using DNS as an aid in the development of an alternative modelling approach, as well as a comparative tool to assess the relative trade-offs between accuracy, ease of model construction and solution times. The high fidelity of DNS allowed the direct modelling of complex heat or mass transfer processes, such as: the exact refrigerated air flow velocity fields;

temperature gradients within individual fruits; and the magnitude of radiation thermal exchange between non-adjacent fruits. Furthermore, DNS represents the 'status quo' of modelling techniques and is well understood among research groups globally. Presenting the new model, with simplified alternative methods for predicting heat and mass transfers, alongside a legacy approach where these exchanges are modelled explicitly with little to no simplification, can assist in the justification of the newly developed modelling methodology.

For these reasons, a DNS model for a single box of kiwifruit was developed. The finite element model was built in the commercial DNS package COMSOL Multiphysics (COMSOL, 2015). A single box scale was decided upon because this thesis is interested in developing a *heat transfer* model for horticultural produce, so that the primary inquiry was the internal resistance to external heat transfer. Separating heat transfer from airflow, it was not wise to model the system at the pallet scale, as this requires knowledge of how the orientation of individual boxes and packaging vents align on the pallet scale to form a complex airflow pathway. If a single box heat transfer model can be developed and validated, then the model can be upgraded to the pallet scale by integrating it with a separate airflow model, which is being developed separately to this thesis by colleagues at the CPRR.

5.2.1: Model Geometry

Validation cooling data was collected in section 3.3, where fruit were stacked into an ordered pattern so that a thermocouple could be placed into the same position within a box between trials. Thus, a geometry with the same stacking pattern was re-created in COMSOL. A stack of fruit was created manually using Blender, where Eq. 4.11 (shape equation for kiwifruit) was used in conjunction with the method outlined in section 4.3 to create 100 kiwifruits. Only 'average' sized count 36 fruit were created, using $D_{X,av}$, $D_{Y,av}$ and L_{av} from Table 4.1, rather than the creation of 100 random fruit sizes. Individual fruits were moved into a digital enclosure with the same inner dimensions of a modular bulk package: 372×292×187mm. This was an arduous and time consuming process, there being great difficulty in finding a correct pattern that would allow all 100 fruit into the enclosure without fruit intersecting with each other or the walls of the package. The final geometry is shown in Figure 5.1.

The “near miss principle” was used (Ferrua and Singh, 2009a; Defraeye *et al*, 2014) which shrinks fruit by a small percentage of total volume to prevent the surface of individual fruits from overlapping. This was done to mitigate COMSOLs tendency to produce errors when attempting to finalise the geometry or mesh geometry with surface conjunctions between objects. Each fruit was reduced in volume by 2%.

The polyliner was created using the methods outlined in section 4.4.5, using the settings: Subdivide = 6, Offset = -0.00035 and Smooth = 5 (Figure 5.2). The Offset being negative created a polyliner with a small degree of perfect contact between the fruit and the polyliner so that there was limited direct contact between fruit and the refrigerated airflow. The need for this direct fruit-air contact area is explored later in section 5.3.3.

The fruit and polyliner geometries were exported from Blender separately as .stl files, and then imported into COMSOL (Figure 5.3) and converted into solids using COMSOLs ‘Form Solid’ function. They were then joined with the ‘Form Union’ Boolean operator. This created new boundaries on the surface of fruits where the polyliner and fruit surfaces overlapped, to represent small areas where there was perfect contact between the fruit and the polyliner. The finalised COMSOL geometry is shown in Figure 5.4 from several viewing angles.

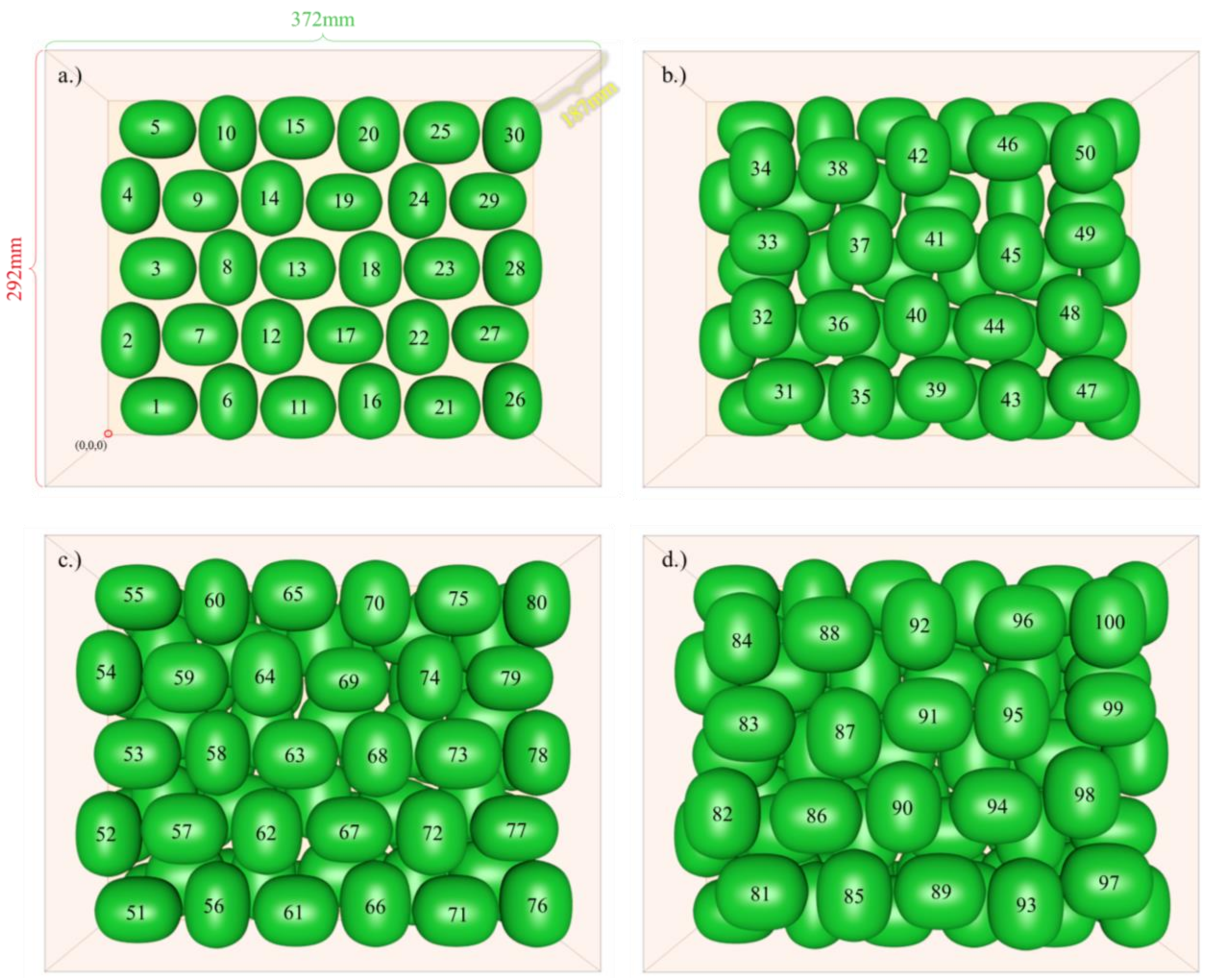

Figure 5.1: Model geometry of 100 kiwifruit stacked manually into 4 orderly layers in Blender within the inner dimensions of a modular bulk package: a.) bottom layer, 30 fruit; b.) 2nd layer, 20 fruit; c.) 3rd layer, 30 fruit; and d.) top layer, 20 fruit.

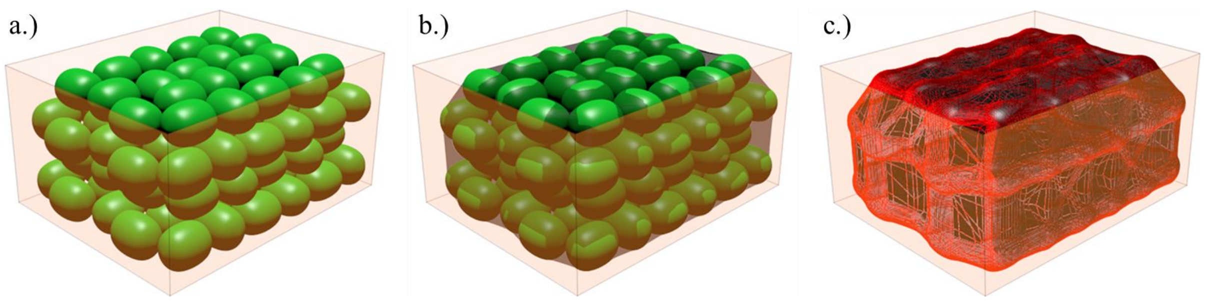

Figure 5.2: Automated polyliner wrapping of the fruit geometry (Subdivide = 6, Offset = -0.00035 and Smooth = 5). a.) fruit geometry; b.) polyliner and fruit; c.) mesh topography of the polyliner.

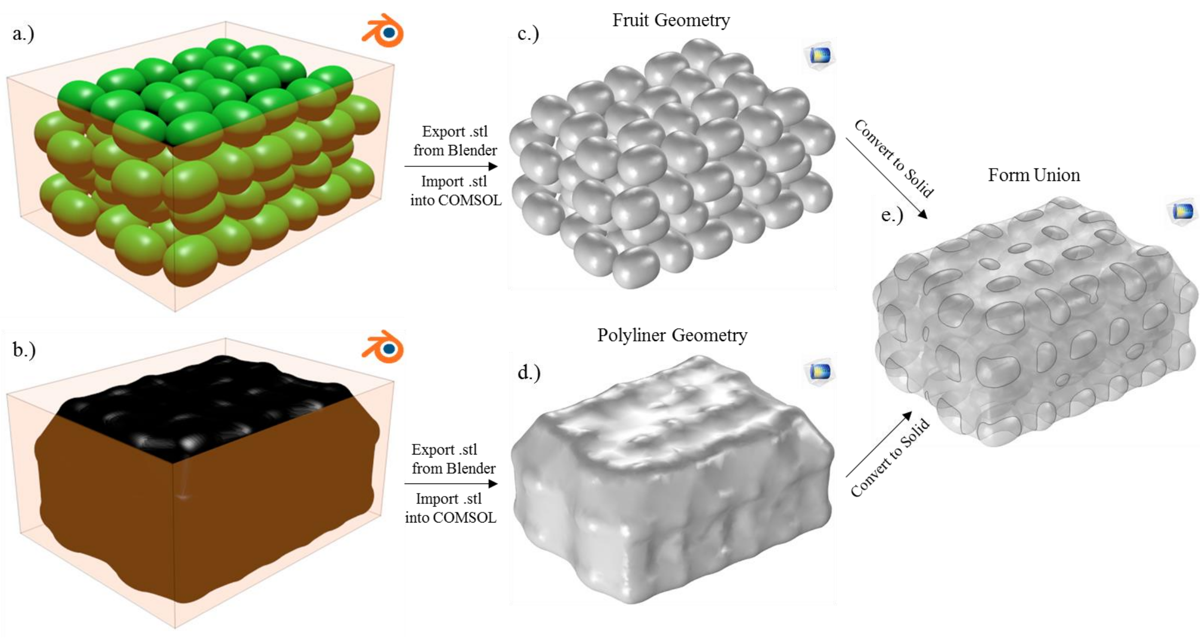

Figure 5.3: Export of fruit and polyliner from Blender as an .stl and then imported into COMSOL (a, b, d and d). Geometries are then converted from surfaces to solid and then joined (d).

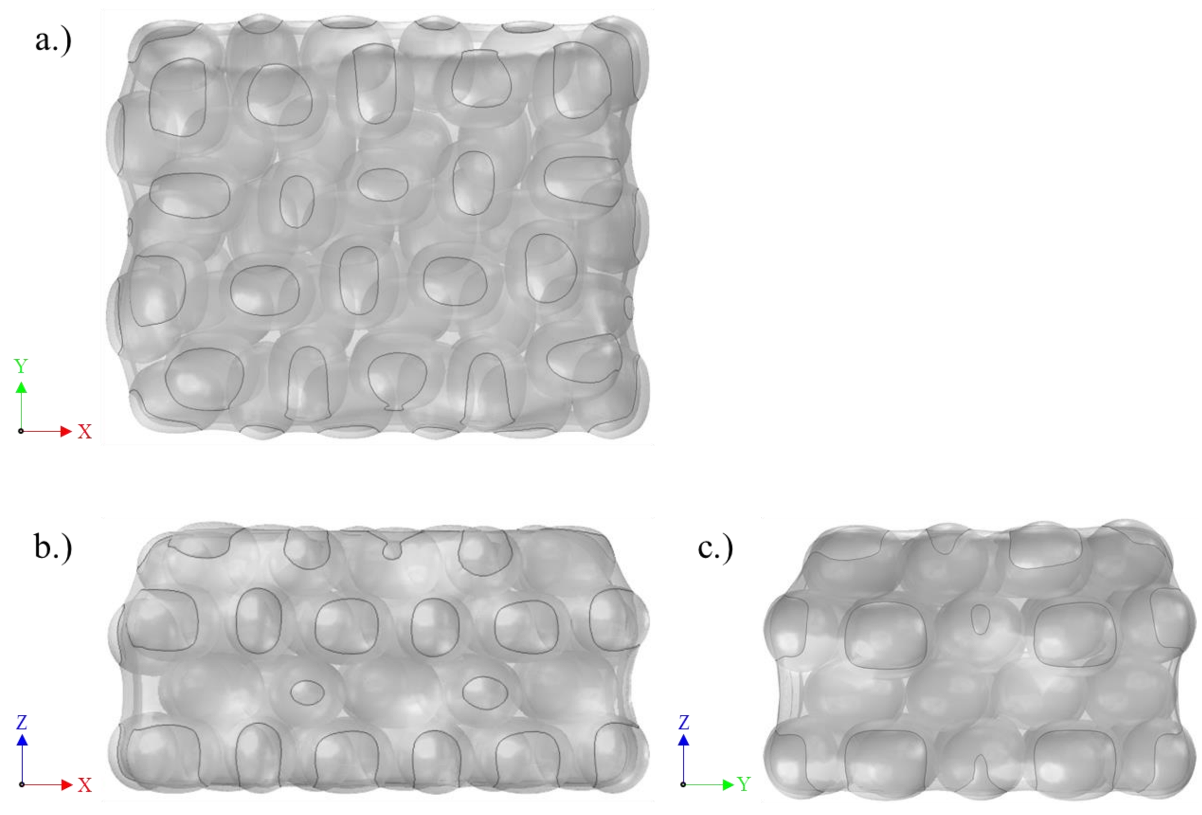

Figure 5.4: Finalised geometry of fruit and polyliner in COMSOL. a.) top down view (Y-X direction); b.) front view (Z-X direction); and c.) side view (Z-Y direction).

5.3: Transport Mechanisms

Creation of a fast and flexible heat transfer model for boxes of polylined kiwifruit requires understanding of which heat, mass and momentum transfer mechanisms occur during pre-cooling. As outlined in section 1.2.4, the following transfer mechanism were identified as possible contributors to fluxes of heat or mass:

- Thermal conduction;
- Forced convection;
- Natural convection;
- Radiation;
- Evaporation;
- Diffusion, and;
- Respiration.

This section explores the relative magnitude of each mechanism so that decisions can be made later during the development of the zonal model pertaining to which must be included. Mechanisms that are significant must be accounted for in some simplified manner, while other mechanisms that contribute little to the overall rate of temperature or mass change can be ignored, further simplifying the model. This exploration utilises the DNS model geometry (section 5.2) as a tool to explicitly model transfer mechanisms.

5.3.1: Conduction

Conduction is the transfer of thermal energy from a high temperature region to a low temperature region. This can only occur within objects or between two objects that are in direct contact with each other. Conduction heat transfer is described by Fourier's equation:

$$\phi_{cond} = \lambda \cdot A \cdot \frac{\Delta T}{x} \tag{5.1}$$

Where ϕ_{cond} is the heat flux due to conduction (W, or J·s^{-1}); λ is the thermal conductivity of the material (W·m^{-1}·K^{-1}), A is the heat transfer surface area (m^2), ΔT is the temperature gradient (K) and x is the distance over which heat transfer is occurring (m). Conduction is expected to play a very important role, as it is the preeminent mode of heat transfer within opaque solids, such as food (Singh and Heldman, 2009). This is expected to apply more so for a polylined system: although convection heat transfer is typical at the surface of objects, the polyliner limits the degree to which refrigerated air can interact with the bulk surface of the fruit, as the forced airflow cannot penetrate the polyliner. Thus, there will not only be conduction heat transfer between touching fruits, but also a significant amount of conduction through the air inside the polyliner.

5.3.2: Convection

Heat transfer via convection involves the exchange of heat between the surface of an object and a moving fluid. The fluid will be in motion because of natural convection, pressure gradients created by temperature differences in the fluid; or because of forced convection, caused by an artificially induced pressure drop. During a forced-air cooling process, there are several domains in which convection could be important. Forced convection is likely to be dominant outside of the polyliner as the fan creates a large pressure drop, resulting in high velocities of air being forced through the package ventilation (Defraeye *et al.*, 2014). Natural convection is likely to occur within the polyliner as the temperature differences between fruit and air cause small convection currents, facilitating the transfer of heat from the fruit (O'Sullivan *et al.*, 2016). These two forms of convection are investigated separately.

5.3.2.1: Forced Convection

Forced convection plays the role of the external rate of heat transfer, described in section 1.2.5.1 and Figure 1.8 as one half of the 'cause' in the overall heat transfer 'effect' – the other half being the internal resistance to heat transfer. The combination of fan speed, fan size, package orientation, vent size, vent shape and vent number, and the shape of the headspace all combine to form a specific airflow pathway. This pathway of refrigerated air carries heat away from the surface of the polyliner and to a more limited degree, fruit within a box, as described by Eq. 5.2 (Holman, 2010):

$$\frac{\phi_{conv}}{A} = -\lambda_A \frac{\partial T}{\partial x}\bigg|_{x=0} \tag{5.2}$$

Where ϕ_{conv} is the heat flux due to convection; A is the heat transfer surface area (m^2); λ_A is the thermal conductivity of air ($W \cdot m^{-1} \cdot K^{-1}$); and $\frac{\partial T}{\partial x}\big|_{x=0}$ is the temperature gradient on the surface as a result of a specific airflow pathway. This temperature gradient cannot be measured easily without disrupting the boundary layer, or it can be determined with complex techniques such as CFD or inferred by particle image velocimetry (Ferrua and Singh, 2009a; Ferrua and Singh, 2009b). However, using Newton's law of cooling:

$$\frac{\phi_{conv}}{A} = h_{ext}(T_{surf} - T_{ref}) \tag{5.3}$$

It can be shown that a simple external heat transfer coefficient, h_{ext}, can be used to represent the convective impact of a complex airflow pattern by combining Eq. 5.2 and Eq. 5.3:

$$h_{ext} = \frac{-\lambda_A(\partial T/\partial x)|_{x=0}}{T_{surf} - T_{ref}} \tag{5.4}$$

In the interests of simplicity, the impact of forced-convection will be explored in this section using representative, imposed values of h_{ext}, rather than explicit modelling of the airflow and consequent heat transfer coefficient. This exploration was done using the DNS model of section 5.2. For this exploration, the cardboard packaging was removed, the implication being that h_{ext} represents the impact of the airflow flowing through the package in the gaps between the surface of the polyliner and the inside surface of the box. Thermal properties are given in section 5.4. The air within the polyliner was considered stagnant to simplify this exploration, with pure conduction through the fruit and polyliner air phases, modelled as:

$$\rho \cdot C \cdot \frac{\partial T}{\partial t} = \nabla(\lambda \cdot \nabla T) \tag{5.5}$$

External cooling was imposed as a Robin boundary condition (Mercier et al, 2017a):

$$-\lambda \nabla T \cdot \boldsymbol{n} = h_{ext} \cdot \left(T - T_{ref}\right) \text{ (at boundary } \Omega\text{)} \tag{5.6}$$

Where $\boldsymbol{n}$ is the normal vector and Ω is the entire external surface of the object – this h_{ext} was applied uniformly across the surface of the polyliner, as well at the smaller areas where there was direct contact between the fruit and polyliner. Realistically, h_{ext} will not be uniform over the entire fruit and polyliner stack, as the airflow pattern will create disparate airflow velocities, in turn creating different magnitudes of convective heat transfer in different locations – for example, there is likely to be greater air flow and therefore a greater convective heat transfer coefficient in the headspace than at the bottom of the box; depending upon the precise configuration of vents etc. However, in this exploratory case these differences are ignored, but are addressed later during model validation (see section 6.3). The initial temperature of all fruit and air inside the polyliner was T_i = 20°C, the temperature of the refrigerated air T_{ref} = 0°C. The geometry was meshed into 117775 tetrahedral elements (Figure 5.5b), and the h_{ext} values investigated were 5, 10, 20 and 40 $W \cdot m^{-2} \cdot K^{-1}$. These values approximately correspond to air velocities ranging from nearly 0.2 $m \cdot s^{-1}$ to 6.0 $m \cdot s^{-1}$; which covers the range expected within the box (ASHRAE, 2010). The simulation predicted the temperature change over 20 hours of cooling. Visualisation of the temperature gradients within the box at 10 hours of cooling are given in Figure 5.5d and e at different cut planes; the volume average temperature of all fruit are plotted over time in Figure 5.6a; and the relationship between h_{ext} and the half-cooling time is shown in Figure 5.6b.

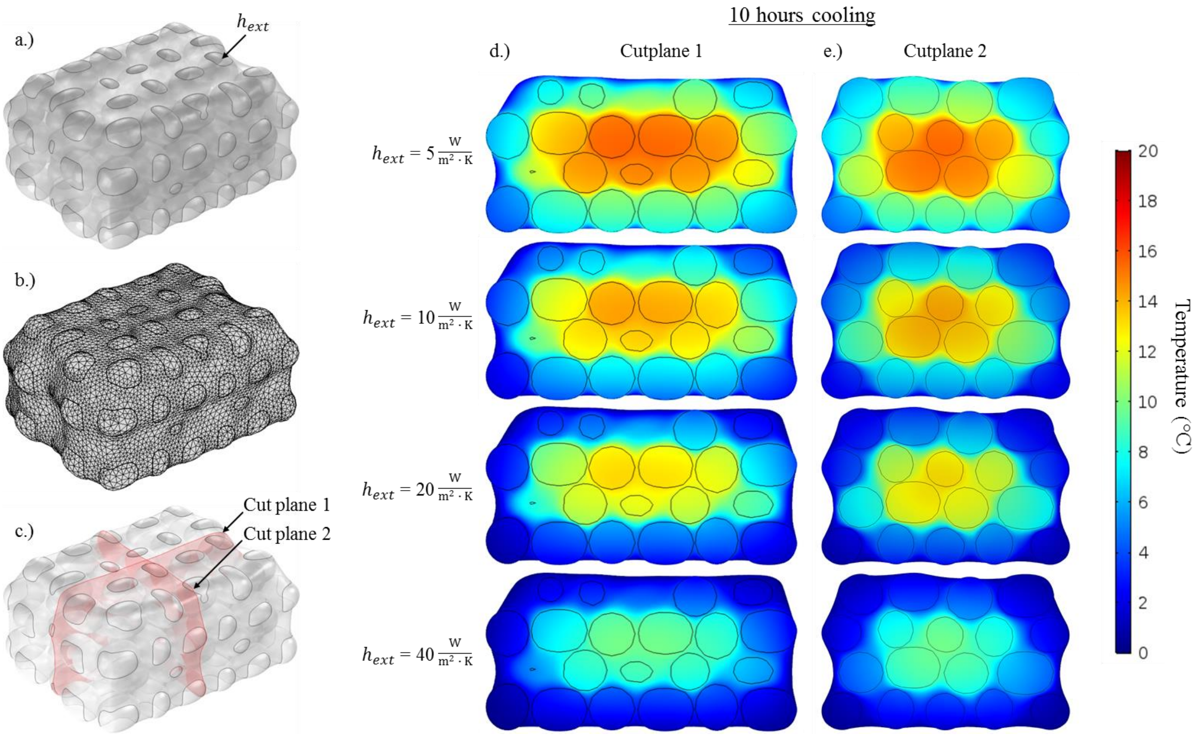

Figure 5.5: Results of DNS model investigating the impact of external convection on the fruit-polyliner stack. a.) geometry of the fruit and polyliner; b.) mesh of the geometry (117775 elements); c.) cutplanes for visualisation of results; d). temperature gradients within the stack at 10 hours of cooling for cut plane 1; d.) temperature gradients within the stack at 10 hours of cooling for cut plane 2.

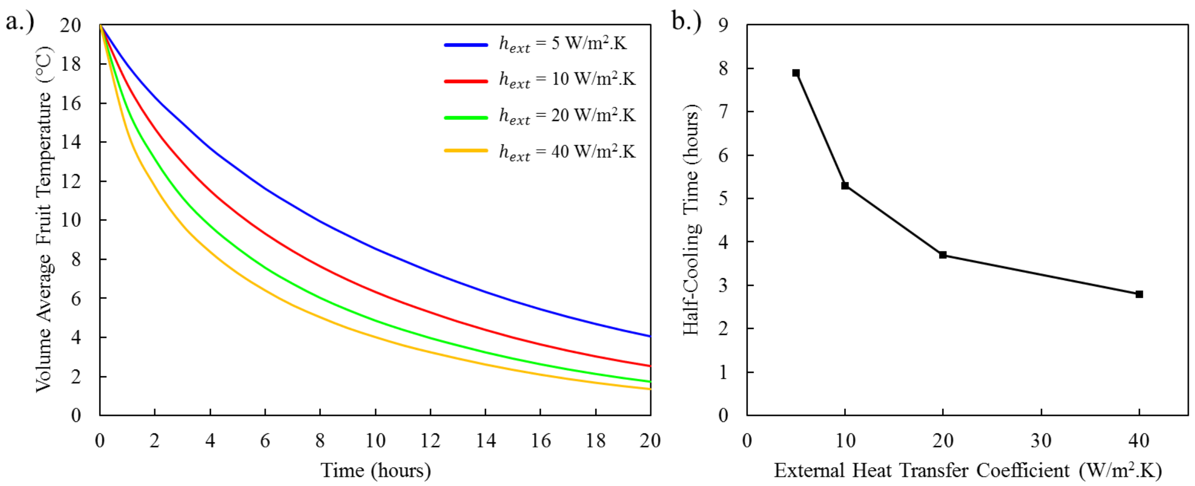

Figure 5.6: Overall impact of external convection on cooling rates: a.) volume average fruit temperature cooling curves; b.) impact of external heat transfer coefficient on volume average HCT.

Figure 5.6 and Figure 5.6 shows conclusively that forced-convection is a vital heat transfer mechanism, and must be accounted for in the zonal model, which is to be expected as the airflow acts as the main driving force for temperature change. This also reveals the internal resistance is surprisingly high. Figure 5.6b shows a diminishing relationship between h_{ext} and the average cooling rate, where the point of diminishing returns appears to be at a relatively low value of h_{ext}. Doubling h_{ext} from 5 to 10 W.m^{-2}.K^{-1} accelerates the HCT by 2.6 hours, while doubling h_{ext} from 20 to 40 W.m^{-2}.K^{-1} only accelerates the HCT by 0.9 hours. This is consistent with empirical observations (section 3.3.4.2.1).

5.3.2.2: Natural Convection

Natural, or free convection, occurs when temperature gradients in a fluid produces convection currents. The degree to which gravity induced buoyancy forces are present are dependent on the size of the system, as a larger enclosure is more likely to allow the development of convection currents. Similarly, the larger the differential in temperature, the larger the currents become as convection currents will not form if the temperature induced pressure differential is not sufficiently high. Natural convection can occur in any region where there is fluid, so there are two regions where buoyancy forces may need to be incorporated into the model. The first is the fan-forced jet stream of refrigerated air flowing into the boxes and around the polyliner and fruit. At certain velocities, the forced-convection may dominate over natural convection, while at lower velocities there is a mixture of natural convection and forced convection. Holman (2010) advises that free convection is significant over forced convection when Gr/Re^2 > 10, Gr being the dimensionless Grashof number (Eq. 5.7) and Re being the dimensionless Reynolds number (Eq. 5.8):

$$\mathrm{Gr} = \frac{g\beta(T_{surf} - T_{ref})H^3}{\nu^2} \tag{5.7}$$

$$\mathrm{Re} = \frac{uH}{\nu} \tag{5.8}$$

Where g is the acceleration due to gravity (g = 9.81 m.s^{-2}); β is the thermal expansion coefficient ($\beta = 1/T_A$; K^{-1}); H is the characteristic length of the system, in this case the height of the box (m); T_{surf} is the temperature of the heated or cooled surface (K); T_{ref} is the temperature of the bulk air (K); ν is the kinematic viscosity of air (m^2.s^{-1}); and u is the velocity of air (m.s^{-1}). Figure 4.47 of section 4.5 suggests a headspace in the box of approximately 25 mm, so this is used as the height, H. ASHRAE (2010) suggests forced air coolers have air velocities in the range of 1-3 m.s^{-1}, so the lower value of 1 m.s^{-1} is taken as at lower air velocities, buoyancy is more likely to become dominant. T_{surf} is the polyliner surface temperature and is taken as half-way between the initial temperature (T_i = 20°C) and the refrigeration temperature (T_{ref} = 0°C), so T_{surf} = 10°C. Properties of air (β and ν) are taken at 10°C (β = 0.0035; ν = 1.345×10^{-5}). This gives Gr = 3.0×10^4 and Re = 1.86×10^3, so that Gr/Re^2 = 0.0087 – so that at even the lower range of expected air velocities, free convection is negligible in the bulk flow of air. Thus, natural convection can be ignored from any future modelling work in this region.

The second region where convection currents can form is in the air inside the polyliner. The polyliner blocks most of the air forced through the packaging from interacting with this 'trapped' air, and is considered by some to be stagnant (Mercier *et al.,* 2017a; Ambaw *et al.,* 2017). However, O'Sullivan *et al.* (2016) argues the contrary with natural convection considered to be vital in the validation of their CFD model. Holman (2010) posits that the use of the dimensionless Rayleigh number (Eq. 5.9) can be used to assess whether there is a significant level of natural convection in a system where there is an absence of forced convection:

$$\mathrm{Ra} = \frac{g\beta(T_{surf} - T_{ref})H^3}{\nu\kappa} \tag{5.9}$$

Where κ is the thermal diffusivity of the air (m^2·s^{-1}). At low Ra values (< 2000), the system has negligible natural convection and the air can be considered 'stagnant', and can be modelled as a solid with the same thermal properties as air. Between Ra = 6×10^3–2×10^5 there is a significant level of natural convection, and the convection currents formed follows a laminar regime, while at Ra = 6×10^5–1.1×10^7 the convection currents are turbulent (Holman, 2010). With the same initial temperature of 20°C and refrigeration temperature of 0°C, with T_{surf} = 10°C and air properties evaluated at T_{surf} (β = 0.0035 K^{-1}; ν = 1.345×10^{-5} m^2·s^{-1}; λ_A = 0.0257 W·m^{-1}·K^{-1}; ρ_A = 1.205 kg·m^3; C_A = 1005 J·kg^{-1}·K^{-1}; κ = $k_A/(\rho_A \cdot C_A)$ = 2.1×10^{-5} m^2·s^{-1}), and the height of the box as H = 0.196 m, this gives Ra = 9.0×10^6. This indicates natural convection currents are very rapid inside the polyliner, and are in the turbulent regime, likely to contribute greatly to the heat and mass transfer rate. However, this result is somewhat disingenuous: this does not take into account that the volume inside of the polyliner is not filled entirely with air, but is rather a combination of fruit and air. The fruit will act as an impediment to the formation of convection currents, the air only able to move in the pores or gaps between fruits. If the vertical height H is instead taken as the vertical spaces between fruit within the polyliner (which might range between 0.01-0.03 m, then Ra might be estimated to range between about 1200 and 3.0×10^4, suggesting that natural convection could instead be either irrelevant or follow laminar regime.

Resolving this ambiguity warranted further investigation using the finite element model. The DNS model, using COMSOL, modelled the velocity field created by minute temperature induced pressure gradients in the air directly. Movement of the air was modelled by using Eq. 5.10 and Eq. 5.11:

$$\rho\frac{\partial u}{\partial t}+\rho(u\cdot\nabla)u=\nabla\cdot[-PI+\mu(\nabla u+(\nabla u)^T)]+F \tag{5.10}$$

$$\rho\nabla\cdot(u)=0 \tag{5.11}$$

The volume force, F was defined as :

$$F=-g\cdot\rho \tag{5.12}$$

The simulation was set up so that it could be compared with the forced convection example of section 5.3.2.1, with the same initial temperature, refrigeration temperature, thermal properties and external cooling conditions of h_{ext} = 5, 10, 20 and 40 W.m^{-2}.K^{-1}. Results are shown in Figure 5.7.

As suspected, the impact of natural convection is not nearly as pronounced as the first calculated Rayleigh number would suggest. The presence of fruit inside of the polyliner significantly increased the resistance to the formation of convection currents, limiting the ability of free convection to convect heat away from the surface of fruits inside the polyliner and deliver it to the surface of the polyliner. Natural convection reduced the internal resistance by approx. 5-10% – though not hugely significant, this is still in a range where it would be remiss to ignore it. Thus, natural convection must be taken into account when modelling the air inside of the polyliner in later sections. Modelling this phenomenon should be done in a much simpler fashion than was done here – as modelling natural convection directly doubled the simulation completion time, from half an hour (section 5.3.2.1) to an hour.

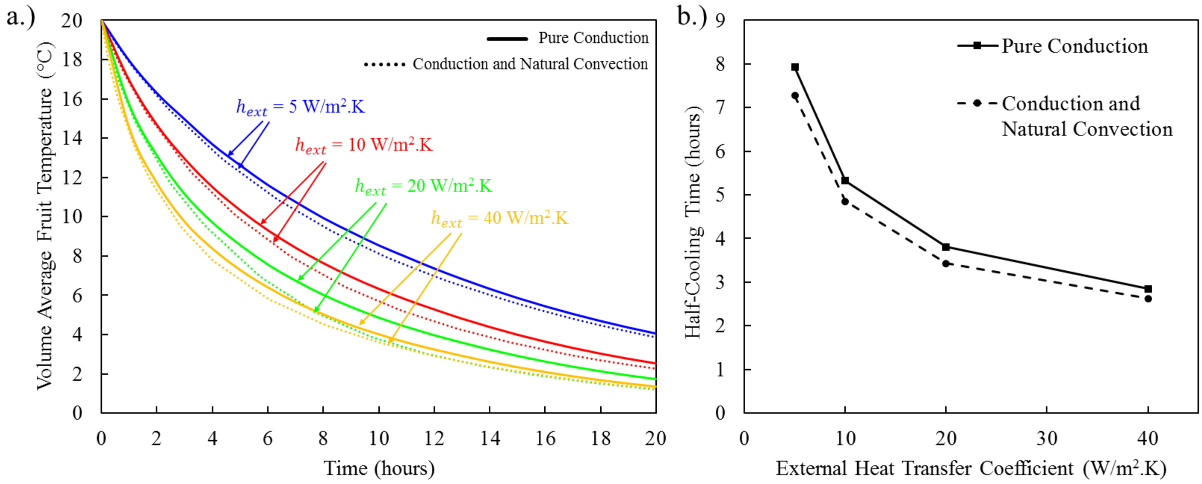

Figure 5.7: Comparative impact of natural convection on cooling rates: a.) volume average fruit temperature cooling curves, with (dotted lines) and without (solid lines) natural convection; b.) impact of external heat transfer coefficient on volume average HCT, with (dashed line, circles) and without (solid line, squares) natural convection.

5.3.3: Direct Contact Between Fruit and Polyliner

Though not necessarily a 'heat or mass transfer mechanism', it was important to explore the decision to create a polyliner with some perfect contact between the fruit and polyliner. This decision increased the difficulty of creating a DNS model, but was necessary because of the following analysis. A polyliner was generated with a 0.5 mm gap between the fruit and the polyliner using the method outlined in section 4.4.5 (Subdivide = 6, Offset = 0.001 and Smooth = 5). Cooling curves comparing this polyliner with that of section 5.3.2.1 are shown in Figure 5.8; and a visualisation of the temperatures of the two cases in Figure 5.9.

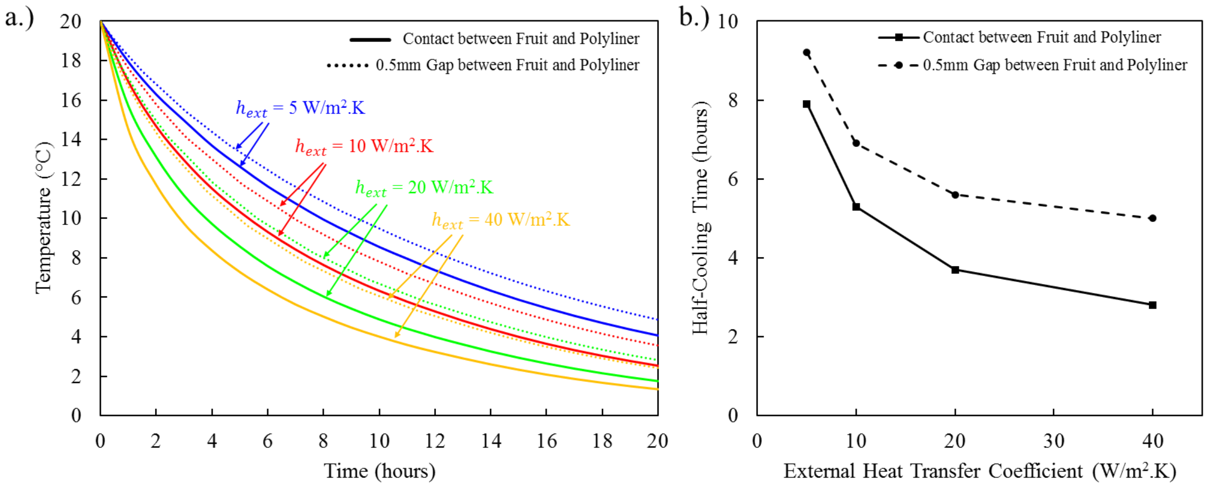

Figure 5.8: Comparative impact of direct contact between fruit and polyliner on cooling rates: a.) volume average fruit temperature cooling curves, with a 0.5mm gap between fruit and polyliner (dotted lines) and with contact between fruit and the polyliner (solid lines); b.) impact of external heat transfer coefficient on volume average HCT, with a 0.5mm gap (dashed line, circles) and with direct contact (solid line, squares).

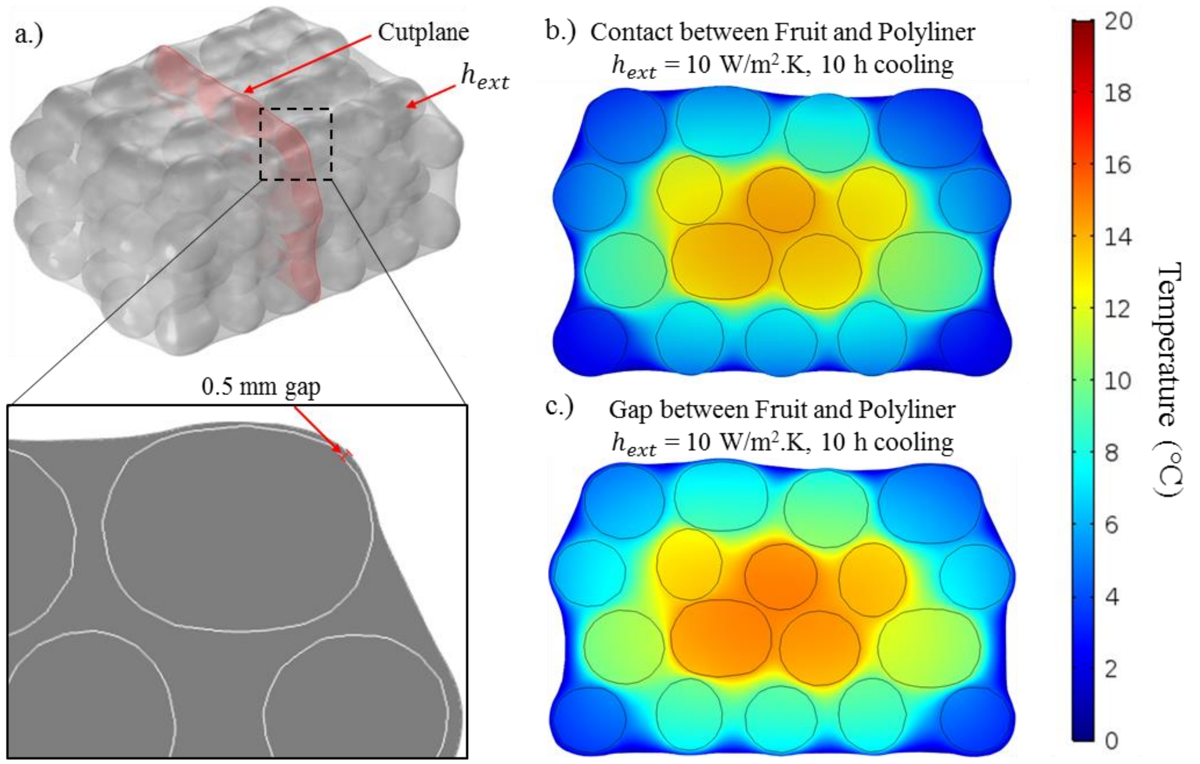

Figure 5.9: Results of DNS model investigating the impact of direct contact between the fruit and polyliner; a.) geometry of fruit and polyliner with a close-up of the 0.5 mm gap between fruit and polyliner; b.) temperature gradients with contact between fruit and polyliner; c.) temperature gradients with a 0.5mm gap between fruit and polyliner.

Even a minute gap of half a millimetre between the fruit and polyliner caused a sharp increase in the internal resistance. Cooling at h_{ext} = 40 W.m^{-2}.K^{-1}, the slight gap in the polyliner impaired the HCT by 2.2 hours. Even though there was a seemingly negligible gap between the fruit and polyliner, air has a very low thermal conductivity, just λ_A = 0.0257 W·m^{-1}·K^{1}. Applying a thin 0.5 mm layer of insulation around the entire polyliner, that has a large surface area, seemingly doubles the internal resistance. This shows conclusively that the geometry of the fruit and polyliner plays a vital role, and that some direct contact between fruit and the polyliner is more realistic. Considering that the polyliner is wrapped tightly around the fruit, it would make sense that the flexible polyliner is forced onto the surface of the fruit, conforming to the bulk exterior shape of the mass of fruit. Accounting for this direct contact was very difficult to implement in a DNS scheme and so in a later section, methods were developed for circumventing these difficulties to increase the flexibility of the model (section 5.5.4).

5.3.4: Respiration

Fruit are living organisms that continue to respire even after they have been picked, converting stored sugars into CO_2 and generating heat. The chemical reaction for respiration is given in Eq. 5.13 (ASHRAE, 2010):

$$\mathrm{C_6H_{12}O_6 + 6O_2 \rightarrow 6CO_2 + 6H_2O + 2667000\ J} \quad (5.13)$$

Fruit respire at lower rates at lower temperatures – a major motivator for pre-cooling to reduce the fruit temperature as quickly as possible. From a heat transfer prediction perspective, it is important to know if heat generated from respiration has an impact on the observed cooling rate. Heyes *et al.* (2009) measured the CO_2 production rate as a function of temperature for Hayward kiwifruit as Eq. 5.14:

$$R_{CO_2} = [3.9037 \times T + 21.782] \times 10^{-9} \quad (5.14)$$

Where R_{CO_2} is the rate of CO_2 production (mol·kg^{-1}·s^{-1}). The heat generated from respiration is therefore Eq. 5.15:

$$\frac{\phi_{respiration}}{V_S} = \frac{2667000}{6} \times [3.9037 \times T + 21.782] \times 10^{-9} \times \rho_S \qquad (5.15)$$

The impact of this mechanism was modelled with the DNS model. Respiration was modelled as a temperature dependent heat source, applying Eq. 5.15 to all of the fruit domains. External airflow was modelled as h_{ext} = 10 W.m^{-2}.K^{-1}, with the same initial conditions, refrigeration temperature and thermal properties as in section 5.3.2.1. Predicted cooling rates with respiration and no respiration are shown in Figure 5.10:

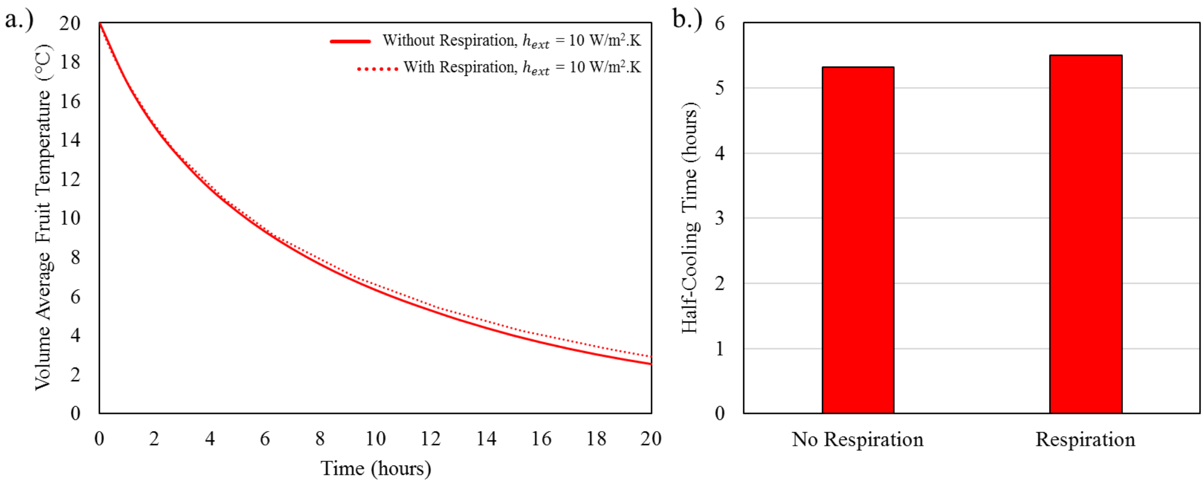

Figure 5.10: Comparative impact of respiration on cooling rates: a.) volume average fruit temperature cooling curves, with (dotted line) and without (solid line) respiration; b.) impact on HCT with and without respiration.

Adding respiration did not impact the cooling profile significantly. No differences appeared until approximately 6 hours, after which respiration raised the temperature by a minute 0.4°C at 20 hours of cooling – a HCT difference of just 0.17 h. Respiration is therefore considered negligible and will be excluded from consideration in further sections. Its insignificance is partially because of the relatively low respiration rate, but is also a consequence of the short time scale. Negligible quantities of heat are generated from respiration over just 20 hours, but in a long-term cold storage scenario where fruit pallets can be kept for up to 12 months, the heat of respiration can be quite considerable and a challenge to remove. When modelling other fruits or different parts of the cold-chain its contribution should be re-examined.

5.3.5: Evaporation, Condensation and Diffusion

Fruit consist mostly of water, where Kiwifruit consists of approx. 80% water (see section 5.4). Evaporation therefore has potential to contribute to the heat load of a pre-cooling process, even if only a small fraction of water weight is lost. This is due to evaporation being a phase change process, where latent heat is removed from the surface of the food product – free water in the fruit is evaporated into gaseous moisture in the air. Seeing as the latent heat of vaporisation is 2260 kJ/kg, even small quantities of evaporation can contribute significantly to the cooling rate. Ferrua and Singh (2009b) modelled the forced-air cooling of strawberries, where a minimal 0.4-0.55% moisture loss contributed to 15-27% of the overall heat removal. This was, however, for an open system with no polyliner and so there was a high degree of convective evaporation, the only barrier to moisture loss being the skin of the strawberries; and was in a system where the product was small, so there was a high surface area to volume ratio, promoting water loss. This is in contrast with the current scenario where kiwifruit is wrapped in a polyliner bag. The design purpose of the polyethylene bag is to promote a high humidity local environment. Some evaporation may occur at the beginning of the cooling process, but the air inside the polyliner very quickly reaches saturation, effectively reducing the moisture gradient between fruit and air to zero. Additionally, the polyliner does not allow refrigerated air to interact directly with the bulk of the fruit, so any convective evaporation is through natural convection only, which subsequently has a small impact (section 5.3.2.2). Huang *et al* (2017) modelled evaporation from fruit in a closed system and found that it had a negligible impact on the predicted temperature profile. In a scenario where the polyliner is not considered perfectly sealed and leakages can occur, evaporation is still expected to be minimal as the air used in pre-cooling processes is high humidity (~80% RH, Bachmann and Earles, 2000). Furthermore, the time scale over which the pre-cooling process takes place is short compared with other parts of the cold chain – pre-cooling takes approximately 12-24 hours, while fruit pallets can spend up to 12 months in cold-storage. Assuming that the rate of moisture loss might be higher during pre-cooling, the time frame over which pre-cooling occurs is orders of magnitude lower than a room-cooling scenario – where the rate of evaporation is likely much lower but occurs over a much greater time period.

Thus, modelling moisture transfers and its associated heat transfers – evaporation and condensation – are unnecessary and will not be considered using the DNS model or in later modelling sections. However, when modelling a non-polylined system, or a different part of the cold-chain, its importance should be reconsidered.

5.3.6: Thermal Radiation

Thermal radiation occurs when two or more surfaces of different temperatures exchange energy via emission of infrared light (Holman, 2010):

$$\phi_{rad} = A \cdot \sigma_{rad} \cdot \epsilon \cdot \Delta(T^4) \tag{5.16}$$

Where A is the area seen by both surfaces (m^2); σ_{rad} is the Stefan–Boltzmann constant (5.67×10^{-8} $W{\cdot}m^{-2}{\cdot}K^{-4}$); ϵ is the emissivity of the surfaces (-); and $\Delta(T^4)$ is the temperature difference of each surface (K).

While radiation is often ignored in models encountered in the literature (Ferrua and Singh, 2009a; Defraeye *et al.,* 2014; Delele *et al.,* 2013), the rationale for its exclusion is its low relative impact compared with convective heat transfer, especially when the exterior surfaces are all relatively similar in temperature. There is reason to doubt this assumption in the current scenario, where the polyliner limits the impact of convective heat transfer greatly. Radiation has potential to play a more significant role in a polylined scenario as it can occur between non-adjacent objects. Heat is difficult to remove from fruit at the centre of the polyliner, so with radiation this may facilitate some heat transfer between these warm fruits and colder fruit within line of sight at the polyliner.

Thermal radiation was therefore investigated by modelling it directly using COMSOL. Fruit were assigned as opaque emissive surfaces with an emissivity of ϵ = 0.9 (Huang *et al.,* 2017). Air and the polyliner are considered transparent. Thermal radiation was modelled as surface-to-surface radiation using the hemi-cube method and a resolution of 256 (see COMSOL, 2015 for details). External airflow was modelled as h_{ext} = 5 $W.m^{-2}.K^{-1}$, with the same initial conditions, refrigeration temperature and thermal properties as in section 5.3.2.1. Unfortunately, this simulation required much greater computational resources than were available (Intel® i7-4770 with 16GB of RAM); so as a compromise, approximately half of the fruit were removed (44 of 100) from the simulation (see Figure 5.11). Comparative cooling profiles of this half box of fruit with radiation and without radiation are shown in Figure 5.12.

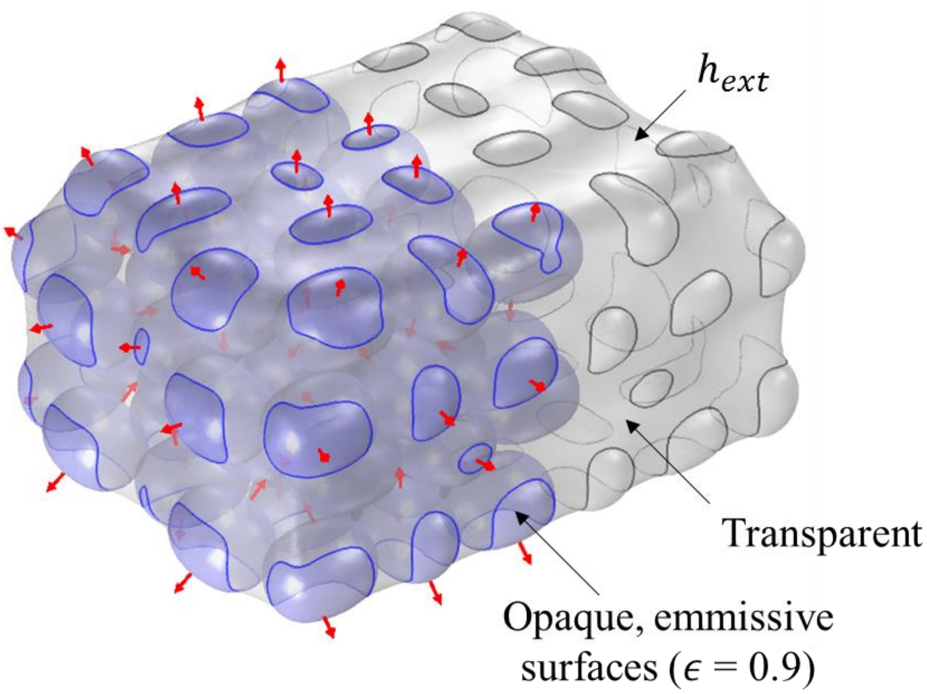

Figure 5.11: Geometry of thermal radiation DNS model, with the normal of emissive surfaces (fruit) as red arrows.

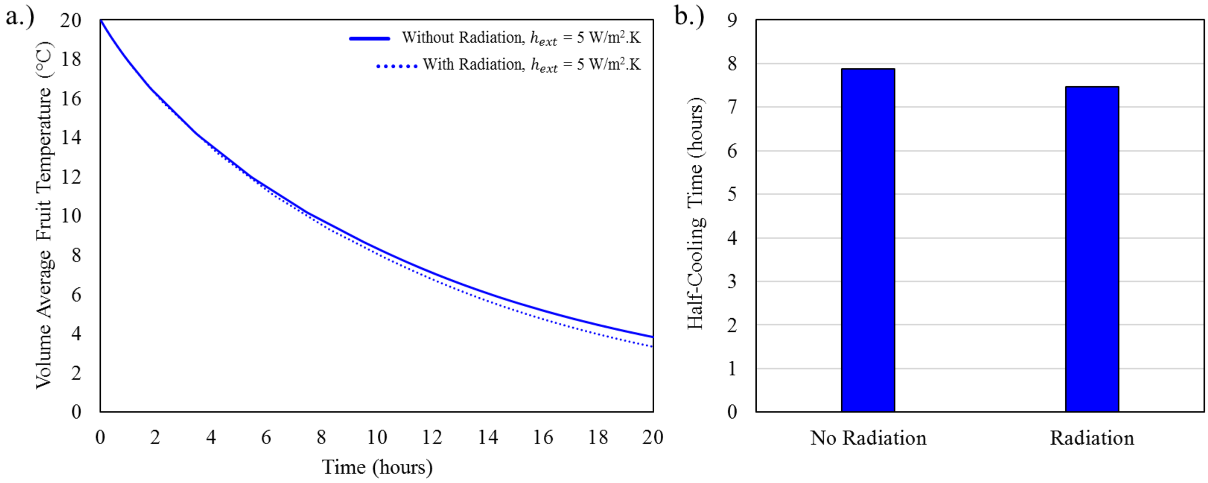

Figure 5.12: Comparative impact of thermal radiation on cooling rates; a.) volume average fruit temperature cooling curves, with (dotted line) and without (solid line) thermal radiation; b) impact on HCT with and without respiration.

Figure 5.12 shows radiation has a negligible impact on the predicted cooling curve. Slight differences began to manifest at ~6 h of cooling, resulting in a drop of 0.5°C at 20 h of cooling – a difference in HCT of only 0.4 h. Including radiation in the COMSOL model had a large negative impact on the computational efficiency – 25-minute solution times with radiation excluded, versus 12-hour solution times with radiation included. Though radiation did achieve some additional removal of heat from the centre of the package, what appears to happen is a minimisation of A or ΔT: in situations where the temperature gradient between fruit surfaces is high, such as fruit in the centre of the box and fruit at the edges, the area seen by both surfaces is low as there are a multitude of other fruit obstructing the field of view. In other cases, where there is a high surface area for radiative transfer, these are between adjacent fruits that have a small surface temperature difference. These phenomena combine to result in a near zero total rate of thermal radiative transfer. Excluded from this DNS model is the packaging, which could potentially provide another surface where a significant amount of radiative heat transfer could occur. However, this is unlikely, for the same reasons as before: fruit at the edges of the polyliner will see a large surface area to exchange thermal radiation, but the temperature of these fruit at the edges and the packaging will be approximately the same; while fruit in the centre of the package will be obstructed by other fruits, severely limiting the view factor of radiative exchange.

Radiation is therefore excluded from further sections. Seeing as it is recommended that radiation be ignored in non-polylined scenarios as well (Ferrua and Singh, 2009a; Defraeye *et al.*, 2014; Delele *et al.*, 2013), it is wise to ignore this phenomenon when modelling other fruits and alternative pre-cooling scenarios as well. Furthermore, it was recommended by Mercier *et al.* (2017a) that radiation does not occur significantly in room cooling scenarios, or between the surfaces of individual boxes on a pallet.

5.4: Thermophysical Properties

The thermophysical properties of note are density (ρ_Z, kg·m^{-3}), specific heat capacity (C_Z, J·kg^{-1}·K^{-1}) and thermal conductivity (λ_Z, W·m^{-1}·K^{-1}). To model a system correctly – and to validate a model against empirical data – accurate estimates of each must be measured or derived for each phase – fruit ($Z = S$), air ($Z = A$) and packaging ($Z = P$). Each of these phases are assumed to be isotropic. O'Sullivan (2016) derived the following properties for kiwifruit and fibreboard packaging based on literature sources.

The kiwifruit density was taken as ρ_S = 1037 kg·m^{-3} as the average of a range of measured values by Jordan *et al.* (2000) and Jordan and Seelye (2009) of 1025.5 – 1038.2 and 1031.3 – 1049.9 kg·m^{-3}, respectively. The thermal conductivity and specific heat capacity for kiwifruit was derived using a series of literature models based on the chemical composition of fruit – the proportion of dry matter and water content. Hayward kiwifruit is reported to have a dry matter content of 15.1 – 19% for an average of 17% (Wang *et al*., 2011), making the water content X_W = 83%. Based on empirical models from the literature, an average specific heat capacity of C_S = 3713 J·kg^{-1}·K^{-1} and thermal conductivity of λ_S = 0.542 W·m^{-1}·K^{-1} were derived (see table 6.2 in O'Sullivan, 2016). The thermal conductivity of fibreboard cardboard was measured in ASHRAE (2013) as λ_P = 0.065, the density measured by Tanner (1998) as ρ_P = 195 W·m^{-1}·K^{-1} and the specific heat capacity measured by Amos (1995) as C_P = 1700 J·kg^{-1}·K^{-1}. Air properties were taken as measured values at 20 ºC from ASHRAE (2013) as ρ_A = 1.205 kg·m^{-3}, C_A = 1005 J·kg^{-1}·K^{-1} and λ_A = 0.0257 W·m^{-1}·K^{-1}. In summary, Table 5.1:

Phase	Fruit			Packaging			Polyliner Air		
Symbol	λ_S	ρ_S	C_S	λ_P	ρ_P	C_P	λ_A	ρ_A	C_A
Value	0.542	1037	3713	0.065	195	1700	0.0257	1.205	1005
Unit	W·m^{-1}·K^{-1}	kg·m^{-3}	J·kg^{-1}·K^{-1}	W·m^{-1}·K^{-1}	kg·m^{-3}	J·kg^{-1}·K^{-1}	W·m^{-1}·K^{-1}	kg·m^{-3}	J·kg^{-1}·K^{-1}

Table 5.1: Summary of thermophysical properties used in modelling activity

5.5: Zonal Model Development

5.5.1: Introduction

Section 5.3, in addition to the plurality of published models in the literature (such as Ferrua and Singh, 2009a; Delele *et al.,* 2013; Defraeye *et al.,* 2014; Dehghannya *et al.,* 2011; and Berry *et al.,* 2017), demonstrates the power of DNS schemes to accurately and directly model heat and mass transfer mechanisms in high fidelity. However, the approach has significant drawbacks as discussed in section 5.2, finalising a geometry and meshing it correctly was prohibitively difficult, and simplifying compromises and manipulations often need to be made to the geometry. Solution times were also excessively high – ranging from half an hour, to over 12 hours using an Intel® i7-4770 and 16GB of RAM (section 5.3). These were clear violations of the philosophies outlined in chapter 2 of this thesis, so the use of an alternative modelling methodology was necessary to achieve our goals. Though the porous medium approach is a more simplified method (section 1.2.5.3), exclusive use of this methodology runs the risk of excluding any scenario where the package to product ratio is below 10; this includes the current scenario, where 100 count 36 kiwifruit in a modular bulk package has a ratio of approximately 6 (Verboven *et al*., 2006; Eisfeld and Schnitzlein, 2001), making this thesis' goal of developing a modelling methodology that can be applied universally, moot. With computational efficiency and flexibility being the key considerations for model development, it was concluded that the zonal modelling approach (Tanner *et al.,* 2002a) had the most potential in these regards (section 1.2.5.4). The potential for speed comes from the approach's division of the model geometry into a relatively small set of space averaged zones, rather than the many hundreds of thousands (or millions) of finite elements seen in CFD models (Frei, 2013). Solving the ODEs for heat and mass transfer within and between adjacent zones can be achieved on the order of seconds, rather than the hours or days typical of CFD models (see section 5.2; Defraeye *et al.,* 2014). This makes the model suitable for integration with an iterative optimization routine – such as a Monte-Carlo simulation (Martines-Hermosilla *et al*., 2016) or genetic algorithm (East *et al.,* 2009) – to identify the best package design or operational conditions in a reasonable time frame. Since there is still some level of volume discretization, the zonal approach is also capable of predicting not only the cooling rate, but also the heterogeneity of cooling by observing the distribution of temperatures throughout the zonal set. If a zonal based model can be developed that is able to be integrated with the previous work of chapter 4 – where the exact 3D geometry inside of a package was appropriated using a CT scanner (section 4.2); or a 3D geometry was generated via the random stacking model (sections 4.4) – the speed of model construction can be greatly accelerated; and if this geometry data is used to automatically determine the heat and mass transfer properties inside of each zone, then this represents a highly flexible approach that can be applied with minimal amendments to a wide range of alternative scenarios: different cooling operations, different horticultural produce, and different package sizes and shapes. The zonal approach also has the opportunity to succeed where the porous medium approach cannot, as the assumption of a local thermal equilibrium is not necessary – different phases, such as fruit and air within the same zone, can be modelled separately.

In this section, a new interpretation of the zonal approach is developed. This modernised take attempts to align the zonal modelling approach as closely as possible with the principles of flexibility, speed and automation with the development of new, novel and generalised techniques to automatically determine the heat and mass transfer properties of each zone as a function of the geometry – properties such as the volume of each phase, the heat transfer surface area between phases and the resistance to heat transfer in a given direction.

5.5.2: General Description of a Zonal System

Similar to DNS, the zonal approach relies on a form of volume discretization; however, rather than a complex meshing strategy where a given geometry is discretized into many thousands of small tetrahedral finite elements, the geometry is instead partitioned into a collection of much larger – and fewer in number – discrete volumes. These are called 'zones', the moniker of this modelling approach. An illustration of this process is given in Figure 5.13, where a geometry of fruit wrapped in a polyliner inside of a package (Figure 5.13a) is divided into a number of cuboid-shaped zones (Figure 5.13b):

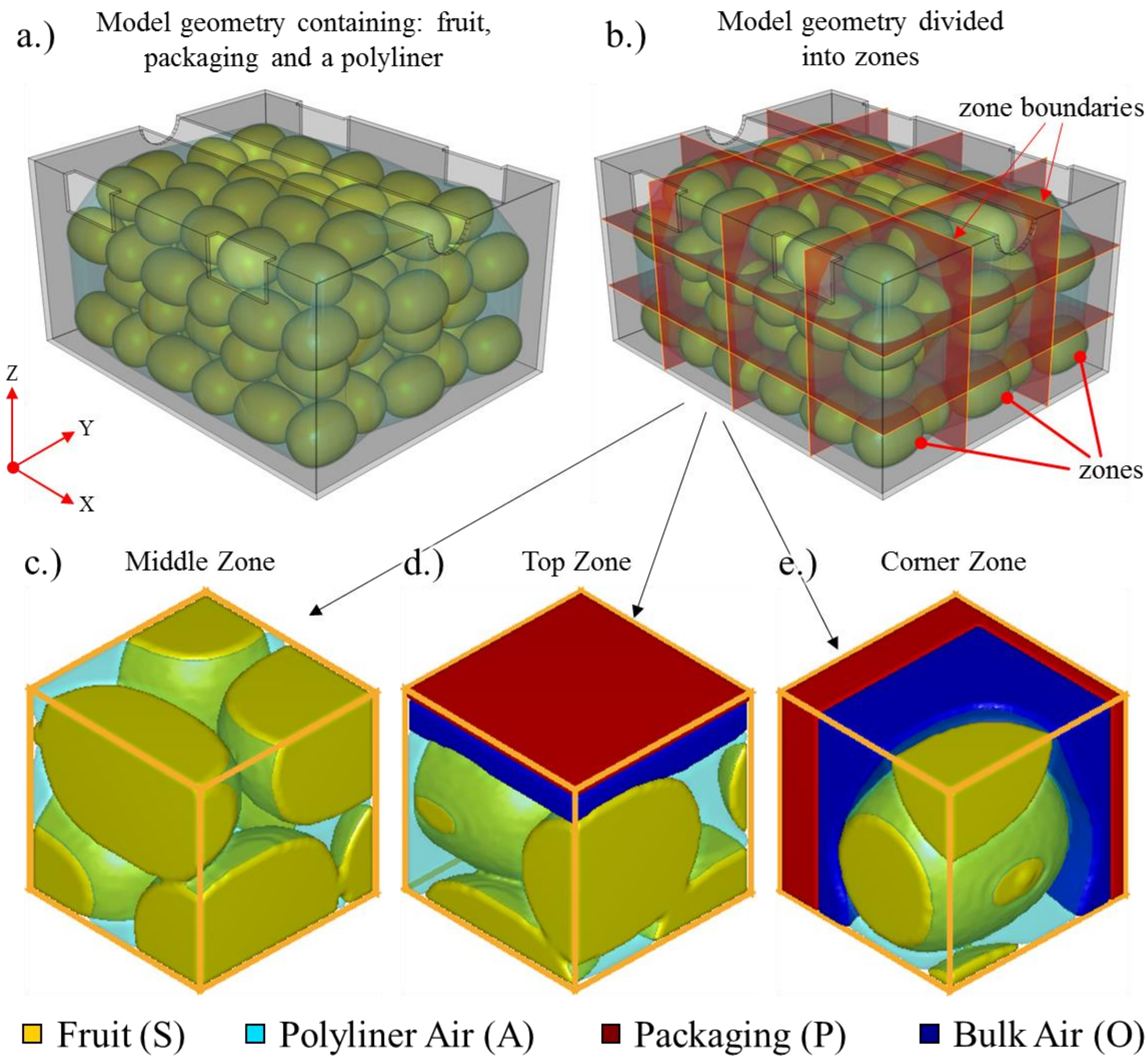

Figure 5.13: a.) an example model geometry: fruit and polyliner inside of a package; b.) the model geometry divided into a number of zones; c, d and e.) illustrations of the geometry within a variety of zones from different locations throughout the model geometry.

Tanner *et al.* (2002a) defines a zone as: "a physical space within a packaging geometry, which may or may not contain product, cooling fluid, packaging materials or other sources of heat and/or mass". Thus, a zone can contain any number of phases, and in any combination or proportion – this is illustrated in Figure 5.13c - e, where the interior of zones from different locations are presented, their multi-phasic nature portrayed. A phase is defined as any region with homogeneous, isotropic and thermophysical properties. Therefore, in context of the current scenario, there are three phases: fruit, air and packaging, as each has a distinct thermal conductivity, density and specific heat capacity. Due to the existence of the polyliner, there is a *de-facto* fourth phase: the air outside of the polyliner, through which refrigerated air flows due to the pressure drop created by the fan which is considered separate to the air inside the polyliner. A specific phase is denoted as Z, so that $Z = S$ corresponds with fruit (or solids), $Z = A$ with the air inside the polyliner, $Z = P$ with packaging and $Z = O$ with air outside the polyliner.

Temperature and moisture changes are predicted by networking adjacent phases and zones, and then numerically solving fluxes of heat and/or moisture over a series of small time intervals. This process utilises a lumped approach (van der Sman, 2003), with each phase inside of each zone being modelled as a separate volume averaged entity. For example, the zone illustrated in Figure 5.13c would contain 2 volume average temperatures modelled independently, one for air and one for fruit; while Figure 5.13d and e would contain 4 volume average temperatures, for fruit, air, packaging and bulk airflow. To better visualise a zonal network, Figure 5.14 shows zonal networks for heat transfer formed between two hypothetical zones: the zone under study, denoted as zone i; and an adjacent zone, denoted as zone j. A network of heat fluxes form within zone i between phases (Figure 5.14a), with heat flowing along each flux line via a specific mechanism, such as conduction, convection or thermal radiation (see section 5.3). These are denoted as 'intra-zonal exchanges', as heat is being transferred *inside* of a zone. The phases within zone i are connected to other phases in different but adjacent zones (Figure 5.14b). As these fluxes occur across the $i \rightarrow j$ zonal boundary, they are denoted as 'inter-zonal exchanges'. Equations must be formulated for each flux, the magnitude of a flux dependent on a number of factors such as the temperature difference, heat transfer surface area, size of the boundary between zones and resistance to heat transfer in a particular direction. The temperature change is dependent on the thermal properties and thermal mass of the phase inside of the zone. These properties are dependent on the geometry of each phase inside of the zone, and must be either estimated or appropriated somehow (more on this later in section 5.5.6). There is also an equivalent moisture transfer network analogous to Figure 5.14 in systems where it is significant (see section 5.3.5).

To solve a realistic problem, inter-zonal networks are formed along all zonal boundaries with all adjacent zones. Doing so directly and indirectly connects all parts of the model together, forming a global zonal network that is capable of predicting temperature and moisture changes at both global and local levels. Such a global network should be self-forming to achieve a flexible modelling methodology. In this sense, self-forming means that the network can be developed algorithmically from simple rules.

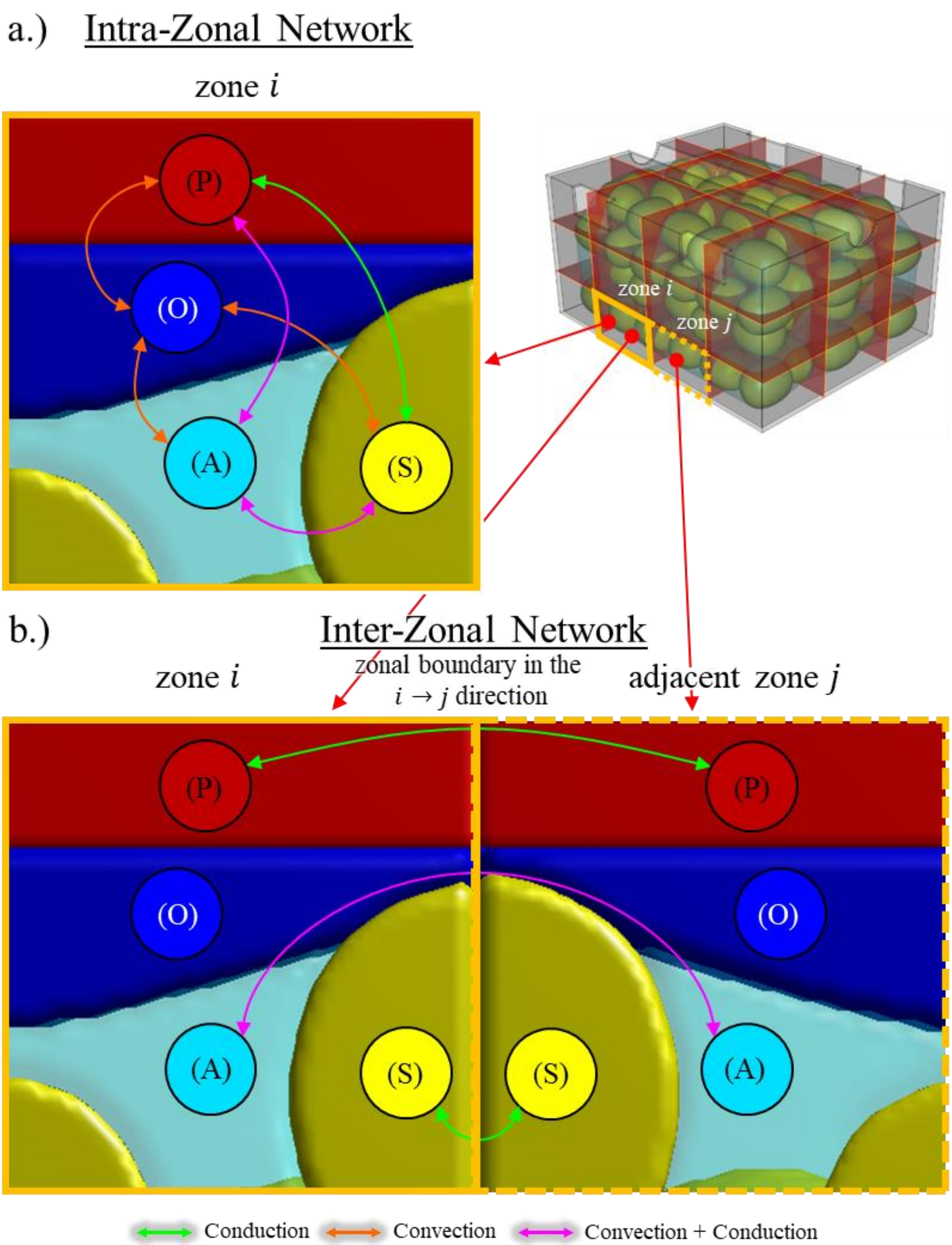

Figure 5.14: Intra- and Inter-Zonal heat transfer networks, connecting: a.) adjacent phases within zones (intra-zonal exchanges; Table 5.2), and b.) adjacent zones (inter-zonal exchanges; Table 5.3)

5.5.3: Formulation of Heat and Mass Transfer Equations

The governing equations for heat and mass transfer were formulated for the simplified two zone system of Figure 5.14, where the zone under study is denoted zone i and the adjacent zone as zone j, and individual phases are referred to as Z. This began with a heat balance, as articulated first in words in Eq. 5.17:

$$\begin{array}{c}\text{change in the} \\ \text{volume average} \\ \text{temperature of} \\ \text{phase } Z \text{ in zone } i\end{array} = \frac{\begin{array}{c}\text{all exchanges of} \\ \text{energy between} \\ \text{phase } Z \text{ and} \\ \text{other phases} \\ \text{inside of zone } i\end{array} + \begin{array}{c}\text{all exchanges of} \\ \text{energy between} \\ \text{phase } Z \text{ and} \\ \text{phases in} \\ \text{adjacent zones } j\end{array}}{\text{thermal mass of phase } Z \text{ within zone } i} \qquad (5.17)$$

The left side of Eq. 5.17 will form the ODE for temperature change that is to be numerically integrated, with the units of $°C{\cdot}s^{-1}$. The numerator of the right side of Eq. 5.17 is concerned with exchanges of heat. An exchange of heat is denoted as ϕ, and has the unit of watts, W or $J{\cdot}s^{-1}$. The first term in the numerator is concerned with exchanges of heat within a zone, an *intra*-zonal exchange. Intra-zonal heat fluxes are denoted as ϕ_{ii} – from zone i to zone i. The second term in the numerator implies exchanges of heat between adjacent zones: an *inter*-zonal exchange. An interzone heat flux is denoted ϕ_{ij} – from zone i to zone j. There are many different modes of energy exchange from a variety of transport mechanisms. Each mode should be considered individually, but all should contribute to the overall energy change within the fruit phase. For example, heat convecting from fruit to air could be denoted as $\phi_{ii,1}$, and separately heat radiating from the fruit to the packaging could be $\phi_{ii,2}$. There is a large number of potential mechanisms that can occur, so the subscript k is used to track separate mechanisms and heat transfer directions. Therefore, the numerator of Eq. 5.17 are denoted $\sum \phi_{ii,k}$ and $\sum \phi_{ij,k}$ to represent the sum of all considered modes of energy transfer, within and between zones. The denominator of Eq. 5.17

is concerned with the temperature impact of an energy change. The units of thermal mass is J·°C^{-1}, and is determined by the volume of phase Z inside zone i multiplied by the density and specific heat capacity of phase Z, thermal properties that are assumed to be isothermal and isotropic (section 5.4). Thus, Eq. 5.17 can be transcribed into a generalised ODE for heat transfer, Eq. 5.18:

$$\frac{d\bar{T}_{Z,i}}{dt} = \frac{\sum \phi_{ii,k} + \sum \phi_{ij,k}}{V_{Z,i} \cdot \rho_Z \cdot C_Z} \tag{5.18}$$

Where $\frac{d\bar{T}_{Z,i}}{dt}$ is the volume averaged temperature change of phase Z within zone i (°C·s^{-1}); $V_{Z,i}$ is the volume of phase Z inside of zone i (m^3), ρ_Z is the density of phase Z (kg·m^{-3}) and C_Z is the specific heat capacity of phase Z (J·kg^{-1}·°C^{-1}).

For the sake of completeness, the formulation for moisture transfers is given in appendix B, to provide readers with a framework for how to construct a zonal model where it is a significant mode of heat transfer (despite the conclusion of section 5.3.5).

Each mechanism of heat transfer for use in Eq. 5.18 is labelled and listed in Table 5.2 for intra-zonal exchanges, and Table 5.3 for inter-zonal exchanges. The subscript k labels each specific mechanism.

In the interests of keeping the approach generalised, it was desirable for as many modes of heat transfer to be described by the same form of equation as possible. Thus, all heat fluxes are described generally by Eq. 5.19:

$$\phi = h_{eff} \cdot A_{eff} \cdot \Delta\bar{T} \tag{5.19}$$

Where h_{eff} is the effective heat transfer coefficient (W·m^{-2}·°C^{-1}), A_{eff} is the effective heat transfer surface area (m^2), and $\Delta\bar{T}$ is the volume averaged temperature difference between the two phases. h_{eff} and A_{eff} are flexible parameters that represent the effective properties of specific phases, specific mechanisms and specific zones: for example, for $\phi_{ii,6}$ (see Table 5.2) that models conduction heat transfer between fruit and packaging, A_{eff} represents the contact area of fruit touching the packaging, while h_{eff} is related to the thickness of the packaging and the thermal conductivities of the two materials. Comparatively, $\phi_{ii,9}$ (see Table 5.2) represents radiation heat transfer between fruit and packaging, and in this case h_{eff} represents the net emissivity of each surface and A_{eff} is the area that both surfaces can see of each other, or the view factor (Holman, 2010). Furthermore, each zone has unique values of h_{eff} and A_{eff} for each transfer mechanism: taking $\phi_{ii,6}$ as an example again, the contact area between fruit and packaging may be large in one zone, or zero in others. Thus, for every mode listed in Table 5.2 and Table 5.3, an accompanying matrix of h_{eff} and A_{eff} values is required for each zone. This can be provided to the model externally, otherwise there must be methods to appropriate h_{eff} and A_{eff} for each zone and each mechanism (more on this later, see section 5.5.6).

Intra-Zone Exchanges:						
Heat Transfer	Mass Transfer	Transfer Mechanism	Phase 1	Phase 2	Sig.?	Ref.
$\phi_{ii,1}$	-	Heat transfer via conduction and convection from air (inside the polyliner) to the surface of fruit	S	A	✓	Section 5.3.1 and 5.3.2.2
$\phi_{ii,2}$	-	Air (outside the polyliner) convects heat away from the surface of the fruit	S	O	✓	Section 5.3.2.1 Section 5.3.2.1
$\phi_{ii,3}$	-	Heat transfer via conduction and convection from air (inside the polyliner) to the surface of packaging	A	P	✓	Section 5.3.1 and 5.3.2.2
$\phi_{ii,4}$	-	Air (outside the polyliner) convects heat away from the surface of the polyliner	A	O	✓	Section 5.3.2.1
$\phi_{ii,5}$	-	Air (outside the polyliner) convects heat away from the surface of the packaging.	P	O	✓	Section 5.3.2.1
$\phi_{ii,6}$	-	Heat conducts from fruit to packaging	S	P	✓	Section 5.3.1
$\phi_{ii,7}$	$\dot{m}_{ii,1}$	Moisture convectively evaporates or condenses from the fruit to the air	S	A	✗	Section 5.3.5
$\phi_{ii,8}$	$\dot{m}_{ii,2}$	Moisture convectively evaporates or condenses from the packaging to the air	P	A	✗	Section 5.3.5
$\phi_{ii,9}$	-	Radiation from fruit to packaging	S	P	✗	Section 5.3.6
-	$\dot{m}_{ii,3}$	Moisture absorbed by the packaging from the fruit by diffusion	P	S	✗	Section 5.3.5
$\phi_{ii,10}$	-	Respiration heat of fruit	S	S	✗	Section 5.3.4

Table 5.2: List of intra-zone heat and mass transport mechanisms that can occur within a zonal system. S = fruit phase, A = air inside the polyliner phase, P = packaging phase, O = bulk air (outside the polyliner) phase.

Inter-Zone Exchanges:						
Heat Transfer	Mass Transfer	Transfer Mechanism	Phase 1	Phase 2	Sig.?	Ref.
$\phi_{ij,1}$	$\dot{m}_{ij,1}$	Heat and moisture flow due to forced-convection of refrigerated air	O	O	✗	Section 5.3.2.1
$\phi_{ij,2}$	-	Heat conduction and free convection from air in one zone to air in another zone	A	A	✓	Section 5.3.1 and 5.3.2.2
$\phi_{ij,3}$	-	Heat conduction from fruit in one zone to fruit in another zone	S	S	✓	Section 5.3.1
$\phi_{ij,4}$	-	Heat conduction from packaging in one zone to packaging in another zone	P	P	✓	Section 5.3.1
-	$\dot{m}_{ij,2}$	Moisture transfer through diffusion from packaging in one zone to packaging in another zone	P	P	✗	Section 5.3.5
$\phi_{ij,5}$	-	Heat conduction from fruit in one zone to packaging in another zone	S	P	✗	Section 5.5.6.2.2
$\phi_{ij,6}$	-	Heat conduction from fruit in one zone to air in another zone	S	A	✗	Section 5.5.6.2.2
$\phi_{ij,7}$	-	Heat conduction from air in one zone to packaging in another zone	A	P	✗	Section 5.5.6.2.2
$\phi_{ij,8}$	$\dot{m}_{ij,3}$	Moisture convectively evaporates or condenses from fruit in one zone to air in another zone	S	A	✗	Section 5.3.5
$\phi_{ij,9}$	$\dot{m}_{ij,4}$	Moisture convectively evaporates or condenses from packaging in one zone to air in another zone	P	A	✗	Section 5.3.5
$\phi_{ij,10}$	-	Radiation heat transfer from fruit in one zone to fruit in another zone	S	S	✗	Section 5.3.6
$\phi_{ij,11}$	-	Radiation heat transfer from packaging in one zone to fruit in another zone	P	S	✗	Section 5.3.6
$\phi_{ij,12}$	-	Radiation heat transfer from packaging in one zone to packaging in another zone	P	P	✗	Section 5.3.6
-	$\dot{m}_{ij,5}$	Moisture transfer through diffusion and free convection in one zone to another zone	A	A	✗	Section 5.3.5
-	$\dot{m}_{ij,6}$	Moisture transfer through diffusion from fruit in one zone to fruit in another zone	S	S	✗	Section 5.3.5

Table 5.3: List of inter-zone heat and mass transport mechanisms that can occur within a zonal system. S = fruit phase, A = air inside the polyliner phase, P = packaging phase, O = bulk air (outside the polyliner) phase.

5.5.4: Voxelisation

The geometric procedures developed later in section 5.5.6 were originally designed for use with CT scan data, which – as described in section 4.2 – is voxelised volume data. It was desirable to maintain this data format to preserve the automation of the model builder, in addition there are further benefits for finalising the geometry of fruit and polyliner, which are discussed later in this section. Therefore, there was a need for a pre-processing step where a model geometry – created either manually, such as in the finite element model of section 5.2; or computationally generated via the random stacking model of section 4.4 – is converted from a surface mesh into a collection of voxels. This process is known as ‘voxelisation’.

Voxelisation discretizes geometric objects from their continuous geometric representation into a set of voxels that best approximates the continuous object (Kaufman *et al.*, 1993). The voxelisation process is illustrated for a simple 2D object in Figure 5.15:

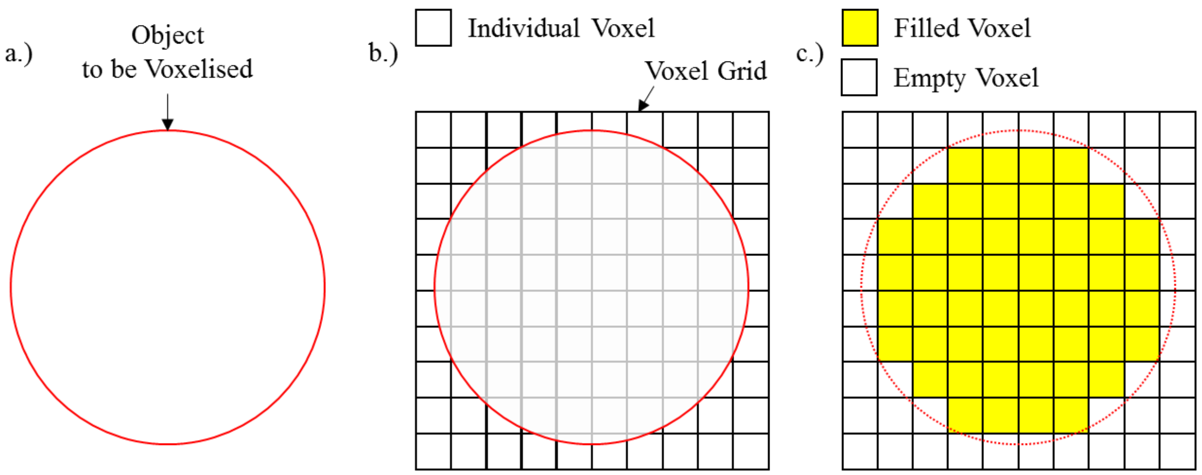

Figure 5.15: Voxelisation, a process through which a continuous geometric shape is converted into a voxelised grid. a.) the object to be voxelised (a circle); b.) a voxel grid laid over the top of the object; c.) the voxelised object with filled (voxels inside the object, yellow) and empty (voxels outside the object, white) voxels.

The object in this case is a circle (Figure 5.15a). A voxel grid is laid over the original object (Figure 5.15b), and an algorithm is used to identify filled (inside the object) and empty (outside the object) voxels (Figure 5.15c). The efficacy of the voxelisation process depends on the resolution of the voxel grid and the algorithm chosen to identify filled and empty voxels. A finer grid will approximate curves better, but at the expense of requiring many more voxels to complete the voxelisation process, potentially being more computationally costly; and the algorithm chosen to identify filled and empty voxels should be computationally efficient and agnostic to the shape of the object to be voxelised, as well as having defined rules pertaining to 'partially filled' voxels, voxels through which the object surface intersects.

A MATLAB program created by Aitkenhead (2013) called 'VOXELISER', originally written for use with medical imaging research, was used to accomplish voxelisation. This code used a ray intersection method similar to that described in Patil and Ravi (2005). It was very flexible in that any voxel size could be chosen so that changes to the voxel grid resolution can be easily incorporated into the modelling methodology. Use of Aitkenhead's (2013) 'VOXELISER' MATLAB function is presented in Figure 5.16 for a familiar 3D object:

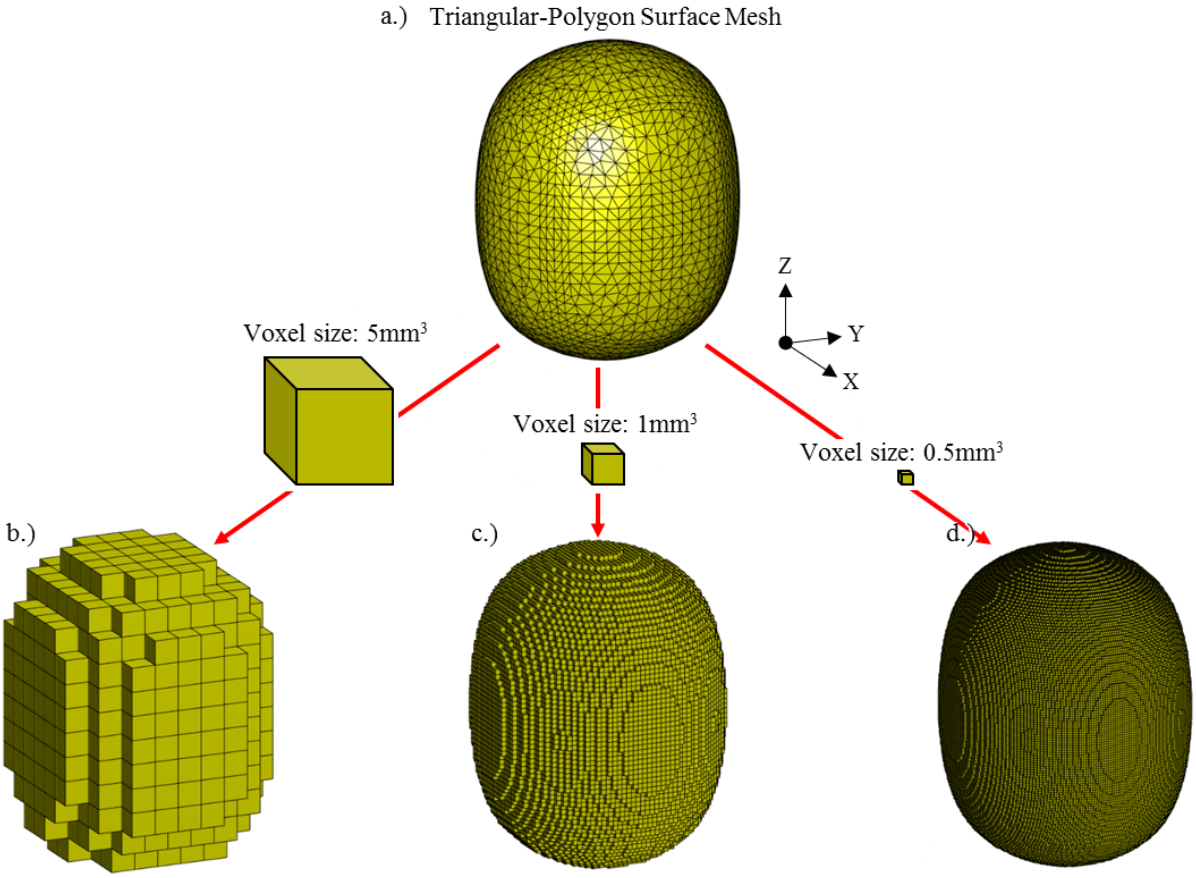

Figure 5.16: Use of Aitkenhead's (2013) voxeliser on an average sized count 36 Hayward kiwifruit, voxelised to a.) 5mm3; b.) 1mm3; and c.) 0.5mm3 resolutions.

Figure 5.16a is an ‘average’ sized count 36 Hayward kiwifruit, created as a triangular-polygon surface mesh using Eq. 4.16 (section 4.3.2.2). The voxeliser reads this information as a collection of vertexes, edges and faces (an .stl file), and then applies Patil and Ravi’s (2005) ray tracing method to voxelise according to a pre-specified voxel size. Figure 5.16b - d show the results of the voxelisation at 5, 1 and 0.5 mm voxel sizes. A low resolution voxel grid (Figure 5.16b) approximates the object poorly, where not only are the curves of the fruit unsatisfactorily estimated, but the predicted fruit volume was 2.2% lower than the original object. Increasing the voxel resolution to 1 mm (Figure 5.16c) improved the shape significantly and only suffered a 0.1% reduction in total volume; while improving voxel resolution even further to 0.5 mm (Figure 5.16d) reduced error to just 0.01%. The routine was fast, with voxelisation times of 0.15, 0.70 and 2.4 seconds for 5, 1 and 0.5 mm voxel sizes.

Expanding the voxeliser for use with a more relevant geometry – an entire stack of fruit wrapped in a polyliner – does not require any significant modification; the .stl file of a single fruit is merely replaced with a triangular polygonal surface mesh of a stack of fruit (either made manually, section 5.2.1; or generated from the random stacking model, section 4.4), and a polyliner, as shown in Figure 5.17. The fruit and polyliner geometries are voxelised separately using the same sized voxel grid (1 mm^3; Figure 5.17b - e) and then combined to form the finalised voxelised geometry (Figure 5.17f). This process was efficient, only 25 seconds for the fruit, and 15 seconds for the polyliner.

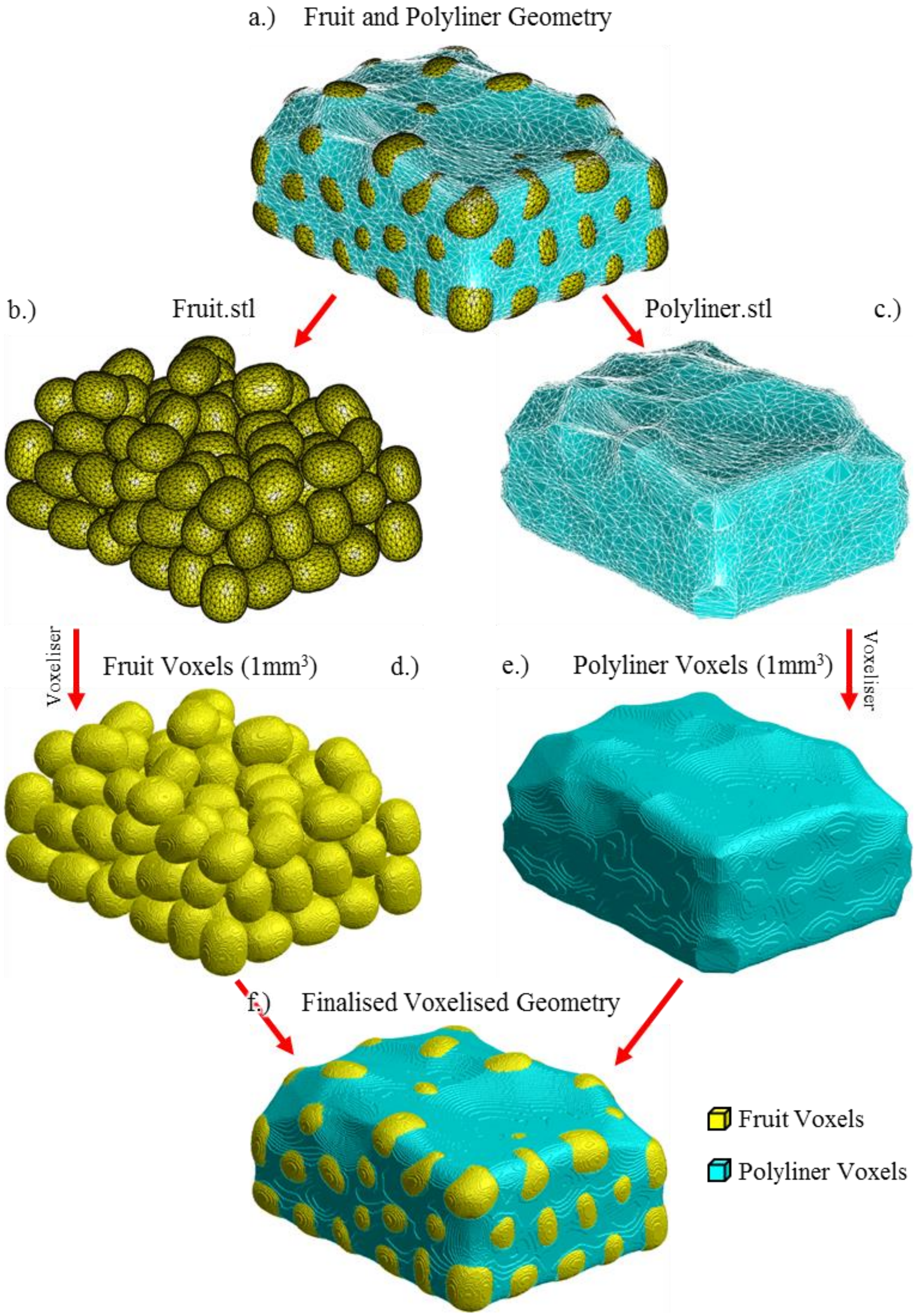

Figure 5.17: Use of Aitkenhead's (2013) voxeliser on a.) a random stack of kiwifruit. The surface meshes (.stl files) of b.) fruit and c.) the polyliner are voxelised separately with a 1mm3 voxel resolution. The voxelised d.) fruit and e.) polyliner are then combined into f.) the finalised voxelised geometry.

The final geometry (Figure 5.17f) is functionally identical to CT scan data, and so the techniques of section 5.5.6 can be applied verbatim. However, the geometric procedures were not the only reason for conducting voxelisation: an additional significant benefit was its ability to quickly and easily resolve the previously difficult fruit-polyliner intersections (section 5.2.1 and 5.3.3). If the fruit and polyliner are voxelised with the same voxel resolution, the two geometries can be joined through a basic combination of matrices. A close up of the joining process of Figure 5.17f is shown in Figure 5.18:

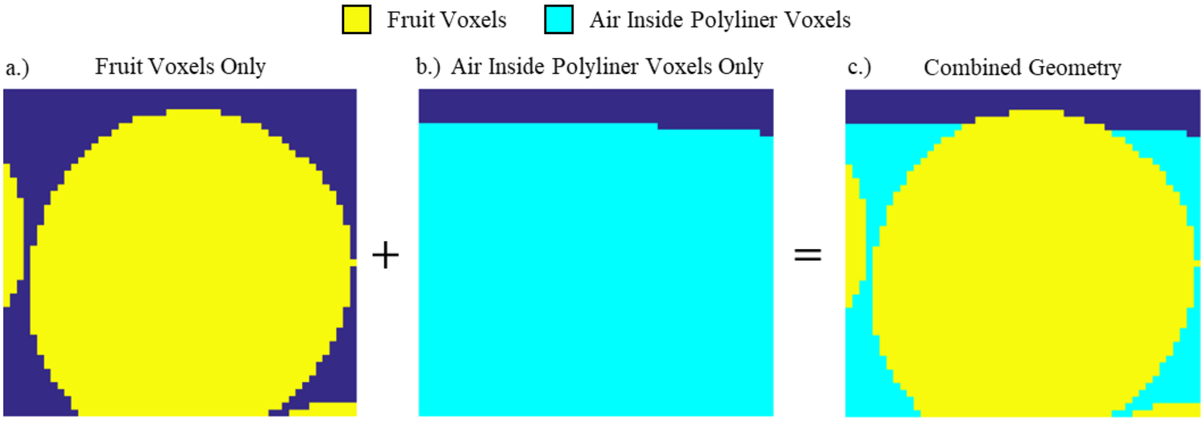

Figure 5.18: Voxel geometry finalisation process through a combination of matrices.

The voxel grid of fruit (Figure 5.18a) is superimposed onto the voxel grid of the polyliner (Figure 5.18b); any voxels of fruit replace voxels of polyliner air, resulting in an instantaneous joining and finalised geometry (Figure 5.18c), resolving the edge detection problems discussed previously using a DNS scheme (section 5.2.1). The determination of the important metric of surface area of fruit in direct contact with the bulk airflow (section 5.3.3) can therefore be determined quickly and easily with procedures described later in section 5.5.6.1.2.

As an aside, it is pertinent to comment on where voxelisation may be inappropriate. The scenario of note, a single box of kiwifruit wrapped in a polyliner, is a simple and fast process. This is in part due to the relatively small size of the global geometry, but also the relative size of the fruit inside of the box – voxelising to a 1mm^3 grid retains the overall shape of individual fruits, while producing a manageable 300×400×196 voxel grid size. A box of similar size filled with grapes (with produce diameter of 0.0201m, Delele *et al.*, 2012) would require a more detailed voxel resolution, perhaps 0.5 mm^3 or 0.25 mm^3 resolutions. This would increase the size of the voxel grids significantly, which may not be possible depending on the hardware that is available. A similar problem occurs when dealing with larger geometries, such as a full pallet or a bin of fruit. For these alternative scenarios, voxelising the entire geometry in one stage is likely not the correct strategy. Instead, it is recommended that voxelisation be done in parts: for a pallet, voxelisation and application of the geometric procedures (section 5.5.6) should be done *per box*, with the zones from separate packages joined in a later step; for a large geometry such as a bin, or a situation where the product size is small, it is recommended that the geometry is divided into zones before it is voxelised, and then each zone is voxelised just prior to its importation into the geometric procedures. The zones should then be re-joined after all zonal properties have been determined.

Though examples were shown where all voxels have the same width, height and depth, this is not mandatory. Skewness is common when using CT scan data, as the slice thickness is usually several times larger than pixel depth (see section 4.2).

5.5.5: Zoning Procedure

The nature through which the global geometry is divided into zones is the cornerstone of the zonal modelling approach. Development of a suitable zoning procedure must take into consideration the size and shape of zones, as well as the number of zones – a higher zonal resolution means a more detailed and potentially better predictive model. Additionally, the zoning procedure must correctly classify the zonal boundaries and zonal adjacency for the successful communication of heat and mass fluxes throughout the zonal network. For the model to retain flexibility, such a procedure must be coded in a way that a geometry can be divided into zones with minimal user input, and in an automated fashion.

A range of zoning strategies were considered and experimented with. It became clear that there was a trade-off between the simplicity of the zonal shape and the ease through which adjacency can be determined, and the simplicity of the intra-zonal boundary. For example, Tanner *et al.* (2002a) suggested a **cuboidal** approach, where rectangular cuboid shaped zones were placed around individual fruits and packaging layers. This approach creates zones that are easily defined, limiting each to just 8 corners and 6 faces. Determining adjacency is thus straightforward: the boundaries between zones are flat and regular, and the number of adjacent zones per zone is 6 or less – one for each face. Regrettably, applying such a simple zoning strategy to the current scenario of a randomly stacked modular bulk package cannot divide individual fruits into individual zones as fruits are not neatly separated by trays as in the case of Tanner *et al* (2002a), hence the geometry inside of individual zones is highly irregular, containing excised parts from multiple fruits in the same zone, or a small piece of the overall packaging material (illustrated in Figure 5.13c - e). Deriving zonal properties, such as volume or heat transfer resistance in a particular direction, from anfractuous shapes may be a significant challenge. An alternative that was explored was the **monophasic** strategy. This created a number of 'fruit-shaped' zones, the boundaries of each zone following the surface of individual fruits exactly, with an accompanying number of 'air-shaped' zones. While this solved the problem of a complex intra-zonal fruit geometry, it exacerbated other problems, namely the definition of the air zones and the determination of inter-zonal boundaries and zonal adjacency. Unlike fruits that have closed surfaces and can be identified individually, air is one interconnected sinuous object. Where and in what quantity air zones should be created were programming challenges that were not able to be resolved. Determining zone adjacency was also much more complex: the zonal boundaries were curved and consisted of many faces and vertices, and depending on how many air zones were created could result in a potential infinite number of adjacent zones in any number of directions. Potential for this zoning procedure to be automating was thus limited.

It was ultimately decided that the need for a simpler zonal shape, the ability to simply calculate inter-zonal boundaries and zonal adjacency trumped concerns for intra-zonal geometry orthodoxy. Techniques were developed for calculating zonal heat and mass transfer properties that were generalised in nature and could be applied to simple objects and highly irregular fruit or air geometries equally (see section 5.5.6.1.3). Thus, the automated zoning procedure that was developed was based on the **cuboid** zoning strategy. This strategy was harmonious with the voxelisation nature of the geometry data (section 5.5.4), as zonal divisions aligned exactly with a voxel grid.

The zoning procedure was programmed thusly: after importing the model geometry, it was divided into rectangular cuboid shaped zones through a series of planar cuts along each axis. Each planar cut intersected through the entire geometry along a given axis, the location of each cut contained in the vectors B_X, B_Y and B_Z. Three different zoning schemes are given as examples in Figure 5.19.

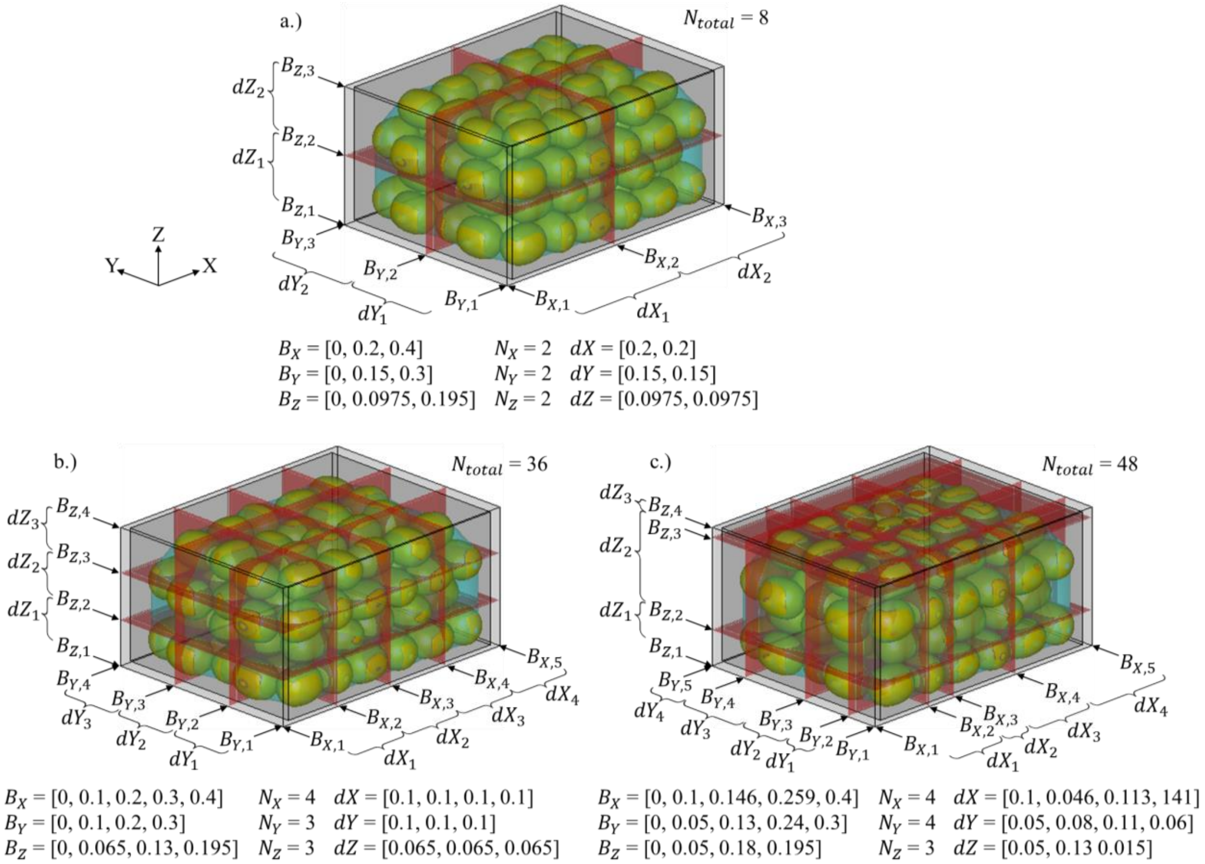

Figure 5.19: The cuboid zoning strategy, where the global geometry is divided into zones through a series of planar cuts. a.) a low resolution zoning strategy; b.) a higher resolution strategy; c.) a skewed zonal strategy, with zones of disparate size and shape.

The first and last planar cut in the X, Y and Z axes are the origin and end of the geometry in that given direction. Additional planar cuts are added to create a collection of zones. The number of zones created in each direction is given by N_X, N_Y and N_Z and is the size of vectors B_X, B_Y and B_Z minus one. The vectors dX, dY and dZ denote the length, width and height of the created zones. Figure 5.19a shows one cut in each the X, Y and Z direction – in addition to the origin and end cut planes – resulting in a geometry with 8 zones, the total number of zones being N_{total}. Figure 5.19b shows a higher resolution zonal grid, with three cuts in the X direction and two in the Y and Z directions. This results in 36 smaller zones and may produce a more detailed and accurate solution compared with Figure 5.19a. The zones of Figure 5.19a and Figure 5.19b are 'homogenous', being the same in size throughout the geometry. Homogeneity is *not* a requirement, and the zonal approach can function with heterogeneous zone sizes, such as in Figure 5.19c where the position of zonal divisions were chosen haphazardly. Heterogeneous schemes may be beneficial if there is heat transfer in a specific direction – for example, perhaps a larger number of zones in the Z axis would give a better solution in a situation where a box is being cooled using a plate freezer, with the cold plate pressed against the top and bottom of the box.

This zoning procedure therefore requires as an input: the model geometry (see section 4.2 or section 5.2.1) and the position of the planar cuts, B_X, B_Y and B_Z.

While individual zones have been referred to as 'zone i' and adjacent zones as 'zone j', these i and j variables must refer to specific zones so that fluxes throughout the zonal network can communicate correctly. This makes two additional matrices necessary: the Coordinate Matrix, C_{XYZ}, which gives each individual zone a unique numerical tag; and the Connectivity Matrix, C_{ij}, which records which zones are adjacent to each other and in what direction. The advantage of using a cuboid zoning procedure is that these matrices can be determined algorithmically, making this entire zoning process automated.

The Coordinate Matrix, C_{XYZ}, is a matrix $N_X \times N_Y \times N_Z$ in size that contains unique numerical values that correspond to each zone, integers from $1 \rightarrow N_{total}$. Given that zones are created in a grid formation, these values are assigned sequentially starting at the bottom-left-most zone, according to Eq. 5.20:

$$C_{XYZ} = \begin{bmatrix} \begin{bmatrix} 1 & \cdots & N_X \\ \vdots & \ddots & \vdots \\ N_X(N_Y - 1) + 1 & \cdots & N_X N_Y \end{bmatrix} \\ \vdots \\ \begin{bmatrix} N_X N_Y (N_Z - 1) + 1 & \cdots & N_X N_Y (N_Z - 1) + N_X \\ \vdots & \ddots & \vdots \\ N_X N_Y (N_Z - 1) + \left(N_X (N_Y - 1)\right) + 1 & \cdots & N_{total} \end{bmatrix} \end{bmatrix} \tag{5.20}$$

A single zone is taken from the centre of the system in Figure 5.20 so that the nature of adjacency in the zonal network can be examined. As the zonal shape has been restricted to cuboids, the 6 faces that form the polyhedron also form the zonal boundaries. Thus, when expressing zones j as those adjacent to zone i, there is a maximum of 6 adjacent zones: 6 if zone i is surrounded by other zones (a zone from the centre of the zonal network) or fewer than 6 is zone i is on the corner or edge of the geometry. j can be used to denote the direction in which an inter-zone exchange is occurring: in the X direction, left, $j = \leftarrow$ or right, $j = \rightarrow$; in the Z direction, up, $j = \uparrow$ or down, $j = \downarrow$; and in the Y direction, forward (or into the page), $j = \otimes$ or backward (or out of the page), $j = \odot$. The Connectivity Matrix is therefore a matrix $6 \times N_{total}$ in size and records which zones – numerical tags derived from the Coordinate Matrix, C_{XYZ} – are adjacent to each zone and in which direction; or Eq. 5.21.

$$C_{ij} = \begin{bmatrix} Zone\ 1: & \leftarrow_1 & \rightarrow_1 & \otimes_1 & \odot_1 & \uparrow_1 & \downarrow_1 \\ \vdots & \vdots & \vdots & \vdots & \vdots & \vdots & \vdots \\ Zone\ N_{total}: & \leftarrow_{N_{total}} & \rightarrow_{N_{total}} & \otimes_{N_{total}} & \odot_{N_{total}} & \uparrow_{N_{total}} & \downarrow_{N_{total}} \end{bmatrix} \quad (5.21)$$

Zones that do not have an adjacent zone in a given direction have a 0 in the C_{ij} matrix, meaning the zonal boundary in that direction is insulated. C_{ij} can also be manipulated to create a periodic boundary condition: for example, if it were desired to model boxes stacked on top of each other, rather than model many boxes at once with a great deal of zones for each box, the model could instead be simplified to a single box where heat conducts from the bottom of the box to the top of the same box. Such a condition can be incorporated into C_{ij} by replacing the 0s in the ↓ direction for the bottom layer of zones with the numerical tag for zones on the top layer, and similarly for the ↑ direction for the top layer of zones.

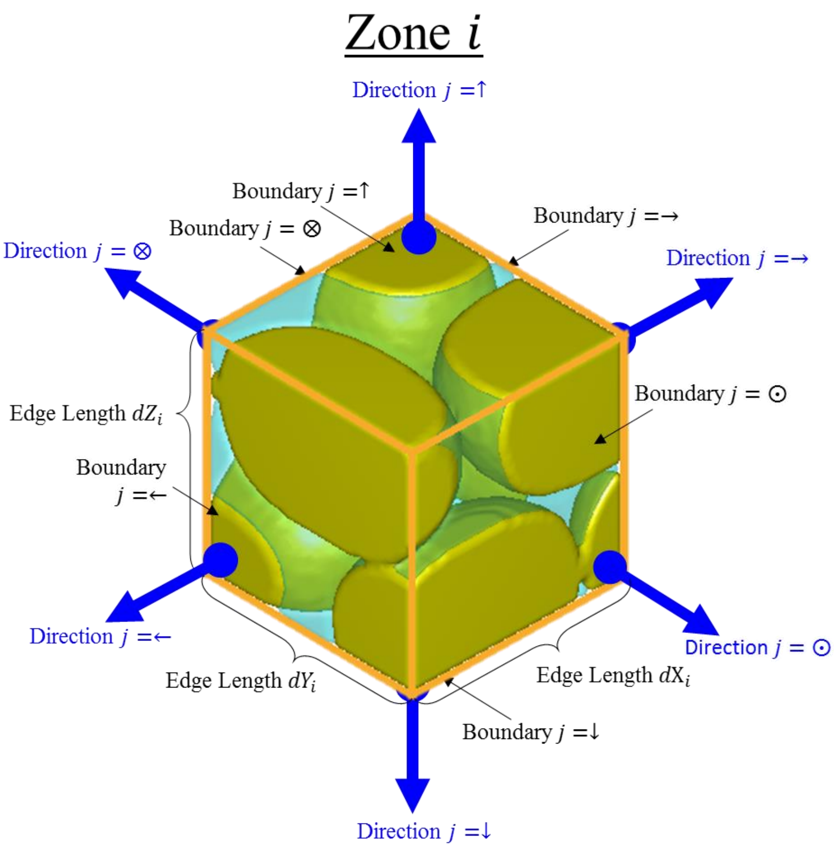

Figure 5.20: Single cuboid-shaped zone taken from the centre of a zonal network to investigate the zonal adjacency.

5.5.6: Zone Builder

The zonal approach has potential to have fast solution times compared to DNS schemes due to the small number of ODEs, but such gains in speed are futile if solutions are not accurate enough. The accuracy of the approach is thus contingent on the zonal properties, and that these are an authentic representation of the real system. The approach is also impractical if the required set of zonal properties must be calculated in an arduous or manual fashion. This new interpretation of a zonal model can only achieve the goals of flexibility and automation if all of the zonal properties can be computed automatically and provided to the user. If a model can be coded in such a way and executed in a relatively short period of time, then this represents a universal approach that can be applied to a wide range of scenarios.

The desired process is presented in Figure 5.21. Figure 5.21a shows the voxelised finalised geometry, a collection of 3D volumes that represent fruit, packaging and air inside and outside of the polyliner, that have been divided into zones according to the user's desired zonal resolution. One by one, zones are removed from the rest of the zonal set and fed through a series of computational routines named 'geometric procedures'. These examine the voxelised geometry of each phase inside of the zone and uses them to estimate zonal properties such as the volume, heat transfer surface area, heat and mass transfer resistances, for each transfer mechanism that the user has decided is relevant.

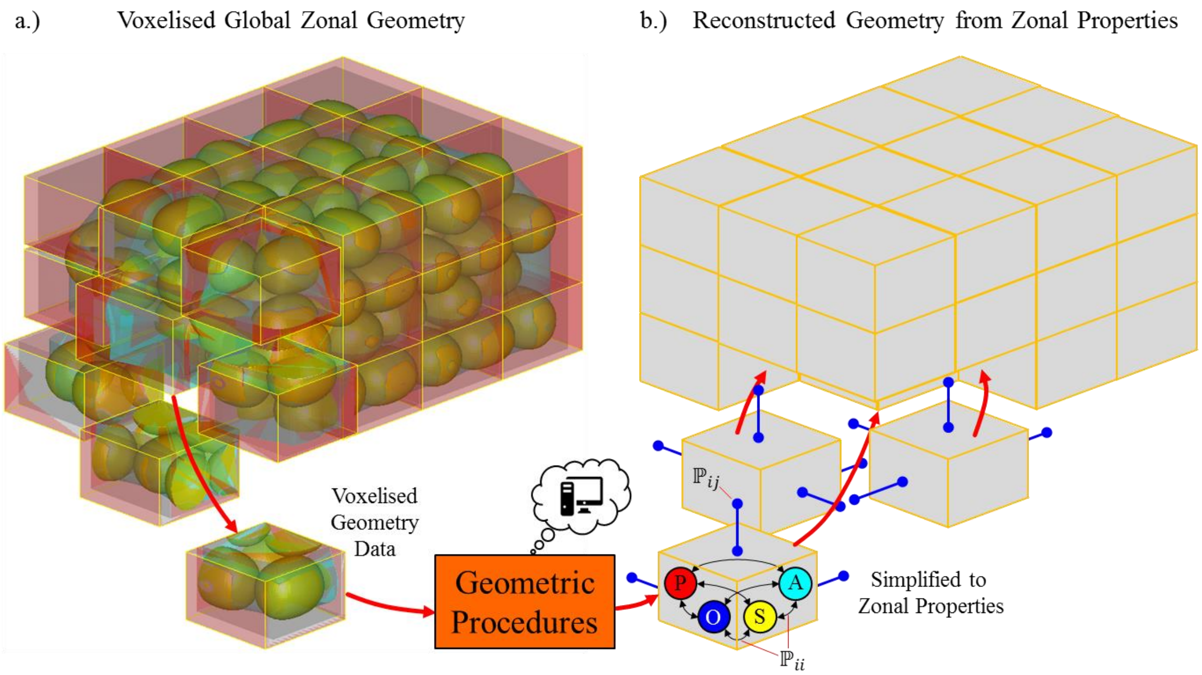

Figure 5.21: Concept of the Zone Builder and the Geometric Procedures: a.) the voxelised fruit, polyliner and packaging geometry is divided into zones, and imported one by one into the Geometric Procedures; b.) a series of computational operations automatically convert the geometrical information into a small set of intra- and inter-zonal properties, $\mathbb{P}_{\mathrm{ii}}$ and $\mathbb{P}_{\mathrm{ij}}$, completing the zonal network.

The zone is then released from the 'geometric procedure' routines, no longer a complex collection of voxels but instead a small set of lumped zonal properties – these are denoted in general terms as $\mathbb{P}_{ii}$ for intra-zonal properties, and $\mathbb{P}_{ij}$ for inter-zonal properties, nested matrices that contain all of the information necessary to predict temperature and moisture changes throughout the zonal network. Examining intra-zonal properties first, $\mathbb{P}_{ii}$ is given as:

$$\mathbb{P}_{ii} = \begin{bmatrix} V_{Z,i} \\ A_{eff\,m,Z_\alpha \to Z_\beta,i} \\ h_{eff\,n,Z_\alpha \to Z_\beta,i} \\ D_{eff\,o,Z_\alpha \to Z_\beta,i} \end{bmatrix} \tag{5.22}$$

$\mathbb{P}_{ii}$ is a data structure of different zonal attributes, where $V_{Z,i}$ is the volume of each phase inside of each zone; A_{eff} is the effective heat transfer surface areas for different mechanisms of transport between different phases inside of each zone; h_{eff} is the effective heat transfer coefficient for different mechanisms between different phases inside of each zone. While moisture transfers aren't modelled explicitly in this thesis, D_{eff} is included for the sake of completion, and is the effective mass transfer coefficient, or permeability. The subscripts are interpreted thusly: i denotes a specific zone in the zonal network ($i = [1,2,\cdots,N_{total}-1,N_{total}]$), controlled by the coordinate matrix, C_{XYZ} (Eq. 5.20). Z is specific phases, for which there are 4 (defined previously in section 5.5.2; $Z = [S,A,P,O]$). m, n and o denote transport mechanisms identified in Table 5.2 ($m = [cond,diff,rad]$ for conduction, diffusion and radiation; and similarly, $n = [cond,conv,rad,ext]$ for conduction, natural convection, radiation and forced convection; and $o = [conv,ext,diff]$ for natural convection, forced convection and diffusion). Akin to how Z refers to a phase, $Z_\alpha \rightarrow Z_\beta$ refers to a phase-pair where an exchange of heat or moisture takes place; for example, in the case of A_{eff}, fruit may be touching the packaging, so $Z_\alpha \rightarrow Z_\beta = S \rightarrow P$.

The inter-zonal properties are stored in a similar vector:

$$\mathbb{P}_{ij} = \begin{bmatrix} A_{eff}{}_{m,Z_\alpha\rightarrow Z_\beta,ij} \\ h_{eff}{}_{n,Z_\alpha\rightarrow Z_\beta,ij} \\ D_{eff}{}_{o,Z_\alpha\rightarrow Z_\beta,ij} \\ \dot{Q}_{ij} \end{bmatrix} \tag{5.23}$$

Where A_{eff}, h_{eff} and D_{eff} are for between adjacent zones. The zone under study is denoted as zone i and any adjacent zones as j, the adjacency defined by the Connectivity Matrix, C_{ij} (Eq. 5.21). While $Z_\alpha \rightarrow Z_\beta$ is included so there is potential for exchanges such as $\phi_{ij,5}$ to be modelled (see Table 5.3), this interpretation of the zonal approach is structured in a way where exchanges are exclusively from one phase to the same phase in an adjacent zone: $Z_\alpha \rightarrow Z_\beta = [S \rightarrow S, A \rightarrow A, P \rightarrow P]$. Finally, $\dot{Q}_{ij}$ is included, which is the flowrate of refrigerated air through the zonal network. This is included in the model formation process to account for the airflow model which is to be developed separately to this heat transfer model, but is not developed in this thesis as it is being worked on separately (section 5.5.6.2.4).

The goal of the geometric procedures are to calculate each of these attributes and populate the vectors $\mathbb{P}_{ii}$ and $\mathbb{P}_{ij}$ as a function of the geometry inside of each zone. Such a system satisfies the flexibility goal of this thesis, as the input geometry (Figure 5.21a) can be easily replaced with an alternative geometry and – given that the geometric procedures are properly formulated to be automated and computationally efficient – the model will re-formulate itself accordingly. Such a process would allow a cooling model to be constructed automatically, expeditiously and universally.

The following geometric procedures were bundled into a MATLAB program named the 'zone builder'.

5.5.6.1: Geometric Procedures for Intra-Zonal Properties

5.5.6.1.1: Volume

The volume of phases is vital to the successful prediction of temperature change, as it is proportional to the thermal mass. Defined previously in section 4.2.3, the voxels inside of a zone are denoted as $\mathbb{v}_n = x$, where n refers to a specific voxel and its position, and x refers to the value of the voxel. The voxel has a width, depth and height, which is denoted as dx, dy and dz. At this stage the voxel information should have been discretised – if the geometry information has come from a CT scan then through Otsu's method (Otsu, 1979, section 4.2.3); or from the voxeliser (Aitkenhead, 2013; section 5.5.4). These discretized values of voxels allow phases to be easily separated by assigning integers to specific phases. In this case the following conventions were implemented: while $\mathbb{v}_n = x$ refers to a generic voxel, $\mathbb{v}_i = Z$ represents a voxel inside of zone i, of phase Z. Considering that all voxels are the same size, the volume of a specific phase can be calculated by summing all voxels with the same Z and multiplying the resulting count by the volume of a single voxel, or $(dx \cdot dy \cdot dz)$:

$$V_{Z,i} = \left(\sum [\mathbb{v}_i = Z]\right) \times (dx \cdot dy \cdot dz) \tag{5.24}$$

This is visualised in Figure 5.22:

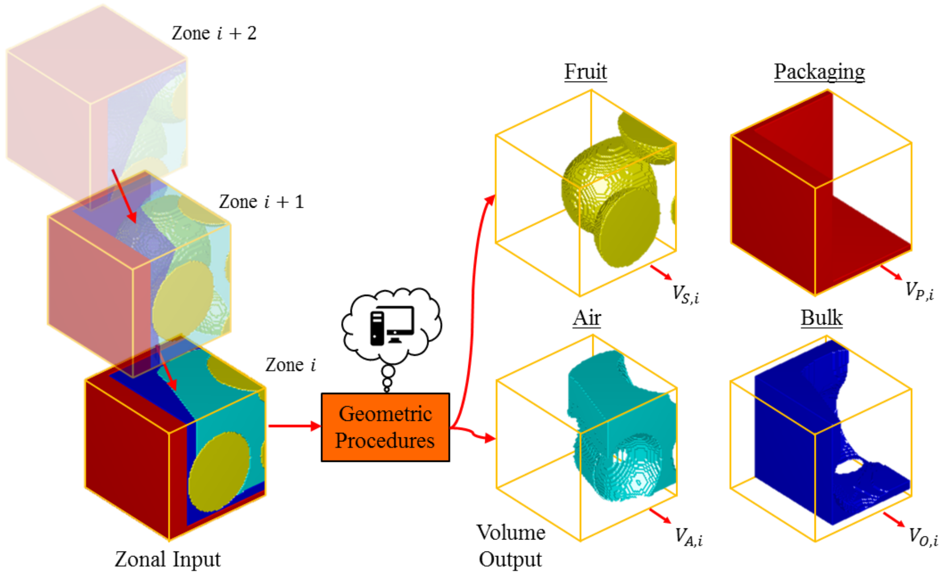

Figure 5.22: Geometric Procedure for appropriating volume from each phase inside a zone, by summing voxels from each phase.

5.5.6.1.2: Heat Transfer Surface Area

A collection of voxels can be processed into a surface mesh with the MATLAB function 'isosurface', resulting in a collection of vertices, edges and triangular faces that conform to the overall shape of the voxels from which it was formed (Figure 5.23):

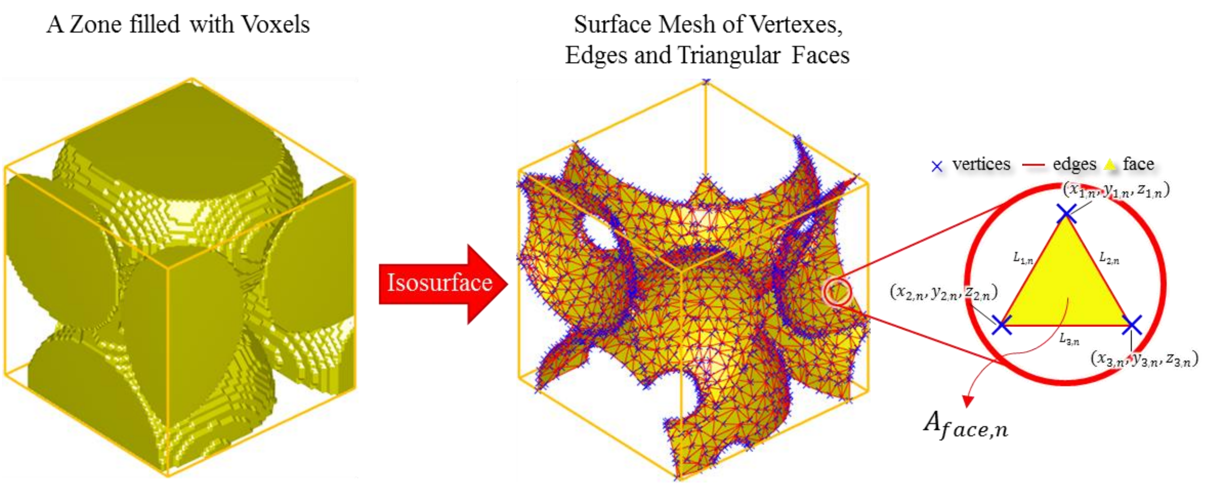

Figure 5.23: Voxels in a zone converted into a surface with 'isosurface' MATLAB function – the total surface area being the sum of the areas of each individual triangular face.

The surface area of a collection of voxels can be derived from the surface mesh by computing the area of each individual triangular face, and then taking the sum. The co-ordinates of the 3 vertexes that make up each face are known, as they are outputs of the 'isosurface' function. These co-ordinates were used to calculate the length of each of the three edges that make up the face:

$$L_{1,n} = \sqrt{\left(x_{1,n} - x_{2,n}\right)^2 + \left(y_{1,n} - y_{2,n}\right)^2 + \left(z_{1,n} - z_{2,n}\right)^2} \tag{5.25}$$

$$L_{2,n} = \sqrt{\left(x_{2,n} - x_{3,n}\right)^2 + \left(y_{2,n} - y_{3,n}\right)^2 + \left(z_{2,n} - z_{3,n}\right)^2} \tag{5.26}$$

$$L_{3,n} = \sqrt{\left(x_{1,n} - x_{3,n}\right)^2 + \left(y_{1,n} - y_{3,n}\right)^2 + \left(z_{1,n} - z_{3,n}\right)^2} \tag{5.27}$$

Heron's formula (Weisstein, 2003) was then used to compute the area of the individual face:

$$A_{face,n} = \frac{1}{4}\sqrt{\begin{matrix}\left(L_{1,n} + L_{2,n} + L_{3,n}\right) \times \left(-L_{1,n} + L_{2,n} + L_{3,n}\right) \times \\ \left(L_{1,n} - L_{2,n} + L_{3,n}\right) \times \left(L_{1,n} + L_{2,n} - L_{3,n}\right)\end{matrix}} \tag{5.28}$$

Where n in this case denotes individual faces in the triangular surface mesh. Repeating this process for each face, the total surface area in zone i is the sum of the areas for all individual faces:

$$A_{eff_{m,Z_\alpha \to Z_\beta,i}} = \sum_{n=1}^{N} A_{face,n} \tag{5.29}$$

This process applies to heat transfer mechanisms that occur through direct contact, namely conduction ($m = cond$ in Eq. 5.22). Mass transfer also occurs through physical contact, so it applies to diffusion/evaporation as well ($m = diff$ in Eq. 5.22). While the example in Figure 5.23 shows a zone with only 2 phases (air and fruit), the method had to be amended when considering a zone with 3 or 4 phases. For example, when computing the surface of the fruit phase, part of the total surface may be in contact with the polyliner air, another part in contact with the packaging, and yet another part with the bulk airflow. Determining the contact area between a specific phase-pair was accomplished through a nominal addition to the 'isosurface' function: while the voxels in the first phase were converted into a surface mesh verbatim, the second phase it is in contact with was used to determine the colour of individual faces. Faces in contact with the second phase are thus considered one colour (in this case, yellow) and faces not in contact are considered another (dark blue). When applying Eq. 5.29, only the 'yellow' faces were included in the surface area calculation, while the others were ignored. This is shown in Figure 5.24, where the primary phase is shown as the solid object, the secondary phase as see-through, and the included and excluded sections of the surface mesh indicated via colour.

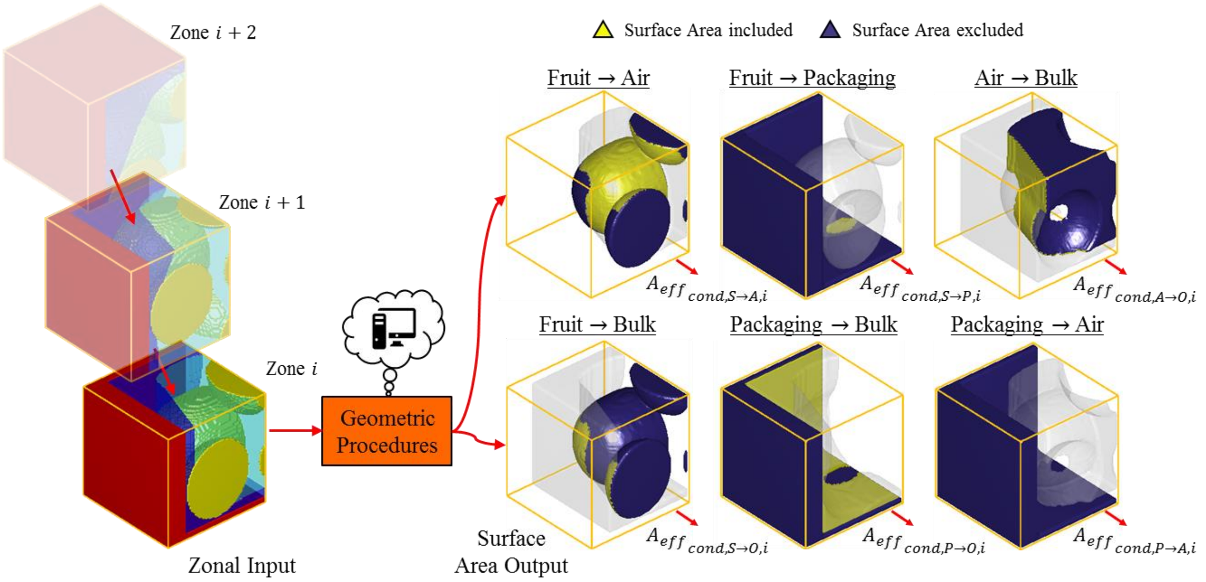

Figure 5.24: Geometric Procedure for appropriating the heat and mass transfer surface area between each of the 6 phase-pairs.

The final mechanism for which A_{eff} is important is radiation ($m = rad$ in Eq. 5.22). Section 5.3.6 and Table 5.2 concluded it is not an important mechanism, so automated methods for appropriating the radiative view factor were not developed and weren't included in the zone builder MATLAB script. However, should others intend to include radiation in a zonal mode, brief suggestions are made in appendix B.

5.5.6.1.3: Conduction: Average Voxel Distance Calculator

Conduction heat transfer is modelled in the zonal approach as a lumped effective heat transfer coefficient $h_{eff,Z_\alpha \to Z_\beta,i}$. Implied from the subscript $Z_\alpha \to Z_\beta$, heat transfer occurs via this mechanism between specific phase-pairs inside of each zone. There being 4 phases, there are 6 separate phase-pairs through which conduction heat transfer could occur. Pure conduction does not occur in all phases, however, as pure conduction only occurs in solids. For example, for $S \to P$, there is pure conduction in both phases; but for $S \to A$, there is conduction in the fruit phase and a combination of conduction and natural convection in the air phase; and for $S \rightarrow O$ there is conduction in the fruit phase and pure convection in the bulk air phase. This section deals primarily with pure conduction and is described mostly in terms of conduction through the fruit, but lays the groundwork for accounting for these additional mechanisms.

The technique developed to determine the lumped heat transfer coefficients within a zone was based on van der Sman (2003). van der Sman (drawing on previous literature) formalised a method for deriving an electrical network analogue-based, lumped, simplified cooling model for regularly shaped foods:

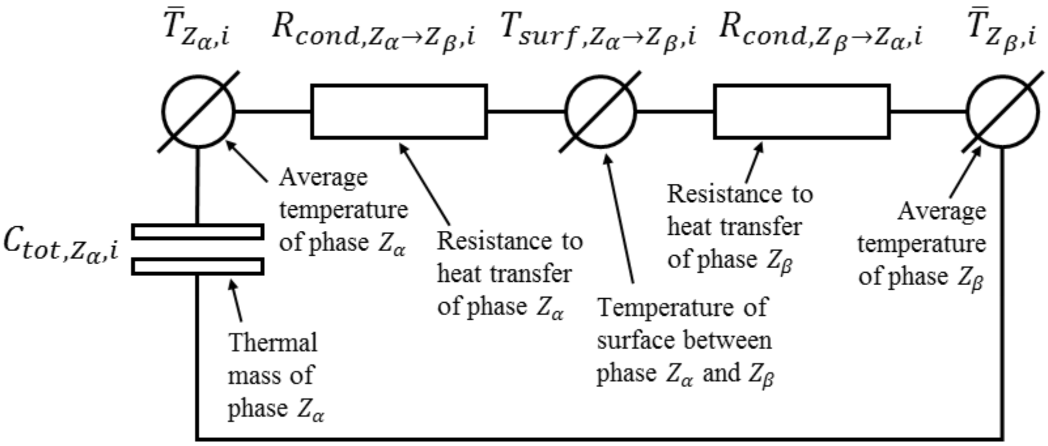

Figure 5.25: Electrical analogue for conduction heat transfer between a specific phase-pair using lumped properties. Image derived from van der Sman (2003).

Figure 5.25 summarises an exchange of heat between two phases inside of zone i, phase Z_α, and phase Z_β. Thus, $\bar{T}_{Z_\alpha,i}$ is the volume average temperature of the primary phase under study, $\bar{T}_{Z_\beta,i}$ is the volume average temperature of the secondary phase it is transferring heat to or from, and $T_{surf,Z_\alpha \rightarrow Z_\beta,i}$ is the temperature of the surface between the two phases. $C_{tot,Z_\alpha,i} = \rho_{Z_\alpha} \cdot C_{Z_\alpha} \cdot V_{Z_\alpha,i}$, or is the thermal mass of phase Z_α inside of zone i. $R_{cond,Z_\alpha \rightarrow Z_\beta,i}$, is the internal resistance to conduction heat transfer to heat transfer of phase Z_α; and $R_{cond,Z_\beta \rightarrow Z_\alpha,i}$, the internal conductive resistance to heat transfer of phase Z_β, both with the units $m^2 \cdot K \cdot W^{-1}$. van der Sman stated that the heat flux away from the surface of phase Z_α is Eq. 5.30:

$$\phi_{ii,k} = h_{eff_{cond,Z_\alpha \rightarrow surf,i}} \cdot A_{eff_{Z_\alpha \rightarrow Z_\beta,i}} \left(\bar{T}_{Z_\alpha,i} - T_{surf,Z_\alpha \rightarrow Z_\beta,i}\right) \quad (5.30)$$

And similarly, the heat flux *from* the surface to phase Z_β is Eq. 5.31:

$$\phi_{ii,k} = h_{eff_{cond,surf \to Z_\beta,i}} \cdot A_{eff_{Z_\alpha \to Z_\beta,i}} (T_{surf,Z_\alpha \to Z_\beta,i} - \bar{T}_{Z_\beta,i}) \tag{5.31}$$

Where $A_{eff_{Z_\alpha \to Z_\beta,i}}$ is the surface area of the contact formed between the two phases being investigated (see section 5.5.6.1.2); and $h_{eff_{cond,Z_\alpha \to surf,i}}$ and $h_{eff_{cond,surf \to Z_\beta,i}}$ are the lumped effective heat transfer coefficients for heat exchanged between phase Z_α and Z_β through conduction. The effective heat transfer coefficients are inversely proportional to the internal resistances of Figure 5.25:

$$h_{eff_{cond,Z_\alpha \to surf,i}} = \frac{1}{R_{cond,Z_\alpha \to Z_\beta,i}} \tag{5.32}$$

$$h_{eff_{cond,surf \to Z_\beta,i}} = \frac{1}{R_{cond,Z_\beta \to Z_\alpha,i}} \tag{5.33}$$

van der Sman through a series of finite element investigations of various objects found that the temperature gradients formed within an object due to conduction were sufficiently linearly correlated to the distance from the surface which was being convectively cooled. The consequence of this was the simplification of the internal resistance to:

$$R_{cond,Z_\alpha \to Z_\beta,i} = \frac{d_{Z_\alpha \to Z_\beta,i}}{\lambda_{Z_\alpha}} \tag{5.34}$$

$$R_{cond,Z_\beta \to Z_\alpha,i} = \frac{d_{Z_\beta \to Z_\alpha,i}}{\lambda_{Z_\beta}} \tag{5.35}$$

Where $d_{Z_\alpha \to Z_\beta,i}$ and $d_{Z_\beta \to Z_\alpha,i}$ were named ‘characteristic distances’ by van der Sman, and in context with this discussion of agnostically shaped phases, represent the characteristic distances of phase Z_α and Z_β respectively, in the direction of the surface formed between the two phases, with the units of meters (m). λ_{Z_α} and λ_{Z_β} are therefore the thermal conductivities of phase Z_α and Z_β, respectively ($W \cdot m^{-1} \cdot K^{-1}$). van der Sman denoted a characteristic distance as d_c and found that they were constants for a number of simple shapes, namely $d_c = L/4$ for a flat plate with thickness L and is cooled on both sides, $d_c = r/3$ for a cylinder with radius r, and $d_c = r/4$ for a sphere with radius r being convectively cooled on the surface.

Attempts to apply these principles to a zonal geometry is problematic as the surface temperature between phases is not considered in the model, only the average temperatures of phases, $\bar{T}_{Z_\alpha,i}$ and $\bar{T}_{Z_\beta,i}$. Seeing as Eq. 5.30 is equal to Eq. 5.31, and the effective heat transfer coefficients are the inverse of the resistances (Eq. 5.32 and Eq. 5.33) the following expansion can be made:

$$\frac{1}{R_{cond,Z_\alpha \to Z_\beta,i}} \cdot A_{eff_{Z_\alpha \to Z_\beta,i}} \left(\bar{T}_{Z_\alpha,i} - T_{surf,Z_\alpha \to Z_\beta,i}\right) \\ = \frac{1}{R_{cond,Z_\beta \to Z_\alpha,i}} \cdot A_{eff_{Z_\alpha \to Z_\beta,i}} (T_{surf,Z_\alpha \to Z_\beta,i} - \bar{T}_{Z_\beta,i}) \tag{5.36}$$

Eq. 5.36 can be rearranged to give an expression for the surface temperature:

$$T_{surf,Z_\alpha \to Z_\beta,i} = \frac{R_{cond,Z_\alpha \to Z_\beta,i} \cdot \bar{T}_{Z_\beta,i} + R_{cond,Z_\beta \to Z_\alpha,i} \cdot \bar{T}_{Z_\alpha,i}}{R_{cond,Z_\alpha \to Z_\beta,i} + R_{cond,Z_\beta \to Z_\alpha,i}} \tag{5.37}$$

Which, when inserted into Eq. 5.30, gives:

$$\phi_{ii,k} = \\ \frac{1}{R_{cond,Z_\alpha \to Z_\beta,i}} \cdot A_{eff_{Z_\alpha \to Z_\beta,i}} \left(\bar{T}_{Z_\alpha,i} - \frac{R_{cond,Z_\alpha \to Z_\beta,i} \cdot \bar{T}_{Z_\beta,i} + R_{cond,Z_\beta \to Z_\alpha,i} \cdot \bar{T}_{Z_\alpha,i}}{R_{cond,Z_\alpha \to Z_\beta,i} + R_{cond,Z_\beta \to Z_\alpha,i}}\right) \tag{5.38}$$

Eq. 5.38 can be simplified to:

$$\phi_{ii,k} = \frac{1}{R_{cond,Z_\alpha \to Z_\beta,i} + R_{cond,Z_\beta \to Z_\alpha,i}} \cdot A_{eff_{Z_\alpha \to Z_\beta,i}} \left(\bar{T}_{Z_\alpha,i} - \bar{T}_{Z_\beta,i}\right) \tag{5.39}$$

Eq. 5.39 takes the same form as Eq. 5.19, which was described in section 5.5.3 as the generalised equation for a heat flux. Therefore, the overall effective heat transfer coefficient $h_{eff_{cond,Z_\alpha \to Z_\beta,i}}$ is:

$$h_{eff_{cond,Z_\alpha \to Z_\beta,i}} = \frac{1}{R_{cond,Z_\alpha \to Z_\beta,i} + R_{cond,Z_\beta \to Z_\alpha,i}} \tag{5.40}$$

Including Eq. 5.32 and Eq. 5.33 with Eq. 5.40:

$$h_{eff_{cond,Z_\alpha \to Z_\beta,i}} = \frac{1}{\frac{d_{Z_\alpha \to Z_\beta,i}}{\lambda_{Z_\alpha}} + \frac{d_{Z_\beta \to Z_\alpha,i}}{\lambda_{Z_\beta}}} \tag{5.41}$$

Given that λ_{Z_α} and λ_{Z_β} are thermophysical properties (see section 5.4) that are constant, it is thus posited that conduction can be modelled between phases inside of a zone by determining the characteristic distances for both phases, $d_{Z_\alpha \to Z_\beta,i}$ and $d_{Z_\beta \to Z_\alpha,i}$.

van der Sman gave d_c values for simple objects like spheres and slabs as a ratio of well-defined dimensions, such as lengths or radius'. However, determining the characteristic distance for the shape formed by individual phases inside of a zone is significantly more challenging, as our chosen cuboid shaped zoning procedure intersects through different parts of fruits, air and packaging to create sinuous 3D geometry that *cannot* be described in regular shape terms (see Figure 5.13). A new technique was therefore needed that could examine the voxelised shape of phases, and use the voxel information to compute equivalent d_c values that result in a realistic resistance to heat transfer. Such a technique should work universally – on simple objects such as cylinders, spheres and slabs; as well as complex shapes, like the phases inside of a zone.

Developing this new geometric procedure began with the recognition that the conduction mechanism occurs in the direction of the temperature gradient, namely *toward* (or *away from*) the surface through which heat is being transferred. For a slab being heated/cooled on one surface, this occurs in only *one* direction; and for spheres or cylinders, this occurs in a *radial* direction. For more complex shapes, it can be generally said that the temperature gradient is occurring along the path of least resistance, or the shortest distance from a position inside of an object to the nearest position along its surface (given an object of homogenous thermal conductivity). As van der Sman (2003) proved, within a certain range of Biot numbers, the temperature gradient within objects has an approximately linear relationship with the distance away from the surface. This forms the basis for a generalised algorithm for predicting the characteristic distance for any shape: if d_{min} is the smallest distance from a position inside an object to the nearest surface position, then $\overline{d_{min}}$ represents the average distance from all positions for the entire object. It is then postulated that $\overline{d_{min}} \approx d_c$. The automated methodology formulated to compute $\overline{d_{min}}$ from a voxelised zonal geometry has been given the moniker 'average voxel distance calculator', or AVDC. The AVDC is described with reference to Figure 5.26, which shows a typical zone filled with voxelised geometry data (to assist in the explanation of the algorithm, this zone is 2 dimensional).

The AVDC requires 4 steps:

1. Determine the position of every voxel in the phase under investigation;
2. Determine the position of every surface voxel;
3. Compute the smallest distance between every voxel and the nearest surface voxel;
4. Estimate the characteristic distance as the average minimum path length.

Remembering that all voxels inside of zone i are denoted as $\mathbb{v}_i$, individual voxels inside of zone i are referred to as $\mathbb{v}_{n,i} = Z$. First, the position of every voxel in the phase under investigation must be known – in Figure 5.26 this is Z_α, where Z_α is fruit: $Z_\alpha = S$. This is a given, as the voxelised zonal geometry has been provided as an input (Figure 5.26a). Second, the voxels that are at the interface between phases Z_α and Z_β (in Figure 5.26, the second phase is air, $Z_\beta = A$) must be identified – these 'surface voxels' are denoted as $\mathbb{v}_{surf,Z_\alpha \to Z_\beta,m,i}$ (Figure 5.26b), where the subscript $Z_\alpha \to Z_\beta$ denotes which phase-pair is being investigated, and m refers to individual surface voxels. Identifying surface voxels and their position is an important part of the AVDC and so automated surface identification algorithms are discussed in more detail later. Third, the smallest distance between each voxel and its nearest surface voxel must be calculated.

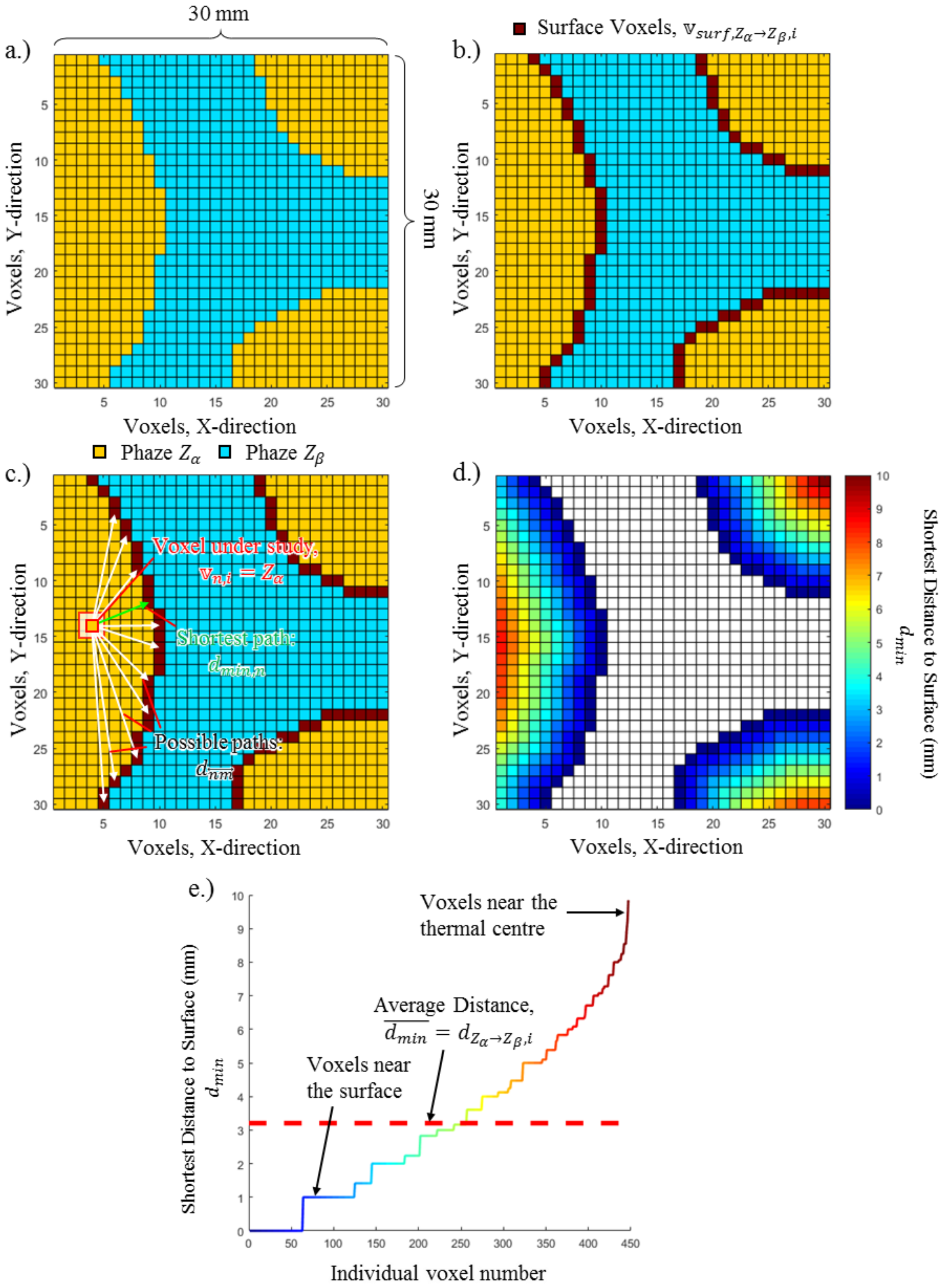

Figure 5.26: Visualisation of the Average Voxel Distance Calculator, as applied to a hypothetical 2 dimensional zone filled with voxels of fruit and air; a.) a 30×30 mm 2 dimensional zone filled with voxels of fruit (yellow) and air (blue); b.) identification of the surface voxels (dark red); c.) paths from a given voxel to all surface voxels (white arrows) to determine the shortest distance from that position (green arrow); d.) shortest distance from each voxel to the nearest surface; e.) computation of the characteristic distance for the zonal geometry as the mean minimum distance, $\overline{\mathrm{d_{min}}}$.

Given that voxels and surface voxels both have X, Y and Z positions in space that are known, the distance between a given couple is:

$$d_{\overleftrightarrow{nm}} = \sqrt{((X_n - X_m)^2 + (Y_n - Y_m)^2 + (Z_n - Z_m)^2)} \tag{5.42}$$

Where $d_{\overleftrightarrow{nm}}$ is the distance between voxel n and surface voxel m (in meters, m); x_n, y_n and z_n is the x, y and z position of voxel n; and x_m, y_m and z_m is the x, y and z position of surface voxel m. The distance between voxel n and all surface voxels are calculated, represented as the plurality of white arrows in Figure 5.26c. The smallest distance is the path of least resistance, represented by the green arrow in Figure 5.26c:

$$d_{min,n} = \min\left[d_{\overleftrightarrow{n,1}}, d_{\overleftrightarrow{n,2}} \cdots d_{\overleftrightarrow{n,M-1}}, d_{\overleftrightarrow{n,M}}\right] \tag{5.43}$$

Where $d_{min,n}$ is the minimum distance from voxel n to the nearest surface voxel; and M is the total number of surface voxels*. Repeating the process for all voxels (Figure 5.26d), the result is proposed to be an approximation of the fully developed temperature gradient in the object, so that the 'characteristic distance' can be taken as the average path of least resistance (Figure 5.26e):

$$\overline{d_{min}} = \frac{\sum\left[d_{min,1}, d_{min,2} \cdots d_{min,N-1}, d_{min,N}\right]}{N} \tag{5.44}$$

Where $\overline{d_{min}}$ is the average minimum distance and N is the total number of voxels. This process has potential to be computationally intensive as an N number of $1 \times M$ vectors must be created, and if there is a high voxel resolution these numbers could be in the range of hundreds of thousands to millions. Methods to compute the minimum distances expeditiously are explored later. As discussed previously, it is postulated that $d_c \approx \overline{d_{min}}$ and $\overline{d_{min}} = d_{Z_\alpha \rightarrow Z_\beta, i}$ for use in Eq. 5.34 and Eq. 5.41 to compute the internal resistance. In the example of Figure 5.26, $d_{S\rightarrow A,i}$ = 3.2 mm, making the internal resistance of the fruit $R_{cond,S\rightarrow A,i} = d_{S\rightarrow A,i}/\lambda_S$ = 0.00321/0.542 = 0.00591 m·K·W^{-2} (see section 5.4). This result

* min denotes minimum

was obtained with no assumptions made about the shape of the fruit phase, using a repeatable algorithm that could be applied verbatim to the remainder of the phases and zones in the zonal set.

The hypothesis that $d_c \approx \overline{d_{min}}$ was partially validated by applying the AVDC algorithm to the same objects investigated by van der Sman (2003) – namely, a slab (Figure 5.27), a cylinder (Figure 5.28) and a sphere (Figure 5.29) – and comparing the $\overline{d_{min}}$ values derived with the d_c figures noted by van der Sman. This investigation also aimed to investigate the role of voxel resolution on the accuracy of the derived $\overline{d_{min}}$ metrics. The AVDC is more thoroughly tested during numerical validation (see section 6.2.2).

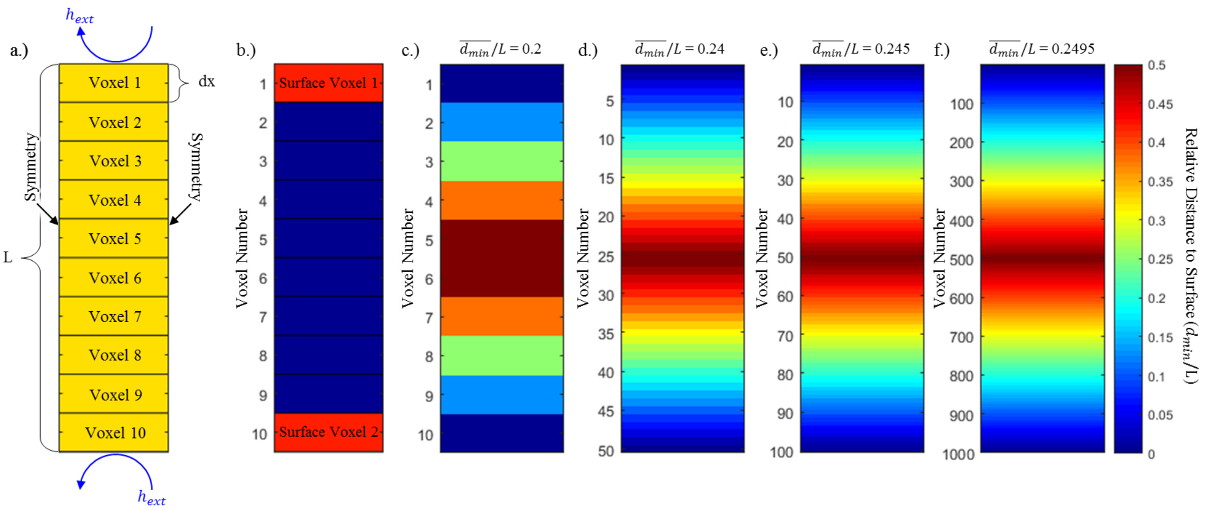

Figure 5.27: The AVDC tested on a 1-D slab. a.) the voxel geometry of the slab; b.) identification of surface voxels; $\overline{\mathrm{d_{min}}}$ *given relative to the length of the slab,* L, *with c.) 10; d.) 50; e.) 100; and f.) 1000 voxels.*

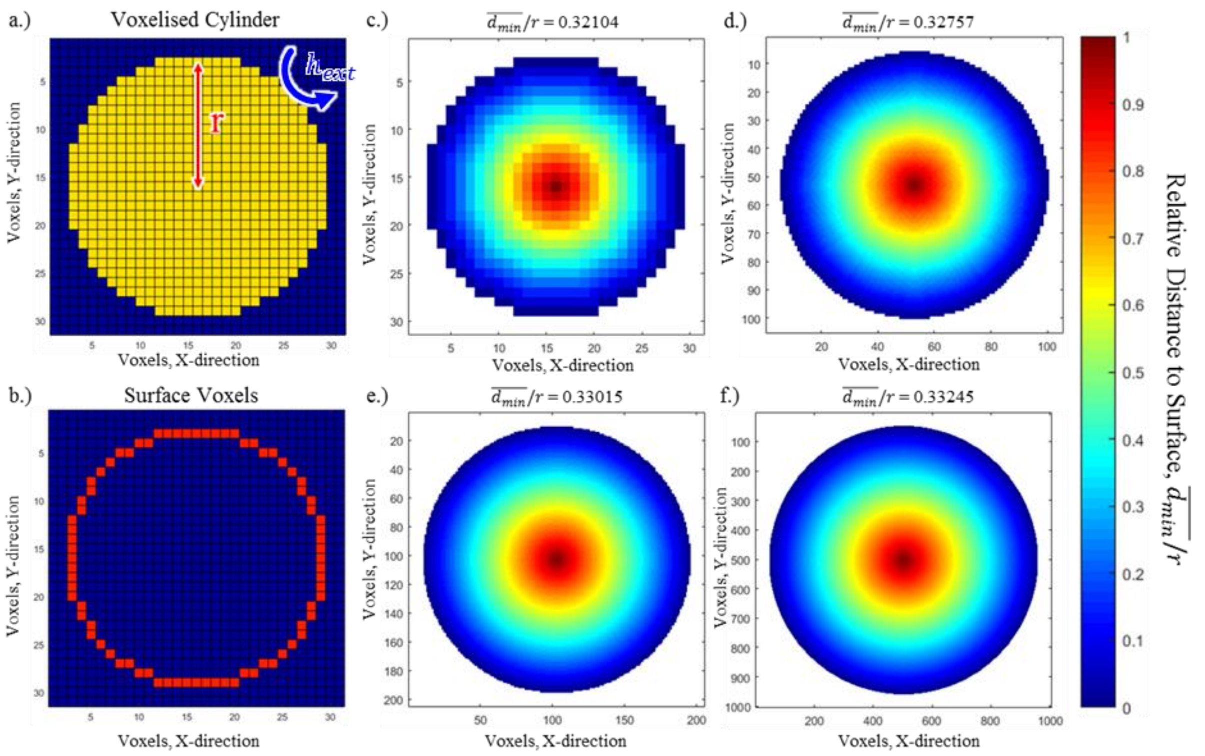

Figure 5.28: The AVDC tested on a 2-D cylinder. a.) the voxel geometry of the cylinder; b.) identification of surface voxels; $\overline{\mathrm{d}_{\mathrm{min}}}$ *given relative to the radius of the cylinder,* r, *with a c.) 30×30; d.) 100×100; e.) 200×200; and f.) 1000×1000 voxel grid.*

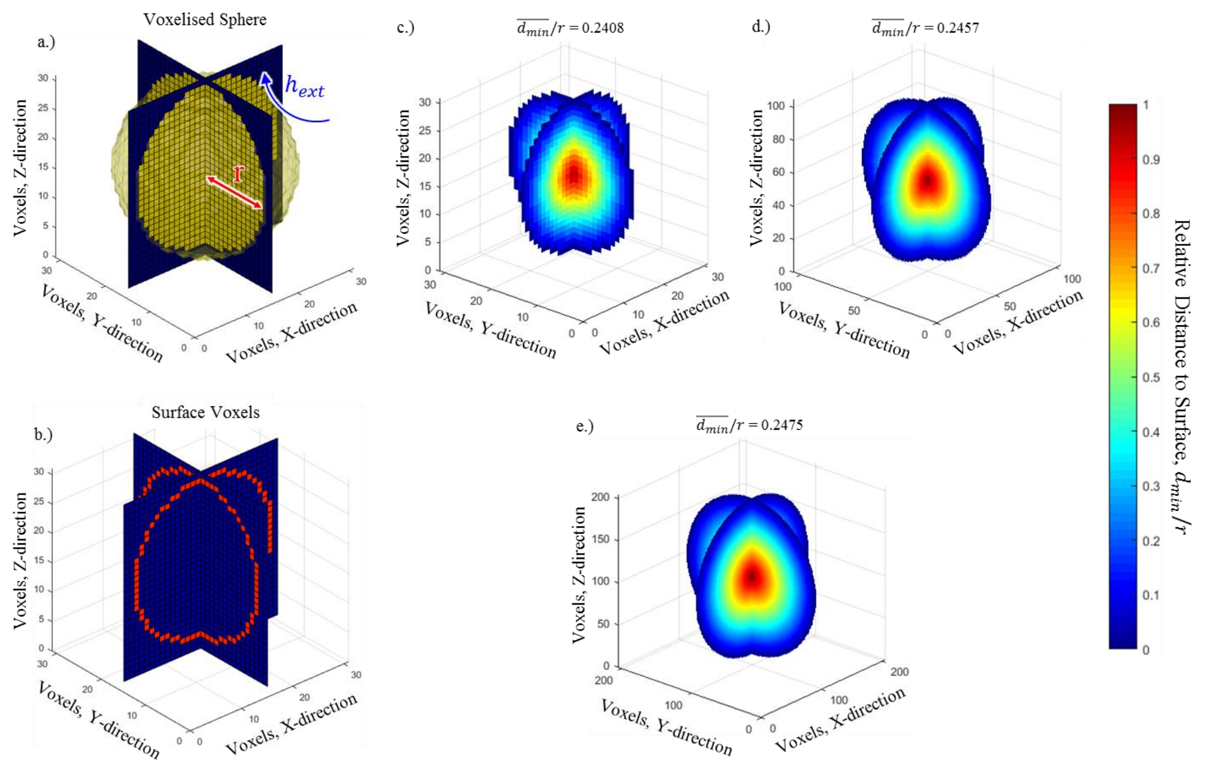

Figure 5.29: The AVDC tested on a 3-D sphere. a.) the voxel geometry of the sphere; b.) identification of surface voxels; $\overline{\mathrm{d}_{\mathrm{min}}}$ *given relative to the radius of the sphere,* r, *with a c.) 30×30×30; d.) 100×100×100; e.) 200×200×200 voxel grid.*

The AVDC was first applied to a 1-dimensional slab, heated/cooled on both surfaces (Figure 5.27). The geometry consisted of a single column of voxels (Figure 5.27a); the number of voxels, N, and the length of the slab, L, determined the thickness of each voxel, $dx = L/N$. Surface voxels were chosen manually as the top and bottom voxels in the column (Figure 5.27b). The shortest distance to the surface was then calculated for each position, d_{min}, and reported relative to the length of the slab; this was repeated for a sequentially higher voxel resolution (Figure 5.27c - f). van der Sman (2003) determined through finite element analysis that the characteristic distance for a slab was $d_c = L/4$, or $d_c/L = 0.25$. It has been posited that $d_c \approx \overline{d_{min}}$, which appears to be an accurate contention but is dependent on the voxel resolution: while at a low voxel resolution of 10 voxels, the AVDC gave a relative characteristic distance of $\overline{d_{min}}/L$ = 0.2 – an error of 22% (Figure 5.27c) – increasing the voxel resolution showed a clear trend toward the characteristic distance reported by van der Sman, with $\overline{d_{min}}/L$ = 0.2495 at a 1000 voxel resolution – just 0.2% error (Figure 5.27f).

Applying the same AVDC to an entirely different geometry, a cylinder, further supported the hypothesis (Figure 5.28). A voxelised circle was created using similar techniques of that in section 5.5.4, creating what can be considered an infinitely long cylinder of a specified radius, r (Figure 5.28a). Surface voxels were chosen using the edge detection MATLAB function, 'edge'. The hypothesis of $d_c \approx \overline{d_{min}}$ appears to remain true even with the change of geometry: van der Sman concluded that a cylinder had a characteristic distance of d_c/r = 1/3, which is reflected by the AVDC with $\overline{d_{min}}/r$ = 0.32104 at a relatively low voxel resolution of 593 voxels – under 4% error (Figure 5.28c) – to $\overline{d_{min}}/r$ = 0.33245 at a high resolution of over 2.6 million voxels – a 0.3% error (Figure 5.28f).

Finally, the same AVDC algorithm was applied again, but to a 3-D object, a sphere being heated/cooled on its outer surface (Figure 5.29). Created with the voxeliser of section 5.5.4 with a specific radius, r, surface voxels were again detected with the 'edge' MATLAB function. The AVDC again reflects the conclusion of van der Sman, where a sphere had a characteristic distance of d_c/r = 0.25: the AVDC predicted $\overline{d_{min}}/r$ = 0.2408 at a relatively low resolution of 12893 voxels – just under 4% error

(Figure 5.29c) – while at a high voxel resolution of over 4 million voxels, $\overline{d_{min}}/r$ = 0.2475 – a 1% error (Figure 5.29e).

This exercise proves in part that the same algorithm, the AVDC, can correctly reproduce the findings of van der Sman (2003), lending credence to its universal application to many other shapes, including highly irregular geometries such as the phases inside of a zone. This also showed that the prediction of the characteristic distance improves as the voxel resolution increases – however, the accuracy of this metric must be balanced closely with the computational efficiency of the AVDC algorithm, which is discussed below. Further validation of the AVDC is performed on a variety of objects later in section 6.2.2.

Pertinent to this section is bringing the AVDC in line with the philosophies of this thesis: while it was developed with flexibility in mind, it is not necessarily automated or computationally efficient. Step 2 of the AVDC requires that the surface voxels, $\mathbb{V}_{surf,Z_\alpha \to Z_\beta,i}$, be identified in an automated fashion. Though Figure 5.26 only had 2 phases (so that there is only one set of surface voxels), there is potentially up to 4 phases per zone, so that there can be up to 6 different sets of surface voxels – one for each phase-pair, $Z_\alpha \to Z_\beta$. There must be an automated technique to detect each of these different sets for any potential intra-zonal geometry. Step 3 of the AVDC has potential to be prohibitive from a computational perspective, as under certain circumstances it requires a very large number of calculations, or the construction of very large matrices. For example, Figure 5.29e is a sphere comprised of 4,028,249 voxels, and 90,883 surface voxels. To compute the entirety of $d_{\overrightarrow{nm}}$ (Eq. 5.42) requires a matrix 4028249 × 90883 in size, which according to MATLAB demands 2728 GB of RAM – where only 16 GB was available. This can be somewhat circumvented by calculating the path lengths from a single voxel to all surface voxels – such as Eq. 5.43 – a much smaller vector of 1 × 90883, and storing the minimum length as the separate variable $d_{min.n}$, discarding the larger paths. However, an incredibly large loop of 4028249 iterations must be executed – in the case of Figure 5.29e, this took 2881 seconds, or 0.8 hours, an unacceptably long period of time for a single object.

The following techniques were developed to mitigate these issues. First, the process for automatically identifying the surface voxels of any phase pair, $Z_\alpha \rightarrow Z_\beta$, is discussed in relation to Figure 5.30a, which shows a zone from the corner of the package that contains 4 phases. Figure 5.30b shows a cross section of the zone to better illustrate the process. Selecting a given phase-pair, for example, $Z_\alpha \rightarrow Z_\beta = S \rightarrow A$, the first step is isolation, where the two phases under investigation are taken separately and the remaining phases temporarily removed (Figure 5.30c). Phase Z_β (in this case, $Z_\beta = A$) is dilated with the 'imdilate' MATLAB function, a process that essentially adds an extra layer of voxels to the surface of the phase (white voxels in Figure 5.30d). Adding the dilated phase Z_β to phase Z_α, the overlapping voxels are taken as the surface voxels (yellow voxels in Figure 5.30e). The process can be repeated for all possible phase-pairs with minimal amendments to the code, to quickly and automatically identify the 6 possible sets of surface voxels (Figure 5.31), an operation that took only 0.2 seconds to execute.

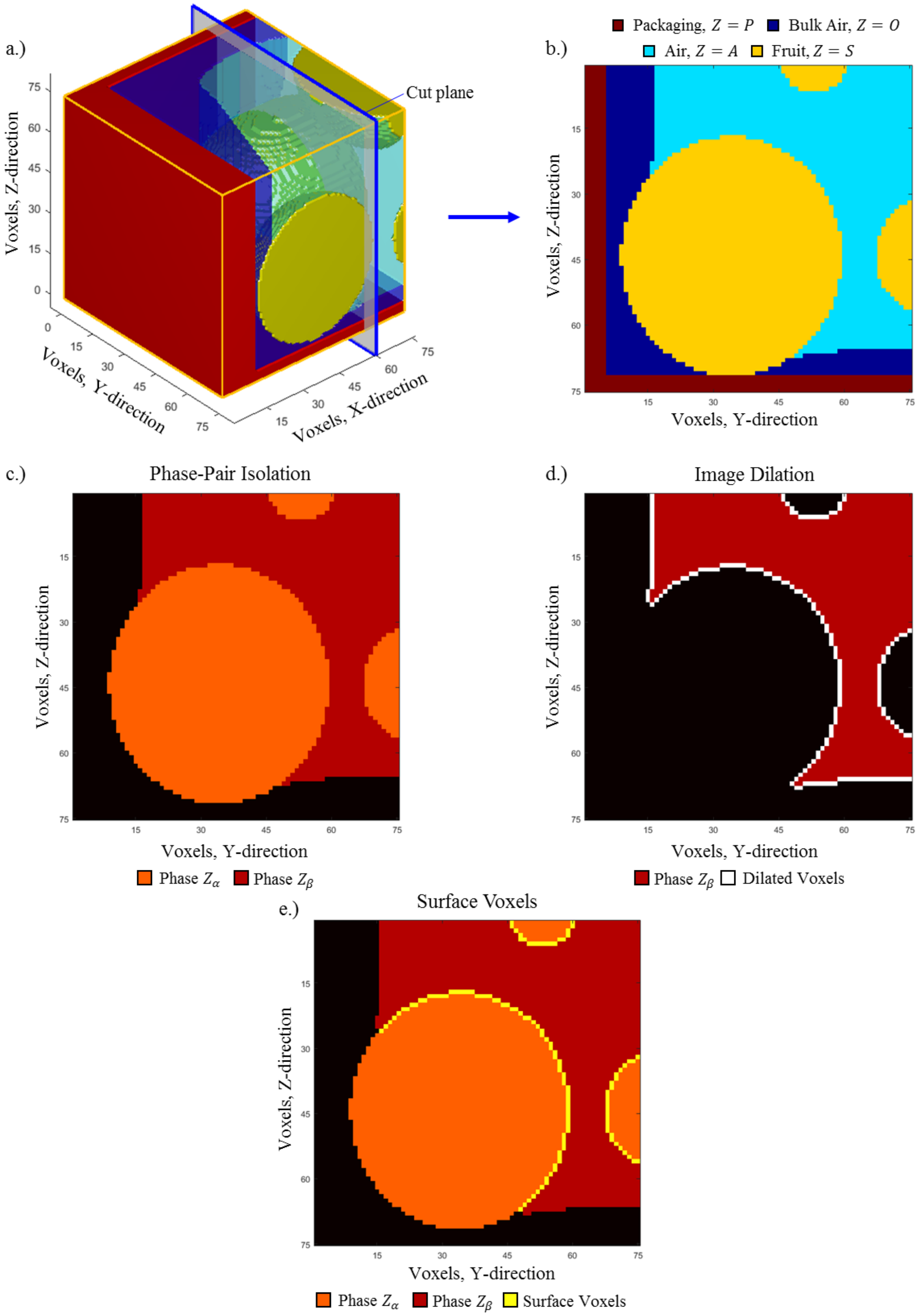

Figure 5.30: Automated surface voxel identification: a.) a voxelised cuboid zone from the corner of a package; b.) a 2-D cross section of the zone; c.) the specific phase-pair is isolated; d.) the secondary phase is dilated by one voxel (white voxels); e.) overlap between the dilated phase Z_β and phase Z_α are the surface voxels (yellow voxels).

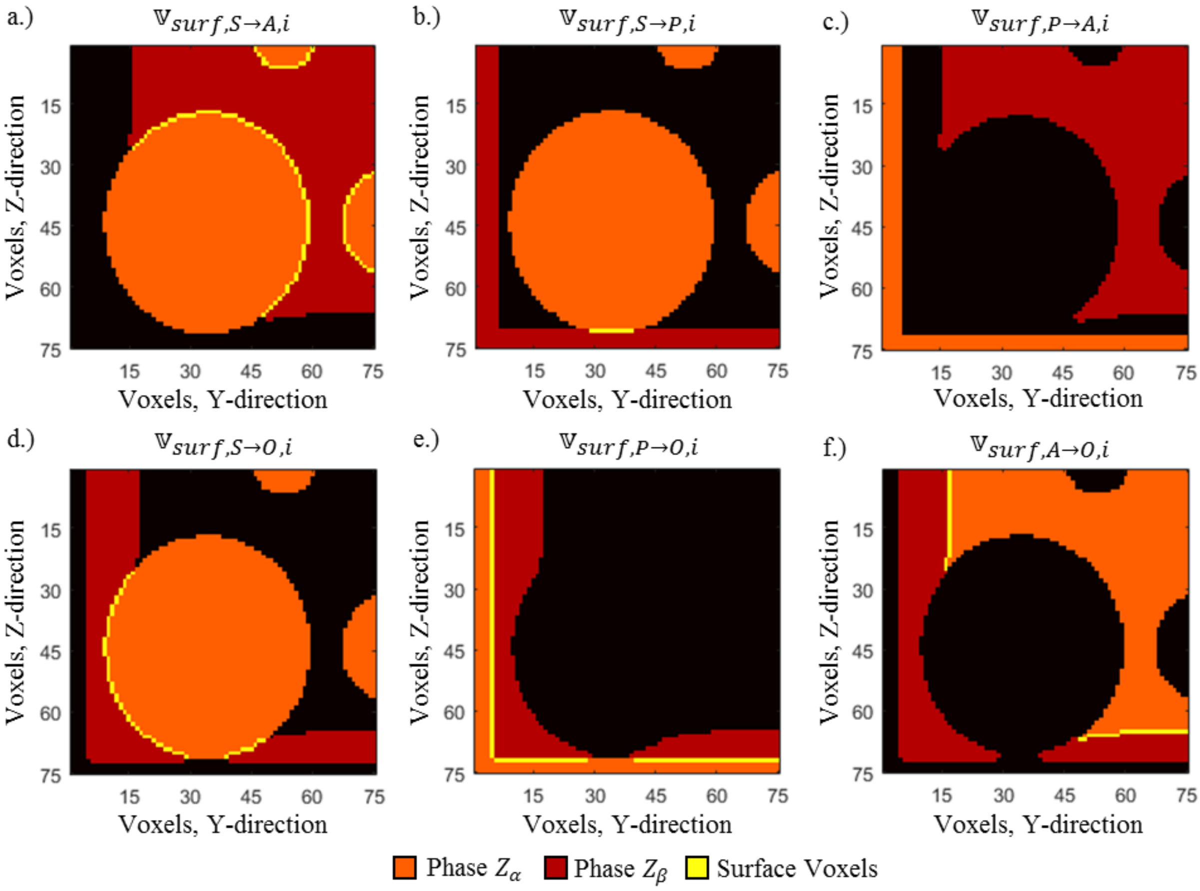

Figure 5.31: Repetition of the automated surface voxel identification algorithm for each of the 6 possible phase pairs.

Next was the expediting of the calculation of $\overline{d_{min}}$. The fruit geometry of Figure 5.30 consisted of 111700 fruit voxels, and 5595 surface voxels when considering its contact with the polyliner air (Figure 5.30e). Executing Eq. 5.42, Eq. 5.43 and Eq. 5.44 took approximately 72 seconds to determine $d_{S\to A,i}$ (Figure 5.32).

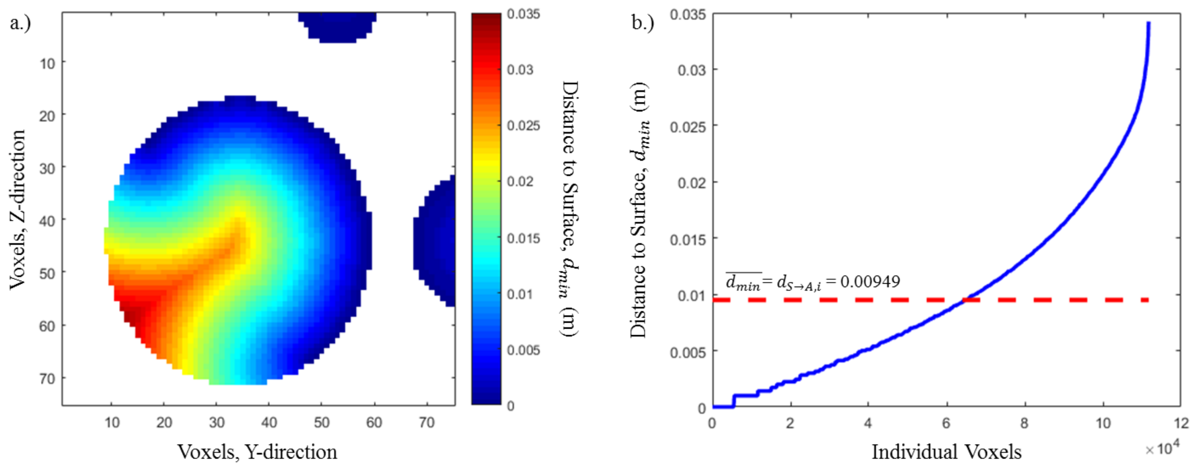

Figure 5.32: Application of the AVDC for $\mathrm{d_{S\to A,i}}$ *(fruit to polyliner air) for a cross section of a corner zone; a.) path of least resistance from each position; b.) path of least resistance from each position, plotted from shortest to longest, to derive* $\mathrm{d_{S\to A,i}}$.

It was pertinent to minimise this period as $d_{S\to A,i}$ is just one of many properties that must be appropriated, and just one zone out of a zonal network of potentially hundreds, so that speed improvements will be carried through to these other areas and expedite the zone builder as a whole. It was realised that it is not necessary to calculate the path of least resistance from every voxel in the geometry to appropriate a good estimate for $\overline{d_{min}}$; rather, a fractional sample of voxels can be taken instead, maintaining the accuracy and flexibility of the AVDC but reducing the number of calculations by an order of magnitude. Rather than calculate the path of least resistance from all 111700 fruit voxels, a smaller sample – in this case, 10%, or 11170 voxels – was taken instead, the position of the 'sampled voxels' being randomly chosen. This is demonstrated in Figure 5.33. A 10% random sample of voxels was taken 100 times and the d_{min} plotted from shortest to longest. This revealed that the shape of the curve closely mirrors that of the full calculation (Figure 5.32b). The difference between curves is minimal, despite each consisting of a unique sample of voxels. The difference between the sampled $\overline{d_{min}}$ values and the full calculation (Figure 5.32b) was found to be at most ±2% (Figure 5.33b), with 52% of the population deviation within ±0.5%. Adding at most 2% error to the calculation of $d_{S\to A,i}$ was considered worthwhile with a new calculation times of only 3.7 seconds.

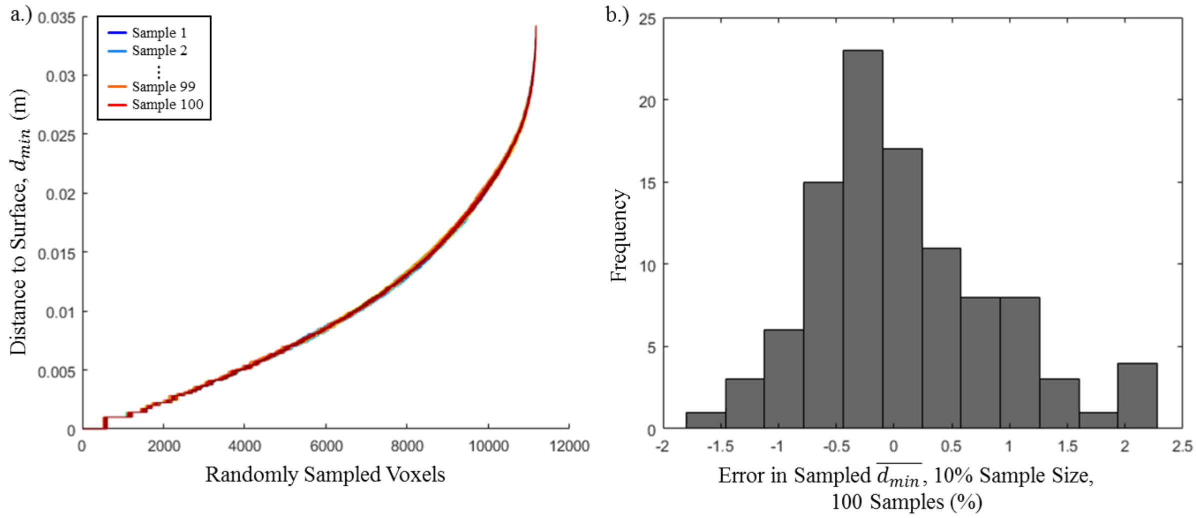

Figure 5.33: a.) path of least resistance distances from 11170 randomly selected voxels (a 10% sample size) from the fruit phase of a zone from the corner of a package, with random selection being repeated 100 times; b.) population of percentage error between the fully calculated and randomly sampled $\overline{\mathrm{d_{min}}}$ *for 100 random samples of 10%.*

Further improvements to the efficiency of the AVDC were found, but only applied to specific zones. The distance transform is an image processing technique that was used previously in section 4.5.1. It can also be used here as an efficient algorithm to determine the closest distance from each voxel to the nearest surface voxel, but as it only applies to binary images, is restricted in its use to zones which have *only 2 phases*, such as zones from the middle of the box. The MATLAB function 'bwdist' computes the distance transform and outputs a new matrix of *voxel distances* to the surface. Voxels at the surface are given a voxel distance of 1 rather than 0, and so prior to the application of 'bwdist', the surface voxel algorithm (Figure 5.31) must be used to remove the surface voxels. The resulting distance matrix must be multiplied by the length, width or height of a voxel, so the condition of $dx = dy = dz$ is necessary. For geometries with voxels that are perfect cubes, this improved efficiency to just 0.18 seconds for a similarly sized zone as Figure 5.31. For geometries with skewness in voxel size (such as a CT scan), a modified 'bwdist' function was used (Mishchenko, 2015), which incorporated the voxel skewness but worsened efficiency slightly to 0.29 seconds. Logic was coded into the zone builder which was able to determine which of these improved AVDC methods would be applied, depending on which zone was being examined.

5.5.6.1.4: Natural Convection

The methods of section 5.5.6.1.3 applied to solid phases where there was pure conduction. When applying these methods to the fluid phase, if it is considered stagnant, then heat is transferred through pure conduction and section 5.5.6.1.3 can be applied verbatim. However, if the temperature gradients in the fluid phase promotes the formation of natural convection currents, there will be a combination of conduction *and* convection, and the resistance will be lower than that predicted by the AVDC. Section 5.3.2.2 showed that natural convection plays a significant role during the pre-cooling process, so the combination of conduction and convection be must accounted for when applying the AVDC to a fluid phase.

The significance of natural convection was not nearly as considerable as the standard Rayleigh number indicated, the dimensionless number used to signify the existence of natural convection currents – with Ra = 9.0×10^6, the natural convection currents inside the polyliner should be turbulent and fast flowing (Holman, 2010; section 5.3.2.2). A lengthy and complex finite element analysis (Section 5.3.2.2) revealed that natural convection contributed perhaps 5-10% to overall cooling, which contradicts the Rayleigh number previously reported. Incorporating natural convection into the zonal model requires that the added resistance to the formation of natural convection currents imposed by the fruit be accounted for in a simplified manner that does not contribute significantly to the computational overhead.

Avila-Acevedo and Tsotsas (2008) described the impact of natural convection in an enclosed granular media by relating the heat transfer rate when there is no natural convection (pure conduction) to the heat transfer rate when there is a combination of conduction and convection:

$$h_{rel} = \frac{h(\text{conduction} + \text{convection})}{h(\text{pure conduction})} \tag{5.45}$$

Where h denotes the perceived heat transfer coefficient ($\mathrm{W{\cdot}m^{-2}{\cdot}K^{-1}}$). As stated previously in Eq. 5.32, the heat transfer coefficient is the reciprocal of the internal resistance in the air phase:

$$h = \frac{1}{R_{int}} = \frac{\lambda_A}{d_c} \tag{5.46}$$

Inserting Eq. 5.46 into Eq. 5.45 gives:

$$h_{rel} = \frac{\lambda_A(\text{conduction} + \text{convection})}{d_c} \bigg/ \frac{\lambda_A(\text{pure conduction})}{d_c} \tag{5.47}$$

The characteristic distance, or d_c as described in section 5.5.6.1.3 is related to the geometry of the air phase inside of the zone and is not impacted by the addition of natural convection. Thus, Eq. 5.47 can be simplified to:

$$h_{rel} = \frac{\lambda_A(\text{conduction} + \text{convection})}{\lambda_A(\text{pure conduction})} \tag{5.48}$$

Thus, it is proposed that natural convection can be accounted for by using a new thermal conductivity for air, $\lambda_A(\text{conduction} + \text{convection})$, which can also be described as an effective thermal conductivity, that is related to the original conductivity, $\lambda_A(\text{pure conduction})$, by the multiplier h_{rel}. Written in a more general sense:

$$\lambda_{A,eff} = \lambda_A \cdot F_{N.C.} \tag{5.49}$$

Where $\lambda_{A,eff}$ is the effective thermal conductivity for air with natural convection and conduction ($W \cdot m^{-1} \cdot K^{-1}$), λ_A is the thermal conductivity for air with pure conduction ($W \cdot m^{-1} \cdot K^{-1}$) and $F_{N.C.}$ is the natural convection correction factor. If the conditions inside the package are such that the air phase is stagnant, then $F_{N.C.}$ = 1 and the resistance is $R_{conv} = d_c/\lambda_A$; but if there is some natural convection, then the resistance is lowered to $R_{conv} = d_c/(\lambda_A \cdot F_{N.C.})$ where $F_{N.C.} > 1$. This section is thus principally concerned with the prediction of $F_{N.C.}$ as a function of physically relevant quantities which contribute to the natural convection phenomenon, such as the geometry of the box, physical properties of the fluid, temperature and porosity.

Holman (2010) and Tanner *et al* (2002b) suggested that natural convention be modelled using the Nusselt number, where Nu is defined as the ratio of the heat transports with and without convection, or Nu = $F_{N.C.}$. Holman (2010) offered the empirically determined correlation which was used by Tanner *et al.* (2002b):

$$\mathrm{Nu} = F_{N.C.} = \frac{\lambda_{A,eff}}{\lambda_A} = 0.073 \cdot \mathrm{Ra}^{1/3} \left(\frac{x_y}{x_x}\right)^{-1/9} \ (2 \times 10^5 < \mathrm{Ra} < 1.1 \times 10^7) \tag{5.50}$$

Which uses relevant physical quantities such as the Rayleigh number (Ra), height (x_y) and width (x_x) of the box. This correlation is clearly not appropriate for the current system, however, as it does not incorporate the presence of the fruit inside of the polyliner, and predicts (using Ra = 9.0×10^6, x_y = 0.196 and x_x = 0.3) a correction factor of $F_{N.C.}$ = 15.9, or a 1590% increase in the thermal conductivity of air due to natural convection – which clearly does not conform with what was observed in section 5.3.2.2. Nonetheless, Eq. 5.50 was the impetus to search the literature for a similar approach that incorporated the missing information pertaining to the airflow resistance caused by the presence fruit.

It was here that concepts from the porous medium approach were turned to for inspiration, specifically for porous media problems in enclosed spaces, as this is similar to the fruit inside of a polyliner scenario. Though the porous medium approach was ruled out for the current scenario (section 1.2.5.3), certain concepts had potential to be useful to the problem at hand, namely the manner in which natural convection problems are managed in solid-liquid packed beds. One such principle is the porous media modified Rayleigh number (Nield, and Bejan, 2017), which has potential to be a more representative dimensionless number for the presence of natural convection than the standard Rayleigh number (see Eq. 5.9):

$$\mathrm{Ra}^* = \frac{K_\varepsilon g \rho_o \beta H}{\mu \kappa^*}\left(T_i - T_{ref}\right) \tag{5.51}$$

Where Ra* is the porous media modified Rayleigh number (-); K_ε is the permeability of the packed bed (m^2); g is the acceleration due to gravity (m·s^{-2}); T_i is the initial temperature (K); T_{ref} is the refrigeration temperature (K); ρ_o is the density of the fluid at the initial temperature (kg·m^{-3}); β is the thermal expansion coefficient (K^{-1}); H is the height of the packed bed (m); μ is the viscosity of the fluid ($kg \cdot m^{-1} \cdot s^{-1}$); and κ^* is the modified bed thermal diffusivity ($m^2 \cdot s^{-1}$). This dimensionless number incorporates information pertaining to the ability for the fluid in a packed bed to form natural convection currents with K_ε, the Darcy–Forchheimer permeability (Chen and Hsiao, 1998):

$$K_\varepsilon = \frac{{d_S}^2 \cdot \varepsilon^3}{150(1-\varepsilon)^2} \tag{5.52}$$

Where d_S is the particle diameter (m); and ε is the porosity of the packed bed (-).

According to Hewitt *et al.*, (2004), Avila-Acevedo and Tsotsas (2008) and Nield, and Bejan (2017), there is a critical Rayleigh number, below which no natural convection occurs, and the air phase acts as a conducting solid (or $F_{N.C.}$ = Nu = 1). For enclosed cavities filled with a porous media, Bories (1987) showed that the theoretical critical Rayleigh number was $\mathrm{Ra}_c^* = 4\pi^2$, or approximately equal to 40. After the critical Rayleigh number, natural convection currents begin to have an impact on the cooling rate. Bories' (1987) theoretical relationship between the Nusselt number and Rayleigh number in enclosed spaces is:

$$\mathrm{Nu} = 1 + \sum_{j=1}^{\infty} k_j \left(1 - \frac{\mathrm{Ra}_{cj}^*}{\mathrm{Ra}^*}\right) \tag{5.53}$$

Where $\mathrm{Ra}_{cj}^* = 4j^2\pi^2$; $k_j = 2$ when $\mathrm{Ra}^* > \mathrm{Ra}_{cj}^*$; and $k_j = 0$ when $\mathrm{Ra}^* < \mathrm{Ra}_{cj}^*$. Nield, and Bejan (2017) showed that (through Cheng, 1978 a; and Cheng, 1978 b) the critical Rayleigh number of $\mathrm{Ra}_c^* \approx 40$ is generally confirmed, and that across a range of experimental comparisons, Eq. 5.53 predicts the general shape of the $\mathrm{Nu}(\mathrm{Ra})$ relationship – though the theoretical values of Nu are generally lower than those observed. In the range of Rayleigh numbers immediately after the critical Rayleigh (the Darcy regime), there was a low spread of Nu across the surveyed experiments, and Elder (1967) offered a simplified relationship of:

$$\mathrm{Nu} = \frac{\mathrm{Ra}^*}{40} \tag{5.54}$$

At higher Rayleigh values (the Forchheimer regime) there was a high spread of Nu across the surveyed experiments, and use of Eq. 5.53 was much less accurate, and Eq. 5.54 is no longer applicable. These correlations are plotted in Figure 5.34. As was observed with the lengthy finite element model of section 5.3.2.2, the effects of natural convection were relatively small; therefore, the system under study is expected to be slightly supercritical, or Ra^* is slightly larger than 40, or in the Darcy regime.

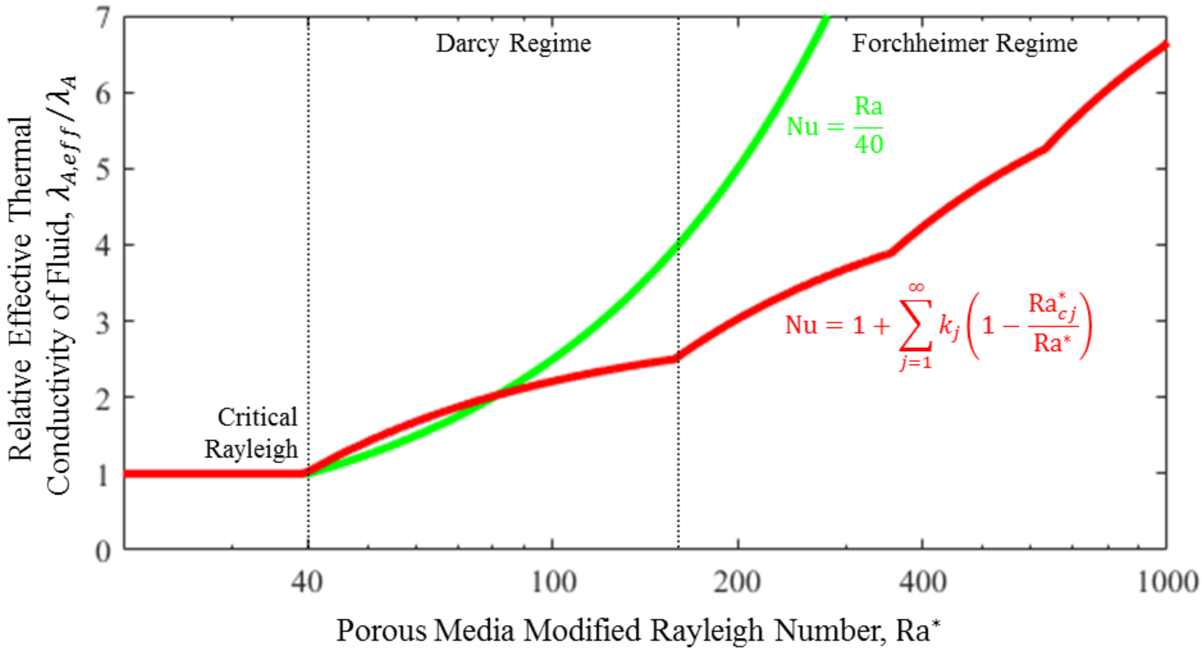

Figure 5.34: Relative effective thermal conductivity of fluids (Nusselt number) as a function of the porous media modified Rayleigh number, various models. Image based on Cheng (1978 a), Cheng (1978 b) and Wang and Bejan 1987.

Computing the porous media modified Rayleigh number for the current scenario – 100 count 36 hayward kiwifruit wrapped in a polyliner – first requires some additional variables be defined. First, computing the Darcy–Forchheimer permeability, K_ε (Eq. 5.52), requires the porosity and particle diameter. The porosity, being the volume ratio of fluid to total volume, is:

$$\varepsilon = \frac{V_{A,tot}}{V_{S,tot} + V_{A,tot}} \tag{5.55}$$

The porosity is not calculated on a per-zone level, but on a global – or package – scale. Thus, $V_{A,tot}$ is the volume of air in all zones (m^3) and $V_{S,tot}$ the volume of fruit in all zones (m^3). These can be calculated by counting the total number of voxels corresponding to each phase, or section 5.5.6.1.1.

Important to note is that only the air *inside* of the polyliner is included in the porosity calculation, as it has already been shown (section 5.3.2.2) that natural convection does not occur in the bulk airflow (phase $Z = O$).

Kiwifruit do not have a definite 'particle diameter' as they are proto-ellipsoids with a major (D_X) and minor (D_Y) diameter, and length (L). Furthermore, there is a variation in these dimensions from fruit to fruit (see section 4.3.3). Therefore, an effective particle diameter is used, which is the radius of a sphere with the same volume as the average volume of all kiwifruit in the stack:

$$d_S = 2 \cdot \left[\frac{V_{S,tot}/N_S}{(4/3) \cdot \pi}\right]^{1/3} \tag{5.56}$$

Where N_S is the number of kiwifruit in a stack, which can be calculated automatically using the technique of section 4.5.1; making $V_{S,tot}/N_S$ the average volume of a single kiwifruit in the stack.

The modified bed thermal diffusivity, κ^*, for a typical porous medium is:

$$\kappa^* = \frac{\lambda_b}{\rho_A \cdot C_A} \tag{5.57}$$

Where λ_b is the effective thermal conductivity of the packed bed ($W \cdot m^{-1} \cdot K^{-1}$); ρ_A is the density of the fluid ($kg \cdot m^{-3}$)and C_A is the specific heat capacity of the fluid ($J \cdot kg^{-1} \cdot K^{-1}$). As has already been shown (section 1.2.5.3), a single effective thermal conductivity does not apply globally to the current scenario as the product-to-package ratio is too low. It is estimated using the parallel effective thermal conductivity model (Delele *et al.*, 2012), with the understanding that it introduces error into the approximation of $F_{N.C.}$, but that some degree of error is acceptable when taking into account the simplicity of Eq. 5.49 when compared to section 5.3.2.2:

$$\lambda_b = \varepsilon \cdot \lambda_A \times (1 - \varepsilon) \cdot \lambda_S \tag{5.58}$$

This allows the modified Rayleigh number to be calculated for the current scenario. The thermal properties and cooling conditions are given in Table 5.4.

Variable	**Value**	**Units**
g	9.81	$m \cdot s^{-2}$
ρ_o	1.20	$kg \cdot m^{-3}$
β	0.00341	K^{-1}
H	0.196	m
μ	1.81×10^{-5}	$kg \cdot m^{-1} \cdot s^{-1}$
T_i	20	°C
T_{ref}	0	°C
$V_{S,tot}$	0.0107	m^3
$V_{A,tot}$	0.00553	m^3
N_S	100	-
d_S	0.0588	m
ε	0.342	-
K_ε	2.13×10^{-6}	m^2
ρ_A	1.20	$kg \cdot m^{-3}$
C_A	1005	$J \cdot kg^{-1} \cdot {}^{o}C^{-1}$
λ_A	0.0257	$W \cdot m^{-1} \cdot K^{-1}$
λ_S	0.542	$W \cdot m^{-1} \cdot K^{-1}$
λ_b	0.365	$W \cdot m^{-1} \cdot K^{-1}$
κ^*	2.12×10^{-5}	$m^2 \cdot s^{-1}$
Ra^*	61.4	-

Table 5.4: Thermal properties and initial conditions used to calculate the porous media modified Rayleigh number.

With an initial temperature of 20ºC and refrigeration temperature of 0ºC, the porous media modified Rayleigh number was Ra^* = 61.4, putting the box of kiwifruit into the slightly supercritical range; this is to be expected, considering the findings of section 5.3.2.2. Applying Eq. 5.53, the natural convection correction factor was $F_{N.C.}$ = 1.71; or applying the simplified Eq. 5.54 gives $F_{N.C.}$ = 1.53. Therefore, instead of the complex process of section 5.3.2.2, the impact of natural convection can be modelled by using λ_A = 0.0441 (Eq. 5.53) or λ_A = 0.0393 (Eq. 5.54) instead of the standard λ_A = 0.0257 for the A phase in the zone builder.

This approach is clearly simpler than the explicit modelling of buoyancy airflow velocities, and is imminently more efficient, capable of automatically appropriating from the imported voxelised geometrical information all of the necessary metrics to compute Ra^* and by extension, $F_{C.N.}$, in only 2 seconds.

5.5.6.1.5: Forced Convection

Forced convection is modelled in this interpretation of the zonal approach as an exclusively intra-zonal phenomenon, taking place within the bulk air phase, $Z_\beta = O$, convecting heat away from the surface of the phases it is in contact with, $Z_\alpha = S$, A or P. Resistance to forced convection is therefore the reciprocal of the external heat transfer coefficient:

$$R_{ext,Z_\beta \to Z_\alpha,i} = \frac{1}{h_{ext,i}} \tag{5.59}$$

Where h_{ext} is the external heat transfer coefficient (W·m^{-2}·K^{-1}) which, as shown in section 5.3.2.1, is the representative proportionality constant of the convective impact of a certain airflow velocity and/or pattern. Set up in this fashion, it is possible for each zone with a bulk air phase to have a unique value of h_{ext}, as indicated by the subscript i, so that the impact of a specific airflow pattern on a bulk of fruit can be explored by linking the velocity through the zone with a certain level of external heat transfer; or a uniform external rate of heat transfer can be applied across the whole system by setting each h_{ext} to the same value. These concepts are explored in more detail during numerical (section 6.2) and experimental validation (section 6.3).

5.5.6.2: Inter-Zonal Properties

5.5.6.2.1: Heat Transfer Surface Area

The heat transfer surface area between zones is related to the geometry at the boundaries of each zone. Given that zone shape was simplified to cuboids, each zone can be connected to a maximum of 6 other zones (section 5.5.5). Heat transfers across zones are limited to conductive fluxes between the same phase (see Table 5.3) of which there are a maximum of 4 phases; therefore, the zone builder needs an automated routine to appropriate up to 24 intra-zonal conductive heat transfer surface areas per zone in the zonal network.

The voxelisation of the zonal geometry was exploited to build such a routine. Voxels at the edge of a zone are easily identifiable as the first or last row/column/aisle in the 3D voxel set, depending on which direction is being studied; therefore, counting the number of voxels at each applicable zonal boundary and multiplying the result by the surface area of one voxel in that particular direction gives the inter-zonal heat transfer surface area in a fast and automated fashion:

$$A_{eff_{cond,Z_\alpha \to Z_\alpha,ij}} = \sum \mathbb{v}_{boundary,ij} \times A_{\mathbb{v},j} \tag{5.60}$$

Where $\mathbb{v}_{boundary,ij}$ are the voxels at the boundary of zone i in the direction of zone j; and $A_{\mathbb{v}}$ is the area of a voxel in a particular direction: $A_{\mathbb{v},j} = dx \cdot dy$ if j = ↑ or ↓, $A_{\mathbb{v},j} = dx \cdot dz$ if j = ⊙ or ⊗, and $A_{\mathbb{v},j} = dy \cdot dz$ if j = → or ← (illustrated in Figure 5.35):

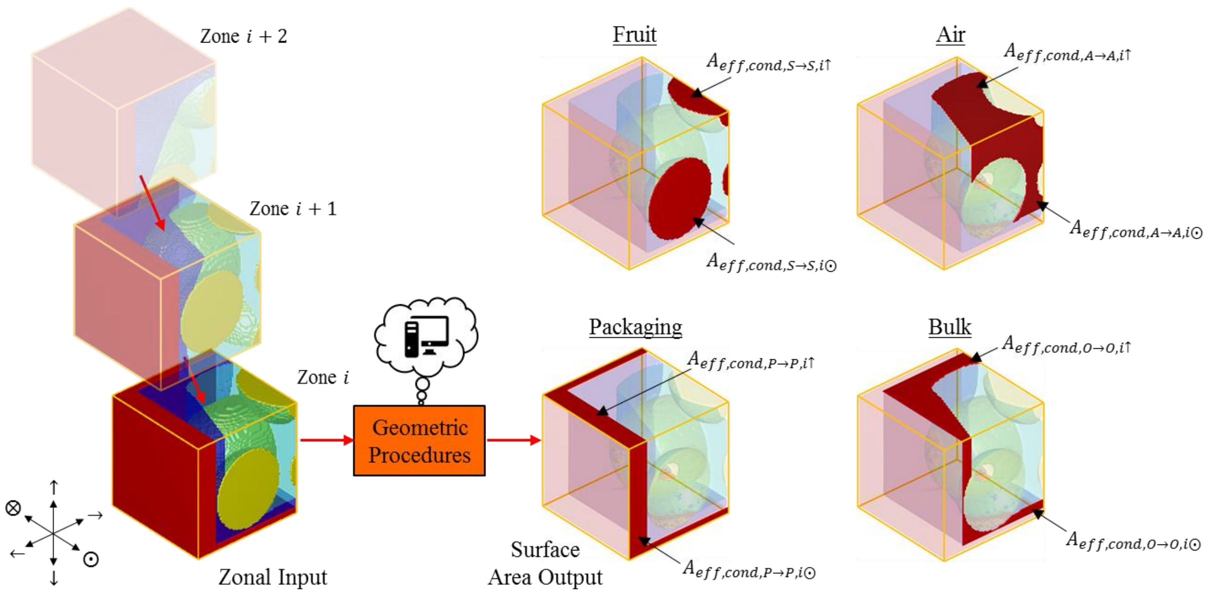

Figure 5.35: Geometric procedure for appropriating the inter-zonal heat transfer surface area between adjacent zones.

5.5.6.2.2: Conduction

Conduction between zones is done through solids phases, namely fruit and packaging. This section outlines the routine developed to appropriate the inter-zonal conductive resistances to heat transfer in these two phases, which lays the groundwork for descriptions of combinations of conduction and natural convection through the polyliner air.

Exchanges across zonal boundaries are restricted to the same phase – for example, fruit in one zone conducts heat to fruit in another zone, but fruit in one zone does not transfer heat to air in another zone – reducing $h_{eff_{n,Z_\alpha \to Z_\beta,ij}}$ (Eq. 5.23) to $h_{eff_{cond,Z,ij}}$.

Van der Sman's (2003) lumped-properties electrical analogue – as was made for an intra-zonal exchange (section 5.5.6.1.3) – is also made for a conductive inter-zonal exchange, Figure 5.36:

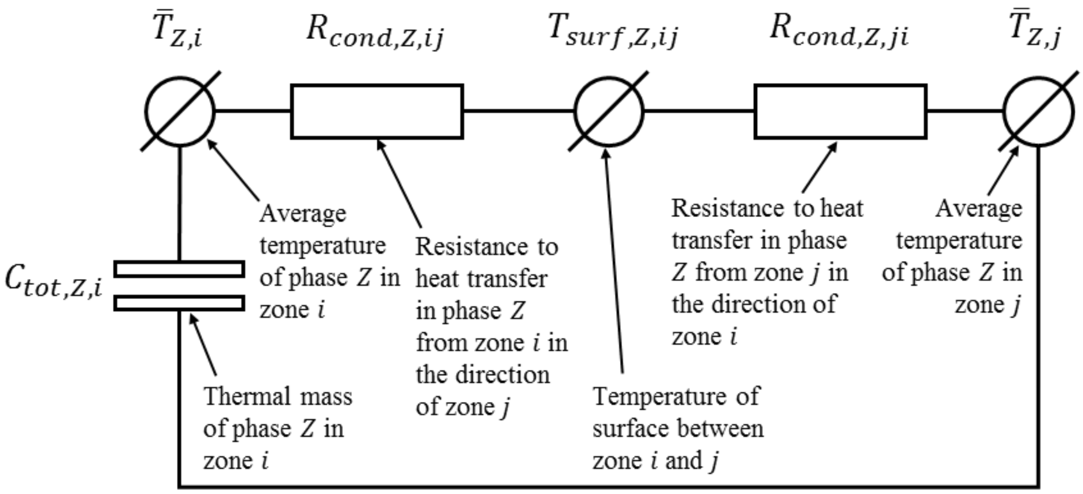

Figure 5.36: Electrical analogue for conduction heat transfer between adjacent zones using lumped properties. Image derived from van der Sman (2003)

Analogous to Eq. 5.40, the effective heat transfer coefficient for a conductive heat flux across zonal boundaries is:

$$h_{eff_{cond,Z,ij}} = \frac{1}{R_{cond,Z,ij} + R_{cond,Z,ji}} \tag{5.61}$$

Where $R_{cond,Z,ij}$ is the conductive resistance of phase Z inside of zone i in the direction of the adjacent zone j; and $R_{cond,Z,ji}$ the conductive resistance of phase Z inside of zone j in the direction of zone i.

The automated algorithm that was developed takes advantage of the voxelised nature of the geometry information to split a zone into slices perpendicular to each of the three directional axes (Figure 5.37). An unsteady-state heat transfer simulation can be performed on the collection of slices to investigate how heat flows through the geometry in each direction, and this information can be used to derive the resistance zonal properties.

The properties necessary to build the heat transfer simulation are the volume and heat transfer surface area per slice. These are trivially obtained by counting all voxels of the phase being investigated in each row/column/aisle in the 3D voxel set, depending on which direction is being studied:

$$A_{slice\ n} = \sum \mathbb{v}_{slice\ n,j} \times A_{\mathbb{v},j} \tag{5.62}$$

$$V_{slice\ n} = \sum \mathbb{v}_{slice\ n,j} \times (dx \cdot dy \cdot dz) \tag{5.63}$$

Where there is an N number of slices, of which specific slices are referred to as slice n; $A_{slice\ n}$ is the heat transfer surface area of slice n (m^2; $A_{\mathbb{v}}$ is the surface area of one voxel in the direction being studied, see section 5.5.6.2.1 and Figure 5.37a - c); $V_{slice\ n}$ is the volume of slice n (m^3); and $\mathbb{v}_{slice\ n,j}$ are the voxels in slice n perpendicular to the direction j (see Figure 5.20).

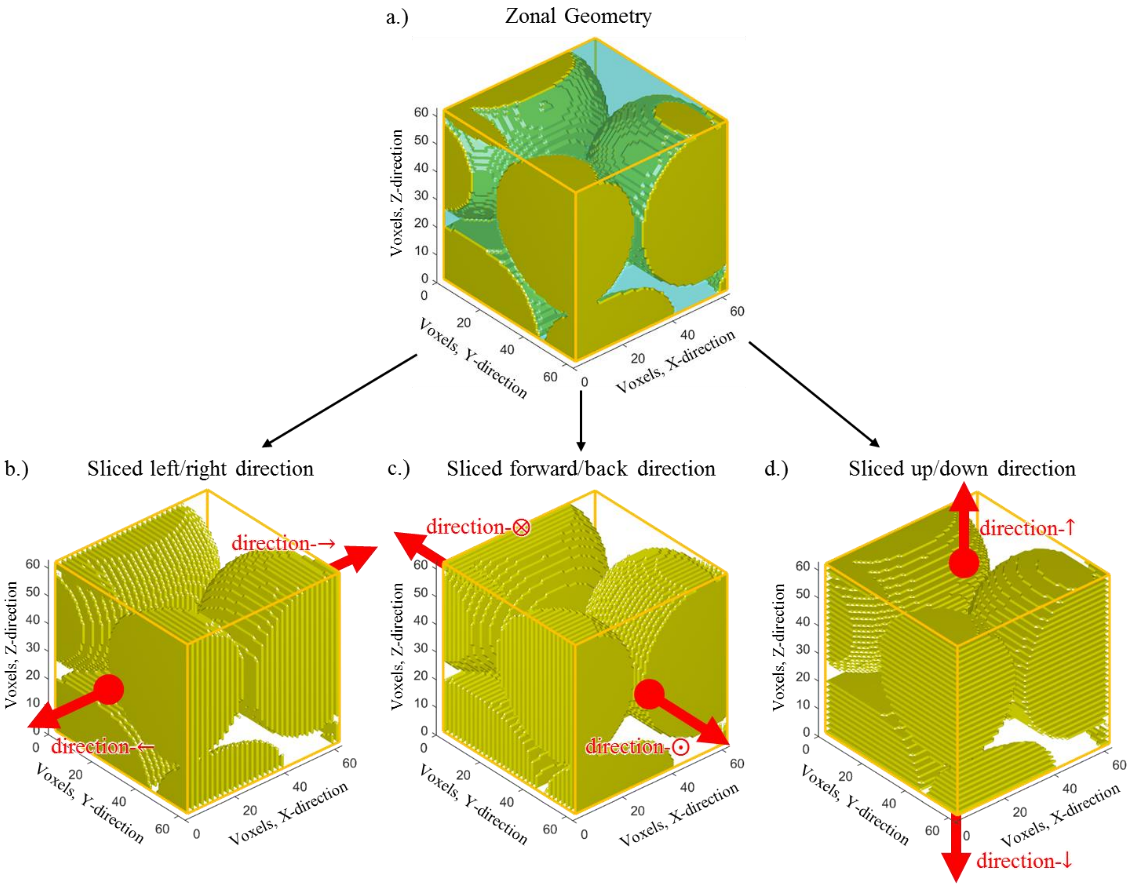

Figure 5.37: a.) original zonal geometry; fruit divided into slices perpendicular to the direction being investigated: b.) left/right direction; c.) forward/back direction; and d.) up/down direction.

Using Eq. 5.62 and Eq. 5.63 builds vectors of areas and volumes that describe the geometry inside of the zone along a single direction, of which there are 6 direction; for the hypothetical zone in Figure 5.37, the area per slice in each direction is presented in Figure 5.38 (given that voxels in this example are 1mm^3 cubes, the volume per slice follows the same shape but is 1×10^{-3} smaller). The ease through which heat can flow in a particular direction is impacted by the shape of these profiles, where regions with a higher area allow heat to flow more quickly and easily, whereas points of low area represent bottlenecks to heat transfer and will increase the conductive resistance of the zone as a whole. The position of high/low surface area changes the overall resistance, for example: if there is a bottleneck near the inter-zonal surface, then the rest of the zone is 'shielded' from the effects of heat transfer, and alternatively if a bottleneck appears on the opposite side of the zone then the entire zone has 'access' to the surface through which heat is being exchanged. These geometrical ramifications for heat transfer are able to be condensed into a single term for resistance through the following methodology:

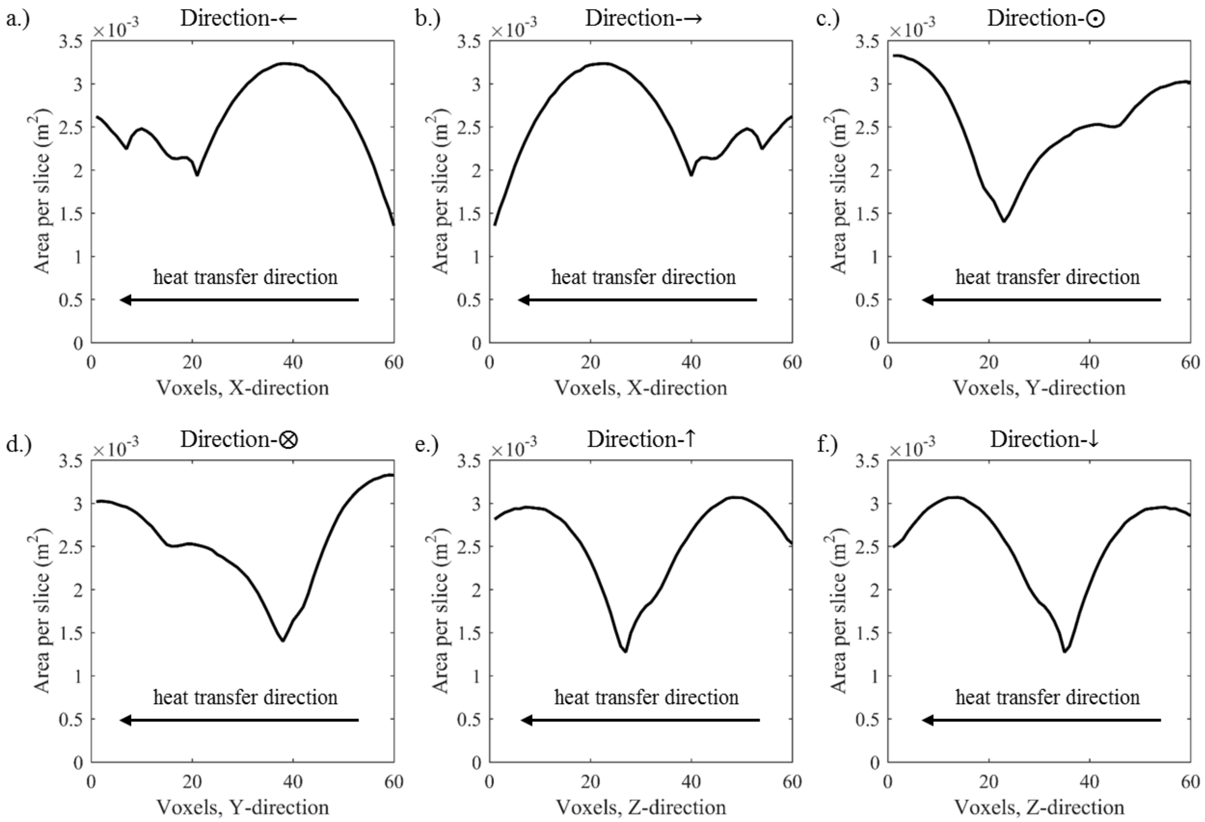

Figure 5.38: Area of slices in the direction of each of the 6 adjacent zones.

A heat transfer simulation through the slices is set up as follows: a slice n is connected to the slice in front of it, $n - 1$, and behind it, $n + 1$; with the exception of the first slice, slice 1, and the last slice, slice N. The conductive heat transfer proportionality constant is the thermal conductivity of the phase, λ_Z, divided by the thickness of the slice, d_{slice}, which in this approach is the thickness of a single voxel in the direction being studied (for direction-→ or direction-←, $d_{slice} = dx$; for direction-⊙ or direction-

⊗, d_{slice} = dy; and for direction-↑ or direction-↓, d_{slice} = dz; Figure 5.39). As the heat transfer in one direction is being investigated, heat entering a slice will come entirely from the slice behind it:

$$\phi_{in,slice\ n} = {}^{\lambda_Z}/_{d_{slice}} \cdot A_{slice} \cdot (T_{slice\ n+1} - T_{slice\ n}) \tag{5.64}$$

And heat exiting a slice will flow into the slice in front of it (Figure 5.39):

$$\phi_{out,slice\ n} = {}^{\lambda_Z}/_{d_{slice}} \cdot A_{slice} \cdot (T_{slice\ n-1} - T_{slice\ n}) \tag{5.65}$$

Combining Eq. 5.64 and Eq. 5.65:

$$\begin{gathered} \Delta\phi_{slice\ n} = \phi_{in,slice\ n} + \phi_{out,slice\ n} \\ = {}^{\lambda_Z}/_{d_{slice}} \cdot A_{slice} \cdot (T_{slice\ n-1} - 2T_{slice\ n} + T_{slice\ n+1}) \end{gathered} \tag{5.66}$$

Which is used to give the ODE for temperature change per slice:

$$\frac{dT_{slice\ n}}{dt} = \frac{{}^{\lambda_Z}/_{d_{slice}} \cdot A_{slice} \cdot (T_{slice\ n-1} - 2T_{slice\ n} + T_{slice\ n+1})}{V_{slice\ n} \cdot \rho_Z \cdot C_Z} \tag{5.67}$$

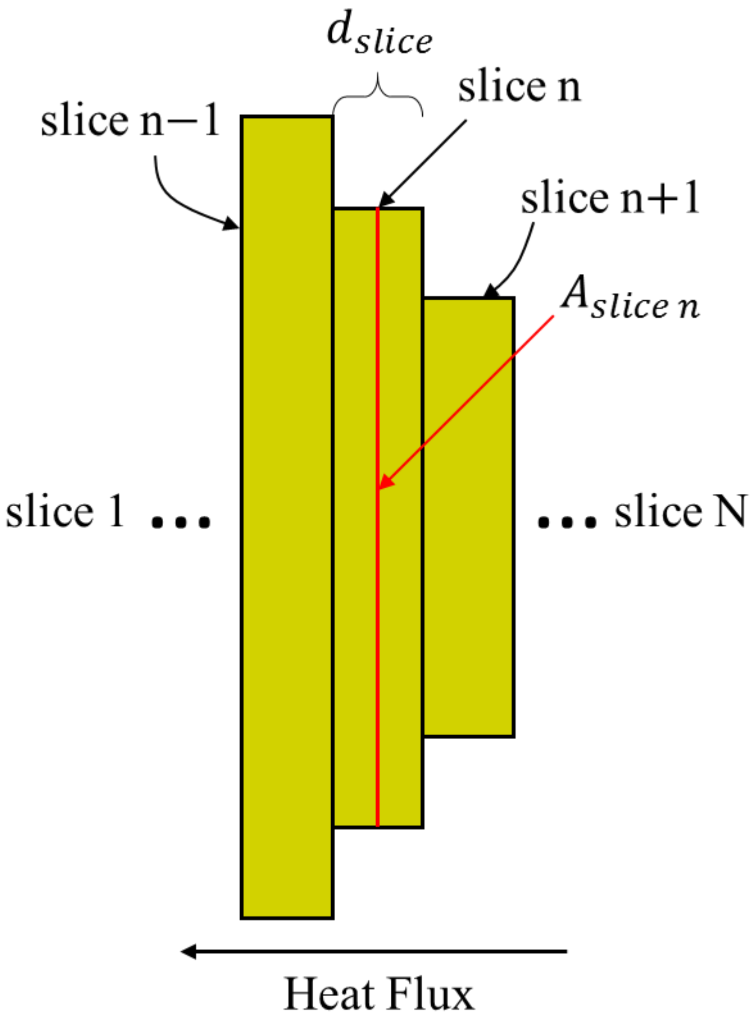

Figure 5.39: Linear slice heat flux simulation, where heat is transferred through slices n *via connectivity to slices in front and behind it, the rate controlled by the thickness of the slices,* d_{slice}*, and the heat transfer surface area,* $A_{slice\ n}$.

Additional boundary conditions are on the first and last slices: slice 1 is held at a constant temperature of T_{ref}:

$$T_{slice\ 1} = T_{ref} \tag{5.68}$$

$$\frac{dT_{slice\ 1}}{dt} = 0 \tag{5.69}$$

And slice N does not have a slice behind it:

$$\frac{dT_{slice\ N}}{dt} = \frac{{}^{\lambda_Z}/_{d_{slice}} \cdot A_{slice} \cdot (T_{slice\ N-1} - T_{slice\ N})}{V_{slice\ N} \cdot \rho_Z \cdot C_Z} \tag{5.70}$$

All slices (except the first) are set to an initial temperature of T_i:

$$T_{slice\ 2}, T_{slice\ 3}, \dots, T_{slice\ N-1}, T_{slice\ N} = T_i \tag{5.71}$$

This set of ODEs were solved numerically via the Runge-Kutta method (MATLAB function 'ode45') to predict the temperature change of each slice and, by extension, the entire zone. From this information, the resistance to heat transfer of the entire zone in a particular direction can be derived by rearranging Newton's law of cooling:

$$\frac{d\bar{T}_Z}{dt} = \frac{\frac{1}{R_{cond,Z,ij}} \cdot A_{eff\,cond,Z_\alpha \to Z_\alpha,ij} \cdot \left(T_{ref} - \bar{T}_Z\right)}{V_{Z,i} \cdot \rho_Z \cdot C_Z} \tag{5.72}$$

$$R_{cond,Z,ij} = \frac{A_{eff\,cond,Z_\alpha \to Z_\alpha,ij} \cdot \left(T_{ref} - \bar{T}_Z\right) \cdot dt}{V_{Z,i} \cdot \rho_Z \cdot C_Z \cdot d\bar{T}_Z} \tag{5.73}$$

Where $\bar{T}_Z$ is the volume average temperature of the entire phase Z inside of zone i, derived from the temperatures and volumes of each slice (ºC); $A_{eff\,cond,Z_\alpha \to Z_\alpha,ij}$ is the inter-zonal heat transfer surface area between zone i and j (calculated previously in section 5.5.6.2.1; m^2); $V_{Z,i}$ is the volume of phase Z inside of the zone (calculated previously in section 5.5.6.1.1; m^3); and $R_{cond,Z,ij}$ is the 'volume averaged' resistance to heat transfer in the direction of zone j ($m^2 \cdot ºC \cdot W^{-1}$).

This process is applied to the zone of Figure 5.37 with results presented in Figure 5.40 for direction-←. For the example, T_i = 20 ºC and T_{ref} = 0 ºC were used (however these numbers are arbitrary and the same $R_{cond,Z,ij}$ can be derived for any combination, as long as $T_i \neq T_{ref}$). Figure 5.40c shows the predicted temperature change of each slice in blue, and the volume average temperature of the entire zone is presented as the dashed red line. This volume average temperature profile was used in Eq. 5.73 to compute the lumped resistance of zone i in the direction of zone j, $R_{cond,Z,ij}$. Because the temperature profile was numerically determined, $d\bar{T}_Z(t) = \bar{T}_Z(t+1) - \bar{T}_Z(t)$ and $dt = (t+1) - t$. The resulting lumped resistance is presented in Figure 5.40d. The resistance is low at the beginning of the simulation as the first slices are the only ones that are exchanging heat (as evidenced by the large amount of lagging slices that can be seen in Figure 5.40c); but as time progressed the remainder of the slices began to cool and the resistance of the zone tends towards a constant value. This constant resistance value is the lumped resistance chosen as representative of the zone as a whole in the direction that is being studied, and is stored in the $\mathbb{P}_{ij}$ vector.

For the remaining 5 directions, this process is repeated; and the process is continually repeated for all zones in the zonal network and for all applicable phases, until the full set of inter-zonal conductive resistances is compiled. The process was fully automated and was very flexible to changes such as a new geometry or different zonal network resolution; and computationally efficient, only ~0.5 seconds per direction.

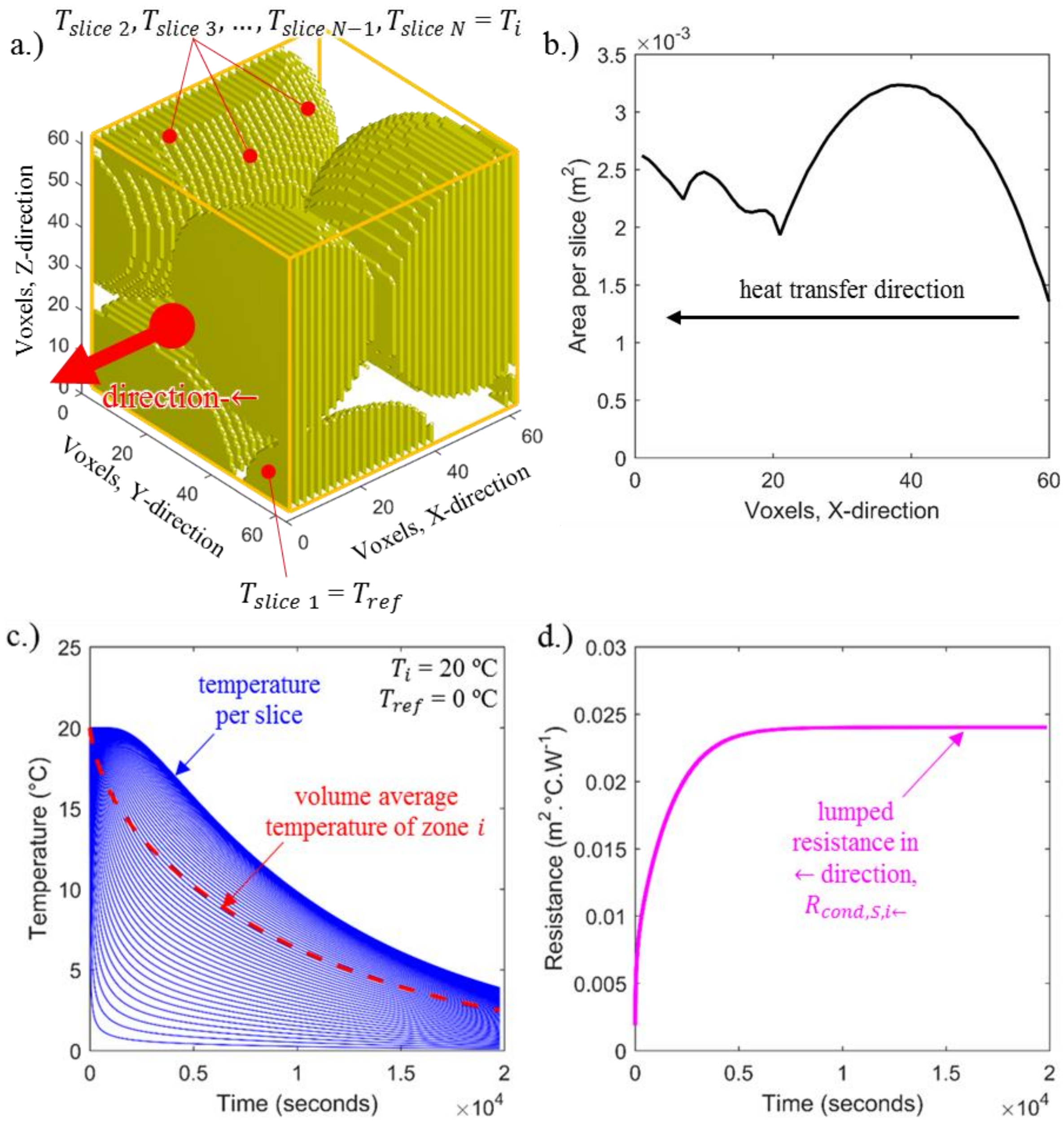

*Figure 5.40: Example of the linear slice heat transfer geometric procedure. A.) the geometry is divided into slices perpendicular to the left direction (*j *=←); b.) the area of each slice in the direction-←; c.) predicted temperatures of all slices (solid blue lines) and the volume average temperature of zone* i *(dashed red line); d.) the derived resistance of zone* i *to conductive heat transfer through the fruit in the direction-←.*

A special case was a so called 'pinch' scenario, where there were at least one or more slices that had zero area and volume. This was not an issue if this occurred at the beginning or end of the zone – at the beginning, there is an infinite resistance between zone i in the direction of zone j and no heat transfer occurs; and at the end, the zone is essentially shortened by the number of slices that do not have a size.

However, it becomes a problem when a ‘pinch’ occurs somewhere in the centre of the zone; for example, Figure 5.41:

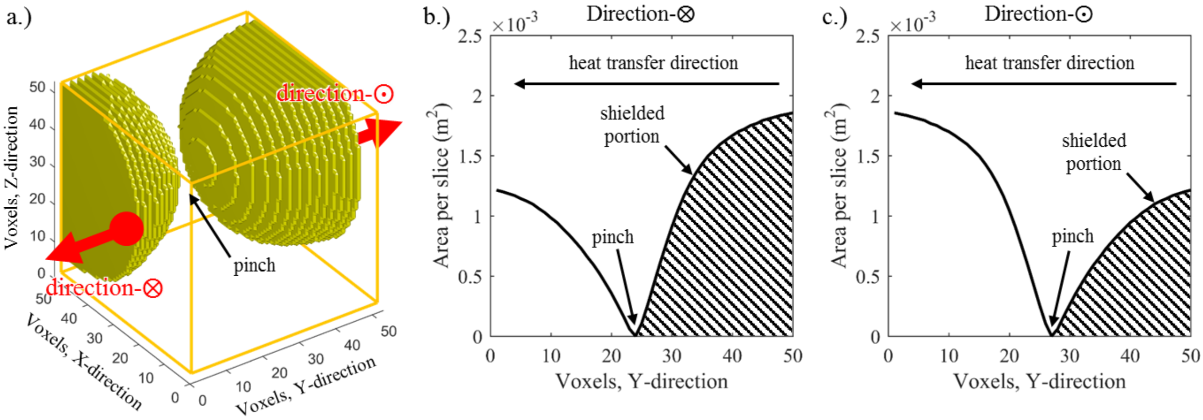

Figure 5.41: A scenario where a ‘pinch’ occurs within a zone, where in a given direction there is a region with zero area, limiting heat transfer access through the entire zone; the shielded portion of the zone is shaded.

In this example, a pinch occurs in approximately the centre of the zone, preventing any heat from flowing from the region highlighted as the ‘shielded portion’. This causes issues with how the resistance is calculated according to Eq. 5.73, as is demonstrated in Figure 5.42 which presents the linear slice heat transfer simulation of Figure 5.41:

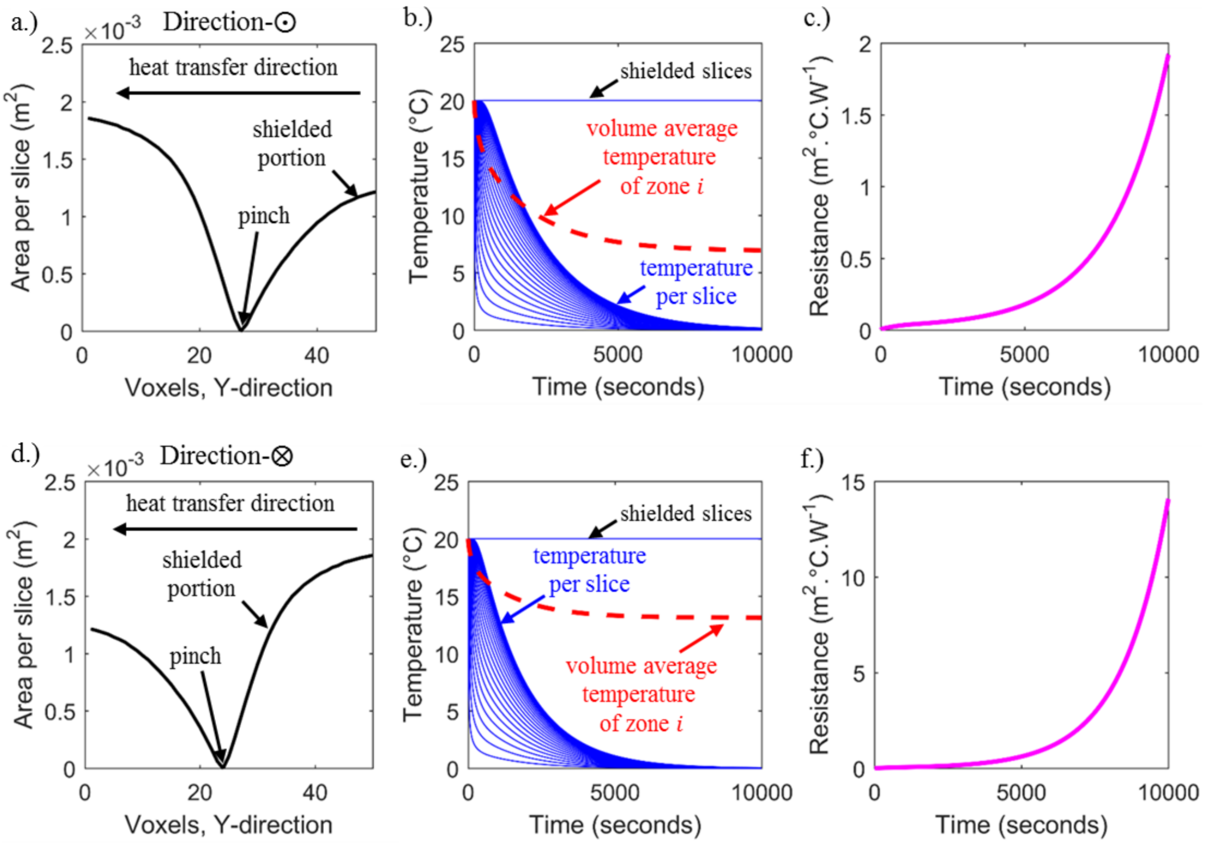

Figure 5.42: Example of how the liner slice heat transfer geometric procedure fails when a 'pinch' occurs, resulting in no tendency toward a constant heat transfer resistance.

The pinch distorts the volume average temperature of the zone, forcing it to tend toward a temperature well above T_{ref} = 0 °C. As a consequence, the resistance (according to Eq. 5.73) does not tend towards a constant value. To account for this, the code for this geometric procedure was amended to recognise a pinch and made adjustments to the slice area and volume vectors before passing them through to the heat transfer simulation. The first slice which has zero volume and area is identified as the pinch position, and all slices after this position – the slices in the 'shielded portion' – are set to 0 area and volume. When using Eq. 5.73 to determine the resistance, the volume of zone i is not that of the whole zone as computed in section 5.5.6.1.1, but of only the portion before the pinch position.

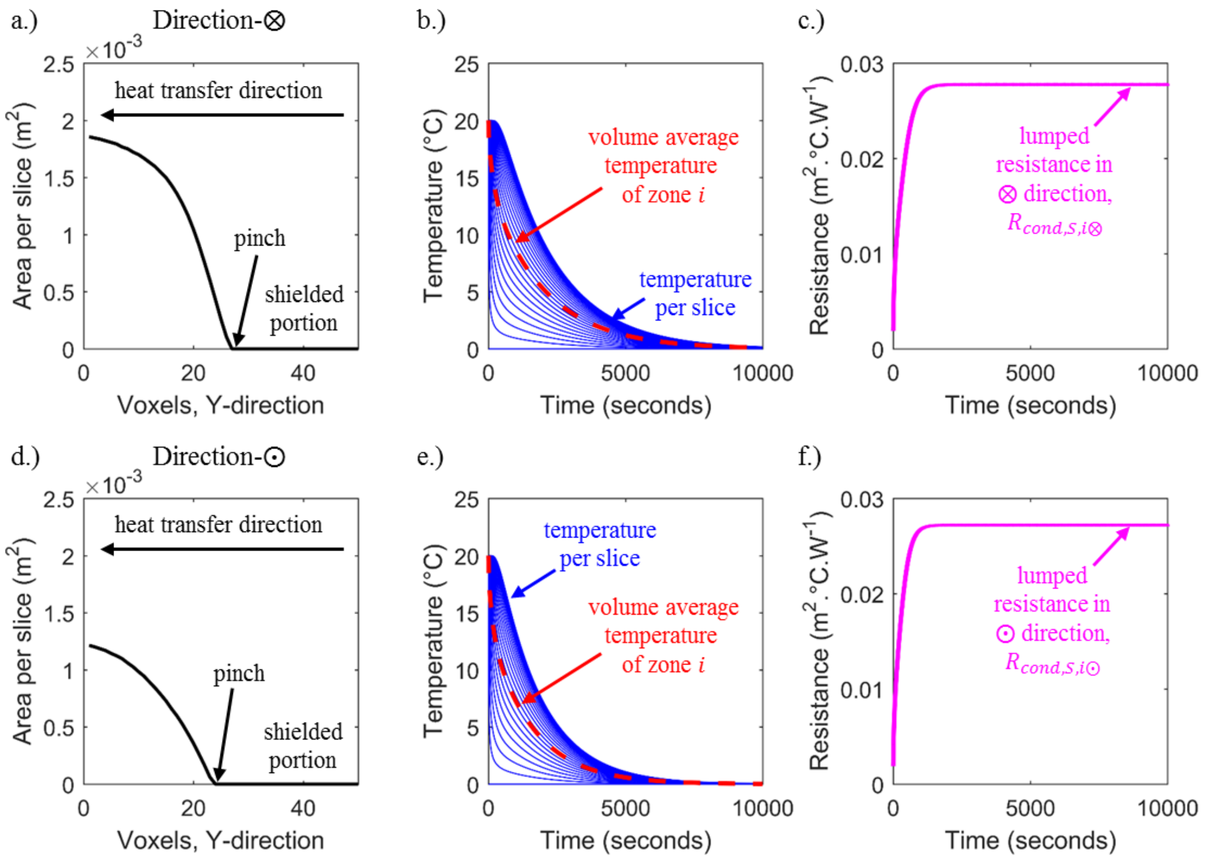

Figure 5.43: The solution to the pinch problem: the shielded portion must be excluded from the simulation in order to derive a representative conductive heat transfer resistance.

5.5.6.2.3: Natural Convection

A combination of conduction and natural convection occurs exclusively in the polyliner air phase, $Z = A$. The same linear slice geometric procedure of section 5.5.6.2.2 is used in this phase, however the thermal conductivity of the slices is $\lambda_{A,eff} = \lambda_A \cdot F_{N.C.}$, where λ_A is the thermal conductivity of stagnant air and $F_{N.C.}$ is the natural convection correction factor, derived in section 5.5.6.1.4.

5.5.6.2.4: Airflow

As discussed previously in section 5.5.6.1.5, the cooling impact of airflow is restricted to an intra-zonal phenomenon and is driven entirely by airflow velocity per zone information (see section 6.3.2); this is due to the decision to focus on developing a simplified heat transfer model. If an equivalently simplified airflow model is to be developed independently, it would require a variety of inter-zonal properties to be sufficiently predictive, especially at the pallet scale where airflow is exchanged between individual packages. Some brief comments on the nature of this information and how to appropriate it in a zonal model framework is given here:

The most important inter-zonal property pertaining to airflow is the volumetric flowrate of air between zones. This information is key to determining the rate of energy transfer through the air as it is pulled from the front to the back of the pallet. Air that enters the system at the refrigeration temperature warms as it absorbs heat from the hot fruit; this elevated air temperature moves into the box behind it, where the temperature gradient between the fruit and air is significantly smaller, resulting in a decelerated rate of cooling; and this trend continues, so that typically the boxes at the back of the pallet cool at the slowest rate (O'Sullivan *et al.*, 2016). In a similar vein, new packaging features such as a different number, size or distribution of vents may promote cross-linkages of airflow on the pallet scale, so that even if boxes near the rear of the pallet receive warmer air, this phenomenon is counter-acted by a degree of by-pass cold air, promoting a more equitable pallet scale cooling profile. It is suggested that an expression similar to the following be used to track the energy exchanges inside of the bulk air in each applicable zone:

$$\phi_{ij,1} = \left(\dot{Q}_{ji} \cdot \rho_A \cdot C_A \cdot \bar{T}_{O,j}\right) - \left(\dot{Q}_{ij} \cdot \rho_A \cdot C_A \cdot \bar{T}_{O,i}\right) \tag{5.74}$$

Eq. 5.74 being based on an energy balance through a finite volume (Datta *et al.*, 2007), where $\dot{Q}_{ji}$ is the volumetric flowrate of air into zone i from adjacent zones j ($m^3 \cdot s^{-1}$), $\dot{Q}_{ij}$ is the volumetric flowrate out of zone i to adjacent zones j ($m^3 \cdot s^{-1}$), and $\bar{T}_{O,j}$ and $\bar{T}_{O,i}$ is the temperature of the air entering and exiting the zone, respectively. To utilise this equation in a solver requires the prediction of the full set of $\dot{Q}_{ij}$; it is suggested that this could be accomplished quickly and simply through the use of a resistance network (Smale, 2004). Adapting a resistance network to a zonal framework represents a significant challenge, where geometric procedures will need to be developed that are capable of converting vent and bulk air phase geometries into representative friction factors, so that a global set of $\dot{Q}_{ij}$ values can be iteratively appropriated.

5.5.7: Zone Solver

This zonal model was designed to have a 'pre-processing' stage, where the model is voxelised (section 5.5.4), zoned (section 5.5.5) and converted into intra- and inter-zonal properties via the zone builder program (section 5.5.6). These processes only need to be executed once for a given geometry or zonal resolution, and the set of stored $\mathbb{P}_{ii}$ and $\mathbb{P}_{ij}$ are used as inputs to predict the flow of heat through the zonal network. The numerical integration is done with a separate program, the 'zone solver'.

The zone solver uses the generalised ODE for temperature change, Eq. 5.18, to predict the cooling rate through the fruit, packaging and air phases (the bulk air phase is held at a constant temperature, T_{ref}; see section 6.3.5) in each zone. For fruit, the temperature change ODE is:

$$\frac{d\bar{T}_{S,i}}{dt} = \frac{\overbrace{[\phi_{ii,1} + \phi_{ii,2} + \phi_{ii,6}]}^{intra-zonal} + \overbrace{\sum_{j=1}^{6} \phi_{ij,3}}^{inter-zonal}}{\underbrace{V_{S,i} \cdot C_S \cdot \rho_S}_{thermal\ mass}} \tag{5.75}$$

Where the fluxes $\phi_{ii,k}$ and $\phi_{ij,k}$ are from Table 5.2 and Table 5.3; and the intra-zonal exchanges are:

$$\phi_{ii,1} = h_{eff_{conv,S\to A,i}} \cdot A_{eff_{cond,S\to A,i}} \cdot \left(\bar{T}_{A,i} - \bar{T}_{S,i}\right) \tag{5.76}$$

$$\phi_{ii,2} = h_{eff_{ext,S\to O,i}} \cdot A_{eff_{cond,S\to O,i}} \cdot \left(T_{ref} - \bar{T}_{S,i}\right) \tag{5.77}$$

$$\phi_{ii,6} = h_{eff_{cond,S\to P,i}} \cdot A_{eff_{cond,S\to P,i}} \cdot \left(\bar{T}_{P,i} - \bar{T}_{S,i}\right) \tag{5.78}$$

And the inter-zonal exchange:

$$\phi_{ij,3} = h_{eff_{cond,S,ij}} \cdot A_{eff_{cond,S,ij}} \cdot \left(\bar{T}_{S,j} - \bar{T}_{S,i}\right)$$

Which are specific forms of the generalised heat flux equation, Eq. 5.19. The properties h_{eff} and A_{eff} are given by the geometric procedures (section 5.5.6) and are stored in the $\mathbb{P}_{ii}$ and $\mathbb{P}_{ij}$ vectors. For the inter-zonal exchange, a sum over 6 is performed, as there are 6 possible adjacent zones, and the directional tag for zone j is replaced by numerals: ← = 1, → = 2, ⊗ = 3, ⊙ = 4, ↑ = 5 and ↓ = 6. For the air phase, the ODE for temperature change is:

$$\frac{d\bar{T}_{A,i}}{dt} = \frac{\left[-\phi_{ii,1} + \phi_{ii,3} + \phi_{ii,4}\right] + \sum_{j=1}^{6} \phi_{ij,2}}{V_{A,i} \cdot C_A \cdot \rho_A} \tag{5.79}$$

Where the intra-zonal exchanges are:

$$\phi_{ii,3} = h_{eff_{conv,A\rightarrow P,i}} \cdot A_{eff_{cond,A\rightarrow P,i}} \cdot \left(\bar{T}_{P,i} - \bar{T}_{A,i}\right) \tag{5.80}$$

$$\phi_{ii,4} = h_{eff_{ext,A\rightarrow O,i}} \cdot A_{eff_{cond,A\rightarrow O,i}} \cdot \left(T_{ref} - \bar{T}_{A,i}\right) \tag{5.81}$$

And the inter-zonal exchange:

$$\phi_{ij,2} = h_{eff_{cond,A,ij}} \cdot A_{eff_{cond,A,ij}} \cdot \left(\bar{T}_{A,j} - \bar{T}_{A,i}\right) \tag{5.82}$$

And for the packaging phase:

$$\frac{d\bar{T}_{P,i}}{dt} = \frac{\left[-\phi_{ii,3} + \phi_{ii,5} - \phi_{ii,6}\right] + \sum_{j=1}^{6} \phi_{ij,4}}{V_{P,i} \cdot C_P \cdot \rho_P} \tag{5.83}$$

Where the intra-zonal exchange is:

$$\phi_{ii,5} = h_{eff_{ext,P\rightarrow O,i}} \cdot A_{eff_{cond,P\rightarrow O,i}} \cdot \left(T_{ref} - \bar{T}_{P,i}\right) \tag{5.84}$$

And the inter-zonal exchange is:

$$\phi_{ij,4} = h_{eff_{cond,P,ij}} \cdot A_{eff_{cond,P,ij}} \cdot \left(\bar{T}_{P,j} - \bar{T}_{P,i}\right) \tag{5.85}$$

The zone solver numerically integrates Eq. 5.75, Eq. 5.79 and Eq. 5.83 using the MATLAB function ‘ode15s’ – this solver performed significantly more efficiently than ode45 which is used previously as it can handle stiff differential equations easier – with inputs pertaining to the initial temperature, T_i, starting time, t_0, and finishing time, t_f. Starting at time t = 0 and zone i = 1 (according to the Coordinate Matrix, section 5.5.5 and Eq. 5.20), the zone solver predicts the heat transfer in, out and inside of the phases of the zone. It then advances to the next zone, zone i = 2, and the process is repeated. This continues until i = N_{total}, where N_{total} is the number of zones in the network. The predicted temperature change is applied across the zonal network over a small time step, Δt, and the 'ode15s' function advances time to $t = t + \Delta t$ and the process is repeated. This continues until $t = t_f$.

An example of the zone solver in action is provided in Figure 5.44. The cooling rate through a geometry with 100 zones, external heat transfer conditions of h_{ext} = 5 W·m^{-2}·K^{-1}, initial temperature of T_i = 20 ºC and refrigeration temperature of T_{ref} = 0 ºC (see section 6.3.5 for more details) was solved over 20 hours of simulated cooling time:

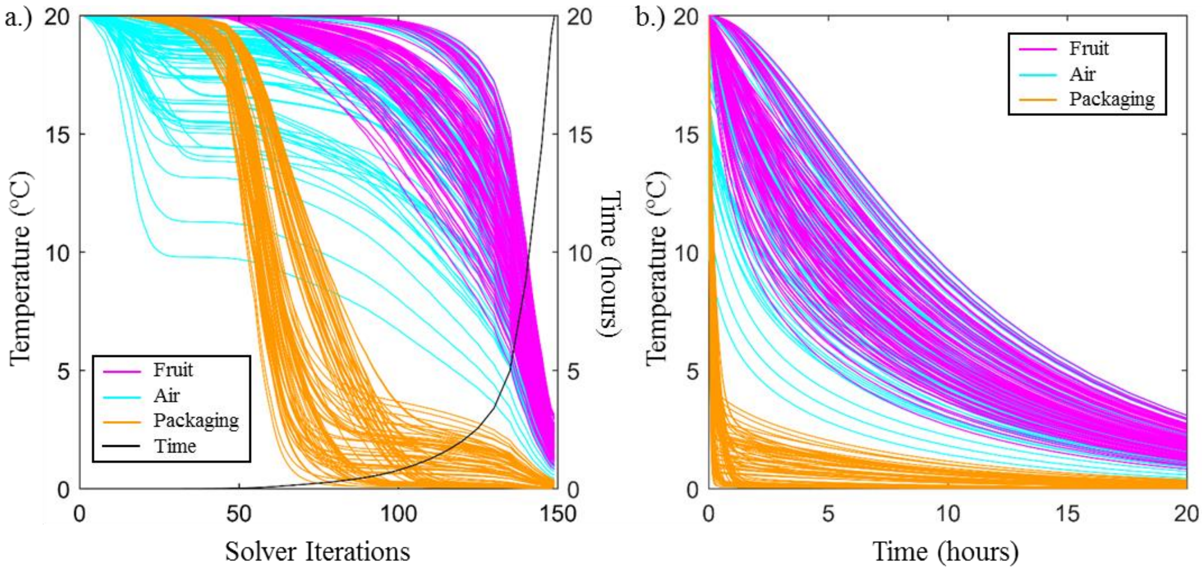

Figure 5.44: The zone solver, applied to a geometry divided into 100 zones: a.) temperature and time versus solver iterations, and; b.) predicted time-temperature curve. Each line represents an individual zone, and colours represent phases (magenta for fruit, cyan for air and orange for packaging).

Figure 5.44a shows results from the zone solver in terms of solver iterations, where each line represents a different zone and colours represent different phases. As it numerically integrates Eq. 5.75, Eq. 5.79 and Eq. 5.83 for each of the 100 zones, a very small time step is chosen at the onset of the simulation, signified by the black line representing the cooling time at each solver iteration. Rapid changes in temperature inside some air zones at the surface of the polyliner before equilibrating with adjacent fruit zones (due to the low thermal mass of the air phase) requires a very small time step to properly account for this stiffness – which is similarly so for the packaging phase, which also has a low thermal mass.

When the network reaches equilibrium and there are less aberrations detected in temperature changes per iteration, the time step is increased to save on computational overhead; in this example, it took approximately 50 solver iterations for the network to reach equilibrium, which is only 0.01 hours of cooling time. The solver continues until $t = t_f$, resulting in Figure 5.44b, the practical output of the zonal modelling approach: predicted temperatures of each zone and phase over time.

The zone solver was exceptionally fast: the example given in this section (a single box geometry with 100 zones; see section 6.3.5) took under 1 second with an Intel® i7-4770 and 16GB of RAM, a significant advantage over DNS (section 5.3) from a computational efficiency perspective with solution times that ranged from 0.5-12 hours, depending on which mechanisms were included.

5.5.8: Overall Model Structure

The computational structure of this new interpretation of a zonal model described thus far is as follows (Figure 5.45):

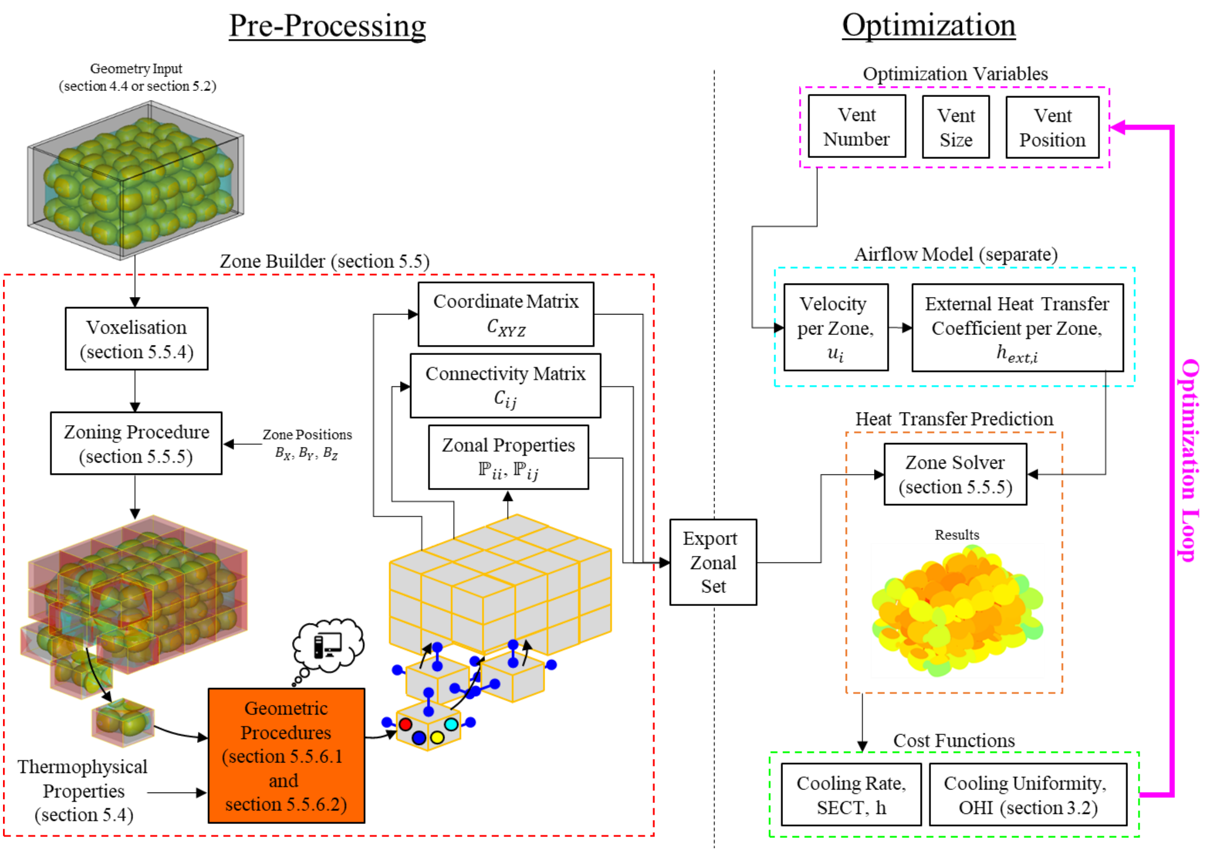

Figure 5.45: The computational structure of this new interpretation of the zonal modelling approach

The model was structured so that there was a significantly larger and more computationally intensive pre-processing step. Calculations done in this part include voxelisation of the input geometry (section 5.5.4), dividing the geometry into zones (section 5.5.5), and converting the voxelised zonal set into a set of representative zonal properties via the geometric procedures (section 5.5.6.1 and section 5.5.6.2), which is exported from the zone builder upon completion. This process, depending on the number of zones, can take 10-20 minutes to complete – however, the data exported from the zone builder at this stage represents R_{int}, the internal resistance to heat transfer (from Figure 1.8 in section 1.2.5.1), one half of the overall heat transfer equation. This being a function of the bulk fruit, polyliner and packaging geometry, as well as the thermophysical properties which are model inputs, this information **only needs to be appropriated once** for a given input geometry.

In the second step, the zone solver uses the outputs from the zone builder and combines it with information about the airflow pathway, which represents h_{ext} (see Figure 1.8 in section 1.2.5.1), the remaining half of the overall heat transfer equation, and is being worked on separately to this thesis, to predict the local and global temperature profile. This process is very computationally efficient, taking under 1 second to produce a result for approximately 100 zones (see section 5.5.7). An optimization loop is therefore possible with the model structured in this manner, with most of the computational overhead shifted into the pre-processing stage to vastly accelerate the speed of each iteration. While the heat transfer solution portion of the optimization loop is satisfactorily expeditious, the speed of the overall loop is still also dependent on the efficiency of the airflow model – this is explored later in section 7.3.1.

5.6: Conclusions

In conclusion, a new interpretation of the zonal modelling approach was developed. In line with this thesis' goals, the model was **fast**, with heat transfer solution times on the order of 1-2 seconds; **flexible**, as the computational subroutines called 'geometric procedures' were designed to be universal, allowing a wide variety of bulk fruit shapes to be valid model inputs; and **automated**, as the 'zone builder' pre-processing step was capable of algorithmically generating the zonal network without manual intervention or decisions. These three features combined make this modelling approach a potentially universal model for heat transfer problems in horticulture, greatly accelerating the rate at which modelling can be used to solve real-world problems. The efficacy of the geometric procedures, the ability for the zone builder to construct the zonal network and the accuracy of the solution produced by the zone solver are all explored later in chapter 6.

Chapter 6

Model Validation

6.1: Introduction

A fast, flexible and automated (i.e. algorithmically generated/configured) heat transfer model was developed in chapter 5. In this section, the model and the assumptions used to construct it are validated, both numerically and experimentally. In section 6.2, the average voxel distance calculator (AVDC) is tested against a variety of objects; and a single box scale zonal network is validated against an equivalent Direct Numerical Simulation geometry under the same simplified cooling conditions to confirm the validity of the other geometric procedures. Finally, in section 6.3 the zonal model is compared at the single box scale to experimental measurements taken in chapter 3; where in lieu of a simplified airflow model, Computational Fluid Dynamics was used to provide airflow velocity information.

6.2: Numerical Validation

6.2.1: Introduction

The geometric procedures developed in section 5.5.5.6 – such as the AVDC, porous media modified Rayleigh number correction of fluid conductivity, and the linear slice inter-zonal resistance procedure – were designed to quickly and automatically construct a zonal model from a given geometry input (which may have also been automatically generated, see section 4.4). Speed, flexibility and automation concerns meant that accuracy was a necessary sacrifice, however the degree to how much additional error has been introduced has not been determined. Therefore, the zonal approach and its associated geometric procedures are tested against a more direct and detailed modelling methodology, namely a DNS scheme.

6.2.2: Validation of Intra-Zonal Geometric Procedures

A seminal element of the zonal models pre-calculation phase is the geometric procedures of section 5.5.5.6, a series of computational operations that were designed to convert individual zones into a small set of zonal properties in an automated fashion. Though parts of the intra-zonal geometric procedures were validated to some extent for simple objects (see section 5.5.6.1.3), it is pertinent to further test the universality of the techniques developed and to demonstrate that a simplified lumped approach can perform similarly to more detailed modelling methodologies, such as DNS schemes, when predicting the rate of heat transfer.

The geometric procedures were validated by applying them to a wide variety of input shapes and then using the small set of derived lumped properties to predict the time-temperature curve. The predicted cooling rate was then compared to a finite element model with an equivalent geometry, thermal properties and external cooling conditions. Each scenario represented a one phase system, with conduction heat transfer within the interior of the object, and convective cooling on the surface of the object. In accordance with Figures 5.25, the lumped approach can be described as an electrical analogue in Figure 6.1:

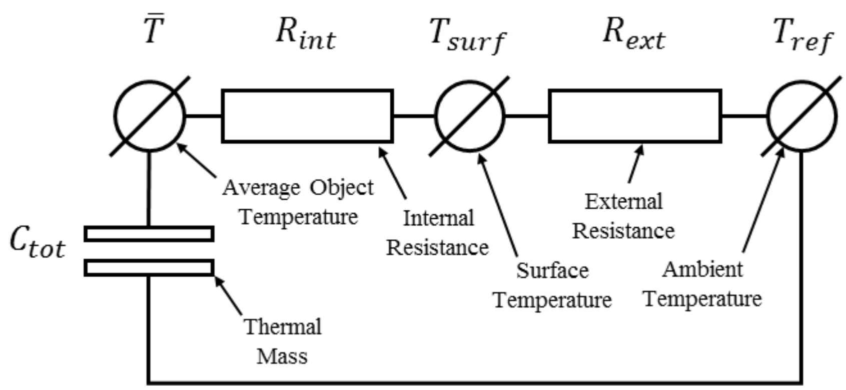

Figure 6.1: Electrical analogue for heat transfer between an object and refrigerated airflow using lumped properties. Image derived from van der Sman (2003).

The generalised ODE for the volume average temperature change – a simplified form of Eq. 5.18 – for the lumped approach is (derived from Figure 6.1):

$$\frac{d\bar{T}}{dt} = \frac{h_{eff} \cdot A \cdot (\bar{T} - T_{ref})}{C_{tot}} \tag{6.1}$$

Where $\bar{T}$ is the volume average temperature of the object (K); T_{ref} is the refrigeration (ambient) temperature (K); A is the heat transfer surface area (m^2); h_{eff} is the effective heat transfer coefficient ($W \cdot m^{-2} \cdot K^{-1}$); and C_{tot} is the thermal mass of the object ($J \cdot K^{-1}$). The effective heat transfer coefficient is the reciprocal sum of the internal and external resistances:

$$h_{eff} = \frac{1}{R_{int} + R_{ext}} \tag{6.2}$$

Where R_{int} is the internal resistance to conductive heat transfer ($m^2 \cdot K \cdot W^{-1}$); and R_{ext} is the external resistance to convective heat transfer ($m^2 \cdot K \cdot W^{-1}$). Defined previously in section 5.5.6.1.3, the internal resistance in the lumped approach is defined as:

$$R_{int} = \frac{\overline{d_{m\imath n}}}{\lambda} \tag{6.3}$$

Where $\overline{d_{m\imath n}}$ is the product of the AVDC (m), and is the average path of least resistance; and λ is the thermal conductivity of the object ($W \cdot m^{-1} \cdot K^{-1}$). The external resistance is the reciprocal of the external heat transfer coefficient:

$$R_{ext} = \frac{1}{h_{ext}} \tag{6.4}$$

Where h_{ext} is the external heat transfer coefficient ($W \cdot m^{-2} \cdot K^{-1}$), which as described in section 5.5.6.1.5, is used to describe the aggregate effect of a particular airflow velocity and pattern. The thermal mass is:

$$C_{tot} = M \cdot C \tag{6.5}$$

Where M is the mass (kg); and C is the specific heat capacity (J·kg^{-1}·K^{-1}). Mass can also be determined by the volume:

$$M = V \cdot \rho \tag{6.6}$$

Where V is the volume of the object (m^3), and ρ the density (kg·m^{-3}). Thus, expanding Eq. 6.1 gives:

$$\frac{d\bar{T}}{dt} = \frac{\dfrac{1}{\dfrac{\overline{d_{min}}}{\lambda} + \dfrac{1}{h_{ext}}} \cdot A \cdot \left(\bar{T} - T_{ref}\right)}{V \cdot \rho \cdot C} \tag{6.7}$$

Examining Eq. 6.7, the hypothesis to be tested in this section is that the geometric information of any object can be condensed into just three lumped properties: the volume (V), heat transfer surface area (A) and average path of least resistance ($\overline{d_{min}}$). These are computed expeditiously and automatically by the geometric procedures using methods outlined in sections 5.5.6.1.1, 5.5.6.1.2 and 5.5.6.1.3, respectively; and assume that the input object has been voxelised, which is also a fast and automated procedure (section 5.5.4). These coupled with the material properties – the specific heat capacity (C), thermal conductivity (λ) and density (ρ) – as well as external cooling conditions – the refrigeration temperature (T_{ref}) and external heat transfer coefficient (h_{ext}) – and initial conditions – initial temperature (T_i) – allows Eq. 6.7 to be solved. Numerical integration of Eq. 6.7 was performed using a Runge-Kutta method implemented in MATLAB as the 'ode45' function.

The resulting time-temperature profiles for the lumped approach (Eq. 6.7) are compared with the finite element approach with the same geometry and external cooling conditions, modelled using COMSOL Multiphysics (version 5.2). Each object is meshed with a high resolution of tetrahedral finite elements. Conduction within the object is modelled as:

$$\rho \cdot C \cdot \frac{\partial T}{\partial t} = \nabla(\lambda \cdot \nabla T) \tag{6.8}$$

Where ∇ the vector differential operator. External cooling was imposed as a Robin boundary condition (Mercier *et al*, 2017a):

$$-\lambda\nabla T \cdot \boldsymbol{n} = h_{ext} \cdot \left(T - T_{ref}\right) \text{ (at boundary } \Omega) \tag{6.9}$$

Where $\boldsymbol{n}$ is the normal vector and Ω is the entire external surface of the object.

All objects were given the same thermal properties as a kiwifruit – λ = 0.542, C = 3713 and ρ = 1037 (see section 5.4). Every scenario had an initial temperature of T_i = 20°C and a refrigeration temperature of T_{ref} = 0°C. To demonstrate the flexibility and automation of the lumped approach, each predicted lumped temperature profile used the exact same MATLAB code, with the exception that a different shaped object was imported at the beginning of the script.

The first set of objects were simple regular shapes (spheres, cubes, finite cylinders and cones; Figure 6.2a - d, respectively). Each scenario had the same external cooling conditions of h_{ext} = 10 W·m^{-2}·K^{-1}, while the size of the objects was changed so that the accuracy of the lumped approach at different length scales could be investigated. Overall it appears that the lumped approach was successful at predicting the cooling rate for the objects studied, successfully computing lumped properties that were representative of the disparate geometries. The lumped approach was least accurate for cubes, with a moderate degree of over prediction across all length scales. Furthermore, the lumped approach performed poorly at larger length scales, with objects at 0.4m and 0.2m dimensions showing larger differences between the simplified and detailed modelling methodologies. As analytical solutions for volume and surface area are also available for each of these objects, comparing these to the algorithms for appropriating V and A from the voxelised geometries showed they were sufficiently accurate – geometric procedures in section 5.5.6.1.1 and section 5.5.6.1.2 predicted a volume and area to within 2% of the analytical solution. This led to the conclusion that at larger length scales the relationship between the fully developed temperature gradient and the geometry of the object is no longer sufficiently linear, so that $\overline{d_{min}}/\lambda$ is not an acceptable approximation of the internal resistance. Additionally, as seen for cubes, cylinders and cones at the 0.4 m length scale, the *shape* of the temperature profiles deviated: the lumped approach and Eq. 6.7 can only predict a perfectly exponentially decaying curve, while a finite element model with a high degree of volume discretization is capable of providing more nuance in the temperature profile. In context with sections 5.5.5 and 5.5.6

and the zonal modelling methodology, this is a favourable result: the lumped approach is more accurate at the 0.1 – 0.025-meter length scale, which is the approximate size range of an individual zone, in the intended examples. However, this gives an additional recommendation for the ideal zoning strategy and zoning size (section 5.5.5), which is explored in further detail later (section 6.2.3.2).

Further testing of the geometric procedures was done on spheroids and cuboids at the recommended small scale of 50 mm radii/lengths, in Figure 6.3. This exercise flattened (Figure 6.3a and c) and stretched (Figure 6.3b and d) these objects into a number of ellipsoids/cuboids of diverse sizes/shapes to demonstrate the flexibility of the simplified approach. Each scenario was cooled at h_{ext} = 10 W·m^{-2}·K^{-1}. The lumped approach showed an agreement to the finite element approach in all scenarios, but the ellipsoids (Figure 6.3a and b) showed a better prediction than the cuboids (Figure 6.3a and b). Thus, it would appear that $\overline{d_{min}}/\lambda$ is a closer approximation of the internal resistance when applied to rounded objects.

The universality of the geometric procedures were pushed to the extreme in Figure 6.4. 4 irregular shapes were chosen, with a fixed scale and cooled at a variety of conditions, ranging from h_{ext} = 2.5 to 40 W·m^{-2}·K^{-1}. First was a helix with 3 curls (Figure 6.4a), followed by a torus (Figure 6.4b). These are objects where the 'centre' temperature is not at a single point, but is distributed throughout the geometry. Despite this paradigm shift from previous comparisons, the lumped approach still performed well compared with the more detailed finite element approach. Figure 6.4c applies the geometric procedures to a shape relevant to this project: a kiwifruit shape, generated using the shape equation of section 4.3. The fruit was an 'averaged' size count 36 Hayward kiwifruit. Across all cooling conditions, the simplified lumped approach predicted the expected cooling curve well. Finally, the object in Figure 6.4d was chosen for its recognisability but more importantly, extreme irregularity: a bust of the Statue of Liberty (credit to jerry7171 who created the 3D model for the statue, taken from https://www.thingiverse.com/thing:508637, accessed on July 1st 2017). Unlike the previous objects which can be described in terms such as lengths, radius', diameters and/or curls, the bust of the Statue of Liberty has no definite dimensions (the 'height' is given to communicate the approximate scale of the object).

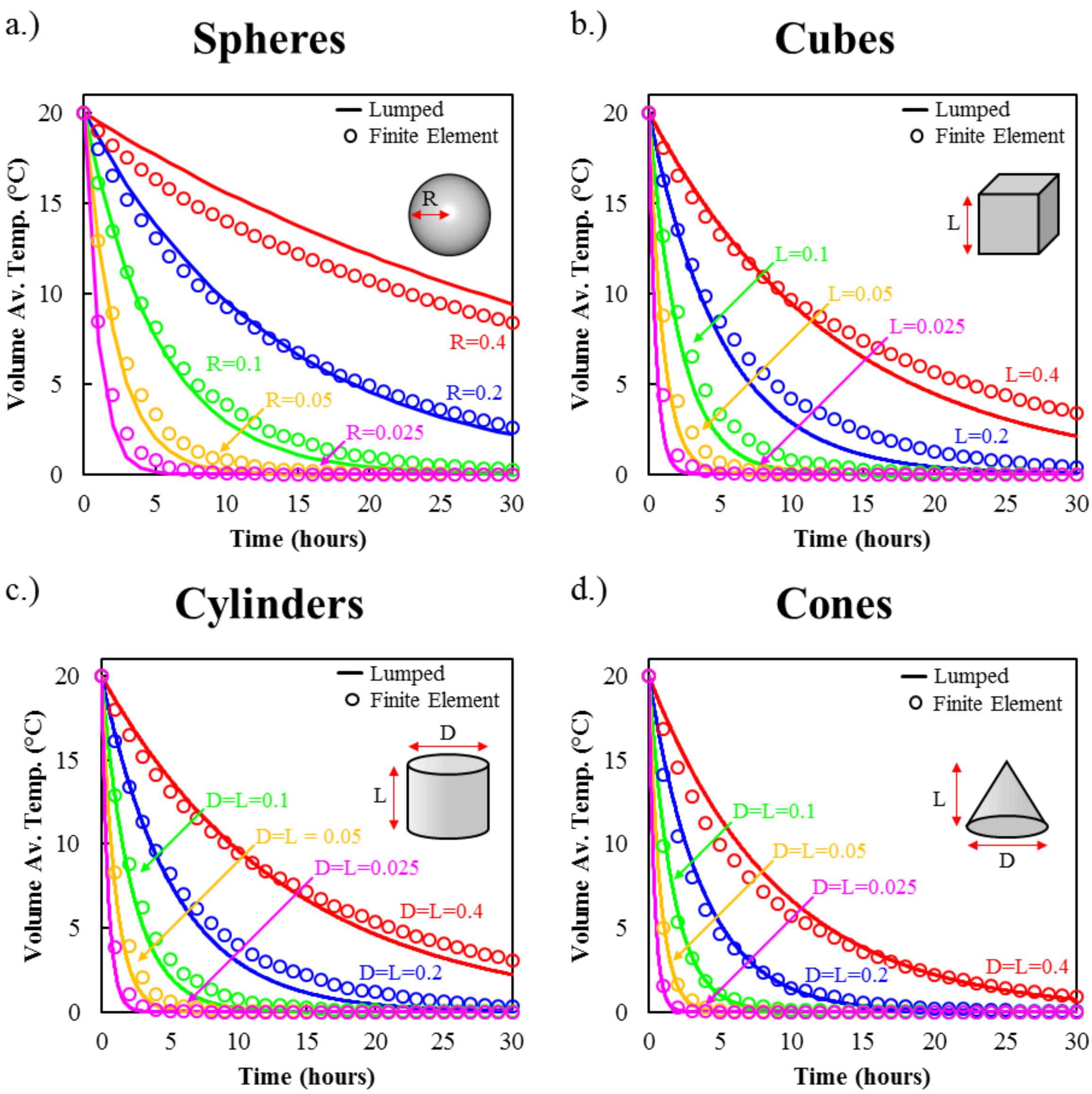

Figure 6.2: Simplified lumped approach (solid lines) versus the finite element approach (circles) for simple objects: a.) spheres; b.) cubes; c.) finite cylinders, and; d) cones. Externally cooled at h_{ext} *= 10* $W{\cdot}m^{-2}{\cdot}K^{-1}$ *in all scenarios. Length scales in meters.*

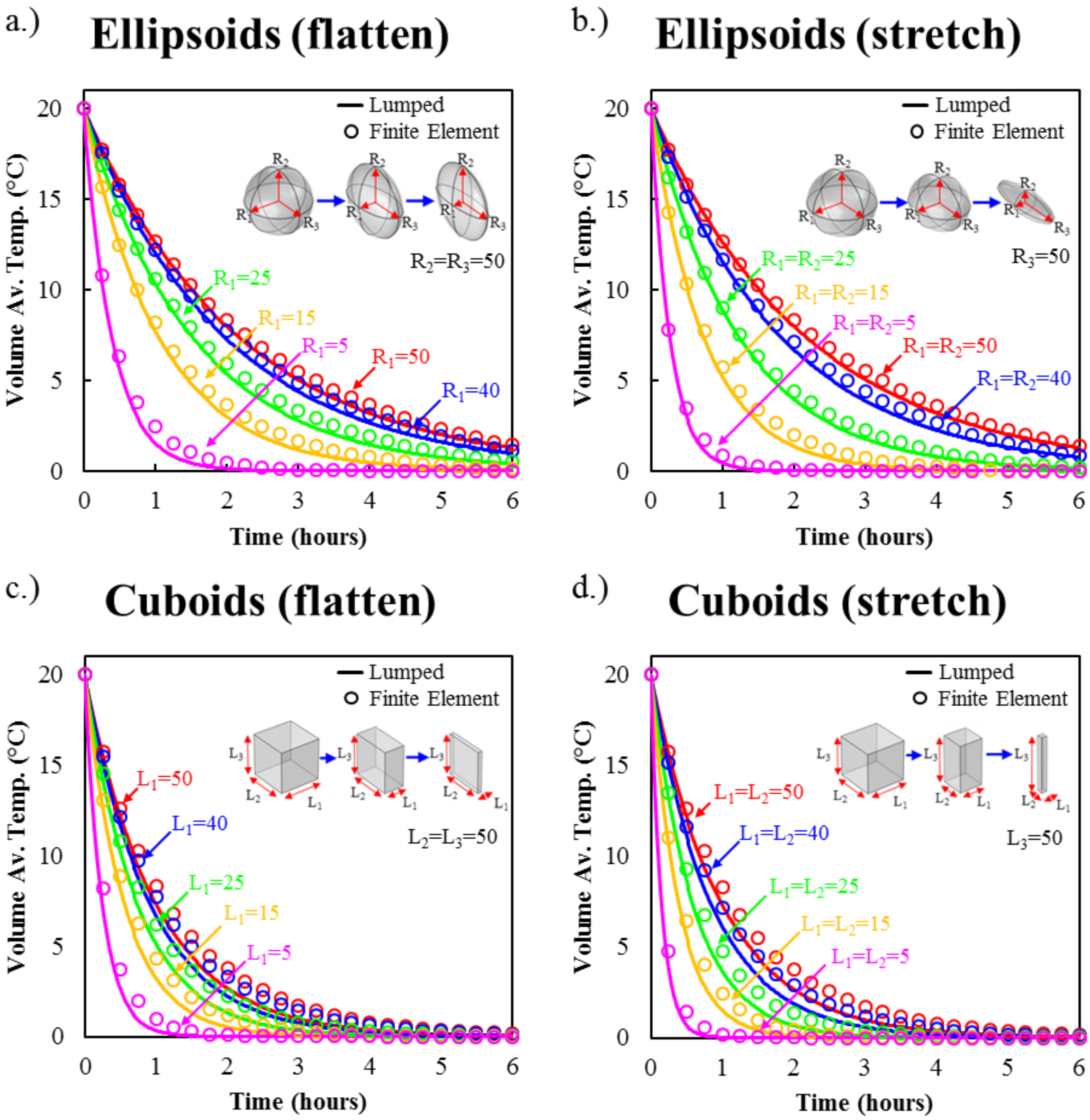

Figure 6.3: Simplified lumped approach (solid lines) versus the finite element approach (circles) for: a.) flattened ellipsoids; b.) stretched ellipsoids; c.) flattened cuboids, and; d.) stretched cuboids. Externally cooled at h_{ext} = 10 W·m^{-2}·K^{-1} in all scenarios. Length scales in millimetres.

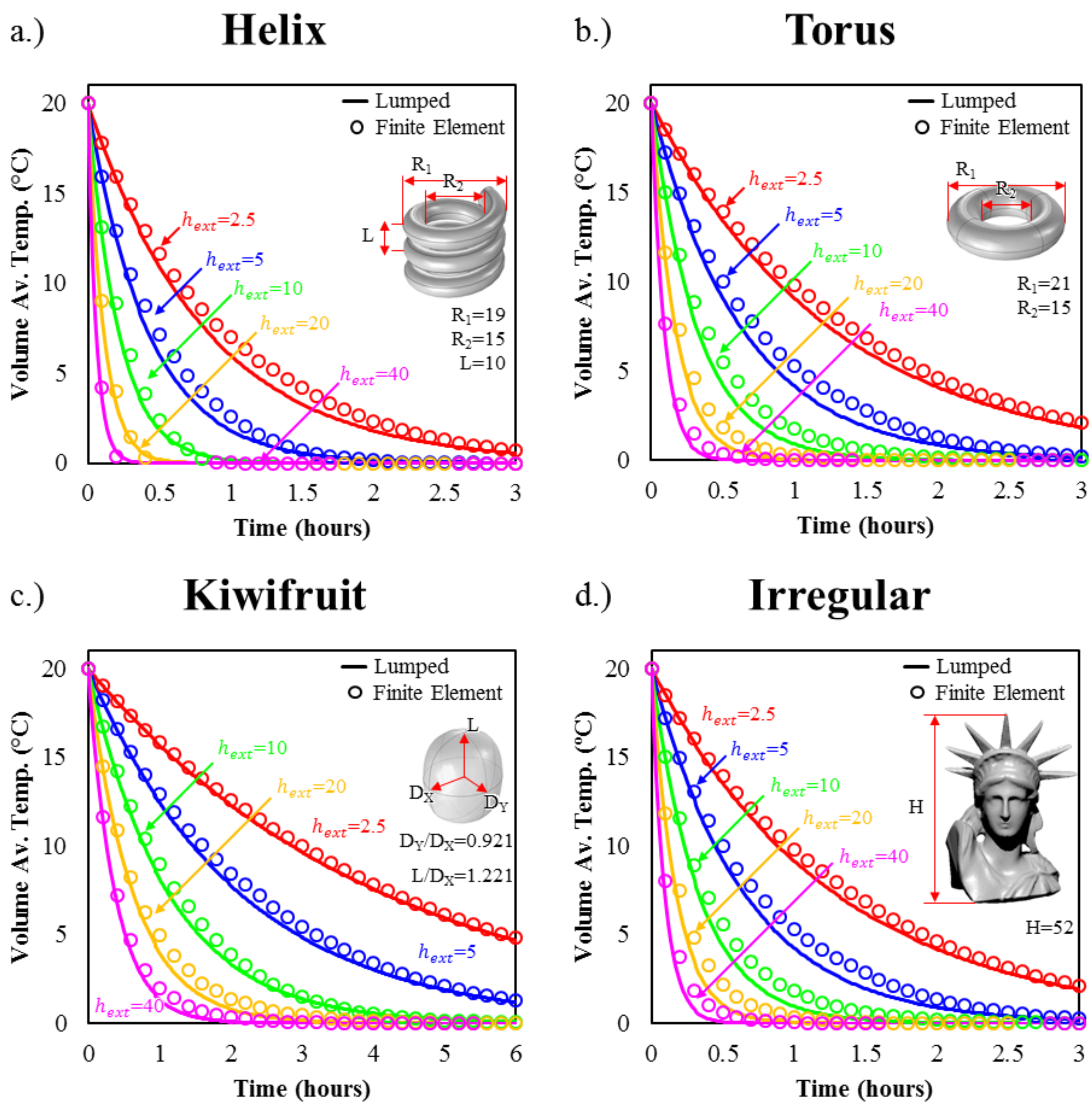

Figure 6.4: Simplified lumped approach (solid lines) versus the finite element approach (circles) for: a.) a helix; b.) a torus; c.) an average sized count 36 kiwifruit , and; d) an irregular shape, a bust of the Statue of Liberty. Externally cooled at from h_{ext} = 2.5 – 40 W·m^{-2}·K^{-1}. Length scales in millimetres.

Despite the bust containing many complex features combined into the one object – such as a crown (consisting of thin pseudo-cylindrical appendages), face (approximately an ellipsoid but with facial features like a brow, nose, mouth and hair) and base (with parts of Lady Liberty's arms and chest, and hints of her robe) – the hypothesis to be tested was that *any* object can be simplified adequately by just 3 lumped properties – A, V and $\overline{d_{min}}$ – with no prior assumptions about the shape of the geometry, and appropriated in a fashion that is easy, fast and automated. This is confirmed by Figure 6.4d, where the simplified lumped properties predicted an average cooling rate close to the result of the finite element approach. Furthermore, producing the lumped approach temperature profiles were much easier than for the finite element case, for these very complex shapes. For the finite element approach, the original surface mesh had to be cleaned manually in Blender by inspecting individual vertices and removing overlapping points and faces before it could be meshed properly in COMOL (Figure 6.5a); this is a time-consuming and manual procedure that would be difficult to perform algorithmically. Figure 6.5a). Alternatively, for the simplified approach, the original surface mesh was imported verbatim into the voxeliser (section 5.5.4), where it was converted into a voxel grid expeditiously and automatically (Figure 6.5b; 7 second voxelisation time) so that the lumped properties could be approximated using the geometric procedures.

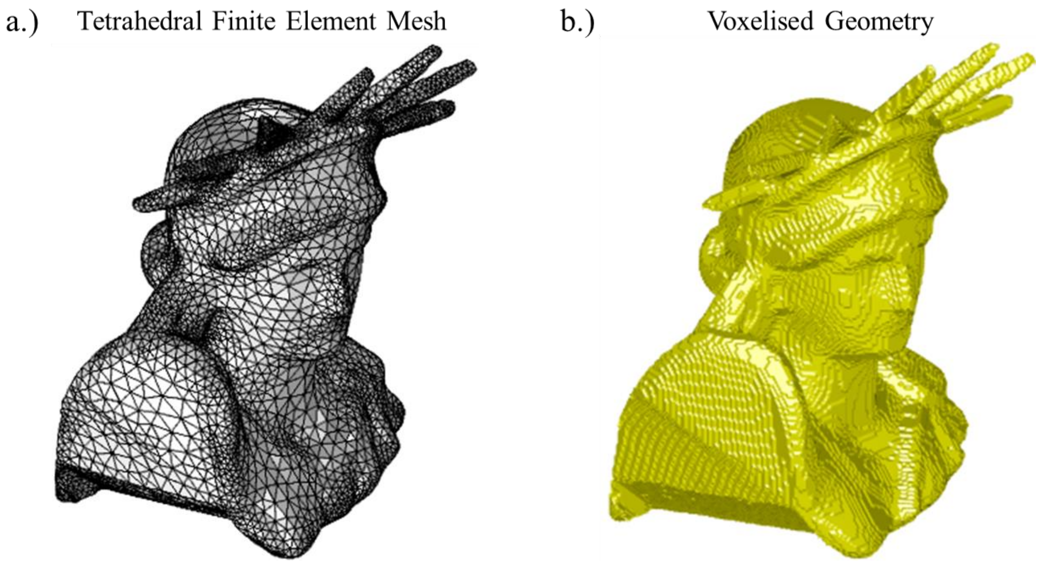

Figure 6.5: Statue of Liberty geometry in both modelling approaches: a.) a tetrahedral finite element mesh; b.) a voxelised geometry (0.25 mm^3 voxel size).

Having demonstrated the efficacy of the intra-zonal geometric procedures across a range of scales and shapes, it is appropriate to conclude this section with an application to a highly relevant geometry: a cuboid shaped zone. The sinuous geometry of individual phases inside of zones as a result of a cuboid zonal shape was of great concern (see section 5.5.5) and was a primary motivator for the development of the AVDC as a universal procedure to handle such complexities. Thus, the lumped approach was applied to a cube-shaped zone, with 63mm length sides, excised from the centre of a CT scan of kiwifruit (see section 4.2), and is shown in Figure 6.6a.

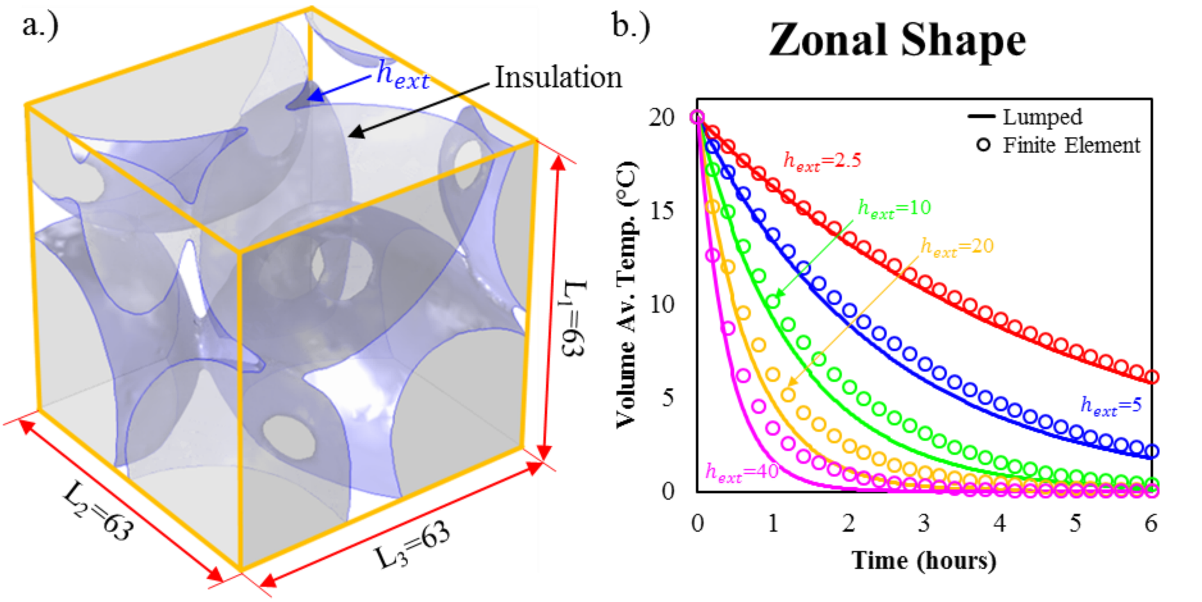

Figure 6.6: a.) a cube shaped zone taken from the centre of a CT scan of fruit, with a complex intra-zonal fruit geometry (length scales in millimetres); b.) predicted cooling curves of the fruit phase inside of the cuboid zone using the simplified lumped approach (solid lines) and finite element approach (circles) cooled on the fruit-air surface at h_{ext} *= 2.5 – 40 W·m*$^{-2}$*·K*$^{-1}$*.*

Figure 6.6a is typical of an intra-zonal geometry when zoning a box into cuboid shaped zones: each zone will most likely contain several bisections from different fruits, with some parts connected and others separated. For this demonstration, only the fruit phase is modelled. The air phase is instead considered as some degree of convective cooling, h_{ext} = 2.5 to 40 W·m^{-2}·K^{-1}, on all internal surfaces – highlighted in blue in Figure 6.6a. As this is an investigation of the intra-zonal cooling rate, the surfaces at the edge of the zone are modelled as insulated, as heat will flow through these 6 boundaries according to the inter-zonal properties, which are separate heat fluxes (see section 5.5.6.2.2, Table 5.3). This complex zonal shape was imported into COMSOL for a finite element comparison by converting the voxelised CT scan data into a surface using the 'isosurface' MATLAB function and exporting it as an .stl file. Again, like with the Statue of Liberty example, the shape data had to be extensively cleaned by hand in Blender before COMSOL was able to mesh the geometry successfully. Conversely, the native voxelised CT scan data was able to be used verbatim by the geometric procedures to appropriate the lumped V, A and $\overline{d_{min}}$ metrics quickly and easily.

The results of the two approaches are compared in Figure 6.6b. The lumped approach follows the cooling trends of the more detailed finite element approach across the different rates of external convection, but the agreement decreases as h_{ext} increases. However, considering a maximum difference of 1.5°C over 6 hours of cooling for the most extreme example (h_{ext} = 40 W·m^{-2}·K^{-1}, magenta lines and circles), this difference could be considered well within the range of acceptability when considering the lumped approach can be universally applied to any zonal geometry, is computationally efficient, and is an automated procedure. Furthermore, a zone with this configuration of fruit is in the centre of the box, which would under normal circumstances have a lower local air velocity, and therefore a lower h_{ext} value, where the accuracy of the lumped approach is much higher.

While the shape of the zone tested in Figure 6.6 was a cube, there is no requirement that zones be equidistant. Should it be desired that skewed – or cuboid shaped – zones be created, then the simplified approach should be able to be applied verbatim without a decrease in accuracy. This is investigated in Figure 6.7.

Figure 6.7a has the same intra-zonal geometry as Figure 6.6 but divided in half along one axis to create a skewed zone. Figure 6.7b was another division along the same axis, creating an even more skewed zonal shape. Comparing the resulting cooling profiles (Figure 6.7c and d) of the simplified approach and the finite element approach, a similar trend as Figure 6.6 is revealed: while the overall accuracy of the simplified approach is satisfactory, it decreases as h_{ext} increases.

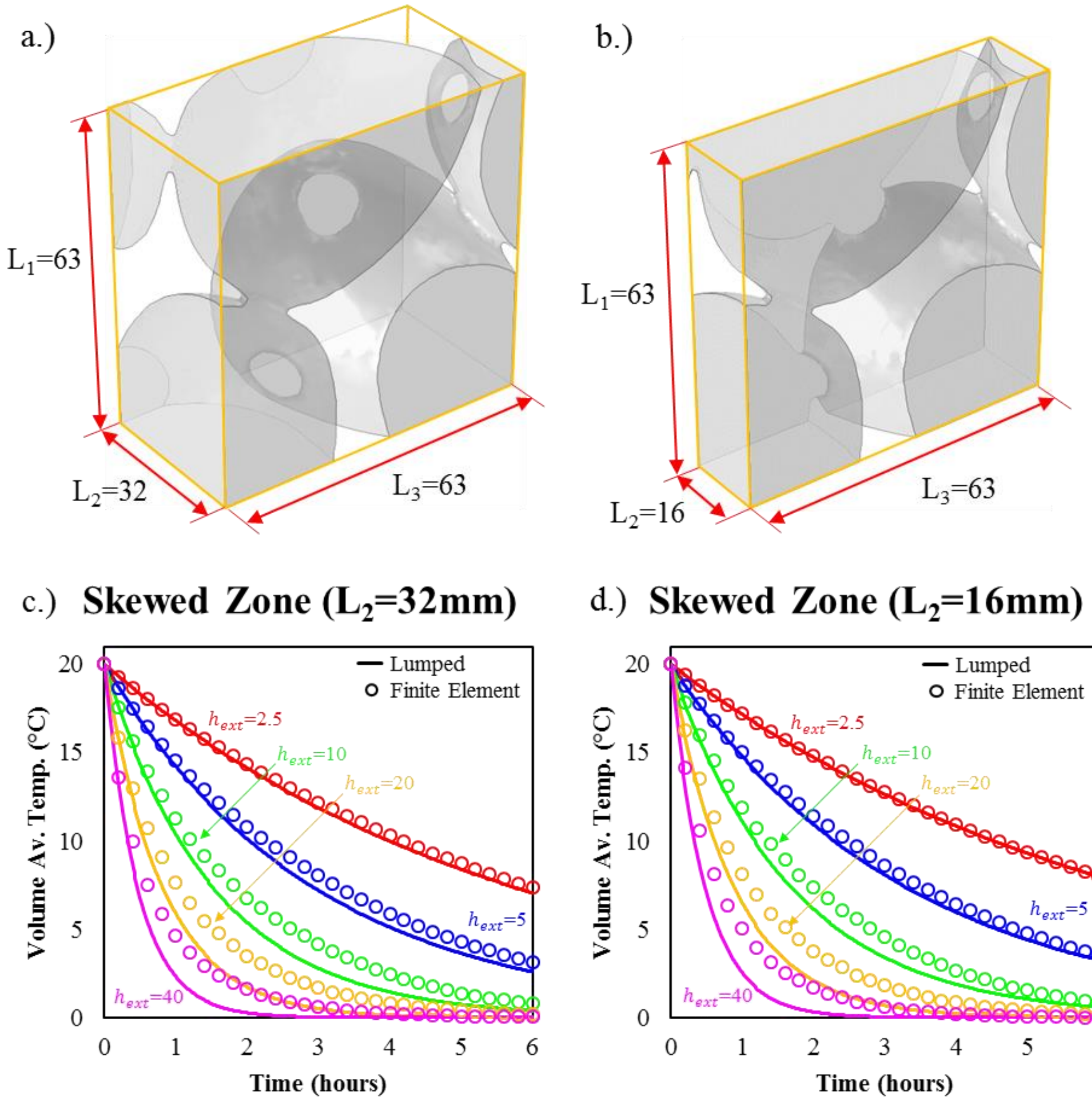

Figure 6.7: a.) a skewed zone taken from the centre of a CT scan of fruit; b.) an increasingly skewed zone taken from the centre of a CT scan of fruit (length scales in millimetres); predicted cooling curves of the fruit phase inside of the zone for the simplified lumped approach (solid lines) and finite element approach (circles) for the c.) skewed zone, and d.) severely skewed zone.

In conclusion, the intra-zonal geometric procedures developed in section 5.5.6.1 are shown to be sufficiently comparable to a more detailed modelling methodology; and also confirms that just three lumped properties, $\overline{d_{min}}$, V and A, can satisfactorily predict the cooling profile of a wide variety of geometries, including a representation of an intra-zonal fruit geometry.

6.2.3: Validation of Zonal Network

6.2.3.1: Introduction

Section 5.5.6 demonstrated the ability for this interpretation of the zonal modelling approach to generate a self-forming zonal network as a function of a generic input geometry. Having validated some of the geometric procedures, for zones in isolation (section 6.2.2 and Figure 6.6), the validation should be expanded to a network of zones, the proper context in which a zonal model will be used. This will demonstrate that the zonal properties appropriated via the automated zone builder (section 5.5.6) and its associated geometric procedures are indeed representative; and when used with the zone solver (section 5.5.7) and integrated numerically, the zones communicate with each correctly to produce the expected time-temperature profile on both a local and global level. Numerical validation is performed in this section by comparing the results derived from the zonal network with an equivalent finite element model.

6.2.3.2: Validation of Single Box Zonal Network

The model geometry chosen for this validation exercise was identical to the fruit-polyliner geometry of the previously used finite element model (section 5.2), which was constructed to mimic the geometry of the manually stacked boxes used during experimental cooling trials (section 3.3 and section 3.4). An important distinction between the two models was rather than applying the near-miss principle as was done in the finite element case (Ferrua and Singh, 2009c), the overlap principle was applied instead: as a small gap between fruit is interpreted by the geometric procedures (section 5.5.6.2.2) as an infinitely high resistance, each fruit was *increased* in volume by a small percentage to *encourage* fruit to touch a small amount. Each fruit volume was increased by 3% in Blender and the overlapping surfaces between fruits removed. The polyliner was generated according to section 4.4.5, with identical settings (Subdivide = 6, Offset = -0.00035 and Smooth = 5). The fruit and polyliner geometries were imported into the Zone Builder as separate .stl files and voxelised to a 1mm^3 voxel resolution, an automated process taking less than 60 seconds. The geometrical identicalness of the two approaches is made clear Figure 6.8. After voxelisation, the fruit-polyliner geometry was divided into cuboid shaped zones (section 5.5.5). The chosen zonal resolution is likely to have an impact on model performance – a smaller number of zones may be beneficial in terms of the efficiency of zone builder, and may also increase the speed of the Zone Solver, but at the expense of a larger zone size which may compromise the ability of the geometric procedures to function correctly, resulting in non-representative zonal properties and a poor prediction of the cooling rate (section 6.2.2). Conversely, a more detailed zonal resolution may improve the accuracy of heat transfer through each zone and by extension, the accuracy of the global solution; but at the expense of a lengthier zone builder and Zone Solver. Investigating changes to zonal resolution are also necessary for validating the geometric procedures ability to adapt to any zone size or intra-zonal geometry. A variety of zonal resolutions were therefore tested, and are shown in Figure 6.9. Zonal Network A divided the geometry into 3 zones along the X-axis, 3 along the Y-axis and 2 along the Z-axis – N_X = 3, N_Y = 3, N_Z = 2 – to create 18 zones (Figure 6.9a). Additional zonal networks had N_X = 4, N_Y = 4, N_Z = 3 for zonal network B, 48 zones (Figure 6.9b); N_X = 5, N_Y = 5, N_Z = 4 for zonal network C, 100 zones (Figure 6.9c); and N_X = 6, N_Y = 6, N_Z = 5 for zonal network D, 180 zones (Figure 6.9d).

a.) Finite Element Geometry b.) Voxelised Geometry

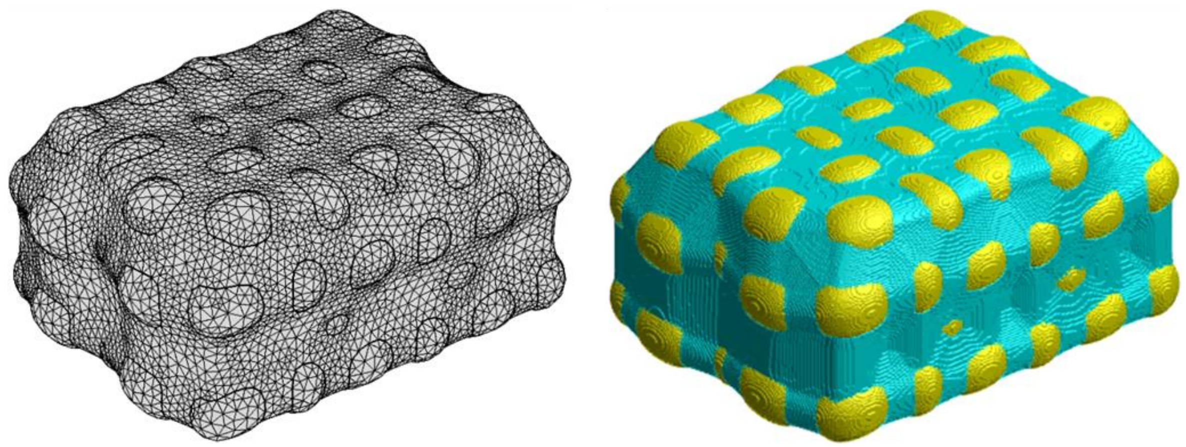

Figure 6.8: Model geometries for each modelling approach: a.) finite element model, meshed into tetrahedral finite elements; b.) zonal model, voxelised into 1 mm^3 cubic voxels.

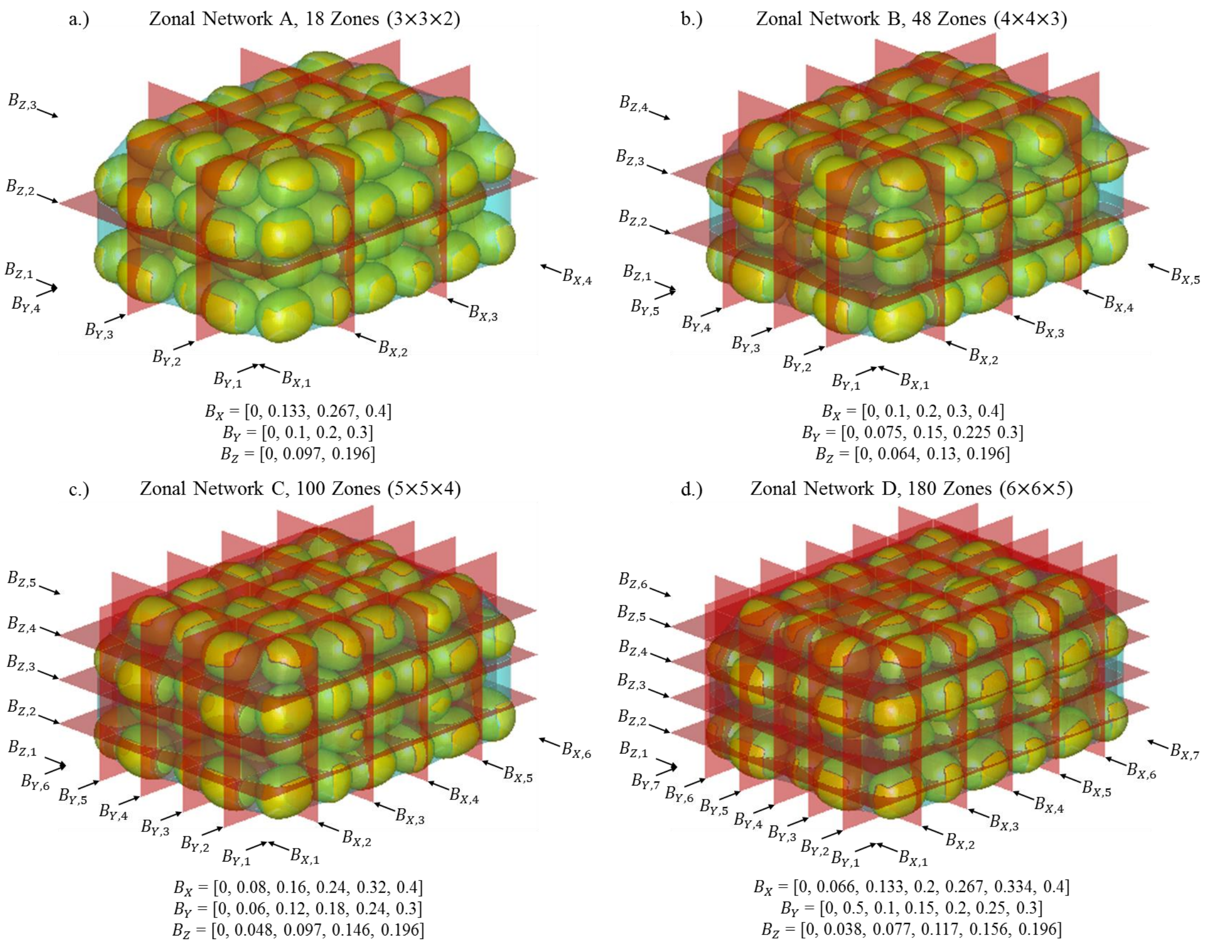

Figure 6.9: Zonal resolutions used in this validation exercise: a.) zonal network A, with 18 zones; b.) zonal network B, 48 zones; c.) zonal network C, 100 zones, and; d.) zonal network D, 180 zones.

As this project is concerned with the development of a *heat transfer* model, the primary matter is to determine the efficacy of a zonal network to correctly predict the internal resistance to heat transfer. Therefore, the same simplified external cooling conditions are imposed on the zonal network as was for the finite element model, with an external heat transfer coefficient, h_{ext}, being applied uniformly across the fruit-polyliner surface, to represent a specific refrigerated airflow velocity and pattern. This h_{ext} is applied as a resistance to external heat transfer, $R_{ext} = 1/h_{ext}$, uniformly across the phase $Z = 0$ (bulk air phase, see section 5.5.6.1.5). The external convection rates explored in this exercise were h_{ext} = 5, 10, 20 and 40 $W{\cdot}m^{-2}{\cdot}K^{-1}$ (these approximately correspond to the expected heat transfer coefficients for air flow rates ranging from nearly 0.2 $m{\cdot}s^{-1}$ to 6.0 $m{\cdot}s^{-1}$ (ASHRAE, 2010). Differences in h_{ext} from zone to zone as a result of airflow patterns are ignored in this exercise, but are explored later during experimental validation (see section 6.3).

The finite element model in this exercise was identical to that of section 5.2 and section 5.3.2.2, with conduction heat transfer through the fruit, and a combination of conduction and natural convection in the polyliner air (with buoyancy induced motion through the air phase modelled explicitly). Respiration, evaporation and thermal radiation were ignored (see section 5.3). The thermal properties were as derived in section 5.4. The simulation predicted the temperature change over 20 hours of cooling.

For the zonal approach, the geometric procedures of the zone builder was applied to each of the zoning strategies of Figure 6.9. Natural convection was incorporated through an effective thermal conductivity for the polyliner air (derived in section 5.5.6.1.4), which was $\lambda_{A,eff}$ = 0.0393 W·m^{-1}·K^{-1} (given that the porous medium modified Rayleigh number was Ra* = 61.4 and Nu = Ra$^*/40$ = 1.53, the effective thermal conductivity was Nu = $\lambda_{A,eff}/\lambda_A$), otherwise the thermal properties were as derived in section 5.4. The Zone Solver was set up to predict the temperature change through each zonal network over a 20-hour time period.

The two approaches were first compared visually, to elucidate the nature of the solutions derived from a zonal model. Fruit temperatures are visualised at different cooling times, with external cooling conditions of h_{ext} = 5 W·m^{-2}·K^{-1}, for the finite element model and all of the studied zonal networks, in Figure 6.10. The finite element approach, being meshed to a high degree of detail, makes predictions of fruit temperature gradients with a high fidelity. It can be seen clearly in Figure 6.10a that the fruit at the edges of the stack are predicted to cool much faster, having direct contact or is in close proximity to the external cooling air. This subsequently forms a warm core of fruit in the centre of the box that are shielded from the effects of the external cooling. This approach is detailed enough to predict gradients through individual fruits, but comes at the expense of having prohibitive solution times of approximately 1 hour. Results from the zonal approach are presented by rendering in 3D the intra-zone fruit geometry of each zone and colouring the result according to the predicted volume average fruit temperature. Given that the zonal approach is a lumped approach, a single volume average fruit temperature is predicted per zone. As a result, at low zonal resolutions such as zonal network A (Figure 6.10b), even though there is an overall change in temperature that appears to be on par with the finite element model, the prediction of temperature gradients through the box is very poor and does not reflect the large levels of temperature heterogeneity that were observed in section 3.3 and predicted in the finite element approach. However, as the zonal resolution increases and more temperature positions are modelled, the expected heterogeneous temperature profiles begins to manifest, with there being the distinctive cold ‘outer shell’ of fruit zones, with a warmer core of fruit zones, as seen in Zonal Network D (Figure 6.10d). This brings the zonal approach into closer agreement with the predictions of the finite element approach, but at a significant savings in computational efficiency – the zone solver operated on the order of seconds, taking approximately 0.3, 0.4, 0.6 and 1.4 seconds to solve the heat transfer rates for 20 hours of simulated cooling through the entirety of zonal networks A, B, C and D, respectively.

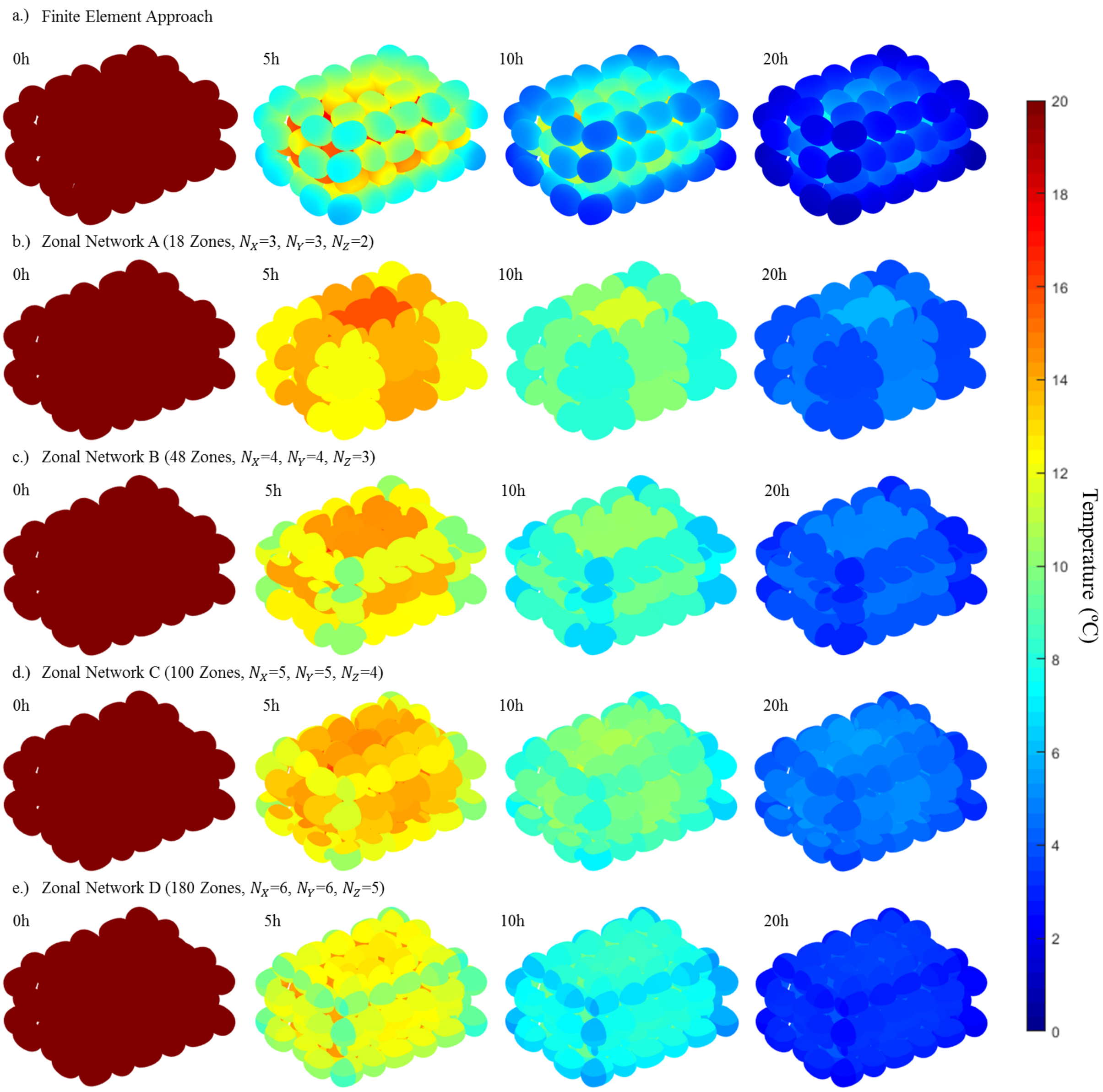

Figure 6.10: Visualisation of the predicted local temperature profile over 20 hours of cooling at 5 W·m^{-2}·K^{-1}: a.) finite element model; zonal model, b.) network A (18 zones); b.) network B (48 zones); c.) network C (100 zones); d.) network D (180 zones).

The quality of the predictions from the zonal approach were further examined through quantitative comparisons of predicted global and local temperature profiles:

Comparisons from a global perspective were made by plotting the volume average time-temperature profiles of all fruit for each modelling approach. Results are shown in Figure 6.11. Generally, it appears that the zonal approach is similar, to the finite element, for predicting the internal response to changes in external cooling conditions. At low zonal resolutions (zonal network A, 18 zones), the predicted internal resistance was appreciably higher than that predicted by the finite element, indicating that the geometric procedures may function poorer at larger zone sizes – this observation aligns with previous work (Figure 6.2a). Increasing the zonal resolution reduced individual zone size, improving the accuracy of individual zonal properties and by extension, the prediction of the global transfer rate – network B, with 48 zones, was potentially still in a range where zone size was too large, and only offered a slight improvement from network A; whereas network C, with 100 zones, showed a very close alignment with the finite element profile; and network D, with 180 zones, showed a negligible difference compared with network C, indicating that zonal network C (Figure 6.9c) was the ideal zonal resolution. The shape of the curves produced by each approach were slightly divergent, with the finite element approach predicting a faster cooling rate at the beginning of the cooling process and a slower rate near the end compared with the zonal approach – an observation also seen in the single zone investigation of cylinders (Figure 6.2c, red line). This is caused by the zonal approach being a simplified approach with lumped properties, where a single zone in isolation is only capable of cooling in a perfectly exponential manner. This is mitigated to an extent in a zonal network environment, where through inter-zonal exchanges of heat there can be non-exponential cooling overall as the temperature gradients in different directions are disparate (this behaviour is observed later when looking at individual zone cooling rates); however, in an overall sense the zonal model follows a more closely exponential cooling profile than the more detailed finite element model, which is capable of producing more nuanced results.

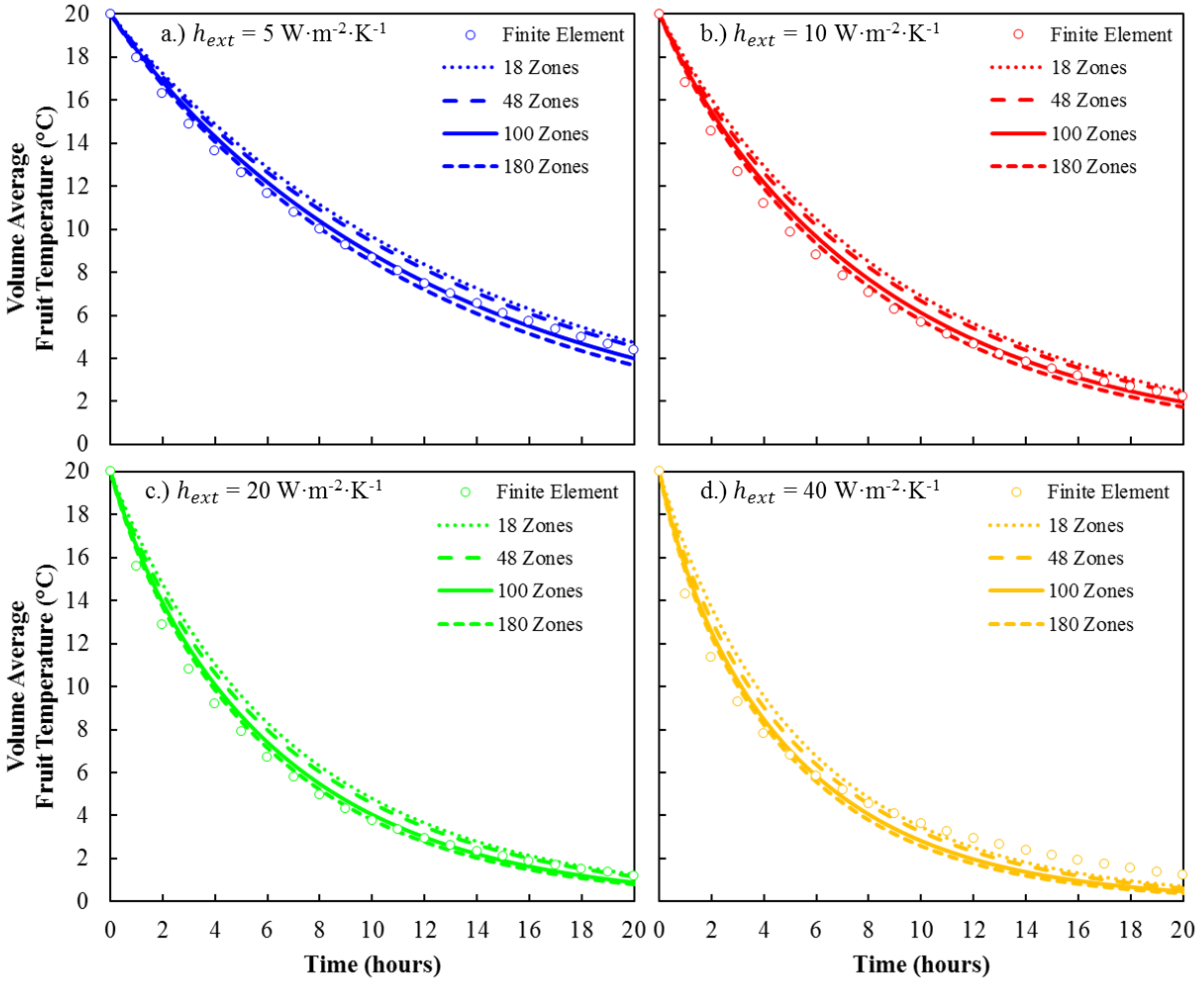

Figure 6.11: Comparison of volume average temperature profile predictions for the finite element model (circles) and zonal approach (lines), over a variety of zonal resolutions and external cooling conditions: a.) 5 W·m^{-2}·K^{-1}; b.) 10 W·m^{-2}·K^{-1}; c.) 20 W·m^{-2}·K^{-1}, and; d.) 40 W·m^{-2}·K^{-1}.

The variation between finite element and zonal predictions was greatest at high external rates of heat transfer, h_{ext} = 40 W·m^{-2}·K^{-1}, or Figure 6.11d, where the time-temperature curve of the zonal model was colder for all zonal networks. This result is echoed in the previous work of Figure 6.6 and Figure 6.7, showing that a lumped approach produces a faster cooling profile than finite element modelling at elevated external cooling rates. However, the maximum difference between network D and the finite element model was 0.9°C over 20 hours of cooling, a degree of error that is probably well within acceptable experimental limits, especially considering the ~1.4 second solution time of the zonal model and the automated nature through which it was produced.

These results support this new interpretation of the zonal approach. It shows that the zone builder can successfully generate a representative set of zonal properties from an input geometry to predict the global internal resistance to heat transfer in an automated fashion; and it also shows that the zone builder is able to adapt to changes in the zonal resolution, zone size and intra-zonal shape. The zone solver also appears to work successfully in communicating transfers of heat throughout the zonal network in an expeditious manner, where increases to the number of zones did not add to the computational overhead significantly.

Further validation of the zonal approach was done by comparing from a local perspective. Comparing the temperature differences on a fruit-to-fruit basis is difficult due to the disparate nature of the data – for example, each fruit is its own distinct object in the finite element model, but in the zonal approach each zone contains excised pieces from a number of different fruits. It was therefore decided that temperatures at specific positions be compared, these being the centre position of the same 12 fruit that were chosen for instrumentation during experimentation (section 3.3 and section 3.4). The chosen 12 temperature positions are illustrated in Figure 6.12. The temperature at these 12 positions are plotted over the 20 hour cooling period in Figure 6.13 for external conditions of h_{ext} = 5 W·m^{-2}·K^{-1} to provide at least one detailed visual study of comparative local performance. The remaining external cooling conditions, h_{ext} = 10, 20 and 40 W·m^{-2}·K^{-1}, are compared using the Overall Heterogeneity Index, or OHI, developed previously in section 3.2 as a quantitative metric that assesses total process heterogeneity.

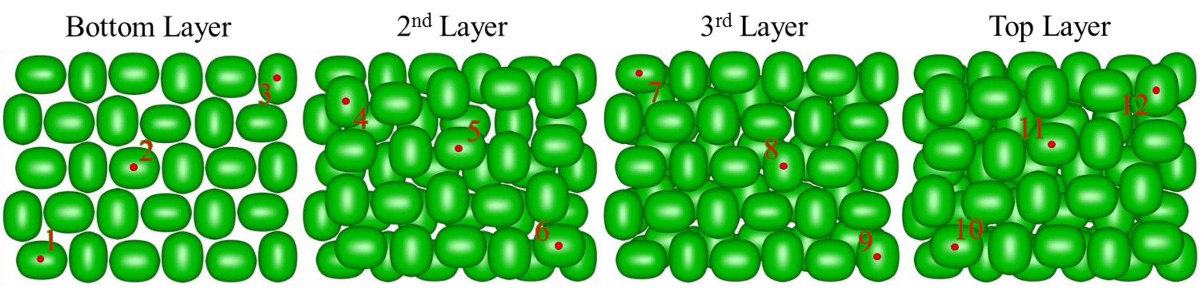

Figure 6.12: Fruit positions used to compare local temperature predictions and heterogeneity; identical to positions used during experimentation (section 3.3).

While at a global level there is near parity between the two approaches (Figure 6.11a), Figure 6.13 reveals there are some notable differences at a local level. Generally speaking, while there is an agreement at positions at the very top and bottom of the stack, such as temperature positions 2 and 11, the zonal approach under-predicts (relative to the finite element method) the cooling rate of fruit at the edges, such as temperature positions 1, 3, 10 and 12; and over-predicts the cooling rate of fruit in the centre of the stack, such as positions 5 and 8. As the zonal resolution increases, the differences between the approaches typically shrinks – though there is some nuance to this statement, with network D performing closer to the finite element method at the edges, but diverges more at the centre, when compared with its alternatives. Some of the differences can be explained due to the differing nature of the predictions. The time-temperature profiles from the finite element model represent *point positions*; while conversely the zonal approach, being a *lumped approach*, represents the volume average temperature of the zone nearest to the position.

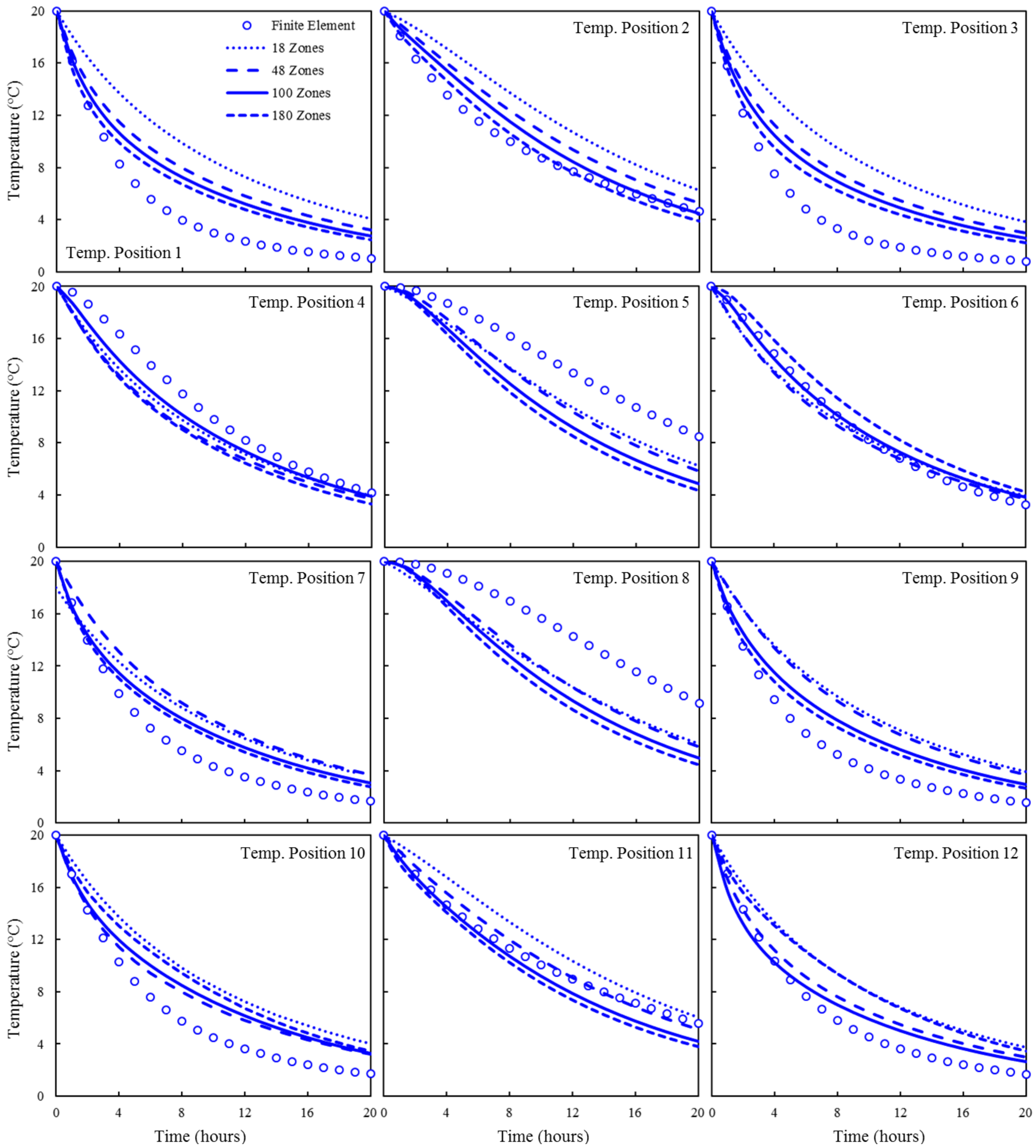

Figure 6.13:Comparison of local temperature profiles between the zonal and finite element models at 12 temperature positions (Figure 6.12) for external cooling conditions of $h_{ext} = 5\ W{\cdot}m^{-2}{\cdot}K^{-1}$.

For cooling scenarios, the volume average temperature is normally cooler than the centre temperature (Holman, 2010), which may explain some of the discrepancies (such as positions 5 and 8), but the opposite is true in other locations (such as positions 1 and 3). The more persuasive explanation is that the divergence is a consequence of volume averaging itself – fruit zones at the edges extend further inside the polyliner than a single fruit would, and these fruit inside of the polyliner are warmer due to being further away from the effects of the refrigerated air. Generating an average temperature for the entire zone results in an overall temperature that is warmer than would be expected if gradients throughout the geometry were modelled explicitly, as is done in the finite element model. Similarly, zones in the centre of the box include sections of fruit that are closer to the edges, which are cooler from closer proximity to the external air, resulting in a volume average temperature that is cooler than the finite element method. Overall, this results in, from a volume average perspective, a seemingly less heterogeneous cooling profile.

Computing the OHI from these 12 temperature positions revealed that the zonal approach predicted an absolute process heterogeneity of approximately half of that of the finite element model: with OHI = 0.115 from the finite element model, and OHI = 0.0532, 0.0592, 0.0622 and 0.0573 for networks A, B, C and D, respectively (note: 20 hours of cooling at h_{ext} = 5 $W \cdot m^{-2} \cdot K^{-1}$ was not enough time for the box to reach the seven eights cooling time, or when the average fractional unaccomplished temperature change reaches $\bar{Y}$ = 0.125, which is the recommended process end time with which the OHI is calculated. Therefore, the process end time was re-defined for this exercise as $\bar{Y}$ = 0.182 as this is was average fractional unaccomplished temperature change for the slowest cooling box at 20 hours of cooling). The error is much less significant when viewing the OHI for the other cooling conditions, such as Figure 6.14 which plots OHI versus h_{ext} for the finite element model and all of the zonal networks. It can be seen that as the external rate of heat transfer increases, the cooling rate becomes more variable and the OHI increases. Although the *absolute* OHI was much lower for the zonal model, the *relative* change in OHI matches that of the finite element approach. Therefore, if using the zonal model as it is intended – in an optimization loop, investigating many package designs/cooling conditions – so long as the same zonal network is used, the relative heterogeneity can be reported with authority and used as a design optimization metric.

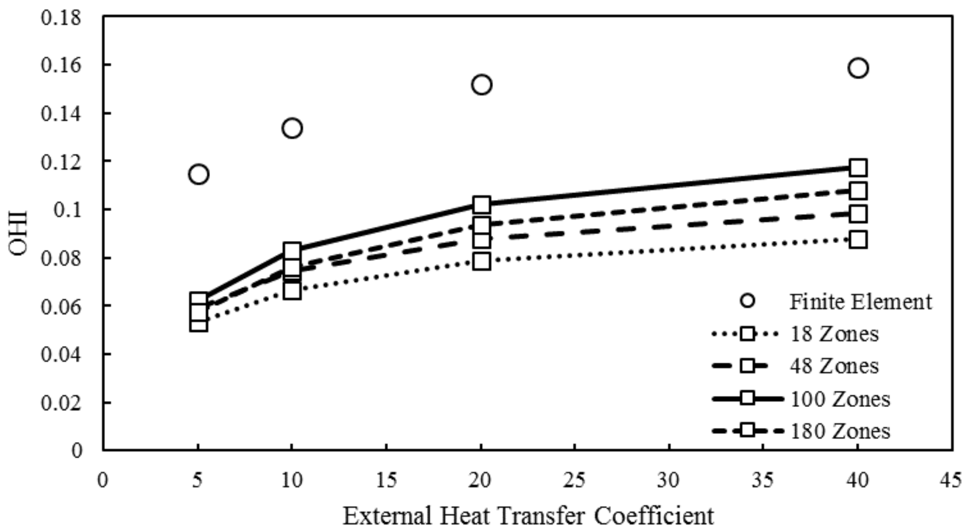

*Figure 6.14: Comparison of overall process heterogeneity (*OHI*) for the finite element model (circles) and the zonal model (squares, lines) over each cooling condition,* h_{ext} *= 5 – 40 W·m-2·K-1.* OHI *was computed with a modified process end time of* $\overline{Y}$ *= 0.182.*

In conclusion, this new interpretation of a zonal modelling approach was shown to be comparable to the much more detailed finite element approach. Small differences at the global level and more substantial differences at the local level were deemed acceptable considering that each zonal model in this exercise was automatically constructed with the zone builder program, and solved in under 2 seconds – in comparison to the laborious meshing process and ~1-hour solution times of the finite element approach. This result validates the geometric procedures of the natural convection correlation (section 5.5.6.1.4) and the inter-zonal linear slice algorithm (section 5.5.6.2.2), each scaling appropriately to different zone sizes and intra-zonal geometries.

6.3: Experimental Validation

6.3.1: Introduction

Finally, the zonal approach was validated with respect to experimentally observed cooling rates and levels of cooling heterogeneity, collected previously in section 3.4. Information pertaining to the pattern and velocity of airflow through the interior of the box was required. Collecting this information could be through empirical means, such as in Tanner *et al.* (2002a) or Smale (2004), where the velocity of air was measured in vital locations via anemometry; or it could be derived from an airflow model of some description. Both of these options represent a problem from the perspective of the limitations imposed on this project: using experimentally determined airflow information places a prohibitive limit on the number of package designs which can be tested, as each will need to be fabricated and measured, a clear violation of the flexibility principle; and alternatively, using established models for airflow prediction, such as Computational Fluid Dynamics (CFD), has potential to be more flexible, but is prohibitively computationally intensive.

It was ultimately decided that the airflow model route would be taken, with care to incorporate the airflow model into this zonal heat transfer model in such a fashion that future work can improve upon the speed and universality of velocity and pressure prediction with minimal to no amendments to the core functionality of the zone solver. This was accomplished by retaining the use of an external heat transfer coefficient, h_{ext}, in the bulk air phase of the zonal model, where each zone is capable of having a unique h_{ext} which reflects the airflow pattern through the interior of the box as a result of the package ventilation and location of the zone, denoted as $h_{ext,i}$ where i denotes a specific zone. $h_{ext,i}$ will be predicted as a function of the velocity of the air flowing through that zone, u_i – as well as other variables such as the geometry of the bulk air phase inside of the zone – with the velocity through each zone predicted using CFD. Developed in this manner, it would be trivial for the CFD part of the model, undeniably the most time consuming and rigid aspect, to be replaced with an alternative simplified approach – such as a resistance network model (Smale, 2004). This simplified airflow model is being actively pursued by different researchers in the CPRR.

The CFD airflow model was developed in COMSOL, the development process and results given in section 6.3.2. The correlation between u_i and $h_{ext,i}$ is explored in section 6.3.3, which also compares the results from the zonal model to experimental data.

6.3.2: Airflow Model (Computational Fluid Dynamics)

The CFD airflow model was developed in COMSOL Multiphysics v.5.2. The fruit and polyliner geometry from section 5.2 were placed inside of packaging with the same outer and inner dimensions, vent number and vent positions as a real modular bulk package. The model geometry is shown in Figure 6.15:

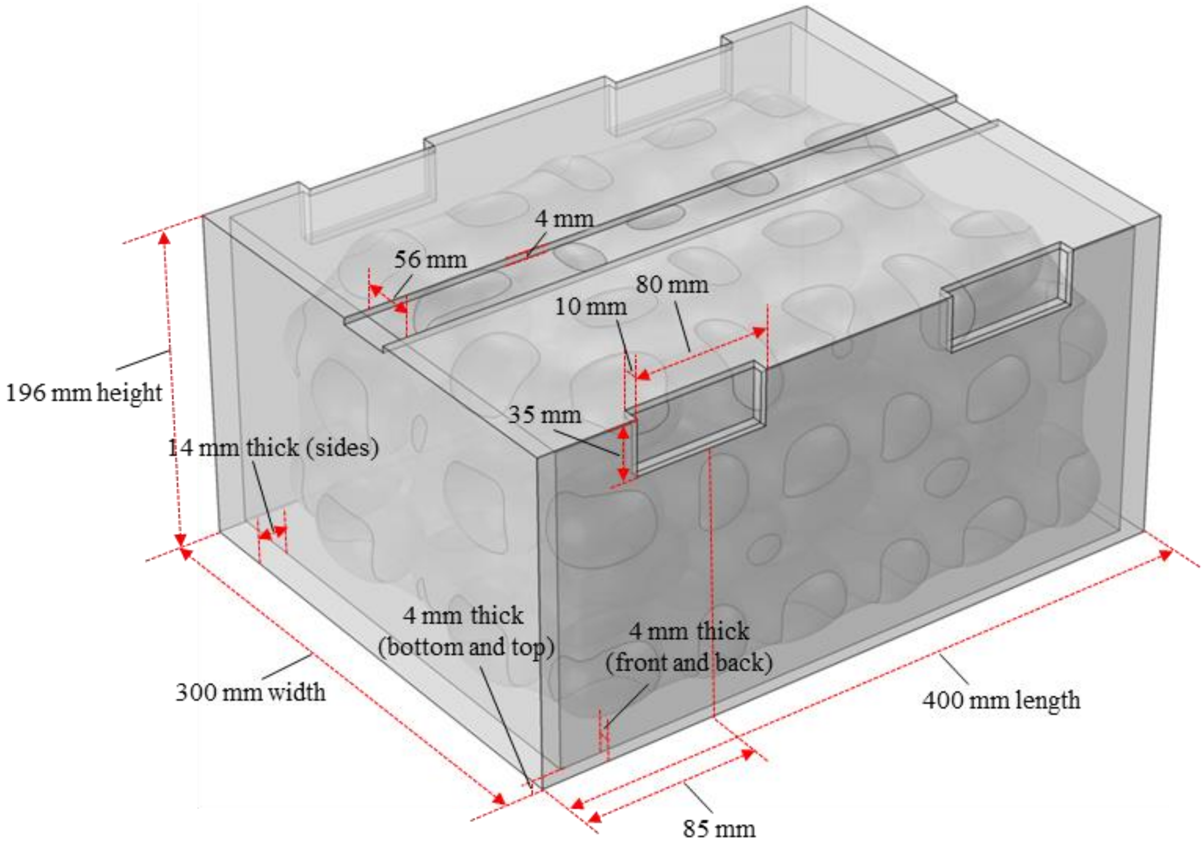

Figure 6.15: COMSOL model geometry of a modular bulk package, 100 count 36 kiwifruit and polyliner for the CFD airflow model.

The intention of this model was to replicate the experimental wind tunnel in which the cooling rate of boxes were empirically measured in section 3.4 (see Figure 3.28). As such, a 200 mm long channel before and 1000 mm long channel after the box was added in Figure 6.16. As described in section 3.4, 6 boxes were cooled simultaneously, each stacked on top of each other. Rather than develop a model for this entire geometry, symmetry and other boundary conditions were exploited to reduce the size of the model geometry to a single box (summarised in Figure 6.17). The packaging, fruit and air inside the polyliner were all considered as solids, while the remaining geometry was considered dry air (Ferrua and Singh, 2009a). The measured pressure drops across the 4 experimental trials – 15, 32, 65 and 118 Pa – were imposed onto the model by applying the same back pressure to the 'Outlet' surface as $-\Delta P_{pallet}$, while the 'Inlet' surface was defined as 0 Pa (see Figure 6.17).

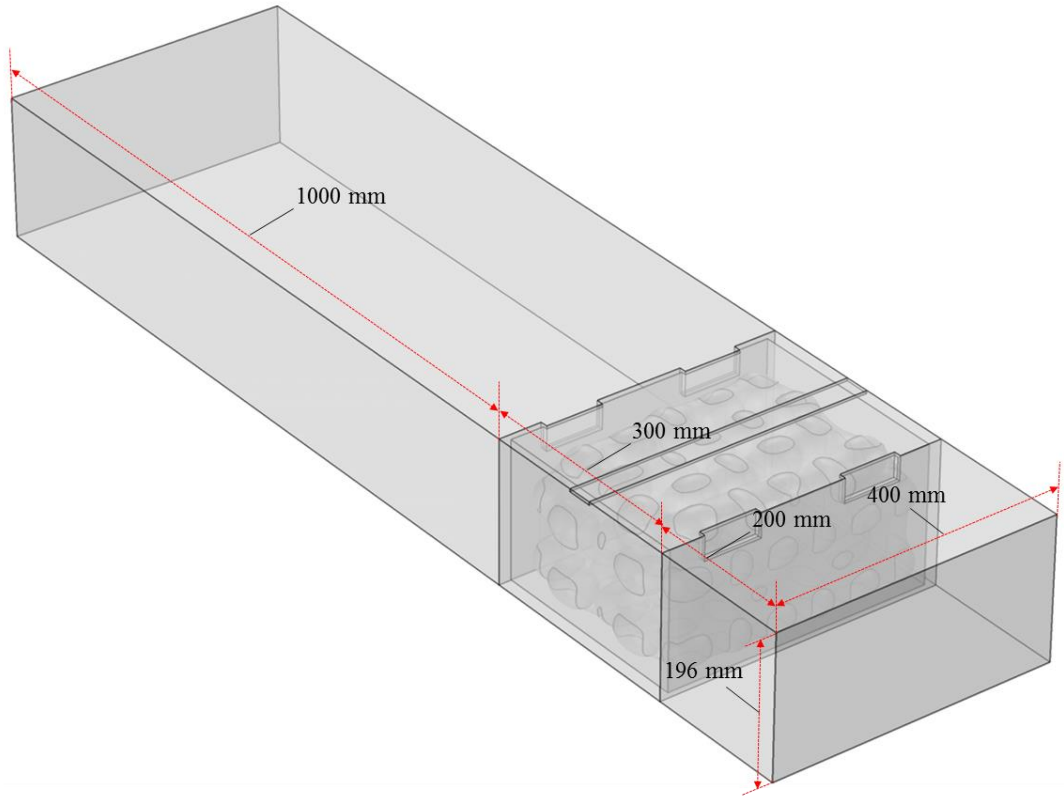

Figure 6.16: Geometry of numerical wind tunnel for the CFD airflow model.

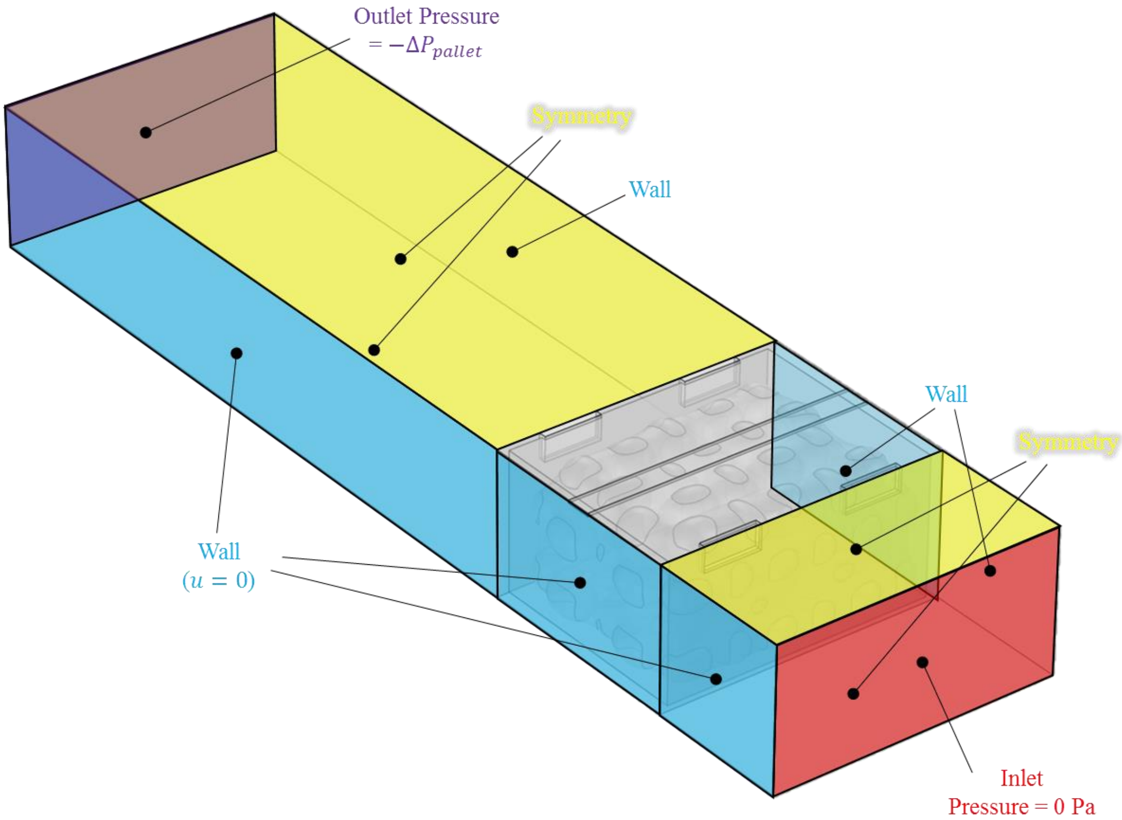

Figure 6.17: Boundary conditions of the CFD airflow model.

Ferrua and Singh (2009c) showed that in scenarios with forced-air cooling through horticulture packaging, the heat and momentum equations for airflow can be decoupled. This enables two important simplifications: first, an airflow solution can be computed independently of considerations pertaining to temperature; and second, a *steady-state* airflow solution can be computed, which has a significantly lower computational overhead than a time-dependent solution. The derived airflow pattern will remain unchanged if used as an input to a separate time-dependent heat transfer model, the consequence for the zonal model being that u_i remains constant throughout all time steps of the Zone Solver, and by extension, $h_{ext,i}$ for each zone remains unchanging over time.

The geometry was meshed into 384295 finite elements. Airflow was modelled as laminar flow according to Eq. 6.10 and Eq. 6.11:

$$\rho_A(\boldsymbol{u}\cdot\nabla)\boldsymbol{u} = \nabla\cdot[-p\boldsymbol{I} + \mu(\nabla\boldsymbol{u} + (\nabla\boldsymbol{u})^T)] \tag{6.10}$$

$$\rho_A\nabla\cdot(\boldsymbol{u}) = 0 \tag{6.11}$$

Each simulation was primed with an initial air velocity of 0.5-3 $m\cdot s^{-1}$ in the direction toward the 'Outlet' (Figure 6.17). The GMRES solver then iteratively solved Eq. 6.10 and Eq. 6.11 until the residual error was below a prescribed level, or 200 iterations had been performed. The appropriateness of each steady-state solution is demonstrated by probing the velocity at the inlet of the left vent as the solver iterates towards convergence. This is shown in Figure 6.18.

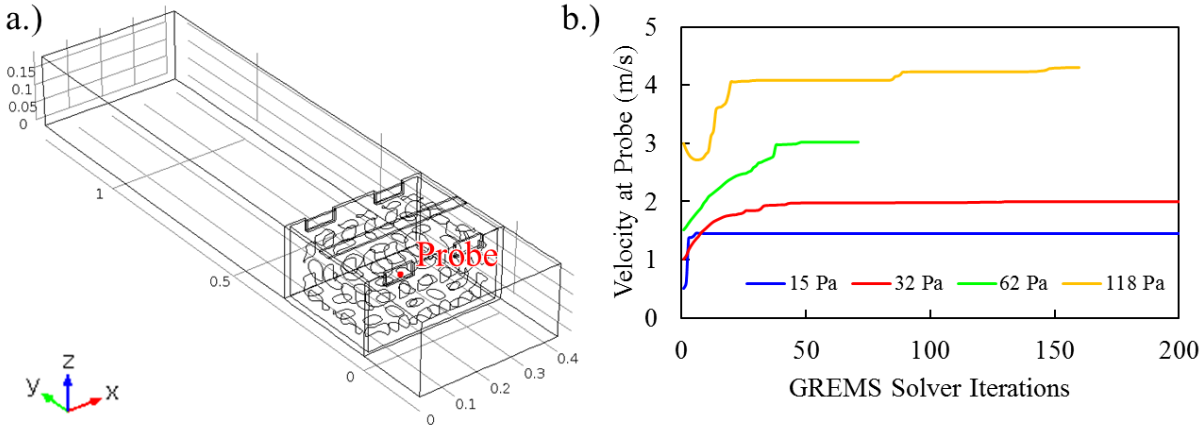

Figure 6.18: Convergence of the CFD airflow simulation: a.) probe location at the centre of the inlet to the left vent; b.) the measured velocity at the probe over GREMS solver iterations.

A velocity plateau is observed across all 4 investigated pressure drops, indicating that each solution has likely converged correctly. In some cases, the simulation was halted before 200 iterations as the residual error was below the prescribed amount, such as the 62 and 118 Pa. In the case of 118 Pa there is a slight increase in the velocity at the probe just convergence; however, moving from 4.23 to 4.30 $m\cdot s^{-1}$ is a 1.7% increase and so can be considered negligible, and the steady-state solution appropriate.

Results of each simulation through the entire wind tunnel are visualised in Figure 6.19 and Figure 6.20:

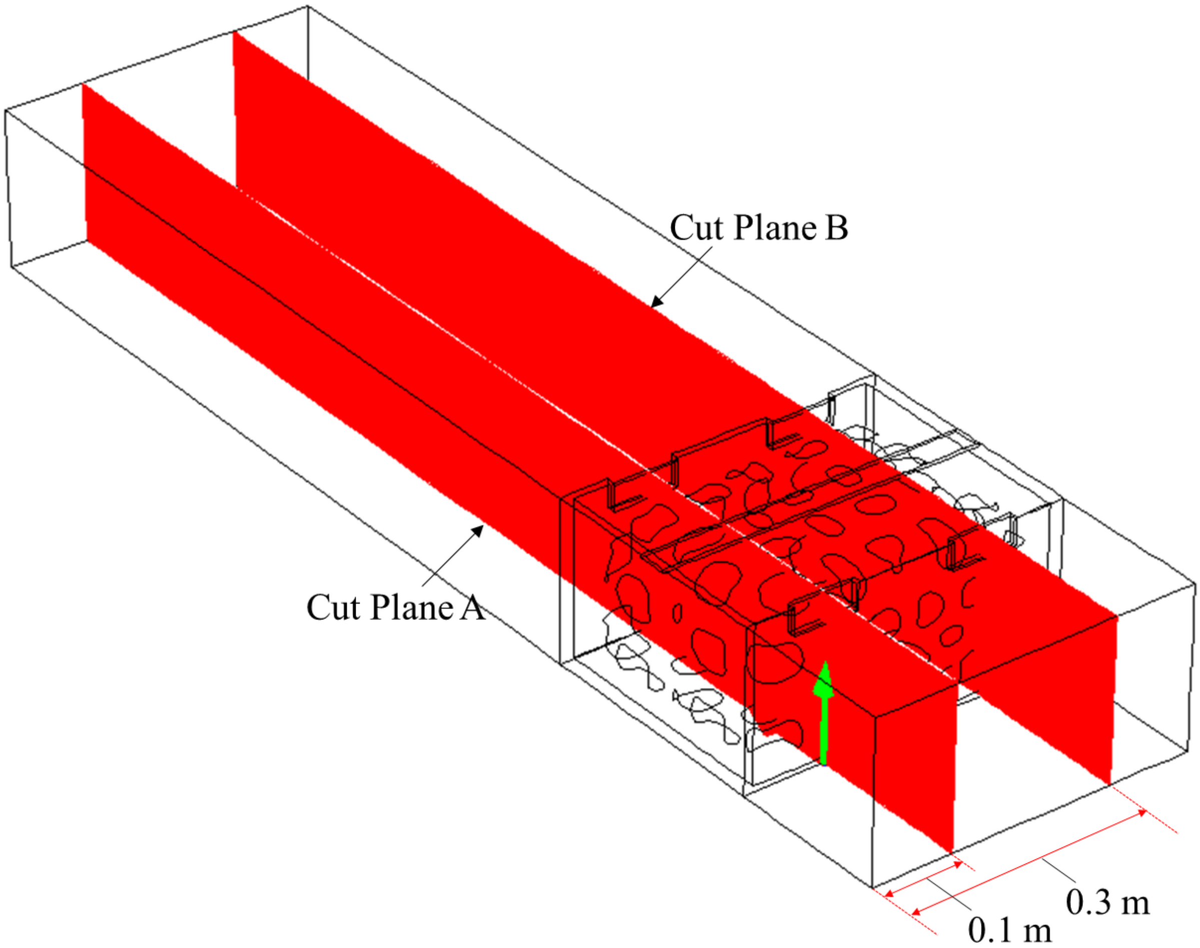

Figure 6.19: Cut planes through model geometry to visualise predicted airflow pattern (Figure 6.20).

Figure 6.20 shows a predicted airflow field that is to be expected: with ventilation at the top of the package and the gap between the top of the box and polyliner forming a fairly large headspace, a majority of the air flows through this region and the velocity of air is at its highest. A minority of the air flows through the sides of the box due to the increased resistance through the narrower channels caused by the presence of fruit and the polyliner; and on the bottom of the box is negligible net flow; and there is no airflow through the air between fruits as the polyliner acts as a barrier. As the pressure drop increases, the relative velocity in each region accelerates – such as comparing the inlet-to-vent velocity of the ΔP_{pallet} = 15 Pa result of ~1.5 m·s^{-1} with the ΔP_{pallet} = 118 Pa result of ~4 m·s^{-1} – however the general distribution (or airflow pattern) remains the same, following the aforementioned trends. Carrying this information over to the heat transfer model should result in a higher degree of external heat transfer due to airflow in zones at the top of the packaging when compared to zones at the sides and bottom, due to the large differences in predicted airflow velocity.

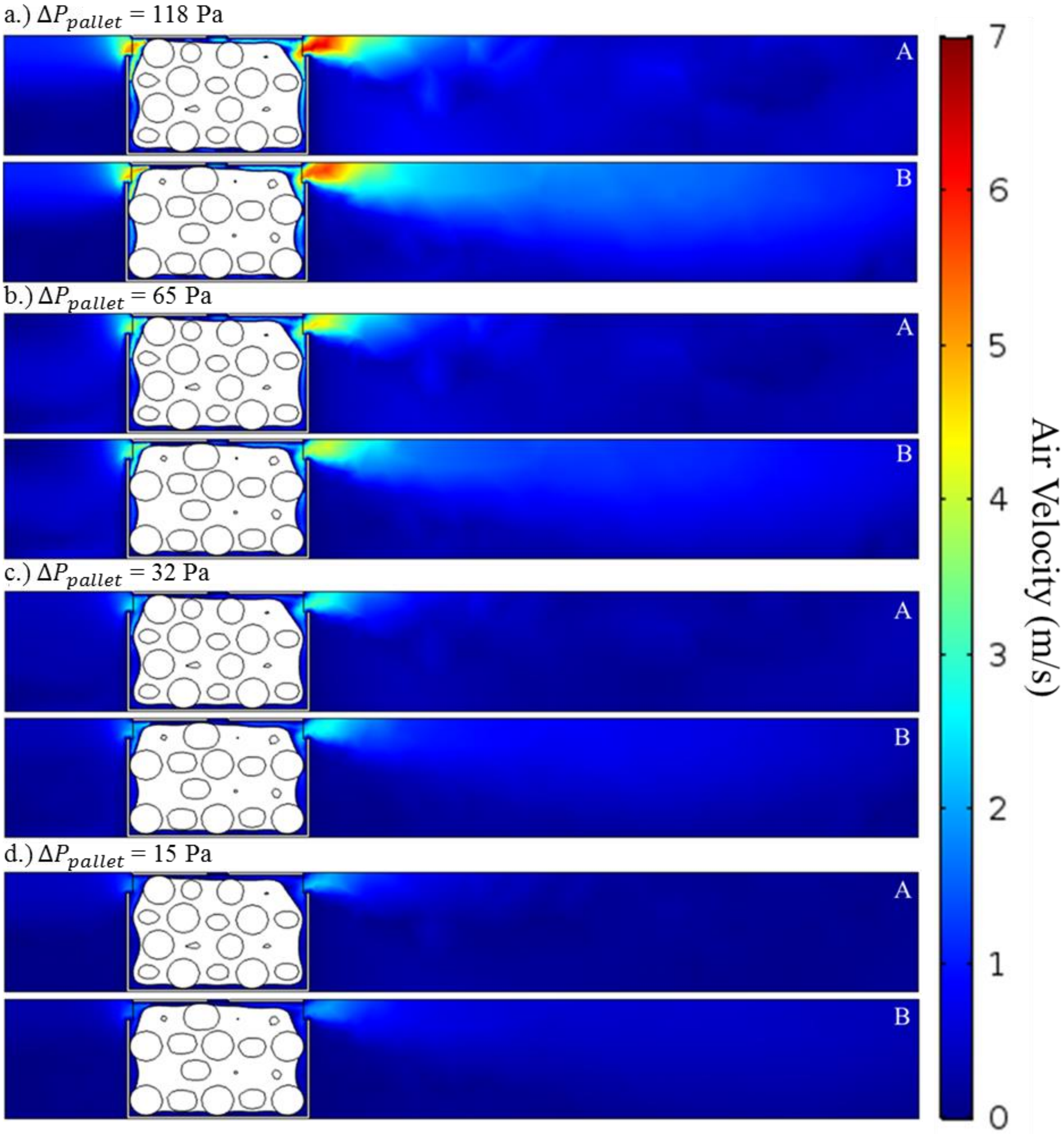

Figure 6.20: Predicted airflow fields at two positions (Figure 6.19) through a single modular bulk package of polylined kiwifruit using CFD at $\Delta \mathrm{P}_{\mathrm{pallet}}$ *of: a.) 118 Pa; b.) 65 Pa; c.) 32 Pa, and; d.) 15 Pa.*

This process for predicting airflow was not efficient, taking approximately 35 minutes to reach convergence for each of the 4 ΔP_{pallet} values. Should a zonal model be sought after with a new bulk fruit geometry or new package design, the airflow field would need to be re-calculated. Incorporating this into an optimization routine, each loop would take ~35 minutes, clearly a violation of the computational efficiency principle. Ideally, it can be replaced at a later date with an airflow model that is similarly fast, flexible and automated as the heat transfer zonal model, a task being actively pursued separately to this thesis.

The next consideration was how to use the CFD airflow information to appropriate the velocity through each zone of the zonal heat transfer model. A technique was developed to acquire this information in a fashion that is flexible to changes in zone size and/or zonal resolution: the 'central position' of the bulk air phase inside of each zone was identified by applying a distance transform to the bulk air phase to determine the position that was 'furthest away' from all other surfaces – fruit, packaging, polyliner or the edges of the zone (Figure 6.21).

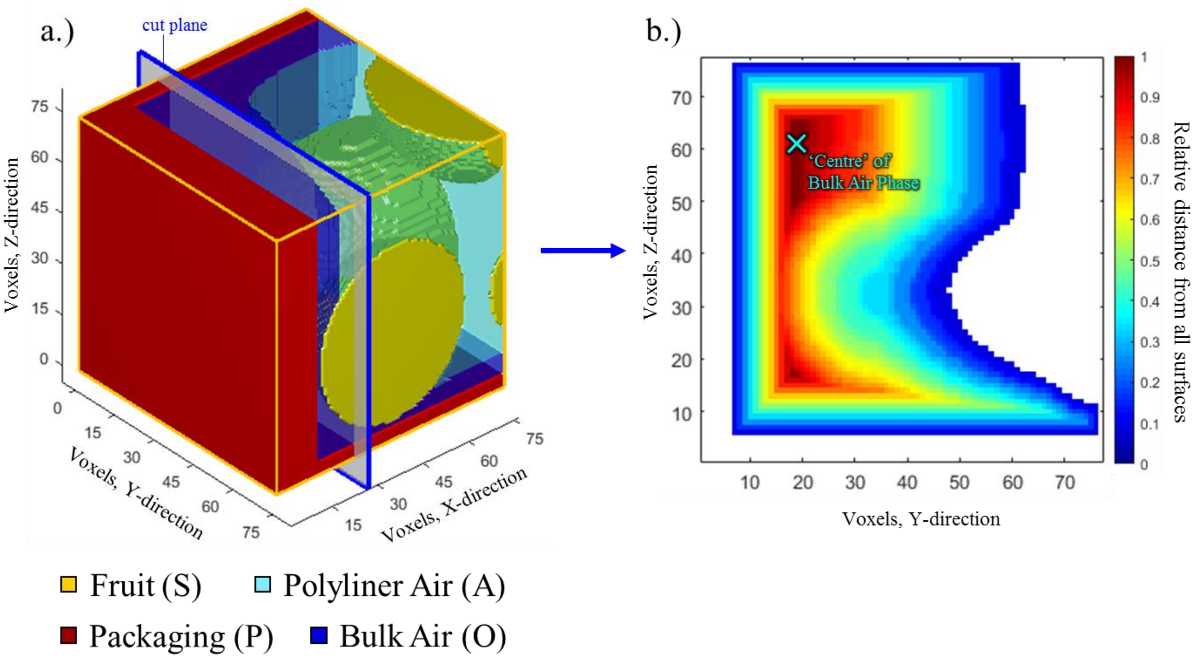

Figure 6.21: Geometric procedure for determining the 'central position' of the bulk air phase: a.) a zone on the corner of the geometry with a bulk air phase; b.) a cutplane of the bulk air phase with the distance transform applied, the largest relative distance from all surfaces being the 'centre' of the phase.

This position is where one would expect an anemometer probe to be placed, if airflow information was collected experimentally. Inserting this procedure into the zone builder was trivial and did not have an impact on computational efficiency. The geometric procedure collates a list of positions that correspond to the centre of each zone through which there is refrigerated airflow, which is then easily imported into COMSOL as a list of positions, with the 'Cut Point 3D' tool used to appropriate the velocity at each of the specified positions, demonstrated in Figure 6.22 and Figure 6.23:

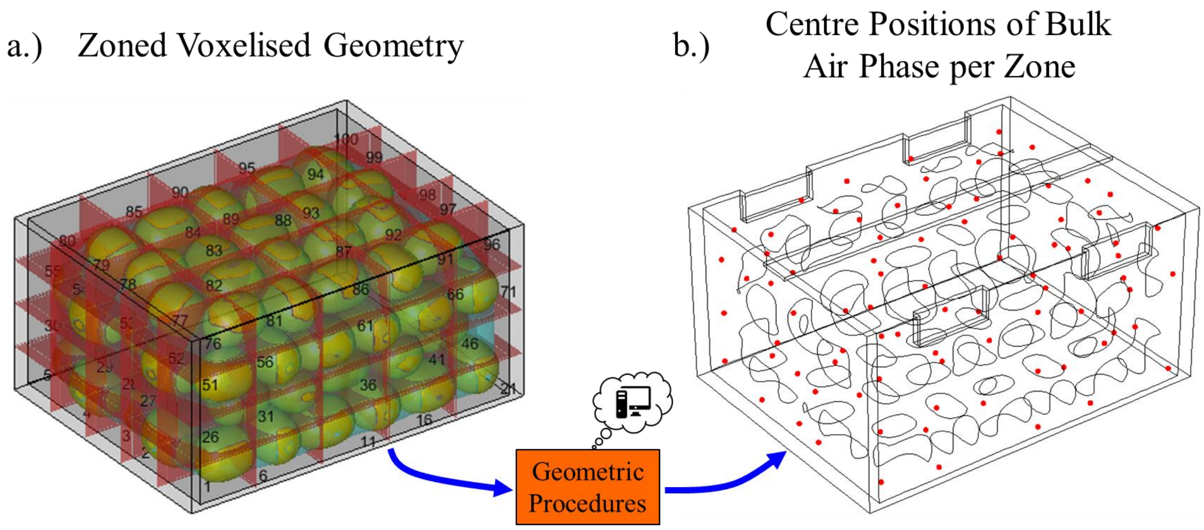

Figure 6.22: a.) list of 'central positions' exported from the zone builder; b.) list imported into COMSOL to generate the velocity at each position, to represent the airflow through each applicable zone.

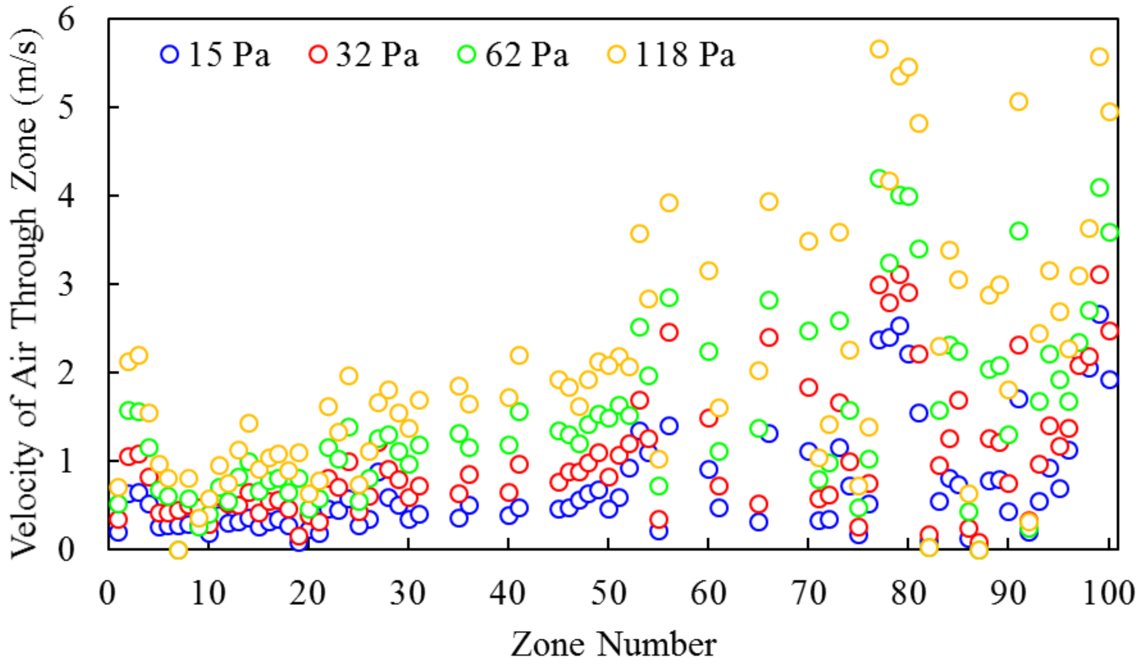

Figure 6.23: Bulk air velocity through each zone, $\mathrm{u_i}$*, appropriated from the CFD airflow model using positions derived from the 'central position' geometric procedure; blue, red, green and yellow circles represent* $\Delta\mathrm{P_{pallet}}$ *= 15, 32, 62 and 118 Pa, respectively.*

Figure 6.23 shows the bulk air velocity through each zone, u_i, derived in an automated fashion from the CFD model for each value of ΔP_{pallet}. Not all zones have airflow, which is why gaps appear in Figure 6.23, representing zones that do not have a bulk air phase (zones in the middle of the package). Zones 1-25 represent zones on the bottom of the box, and have a very low velocity due to the higher resistance to airflow due to the fruit and polyliner stack. Zones 76-100 represent zones on the top of the box, nearest to the vent openings, and so in general have a higher velocity. The differences in velocity are caused by the airflow pattern, which is a result of the pressure drop as well as the geometry of the fruit, polyliner and box. This information will be used to derive a unique $h_{ext,i}$ for each zone (section 6.3.3).

6.3.3: External Heat Transfer Coefficient Correlation

With a zonal heat transfer model (section 5.5.6) and an airflow model capable of predicting the velocity through each zone (section 6.3.2), combining these into a unified predictive model for fruit inside of horticultural packaging and validating it on a global and local level with empirical cooling data (section

3.4) requires that the velocity information per zone, u_i, is related to an external heat transfer coefficient, $h_{ext,i}$, through an appropriate correlation.

By way of a theoretical examination of the fluid boundary layer (Pohlhausen's Method in Kakaç *et al*, 2014), the relationship between $h_{ext,i}$ and u_i is typically given through a $\mathrm{Nu} = f(\mathrm{Pr}, \mathrm{Re})$ correlation:

$$\mathrm{Nu} = \frac{h_{ext} \cdot L}{\lambda_A} \tag{6.12}$$

$$\mathrm{Pr} = \frac{C_A \cdot \mu}{\lambda_A} \tag{6.13}$$

$$\mathrm{Re} = \frac{u \cdot \rho_A \cdot L}{\mu} \tag{6.14}$$

$$\mathrm{Nu} = a \cdot \mathrm{Pr}^b \cdot \mathrm{Re}^c \tag{6.15}$$

Where Nu, Pr and Re are the dimensionless Nusselt, Prandtl and Reynolds numbers. These are related through coefficients a, b and c in Eq. 6.15, and are either derived analytically, such as Eq. 6.16 (derived by Pohlhausen, taken from Kakaç *et al*, 2014) for convection over a flat plate:

$$\mathrm{Nu} = 0.332 \cdot \mathrm{Pr}^{\frac{1}{3}} \cdot \mathrm{Re}^{\frac{1}{2}} \tag{6.16}$$

Or they are empirically determined, such as Eq. 6.17 which describes cooling through smooth pipes (Dittus and Boelter, 1930):

$$Nu = 0.023 \cdot \mathrm{Pr}^{0.3} \cdot \mathrm{Re}^{0.8} \tag{6.17}$$

Producing a general relationship between u_i and $h_{ext,i}$ can therefore be achieved by using Eq. 6.15 and determining representative a, b and c coefficients. Deriving these through analytical means was not feasible, given the reduced focus of this thesis on the details of airflow and also the significant undertaking that derivation of an analytical solution represents. Airflow through the interior of the box could be considered ‘pipe like’, especially in the headspace region where there is a substantially large channel created between the top of the box and the top of the polyliner. As such, Eq. 6.17 may be suitable for this project. In the event that it is inadequate, a new correlation could be empirically developed through an iterative routine to produce a, b and c coefficients with the smallest difference between simulated and measured cooling rates. The short solution times of the zonal model (0.6 seconds for a model with 100 zones, see section 6.2.3.2) facilitates such an iterative approach. These are explored later (section 6.3.6.2).

6.3.4: Characteristic Dimension of Bulk Air Phase

Use of a $\mathrm{Nu} = f(\mathrm{Pr}, \mathrm{Re})$ airflow correlation requires a Reynolds number. According to Eq. 6.14, the velocity through zones, u, is given by the CFD airflow model of section 6.3.2; and ρ_A and μ are physical properties of the fluid (ρ_A = 1.205 kg·m^{-3} and μ = 1.72×10^{-5} Pa·s). The remaining unknown is L, the 'length' or characteristic dimension of the system under study. The definition of a characteristic length changes depending on the system: for example, it is the *diameter* of a pipe, or it the *length* of a flat plate. In the current scenario, defining a characteristic length for an intra-zonal bulk air phase geometry was more challenging, it being highly irregular. In many applications, L is defined as the hydraulic diameter (ASHRAE, 2013), $L = 4 \cdot A/P$, where A is the cross sectional area perpendicular to direction of fluid flow (m^2) and P is the total wetted perimeter (m). Such a definition is difficult to implement in the current model as flow occurs in a multitude of directions (the direction at any point is information that is not known), and a wetted perimeter is difficult to derive from a convoluted bulk air phase geometry. An alternative technique was settled upon, which was to compute an effective characteristic length, L_{eff}, as the ratio between the volume of the bulk air phase and the surface area of airflow interaction (Eq. 6.18 and Figure 6.24):

$$L_{eff,i} = \frac{V_{O,i}}{A_{eff,cond,S\to O,i} + A_{eff,cond,P\to O,i} + A_{eff,cond,A\to O,i}} \tag{6.18}$$

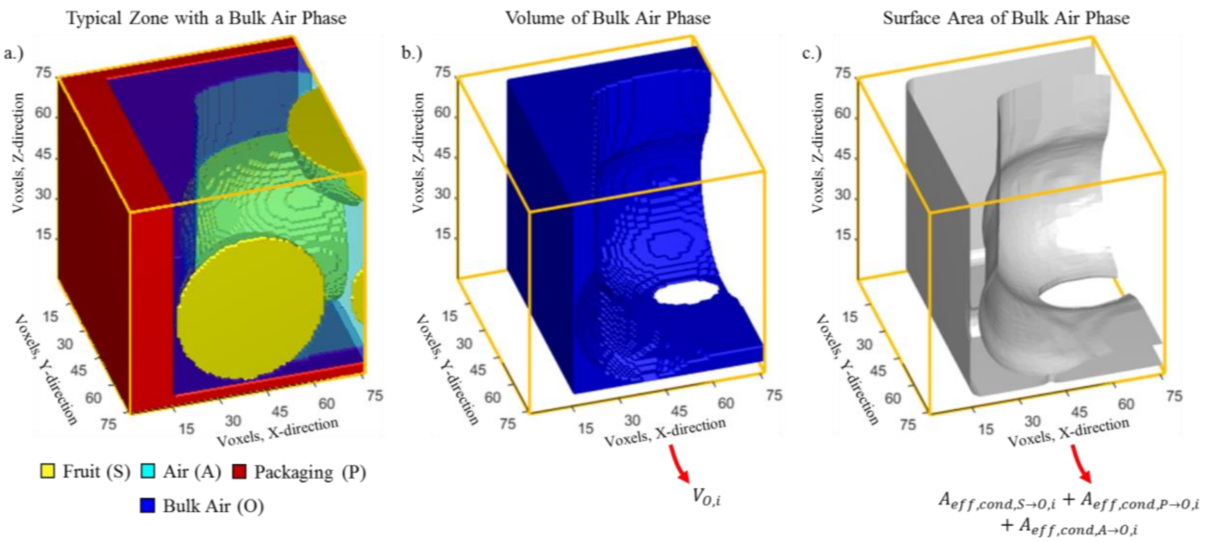

Figure 6.24: Geometric procedure for appropriating the effective characteristic length for use in Reynolds number calculations, $\mathrm{L_{eff}}$*, by dividing the volume of the bulk air phase by the surface area of airflow interaction.*

As each term in Eq. 6.18 has been computed previously by another geometric procedure, (section 5.5.6.1), inserting the derivation of L_{eff} into the zone builder was trivial.*

6.3.5: Experimental Validation Model Set-Up

This iteration of the zonal model aimed to compare predicted cooling rates with empirical cooling data (section 3.4) and to investigate the performance of $\mathrm{Nu} = f(\mathrm{Pr}, \mathrm{Re})$ correlations (section 6.3.3). As such, the fruit and polyliner geometry from the previous iteration (section 6.2.3.2) were used again, being analogous to the fruit stacking pattern imposed experimentally. The packaging phase ($Z = P$) was added for this iteration with the same dimensions as a modular bulk package (Figure 6.25a). The new geometry was voxelised to a 1mm^3 resolution (Figure 6.25b) and zoned into 100 zones, an appropriate zonal resolution given the results of section 6.2.3.2 (Figure 6.25c).

The voxelised and zoned geometry was passed through the zone builder (section 5.5.6) to automatically construct the zonal network. The boundary conditions of the network were amended to simplify the

* Note: in a case where there is a zone filled entirely with the bulk air phase, the surface area of airflow interaction will be 0, so the effective length will be $L_{eff} = \infty$, the consequence being $h_{ext} = \infty$, which is an obvious error. However, given that h_{ext} is restricted to being an intra-zonal phenomenon (section 5.5.6.1.5), this infinite level of external heat transfer is not applied to any other phases and so has no impact on the cooling results.

model and ensure that it was a close representative of the experimental set up. The surface of selected boundaries were defined as Ω with the subscripts ↑, ↓, ←, →, ⊙, and ⊗ to represent each of the 6 boundaries of the box (Figure 6.26a).

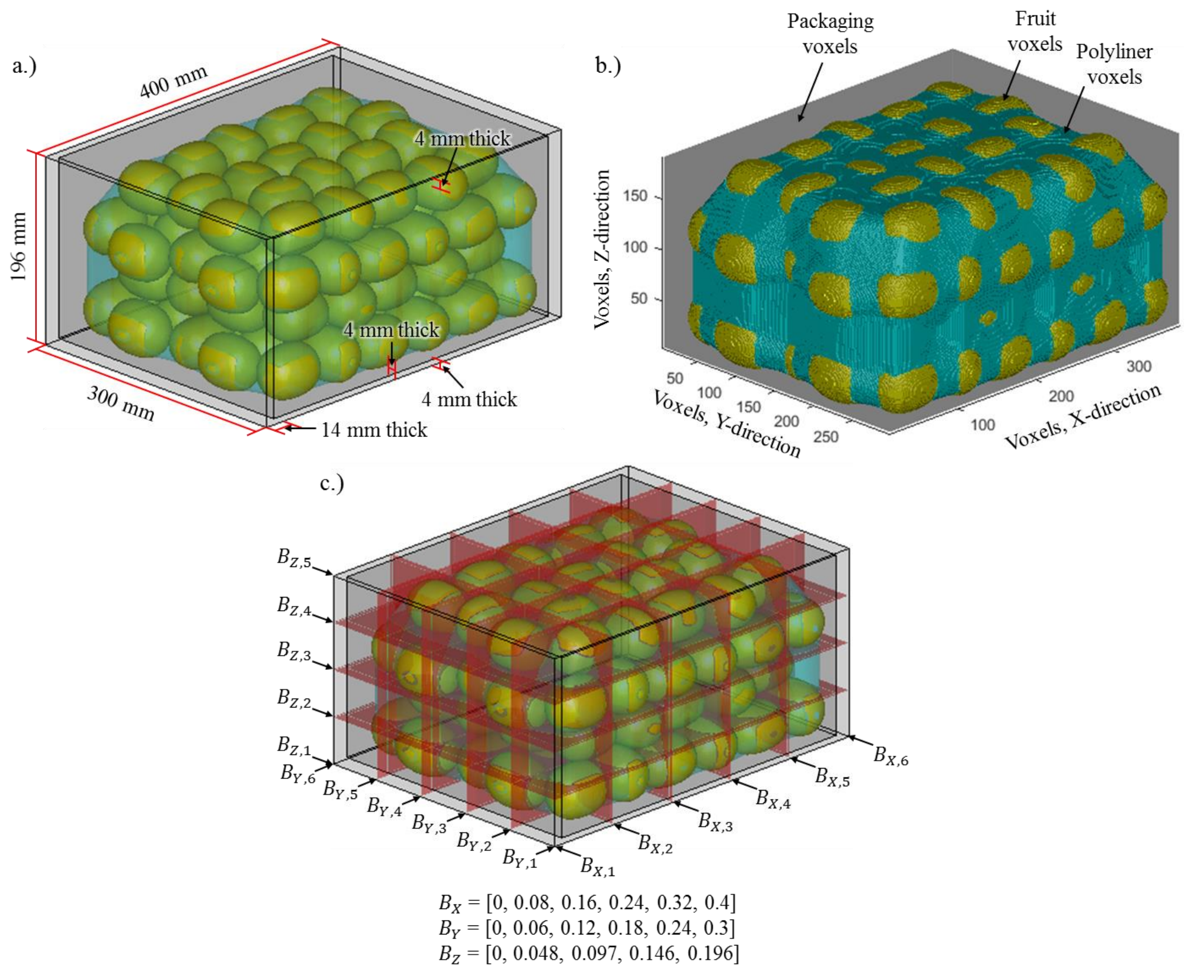

Figure 6.25: Experimental validation zonal model set-up: a.) model geometry of a modular bulk package filled with 100 count 36 kiwifruit, wrapped in a polyliner; b.) the model geometry voxelised to 1 mm³; c.) the voxelised model geometry zoned into a zonal network with N_X *= 5,* N_Y *= 5 and* N_Z *= 4 (*N_{total} *= 100 zones).*

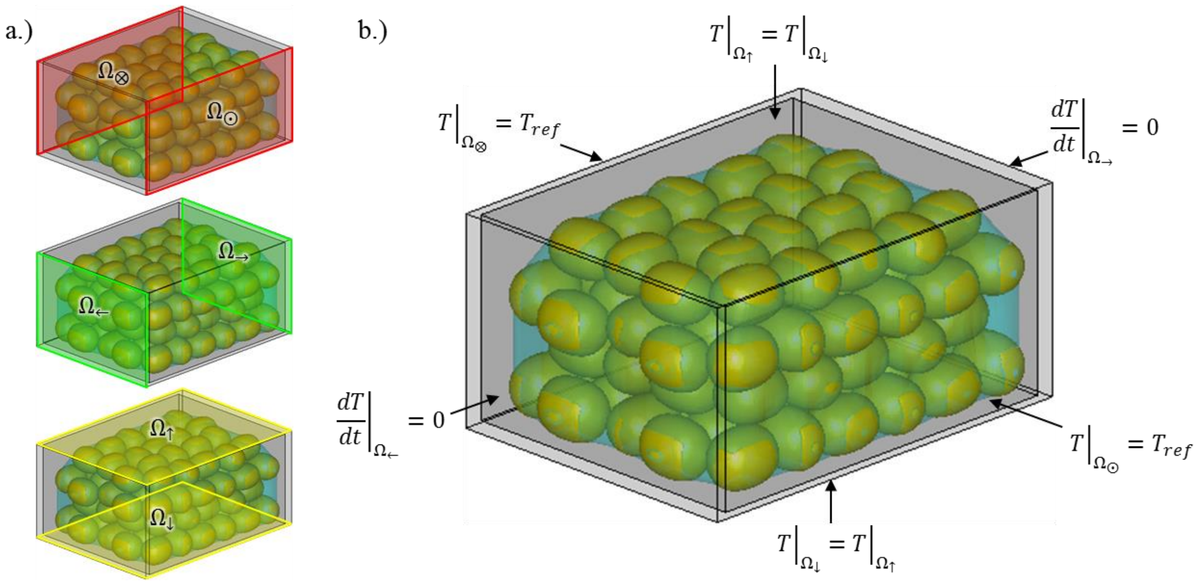

Figure 6.26: Boundary conditions for the zonal model.

The sides of the box ($\Omega_\leftarrow$ and $\Omega_\rightarrow$) in the experimental set up were insulated with thick slabs of polystyrene; therefore from a heat transfer perspective there is no heat flux through these boundaries, or $dT/dt|_{\Omega_\leftarrow} = 0$ and $dT/dt|_{\Omega_\rightarrow} = 0$ (see Figure 6.26b). 6 boxes were stacked on top of one another in the experiment, with the 3 centre boxes instrumented with temperature logging equipment. Rather than create a zonal model comprising of 6 boxes stacked on top of one another, adding a periodic boundary condition connecting the top and bottom surfaces ($\Omega_\uparrow$ and $\Omega_\downarrow$, respectively) allows the geometry to be simplified to a single box, the intention being that this box represents the 'average' box that sits in the centre of a pallet: $T|_{\Omega_\uparrow} = T|_{\Omega_\downarrow}$ and $T|_{\Omega_\downarrow} = T|_{\Omega_\uparrow}$. Finally, the front and back surfaces ($\Omega_\odot$ and $\Omega_\otimes$, respectively) are exposed to the cooling airflow directly, thus it is presumed that the velocity and tortuosity of this airflow is sufficient across all experimental pressure drops to assume a constant refrigeration temperature on these surfaces, or $T|_{\Omega_\odot} = T_{ref}$ and $T|_{\Omega_\otimes} = T_{ref}$. These boundary conditions were imposed on the Zone Solver through amendments to the Connectivity Matrix (see section 5.5.5).

The airflow model was integrated with the zone solver thusly: the combination of convective heat transfers via the flow of refrigerated air and conductive heat transfer through the packaging, fruit and polyliner air is described as an intra-zonal effective heat transfer coefficient in each zone with a bulk air phase:

$$h_{eff,conv,S\to O,i} = \frac{1}{R_{cond,S\to O,i} + \frac{1}{h_{ext,i}}} \tag{6.19}$$

$$h_{eff,conv,A\to O,i} = \frac{1}{R_{cond,A\to O,i} + \frac{1}{h_{ext,i}}} \tag{6.20}$$

$$h_{eff,conv,P\to O,i} = \frac{1}{R_{cond,P\to O,i} + \frac{1}{h_{ext,i}}} \tag{6.21}$$

$R_{cond,S\to O,i}$, $R_{cond,A\to O,i}$ and $R_{cond,P\to O,i}$ are computed via the AVDC of section 5.5.6.1.3. $h_{ext,i}$ is related to the physical properties of the fluid, the velocity of refrigerated airflow (via the CFD model, section 6.3.2) and the effective length of the bulk air phase (section 6.3.4) by means of a rearranged $\mathrm{Nu} = f(\mathrm{Pr}, \mathrm{Re})$ correlation:

$$h_{ext,i} = a \cdot \left[\frac{C_A \cdot \mu}{\lambda_A}\right]^b \cdot \left[\frac{u_i \cdot \rho_A \cdot L_{eff,i}}{\mu}\right]^c \cdot \left[\frac{\lambda_A}{L_{eff,i}}\right] \tag{6.22}$$

The bulk air phase, $Z = O$, is not modelled in the same way as its counterparts. During the execution of the zone solver, fruit, air inside of the polyliner and packaging change temperature in proportion to the magnitude of heat flux and their thermal mass over each time step; the bulk air phase, however, is kept at a constant refrigeration temperature, T_{ref}, over all time steps. In reality, the cold air will leave the package at an elevated temperature as it has absorbed heat from the hot fruit. Temperature change in the bulk air phase is not included in this iteration of the model as more information would need to be known about airflow in order to properly describe the inter-zonal hat exchanges through the air – specifically, $\dot{Q}_{ij}$, the matrix of volumetric flow rates from zone-to-zone (see section 5.5.6). Instead, it is assumed at there is a sufficient degree of air replacement through the box for the bulk air phase to practically always be at T_{ref}. This assumption seems appropriate at a single box scale, where air travels a small distance and is then expelled into the environment; however, at larger more industrially relevant scales, such as the pallet scale, this assumption will introduce an unacceptable level of error. The air being warmer at the back of the pallet due to absorbing heat from the front of the pallet is the reason why boxes at the rear of a pallet cool slower – see O'Sullivan (2016) for a practical example of this.

When integrating this zonal heat transfer model with an equivalently simplified airflow model, the warming of refrigerated air will need to be incorporated.

The fruit, packaging and air inside of the polyliner are all set to the initial temperature, T_i,at time $t = 0$; and the bulk air phase is set to a constant refrigeration temperature, T_{ref}. These are taken from the measured values from the experiment, with T_i being the average fruit temperature before the experiment begins, and T_{ref} the average measured air temperature at the inlet to all three boxes (Table 6.1 and section 3.4):

ΔP_{pallet} (Pa)	15	32	65	118
T_i (°C)	22.03	20.68	21.58	21.09
T_{ref} (°C)	0.05	0.05	0.03	0.14

Table 6.1: Measured initial temperatures and refrigeration temperatures

6.3.6: Results and Discussion

6.3.6.1: Preliminary $\mathrm{Nu} = f(\mathrm{Pr}, \mathrm{Re})$ correlation

The zone solver was executed for each of the four sets of velocity information derived from the airflow model of section 6.3.2 corresponding to the experimentally observed pressure drops of ΔP_{pallet} = 15, 32, 65 and 118 Pa (Figure 6.23). The $\mathrm{Nu} = f(\mathrm{Pr}, \mathrm{Re})$ correlation that was tried initially was that of Dittus and Boelter (1930), derived empirically for flow through smooth pipes (Eq. 6.17). It is acknowledged that the suitability of this correlation is debatable given the current scenario involves air flowing through horticultural packaging; as well as that the correlation being originally derived using a different definition of the Reynolds number, with Dittus and Boelter using the pipe diameter, while in the current case the effective length L_{eff} was used. Eq. 6.17 and the corresponding a = 0.023, b = 0.3 and c = 0.8 coefficients are therefore treated as a starting position to test the need for a more representative correlation.

Preliminary results are presented for global comparisons in Figure 6.29, and for local comparisons in Figure 6.27 and Figure 6.28. For local comparisons, each experiment had 3 replicates of single boxes, where fruit were stacked into the same repeatable pattern so that thermocouples could be inserted into the same 12 positions across all trials (positions are given in Figure 6.12). Empirical local cooling rates are presented as the average of the recorded temperatures at each temperature position, with the associated error bars representing the standard deviation in the 3 measurements over time. Empirical cooling rates are compared with results from the zonal model, where in a similar fashion to section 6.2.3.2, the volume averaged fruit temperature of the zone closest to each of the 12 temperature positions are plotted. For global comparisons, the average temperature across all 3 replicates (36 temperature positions) are plotted, with the error bars being the 95% confidence interval. This is compared with the zonal model, where the average temperature of the 12 zones closest to the 12 selected temperature positions are plotted.

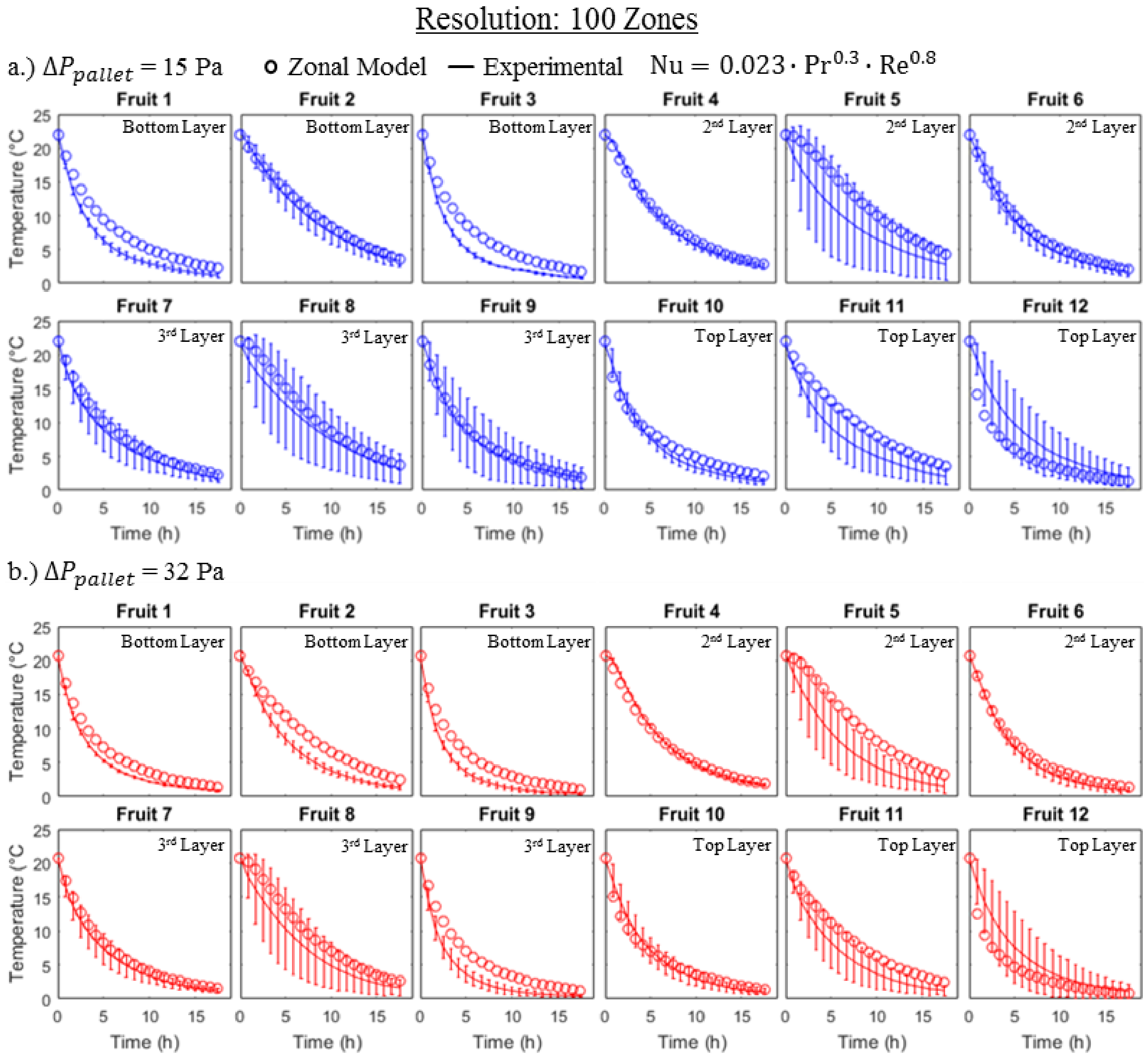

Figure 6.27: Preliminary empirical validation of zonal model, comparing simulation results at the local level, for $\Delta \mathrm{P}_{\mathrm{pallet}}$ of a.) 15 Pa and; b.) 32 Pa. Circles are the zonal model, lines empirical data, error bars are the standard deviation.

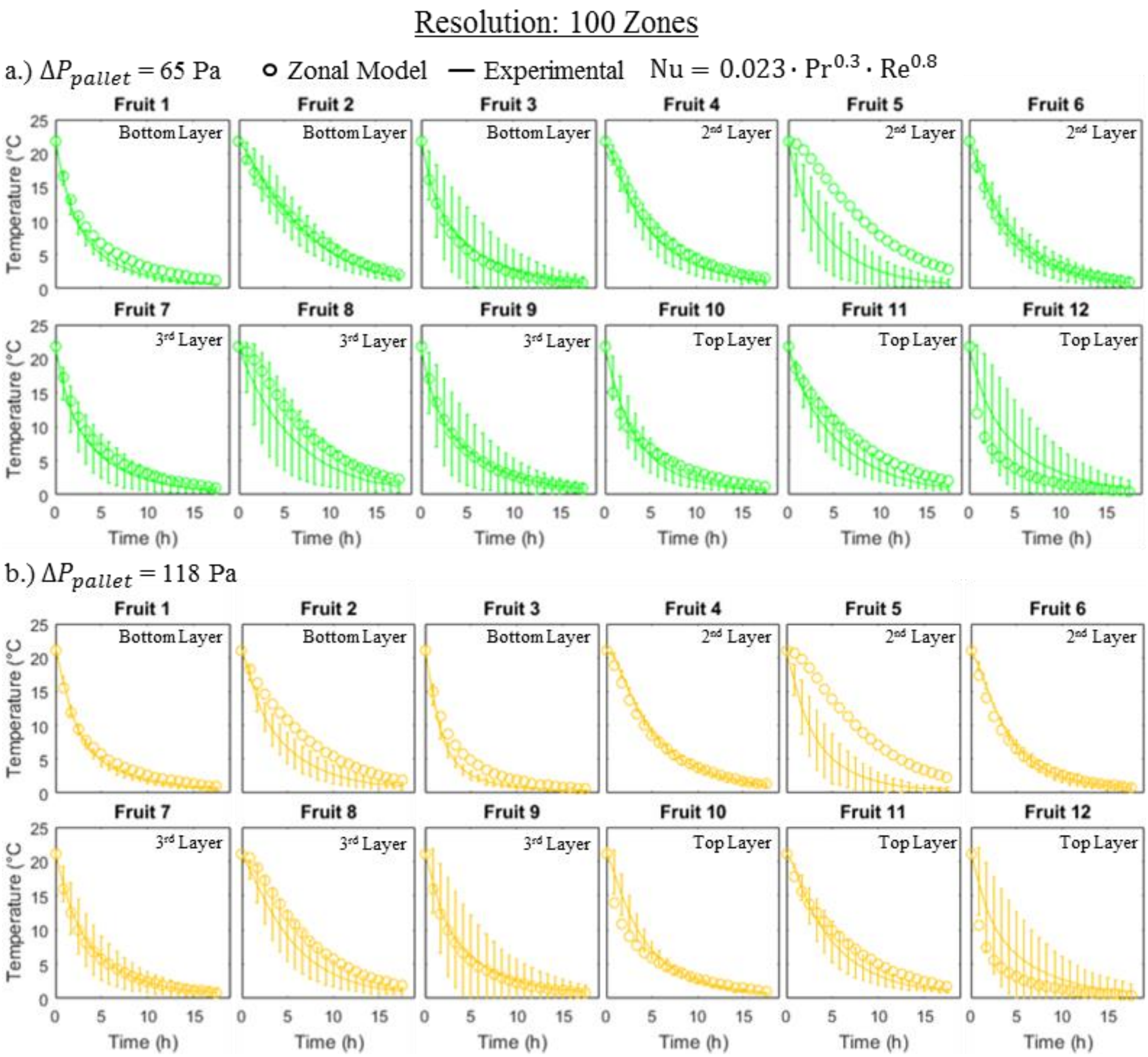

Figure 6.28: Preliminary empirical validation of zonal model, comparing simulation results at the local level, for ΔP_{pallet} *of a.) 65 Pa and; b.) 118 Pa. Circles are the zonal model, lines empirical data, error bars are the standard deviation.*

Figure 6.27 and Figure 6.28 shows that assuming air flowing through a horticultural package has similar heat transfer properties as pipe flow was moderately successful. Though there were some notable locations where the differences between the model and experimental temperature profiles were large enough to be outside the bounds of experimental error – such as the bottom layers (fruits 1, 2 and 3); and the centre of the package (fruit 5) – the overall fit across the 4 experiments could be considered satisfactory. Some of the agreement may be partially due to the large degree of experimental error (see section 3.4 for a discussion on potential causes), such as fruit 12 where the model consistently predicts a faster cooling rate than the average measured rate, but (due to the large experimental uncertainty at this position) lies within the experimental data. A similar analysis can be applied to fruits 8 and 11, which have a slower predicted rate than the average measured rate but are still within the relatively large bounds of variability.

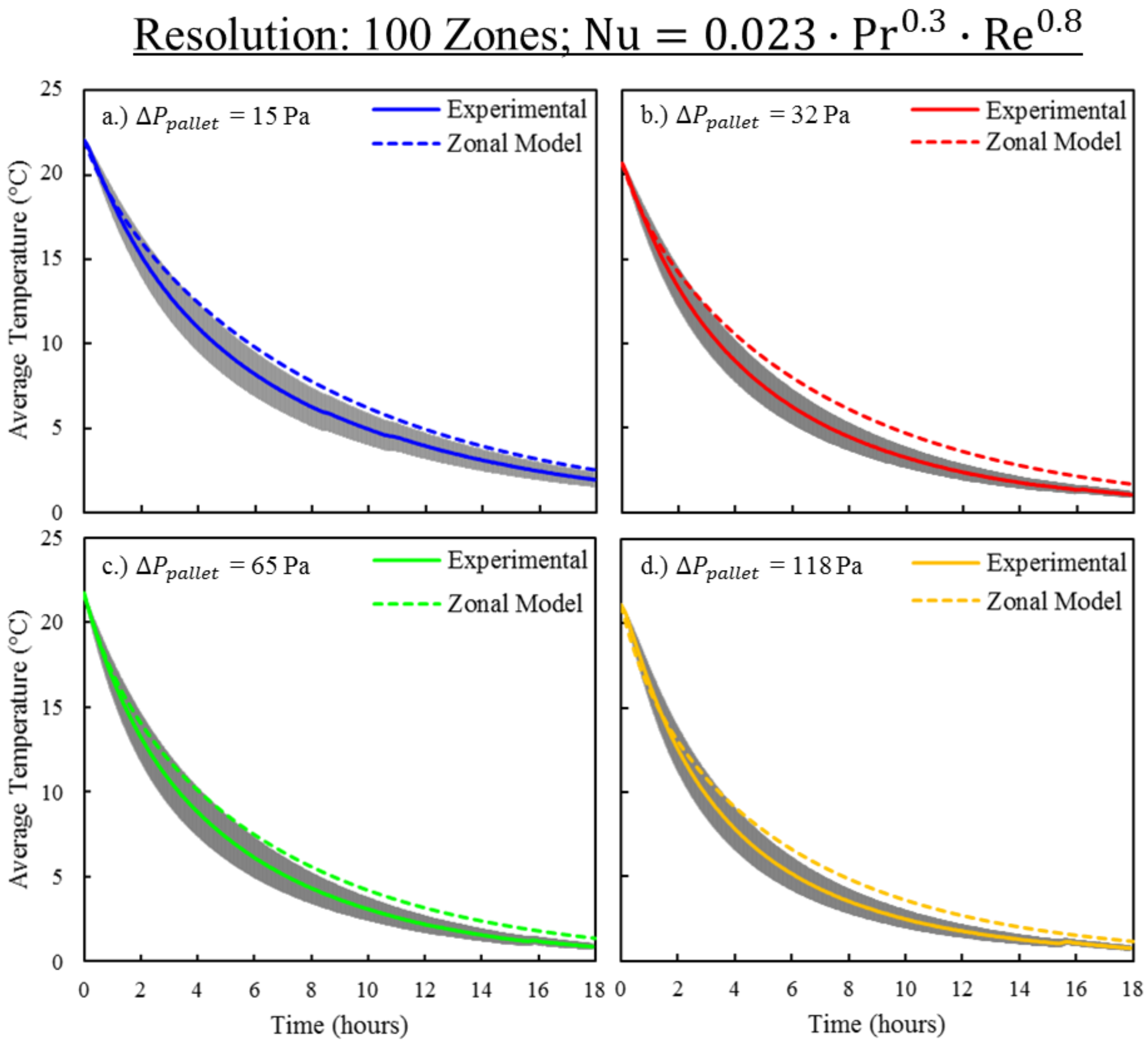

Figure 6.29: Preliminary empirical validation of zonal model, comparing simulation results at the global level, for ΔP_{pallet} of a.) 15 Pa; b.) 32 Pa; c.) 65 Pa, and; d.) 118 Pa. Solid lines are empirical data where error bars are the 95% confidence interval, and dashed lines are the zonal model.

Figure 6.29 clarifies the deficiencies of using a pipe flow correlation, showing this preliminary model universally under-predicts the experimentally observed cooling rate, and the degree of under-performance is significant enough for the predicted rate to fall outside of the margin of experimental error in all cases. This coupled with several local positions predicting the true rate poorly leads to the conclusion that the airflow correlation requires more representative a, b and c coefficients that are representative not of pipe flow, but of airflow through a horticultural package.

6.3.6.2: Derivation of New Airflow Correlation

Having concluded previously in section 6.3.6.1 that the initial airflow correlation Eq. 6.17 is not sufficient for use in airflow through horticultural packaging, the need for a new, more representative correlation became apparent. This section aims to develop this new correlation, taking advantage of the speed of the zonal model to iteratively test many combinations of a, b and c coefficients for the generalised Eq. 6.15 ($\mathrm{Nu} = a \cdot \mathrm{Pr}^b \cdot \mathrm{Re}^c$) until the differences between the model and experiment are minimised.

This exercise begins with determining the definition of the **residual**, or **error**, a metric that represents the overall difference between the model and experiment, which is to be minimised through changes to the a, b and c coefficients. It was decided that optimization would be done with respect to *local rates of heat transfer*, as this gives more optimization points to minimise than a single average cooling curve. Therefore, the total residual was taken as the sum of differences in temperature over the entire cooling period, or Figure 6.30 and Eq. 6.23:

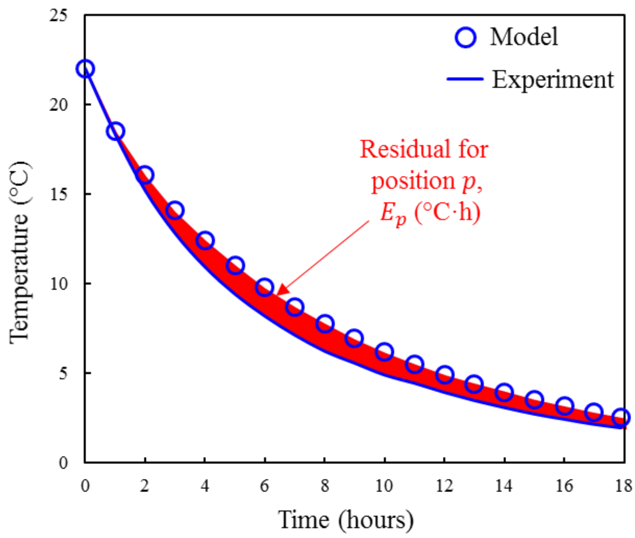

Figure 6.30: Definition of a residual for one temperature position, the total temperature difference between the experiment and model prediction over all times.

$$E_p = \sum_{t=t_i}^{t_f} \left| T_{Exp,t,p} - T_{Mod,t,p} \right| \tag{6.23}$$

Where $T_{Exp,t,p}$ is the experimental temperature of position p at time t; and $T_{Mod,t,p}$ is the temperature predicted by the model at position p and time t; t_i is the starting time (t_i = 0 hours) and t_f is the process end time (t_i = 18 hours); and E_p is the residual of position p, which has the units of degree hours (°C·h; the red shaded area of Figure 6.30).

This process is repeated for all 12 positions and all 4 experiments, to give the total residual, E_{total}:

$$E_{total} = \sum_{e=1}^{4} \sum_{p=1}^{12} \sum_{t=t_i}^{t_f} \left| T_{Exp,t,p,e} - T_{Mod,t,p,e} \right| \tag{6.24}$$

Where e is the number of experiments, which in this case is 4.

With E_{total} representing the cost function, an optimization routine can be constructed around its minimisation. The overall structure of the routine that was developed is presented in Figure 6.31:

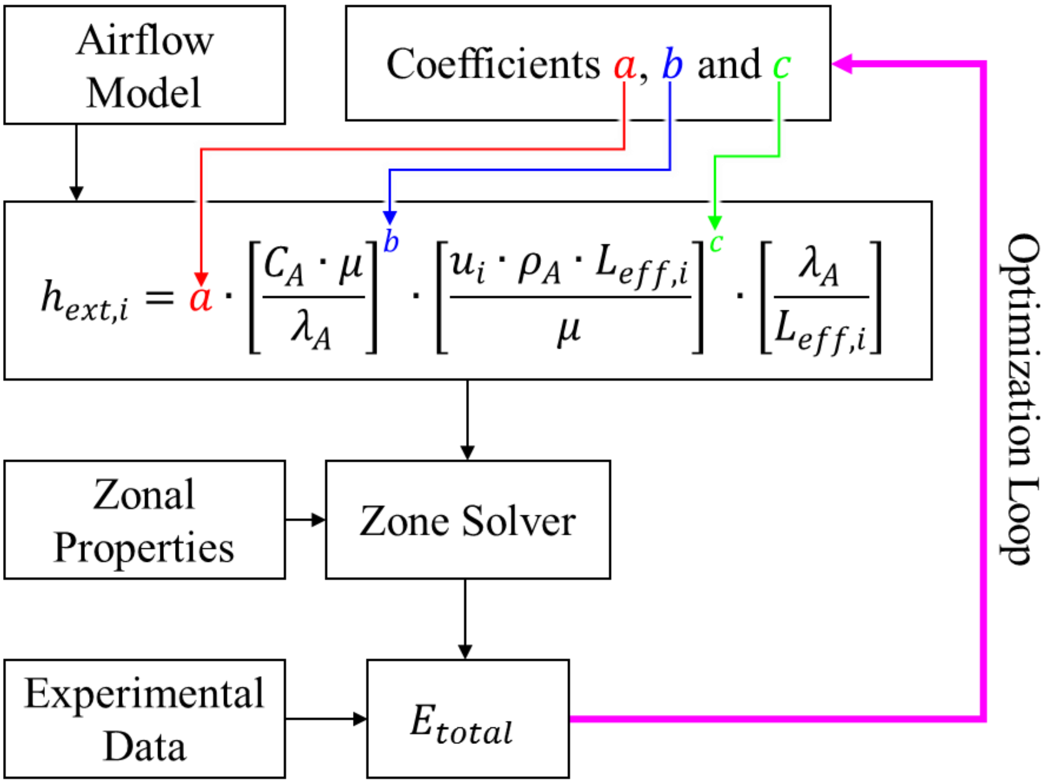

Figure 6.31: Structure of the optimization routine designed to derive a more representative airflow correlation.

This routine relied on inputs from the airflow model (to provide u_i, section 6.3.2), zone builder (to provide the zonal properties, section 5.5.6) and experimental data (section 3.4). The results from the

Zone Solver was then used to compute the total residual, E_{total}, of a specific set of a, b and c coefficients. A new set of a, b or c coefficients were then inserted into the beginning of the routine – these being small adjustments to the previously used numbers – and their impact scored as having a positive or negative impact on E_{total}. The speed of the zone solver was exploited, as with a ~1 second solution time, this process could be repeated hundreds of times in only a few minutes, until a set of a, b and c values were found that minimised E_{total} as much as possible.

The routine was coded in MATLAB, with the function 'lsqnonlin' controlling the changes to a, b and c per iteration to minimise E_{total}. The starting position were the coefficients used during the preliminary experimental validation: that is a = 0.023, b = 0.3 and c = 0.8. The routine was restricted to values between 0 and 1 only. The results of the optimization and derivation of a new airflow-heat transfer correlation are given in Figure 6.32.

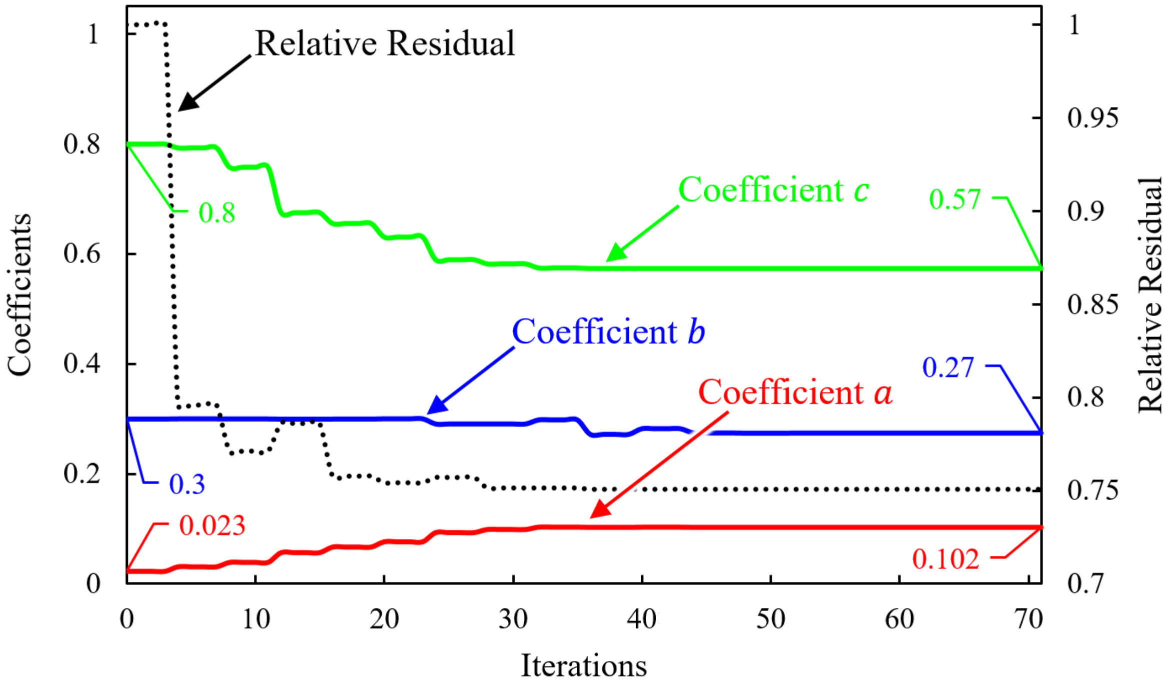

Figure 6.32: Results of the iterative optimization routine, tracking the chosen coefficients a, b *and* c *and the residual over each iteration.*

The residual is given in relative terms, which is $E_{total}/E_{total,0}$, where $E_{total,0}$ is the residual computed after the first iteration. Overall, the routine took 70 iterations to reduce E_{total} to its minimum, a process that only took under 2 minutes due to the computational efficiency of the zonal model. The routine returned a new airflow correlation of:

$$\mathrm{Nu} = 0.102 \cdot \mathrm{Pr}^{0.27} \cdot \mathrm{Re}^{0.57} \tag{6.25}$$

The efficacy of the new correlation was demonstrated through the same global and local comparisons as previously (section 6.3.6.1) in Figure 6.33, Figure 6.34 and Figure 6.35:

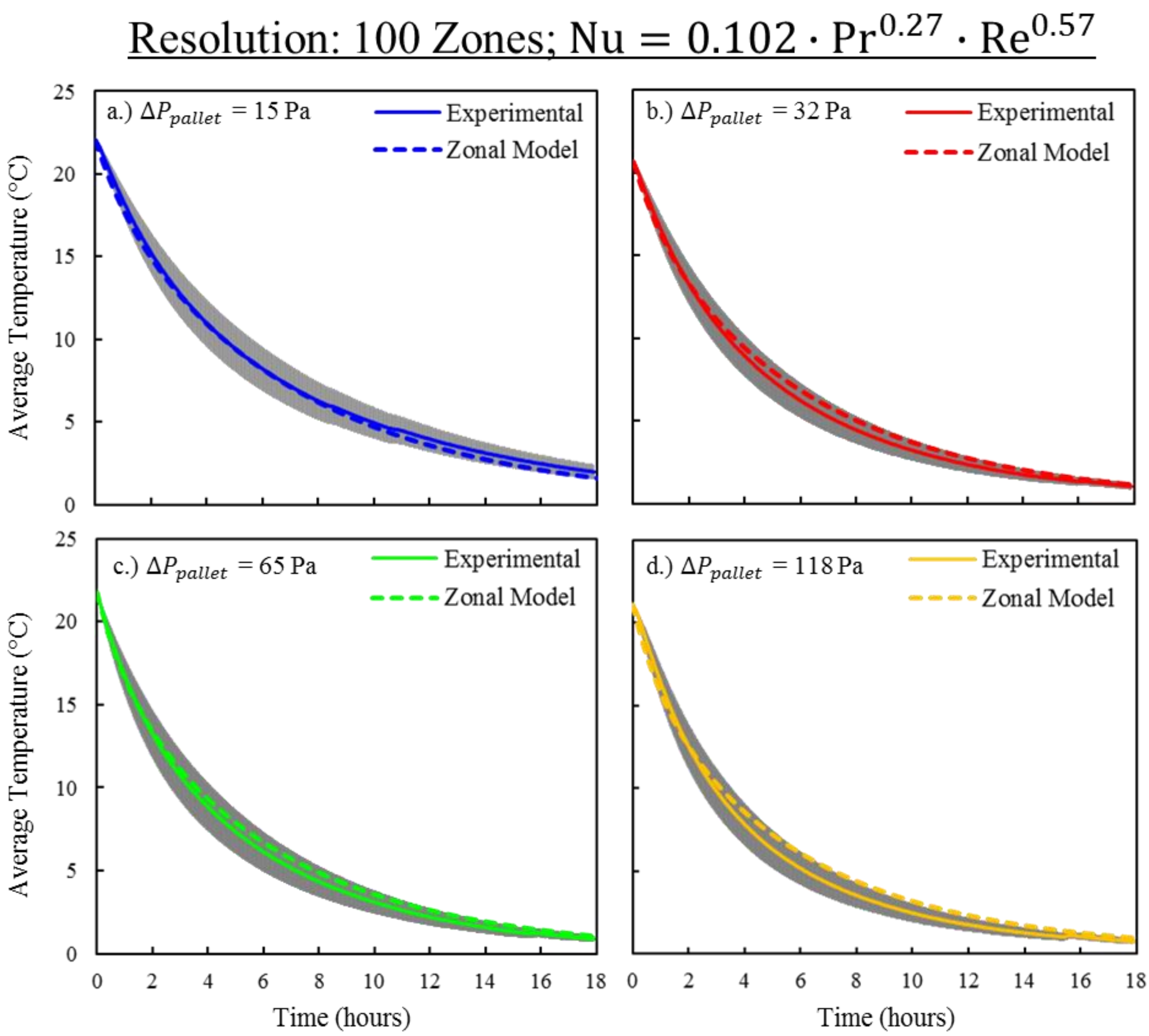

Figure 6.33: Empirical validation of zonal model with the new airflow correlation, comparing simulation results at the global level, for ΔP_{pallet} *of a.) 15 Pa; b.) 32 Pa; c.) 65 Pa, and; d.) 118 Pa. Solid lines are empirical data, error bars are the 95% confidence interval, and dashed lines are the zonal model.*

It is clear from Figure 6.33 that the new correlation is more suitable, with the predicted and measured rates being much closer than in the preliminary case (Figure 6.29). ΔP_{pallet} = 15 Pa shows the closest agreement (Figure 6.29a) with minimal over-prediction at the beginning and end of the cooling process. ΔP_{pallet} = 32 and 65 Pa were less accurate (Figure 6.29b and c), with a slight degree of under-prediction across the entire cooling process – however, this was within the bounds of experimental uncertainty. The least accurate was ΔP_{pallet} = 118 Pa (Figure 6.29d), where the under-prediction was large enough to be on the edge of the upper-bound of experimental uncertainty. Loss of accuracy at very high pressure drops is not a major concern, considering the difference in predicting cooling rates is a maximum of

0.9 ºC over 18 hours of cooling and that typically pre-coolers operate at a pallet scale pressure drop of ~100 Pa (Shim *et al.*, 2016), so that the pressure drop through single boxes is on the order of ~25 Pa (through the 4 boxes stacked in the middle of the pallet, assuming an equal pressure drop through each box in series) where the model performs satisfactorily.

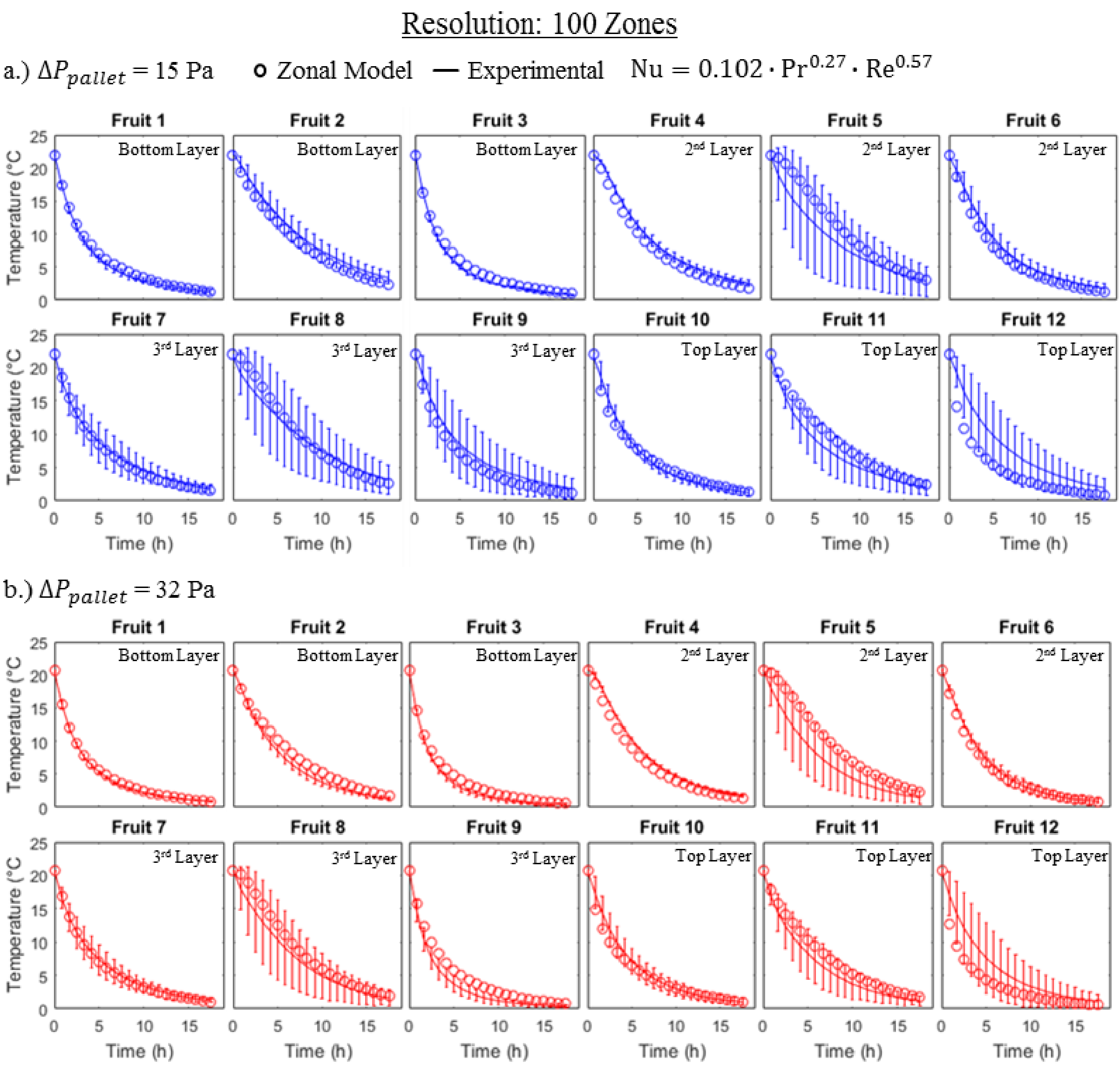

Figure 6.34: Empirical validation of zonal model with the new airflow correlation, comparing simulation results at the local level, for $\Delta P_{\mathrm{pallet}}$ *of a.) 15 Pa and b.) 32 Pa. Circles are the zonal model, lines empirical data, error bars are the standard deviation.*

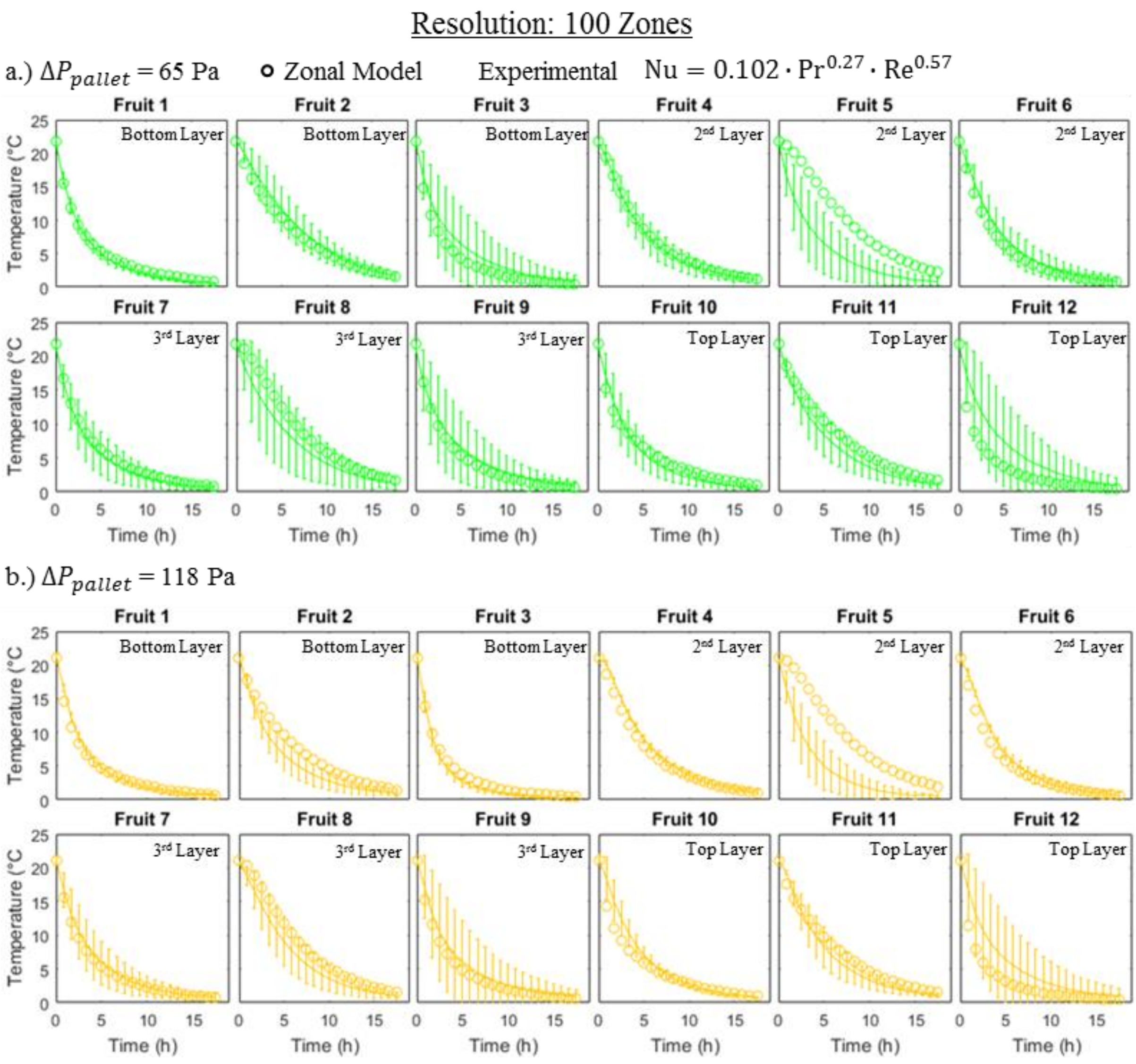

Figure 6.35: Empirical validation of zonal model with the new airflow correlation, comparing simulation results at the local level, for $\Delta \mathrm{P}_{\mathrm{pallet}}$ *of a.) 65 Pa and b.) 118 Pa. Circles are the zonal model, lines empirical data, error bars are the standard deviation.*

The prediction is notable improved on a local level compared with the preliminary case, with the errors on the bottom of the package (section 6.3.6.1) vanishing. A single position performs poorly, which is fruit 5, the fruit at the centre of the package (see Figure 6.12); in ΔP_{pallet} = 65 and 118, the model under-predicts the rate to a degree where it is outside the bounds of experimental error. This could be problematic, considering the thermal centre is an important location for determining system performance in some industrial practices. However, this inaccuracy does not occur at lower airflow rates, which is the expected industrial range (Shim *et al.*, 2016; Figure 6.34); and the OHI was developed (section 3.2) specifically as a more powerful tool for measuring and reporting process heterogeneity than a simplistic single point analysis, a key feature of the OHI being the incorporation of all data points into a single metric so that this single position of inaccuracy has a minimal impact on the measured vs. predicted level of heterogeneity.

The new airflow correlation (Eq. 6.25) could be used for future work involving airflow through polylined horticultural packaging, as is done later in section 7.3.1. To develop an even stronger correlation, it is suggested that the heat transfer coefficient at several locations inside of a box is measured empirically, rather than derived through modelling as was done in this section. Smale (2004) developed a thermistor anemometry system, of which a similar system could be adapted for this task. A more robust $\mathrm{Nu} = a \cdot \mathrm{Pr}^{b} \cdot \mathrm{Re}^{c}$ expression could potentially be derived from this exercise.

6.3.7: Zonal Resolution

The techniques developed in this section to combine the airflow information with the zonal heat transfer model were formulated to be automated as well as flexible to changes in the zonal resolution. It was pertinent to demonstrate this flexibility by repeating the processes of sections 6.3.2: to 6.3.5: for higher zonal resolutions, to directly test the scalability of the approach.

For this exercise, the original Zonal Network of 100 zones (N_X = 5, N_Y = 5, N_Z = 4) is compared with a 180 (N_X = 6, N_Y = 6, N_Z = 5) and 245 (N_X = 7, N_Y = 7, N_Z = 5) zonal network. These are presented in Figure 6.36:

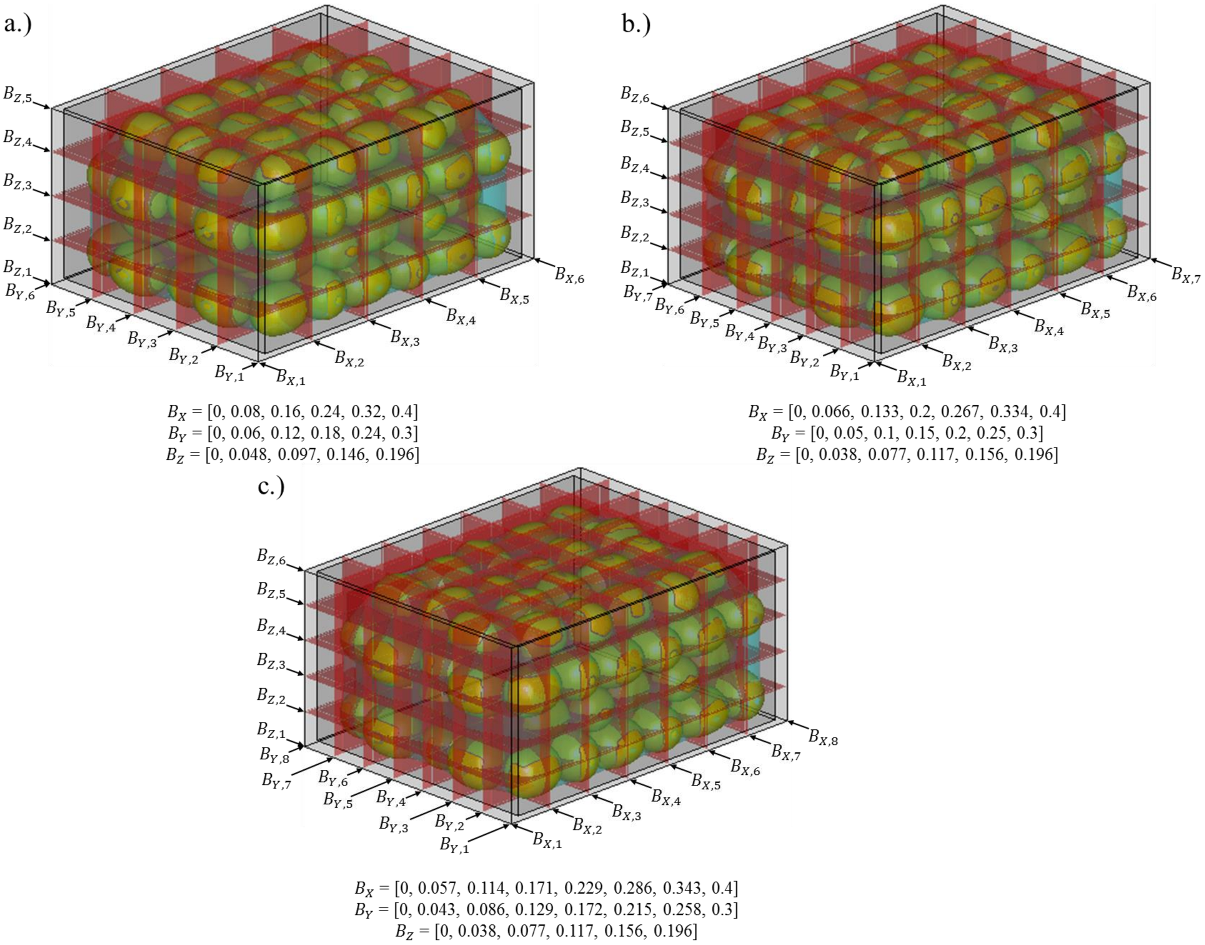

Figure 6.36: Zonal resolutions used to validate the flexibility of the zonal approach: a.) 100 zones (N_X = 5, N_Y = 5, N_Z = 4); b.) 180 zones (N_X = 6, N_Y = 6, N_Z = 5), and; c.) 245 zones (N_X = 7, N_Y = 7, N_Z = 5).

The zone builder was used to automatically appropriate the zonal properties for heat transfer for each of these zonal resolutions (section 5.5.5 and section 5.5.6). This section puts to the test the flexibility of the additional geometric procedures developed in chapter 6 for generating the velocity of air through each zone, u_i, and if they scale appropriately for different zone sizes and geometries, specifically: the calculation of the centroid position of each zone with a bulk air phase (section 6.3.2, Figure 6.21); the effective length of the bulk air phase ($L_{eff,i}$, section 6.3.4, Figure 6.24); and the use of the new airflow correlation (Eq. 6.25, section 6.3.6.2) to calculate $h_{ext,i}$.

Appropriating zonal airflow velocities was performed by collating a list of centroid positions (see section 6.3.2) and importing it into the COMSOL airflow model. The list was automatically generated via the zone builder and therefore this process was trivial to enact for the higher zonal resolutions. The resulting set of zonal airflow velocities are presented in Figure 6.37:

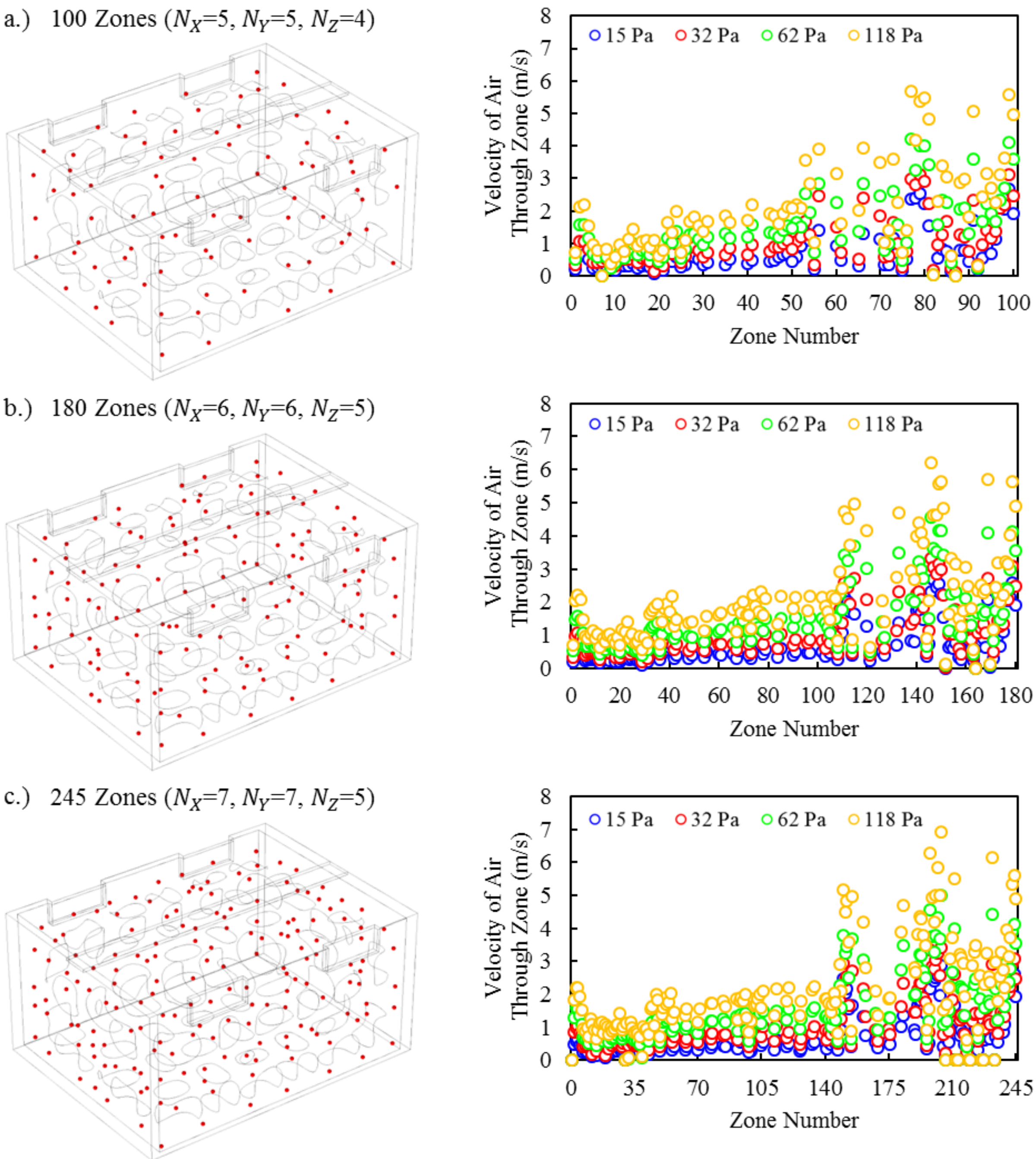

Figure 6.37: Centroid positions representing each zone and airflow velocities representing the velocity of air through each zone for three zonal resolutions: a.) 100 zones ($N_X = 5$, $N_Y = 5$, $N_Z = 4$); b.) 180 zones ($N_X = 6$, $N_Y = 6$, $N_Z = 5$) and; c.) 245 zones ($N_X = 7$, $N_Y = 7$, $N_Z = 5$).

Each zonal network was set up identically to section 6.3.5, with the same boundary conditions, initial and refrigeration temperatures (Table 6.1), and with $h_{ext,i}$ per zone determined from the new airflow correlation, Eq. 6.25. Each network was solved with the zone solver for each ΔP_{pallet} value investigated, with the predicted volume average temperature profiles compared in Figure 6.38:

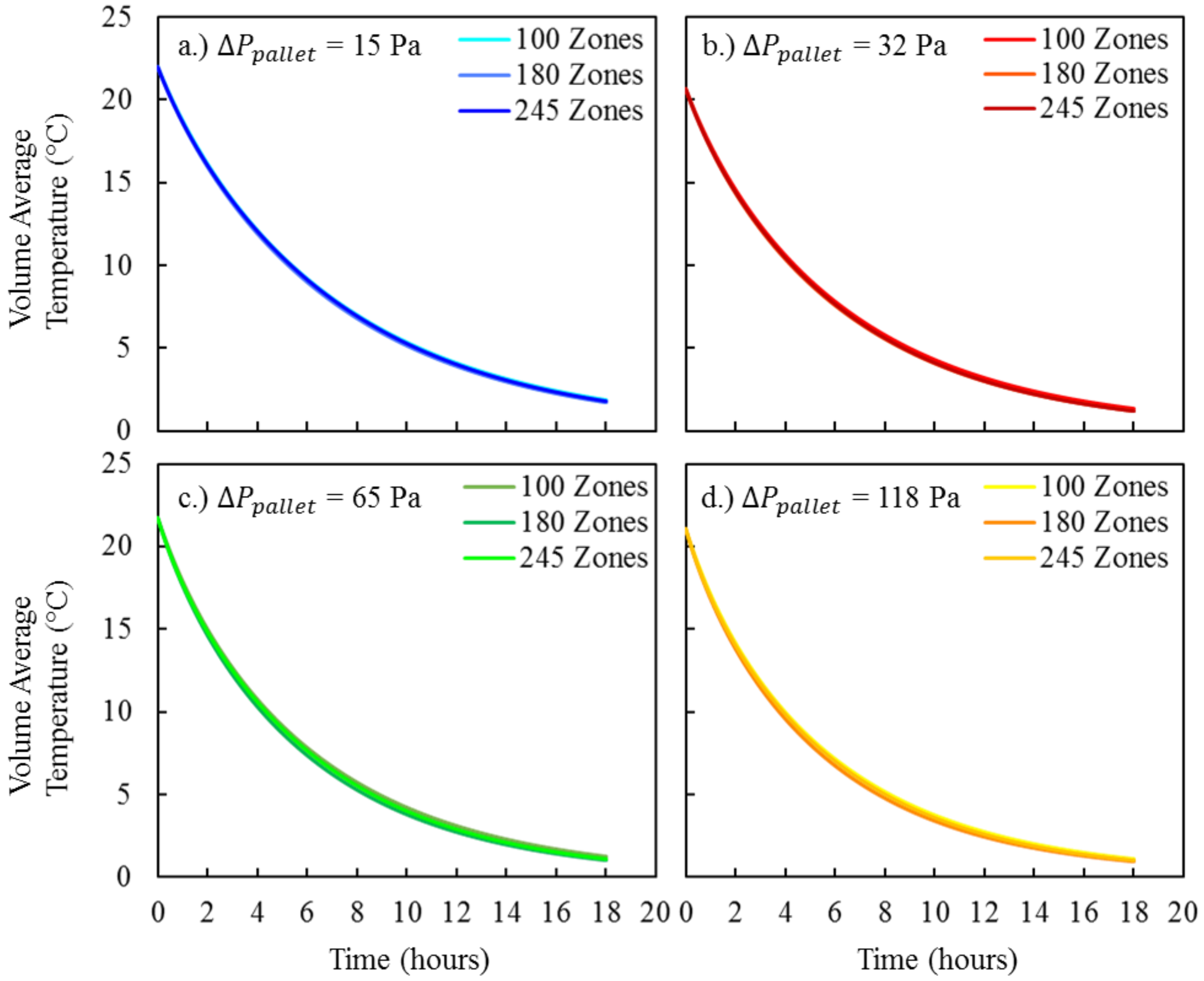

Figure 6.38: Validation of model flexibility, comparing predicted cooling rates of three separate zonal networks across four different airflow rates/pressure drops

For each value of ΔP_{pallet} there was a practically identical cooling profile between zonal resolutions, with a maximum difference of 0.5 °C over 18 hours across all comparisons. Even though the zone builder generated a unique set of heat transfer ($\mathbb{P}_{ii}$ and $\mathbb{P}_{ij}$) and airflow properties (u_i and $h_{ext,i}$) for each zonal network, when combined they resulted in the same or similar predicted cooling profiles. This adds weight to the robustness of the model, and implies that the methods developed in chapter 6 to appropriate u_i, $L_{eff,i}$ and $h_{ext,i}$ are flexible and representative of the true cooling rate.

6.3.8: Conclusions

The accuracy of the heat transfer zonal model was demonstrated in this section on the single box scale through comparisons with empirical cooling data. The model relied on inputs from a laminar flow (see below for discussion about turbulence options) CFD airflow model, which – in the absence of a similarly simplified, fast and flexible airflow model – provided the velocity of refrigerated air through each zone, which was converted into an external heat transfer coefficient using a dimensionless correlation. Assuming airflow through horticultural packaging had similar heat transfer properties as pipe flow was not sufficiently accurate. By taking advantage of the speed of the zonal approach, a new airflow correlation was derived through an iterative optimization routine, resulting in $\mathrm{Nu} = 0.102 \cdot \mathrm{Pr}^{0.27} \cdot \mathrm{Re}^{0.57}$. It is recommended that this new correlation be used in future work where there is airflow through polylined horticultural packaging.

The differences between the average cooling rates predicted by the zonal model and observed experimentally were only a maximum of 0.9 ºC over 18 hours of cooling, a level of error that is more than acceptable considering the zonal model was automatically constructed via the zone builder, and had solution times on the order of 1-2 seconds. Moreover, changing the zonal resolution had a negligible impact on the predicted rate, showing that the assortment of geometric procedures is indeed flexible, and scale appropriately to changes in zone size and intra-zonal geometry.

The level of experimental error was large, and could have had an impact on the model performance, where predicted local cooling rates differed substantially from the mean, but not outside of the sizable error bars. More experimental replicates may be necessary to properly ascertain the true cooling rate at each of the 12 measured positions.

One possible area for improvement is the inclusion of turbulence. Turbulence is likely occurring within the package, especially at the vent inlet and outlet due to the rapid contraction of air through a small channel, and is more likely to occur at higher flow rates/pressure drops. Incorporating turbulence into the zonal heat transfer model is still possible through the simplification of airflow information into a zonal $h_{ext,i}$, however the presence of turbulence will increase the apparent external heat transfer rate.

Alvarez *et al.* (2003) recommends the following correlation:

$$\mathrm{Nu} = a \cdot \mathrm{Pr}^{b} \cdot \mathrm{Re}^{c} \cdot (1 + d \cdot Tu) \tag{6.26}$$

Where Tu is the turbulence intensity, or $Tu = \sqrt{2 \cdot TKE}/u$ and TKE is the turbulent kinetic energy (m^2/s^2); and d is an additional empirical coefficient.

Chapter 7

Discussion and Conclusions

7.1: Conclusions

This project has developed and validated a numerical model capable of predicting the cooling rate and levels of cooling heterogeneity inside of boxes of polylined kiwifruit undergoing the forced-air cooling process. The model is a new interpretation of the zonal modelling approach and was fast, flexible and automated.

A random stacking model was developed and validated which, when coupled with a shape equation for kiwifruit and an input weight distribution, added even more flexibility to the approach by automatically generating the internal bulk fruit geometry.

As cooling heterogeneity was identified as a vital metric for determining a systems performance, a new heterogeneity index was developed: the overall heterogeneity index, or OHI.

Now that this suite of tools has been developed, a number of things are achievable: the zone builder program, being capable of taking any input geometry and self-forming a zonal network and all of the zonal properties, allows the rapid construction of heat transfer models for a wide variety of products and cooling scenarios, greatly accelerating the rate at which modelling can be used to solve real-world horticultural refrigeration problems; the zone solver, with solution times on the order of 1-2 seconds, facilitates the creation of iterative optimization routines, where a large number of package designs can be tested in a short period of time; and the random stacking model, capable of automatically generating a realistic fruit bulk geometry inside of any package shape and/or size, opens up the design space considerably. These are explored in section 7.3.

7.2: Research Outputs

7.2.1: New Heterogeneity Index

The new heterogeneity index (section 3.2) allows the variability of cooling rates throughout an entire cooling process to be collapsed into one quantitative, dimensionless number: the overall heterogeneity index, or OHI. The OHI is significantly more powerful than the previously used relative standard deviation, as it is mathematically stable, is not unit specific, and can reveal the minutiae of how a temperature distribution changes over the cooling process. It is hoped that the OHI becomes the new standard for reporting process heterogeneity in postharvest cooling operations (and potentially other batch operations, such as thawing and drying), and is currently being adopted in the literature (Mercier *et al.,* 2017b; Han *et al.,* 2017; Defraeye *et al.,* 2017).

The new heterogeneity index was bundled into a piece of software called 'Varicool' which processes input raw time-temperature data into all of the relevant heterogeneity information automatically – including heterogeneity plots and maps, the OHI of the system, and the shape of the temperature profile at specific characteristic times. Therefore, the new heterogeneity index is a deliverable output of this project, with industrial partners and interested 3rd parties having access to the 'Varicool' software through inquiry.

7.2.2: New Interpretation of a Zonal Modelling Approach

This project was completed at a time when DNS studies (finite element modelling and computational fluid dynamics modelling) were becoming increasingly popular (Han *et al.,* 2017, Berry *et al.*, 2017, Gruyters *et al.,* 2018). This project represents a shift away from this trend, resurrecting an older and seldom used methodology (pioneered by Tanner *et al.*, 2002a), updating it and bringing it into the modern era. While DNS models are superb at producing highly detailed predictions and are typically very accurate, their practicality as a *design tool* is limited due to large computational resource requirements, a lengthy, complex and highly manual geometry creation process, and long solution times. DNS models also often make some simplifications for complex geometries in order to produce reasonable geometry meshes. It is hoped that with this new zonal model, industry and academia will recognise the utility of models that focus on speed and universality, and are thus easy to set up and capable of predicting the performance of many package designs expeditiously. It is especially useful as a preliminary tool, where a broad set of designs can be tested numerically and narrowed down to a few key options quickly, and further refinement can be done experimentally or with a detailed model. This is particularly important in the field of postharvest technology, where being able to identify new and improved package designs has a real tangible benefit to the economy and environment. Application of the zonal model as a design tool is explored later in section 7.3.1.

The zonal model developed in this thesis represents a tangible, deliverable output, as it is contained within the 'zone builder' and 'zone solver' MATLAB scripts. With sufficient training, the zonal model could be transferred to industrial partners for use – however, the model still requires an equally simplified airflow model, which is being actively worked on separately within the larger packaging project at the CPRR (section 1.2.5.1).

7.2.3: Random Stacking Model

A major obstacle to model creation is the production of the bulk fruit geometry inside of a package. The random stacking model can produce this geometry automatically and expeditiously (~2.5-minute computation time), representing a significant opening of the design space, where a package of any size and shape can now be investigated. The model also facilitates the rapid creation of models for new product types, as the stacking model is agnostic to the shape and size of individual fruits. Beyond use as a geometry generator for heat transfer modelling, the random stacking model has potential as a tool to investigate the volumetric efficiency of new package designs before they are fabricated.

The random stacking model was created in Blender, a free and open source software program, available online at www.blender.org. Blender accepts Python scripts, which can drive the software through a text-editor, making the model automated once information about the size distribution of the fruit in inputted, along with some configuration settings. Therefore, the random stacking model can be transferred to industrial partners and interested 3rd parties, making it a deliverable output of this project.

7.3: Potential Model Applications

The models developed in this project have potential for a variety of applications. Some pertinent examples of model applications are explored here, to give a framework for what is achievable now that this modelling work is concluded.

7.3.1: Iterative Vent Optimization

A major motivation for developing this suite of modelling methodologies was to advance toward having an iterative optimization routine that can inform of the ideal package design. Unfortunately, without a pallet scale airflow model (see section 1.2.5.1, section 6.3.1 and section 6.3.2), this cannot be accomplished with the model in its current form. Nonetheless, it was deemed pertinent to provide at least an exploratory exercise in package optimization using the tools developed in this thesis to give a framework for how such an optimization routine could be performed, and how results should be interpreted.

Section 3.3 showed that packages with 3 vents were superior in terms of cooling uniformity, with only a small penalty to the cooling rate (when compared with a current modular bulk package). This result is carried through to this exercise, where a package with the same outer and inner dimensions of a modular bulk package but with 3 vents is explored. Rather than make educated guesses on what the best combination of vent sizes and vent positions are, these packaging features were turned into variables that can be altered within an iterative loop. Thus, the ventilation of the package is controlled by the variables L_1, L_2 and L_3; H_1, H_2 and H_3; and P_1, P_2 and P_3; which are the length, height and position of vent 1 (left), 2 (middle) and 3 (right), respectively (see Figure 7.1 (a)).

This exercise also provided an opportunity to demonstrate the capability of the random stacking model to rapidly generate the model geometry. A cavity with the same inner dimensions of a modular bulk package was filled with digital kiwifruit analogues using the methodology prescribed in section 4.4. The distribution of fruit sizes was that of the 2016 industry distribution (Figure 4.23), and resulted in 100 kiwifruits after overfills were eliminated. The polyliner was generated according to the methodology of section 4.4.5 (with the settings of Subdivide = 6, Offset = -0.00035 and Smooth = 5).

This whole process was fully automated and took ~2.5 minutes, resulting in the geometry presented in Figure 7.1 (b). Concurrently, this offered a chance to demonstrate the flexibility and universality of the zone builder by applying it to the new fruit geometry to establish that the geometric procedures within are capable of self-forming the zonal network and zonal properties of any input model geometry.

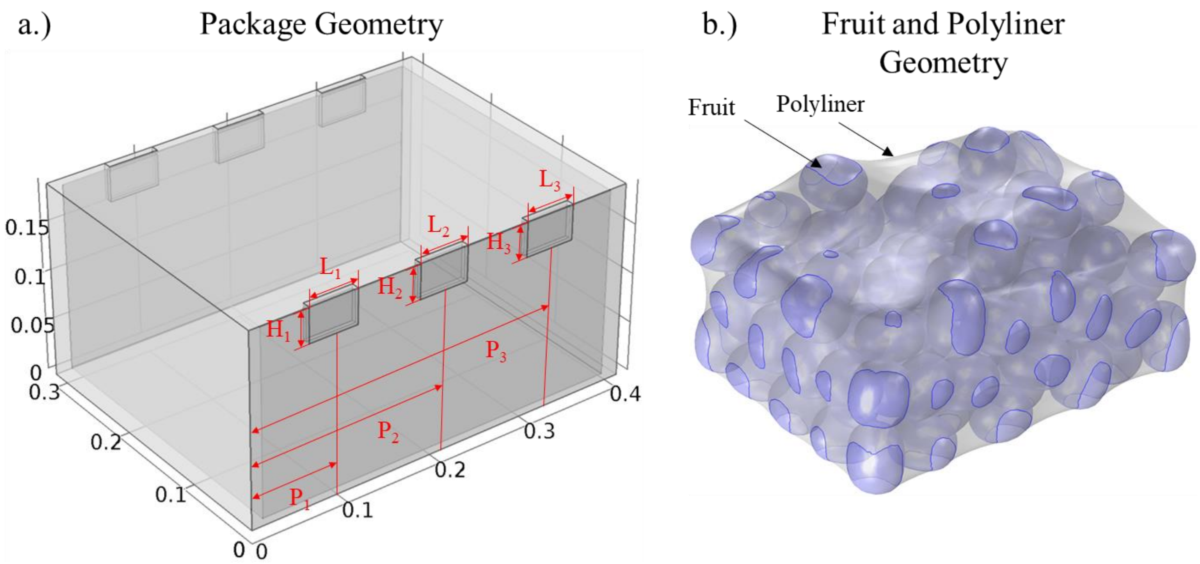

Figure 7.1: a.) Model geometry of a modular bulk package with 3 vents, the size, shape and position of which are controlled by optimization variables L_1, L_2 *and* L_3*;* H_1, H_2 *and* H_3*; and* P_1, P_2 *and* P_3*; which are the length, height and position of vent 1 (left), 2 (middle) and 3 (right), respectively; b.) Model geometry of fruit and polyliner, computationally generated with the random stacking model.*

The overall optimization routine structure was as presented in Figure 7.2.

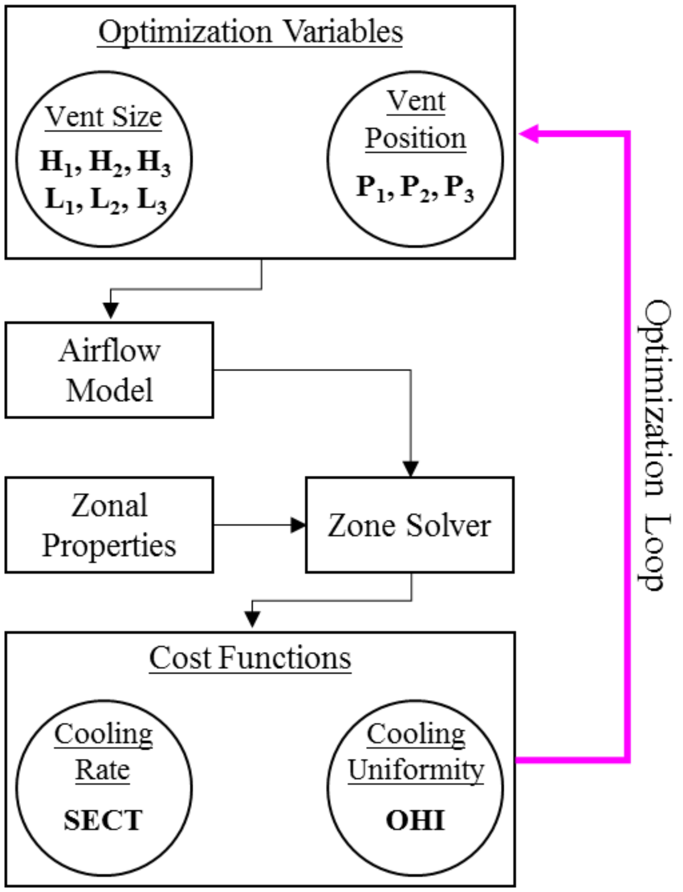

Figure 7.2: Monte-Carlo optimization routine structure.

At the start of each iteration, a new and unique package design was generated through random selection of L_1, L_2, L_3, H_1, H_2, H_3, P_1, P_2 and P_3 values, each within a certain range as given in Table 7.1. This makes this optimization routine a Monte-Carlo routine. Any number of unique package designs are able to be generated in this manner, with four examples shown in Figure 7.3. The airflow through each package design was then predicted using COMSOL. The airflow model had identical boundary conditions and GMRES solver settings as section 6.3.2. For this exercise, the pressure drop across the single package was ΔP_{pallet} = 15 Pa. Examples of the diversity of airflow fields generated through this process is demonstrated in Figure 7.4.

	P_1	P_2	P_3	H_1	H_2	H_3	L_1	L_2	L_3
Minimum	0.065	0.18	0.295	0.005	0.005	0.005	0.005	0.005	0.005
Maximum	0.105	0.22	0.335	0.05	0.05	0.05	0.1	0.1	0.1

Table 7.1: Limits imposed on the random selection of vent size, shape and position variables within the Monte-Carlo loop.

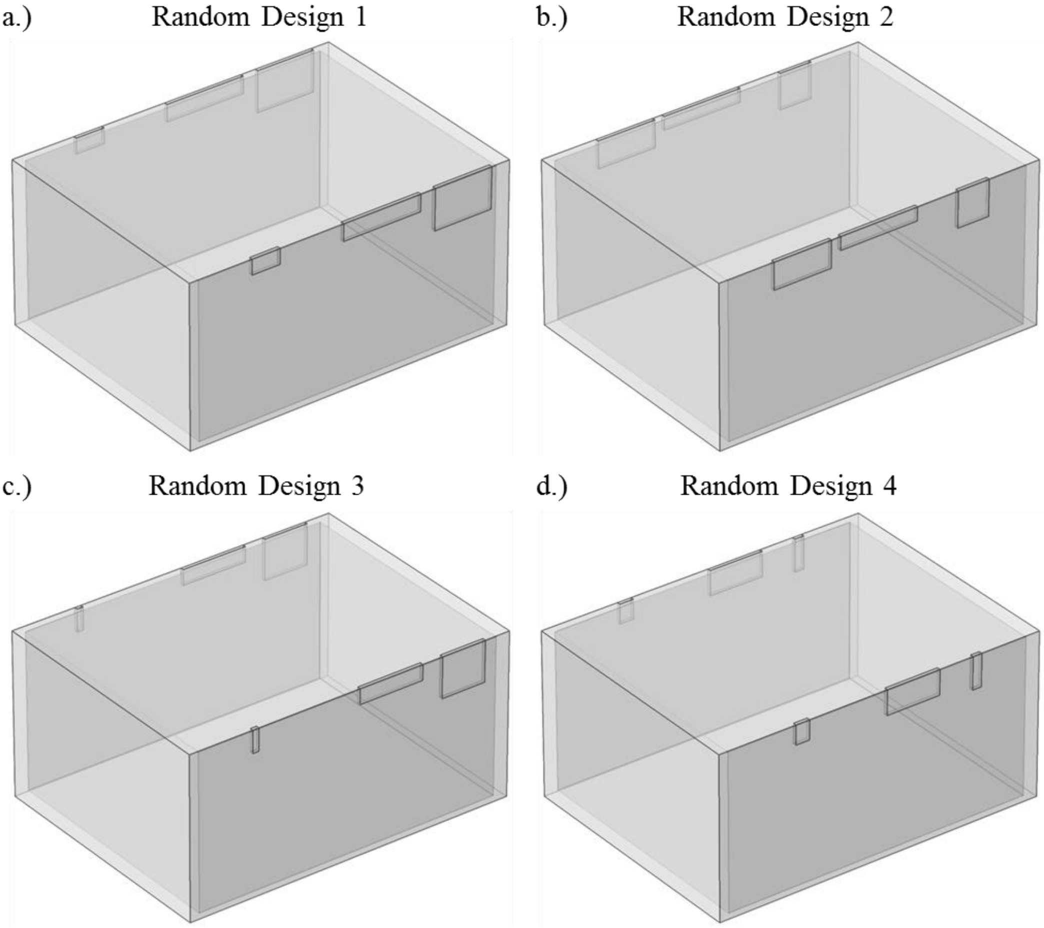

Figure 7.3: 4 examples of randomly generated package designs, the result of random selection of vent size, shape and position.

As in section 6.3.2, the CFD airflow model provides the zonal heat transfer model with u_i for each zone where there is a bulk air phase, which is converted into an external heat transfer coefficient per zone, $h_{ext,i}$, through the airflow correlation $\mathrm{Nu} = 0.102 \cdot \mathrm{Pr}^{0.27} \cdot \mathrm{Re}^{0.57}$ (derived in section 6.3.6.2; Eq. 6.25). Each package design has a unique airflow pattern and therefore unique distribution of $h_{ext,i}$; however the zonal properties – the internal resistances as predicted from the zone builder – are the same for each iteration as the fruit geometry is not changing. Therefore, the fruit, packaging and polyliner geometries only need to be passed through the zone builder once. The fruit and polyliner geometry was voxelised to a $1\mathrm{mm}^3$ resolution (Figure 7.5 (a)) and passed through the zone builder with a 100 zone resolution (Figure 7.5 (b)), automatically constructing the zonal network for the zone solver to use.

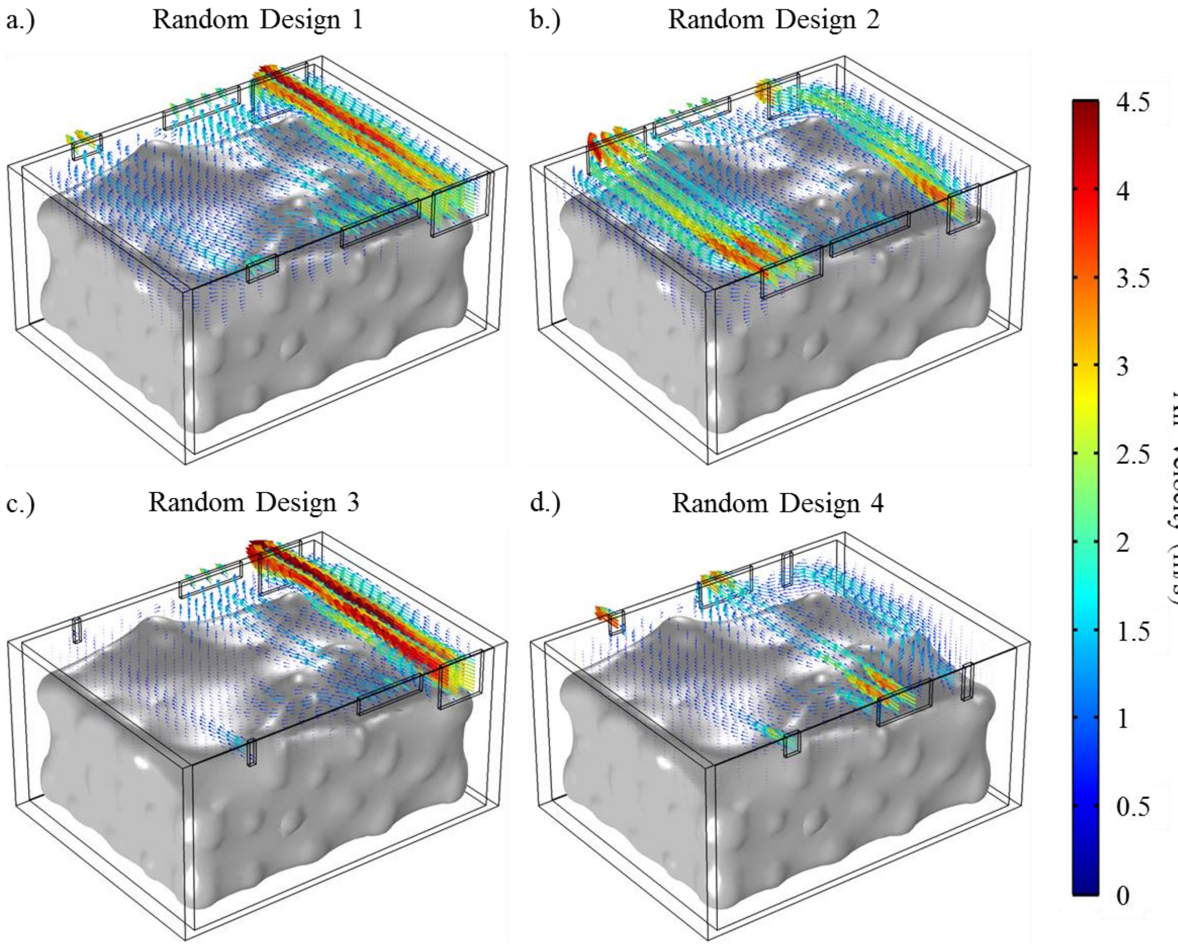

Figure 7.4: Predicted airflow velocities at $\Delta\mathrm{P}_{\mathrm{pallet}}$ *= 15 Pa through 4 randomly generated package designs, using COMSOL.*

The zone solver was then used to predict the cooling rate of each package design using an initial temperature of T_i = 20 °C, refrigeration temperature of T_{ref} = 0 °C and the same boundary conditions as section 6.2.3.2. The performance of each package was determined through two quantitative metrics: the SECT to quantify the rate of cooling; and the OHI (see section 3.2) to quantify the uniformity of cooling.

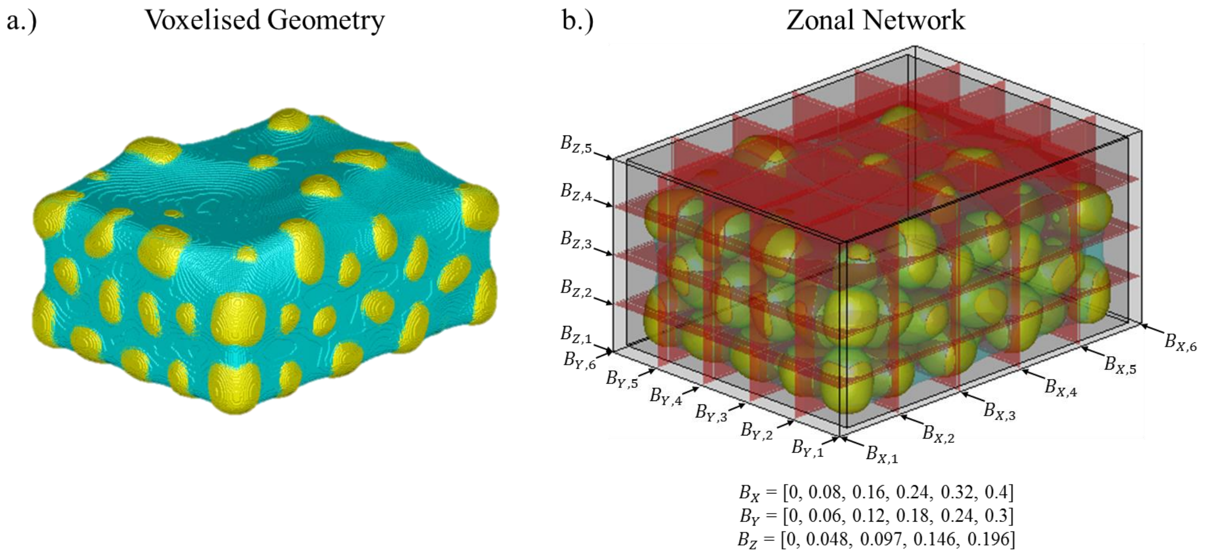

Figure 7.5: a.) Voxelised fruit and polyliner geometry (1mm3 voxel size); b.) the model geometry divided into a zonal network of 100 zones.

This optimization routine was automated and could be repeated any number of times without supervision, until the performance of a wide distribution of package designs have been studied. The major bottleneck of any iterative loop is the computational efficiency, where the faster each component is, the more designs can be investigated per unit of real time. The zonal model was developed with this goal in mind and succeeded in this pursuit, taking only 1-2 seconds per iteration. The CFD airflow model, however, was not efficient, taking between 30-60 minutes to reach convergence per iteration. This time constraint meant that the routine in its current form could only be repeated a moderate number of times: the COMSOL airflow model was permitted to continue cycling through random designs until the airflow pathway of 70 designs was produced, an exercise that took approximately 72 hours (using an Intel® i7-4770 with 16GB of RAM).

A Monte-Carlo optimization routine is useful for 'casting a wide net' over a design space, which if interpreted correctly can generate useful generalizations for package designers. The relative performance of the randomly generated designs are compared to each other in Figure 7.6, where there are two performance metrics: the box average cooling rate, determined by the SECT (h); and the cooling uniformity, determined by the OHI (-). By plotting the new designs (yellow circles, numbers indicating the iteration number) versus the status quo of the modular bulk package, with 2 vents and a 7.5% TOA (blue circle), revealing the distribution of performance gains/losses that can be achieved through package design changes: the majority of the randomised designs cluster around the status quo, indicating that the current package is already moderately optimized; that it is easier to make a package worse than better; and that while a majority of the new packages perform on par with the modular bulk package in terms of cooling rate, there is a much greater variability in predicted cooling uniformities due to package design changes. The plot also reveals that there is a fairly strong correlation between cooling rate and cooling uniformity, a finding that was similar to what was experimentally observed in section 3.3: a more ventilated box promotes the outer layer of fruit to cool very quickly, while the core lags behind due to the polyliner shielding the fruit from the effects of the refrigerated airflow.

Continued analysis plotted performance metrics (SECT or OHI) versus design parameters to determine if correlations can be derived. First, total vent opening area is explored in Figure 7.7.

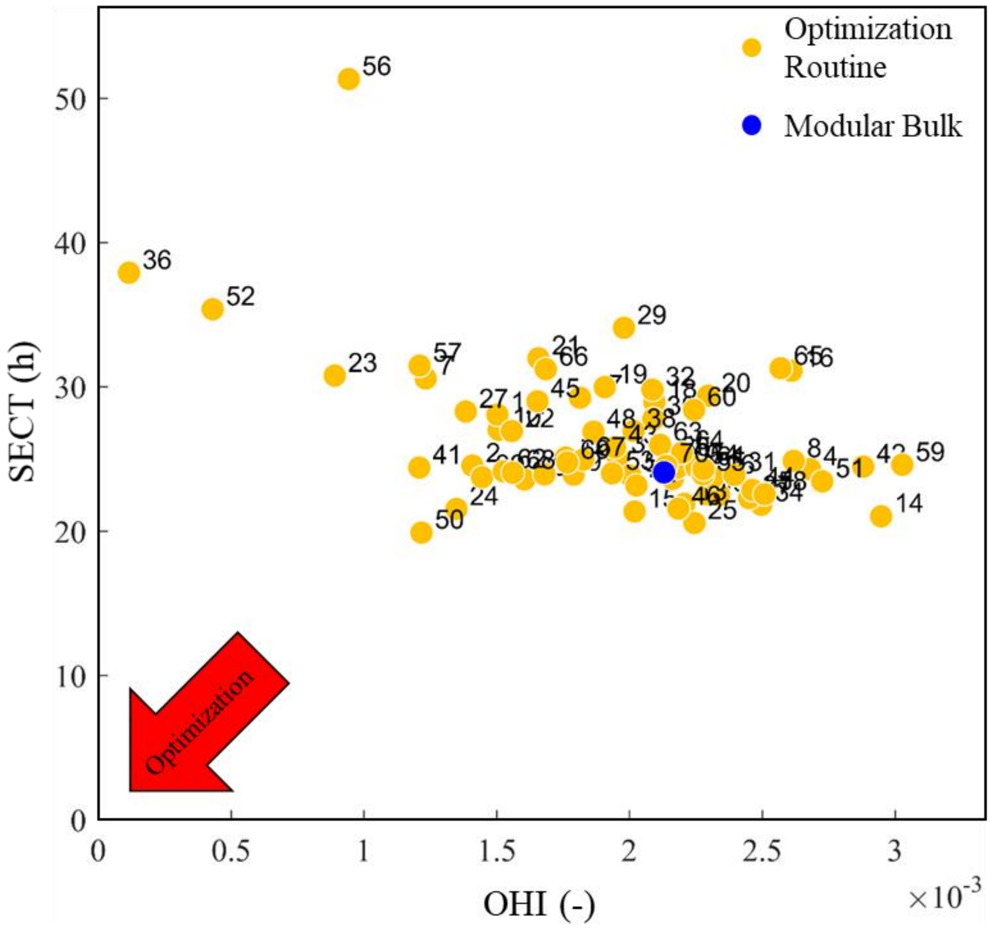

*Figure 7.6: Packaging performance plot, comparing the performance of each randomly generated package design in terms of cooling rate (SECT, Y-axis) and cooling uniformity (*OHI*, X-axis). The package optimization direction is as indicated by the arrow.*

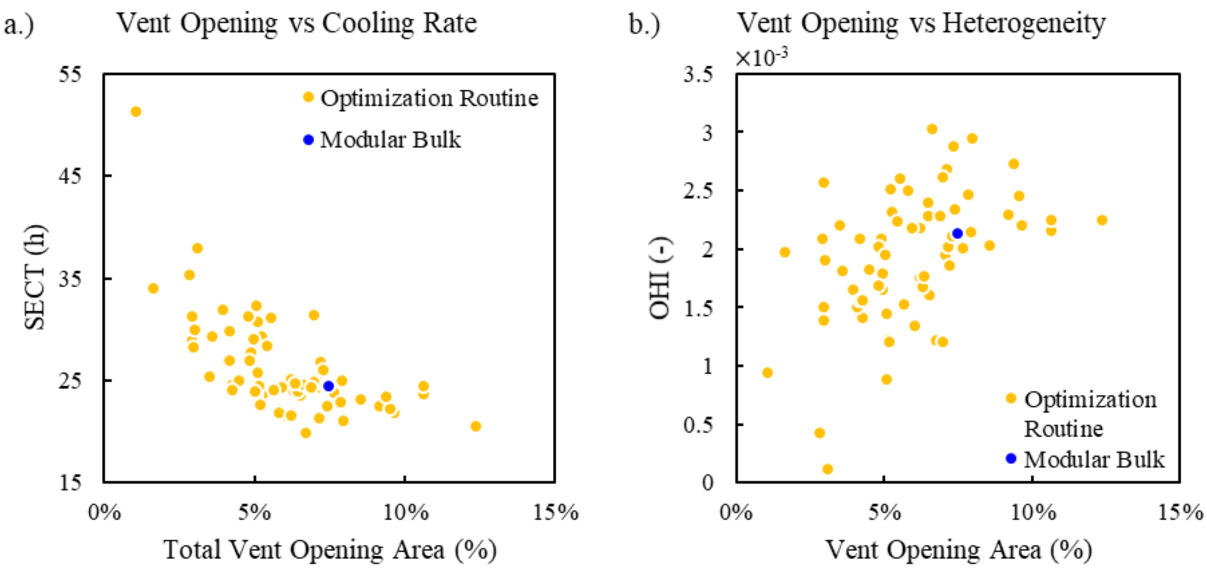

Figure 7.7: Design parameter 'total vent opening area' versus a.) SECT, and b.) OHI.

A relatively strong negative correlation between the SECT and TOA is revealed, where generally speaking the larger the total vent holes, the faster the package cools (a lower SECT). The relationship appears to be non-linear, curving toward a plateau SECT of roughly 20 hours, beginning at approximately 7% TOA. This is the maximum TOA discussed previously in section 1.2.3.2. As this is unique for each system (Pathare *et al.*, 2012), the zonal model could be used as a fast way for package designers to determine this important parameter for new package shapes and sizes or new products. A weak but visible correlation exists between the TOA and the cooling uniformity, where higher vent openings appear to promote a less uniform cooling profile. The relationship is scattered, however, and does not have a threshold like the SECT.

Observing the impact of individual vent size on performance (Figure 7.8) shows that the general trend of larger vents promoting faster cooling rates is repeated, but the correlation is weaker, with no singular vent having a greater influence on the cooling rate. Individual vent impact on cooling uniformity was more meaningful: a larger vent 3 showed a strong correlation to a less uniform cooling profile, while a smaller vent 1 showed a weak correlation to a more uniform profile.

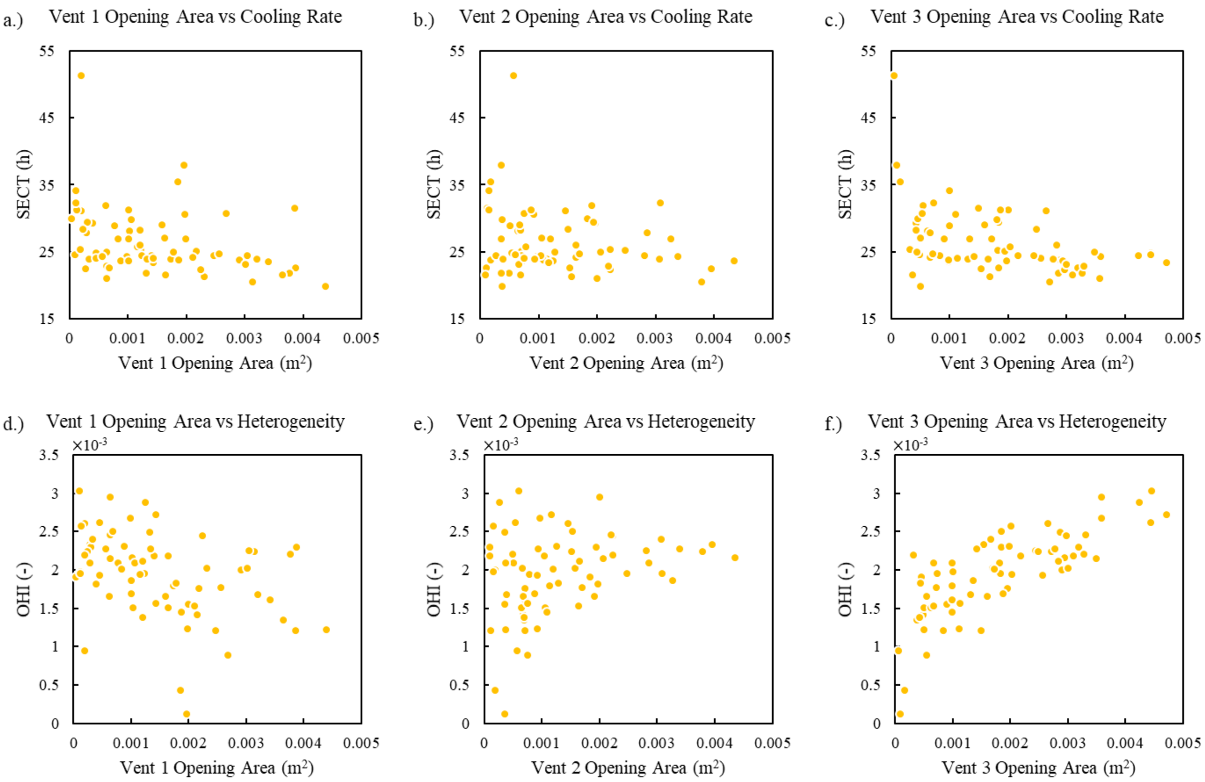

Figure 7.8: Design parameter 'individual vent size' versus SECT and OHI.

Although this appears to show that package design changes have a much greater impact on cooling uniformity than cooling rate, it is in fact the opposite that is true: these differences in OHI are primarily due to the fruit and polyliner geometry, specifically the randomness of the stack, which is not a controllable feature in an industrial setting. Looking at the headspace geometry at the top of the package (Figure 7.1 (b)), the fruit are stacked in a way that produces more direct fruit-to-polyliner contact area on the right side of the package; and the fruit are stacked higher in the box on this side, creating a shallower headspace cavity and therefore a higher air velocity, translating to a higher external rate of heat transfer.

Figure 7.9 investigates if the position of individual vents has an impact on package performance, where it is revealed that – on a single box scale at least – there is no correlation, or that vent size is much more important.

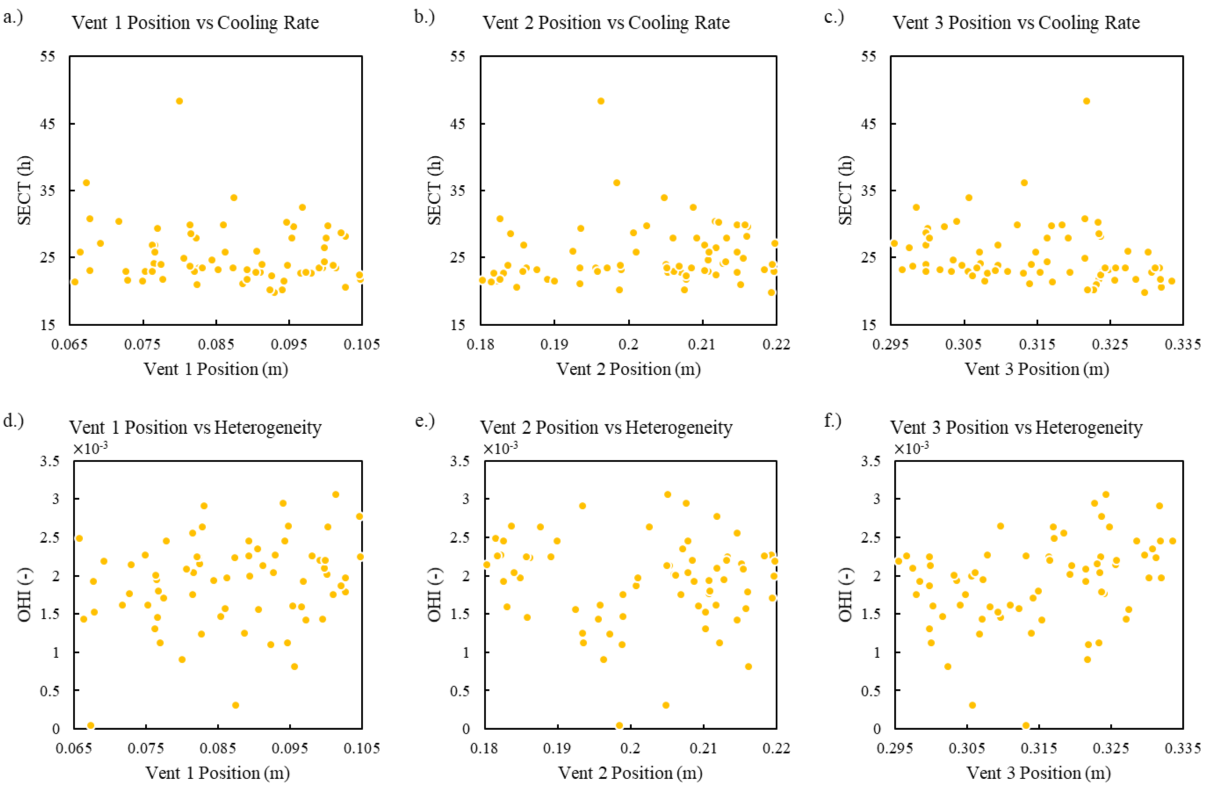

Figure 7.9: Design parameter 'vent position' versus SECT and OHI.

Specific packages that performed exceptionally well (or poorly) are inspected in Figure 7.10. The 'best' package design, with the lowest combination of SECT and OHI, was design 50 (Figure 7.10 (a); see Figure 7.6). The first (left most) vent was large compared to the others, reducing airflow over the right-hand side of the headspace and the preferential stacking pattern of fruit on this side of the box, while still maintaining a large 6.7% TOA, which is near the maximum vent opening area, maximising the cooling rate. Interestingly, the least uniform design, with the highest OHI, was design 59 (Figure 7.10 (b); see Figure 7.6) which is essentially the horizontal mirror image to design 50 – a 6.6% TOA but with the third (right most) vent the largest. This conforms to Figure 7.8 (f), and the right-hand side of the fruit bulk cools disproportionately quickly while the core fruit are shielded from the effects of cooling air, resulting in a very uneven cooling profile. Design 36 (Figure 7.10 (c)) had a preferential airflow through the left-hand side of the box and a long cooling time (37.9 h from a small 3.1% TOA), combining to give the most uniform cooling profile of all randomly generated designs. The slowest design, design 56 (Figure 7.10 (d)) was due to it having the smallest TOA, only 1.1%.

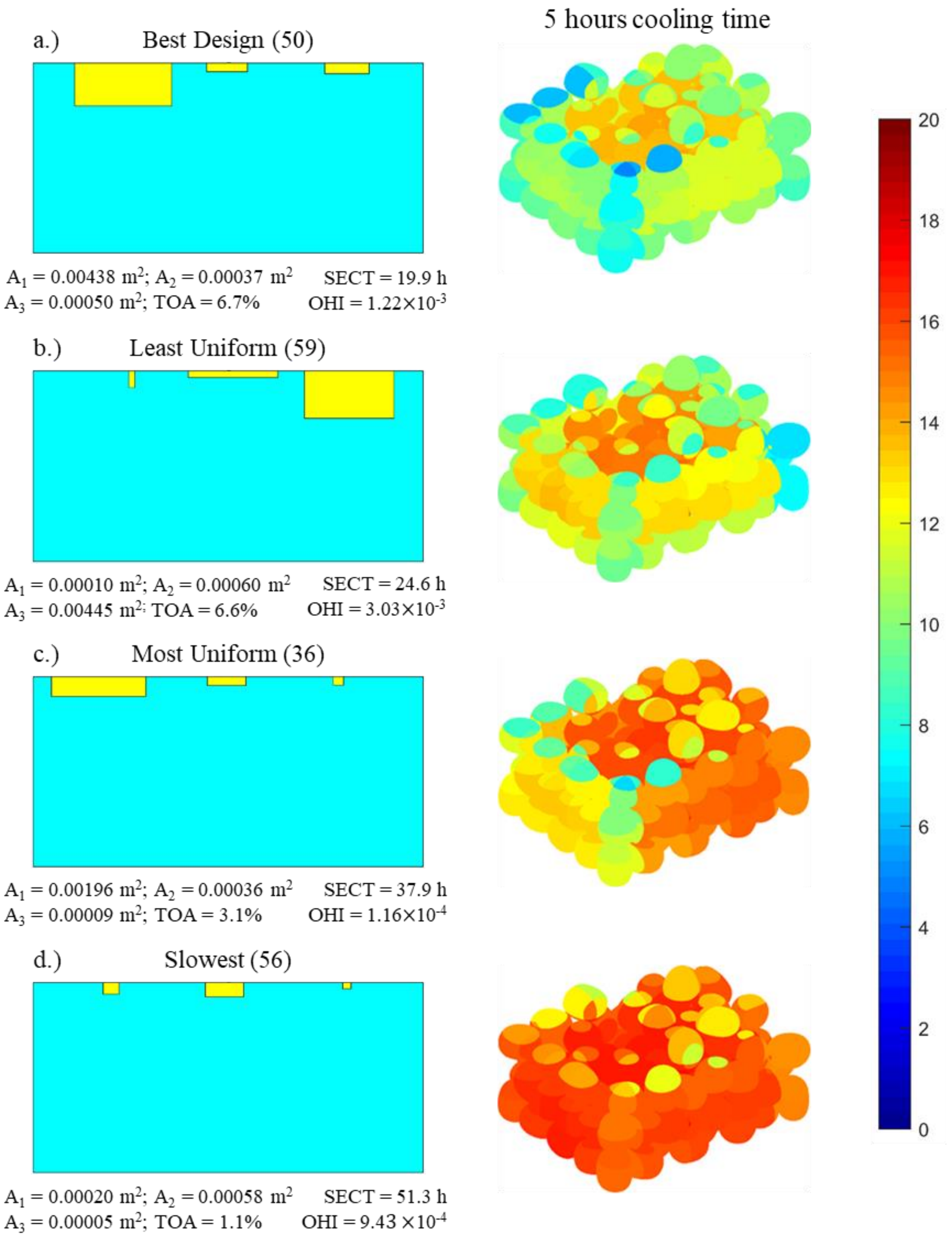

Figure 7.10: Notable randomly generated package designs: a.) the 'best' design, having the most improved combined cooling rate and cooling uniformity; b.) the least uniform design, with the highest OHI*; c.) the most uniform design, with the smallest* OHI*; d.) the slowest design, with the longest SECT.*

In conclusion, this exercise provides a worked example for how a fast and flexible zonal model can be used to quickly learn about the performance implications of package design. Using an interative Monte-Carlo loop, a great number of new designs were randomly generated and tested in a short period of time, generating a distribution of performance results that revealed a maximum TOA of 7% and that the uniformity of cooling is determined more by the randomness of the fruit stacking than by package design, meaning – on a single box scale – heterogeneity is not a controllable feature. While a Monte-Carlo simulation is good for exploring a design space to rapidly determine what is possible, a more ‘driven’ iterative optimization routine could be useful. For example, a genetic algorithm (East *et al.*, 2009) would function similarly to Figure 7.2, but with the new vent variables at each iteration chosen as small adjustments to the previous set, discarding changes that worsen the SECT and OHI and keeping changes that minimize these performance metrics; and over several dozen iterations, the optimal package design would be revealed.

A similar iterative routine will be much more powerful at a pallet scale, where variables like vent position, height and length will become very important as the air flows between packages connected to one another by touching vents, delivering cold/hot air to different regions of the pallet, impacting cooling rates significantly. However, without a simplified pallet airflow model, this cannot be achieved at this time.

7.3.2: Rapid Model Development

The bulk fruit geometry is significantly complex, even in scenarios where the package shape is relatively simple, such as the current case where a modular bulk package is a basic cuboid. Constructing the model geometry manually for this primitive shape was a substantial challenge, as outlined in section 5.2. If the performance of more complex package designs is to be explored in the digital space via modelling, the construction of the bulk fruit geometry is the major bottleneck that prevents such solutions from being investigated.

One of the major motivations for developing the random stacking model of section 4.4 was to mitigate this problem by accelerating and simplifying the model construction process. This was demonstrated in section 4.4.3 for larger and smaller packages (Figure 4.37). It was pertinent to further demonstrate the models usefulness by applying it to new and novel package designs to showcase its potential as a tool to facilitate design.

The new packages in this exercise were designed around the idea that if incoming refrigerated air could be redirected toward the centre of the pallet and insulated from interacting with the warm fruit, this may promote a faster and more uniform cooling rate throughout the pallet. This manifested as ‘airflow bypass vents’, new packaging features erected at the bottom of the box to provide new channels for airflow. Two variants of this concept are tested in this exercise, with a single bypass vent at the centre of one package (Figure 7.11a), and another package design with two bypass vents at each corner (Figure 7.11b):

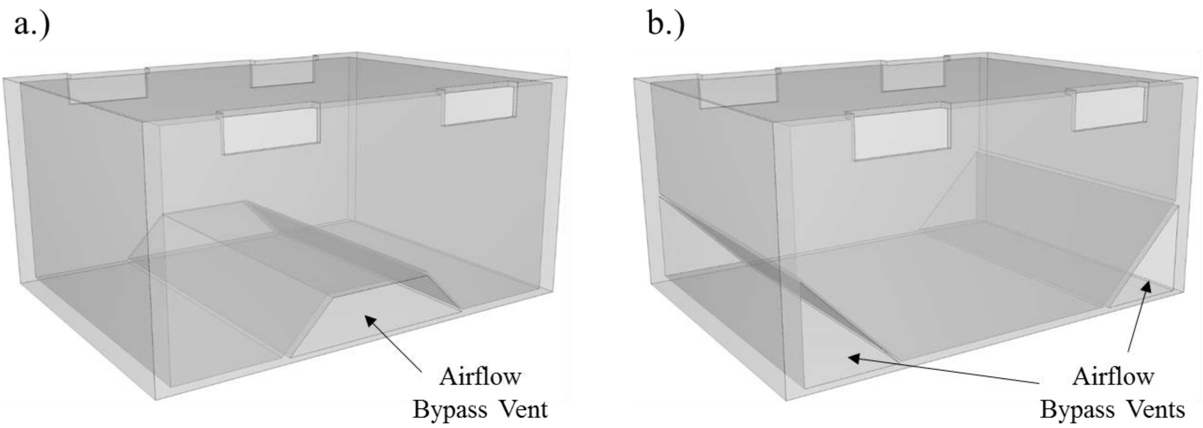

Figure 7.11: Hypothetical new package designs with bypass airflow vents: a.) a single central bypass vent, and; b.) two corner bypass vents.

Populating these new designs with fruit represents a significant challenge. Placing fruit by hand into these digital enclosures would not only be arduous and time consuming, but also runs a significant risk of producing inaccurate stacking pattern that have fewer fruit than the maximum possible, a different degree of fruit-to-packaging contact area – especially for fruit in contact with the airflow bypass vents that may have a high degree of external heat transfer due to high velocities of refrigerated airflow – and an unrealistic headspace size and/or shape. Failing to produce a bulk fruit geometry that correctly incorporates these features would result in a heat transfer model that is incorrect: a wrongful prediction of performance losses representing a lost opportunity for system optimization; or conversely a wrongful prediction of performance gains representing a loss of time and money when validating the design experimentally or industrially.

These concerns are mitigated through the use of the random stacking model. Incorporating the new vents into the model was a simple process of adding new passive walls that represent the bypass ventilation for which the fruit can collide with. The stacking process was automated and expeditious, with just 2.5 minutes of processing time to produce realistic bulk fruit geometries for each package, the result of which is shown in Figure 7.12:

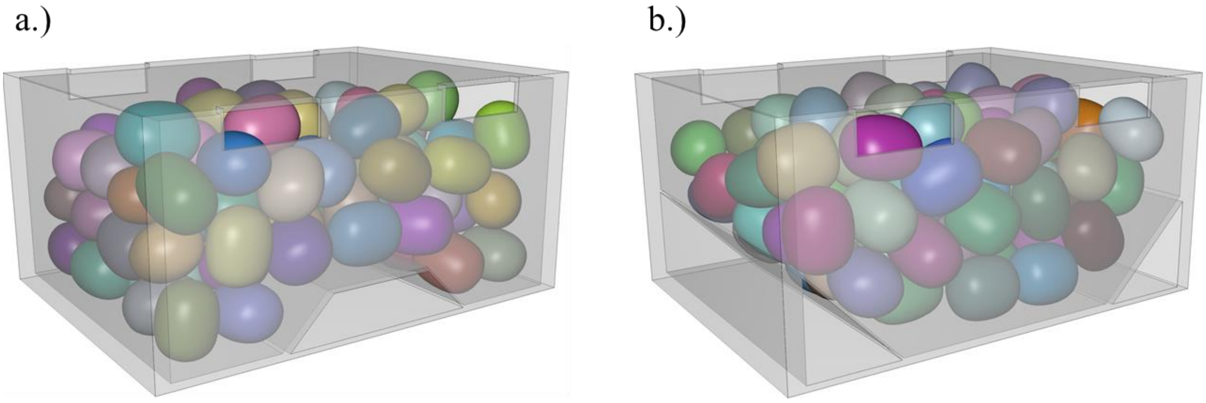

Figure 7.12: Results of the random stacking model, applied to the new bypass vent package designs. The internal geometry was automatically generated for each case in just 2.5 minutes.

The stacking model also provides an opportunity to explore the variability in cooling rates and uniformity as a result of random stacking processes. With everything else held equal – the same sized box with vents of the same size and in the same position – many different random stacks of fruit could be generated quickly, and using the numerical heat transfer model, the variability in performance quantified. This is much closer to an industrial setting where it is not feasible to impose an ordered stacking pattern on boxes of fruit.

7.3.3: Package Design

The random stacking model (section 4.4) has potential to be useful beyond facilitating the construction of heat transfer models. Package designers could also use the model to investigate the shipping efficiency consequences of new package designs.

An example of how the model can be used to inform designers of volumetric efficiency penalties or benefits is performed here. This exercise compares a pallet of fruit made of modular bulk packages (Figure 7.13 (a)) with an alternative design that has a wider footprint and is shallower (Figure 7.13 (b)). The new package, a "Bulk Tray" package, is a design that may conform better to shelving in Asian grocery stores.

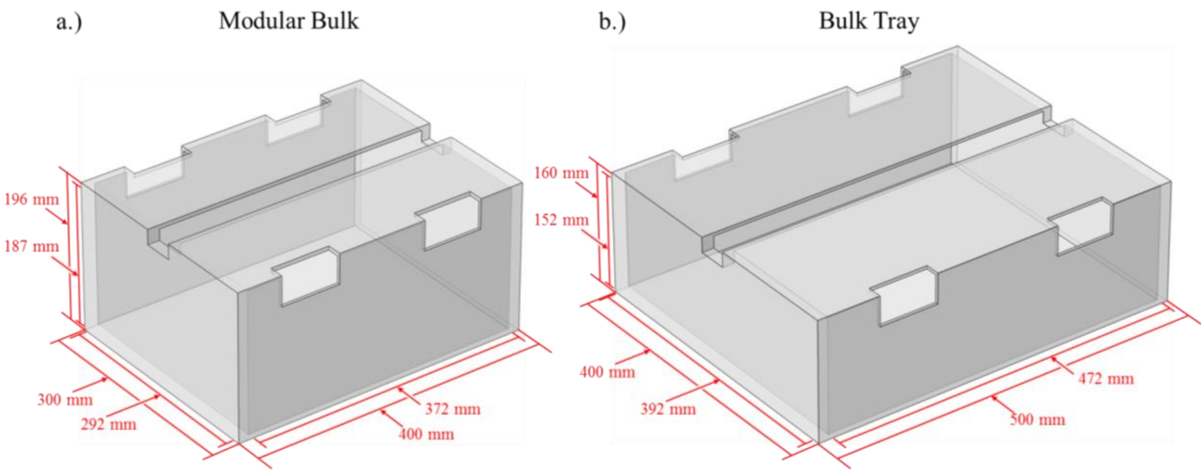

Figure 7.13: a.) the current package design, a modular bulk package, versus; b.) a new, wider and shallower design, dubbed the "Bulk Tray" package.

10 modular bulk packages can fit into a pallet layer according to the orientation of Figure 7.14 (a), and pallets are stacked 10 boxes high (Figure 7.14 (c)). With the target weight of 10.3 kg of count 36 kiwifruit per box, the total weight per pallet is 1030 kg. The bulk tray package has a larger footprint, so only 8 packages can fit per pallet layer (Figure 7.14 (b)). Each package is shallower than a modular bulk package, so that a pallet made of bulk trays is 12 packages tall (Figure 7.14 (d)). The question that can be answered through use of the random stacking model is: can a pallet of bulk tray packages ship more fruit per pallet, and by how much?

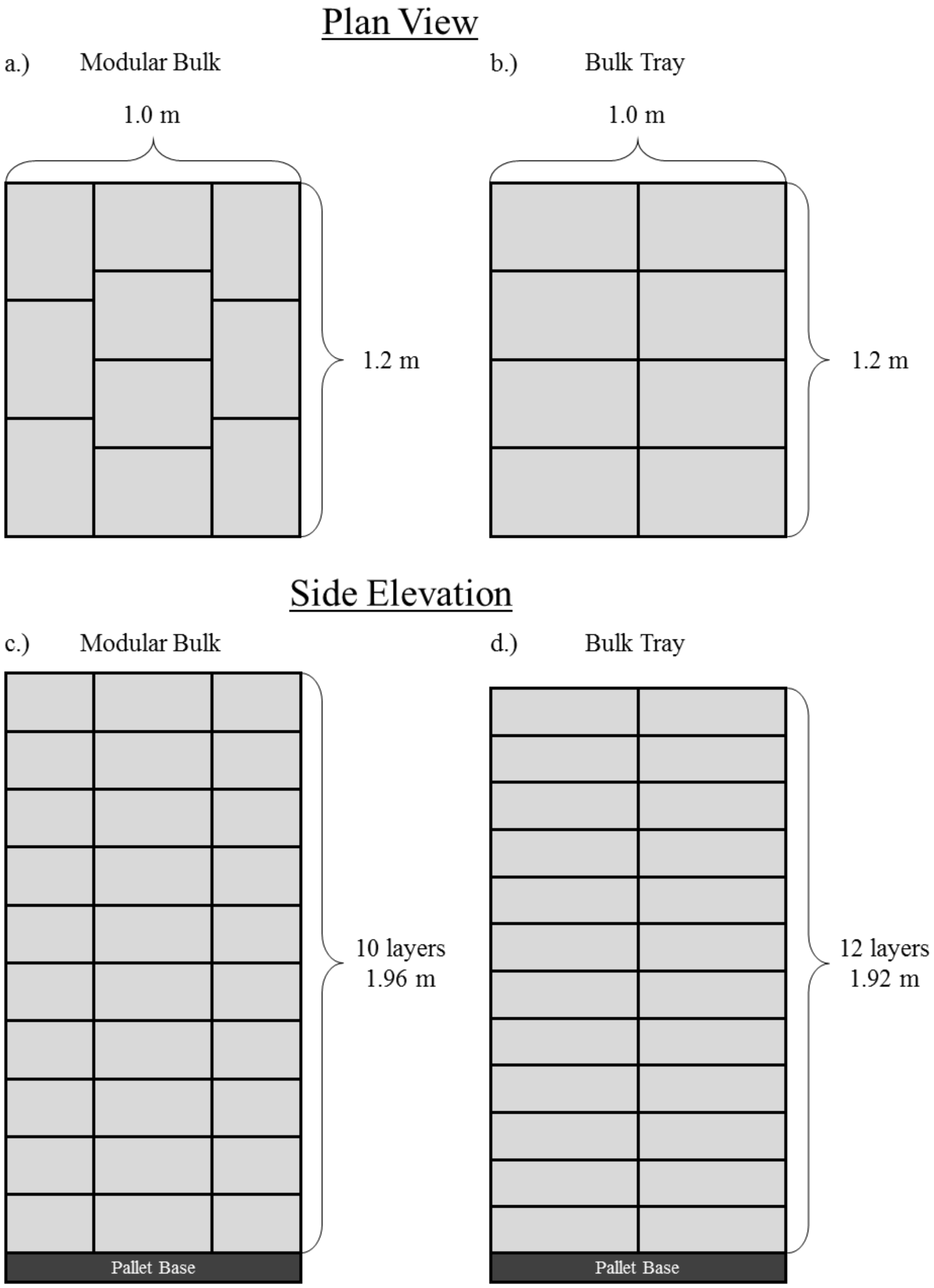

Figure 7.14: Package layer orientation and height for a.) and c.) modular bulk packages; and b.) and d.) Bulk Tray packages.

The stacking model was used to predict the bulk fruit weight that can fit inside of the bulk tray package. The model was amended so that the space to be filled had the same dimensions as the inner dimensions of the bulk tray - 472×392×152 mm. Packages were filled with 150 randomly generated count 36 kiwifruits (using the 2016 industry distribution, see section 4.3.3) and the overfill was eliminated after settling had finished. The weight of fruit inside the box was measured by multiplying the final fruit volume by the fruit density (ρ_S = 1037 kg·m^{-3}, see section 5.4). Fruit size variability and the chaotic nature of the stacking process means that each stack produced is unique, which in turn means the predicted number of fruit and predicted box weight varied. For a more holistic solution it is necessary to repeat the stacking model a moderate number of times and observe the population of answers produced. 50 boxes of the new design were digitally stacked, the resulting distribution of predicted box weights and number of fruits per box presented in Figure 7.15:

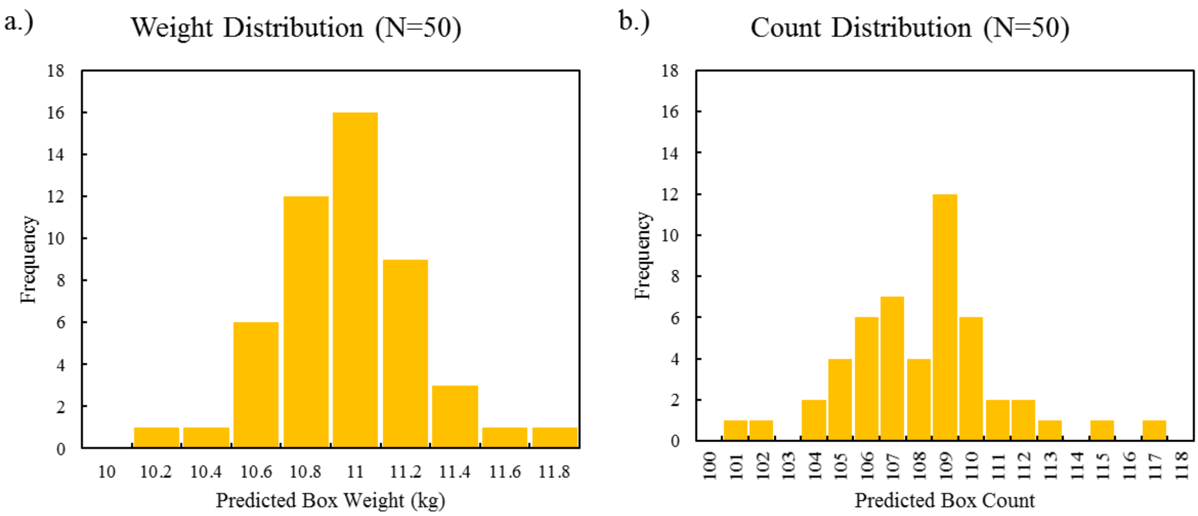

Figure 7.15: Distribution of a.) bulk fruit weight, and b.) number of kiwifruit inside a box over 50 iterations of the random stacking model.

The stacking model predicted box weights ranging from 10.14 to 11.75 kg, with an average of 10.9 kg per box. Extrapolating the predicted box weights from each simulation to the pallet scale – with 8 boxes per layer and 12 layers per pallet – gave pallet weights ranging from 973 to 1128 kg. Though the model predicted both gains and losses, the distribution fell slightly in favour of a higher fruit yield per pallet: with reference to Figure 7.16, of the 50 simulations, 33 produced a pallet weight higher than the status quo (from 0 to 9.6% w/w), while 17 produced a worse pallet weight (from 0 to -5.5% w/w).

In conclusion, this application of the random stacking model informs package designers that this new design is tenable, and may improve the profitability of exports. This conclusion is able to be reached with no material cost investment and in a relatively short time period (50 applications of the stacking model took just over 2 hours to complete). Similar studies could be performed to create customized packages for each individual market.

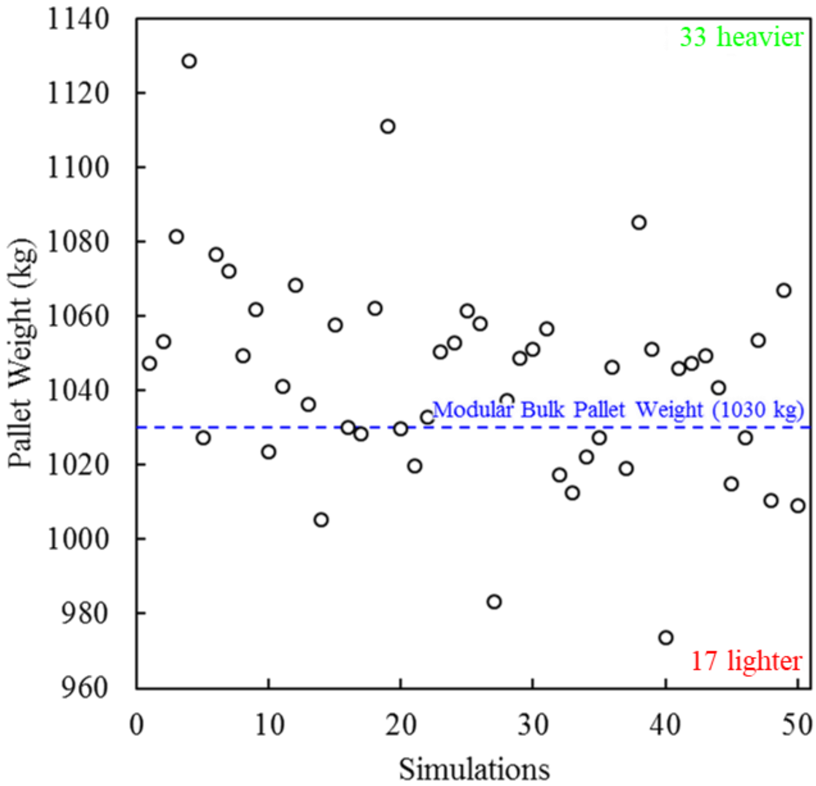

Figure 7.16: Weight of a pallet of Bulk Tray packages for each iteration of the predicted box weight; compared to a modular bulk pallet, 33 simulations showed an improved volumetric efficiency, while only 17 showed a worsened efficiency.

7.4: Challenges and Data Sets Required

Writing code was a significant challenge and required learning two languages to a high proficiency: MATLAB and Python. The number and variety of scripts produced for this project was vast, and consumed a majority of the project time. Particularly challenging was producing efficient code, which added a new layer of complexity and required significant rewrites of the zone builder and zone solver to take advantage of the speed at which MATLAB processes vectors over loops. If there had been more time, it would have been preferable to expand the coding work even further to produce stand alone software packages with graphical user interfaces, so that industrial partners could easily use the models, or so that the models could be sold to interested 3rd parties.

Laboratory work was also challenging as there was a limited time period every year when fruit was available. The pallet scale experiments were performed over a 2-year period, and the single box experiments a year later. Experiments were labour and time intensive, taking approximately 40 hours of labour (approximately one full work week) to complete one trial. If the seasonal availability of fruit were longer, it would have been preferable to examine medium and high flowrates (245 Pa and 335 Pa, respectively) through the different package designs at the pallet scale (section 3.3); as well as measuring the performance of the different packaging designs at the single box scale (section 3.4), so that the zonal model could be validated against package design changes as well as flowrates.

The key data sets required for this project were measurements of the fruit and air temperature, as well as the pressure drop across the pallet/box. The kiwifruit in the model are generated with a shape equation, so the average length and diameter of the fruit are necessary inputs; and if it is desired that a realistic population of fruit shapes and sizes is generated, a fruit weight distribution of the specific count size is also needed. CT scan data was also a required data set to validate the shapes produced by the random stacking model. Another vital data set was refrigerated airflow velocities per zone inside of a box. This project did not develop an equivalently simplified and flexible airflow model, so this information is provided to the model via CFD (section 6.3.2). An alternative method for appropriating this key data set could be with empirical measurement, such as Tanner *et al.* (2002b), where an anemometer measured certain key locations (e.g. vent inlet, centre of packaging, vent outlet) and used extrapolation to estimate airflow velocities for each zone.

7.5: Recommendations

The level of experimental error and was relatively high, on both the pallet (section 3.3) and single box scales (section 3.4). Conducting replicate experiments on the pallet scale is recommended to ascertain the variability in expected results. Reducing error could be done by using 'fruit simulators' to standardise the shape, thermal properties, location of thermocouples and stacking pattern of fruit (Redding *et al.*, 2016; Defraeye *et al.*, 2017). This would also allow experimental work outside of the seasonal availability window. Another possible source of error is sample size and sample location. The performance metrics of SECT and OHI derived from the 12% and 16% samples sizes (section 3.3) may not reflect the 'true' cooling rate or cooling uniformity if all the fruit were measured. As measuring all fruit in a pallet is impractical, the ideal sample size and sampling location could be determined by using the validated numerical model. Apparent SECT and OHI values from different sample sizes can then be compared to the 'true' value, and the sampling error quantified.

This interpretation of the zonal model was designed to be a universal model; however, it was not validated outside of the primary context of polylined count 36 kiwifruit inside a modular bulk package. It is therefore recommended that this zonal model be further validated through comparisons with other fruit and packaging systems, the priority being the industrially relevant pallet scale (see section 3.3). This would require the development of a pallet scale airflow model, where the exchanges of air between boxes through touching vents is vital for model validation. It is recommended that a simplified, flexible and time efficient approach is taken, such as a resistance network (Smale, 2004). Resistance networks operate by having two nodes where the pressure is known and a network of nodes in-between that are unknown. With the resistance to airflow between nodes as a model input, the pressure at each node can be iteratively solved through a series of mass flow balances. Resistances in this case could be from vents or from the headspace – the relationship between vent size and the headspace geometry to airflow resistance will need to be investigated in detail. The number of nodes would likely be far fewer than the number of zones, possibly having only one node to represent one box, and the connections to other nodes being the air entering/exiting through connected ventilation; the output would be a collection of volumetric flow rates through and between boxes on the pallet scale. Another important system to expand the model towards is non-polylined systems. Such a model will require the development of new geometric procedures for moisture transfer and an investigation into the heat transfer effects of airflow through the bulk of fruit. With a polyliner, it was shown that airflow through the head space is similar to pipe flow (section 6.3.6.1), but to improve the predictive power of the zonal model further, new correlations would be necessary for different regions.

The random stacking model (section 4.4) would have more clout if the shape equation for kiwifruit (section 4.3) were replaced with a more universal alternative – for example, the Fourier series method of Rogge *et al*. (2015). As part of the random stacking model, a technique was developed to automatically generate a polyliner geometry around a bulk of digital fruit. The shape of this polyliner and the resulting fruit-polyliner contact area and volume inside the polyliner was not experimentally confirmed. Measuring the exact shape of a real-world fruit-polyliner geometry inside of a box and comparing it to the computationally generated version would afford authority to the routine. Attempts to collect this information were made with CT scans, however the thickness was below the 0.8 mm maximum resolution (section 4.2). A possible solution is by using a 3D scanner (Campanelli *et al.*, 2016) to measure the surface topography directly.

The stacking model assumed a rigid body system, an acceptable assumption based on the firmness of kiwifruit at the time of picking (section 4.4.3). A consequence of this is that the stacking model cannot be used to investigate mechanical damage as a result of the stacking process, a potentially important area for optimization. The random stacking model could be upgraded by converting it into a soft body model. The conversion process would be relatively simple, as soft body problems are incorporated into Blender's bullet physics platform (Coumans, 2012), but requires the elastic and friction properties of fruit (see section 4.4.3).

References

1. Afrodita, M., Rui, G., Pieter, R., Beate, S., David, F., Wim, V., Julie, B. (2014). *Analogies, metaphors, and wondering about the future: Lay sense-making around synthetic meat.* Public Understanding of Science, 24(5), 547-562.
2. Aitken, A.G., Hewett, E.W. (2016). *Fresh Facts – New Zealand Horticulture 2016*. Horticulture New Zealand, Plant and Food Research.
3. Aitkenhead, A.H. (2013). *Mesh voxelisation.* Retrieved from https://au.mathworks.com/matlabcentral/fileexchange/27390-mesh-voxelisation.
4. Alcobendas, R., Mirás-Avalos, J.M., Alarcón, J.J., Nicolás, E. (2013). *Effects of irrigation and fruit position on size, colour, firmness and sugar contents of fruits in a mid-late maturing peach cultivar.* Scientia Horticulturae, 164, 340-347.
5. Alvarez, G., Bournet, P.E., Flick, D. (2003). *Two-dimensional simulation of turbulent flow and transfer through stacked spheres.* International Journal of Heat and Mass Transfer, 46(13), 2459-2469.
6. Alvarez, G., Cantre, D., Verboven, P., Ndoye, F.T., Warren, M., Hartel, W.R., Nicolai, B. (2015). *X-Ray micro-tomography to quantify frozen ice cream structure.* Proceedings of the International Congress of Refrigeration, Yokohama, Japan. ID: 685.
7. Alvarez, G., Flick, D. (1999a). *Analysis of heterogeneous cooling of agricultural products inside bins Part I: aerodynamic study.* Journal of Food Engineering, 39, 227-237.
8. Alvarez, G., Flick, D. (1999b). *Analysis of heterogeneous cooling of agricultural products inside bins Part II: thermal study.* Journal of Food Engineering, 39, 239-245.
9. Ambaw, A., Mukama, M., Opara, U.L. (2017). *Analysis of the effects of package design on the rate and uniformity of cooling of stacked pomegranates: Numerical and experimental studies.* Computers and Electronics in Agriculture, 136, 13-24.
10. Amos, N.D. (1995). *Mathematical modelling of heat and mass transfer and water vapour transport in apple coolstores* (PhD thesis). Massey University, Palmerston North, New Zealand.

11. Anonymous. (1997). *Hayward Plots.*

12. Arendse, E., Fawole, O.A., Magwaza, L.S., Opara, U.L. (2016). *Non-destructive characterization and volume estimation of pomegranate fruit external and internal morphological fractions using X-ray computed tomography*. Journal of Food Engineering, 186, 42-49.

13. ASHRAE (2010). *ASHRAE Handbook: Refrigeration*. Atlanta, GA: American Society of Heating, Refrigeration and Air-Conditioning Engineers.

14. ASHRAE (2013). *ASHRAE Handbook: Fundamentals.* Atlanta, GA: American Society of Heating, Refrigeration and Air-Conditioning Engineers.

15. Avila-Acevedo, J.G., Tsotsas, E. (2008). *Transient natural convection and heat transfer during the storage of granular media.* International Journal of Heat and Mass Transfer, 51(13-14), 3468-3477.

16. Bachmann, J., Earles, R. (2000). *Postharvest handling of fruits and vegetables.* Appropriate Technology Transfer for Rural Areas.

17. Baird, C.D., Gaffney, J.J. (1976). *A numerical procedure for calculating heat transfer in bulk loads of fruits or vegetables*. Presented at the annual Meeting of American Society of Heating, Refrigerating, and Air Conditioning Engineers. Seattle, WA.

18. Banks, N.H., Cleland, D.J., Cameron, A.C., Beaudry, R.M., Kader, A.A. (1995). *Proposal for a Rationalised System of Units for Postharvest Research in Gas Exchange.* Journal of the American Society for Horticultural Science. 30(6), 1129-1131.

19. Barbin, D.F., Neves Filho, L.C., Silveira, V. (2012). *Portable forced-air tunnel evaluation for cooling products inside cold storage rooms.* International Journal of Refrigeration. 35(1), 202-208.

20. Baudrit, C., Hélias, A., Perrot, N. (2009). *Joint treatment of imprecision and variability in food engineering: Application to cheese mass loss during ripening.* Journal of Food Engineering, 93(3), 284-292.

21. Becker, B.R., Fricke, B.A. (1996). *Transpiration and respiration of fruits and vegetables.* Science et Technique du Froid (France).

22. Becker, B.R., Misra, A., Fricke, B.A. (1996). *Bulk refrigeration of fruits and vegetables. Part I: theoretical considerations of heat and mass transfer*. Heating, Ventilating, Air-Conditioning, and Refrigerating Research, 2(2), 122–134.

23. Bennett, A.H., Soule, J., Yost, G.E. (1996). *Temperature response of citrus to forced-air precooling.* ASHRAE Journal, 8(4), 48.

24. Berry, T.M. (2017). *Optimisation of multi-scale ventilated package design for next-generation cold chain strategies of horticulture produce* (PhD thesis). Stellenbosch University, Stellenbosch, South Africa.

25. Berry, T.M., Fadiji, T.S., Defraeye, T., Opara, U.L. (2017). *The role of horticultural carton vent hole design on cooling efficiency and compression strength: A multi-parameter approach.* Postharvest Biology and Technology, 124, 62-74.

26. Blaschke, P., Ngapo, N. (2003). *Review of New Zealand environmental farm plans.* New Zealand Ministry for the Environment. Retrieved 18 December 2017, from www.mfe. govt.nz/sites/default/files/environmental-farm-plans-review-may03.pdf

27. Blender Foundation. (2017). Blender 2.78a Reference Manual. Retrieved from [www.docs.blender.org/manual/en], accessed January 2017.

28. Bories, S.A. (1987). *Natural convection in porous media.* In J. Bear and M.Y. Corapcioglu (Eds.) Advances in Transport Phenomena. Martinus Nijhoff, The Netherlands, 77–141.

29. Boyette, M.D., Wilson, L.G., Estes. E.A. (1989). *Forced-air cooling.* North Carolina Agricultural Extension Service.

30. Boyette, M.D., Wilson, L.G., Estes. E.A. (1990). *Postharvest cooling and handling of apples.* North Carolina Agricultural Extension Service.

31. Brosnan, T., Sun, D.W. (2001). *Precooling techniques and applications for horticultural products — a review.* International Journal of Refrigeration, 24(2), 154-170.

32. Bryant, J.A., Drage, N.A., Richmond, S. (2012). *CT number definition.* Radiation Physics and Chemistry, 81(4), 358-361.

33. Burdon, J., Punter, M., Billing, D., Pidakala, P., Kerr, K. (2014). *Shrivel development in kiwifruit.* Postharvest Biology and Technology, 87, 1-5.

34. Campanelli, V., Howell, S.M., Hull, M.L. (2016). *Accuracy evaluation of a lower-cost and four higher-cost laser scanners.* Journal of Biomechanics, 49(1), 127-131.

35. Capehart, B.L., Turner, W.C., Kennedy, W.J. (2003). *Guide to energy management* (pp. 292-329). Lilburn, GA: Fairmont Press.

36. Carson, J.K., East, A.R. (2017). *The cold chain in New Zealand – A review*. International Journal of Refrigeration. Advance online publication, doi:10.1016/j.ijrefrig.2017.09.019.

37. Cartz, L. (1999). *Nondestructive testing: radiography, ultrasonics, liquid penetrant, magnetic particle, eddy current.* Materials Park, Ohio: ASM International.

38. Chen, C.K., Hsiao, S.W. (1998). *Transport phenomena in enclosed porous cavities.* In Ingham, D.B., Pop, I. (Eds.), Transport Phenomena in Porous Media (1st Ed.). 31-56. Oxford: Elsevier.

39. Cheng, A.K. (2001). *Teaching mathematical modelling in Singapore schools.* The Mathematics Educator, 6(1), 63-75.

40. Cheng, P. (1978a). *Convective heat transfer in porous layers by integral methods.* Letters in Heat Mass Transfer 5, 243–252.

41. Cheng, P. (1978b). *Heat transfer in geothermal systems.* Advanced Heat Transfer 14, 1–105.

42. Cohen-Or, D., Kaufman, A. (1995). *Fundamentals of Surface Voxelization.* Graphical Models and Image Processing, 57(6), 453-461.

43. COMSOL (2015). COMSOL Multiphysics® Reference Manual.

44. Coriolis and New Zealand Ministry of Business, Innovation and Employment. (2017). *The Investor's Guide to the New Zealand Produce Industry 2017*. Retrieved 2 November 2017, from www.mbie.govt.nz/info-services/sectors-industries/food-beverage/documents-image-library/folder-2017-investors-guides/investors-guide-to-the-new-zealand-produce-industry-2017.pdf

45. Coumans, E. (2012). *Bullet 2.80 physics SDK manual (Bullet physics library).* Available from: http://bulletphysics.org/.

46. Coutinho, M.G. (2013). *Dynamic Simulations* in M.G. Coutinho (Ed.), Guide to dynamic simulations of rigid bodies and particle systems (pp. 3-27). London: Springer.

47. Crisosto, G., Hasey, J.K., Zeqbe, J.A., Crisosto, C.H. (2012). *New Quality Index Based on Dry Matter and Acidity Proposed for Hayward Kiwifruit.* California Agriculture, 66(2).

48. Datta, A., Dhall, A. (2011). M*odeling food process, quality and safety: Frameworks and practical aspects*. Procedia Food Science, 1, 1202-1208.

49. Datta, A.K. (2007*). Porous media approaches to studying simultaneous heat and mass transfer in food processes. I: Problem formulations.* Journal of Food Engineering, 80(1), 80-95.

50. de Castro, L.R., Vigneault, C., Cortez, L.A.B. (2004). *Container opening design for horticultural produce cooling efficiency.* Journal of Food, Agriculture and Environment, 2(1), 135–140.

51. de Castro, L.R., Vigneault, C., Cortez, L.A.B. (2005). *Cooling performance of horticultural produce in containers with peripheral openings.* Postharvest Biology and Technology, 38(3), 254-261.

52. Defraeye, T., Cronjé, P., Berry, T., Opara, U. L., East, A.R., Hertog, M., Verboven, P., Nicolai, B. (2015). *Towards integrated performance evaluation of future packaging for fresh produce in the cold chain.* Trends in Food Science & Technology, 44(2), 201-225.

53. Defraeye, T., Lambrecht, R., Delele, M. A., Tsige, A. A., Opara, U. L., Cronjé, P., Verboven, P., Nicolai, B. (2014). *Forced-convective cooling of citrus fruit: Cooling conditions and energy consumption in relation to package design.* Journal of Food Engineering, 121, 118-127.

54. Defraeye, T., Lambrecht, R., Tsige, A.A., Delele, M.A., Opara, U. L., Cronjé, P., Verboven, P., Nicolai, B. (2013). *Forced-convective cooling of citrus fruit: Package design.* Journal of Food Engineering, 118(1), 8-18.

55. Defraeye, T., Wu, W., Prawiranto, K., Fortunato, G., Kemp, S., Hartmann, S., Cronje, P., Verboven, P., Nicolai, B. (2017). *Artificial fruit for monitoring the thermal history of horticultural produce in the cold chain.* Journal of Food Engineering, 215(Supplement C), 51-60.

56. Dehghannya, J., Ngadi, M., & Vigneault, C. (2011). *Mathematical modeling of airflow and heat transfer during forced convection cooling of produce considering various package vent areas.* Food Control, 22(8), 1393-1399.

57. Dehghannya, J., Ngadi, M., Vigneault, C. (2010). *Mathematical modeling procedures for airflow, heat and mass transfer during forced convection cooling of produce: A review.* Food Engineering Reviews, 2(4), 227-243.

58. Delele, M.A., Ngcobo, M.E.K., Getahun, S.T., Chen, L., Mellmann, J., Opara, U.L. (2013). *Studying airflow and heat transfer characteristics of a horticultural produce packaging system using a 3-D CFD model. Part II: Effect of package design.* Postharvest Biology and Technology, 86, 546-555.

59. Delele, M.A., Ngcobo, M.E.K., Opara, U.L., Meyer, C.J. (2012). *Investigating the Effects of Table Grape Package Components and Stacking on Airflow, Heat and Mass Transfer Using 3-D CFD Modelling.* Food and Bioprocess Technology, 6(9), 2571-2585.

60. Delele, M.A., Tijskens, E., Atalay, Y.T., Ho, Q.T., Ramon, H., Nicolaï, B.M., Verboven, P. (2008). *Combined discrete element and CFD modelling of airflow through random stacking of horticultural products in vented boxes.* Journal of Food Engineering, 89(1), 33-41.

61. Dintwa, E., Van Zeebroeck, M., Ramon, H., & Tijskens, E. (2008). *Finite element analysis of the dynamic collision of apple fruit.* Postharvest Biology and Technology, 49(2), 260-276.

62. Dittus, F.W., Boelter, L.M.K. (1930). *Heat transfer in automobile radiators of the tubular type*. Engineering, University of California, Berkeley, (2)443.

63. East, A., Smale, N., Kang, S. (2009). *A method for quantitative risk assessment of temperature control in insulated boxes.* International Journal of Refrigeration, 32(6), 1505-1513.

64. Eisfeld, B., Schnitzlein, K. (2001). *The influence of confining walls on the pressure drop in packed beds.* Chemical Engineering Science, 56(14), 4321-4329.

65. Elder, J.W. (1967). *Steady free convection in a porous medium heated from below.* Journal of Fluid Mechanics, 27, 29–48.

66. El-Hassan, M., Meslem, A., Abed-Meraim, K. (2011). *Experimental investigation of the flow in the near-field of a cross-shaped orifice jet.* Physics of Fluids, 23(4), 045101.

67. Ergun, S. (1952). *Fluid flow through packed columns.* Chemical Engineering Progress, 48, 89-94.

68. Everington, D.W. (1993). *Vacuum technology for food processing.* Food technology international Europe, 993, 71-74.

69. Fahimnia, B., Sarkis, J., & Davarzani, H. (2015). *Green supply chain management: A review and bibliometric analysis.* International Journal of Production Economics, 162, 101-114.

70. Faux I.D., Pratt M.J. (1979) *Computational Geometry for Design and Manufacture*. (pp. 89) John Wiley & Sons.

71. Ferrua, M.J. (2007). *Modeling the forced-air cooling process of fresh horticultural products* (PhD thesis). University of California Davis, California, USA.

72. Ferrua, M.J., Singh, R.P. (2009a). *Modeling the forced-air cooling process of fresh strawberry packages, Part I: Numerical model.* International Journal of Refrigeration, 32(2), 335-348.

73. Ferrua, M.J., Singh, R.P. (2009b). *Modeling the forced-air cooling process of fresh strawberry packages, Part II: Experimental validation of the flow model.* International Journal of Refrigeration, 32(2), 349-358.

74. Ferrua, M.J., Singh, R.P. (2009c). *Modeling the forced-air cooling process of fresh strawberry packages, Part III: Experimental validation of the energy model.* International Journal of Refrigeration, 32(2), 359-368.

75. Fraser, H.F. (1998). *Tunnel Forced-Air Coolers for Fresh Fruits & Vegetables.* Ontario Ministry of Agriculture, Food and Rural Affairs.

76. Frei, W. (2013). *Meshing your Geometry: When to Use the Various Element Types.* COMSOL Blog. Accessed June 2014. http://www.comsol.com/blogs/meshing-your-geometry-various-element-types/.

77. Geankoplis C.J. (1993*). Transport processes and unit operations.* 3rd Ed. Boston: Allyn and Bacon.

78. Giordano, F., Fox, W. P., Horton, S. (2013). *A first course in mathematical modeling.* (pp. 59), Nelson Education.

79. Gowda, B.S., Narasimham, G.S.V.L., Murthy, M.V.K. (1997). *Forced-Air Precooling of Spherical Foods in Bulk: A Parametric Study.* International Journal of Heat and Fluid Flow, 18(6), 613-624.

80. Gruyters, W., Rogge, S., Vanmaercke, S., Delele, M., Ramon, H., Verboven, P., Nicolai, B. (2016). *DEM-CFD- of cooling of packed fruit using 3D shape models*. Proceedings from the International Conference on Agricultural Engineering, Aarhus, Denmark.

81. Gruyters, W., Verboven, P., Delele, M., Gwanpua, S.G., Schenk, A., Nicolaï, B. (2018). *A numerical evaluation of adaptive on-off cooling strategies for energy savings during long-term storage of apples.* International Journal of Refrigeration, 85, 431-440.

82. Gupta, M.K., Bumtariya, K.J., Shukla, H.A., Patel, P., Khan, Z. (2017). *Methods for Evaluation of Radiation View Factor: A Review.* Materials Today: Proceedings, 4(2), 1236-1243.

83. Han, J. H. (2014). *Innovations in food packaging.* (pp. 5-6). London, Elsevier Academic Press.

84. Han, J.W., Qian, J.P., Zhao, C.J., Yang, X.T., Fan, B.L. (2017). *Mathematical modelling of cooling efficiency of ventilated packaging: Integral performance evaluation.* International Journal of Heat and Mass Transfer, 111(Supplement C), 386-397.

85. Han, J.W., Zhao, C.J., Yang, X.T., Qian, J.P., Fan, B.L. (2015). *Computational modeling of airflow and heat transfer in a vented box during cooling: Optimal package design.* Applied Thermal Engineering, 91, 883-893.

86. Hardenburg, R.E., Watada, A.E., Yang, C.Y. (1990). *The commercial storage of fruits, vegetables, and florist and nursery stocks.* Agriculture Handbook, 66: Washington.

87. Hedley, C. (2015). *The role of precision agriculture for improved nutrient management on farms.* Journal of the Science of Food and Agriculture, 95(1), 12-19.

88. Hewitt, D.R., Neufeld, J.A., Lister, J.R. (2014). *High Rayleigh number convection in a three-dimensional porous medium.* Journal of Fluid Mechanics, 748, 879-895.

89. Heyes, J.A., Tanner, D.J., East, A.R. (2009). *Kiwifruit respiration rates, storage temperatures and harvest maturity.* Acta Horticulturae, 880, 167-173.

90. Ho, Q.T., Rogge, S., Verboven, P., Verlinden, B.E., Nicolaï, B.M. (2016). *Stochastic modelling for virtual engineering of controlled atmosphere storage of fruit.* Journal of Food Engineering, 176, 77-87.

91. Holman, J.P. (2010). *Heat Transfer, Tenth Edition*. New York, United States of America: McGraw-Hill Publishers.

92. Huang, H., Tunnicliffe, M., Shim, Y.M., Bronlund, J.E. (2017). *Model based development of fruit simulators.* Proceedings from 20th International ESA form Conference on Material Forming. Dublin, Ireland.

93. Hundy, G.F., Trott, A.R., Welch, T., Trott, A.R. (2008). *Refrigeration and air-conditioning.* Amsterdam: Butterworth-Heinemann/Elsevier.

94. Incropera F.P, DeWitt D.P. (1981). *Fundamentals of heat transfer. (1st Ed.).* USA: John Wiley and Sons.

95. Ishikawa, K. (1982). *Guide to quality control.* Tokyo: Asian Productivity Organization.

96. Izadi, E., Bezuijen, A. (2015). *Simulation of granular soil behaviour using the Bullet physics library.* Geomechanics from Micro to Macro. 1565-1570.

97. Jabbar, A., East, A.R., Jones, G., Tanner, D.J., Heyes, J.A. (2014). *Modelling batch variability in softening of 'Hayward' kiwifruit from at-harvest maturity measures.* Postharvest Biology and Technology, 90, 7-14.

98. James, S.J., James, C. (2010). *The food cold-chain and climate change.* Food Research International, 43(7), 1944-1956.

99. Jodrey, W.S., Tory, E.M. (1985). *Computer simulation of close random packing of equal spheres.* Physical Review A, 32(4), 2347-2351.

100. Jordan, R.B., Seelye, R.J. (2009). *Relationship between taste perception, density and soluble solids concentration in kiwifruit (*Actinidia Deliciosa). New Zealand Journal of Crop and Horticultural Science, 37(4), 303-317.

101. Jordan, R.B., Walton, E.F., Klages, K.U., Seelye, R.J. (2000). *Postharvest fruit density as an indicator of dry matter and ripened soluble solids in kiwifruit.* Postharvest Biology and Technology, 20(2), 163-173.

102. Kak, A.C., Slaney, M. (1988). *Principles of computerized tomographic imaging.* Philadelphia, PA: SIAM.

103. Kakaç, S., Yener, Y. Pramuanjaroenkij, A. (2014). *Convective heat transfer (3rd Ed.).* (pp. 86), Boca Raton, Florida: CRC Press, Taylor & Francis Group.

104. Kaufman, A., Cohen, D., Yagel, R. (1993). *Volume graphics.* Computer, 26(7), 51-64.

105. Kretz, D., Callau-Monje, S., Hitschler, M., Hien, A., Raedle, M., Hesser, J. (2016). *Discrete element method (DEM) simulation and validation of a screw feeder system.* Powder Technology, 287, 131-138.

106. Kuwabara, G., Kono, K. (1987). *Restitution coefficient in a collision between two spheres.* Japanese Journal of Applied Physics, 26, 1230-1233.

107. Larsen, L.E., Jacobi. J.H. (1986). *Medical applications of microwave imaging.* New York: The Institute of Electrical and Electronics Engineers.

108. Löhner, R. (2008). *Applied computational fluid dynamics techniques: an introduction based on finite element methods.* (pp. 137), Chichester: John Wiley & Sons.

109. Lorestani, A.N., Tabatabaeefar, A. (2006). *Modelling the mass of kiwifruit by geometrical attributes.* International Agrophysics, 20 (135-139).

110. Lu, L.X., Chen, X.Q., Wang, J. (2014). *Modeling and thermal analysis of tray-layered fruits inside packages during forced-air precooling process.* Packaging Technology and Science, 29(2), 105,119.

111. Maguire, K.M., Banks, N.H., and Opara, L.U. (2010). *Factors affecting weight loss of apples.* (pp. 197-234), Horticultural Reviews: John Wiley & Sons, Inc.

112. Mangate, L.D., Chaudhari M.B. (2015). *Heat transfer and acoustic study of impinging synthetic jet using diamond and oval shape orifice*. International Journal of Thermal Sciences, 89, 100-109.

113. Marczewska, I., Rojek, J., Kačianauskas, R. (2016). *Investigation of the effective elastic parameters in the discrete element model of granular material by the triaxial compression test.* Archives of Civil and Mechanical Engineering, 16(1), 64-75.

114. Martines-Hermosilla, G.A., Bronlund, J.E., Kueh, C., Dahm, K. (2016). *Food packaging strength with handholes defined by fourier series shape descriptor.* Poster presented at 13th Conference of Food Engineering, Columbus Ohio, USA.

115. McDonald, K., Sun, D.W. (2000). *Vacuum cooling technology for the food processing industry: a review.* Journal of food engineering, 45(2), 55-65.

116. Mercier, S., Marcos, B., Uysal, I. (2017a). *Identification of the best temperature measurement position inside a food pallet for the prediction of its temperature distribution.* International Journal of Refrigeration, 76, 147-159.

117. Mercier, S., Villeneuve, S., Mondor, M. and Uysal, I. (2017b). *Time–temperature management along the food cold chain: A review of recent developments.* Comprehensive Reviews in Food Science and Food Safety, 16(647-667).

118. Mishchenko, Y. (2015) *A fast algorithm for computation of discrete Euclidean distance transform in three or more dimensions on vector processing architectures.* Signal, Image and Video Processing, 9(1), 19-27.

119. Mitchell, G.F. (1987). *Postharvest physiology and technology of kiwifruit.* In I International Symposium on Kiwifruit 282 (pp. 291-307).

120. Moreda, G.P., Muñoz, M.A., Ruiz-Altisent, M., Perdigones, A. (2012). *Shape determination of horticultural produce using two-dimensional computer vision – A review.* Journal of Food Engineering, 108(2), 245-261.

121. Nield, D. A. Bejan, A. (2006). *Convection in porous media.* New York: Springer.

122. Nield, D. A., Bejan, A. (2017). Internal Natural Convection: Heating from Below. In Nield, D.A., Bejan, A. (Eds.), Convection in Porous Media (5th Ed). 241-361. Cham, Switzerland: Springer.

123. Norton, T., Sun, D.W. (2006). *Computational fluid dynamics (CFD) – an effective and efficient design and analysis tool for the food industry: A review.* Trends in Food Science & Technology, 17(11), 600-620.

124. O'Sullivan, J. (2016). *Significant factors affecting the forced-air cooling process of polylined horticultural produce* (PhD thesis). Massey University, Palmerston North, New Zealand.

125. O'Sullivan, J., Ferrua, M. J., Love, R., Verboven, P., Nicolaï, B., East, A.R. (2016). *Modelling the forced-air cooling mechanisms and performance of polylined horticultural produce.* Postharvest Biology and Technology, 120, 23-35.

126. O'Sullivan, J., Ferrua, M.J., Love, R.J., Verboven, P., Nicolaï, B.M., East, A.R. (2013), *Performance of the forced-air cooling process of fruit packed in polyethylene liners as a function of pallet orientation.* Proceedings of the 2nd IIR International Conference on Sustainability and the Cold Chain.
127. O'Hagan, A., Leonard, T. (1976). *Bayes estimation subject to uncertainty about parameter constraints.* Biometrika, 63(1), 201-203.
128. Olatunji, J.R. (2012). *Mathematical modelling of a proton exchange membrane electrolysis cell.* Massey University, School of Engineering and Advanced Technology.
129. Olatunji, J.R., Shim, Y.M., Love, R.J., Ferrua, M.J., East, A.R. (2015). *Numerical determination of kiwifruit shape, volume and surface area.* Poster presented at 12th International Congress on Engineering and Food, Quebec City, Canada.
130. Otsu, N. (1979). *A threshold selection method from gray-level histograms.* IEEE Transactions on Systems, Man, and Cybernetics, 9(1) 62-66.
131. Owen, D.B. (1956). *Tables for computing bivariate normal probabilities.* The Annals of Mathematical Statistics. 27(4), 1075-1090.
132. Pathare, P.B., Opara, U.L. (2014). *Structural design of corrugated boxes for horticultural produce: A review.* Biosystems Engineering, 125, 128-140.
133. Pathare, P.B., Opara, U.L., Vigneault, C., Delele, M.A., Al-Said, F.A.J. (2012). *Design of packaging vents for cooling fresh horticultural produce.* Food and Bioprocess Technology, 5(6), 2031-2045.
134. Patil, S., Ravi, B. (2005). *Voxel-based representation, display and thickness analysis of intricate shapes.* Ninth International Conference on Computer Aided Design and Computer Graphics.
135. Pons, O. (2014). *Nonparametric tests for one sample.* In O. Pons (Ed.), Statistical tests of nonparametric hypotheses: asymptotic theory (pp. 65-68 & 107-109). Singapore: World Scientific Publishing Company.

136. Rashidi, M., Gholami, M. (2008). *Determination of Kiwifruit Volume Using Ellipsoid Approximation and Image-Processing Methods.* International Journal of Agriculture and Biology. 10 (375-380).

137. Rashidi, M., Seyfi, K. (2007). *Classification of fruit shape in kiwifruit applying the analysis of outer dimensions.* International journal of agriculture and biology, 9(5), 759-762.

138. Razavi, S.M.A., Bahram-Parvar, M. (2007). *Some physical and mechanical properties of kiwifruit.* International Journal of Food Engineering 3(6).

139. Redding, G.P., Yang, A., Shim, Y.M., Olatunji, J.R, East, A.R. (2016). *A review of the use and design of produce simulators for horticultural forced-air cooling studies.* Journal of Food Engineering, 190, 80-93.

140. Restuccia, D., Spizzirri, U.G., Parisi, O.I., Cirillo, G., Curcio, M., Iemma, F., Puoci, F., Vinci, G., Picci, N., (2010). *New EU regulation aspects and global market of active and intelligent packaging for food industry applications.* Food Control, 21(11), 1425-1435.

141. Riddle, D.F. (1974). *Calculus and analytic geometry*. Belmont, Calif.: Wadsworth Pub. Co.

142. Risi, D. (2017). *Future of the family farm.* Accessed 18 December 2017. www.youngfarmers.co.nz/assets/ANZ-Scholarship-2016/Daniel-Risi-ANZ-Scholarship-Report-Final.pdf

143. Robb, R.A. (1985). *Three-dimensional biomedical imaging.* Boca Raton, Fla., CRC Press.

144. Rogge, S., Defraeye, T., Herremans, E., Verboven, P., Nicolaï, B.M. (2015). *A 3D contour based geometrical model generator for complex-shaped horticultural products.* Journal of Food Engineering, 157(0), 24-32.

145. Sargent, S.A., Ritenour, M.A., Brecht, J.K., Bartz, J.A. (2007). *Handling, Cooling and Sanitation Techniques for Maintaining Postharvest Quality*. University of Florida.

146. Serway, R., Jewett, J. (2013). *Physics for scientists and engineers with modern physics.* (pp. 561-576). Nelson Education.

147. Shäfer, J., Dippel, S., Wolf, D. (1996). *Force schemes in simulations of granular materials.* Journal de Physique I, 6(5–20).

148. Shapiro, S.S., Wilk, M.B. (1965). *An analysis of variance test for normality (complete samples).* Biometrika, 52(3/4), 591-611.

149. Shim, Y.M., Olatunji, J.R., Zhou, J., Love, R.J., Ferrua, M.J., East, A.R. (2016). *Industry survey on the pressure drop across palletised horticulture produce during precooling.* 4th International Institute of Refrigeration International Conference on Sustainability and the Cold Chain, Auckland, New Zealand, 7-9 April 2016.

150. Singh, R.P., Heldman, D.R. (2009). *Introduction to food engineering.* Burlington, Mass.: Academic Press/Elsevier.

151. Smale, N.J. (2004). *Mathematical modelling of airflow in shipping systems: model development and testing* (PhD thesis). Massey University, Palmerston North, New Zealand.

152. Statistics NZ. (2017a). Data retrieved from the website of the New Zealand Government's Statistics department: http://www.stats.govt.nz/.

153. Statistics NZ. (2017b). *New Zealand's goods and services trade – Imports and exports for the year ended June.* Retrieved 25 October 2017, from http://www.stats.govt.nz/StatsMaps/New-Zealands-goods-and-services-trade.

154. Stewart, J.K., Lipton, W.J. (1960). *Factors influencing heat loss in cantaloups, during hydrocooling.* Marketing Research Report. United States Department of Agriculture, 421.

155. Stockin, K.A., Wiseman, N., Hartman, A., Moffat, N., Roe, W.D. (2008). *Use of radiography to determine age class and assist with the post‐mortem diagnostics of a Bryde's whale* (Balaenoptera brydei). New Zealand Journal of Marine and Freshwater Research, 42(3), 307-313.

156. Tanner, D.J. (1998). *Mathematical modelling for design of horticultural packaging* (PhD thesis). Massey University, Palmerston North, New Zealand.

157. Tanner, D.J., Cleland, A.C., Opara, L.U., Robertson, T.R. (2002a). *A generalised mathematical modelling methodology for design of horticultural food packages exposed to refrigerated conditions: part 1, formulation.* International Journal of Refrigeration, 25(1), 33-42.

158. Tanner, D.J., Cleland, A.C., Opara, L.U., Robertson, T.R. (2002b). *A generalised mathematical modelling methodology for the design of horticultural food packages exposed to refrigerated conditions Part 2. Heat transfer modelling and testing.* International Journal of Refrigeration, 25(1), 43-53.

159. Tanner, D.J., Cleland, A.C., Robertson, T.R. (2002c). *A Generalised Mathematical Modelling Methodology for Design of Horticulture Food Packages Exposed to Refrigerated Conditions: Part 3, Mass Transfer Modelling and Testing.* International Journal of Refrigeration, 25(1), 54-65.

160. Tassou, S.A., De-Lille, G., Ge., Y.T. (2009). *Food transport refrigeration – approaches to reduce energy consumption and environmental impacts of road transport.* Applied Thermal Engineering, Elsevier. 29(8-9), 1467.

161. Terrell, D., Fomby, T.B. (2006). *A multi-variate skew-garch model.* In D. Terrel (Ed.), Econometric analysis of financial and economic time series (pp. 36-38). Amsterdam: Elsevier JAI.

162. Thompson, J.F., Mitchell, F.G., Rumsey, T.R., Kasmire, R.F., Crisosto, C.H. (2008). *Commercial Cooling of Fruits, Vegetables, and Flowers.* (pp. 11). Oakland, CA: University of California, Division of Agriculture and Natural Resources.

163. Tijskens, E., Ramon, H., Baerdemaeker, J. D. (2003). *Discrete element modelling for process simulation in agriculture.* Journal of Sound and Vibration, 266(3), 493-514.

164. van der Sman, R.G.M. (2002). *Prediction of airflow through a vented box by the Darcy–Forchheimer equation.* Journal of Food Engineering, 55, 49-57.

165. van der Sman, R.G.M. (2003). *Simple model for estimating heat and mass transfer in regular-shaped foods.* Journal of Food Engineering, 60(4), 383-390.

166. van Rossum, G. (1995). *Python tutorial*. Technical Report CS-R9526, Centrum voor Wiskunde en Informatica (CWI), Amsterdam

167. Van Zeebroeck, M., Lombaert, G., Dintwa, E., Ramon, H., Degrande, G., Tijskens, E. (2008). *The simulation of the impact damage to fruit during the passage of a truck over a speed bump by means of the discrete element method.* Biosystems Engineering, 101(1), 58-68.

168. Van Zeebroeck, M., Tijskens, E., Dintwa, E., Kafashan, J., Loodts, J., De Baerdemaeker, J., Ramon, H. (2006). *The discrete element method (DEM) to simulate fruit impact damage during transport and handling: model building and validation of DEM to predict bruise damage of apples.* Postharvest Biology and Technology, 41(1), 85-91.

169. Verboven, P., Flick, D., Nicolaï, B. M., Alvarez, G. (2006). *Modelling transport phenomena in refrigerated food bulks, packages and stacks: basics and advances.* International Journal of Refrigeration, 29(6), 985-997.

170. Wang, M., and Bejan, A. (1987). *Heat transfer correlation for Bénard convection in a fluid saturated porous layer.* International Communications in Heat and Mass Transfer, 14, 617-626.

171. Wang, M.Y., MacRae, E., Wohlers, M., March, K. (2011). *Changes in volatile production and sensory quality of kiwifruit during fruit maturation in* Actinidia Delociosa *'Hayward' and* Actinidia Chinensis *'Hort 16A'.* Postharvest Biology and Technology, 59(1), 16-24.

172. Watada, A.E., Ko, N.P., Minott, D.A. (1996). *Factors affecting quality of fresh-cut horticultural products.* POSTEC Postharvest Biology and Technology, 9(2), 115-125.

173. Weisstein, E.W. (2018). *Heron's Formula.* MathWorld--A Wolfram Web Resource. Retrieved 25 January 2018, from http://mathworld.wolfram.com/HeronsFormula.html.

174. Wong, S., Gower, P. (2017). *Labour confirms plans to cut immigrant numbers by up to 30,000.* Newshub. Retrieved 18 December 2017, from www.newshub.co.nz/home/politics /2017/06/labour-confirms-plans-to-cut-immigrant-numbers-by-up-to-30-000.html

175. Xu, Y., Burfoot, D. (1999). *Simulating the bulk storage of foodstuffs.* Journal of Food Engineering, 39(1), 23-29.

176. Zeng, G.L. (2010). *Medical image reconstruction: A conceptual tutorial.* (pp. 67-80,175-187), Berlin, Heidelberg: Springer Berlin Heidelberg.

177. Zespri International (2011). *Nutrition Table of the Zespri Kiwifruit varieties*. Retrieved from: http://www.zespri.com/Documents/Nutrition-table.pdf. [Accessed 10 January 2017].

178. Zespri International. (2017). *Kiwifruit GDP on track to hit $6.14 billion, 29,000 new jobs by 2030: University of Waikato*. Retrieved 28 June 2017, from http://www.zespri.com/ companyinformation/newsroom/kiwifruit-gdp-increase.

179. Zhao, J.M., Bronlund J.E., East A.R. (2014). *Effect of cooling rates on kiwifruit firmness and rot incidence in subsequent storage.* Proceedings of the 5th Postharvest Unlimited Conference, Cyprus. (pp. 313-318).

180. Zou, Q., Opara, L.U., McKibbin, R. (2006a). *A CFD modeling system for airflow and heat transfer in ventilated packaging for fresh foods: I. Initial analysis and development of mathematical models.* Journal of Food Engineering, 77(4), 1037-1047.

181. Zou, Q., Opara, L.U., McKibbin, R. (2006b). *A CFD modeling system for airflow and heat transfer in ventilated packaging for fresh foods: II. Computational solution, software development, and model testing.* Journal of Food Engineering, 77(4), 1048-1058.

Appendix A

Experimental Cooling Results

A.1: Introduction

Section 3.2 involved the collection of pallet scale cooling data for a wide variety of package designs and operational conditions, reiterated in Table A.1:

Case Study:	**Label:**	**Number of Vents:**	**Total Opening Area:**	**Pressure Drop:**
Baseline				
Current Package	**CP1**	2	7.5%	130 Pa
Changes to Pressure Drop				
Medium Flowrate	**CP2**	2	7.5%	245 Pa
High Flowrate	**CP3**	2	7.5%	335 Pa
Increase in Vent Size				
Larger Vents, 1	**LV1**	2	8.9%	130 Pa
Larger Vents, 2	**LV2**	2	13.1%	130 Pa
Decrease in Vent Size				
Smaller Vents, 1	**SV1**	2	3.4%	130 Pa
Smaller Vents, 2	**SV2**	2	4.5%	130 Pa
Changes to Vent Number				
Vent Number, 1	**VN1**	3	7.0%	130 Pa
Vent Number, 2	**VN2**	1	7.0%	130 Pa

Table A.1: Vent number, ventilation total opening area and pressure drop of each experiment.

The remaining results are presented in this appendix. Section A.2 contains the raw cooling profiles for each pallet layer; section A.3 the experimental heterogeneity plots; section A.4 the experimental heterogeneity maps; and section A.5 shows the comparison between the empirical dimensionless temperature distribution and the representative skew-normal distribution for each pallet at a number of process progression indexes.

A.2: Cooling Profiles

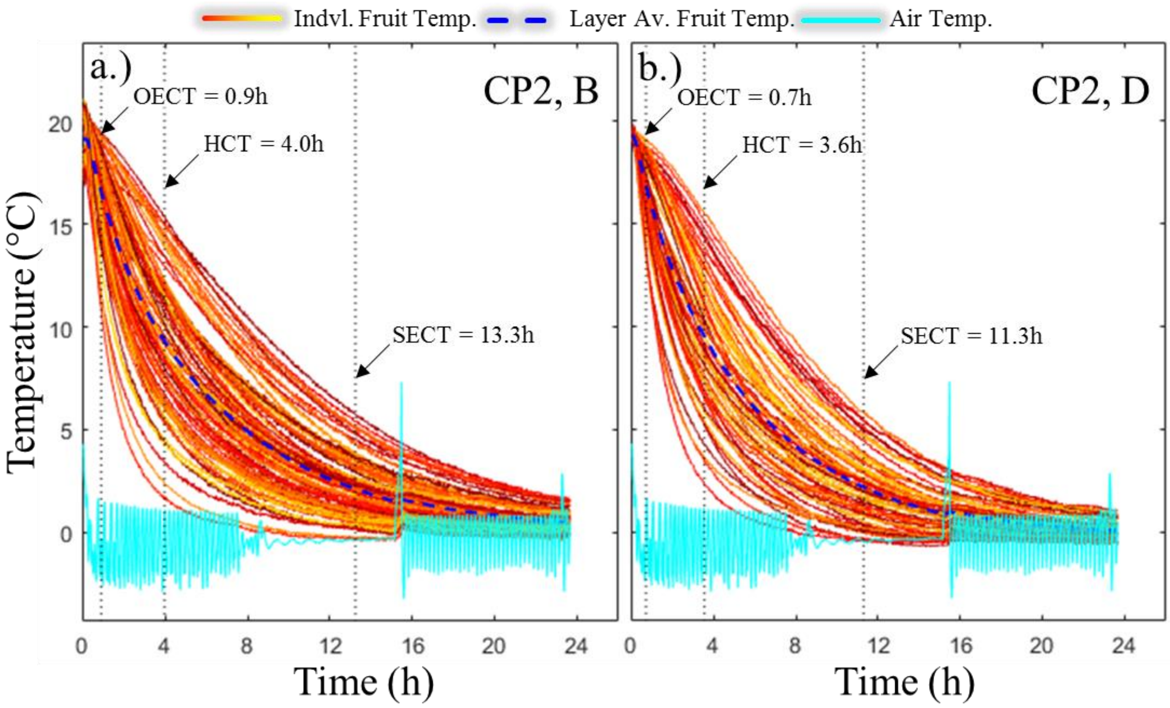

Figure A.1: Empirical cooling curve for pallet CP2: 2 vents, 7.5% TOA, 245 Pa pressure drop. a.) Layer B, and b.) Layer D.

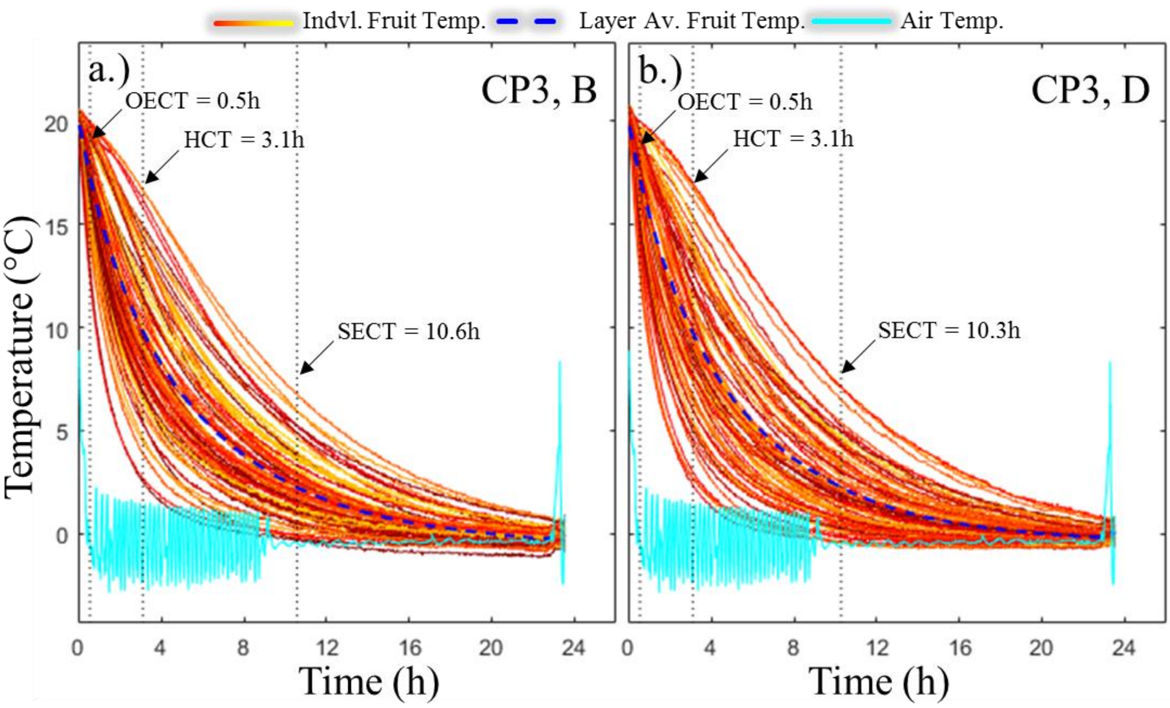

Figure A.2: Empirical cooling curve for pallet CP3: 2 vents, 7.5% TOA, 335 Pa pressure drop. a.) Layer B, and b.) Layer D.

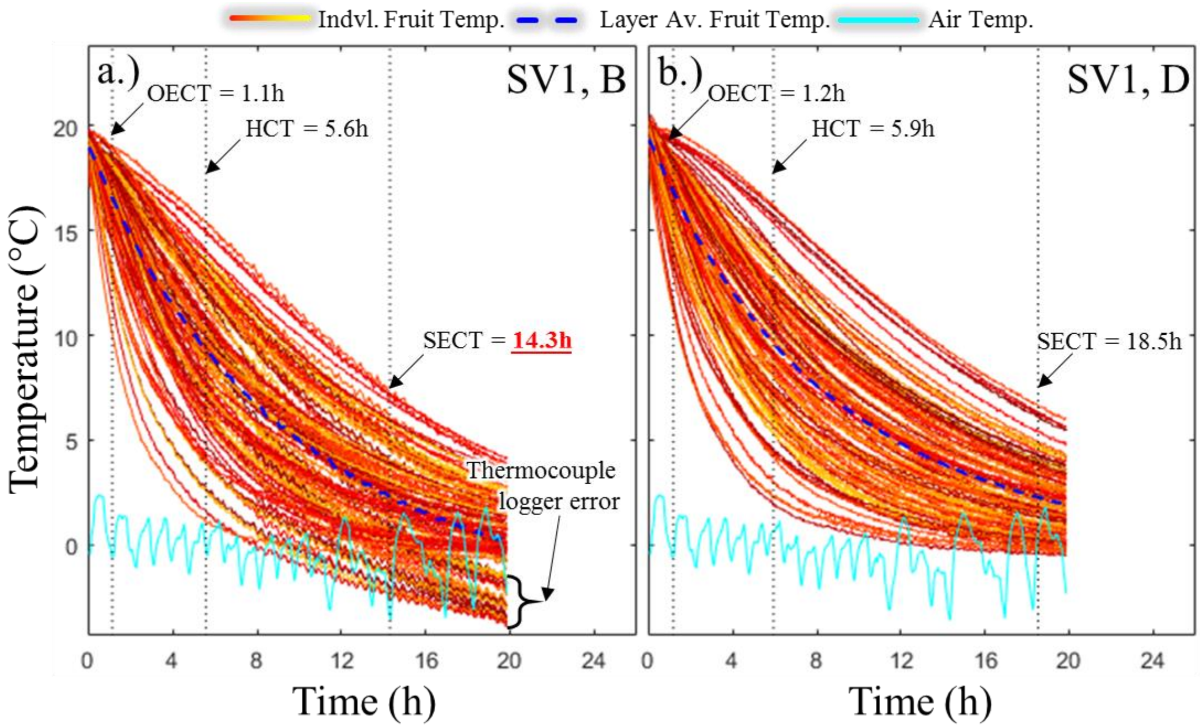

Figure A.3: Empirical cooling curve for pallet SV1: 2 vents, 3.4% TOA, 130 Pa pressure drop. a.) Layer B, and b.) Layer D.

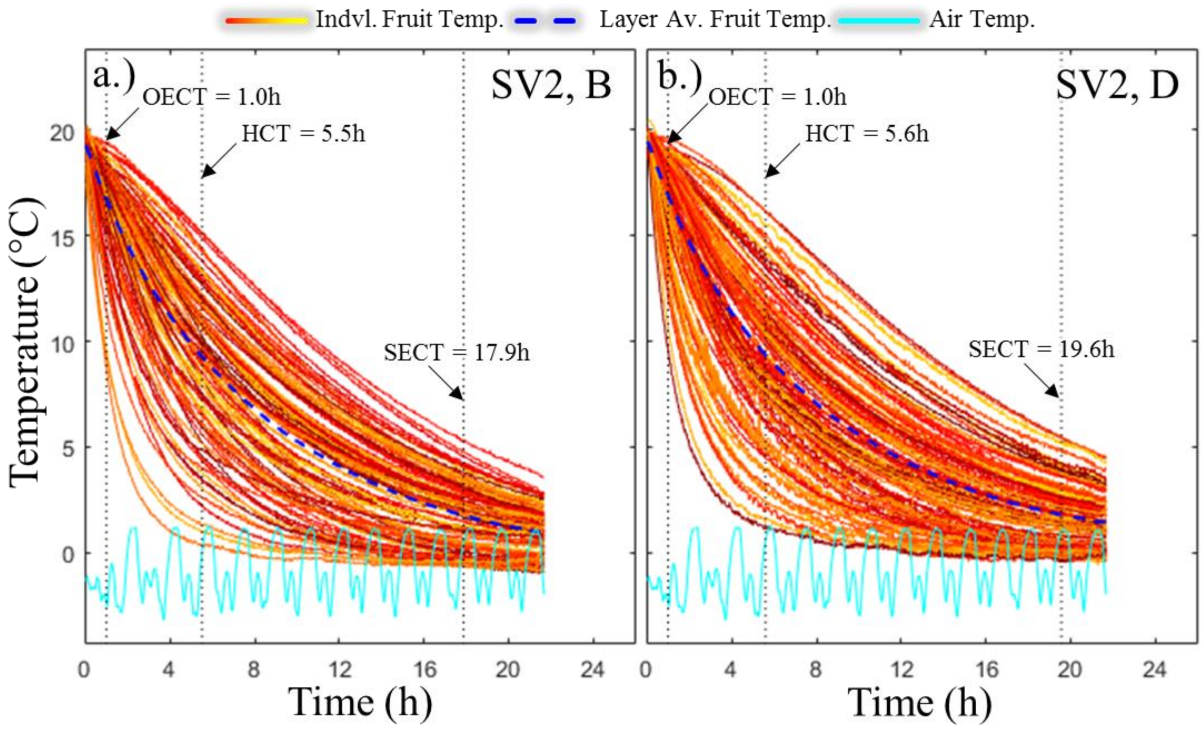

Figure A.4: Empirical cooling curve for pallet SV2: 2 vents, 4.5% TOA, 130 Pa pressure drop. a.) Layer B, and b.) Layer D.

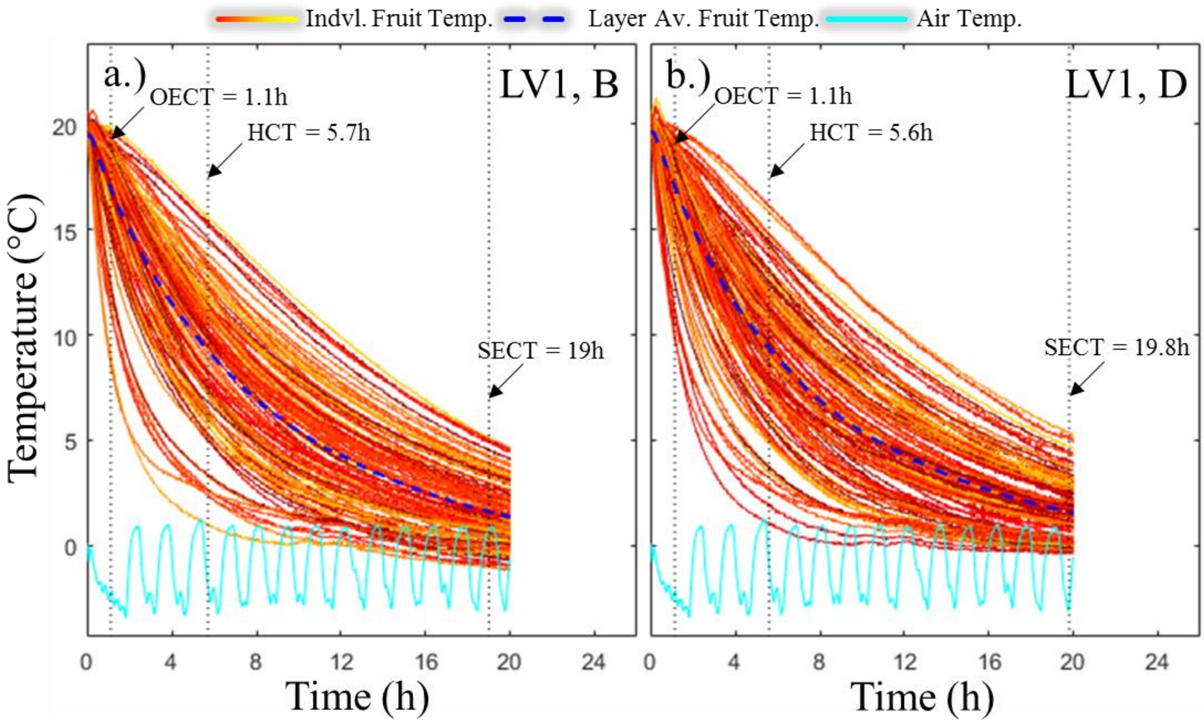

Figure A.5: Empirical cooling curve for pallet LV1: 2 vents, 8.9% TOA, 130 Pa pressure drop. a.) Layer B, and b.) Layer D.

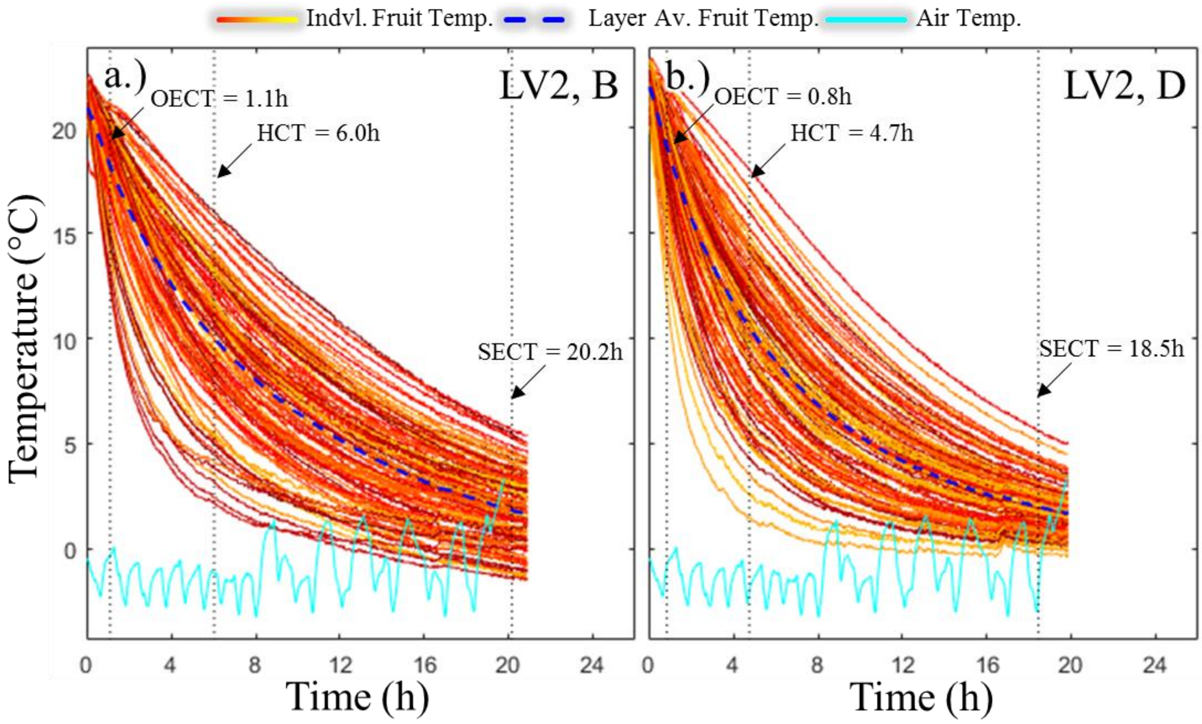

Figure A.6: Empirical cooling curve for pallet LV2: 2 vents, 13.1% TOA, 130 Pa pressure drop. a.) Layer B, and b.) Layer D.

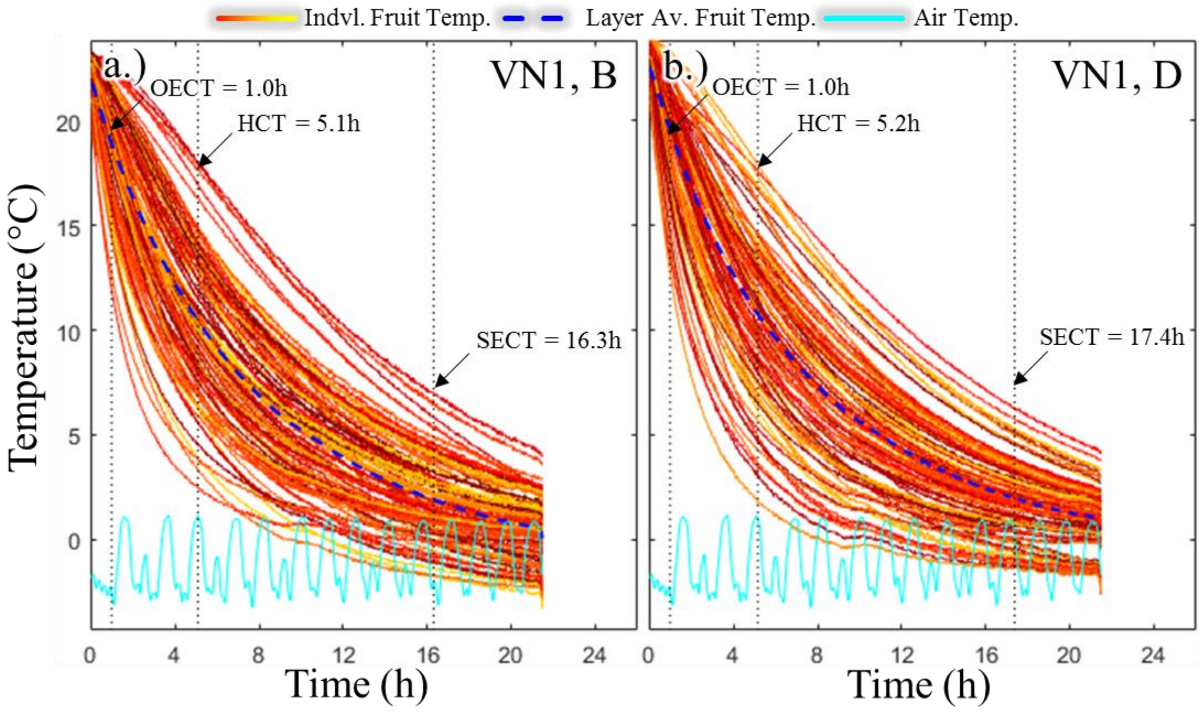

Figure A.7: Empirical cooling curve for pallet VN1: 3 vents, 7.0% TOA, 130 Pa pressure drop. a.) Layer B, and b.) Layer D.

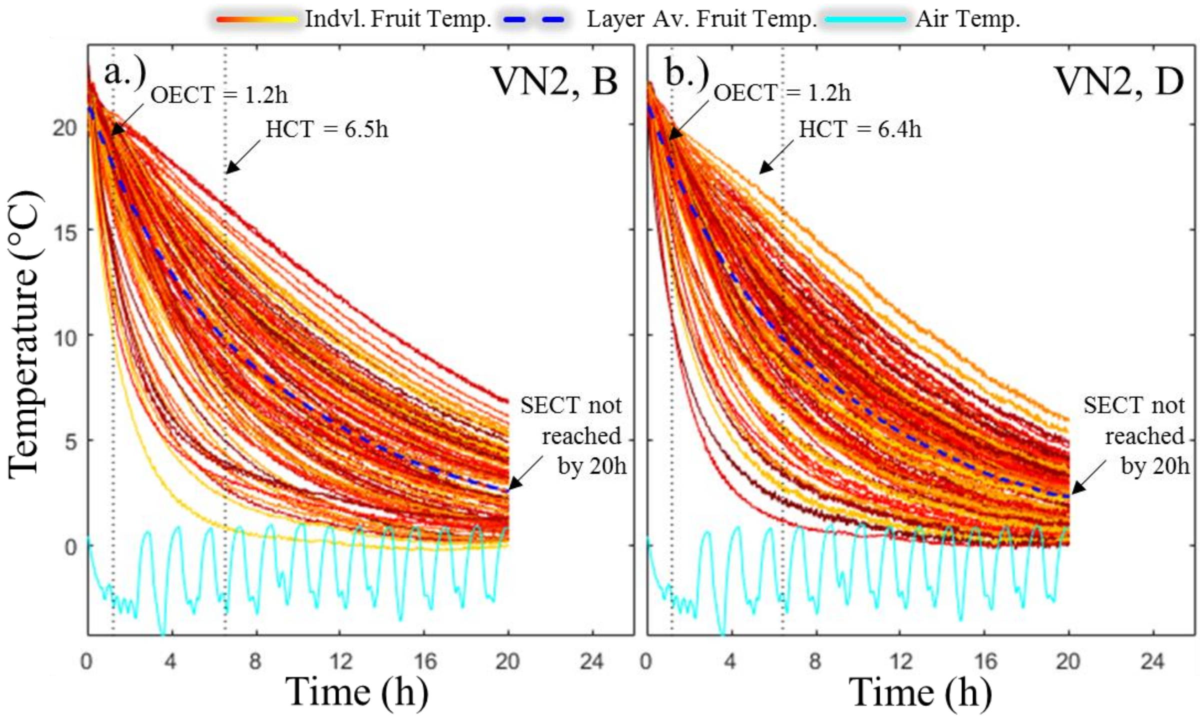

Figure A.8: Empirical cooling curve for pallet VN1: 1 vents, 7.0% TOA, 130 Pa pressure drop. a.) Layer B, and b.) Layer D.

A.3: Heterogeneity Plots

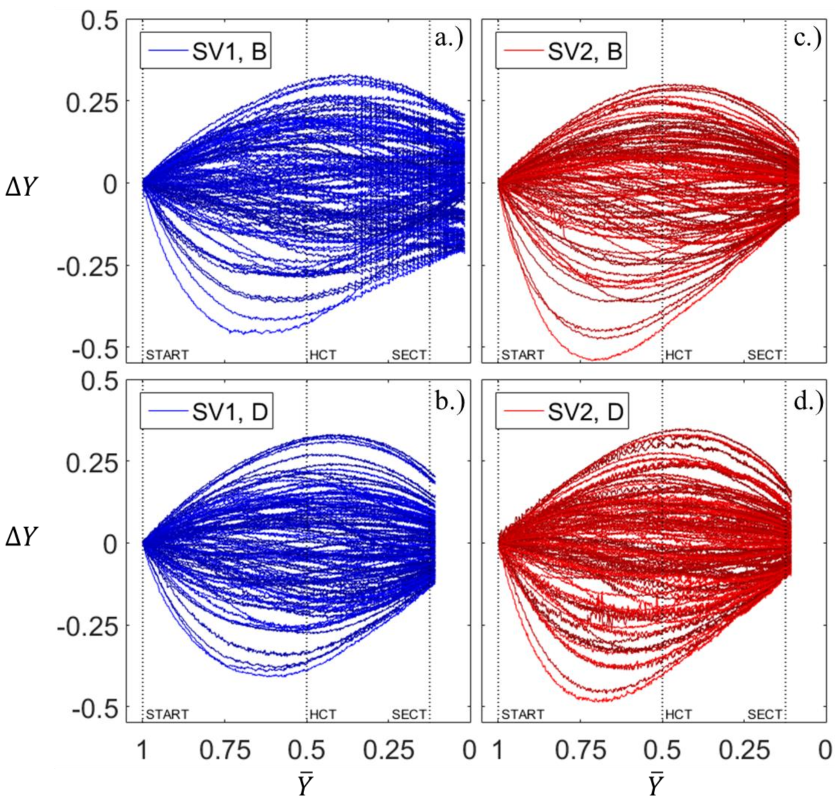

Figure A.9: Experimental heterogeneity plots for pallets SV1 and SV2.

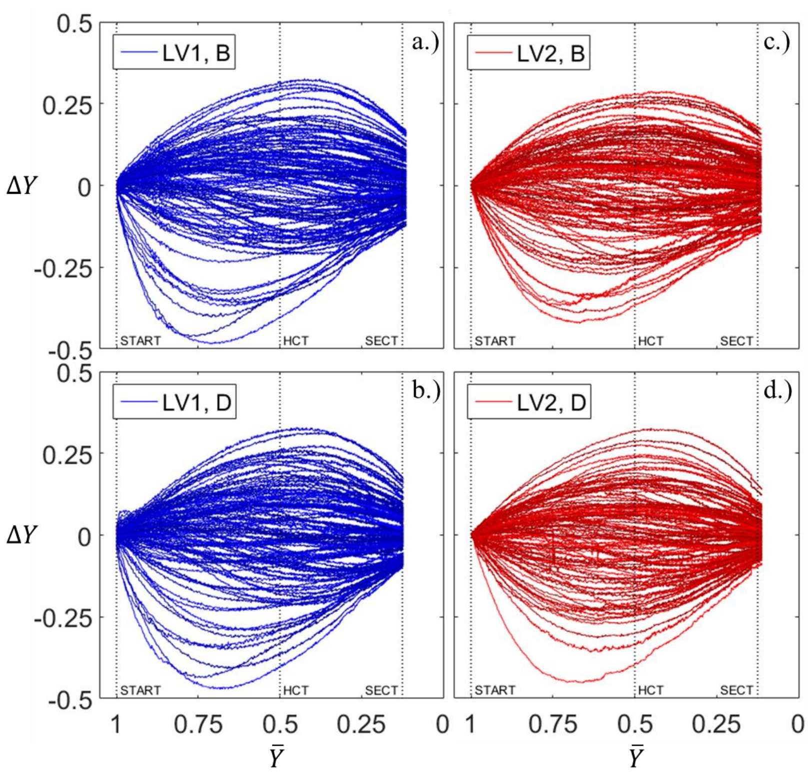

Figure A.10: Experimental heterogeneity plots for pallets LV1 and LV2.

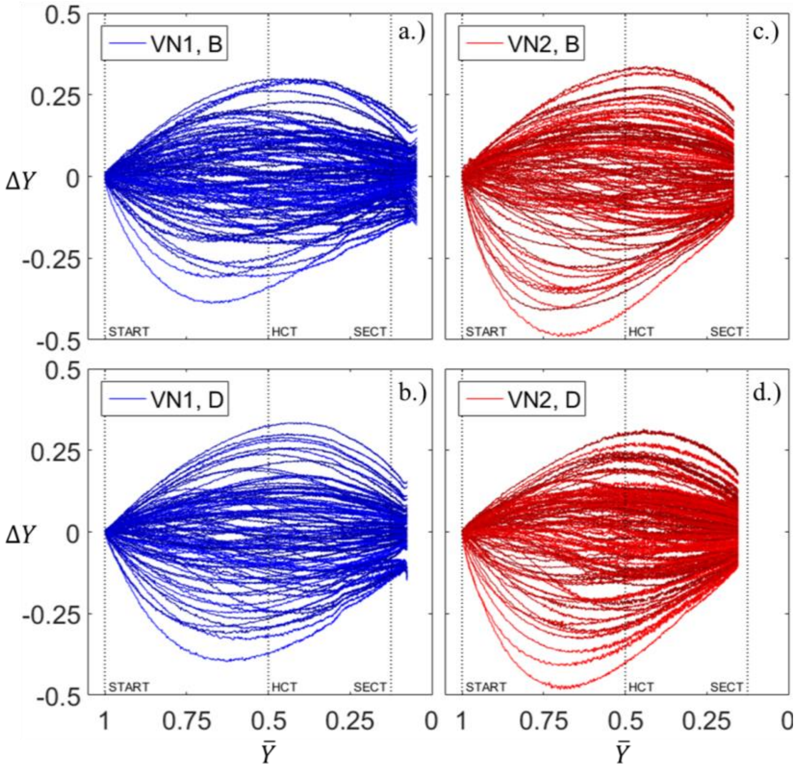

Figure A.11: Experimental heterogeneity plots for pallets VN1 and VN2.

A.4: Heterogeneity Maps

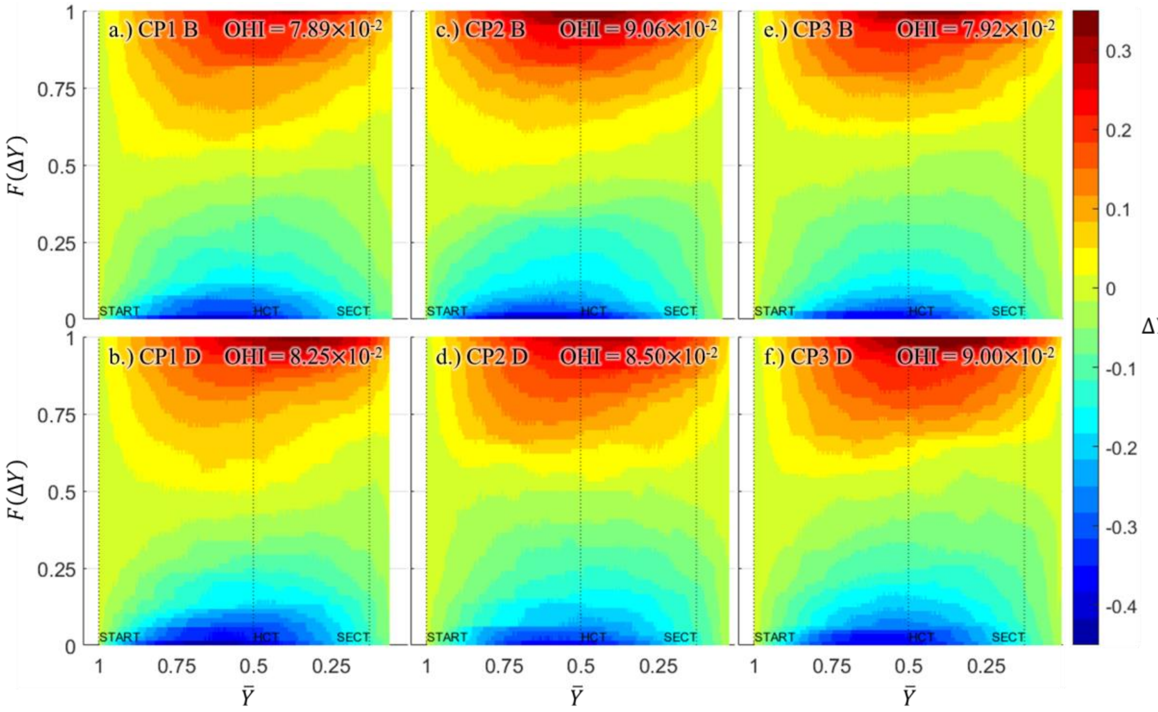

Figure A.12: Experimental heterogeneity maps for pallets CP1, CP2 and CP3.

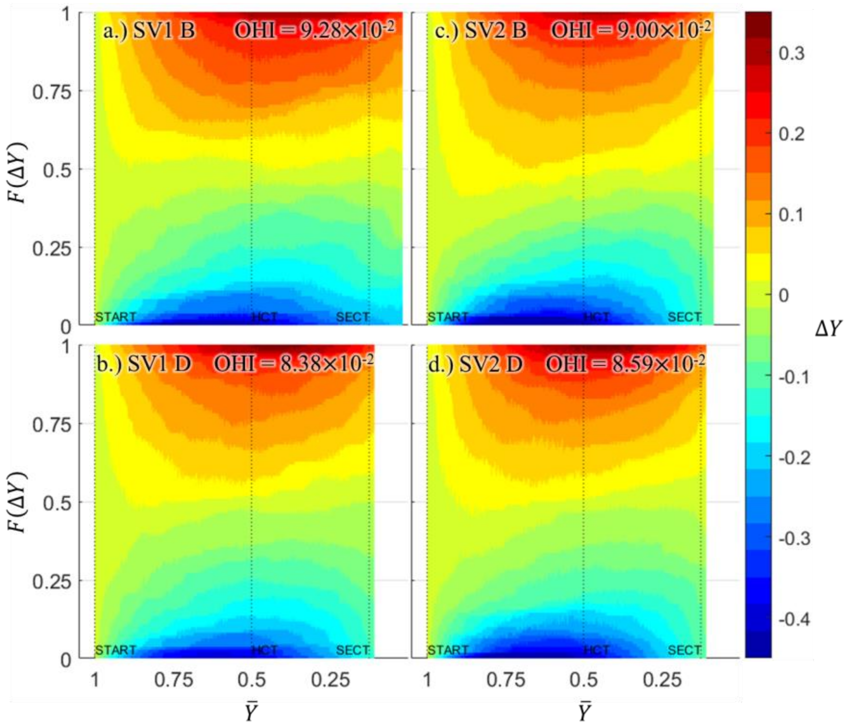

Figure A.13: Experimental heterogeneity maps for pallets SV1 and SV2.

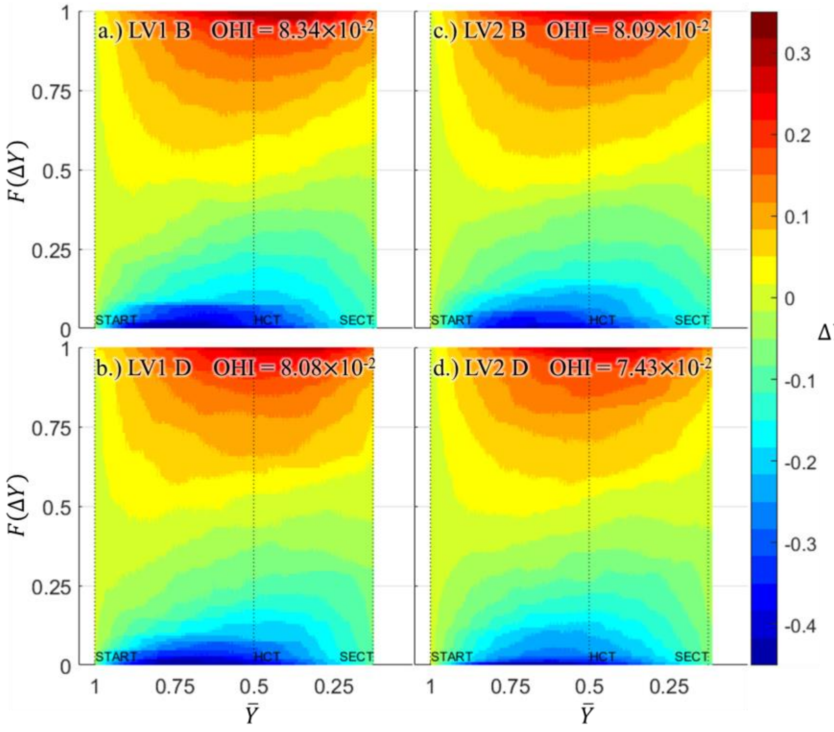

Figure A.14: Experimental heterogeneity maps for pallets LV1 and LV2.

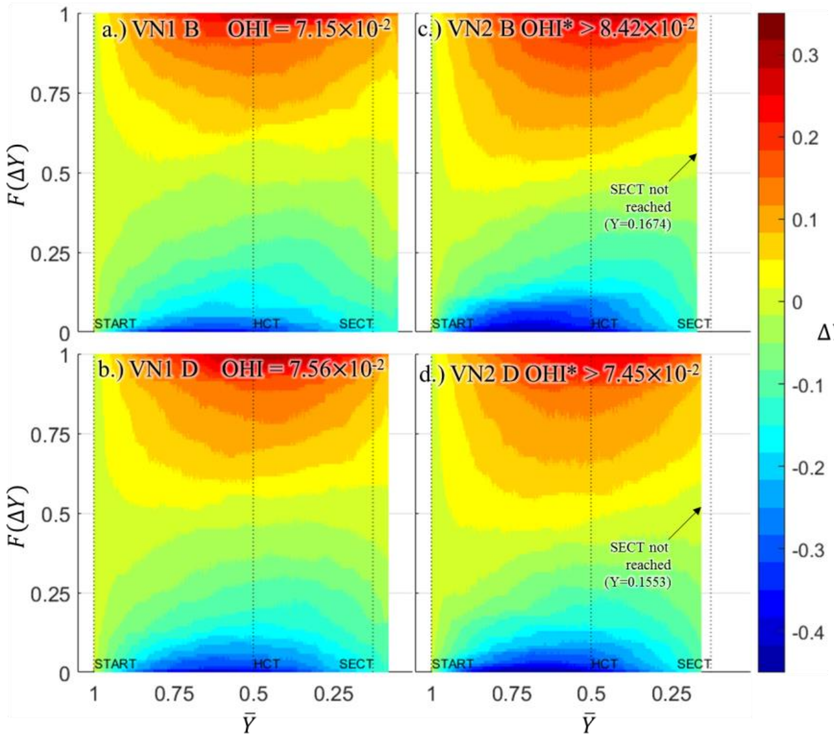

Figure A.15: Experimental heterogeneity maps for pallets VN1 and VN2.

A.5: Validation of Representative Skew-Normal Distributions

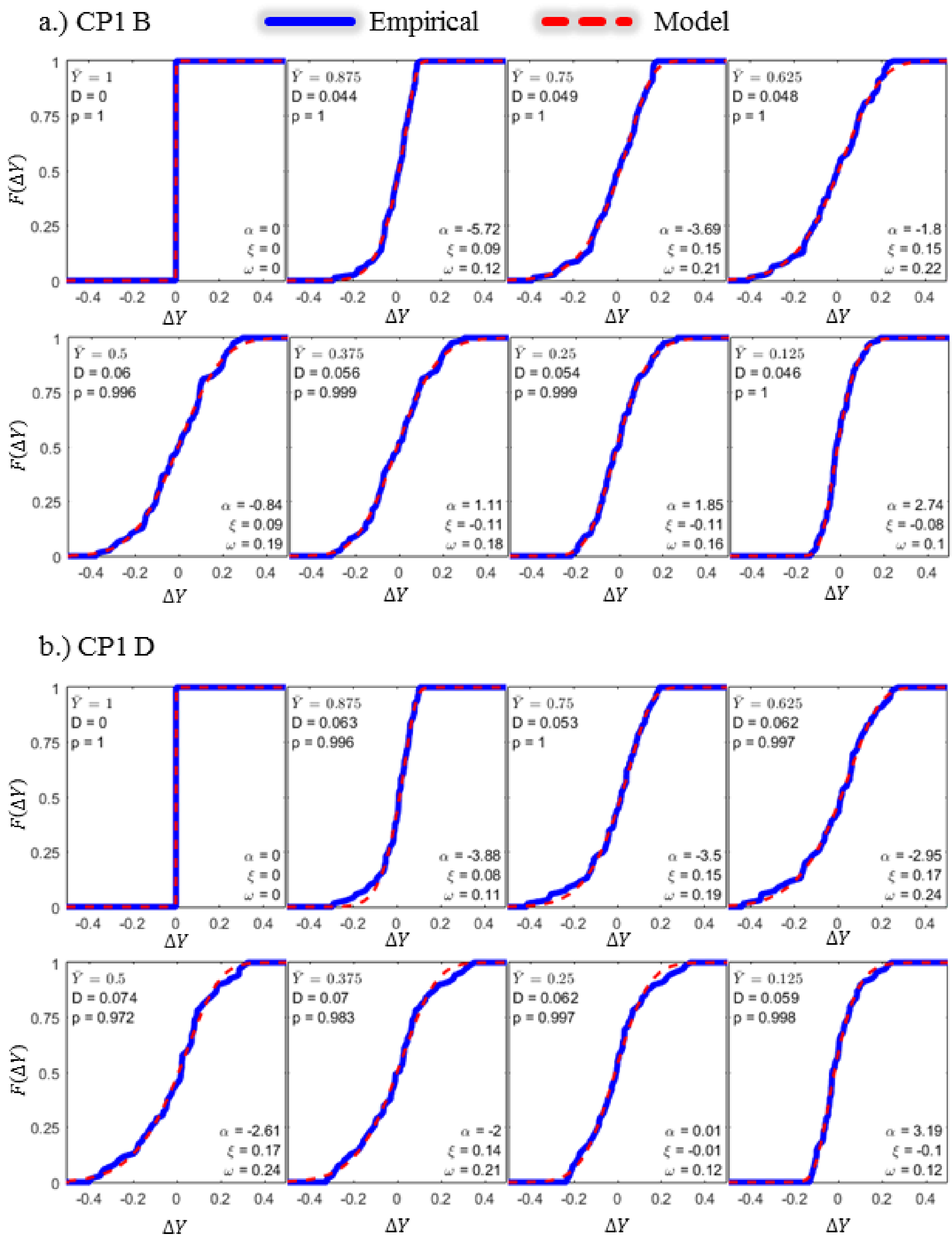

Figure A.16: Experimental cumulative distribution of ΔY (solid blue lines) for cooling of pallet CP1, with fitted Skew-Normal distributions (dashed red lines) for a.) layer B, and b.) layer D at 8 cooling stages: $\overline{Y}$ = 1, 0.875, 0.75, 0.625, 0.5, 0.375, 0.25 and 0.125. D = Kolmogorov-Smirnov test statistic, p = p-value, α = shape, ξ = location and ω = scale.

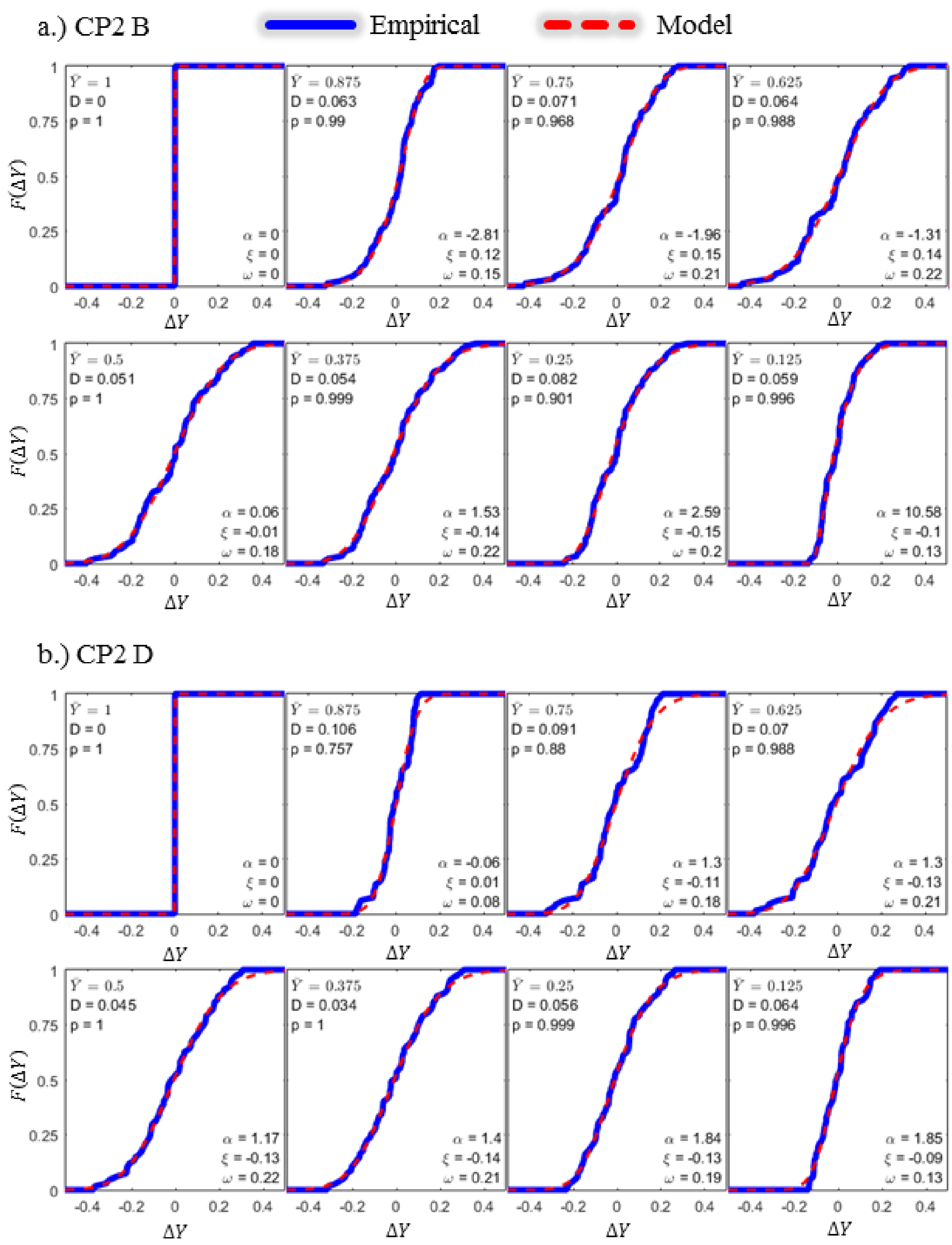

Figure A.17: Experimental cumulative distribution of ΔY (solid blue lines) for cooling of pallet CP2, with fitted Skew-Normal distributions (dashed red lines) for a.) layer B, and b.) layer D at 8 cooling stages: $\bar{Y}$ = 1, 0.875, 0.75, 0.625, 0.5, 0.375, 0.25 and 0.125. D = Kolmogorov-Smirnov test statistic, p = p-value, α = shape, ξ = location and ω = scale.

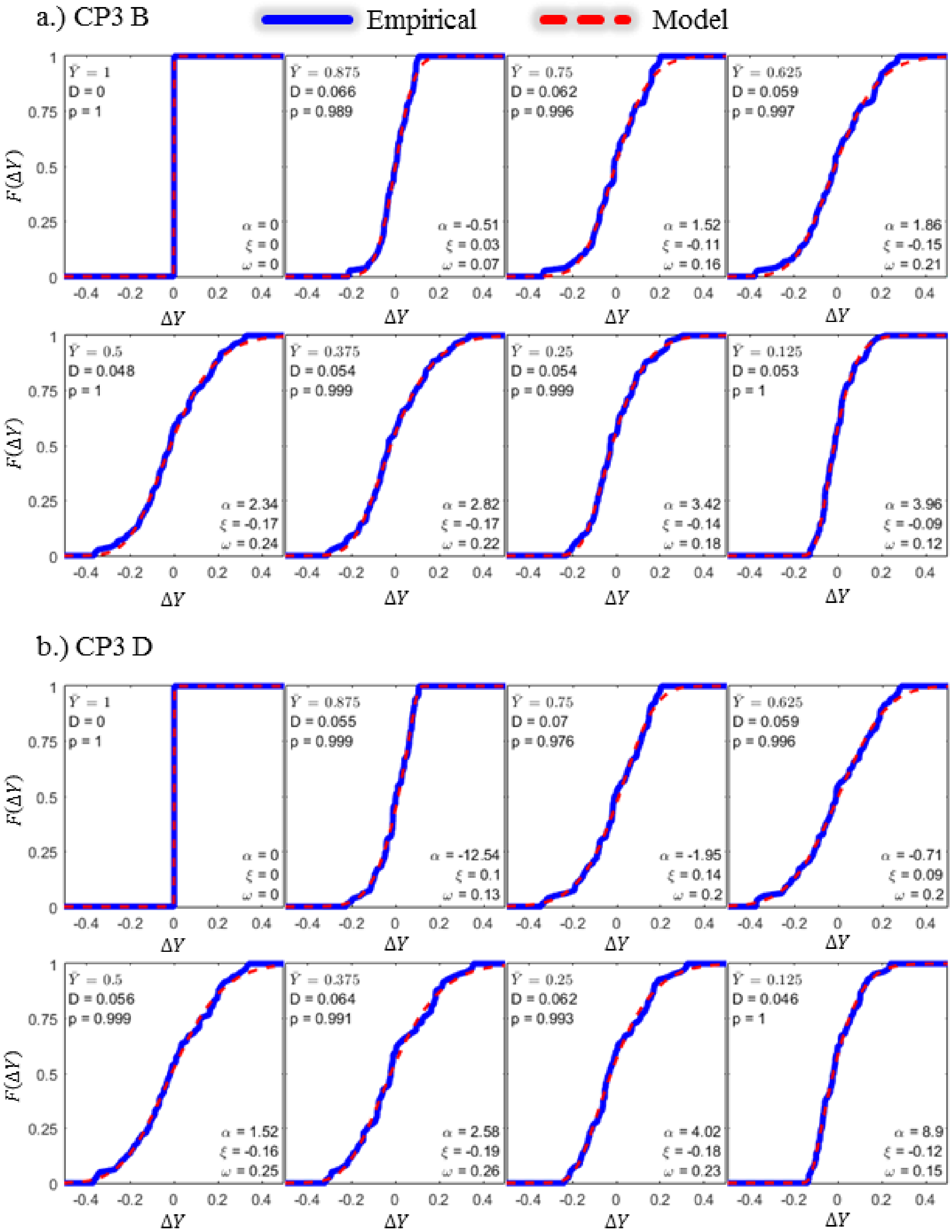

Figure A.18: Experimental cumulative distribution of ΔY (solid blue lines) for cooling of pallet CP3, with fitted Skew-Normal distributions (dashed red lines) for a.) layer B, and b.) layer D at 8 cooling stages: $\bar{Y}$ = 1, 0.875, 0.75, 0.625, 0.5, 0.375, 0.25 and 0.125. D = Kolmogorov-Smirnov test statistic, p = p-value, α = shape, ξ = location and ω = scale.

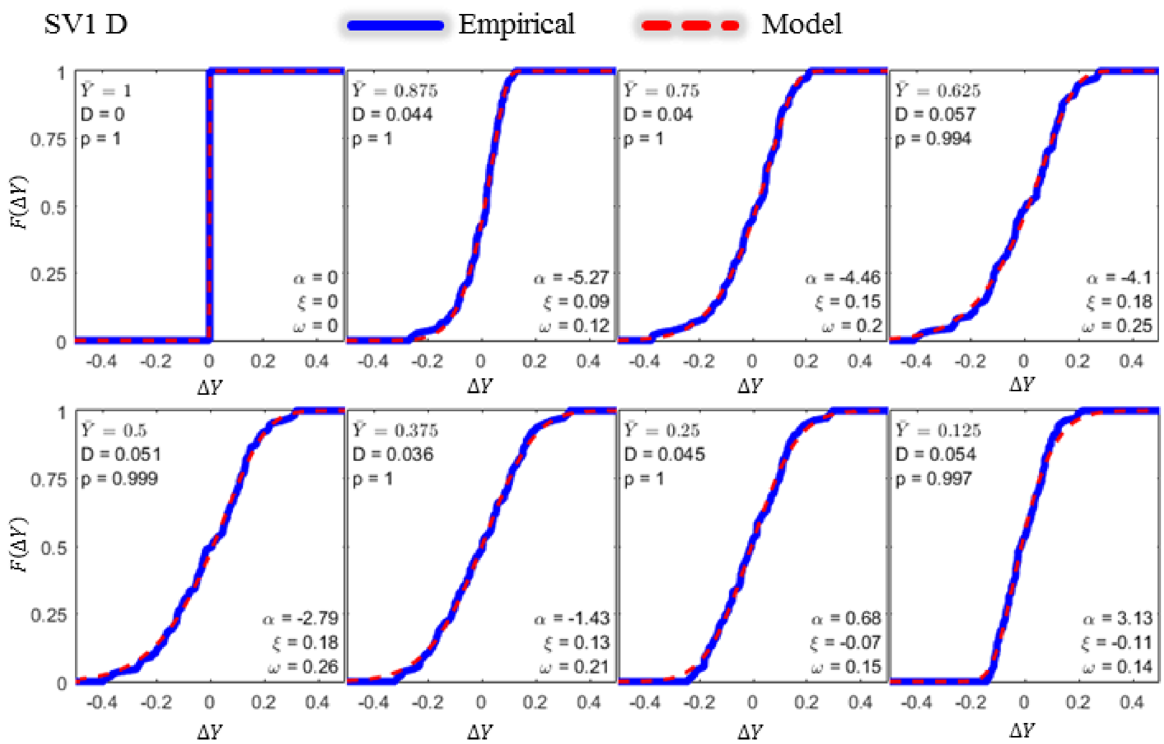

Figure A.19: Experimental cumulative distribution of ΔY (solid blue lines) for cooling of pallet SV1, with fitted Skew-Normal distributions (dashed red lines) at 8 cooling stages: $\bar{Y}$ = 1, 0.875, 0.75, 0.625, 0.5, 0.375, 0.25 and 0.125. D = Kolmogorov-Smirnov test statistic, p = p-value, α = shape, ξ = location and ω = scale. Layer B has been omitted due to a high level of experimental error.

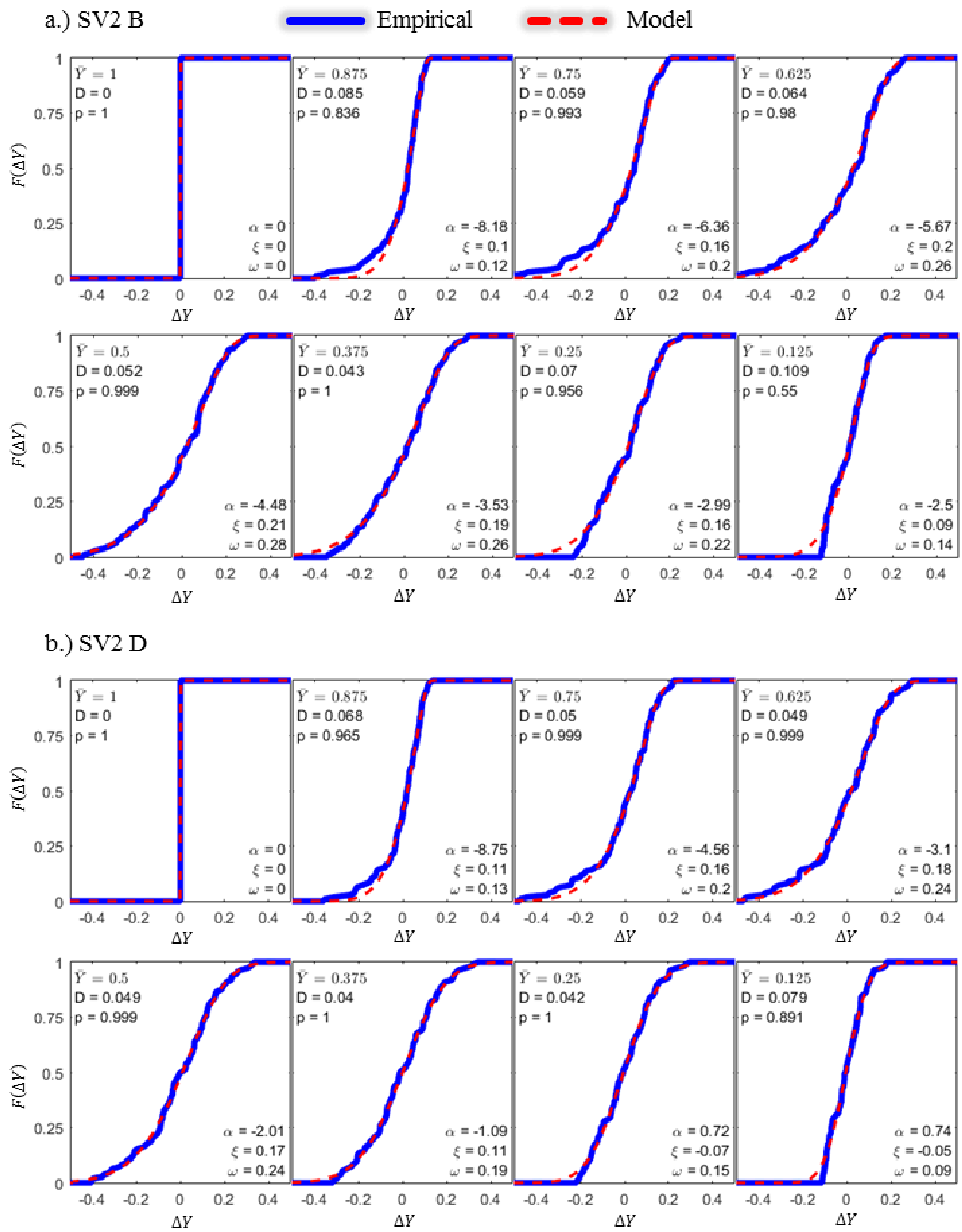

Figure A.20: Experimental cumulative distribution of ΔY (solid blue lines) for cooling of pallet SV2, with fitted Skew-Normal distributions (dashed red lines) for a.) layer B, and b.) layer D at 8 cooling stages: $\overline{Y}$ = 1, 0.875, 0.75, 0.625, 0.5, 0.375, 0.25 and 0.125. D = Kolmogorov-Smirnov test statistic, p = p-value, α = shape, ξ = location and ω = scale.

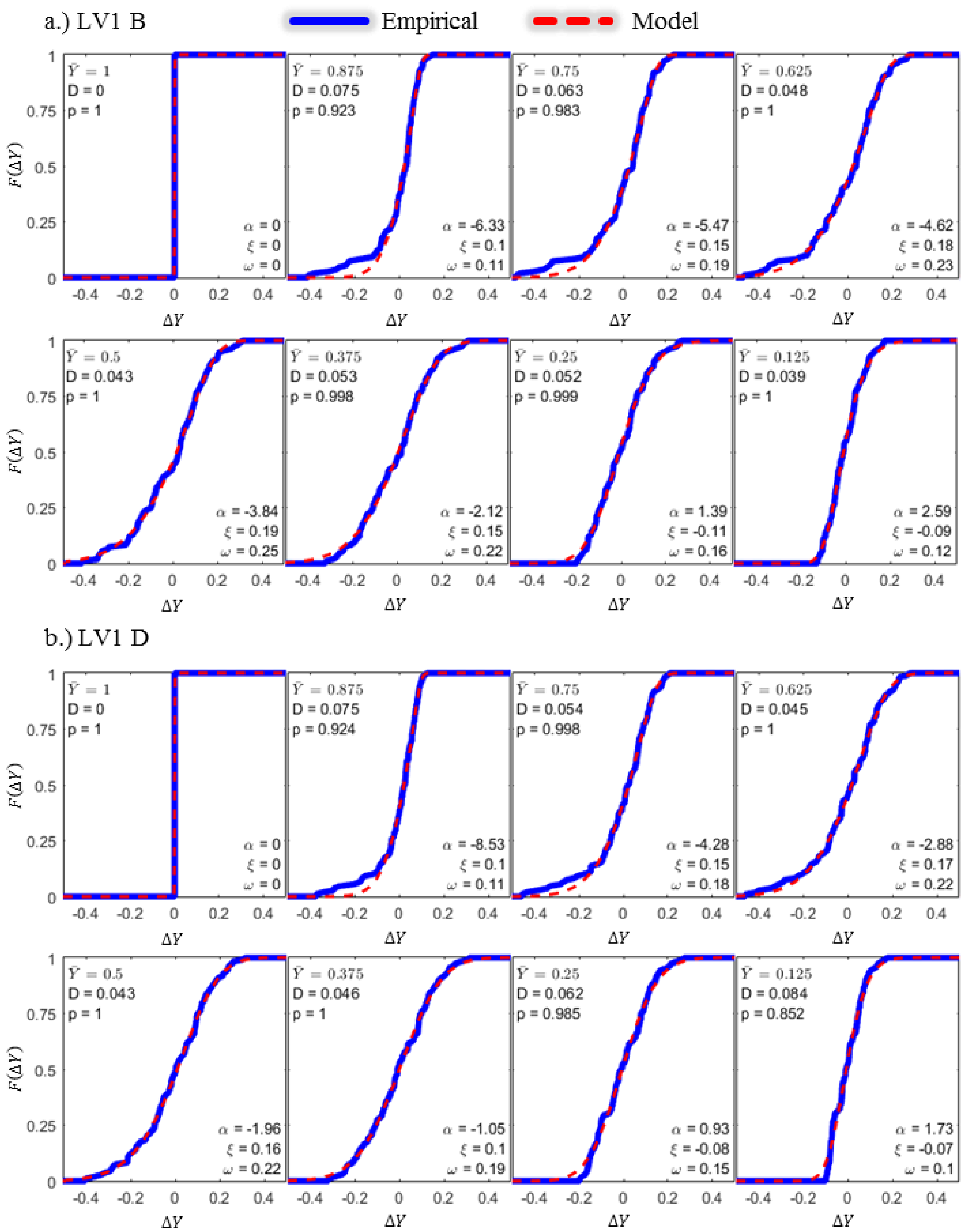

Figure A.21: Experimental cumulative distribution of ΔY (solid blue lines) for cooling of pallet LV1, with fitted Skew-Normal distributions (dashed red lines) for a.) layer B, and b.) layer D at 8 cooling stages: $\overline{Y}$ = 1, 0.875, 0.75, 0.625, 0.5, 0.375, 0.25 and 0.125. D = Kolmogorov-Smirnov test statistic, p = p-value, α = shape, ξ = location and ω = scale.

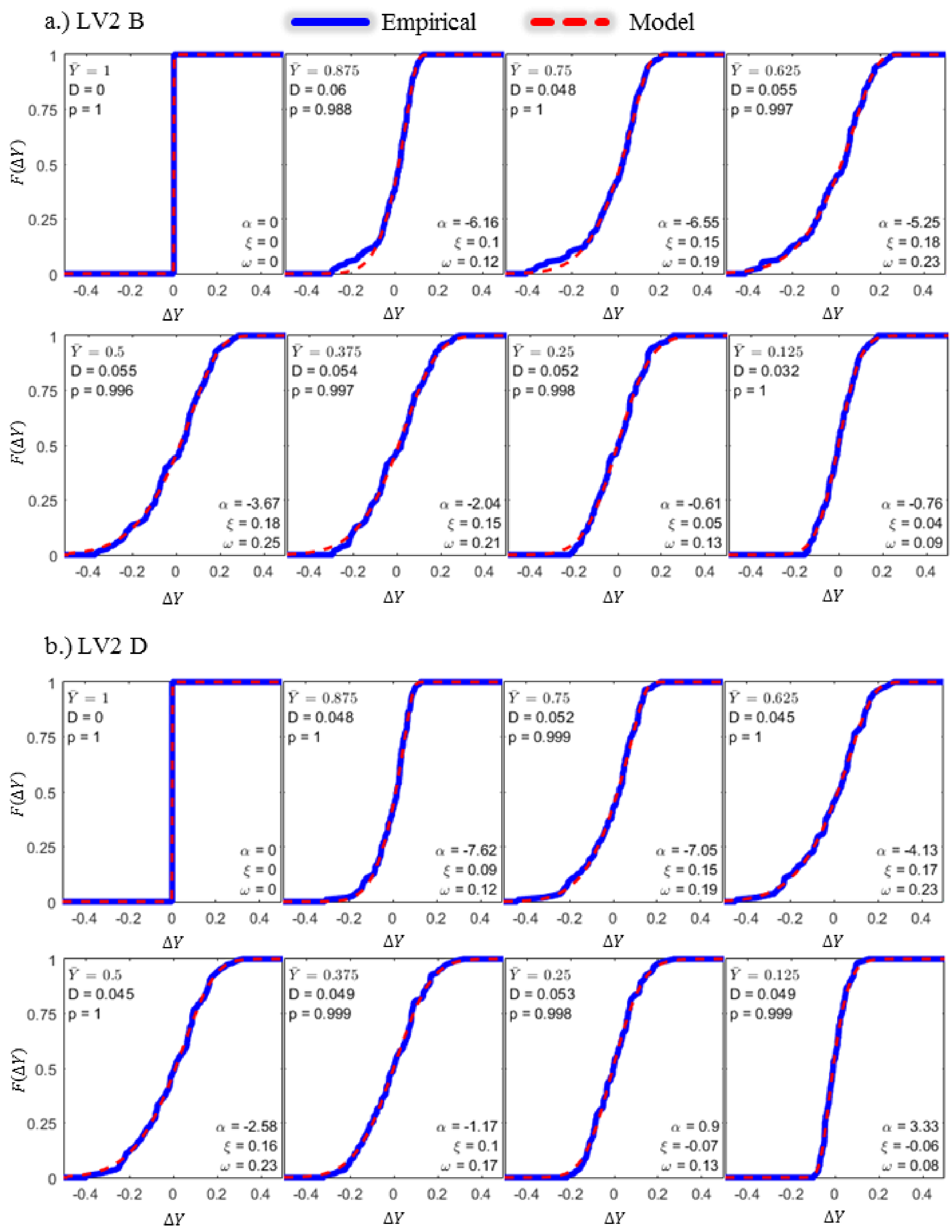

Figure A.22: Experimental cumulative distribution of ΔY (solid blue lines) for cooling of pallet LV2, with fitted Skew-Normal distributions (dashed red lines) for a.) layer B, and b.) layer D at 8 cooling stages: $\overline{Y}$ = 1, 0.875, 0.75, 0.625, 0.5, 0.375, 0.25 and 0.125. D = Kolmogorov-Smirnov test statistic, p = p-value, α = shape, ξ = location and ω = scale.

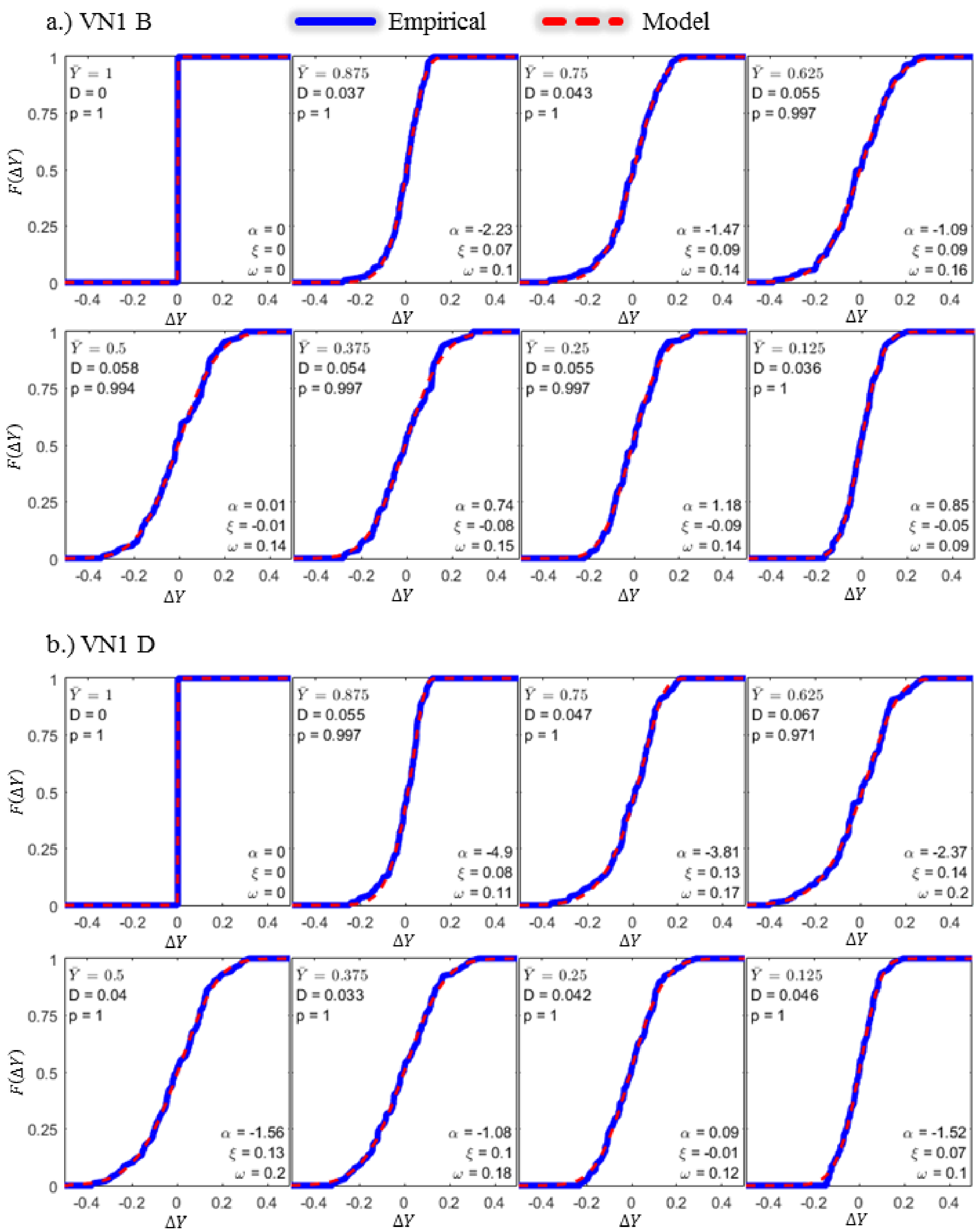

Figure A.23: Experimental cumulative distribution of ΔY (solid blue lines) for cooling of pallet VN1, with fitted Skew-Normal distributions (dashed red lines) for a.) layer B, and b.) layer D at 8 cooling stages: $\bar{Y}$ = 1, 0.875, 0.75, 0.625, 0.5, 0.375, 0.25 and 0.125. D = Kolmogorov-Smirnov test statistic, p = p-value, α = shape, ξ = location and ω = scale.

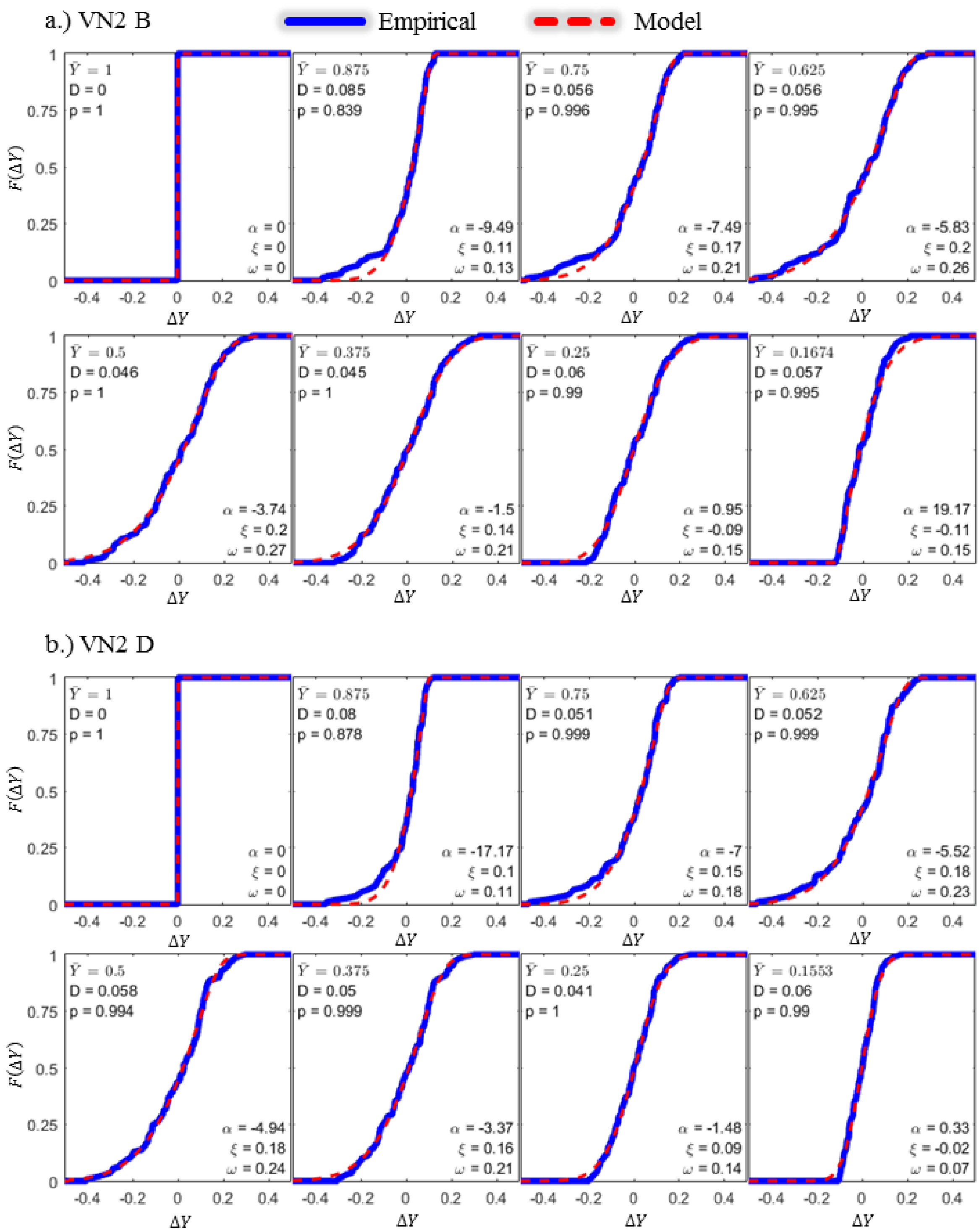

Figure A.24: Experimental cumulative distribution of ΔY (solid blue lines) for cooling of pallet VN2, with fitted Skew-Normal distributions (dashed red lines) for a.) layer B, and b.) layer D at 8 cooling stages: a.) $\overline{Y}$ = 1, 0.875, 0.75, 0.625, 0.5, 0.375, 0.25 and 0.1674 and b.) $\overline{Y}$ = 1, 0.875, 0.75, 0.625, 0.5, 0.375, 0.25 and 0.1553. The SECT is not analysed as the VN2 pallet did not reach the SECT. D = Kolmogorov-Smirnov test statistic, p = p-value, α = shape, ξ = location and ω = scale.

Appendix B

Additional Heat and Mass Transfer Mechanisms

B.1: Introduction

Some heat and mass transfer mechanisms were excluded from the modelling work of this thesis, as they were determined to be insignificant to the current scenario of pre-cooling polylined kiwifruit in a modular bulk package (see section 5.3). In the interests of completeness, it is pertinent to offer some suggestions for how these additional heat and mass transfer mechanisms could be included with a zonal model, for alternative systems where they play a more significant role.

B.2: Formulation of Mass Transfer Equations

Formulating the moisture transfer governing equation is done similarly as heat transfer, with a mass balance within and across zone i, also expressed as a verbal equation in Eq. B.1:

change in the volume average moisture content of phase Z in zone i	=	all exchanges of moisture between phase Z and other phases inside of zone i	+	all exchanges of moisture between phase Z and phases in adjacent zones j	(B.1)

In a fashion synonymous with the previous heat transfer discussion, $\dot{m}$ was chosen as the symbol for a moisture flux, with units kg water·s^{-1}. The same notation for intra- and inter-zonal exchanges was used: $\sum \dot{m}_{ii,k}$ and $\sum \dot{m}_{ij,k}$, which gives Eq. B.2:

$$\frac{d\bar{M}_{Z,i}}{dt} = \sum \dot{m}_{ii,k} + \sum \dot{m}_{ij,k} \qquad \text{(B.2)}$$

Where $\frac{d\bar{M}_{Z,i}}{dt}$ is the mass average moisture change of phase Z within zone i (kg water·s^{-1}).

Mass transfers are denoted as the generalised Eq. B.3:

$$\dot{m} = K_{eff} \cdot A_{eff} \cdot \Delta\bar{p} \qquad \text{(B.3)}$$

Where K_{eff} is the effective mass transfer coefficient (kg water·m^{-2}·s^{-1}·Pa^{-1}), A_{eff} is the effective mass transfer surface area (m^2), and $\cdot\, \Delta\bar{p}$ is the volume averaged water partial pressure difference (Pa).

B.3 Intra-Zonal Radiation

Radiation is distinct from the other mechanisms because the temperature difference is considered to be between *surfaces*, and the temperature gradient is to the *fourth power*:

$$\phi_{ii,9} = h_{eff_{rad,Z_\alpha \to Z_\beta,i}} \cdot A_{eff_{rad,Z_\alpha \to Z_\beta,i}} \cdot \left({T_{surf,Z_\alpha \to Z_\beta,i}}^4 - {T_{surf,Z_\beta \to Z_\alpha,i}}^4 \right) \tag{B.4}$$

Where $h_{eff,rad}$ is the effective radiative heat transfer coefficient (W·m^{-2}·K^{-4}); $A_{eff,rad}$ the effective surface area or view factor (m^2); and T_{surf} the surface temperature; with subscripts $Z_\alpha \to Z_\beta$ denoting a specific phase-pair and i the zone under study (see Table 5.2).

Computing the view factor, $A_{eff,rad,Z_\alpha \to Z_\beta,i}$, in an expeditious and automated fashion poses a significant coding challenge due to the sinuous potential surface shapes in each individual zone. Solutions could come in the form of an efficient ray tracing algorithm similar to Patil and Ravi (2005), which could search for unobstructed faces in the second phase from each face in the first. A variety of methods are given by Gupta *et al.*, 2017 in a review of methods for evaluating the radiation view factor.

The effective radiative heat transfer coefficient is:

$$h_{eff_{rad,Z_\alpha \to Z_\beta,i}} = \sigma_{rad} \cdot \epsilon \tag{B.5}$$

Where σ_{rad} is the Stefan–Boltzmann constant (5.67×10^{-8} W.m^{-2}.K^{-4}); and ϵ is the emissivity of the surfaces (-). It is recommended that an emissivity of 0.9 is used for fruit (taken from Huang *et al.*, 2017).

Determining the surface temperature of the two phases through which there is thermal radiative exchange is more challenging, as the surface temperature is not modelled explicitly in the zonal approach, rather the lumped – or volume averaged – temperature. The approach could be modified to track this temperature, or it could be estimated as a function of the conductive resistances, as it was in section 5.5.6.1.3.

B.4: Intra-Zonal Evaporation

Moisture transfers should be modelled in a fashion analogous to heat transfers, namely via lumped properties. An electrical analogue for moisture transfers between fruit and polyliner air inside of a zone is given in Figure B.1. Moisture partial pressures form the gradient for mass transfers; and moisture transfer resistances are related to the permeability of moisture through the fruit and air:

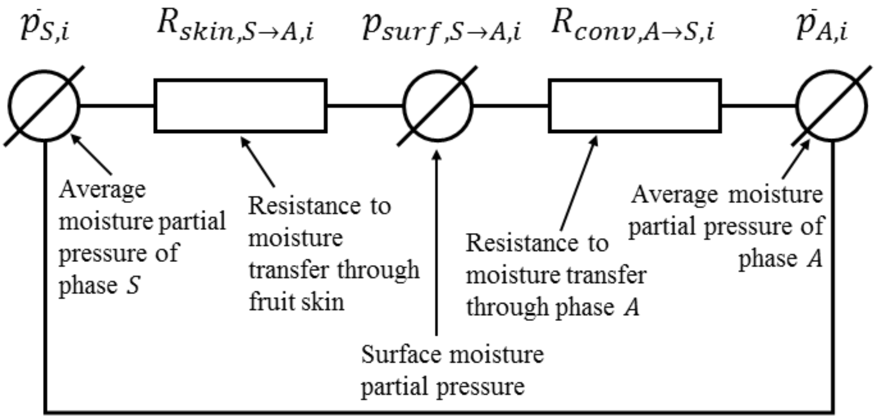

Figure B.1: Electrical analogue for evaporation moisture transfer between the fruit and air, using lumped properties. Image based on van der Sman (2003).

Kiwifruit are moisture rich, with a water content of approx. 80% (Zespri® International, 2011), which is typical for fruit in general. The moisture content inside of a fruit can therefore be considered constant and the surface as fully saturated. Thus, there is no 'internal resistance' to moisture transfer through the flesh of the fruit, and instead the resistance to moisture transfer from the fruit is entirely contingent on the *skin permeance*, D_{skin} (kg water·s^{-1}·m^{-2}·Pa^{-1}). Typically, D_{skin} is difficult to predict/model, so is empirically determined as a physical constant intrinsic to the fruit and cultivar (Maguire *et al.*, 2010; Banks *et al.*, 1995). The moisture transfer resistance from the fruit is therefore:

$$R_{skin,S\to A,i} = \frac{1}{D_{skin}} \tag{B.6}$$

Moisture transfer resistance through the air is:

$$R_{conv,A\to S,i} = \frac{d_{A\to S,i}}{K_A \cdot F_{N.C.}} \tag{B.7}$$

Where $d_{A\rightarrow S,i}$ is the 'characteristic length' of air inside of zone i (it is recommended that the AVDC method is used; see section 5.5.6.1.3; m); K_A is the moisture diffusion coefficient, or permeability, through the air (kg water·s^{-1}·m^{-1}·Pa^{-1}) and $F_{N.C.}$ is a correction factor due to natural convection – this may or may not be the same proportionality constant as is used for heat transfer, see section 5.5.6.1.4. Thus, the effective mass transfer coefficient between fruit and polyliner air is:

$$D_{eff\,conv,S\rightarrow A,i} = \frac{1}{R_{skin,S\rightarrow A,i} + R_{conv,A\rightarrow S,i}} = \frac{1}{\frac{1}{D_{skin}} + \frac{d_{A\rightarrow S,i}}{K_A \cdot F_{N.C.}}} \tag{B.8}$$

Evaporation involves both heat and mass transfer. Mass transfers are controlled by Eq. B.3, the generalised ODE for mass transfer; and evaporative heat transfer from the fruit is modelled as:

$$\phi_{ii,7} = \dot{m} \cdot L_{vap} \tag{B.9}$$

Where $\dot{m}$ is the mass transfer rate of water, determined by Eq. B.3 (kg water·s^{-1}), and L_{vap} is the latent heat of vaporisation, which is a constant 2260 kJ·kg water^{-1} (taken from Serway and Jewett, 2013).

In a scenario where there isn't a polyliner, bulk air flows directly over the fruit, evaporating moisture from the fruit surface and evacuating the moisture from the system. In this case the moisture transfer resistance in the bulk air phase ($Z = O$) will be dependent on the air velocity through the zone. The forced-air moisture transfer resistance can be determined through a dimensionless correlation (Becker and Frike, 1996):

$$\mathrm{Sh} = f(\mathrm{Re}, \mathrm{Sc}) \tag{B.10}$$

Where the Sherwood number is:

$$\mathrm{Sh} = \frac{\frac{1}{R_{ext,A\rightarrow S,i}} \cdot L_{eff}}{K_A} \tag{B.11}$$

The Reynolds number, Re, and the effective length, L_{eff}, is as described in section 6.3.4; and the Schmidt number is:

$$\mathrm{Sc} = \frac{\mu}{\rho_A \cdot K_A} \tag{B.12}$$

So that the effective mass transfer coefficient between the fruit and the bulk airflow is:

$$D_{eff\,conv,S\to A,i} = \frac{1}{\frac{1}{D_{skin}} + R_{ext,A\to S,i}} \tag{B.13}$$

Becker and Frike (1996) suggest Eq. B.14 for spherical fruits or vegetables:

$$\mathrm{Sh} = 2.0 + 0.552 \cdot \mathrm{Re}^{0.53} \cdot \mathrm{Sc}^{0.33} \tag{B.14}$$

However, its efficacy to the current scenario is not explored in this thesis.

B.5: Intra-Zonal Diffusion

Diffusion is also ignored from this zonal model as its impact is negligible over the relatively short time period of the pre-cooling process (0). If the mechanism were to be included, the same electrical analogue as Figure B.1 can be drawn in this scenario, replacing the air components with packaging components:

$$D_{eff\,diff,S\to P,i} = \frac{1}{\frac{1}{D_{skin}} + \frac{d_{P\to S,i}}{K_P}} \tag{B.15}$$

Where $d_{P\to S,i}$ is the 'characteristic length' to the surface formed between fruit and packaging (m), and K_P is the moisture permeability of the packaging material (kg water·s^{-1}·m^{-1}·Pa^{-1}), which should be empirically measured (Tanner *et al.*, 2002c).

B.6: Inter-Zonal Diffusion

Transfers of *moisture* between zones should be handled in much the same fashion as the linear slice geometric procedure of section 5.5.6.2.2, but with the thermal conductivity replaced with the moisture permeability:

$$\frac{M_{slice\ n}}{dt} = {}^{K_Z}\!/_{d_{slice}} \cdot A_{slice} \cdot (p_{slice\ n-1} - 2p_{slice\ n} + p_{slice\ n+1}) \tag{B.16}$$

After setting an initial water partial pressure, p_i, and setting the first slice as p_0, the set of ODEs are solved in a similar fashion as was done in the heat transfer case, and the lumped moisture transfer resistance in a particular is derived from the result via:

$$\frac{d\bar{M}_Z}{dt} = \frac{1}{R_{diff,Z,ij}} \cdot A_{eff\ diff,Z,i} \cdot (p_0 - \bar{p}_Z) \tag{B.17}$$

$$R_{diff,Z,ij} = \frac{A_{eff\ diff,Z,i} \cdot (p_0 - \bar{p}_Z) \cdot dt}{d\bar{M}_Z} \tag{B.18}$$

So that the effective mass transfer coefficient in a particular direction is:

$$D_{eff\ diff,Z,ij} = \frac{1}{R_{diff,Z,ij} + R_{diff,Z,ji}} \tag{B.19}$$

Inter-zonal moisture transfers between fruits should be ignored even if mass transfers are incorporated into the zonal model, as the fruit is considered fully wetted. For packaging, $Z = P$, the approach above is sufficient; however for air, $Z = A$, the permeability of moisture through air, K_A, should be $K_{A,eff} = K_A \cdot F_{N.C.}$ where $F_{N.C.}$ is the natural convection correction factor. It may be the same as that derived in section 5.5.6.1.4, but this should be verified.

B.7: Inter-Zonal Radiation

The energy transfer through this mechanism is:

$$\phi_{ij,k} = h_{eff_{rad,Z_\alpha \rightarrow Z_\beta,ij}} \cdot A_{eff_{rad,Z_\alpha \rightarrow Z_\beta,ij}} \cdot \left(T_{surf,Z_\alpha \rightarrow Z_\beta,j}{}^4 - T_{surf,Z_\beta \rightarrow Z_\alpha,i}{}^4 \right) \quad \text{(B.20)}$$

For k = 10, 11 or 12 (see Table 5.3). The effective heat transfer coefficient in the case of radiative heat transfer is a constant:

$$h_{eff_{rad,Z_\alpha \rightarrow Z_\beta,ij}} = \sigma_{rad} \cdot \epsilon \quad \text{(B.21)}$$

The temperature difference between surfaces, $T_{surf,Z_\alpha \rightarrow Z_\beta,j}{}^4 - T_{surf,Z_\beta \rightarrow Z_\alpha,i}{}^4$, is determined over time through numerical integration, making the primary challenge of incorporating radiation into a zonal model the development of a fast and automated geometric procedure that can produce the inter-zonal radiative view factors, $A_{eff_{rad,Z_\alpha \rightarrow Z_\beta,ij}}$. While zones are limited in other mechanisms to exchanges in a maximum of 6 directions, this limitation does not exist for radiation heat transfer. It is possible for a single zone to exchange thermal radiation with every other zone in the network, given that A_{eff} is greater than 0 for a given combination of zone i and zone j, adding significantly to the number of calculations that must be performed by this theoretical geometric procedure. A ray tracing algorithm, such as the one suggested previously (Patil and Ravi, 2005), would need to be able to detect obstructions between the two zones being studied: for example, a zone in the centre of the package would likely have an $A_{eff} = 0$ with a zone at the edge because of interference by the zones in between.

MASSEY UNIVERSITY
GRADUATE RESEARCH SCHOOL

STATEMENT OF CONTRIBUTION TO DOCTORAL THESIS CONTAINING PUBLICATIONS

(To appear at the end of each thesis chapter/section/appendix submitted as an article/paper or collected as an appendix at the end of the thesis)

We, the candidate and the candidate's Principal Supervisor, certify that all co-authors have consented to their work being included in the thesis and they have accepted the candidate's contribution as indicated below in the *Statement of Originality*.

Name of Candidate: Jamal Olatunji

Name/Title of Principal Supervisor: Dr. Richard Love

Name of Published Research Output and full reference:

Journal Article: Olatunji, J.R., Love, R.J., Shim, Y.M., Ferrua, M.J., East, A.R. (2016). Quantifying and visualising variation in batch operations: A new heterogeneity index. Journal of Food Engineering, 196, 81-93
Conference Paper (1): Olatunji, J.R., Shim, Y.M., Love, R.J., Ferrua, M.J., East, A.R. (2015). Exploring a new heterogeneity index to quantify the variation of cooling rates within systems that undergo the forced-air cooling process. Proceedings of the 24th IIR International Congress of Refrigeration, Yokohama, Japan.
Conference Paper (2): Olatunji, J.R., Shim, Y.M., Ferrua, M.J., Love, R.J., East, A.R. (2016). Toward a fast and flexible heat transfer model for horticultural products packaged into boxes. Proceedings of the 4th IIR International Conference on Sustainability and the Cold Chain, Auckland, New Zealand.
Conference Paper (3): Olatunji, J.R., O'Sullivan, J., Shim, Y.M., Ferrua, M.J., Love, R.J., East, A.R. (2016). Developing cooling models for rapid determination of optimized package designs. Proceedings of the 20th IAPRI World Conference on Packaging, Sao Paulo, Brazil

In which Chapter is the Published Work: Chapter 3

Please indicate either:

- The percentage of the Published Work that was contributed by the candidate:

  and / or

- Describe the contribution that the candidate has made to the Published Work:

  The candidate carried out experimental work, data analysis and model development. Co-authors edited the articles and helped collect experimental data.

Jamal Olatunji Digitally signed by Jamal Olatunji Date: 2018.01.31 12:11:37 +13'00'

Candidate's Signature

31-01-2018

Date

Digitally signed by Richard Love Date: 2018.01.31 16:25:14 +13'00'

Principal Supervisor's signature

31-01-2018

Date

Journal of Food Engineering 196 (2017) 81–93

Contents lists available at ScienceDirect

Journal of Food Engineering

journal homepage: www.elsevier.com/locate/jfoodeng

Quantifying and visualising variation in batch operations: A new heterogeneity index

J.R. Olatunji*, R.J. Love, Y.M. Shim, M.J. Ferrua, A.R. East

Centre for Postharvest and Refrigeration Research, Massey University, Private Bag 11-222, Palmerston North 4442, New Zealand

A R T I C L E I N F O

Article history:
Received 29 June 2016
Received in revised form
26 September 2016
Accepted 1 October 2016
Available online 7 October 2016

Keywords:
Heterogeneity index
Agri-food products
Cooling
Freezing
Drying
Batch process

A B S T R A C T

Heterogeneity, a distribution of rates and achieved temperatures, during bulk chilling, drying and freezing processes can be a leading cause of losses and quality decline in the food manufacturing industry. Assessing or comparing system performance would benefit from a set of robust tools to report, compare and contrast the levels of heterogeneity; at specific times and over the entire operational period. A new heterogeneity index is presented here, including novel methods to model, visualise and quantify heterogeneity. The new index describes temperature or moisture distributions as a Skew-Normal distribution; introduces the heterogeneity plot to visualise heterogeneity over time; and quantifies total system heterogeneity with the Overall Heterogeneity Index (*OHI*). These methods were applied to the forced-air cooling of polylined kiwifruit. The index and methods can now be used to quantify benefits in package design and operational variation, thus providing a rigorous, substantive approach to evaluating innovations.

1. Introduction

Batch chilling, freezing and drying operations are common operations in food processing (Petrova et al., 2015; Singh and Heldman, 2009a; O'Sullivan et al., 2014). Reducing the temperature or moisture content of fresh food products can significantly decelerate natural degradation and halt microbial action, thus maintaining product quality during transport from farm to consumer and extending shelf life.

Many cooling and drying operations are based on the heat or moisture exchange between a food product and a constant supply of airflow through the system (O'Sullivan et al., 2014), so that the surface velocity, distribution, temperature and moisture content of the transfer fluid ultimately determines the rate, uniformity and efficiency of these batch operations. For example, forced-air cooling is widely used in the horticulture industry to quickly and efficiently bring freshly picked produce down to storage temperature. Large batches of produce are packed into boxes, stacked into pallets and placed into a refrigerated room. A fan is then used to create a pressure drop across the pallet, forcing cold air to penetrate through the pallet structure and exchange heat convectively with the product inside (O'Sullivan et al., 2014; Pathare et al., 2012). Many drying processes are similarly designed around the supply of dry air to treat a product, such as in the case of dry-cured hams. Large quantities of ham are placed into a drying chamber that is flooded with a constant supply of dry air, circulated around the chamber using fans (Bantle et al., 2015; Petrova et al., 2015). Moisture is driven from the meat due to the moisture gradient between the surface of the hams and the low humidity air. Thus the rate of heat or moisture transfer can be dependent on the 'ventilation efficiency', or how evenly airflow is delivered throughout a space, and how quickly the space is replaced with fresh air – a notion that is used frequently in building and room sciences and summarised by the mean age of air concept (or MAA), generally defined as the average time for air to travel from a supply inlet area to any location in a ventilated room (Chanteloup and Mirade, 2009). Batch systems can suffer from heterogeneity as a result of poor ventilation, where the rate of heat or moisture transfer for individual products varies significantly with location due to there being suboptimal (or over-optimal) interaction with the supply of air (Delele et al., 2013; Defraeye et al., 2014; Ferrua and Singh, 2009a). For example, in chilling and freezing operations, there may be regions within a system that are shielded from the effects of refrigerated airflow. This can negatively impact the performance of the process, as these products may experience a shortened shelf life compared to other products from the same batch, due to extended

* Corresponding author.
E-mail address: J.Olatunji@massey.ac.nz (J.R. Olatunji).

http://dx.doi.org/10.1016/j.jfoodeng.2016.10.004
0260-8774/

periods of time at elevated temperatures – apples, for example, respire twice as quickly at 4 °C as at 0 °C, and six times as fast at 15 °C (Morris and Brady, 2005); and one additional hour at elevated temperatures corresponds to a shortening in shelf-life of one day (Yahia and Elansari, 2011). Conversely, a system may have regions that are positioned closely to the inlet supply of refrigerated air, so that products in these positions cool disproportionately quickly compared to the average cooling rate. This also can negatively impact the performance, as these products have a higher risk of suffering from chilling injury, where cold shock can impact the texture, taste and shelf life of food products (Zhao et al., 2014; Defraeye et al., 2016). For drying processes, under-dried products risk mould and bacterial growth, while over-dried product represents product sale weight loss.

When exploring the feasibility of upgrading existing facilities, or designing new and improved batch processes, engineers and technologists must be able to fairly compare and contrast differences between systems in a quantifiable manner. The MAA concept and its related performance metrics can be used to compare the quality of ventilation between two or more batch processes from an airflow-side perspective; however, it is also important to have performance metrics from a product-side perspective. For example, comparing chilling operations is commonly achieved by reporting the average cooling rate – such as the half-cooling time (HCT) or seven-eighths-cooling time (SECT). While the average rate of removal is important, when reported in isolation it ignores other factors that impact performance, such as heterogeneity. Previously, temperature variability has been reported as the relative standard deviation (Eq. (1)).

$$HI = \frac{1}{\overline{T}}\sqrt{\frac{1}{m-1}\sum_{n=1}^{m}\left(T_n - \overline{T}\right)^2} \tag{1}$$

where T_n is the temperature of product n out of a total m number of products, and $\overline{T}$ is the average temperature (Dehghannya et al., 2011; Han et al., 2015; Defraeye et al., 2015; Lu et al., 2014; Barbin et al., 2012). Reporting heterogeneity this way has significant shortcomings, such as:

- Only being applicable at single points of time. Although a time series of *HI* values can be plotted to indicate changes in heterogeneity over time, it would be preferable to have a single value that represents total process heterogeneity over the entire processing time;
- Eliminates information concerning whether a product is hotter or colder than the average temperature, and does not provide information pertaining to the shape of the temperature or moisture distribution, or how the shape of the distribution changes over time. The performance may be different comparing a batch cooling process that is dominated by colder than average temperatures (more products susceptible to chilling injury) to a process that favours warmer than average temperatures (higher rates of senescence). For example, kiwifruit quality declines more rapidly due to chilling injury than from senescence (Zhao et al., 2014). Similarly, a drying process dominated by over-dried products will be inefficient in terms of loss of saleable weight, but the consequences of this are far different compared to a system where under-drying has resulted in rotting and total loss of sale. Therefore, it would be preferable to have a heterogeneity index that includes tools to compare the shape of temperature or moisture distributions;
- Becomes mathematically unstable when the refrigeration temperature approaches zero, or is less than zero. As $\overline{T}$ is the denominator in Eq. (1), and many cooling operations are conducted near or below 0 °C, the *HI* approaches infinity or becomes negative. As suggested by Defraeye et al. (2015), this problem can be addressed by using an appropriate offset, namely the Kelvin temperature scale (K). Although this solves one issue, others then arise: $T_n - \overline{T}$ remains the same when using °C or K, but $\overline{T}$ is much larger when using K, resulting in disparate *HI* values from the same set of data, where only the units of temperature have been changed. It would be preferable to have a heterogeneity index that is dimensionless so that a wide number of systems can be fairly compared.

Therefore, in assessing performance of batch operations from a product-side perspective, in addition to the average rate of removal, a robust heterogeneity index is required to quantify the variability in a given process, and hence fairly compare different systems. In this paper, a new heterogeneity index is presented. It was developed and applied to forced-air cooling of fresh horticultural produce, and as a result the language used throughout this paper is appropriate for a chilling scenario (i.e. temperature and cooling, rather than moisture and drying). However, application of the heterogeneity index to other batch operations – such as heating, drying, freezing and thawing – is possible. The aim was to develop a suite of tools that can be used to model, visualise and quantify the levels of process heterogeneity over the entire process time for a batch process. Section two gives details of a laboratory scale forced-air cooling experiment of two pallets of polylined Hayward kiwifruit, each weighing 500 kg and subjected to different airflow rates of 0.38 and 0.77 $m^3\ s^{-1}$, respectively. Section two also explains the development of the new tools used to describe heterogeneity: detailing how to process raw temperature and time data into dimensionless equivalents for fair comparisons between systems, and offers suggestions for how to process data from alternative batch operations, such as drying and freezing; it also includes methods to describe temperature distributions at specific points in time, and how to compare two or more distributions; how heterogeneity over the entire process is visualised using the heterogeneity plot; and introduces the Overall Heterogeneity Index (*OHI*), a continuous, quantitative metric for total process heterogeneity that is dimensionless in terms of temperature and time. Finally, section three presents results from the forced-air cooling experiments, and applies the new methods and tools to give a total description of process heterogeneity, and how changes in important operational settings – in this case, the airflow rate – impacts the total process heterogeneity, and how heterogeneity changes over time.

2. Methods and materials

2.1. Laboratory scale forced-air cooling of kiwifruit pallets

Forced-air cooling is the most commonly used batch precooling process in the horticulture industry (Opara and Zou, 2007), so it was fitting to demonstrate the new heterogeneity index based on this popular application. A laboratory scale forced-air cooling trial was performed, where one hundred (100) boxes of average weight 100 g Hayward kiwifruit (*Actinidia deliciosa)* weighing approximately 10 kg per box (i.e. 100 kiwifruit per box), were supplied by Zespri International Ltd. These were stacked into two pallets of 50 boxes each (10 boxes per layer, 5 layers per pallet, Fig. 1c), weighing 500 kg each – half the size of an industry standard pallet, which typically has 10 layers (O'Sullivan et al., 2016). Polystyrene and aluminium foil insulation was attached to the top and sides of each pallet so the predominant mode of heat transfer was convection with the bulk flow of refrigerated air through the pallet, rather than convection or thermal radiation between the pallet and the cold

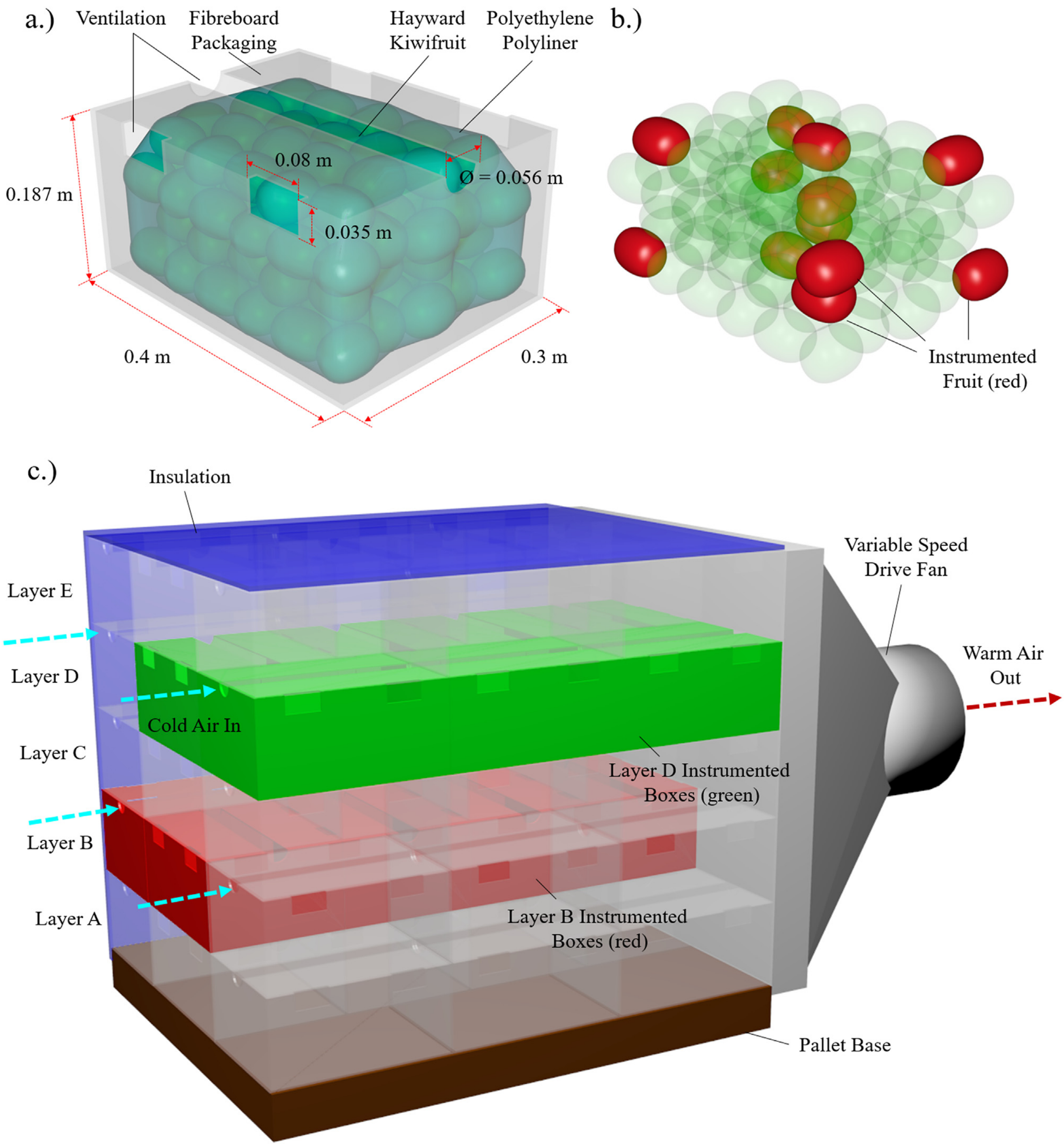

Fig. 1. Details of the experimental forced-air cooling setup for pallets of polylined kiwifruit. a.) a modular bulk package of Hayward kiwifruit, containing approx. 10 kg of fruit (100 per box), with package and ventilation dimensions. b.) ordered stacking pattern of kiwifruit within instrumented boxes, with thermocouples inserted into the centre of fruit highlighted in red. c). experimental forced-air cooling set up: 50 boxes of kiwifruit stacked into a pallet, connected to a VSD fan. 14 boxes were instrumented: 7 in layer B (highlighted in red) and 7 in layer D (highlighted in green) for a total of 168 temperature positions. (For interpretation of the references to colour in this figure legend, the reader is referred to the web version of this article.)

room (Fig. 1c). In practice, pallets are cooled in large row batches, so interaction with the air pulled through the pallet is the only available heat transfer mechanism for the majority of pallets (O'Sullivan et al., 2014). The boxes were made from corrugated fibreboard, with a total front ventilation opening area of 7.5% and side ventilation opening area of 2% (Fig. 1a). The kiwifruit were wrapped in a polyethylene liner to prevent moisture loss and product shrivelling (Fig. 1a). Within the polyliner, kiwifruit were stacked into 4 ordered rows (Fig. 1b), so that the impact on the cooling rate and heterogeneity is due to differences in operational settings between pallets, rather than an artefact of different random stacking patterns between boxes. 14 boxes were selected to be instrumented: 7 in row B (highlighted in red, Fig. 1c) and 7 in row D (highlighted in green, Fig. 1c). Type-T thermocouples were inserted into the centre of 12 kiwifruit per selected box (highlighted in red, Fig. 1b) and connected to 64-channel data-loggers

(1000 Series Squirrel Meter/Logger, Eltek Ltd. Cambridge, UK). These boxes and fruit were selected to give a wide spatial sample of 168 temperature positions throughout the pallet. Kiwifruit were equilibrated to 20 °C for 48 h for a uniform initial temperature. Pallets were connected to a variable speed drive (VSD) fan (AP0502AA5/16, Fantech, Wellington, New Zealand; Fig. 1c), where each pallet was subjected to a different airflow rate. For the first pallet, the VSD was set to 22 rotations per second (RPS). This setup resulted in a pressure drop across the pallet (measured using a Honeywell SSCDRRN005ND2A5, USA barometer) of 130 Pa, and a volumetric flow rate of 0.38 $m^3\ s^{-1}$ (0.76 L s^{-1} kg product^{-1}). For the second pallet the airflow rate was approximately doubled, with a VSD setting of 35 RPS, corresponding to a pressure drop of 335 Pa across the pallet, with a volumetric flowrate of 0.77 $m^3\ s^{-1}$, or 1.54 L s^{-1} kg product^{-1}. Pallets were cooled separately inside of a refrigerated room situated at the laboratories of the Centre for Postharvest and Refrigeration Research, with a refrigeration temperature of 0 °C. Although a typical forced-air cooling process is halted at the SECT (typically a time period of ~12 h, O'Sullivan et al., 2016), each pallet was cooled for a 24-h period to ensure cooling had reached completion. All temperatures were recorded at one minute intervals. It was hypothesised that a doubling of the airflow rate through the second pallet of kiwifruit would result in an elevated overall cooling rate, as well as a more uniform cooling profile. It was thought that at this elevated airflow rate, the overall MAA would be improved, as air is replaced more rapidly with fresh refrigerated air. As a result, a high temperature gradient between the fruit and air will be better maintained, and the higher pressure drop will ensure that cold air is delivered to previously hard to reach locations within the pallet structure.

2.2. Development of new heterogeneity index

2.2.1. Dimensionless units

Collected temperature and time data must be non-dimensionalised so that different systems can be fairly compared (Brosnan and Sun, 2001). Suggestions for how to achieve this for chilling, freezing and drying operations are provided in this section. For clarity, a chilling process is defined as one where the refrigeration temperature, T_{ref}, is greater than the product freezing point, T_{fr}, typically >0 °C. A freezing process is where the refrigeration temperature is less than the product freezing point, <0 °C; and a drying process is one focused on mass transfer – namely moisture – rather than heat transfer.

2.2.1.1. Dimensionless quantity change. In the case of a chilling processes, the Fractional Unaccomplished Temperature Change (FUTC) is a parameter commonly used (Brosnan and Sun, 2001):

$$Y_{t,n} = \frac{T_{t,n} - T_{fl}}{T_{i,n} - T_{fl}} \quad (2)$$

Adjustments are made to Eq. (2) to incorporate drying and freezing operations. For drying, temperature is substituted for the partial pressure of water vapour in the product, P (Pa):

$$Y_{t,n} = \frac{P_{t,n} - P_{fl}}{P_{i,n} - P_{fl}} \quad (3)$$

During the latent phase of a freezing process, there may be temperature uniformity between proximate products; however, some products will be further along in freezing than others. Therefore, in a freezing scenario, the enthalpy method is used (Hu and Argyropoulos, 1996), where temperature is replaced by enthalpy, E (J.kg^{-1}):

$$Y_{t,n} = \frac{E_{t,n} - E_{fl}}{E_{i,n} - E_{fl}} \quad (4)$$

Eq. (5) summarises the changes to Eq. (2):

$$Y_{X,t,n} = \frac{X_{t,n} - X_{fl}}{X_{i,n} - X_{fl}} \quad (5)$$

where Y is the fractional unaccomplished change of the quantity X, where X is temperature (T), enthalpy (E), or vapour pressure (P). Subscripts t is time; n is an individual product out of a total number of recorded products, m; and i is initial quantity.

For chilling, T_{fl} is the refrigeration temperature, $T_{fl} = T_{ref}$.

For drying, P_{fl} is the partial pressure of water in the incoming air. For air (at 101.3 kPa or standard atmosphere), this is (Maguire et al., 2010):

$$P_{fl} = 611 \cdot \exp\left[17.27\left(\frac{T_{ref}}{T_{ref} + 237.3}\right)\right] \times \frac{RH}{100} \quad (6)$$

where RH is the relative humidity of the air.

For a freezing process, $E_{fl} = 0$. The initial enthalpy, E_i, is the sum of the three stages of freezing:

$$E_i = E_{cool} + E_{fusion} + E_{freeze} \quad (7)$$

where E_{cool} is the pre-cooling phase ($T_n > T_{fr}$), estimated by:

$$E_{cool} = C_{p,cool} \cdot \left(T_i - T_{fr}\right) \quad (8)$$

where $C_{p,cool}$ is the specific heat capacity of the product above the freezing point (J.kg^{-1} K^{-1}); E_{fusion} is the latent phase ($T_n = T_{fr}$):

$$E_{fusion} = L_{fusion} \quad (9)$$

where L_{fusion} is the latent heat of fusion (J.kg^{-1}); and E_{freeze} is the subcooling phase ($T_n < T_{fr}$), which can be estimated by:

$$E_{freeze} = C_{p,freeze} \cdot \left(T_{fr} - T_{ref}\right) \quad (10)$$

where $C_{p,freeze}$ is the specific heat capacity of the product below the freezing point (J.kg^{-1} K^{-1}). For the latent heat of fusion and freezing temperatures for a wide variety of food products and methods to estimate these values, see ASHRAE (2010).

Although not considered here, heating and thawing processes can be approached in a similar manner to cooling and freezing, respectively.

2.2.1.2. Characteristic index of process progression. Temperature distributions should not be compared at absolute times (seconds, minutes, hours etc.), as this introduces bias. To illustrate, take two hypothetical chilling processes, where system A has a HCT of 150 min, and system B has a HCT of just 50 min. A comparison at 150 min of absolute process time would see system A at the HCT, when temperature variability is expected to be near its maximum. At this same absolute time, system B is near the SECT, when temperature variability is expected to be low, as cooling is near commercial completion. As a result, the faster system appears to be more uniform, a clear bias that is an artefact of the cooling rate. Hence, it would seem that a more appropriate comparison of two systems would be at the same characteristic time, such as at the HCT of each operation, (150 and 50 min for system A and B, respectively) or the SECT (450 and 150 min for system A and B, respectively). This can be achieved by creating a dimensionless time scale, a characteristic index of process progression.

The average fractional unaccomplished quantity change is one option to accomplish this:

$$\overline{Y}_{X,t} = \sum_{n=1}^{m} Y_{X,t,n}/m \tag{11}$$

Using $\overline{Y}$ ensures each system is continuously compared at the same average cooling state. Every system will begin at $\overline{Y} = 1$, and as cooling progresses, $\overline{Y}$ will tend towards 0. For a chilling process, the HCT occurs at $\overline{Y} = 0.5$; and the SECT at $\overline{Y} = 0.125$.

While it is recommended that $\overline{Y}$ is used wherever possible, there may be scenarios where it's not appropriate. For example, short operational changes are often made to a batch chilling process, such as ceasing cooling momentarily to rotate the pallet and change the direction of airflow (Ferrua and Singh, 2009b); or an intermediary warming period. These scenarios would cause a discontinuity on the progression of the process, and interferes with further analysis. An alternative is to use the fractional unaccomplished cooling completion time, τ:

$$\tau_{X,t} = 1 - t/t_f \tag{12}$$

Calculating τ requires a consistent definition of t_f, the time at which the process ends. For example ceasing precooling operations at the SECT is often recommended; therefore t_f would be the SECT for each system under study. In this scenario, each system will begin at $\tau = 1$, and will cease at $\tau = 0$. For a chilling process, the HCT occurs at $\tau = 0.66$; and the SECT at $\tau = 0$.

It should be stressed that a system analysed using $\overline{Y}$ *cannot* be compared to a system analysed using τ; comparisons can only be made between systems analysed using the same methodology. Both process progression indexes are discussed further in section 2.2.3.1.

2.2.2. Heterogeneity at single time points

Throughout most batch chilling processes, a majority of the products cool at near the average rate. However, there will be other products that cool quickly, and others that cool slowly, giving a multitude of hot and cold spots. The number and magnitude of these positions is expressed by the dimensionless temperature difference, ΔY:

$$\Delta Y_{X,t,n} = Y_{X,t,n} - \overline{Y}_{X,t} \tag{13}$$

When ΔY is plotted as a histogram, the distribution of temperatures at a given point in time will form a bell curve (Fig. 2a), although potentially skewed in either direction. By definition, the mean value of the ΔY bell curve is 0. Positive numbers represent products warmer than the average and hence cooling slowly (hot spots); while negative numbers represent products colder than the average, and hence cooling faster (cold spots). For a low variation in temperatures, the ΔY bell curve is tall and narrow; while a ΔY bell curve indicating high levels of variability is short and wide.

Temperature variability at a given point in time can therefore be modelled as a population bell curve with a mean of zero, and a standard deviation representing the standard deviation of ΔY. This bell curve is described using a Gaussian function (Terrell and Fomby, 2006):

$$f_N(\Delta Y) = \frac{1}{\sigma\sqrt{2\pi}} \cdot exp\left(-\frac{(\Delta Y - \mu)^2}{2\sigma^2}\right) \tag{14}$$

where $f_N(\Delta Y)$ is the frequency of a given value of ΔY, μ is the mean of ΔY ($\mu = 0$), and σ is the standard deviation of ΔY.

Equation (14) and Fig. 2a assumes a normally distributed ΔY bell curve. However, there are many reasons for a non-normal distribution to occur. Products in preferential locations with respect to the cold airflow may cool disproportionately quickly compared to the average rate, while other products may be shielded from the refrigerated air and cool disproportionately slowly. Differences in product size, thermal properties, a poor selection of sample temperature positions, or equipment error could also contribute to a skewed temperature distribution. Regardless of the cause, these effects need to be accounted for mathematically for the heterogeneity index to be robust. The skew-normal (SN) distribution (O'Hagan and Leonard, 1976; Terrell and Fomby, 2006) extends the normal Gaussian distribution (Eq. (14)) to incorporate skewness through the use of α, a shape factor. When $\alpha = 0$, skewness vanishes and the distribution reverts back to normality. When $\alpha > 0$, the distribution is skewed to the right, representing a temperature profile that has a higher proportion of warmer temperatures; and when $\alpha < 0$ the distribution is skewed to the left, a temperature profile with a higher magnitude of colder temperatures (Fig. 2b). The SN density function is (Terrell and Fomby, 2006):

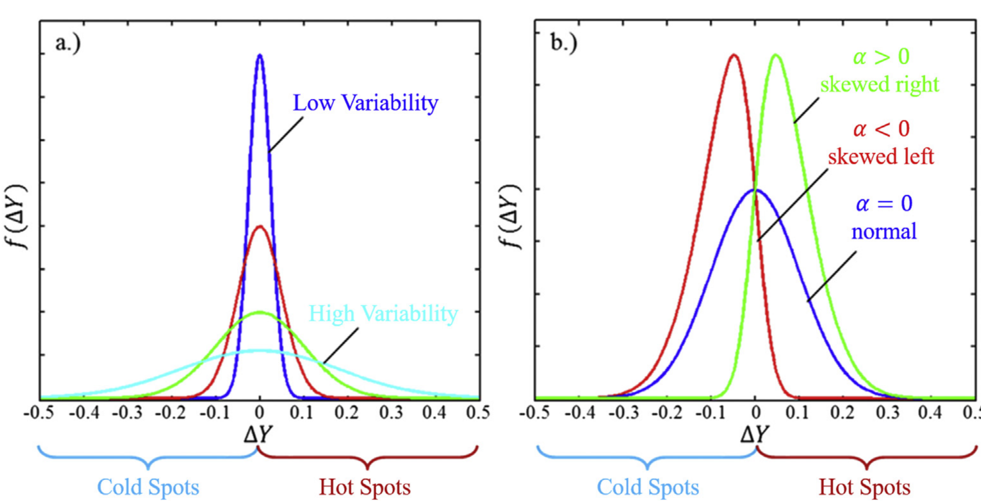

Fig. 2. a.) Potential heterogeneity at a single point of time modelled using a normal Gaussian distribution; b.) Potential heterogeneity at a single point of time modelled using a Skew-Normal distribution, to account for non-normal distributions of ΔY.

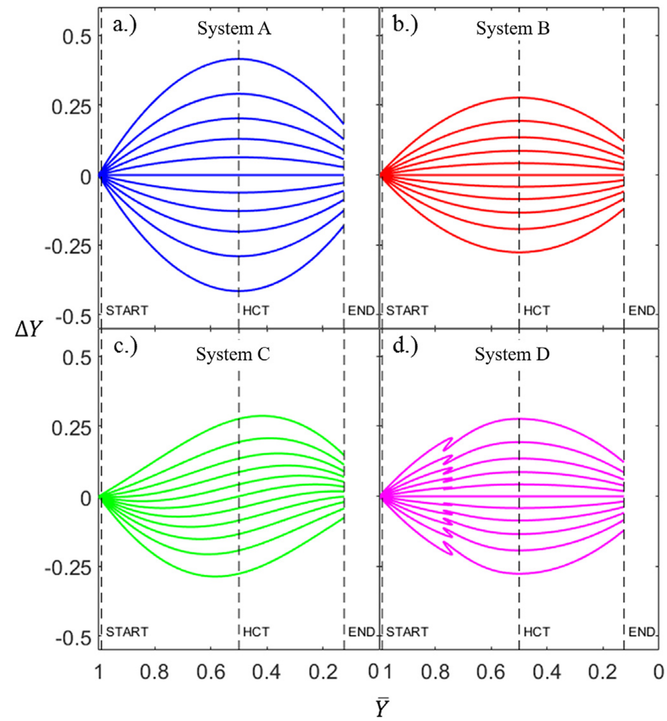

Fig. 3. Idealised heterogeneity plots, plotting ΔY for each individual product against $\overline{Y}$, for four theoretical systems: a.) System A, with a normal distribution of hot and cold spots, and a high level of heterogeneity; b.) System B, with a normal distribution of hot and cold spots, and a lower level of heterogeneity; c.) System C, with skewness-over-time behaviour, and; d.) System D with a short intermediary warming period, making $\overline{Y}$ an inappropriate process progression index.

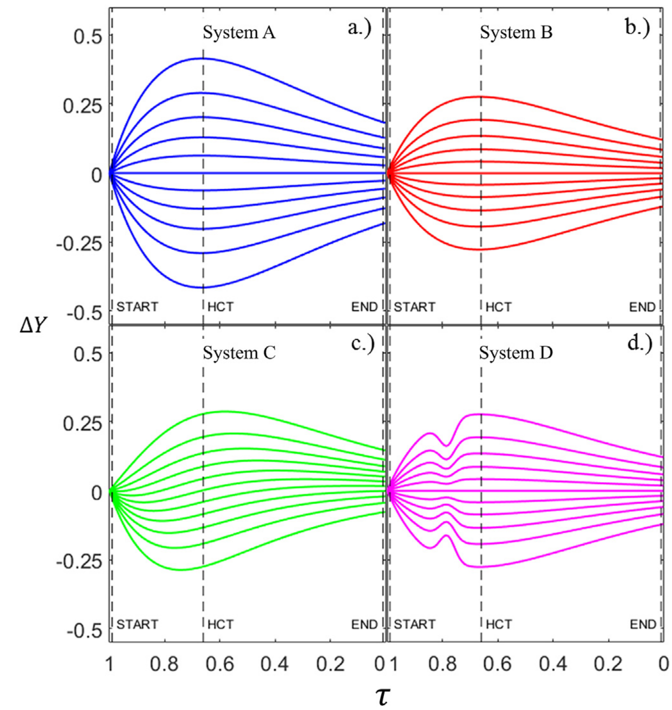

Fig. 4. Idealised heterogeneity plots, plotting ΔY for each individual product against τ for four theoretical systems: a.) System A, with a normal distribution of hot and cold spots, and a high level of heterogeneity; b.) System B, with a normal distribution of hot and cold spots, and a low level of heterogeneity; c.) System C, with skewness-over-time behaviour, and; d.) System D, with a short intermediary warming period, making τ the appropriate process progression index.

$$f_{SN}(\Delta Y) = 2\phi\left(\frac{\Delta Y - \xi}{\omega}\right)\Phi\left(\alpha\frac{\Delta Y - \xi}{\omega}\right) \tag{15}$$

where ϕ is the standard normal distribution and Φ is the standard normal cumulative distribution. The two additional terms: ξ, defined as location; and ω, defined as scale; are the SN analogues to the mean (μ) and standard deviation (σ), respectively. The SN cumulative density function is (Terrell and Fomby, 2006):

$$F_{SN}(\Delta Y) = \Phi\left(\frac{\Delta Y - \xi}{\omega}\right) - 2T_{Owen}\left(\frac{\Delta Y - \xi}{\omega}, \alpha\right) \tag{16}$$

where T_{Owen} is Owen's T function (Owen, 1956). Hence, a temperature distribution at a given point in time can be summarised quantitatively using just three parameters: α, ξ and ω.

2.2.3. Heterogeneity over time

Analysis of the distribution of ΔY only offers information at single stages of the process. There must also be methods to visualise and quantify heterogeneity over the entire bulk chilling process.

2.2.3.1. Visualising heterogeneity over time. Plotting ΔY (Y-axis) against $\overline{Y}$ or τ (X-axis) produces a variability over time plot that's dimensionless in terms of both temperature and time. Named the heterogeneity plot, it provides engineers and technologists with a useful visual tool to compare the variability of two or more systems over the entire processing time. To introduce the heterogeneity plot, theoretical heterogeneity plots are presented in Figs. 3 and 4 (empirical heterogeneity plots given later, see Fig. 9a and b). These plots represent hypothetical chilling operations that follow expected heterogeneity trends, with temperature uniformity at the beginning of the process, maximum heterogeneity at the HCT, and temperature uniformity again when $t \to \infty$ and all products are at the storage temperature. Each was constructed to show how the heterogeneity plot is interpreted and how to visually identify differences between systems. Lines are the ΔY of individual products over time; thus, Figs. 3 and 4 show a representative sample of 11 temperature positions from four hypothetical operations, using both process progression indexes, $\overline{Y}$ and τ. A larger proportion of products have ΔY close to 0 at all times, as they are cooling similarly to the average cooling rate. Hence, lines on the heterogeneity plot are denser nearby $\Delta Y = 0$. The proportion of products hotter and colder than the average diminishes away from $\Delta Y = 0$, so that the lines of the heterogeneity plot separate toward highly positive or negative values of ΔY. This gives all heterogeneity plots a characteristic 'eye' shape, where it is tapered at both ends, as heterogeneity is low at the beginning and end of a bulk chilling process; and a bulge at approximately the HCT, where variability is highest.

System A (Figs. 3a and 4a) shows a system with a normal distribution of hot and cold spots, with a high level of total process heterogeneity. System B (Figs. 3b and 4b) is again normally distributed, but represents a system with low total process heterogeneity. System C (Figs. 3c and 4c) shows a system that has skewness over time behaviour. System D (Figs. 3d and 4d) shows a process with a short intermediary warming period. Visually comparing system A to B, it is readily apparent that system B has a lower spread of temperatures over time; thus system B would be considered superior in terms of homogeneity. Comparing system B to C makes the presence of skewness visually evident; System C clearly showing a higher proportion of cold spots at the beginning of the chilling process, and a higher proportion of hot spots toward the end. System D illustrates a scenario where $\overline{Y}$ is an inappropriate

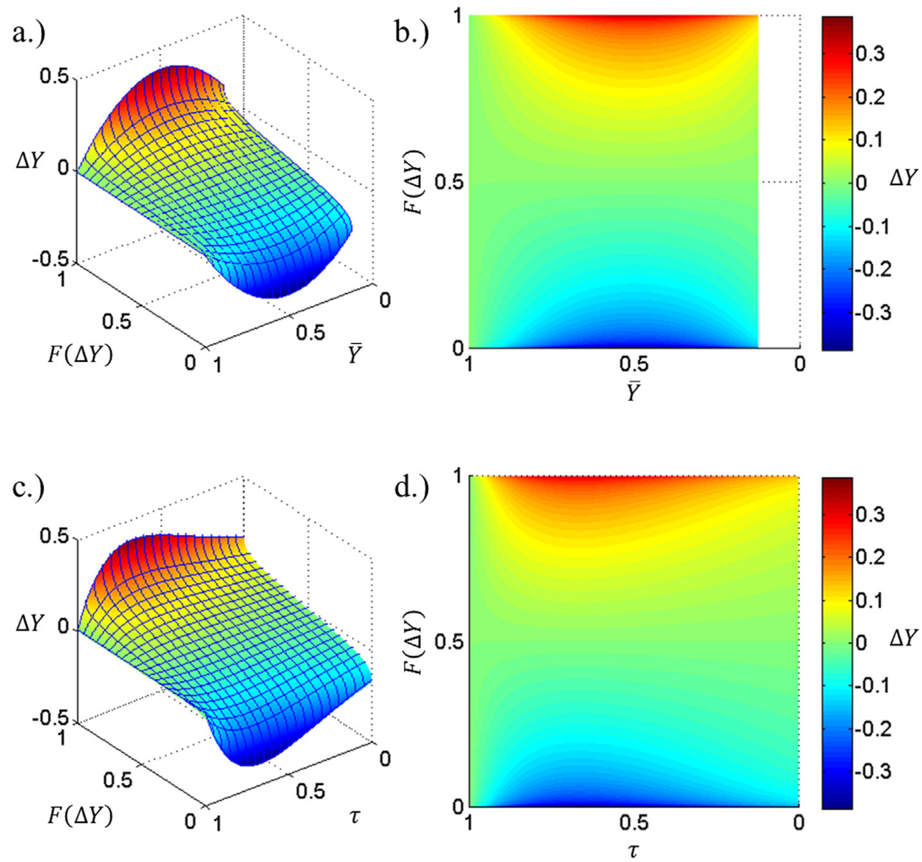

Fig. 5. Idealised heterogeneity maps. 3-D heterogeneity maps (a and c) plot ΔY on the Z-axis, while 2-D heterogeneity maps (b and d) displays ΔY as a colour spectrum. a and b use $\bar{Y}$ as the process progression index, c and d use τ. (For interpretation of the references to colour in this figure legend, the reader is referred to the web version of this article.)

process progression index. Because of the short warming period, $\bar{Y}$ increases for a short period, causing the heterogeneity plot to go backwards on the X-axis. This inconsistency is solved by using τ instead of $\bar{Y}$.

2.2.3.2. Quantifying heterogeneity over time. While a heterogeneity plot is a useful visual tool, a quantitative metric for heterogeneity over time is necessary. The heterogeneity map was developed for this purpose, shown for idealised systems in Fig. 5. It is a 3-D plot with the dimensionless temperature difference (ΔY) on the Z-axis, the chosen process progression index – $\bar{Y}$ or τ – on the X-axis, and the cumulative distribution of ΔY on the Y-axis ($F(\Delta Y)$) (Fig. 5a). Alternatively, for a 2-D heterogeneity map, the Z-axis can be replaced by contours or a colour spectrum across the ΔY range (Fig. 5b). From this data plot, the Overall Heterogeneity Index (*OHI*) is derived: a single, continuous and quantitative metric for total process heterogeneity that is dimensionless in terms of temperature and time.

The theoretical best case scenario in terms of temperature uniformity is represented by a heterogeneity map with a perfectly flat plane at $\Delta Y = 0$ (Fig. 6a). This scenario has an $OHI = 0$, as it is not possible to have a more homogenous system. Systems with some level of heterogeneity will have curvature: products that cool faster than the average rate will drop below, and products that cool slower than the average rate will rise above the Z-axis origin. Deviation from the best case scenario will have an $OHI > 0$; and by extension, the higher the *OHI*, the higher the total process heterogeneity. Individual products that are at or near to the average temperature contribute minimally to the *OHI*, while products that are significantly hotter or colder than the average temperature contribute greatly to the *OHI*. Therefore the *OHI* is equal to the volume that the surface of the heterogeneity map encompasses above and below the Z-axis origin – as represented by the magenta coloured volume in Fig. 6b and c. This volume (the *OHI*) can be determined by:

$$OHI = \int_0^1 \int_{\mathscr{T}_{END}}^{\mathscr{T}_{START}} |\Delta Y| \mathrm{d}F(\Delta Y) \mathrm{d}\mathscr{T} \tag{17}$$

where *OHI* is the Overall Heterogeneity Index, $|\Delta Y|$ is the absolute dimensionless temperature difference for all temperature positions and times, $\int_0^1 \mathrm{d}F(\Delta Y)$ is the integral along the Y-axis, and $\int_{\mathscr{T}_{END}}^{\mathscr{T}_{START}} \mathrm{d}\mathscr{T}$ is the integral along the process progression index, X-axis (either $\bar{Y}$ or τ) of the heterogeneity map.

When using $\bar{Y}$, $\mathscr{T}_{START} = 1$ and $\mathscr{T}_{END} = 0.125$:

$$OHI_{\bar{Y}} = \int_0^1 \int_{0.125}^1 |\Delta Y| \mathrm{d}F(\Delta Y) \mathrm{d}\bar{Y} \tag{18}$$

When using τ, $\mathscr{T}_{START} = 1$ and $\mathscr{T}_{END} = 0$:

$$OHI_{\tau} = \int_0^1 \int_0^1 |\Delta Y| \mathrm{d}F(\Delta Y) \mathrm{d}\tau \tag{19}$$

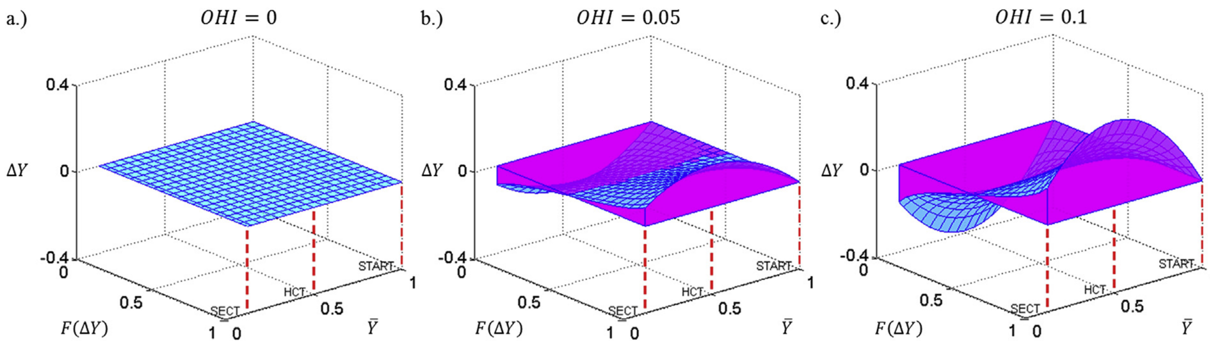

Fig. 6. Idealised heterogeneity maps of three hypothetical systems with varying levels of process heterogeneity: a.) A system with perfect temperature uniformity, and an $OHI = 0$; b.) A system with a low level of heterogeneity, $OHI = 0.05$, and; c.) A system with a high level of heterogeneity, $OHI = 0.1$.

The *OHI* is robust to comparisons between systems where a different number of temperature positions are used, as the integral along the Y-axis is consistently $0 \rightarrow 1$ in all cases, so that the *OHI* scales appropriately. The *OHI* is also not overly sensitive to measurement error, such as thermocouple failure (elimination of a temperature position) or rogue data points; as the *OHI* incorporates the ΔY of each individual product, one or two outliers has a minimal impact on the overall value.

Again it should be emphasised that an *OHI* derived using $\overline{Y}$ is not comparable to an *OHI* derived using τ. A shortcoming of the *OHI* is

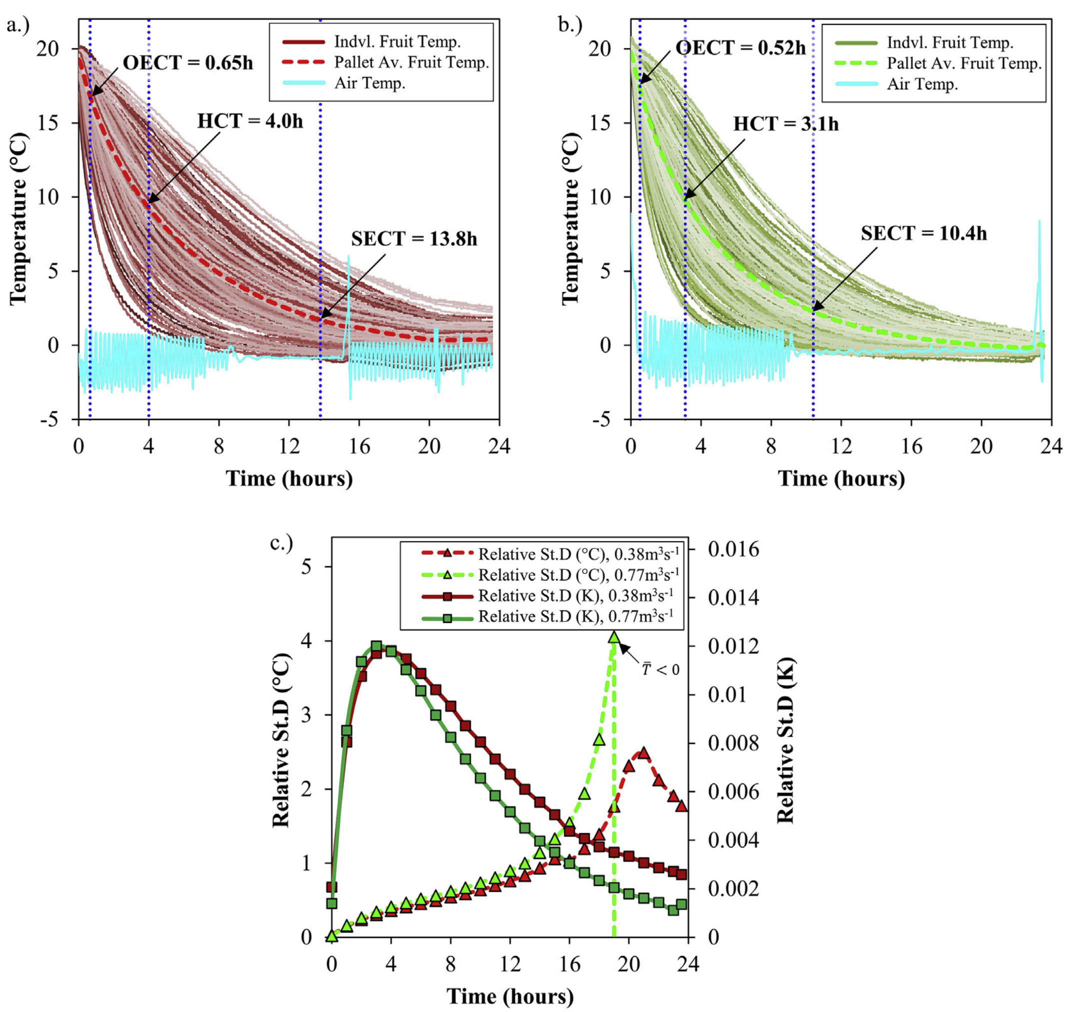

Fig. 7. Experimental kiwifruit forced-air cooling profiles for a.) the first pallet, with an airflow rate of $\dot{Q} = 0.38$ m^3 s^{-1} and; b.) the second pallet, with an airflow rate of $\dot{Q} = 0.77$ m^3 s^{-1}. Individual fruit temperatures marked as solid lines, pallet average temperatures marked as dashed lines; air temperatures marked as a light blue lines. Dotted blue lines mark important process times for each pallet: OECT = One-Eighths Cooling Time, $\overline{Y} = 0.875$; HCT = Half-Cooling Time, $\overline{Y} = 0.5$; and SECT = Seven-Eighths Cooling Time, $\overline{Y} = 0.125$. c.) heterogeneity analysis of both pallets using the relative standard deviation over time (Eq. (1)), using °C (dashed lines, triangles) and K (solid lines, squares) as temperature units. The heterogeneity trends are not accurate due to mathematical instability in the case of °C, and artefacts of the differences in overall cooling rate between pallets in the case of K. (For interpretation of the references to colour in this figure legend, the reader is referred to the web version of this article.)

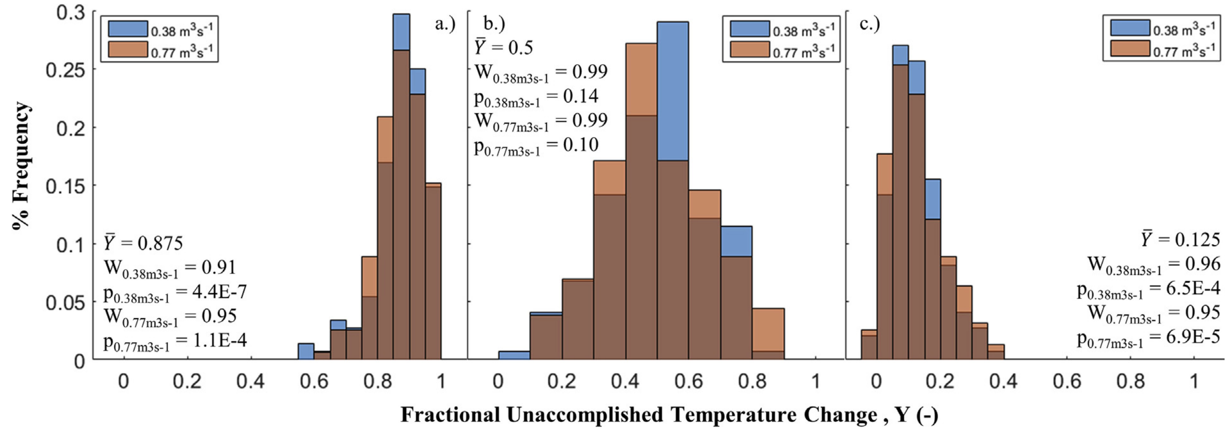

Fig. 8. Temperature distributions from pallet one ($\dot{Q} = 0.38\ m^3\ s^{-1}$, blue) and two ($\dot{Q} = 0.77\ m^3\ s^{-1}$, orange) at a.) $\overline{Y} = 0.875$ (OECT), b.) $\overline{Y} = 0.5$ (HCT) and c.) $\overline{Y} = 0.125$ (SECT). W = Shapiro-Wilks test statistic; p = p-value. (For interpretation of the references to colour in this figure legend, the reader is referred to the web version of this article.)

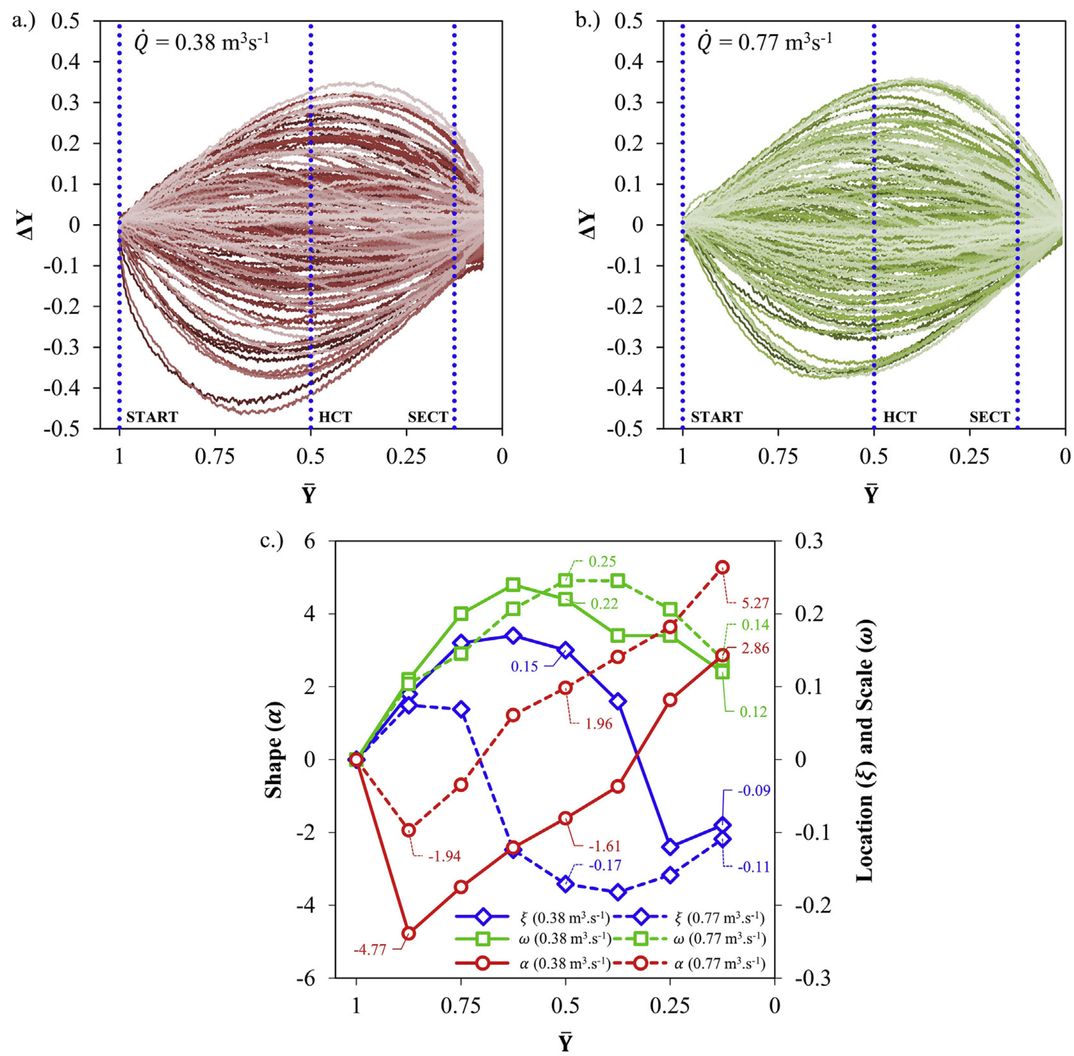

Fig. 9. Experimental heterogeneity plots for the forced-air cooling of kiwifruit, plotting the ΔY of individual fruits against $\overline{Y}$, the chosen process progression index for a.) pallet one, $\dot{Q} = 0.38\ m^3\ s^{-1}$ and b.) pallet two, $\dot{Q} = 0.77\ m^3\ s^{-1}$ c.) Shape (red circles), scale (green squares) and location (blue diamonds) values for representative Skew-Normal distributions at $\overline{Y} = 1$, 0.875, 0.75, 0.625, 0.5, 0.375, 0.25 and 0.125 for pallet one (solid lines) and pallet two (dashed lines). (For interpretation of the references to colour in this figure legend, the reader is referred to the web version of this article.)

that in isolation it does not indicate the extent to which it is dominated by products hotter or colder over time. However, as $F(\Delta Y)$ in Eqs (17)–(19) can be modelled as a SN distribution (Eq. (16)), representative α, ξ and ω can be assigned at various process times and reported in conjunction with the *OHI* to give a total description of process heterogeneity over time.

3. Results and discussion

3.1. Experimental results

Experimental cooling curves for both pallets of kiwifruit are shown in Fig. 7. The first pallet – with a flowrate of $\dot{Q} = 0.38\ \mathrm{m^3\ s^{-1}}$ – is shown in Fig. 7a, and the second pallet – with a flowrate of $\dot{Q} = 0.77\ \mathrm{m^3\ s^{-1}}$ – in Fig. 7b. Individual product temperatures are plotted over the 24 h cooling period, displayed as solid lines. The average fruit temperature (dashed lines) and refrigerated air temperature (light blue line) are overlaid. Important temperature milestones – the 1/8th cooling time (OECT), $\overline{Y} = 0.875$; half-cooling time (HCT), $\overline{Y} = 0.5$; and 7/8th cooling time (SECT), $\overline{Y} = 0.125$ – are marked with dotted blue lines. At the beginning of the cooling process ($t = 0$ h), the individual fruits were at a similar initial temperature of 20 °C, so that there was near temperature uniformity. As cooling progressed, individual fruits experienced disparate cooling rates, so that at the HCT there was a high level of heterogeneity in each system. As the second pallet was cooled with approximately double the airflow rate, this pallet experienced an overall accelerated cooling rate, where the HCT was reached after $t = 3.1$ h for $\dot{Q} = 0.77\ \mathrm{m^3\ s^{-1}}$ (Fig. 7b) compared with $t = 4.0$ h for $\dot{Q} = 0.38\ \mathrm{m^3\ s^{-1}}$ (Fig. 7a). As the fruit continued to cool, the fruit began to approach the refrigeration temperature of approximately 0 °C. Therefore, at the SECT – when the forced-air cooling process is typically halted, and the pallets are moved into cold storage; $t = 13.8$ h for the first pallet (Fig. 7a) and $t = 10.4$ h for the second (Fig, 7b) – there was a narrower separation of temperatures, so that heterogeneity was again low. This separation in temperatures continued to narrow as each pallet continued to be cooled over the whole 24-h period.

Using Celsius (°C) as the temperature scale, the expected heterogeneity trends are not reflected by the relative standard deviation (Eq. (1); Fig. 7c). Rather, the heterogeneity is shown to constantly increase, with a greater apparent level of heterogeneity at the SECT when compared to the HCT for both systems. This is a product of mathematical instability, where as $\overline{T}$ approaches the refrigeration temperature of approximately 0 °C, the *HI* is artificially inflated; and becomes negative in the case of the second pallet at $t = 19.8$ h, as the average pallet temperature has fallen slightly below 0 °C. These problems were addressed by using an appropriate offset, namely the Kelvin temperature scale (K), as suggested by Defraeye et al. (2015; Fig. 7c). It would seem that the second pallet is superior in terms of heterogeneity, displaying lower values of *HI* at the same absolute times. This is not accurate, and – in relation to the discussion pertaining to the necessity of a dimensionless process progression index for fair comparisons (section 2.2.1.2) – is an artefact of the second pallet having an accelerated overall cooling rate.

Additionally, important information pertaining to the shape of the temperature distributions was masked by only using the relative standard deviation. A closer examination of the temperature profiles at the important process milestones are shown in Fig. 8. It was observed that at the OECT (Fig. 8a), the temperature profile was heavily skewed to the left, as a significant proportion of fruit have cooled disproportionately faster than the average rate, most likely from being in preferential locations with respect to the incoming cold airflow – such as fruit in contact with the polyliner. At the HCT (Fig. 8b), this level of skewness seemed to have reduced so that there was a more even spread of hot and cold temperatures around the average fruit temperature. At the SECT (Fig. 8c), a level of skewness had returned, but was instead skewed to the right, as a large proportion of fruit had lagged behind the average cooling rate due to being shielded from the forced air – such as fruit stacked near the centre of a box. These observations were further supported by Shapiro-Wilks tests (Shapiro and Wilk, 1965), where only the distributions at the HCT can be considered to be normally distributed (Fig. 8b, $p > 0.05$). It is important to again emphasise that a typical forced-air cooling process is halted at the SECT. The temperature distributions shown in Fig. 8c are likely to persist for a long period of time after the pallet is moved into cold-storage, as the primary mode of heat transfer is shifted from forced-convection to natural convection, conduction and radiation with a cold room, heat transfer mechanisms that are substantially slower (Singh and Heldman, 2009b). Therefore, quantifying, comparing and contrasting the temperature distributions at the process end time offers an additional pathway toward optimization, information that is otherwise ignored if only the relative standard deviation is used.

3.2. Application of the new heterogeneity index

The new heterogeneity index was then applied. Recorded temperature data from each pallet was non-dimensionalised using Eq. (2). $\overline{Y}$ (Eq. (11)) was deemed an appropriate dimensionless process progression index as cold air was constantly supplied to each system throughout the 24 h of cooling. Experimental heterogeneity plots for each system are shown in Fig. 9a and b. These empirical heterogeneity plots correctly reflect the expected heterogeneity behaviour over time from the theoretical plots displayed previously: the characteristic 'eye' shape is distinct, and the skewness over time behaviour is visually conspicuous by the absence of longitudinal symmetry – similar to the hypothetical system C from Fig. 3c, where colder than average temperatures are favoured at the beginning of the cooling process, and then hotter than average temperatures toward the end. Empirical heterogeneity maps for each system are shown in Fig. 10, where $OHI_{\overline{Y},0.38\mathrm{m^3s^{-1}}} = 0.0817$ and $OHI_{\overline{Y},0.77\mathrm{m^3s^{-1}}} = 0.0845$ were derived. Thus, a doubling of the airflow rate has resulted in a small 3.4% increase in total process heterogeneity. More details about how the temperature distribution within each system changed over the processing time were derived by using the skew-normal distribution. SN distributions (Eq. (16)) were fitted to empirical temperature distributions at 8 stages of the cooling process ($\overline{Y} = 1$, 0.875, 0.75, 0.625, 0.5, 0.375, 0.25 and 0.125) using non-linear regression. Shape, scale and location (α, ω and ξ) values were derived from the fitted model distributions, which can be considered representative as the application of the one-sample Kolmogorov-Smirnov test (Pons, 2014) was $p \gg 0.05$ in all cases (Fig. 11). These representative α, ω and ξ values are summarised in Fig. 9c, providing a quantitative review of system performance from a heterogeneity perspective. Temperature uniformity at the process start time was confirmed for both systems, with scale values – the SN equivalent to standard deviation, σ – of $\omega_{0.38\mathrm{m^3s^{-1}}} = 0$ and $\omega_{0.77\mathrm{m^3s^{-1}}} = 0$ when $\overline{Y} = 1$. This increased over process time for both systems so that there was a considerably higher level of temperature variability at the HCT, with $\omega_{0.38\mathrm{m^3s^{-1}}} = 0.22$ and $\omega_{0.77\mathrm{m^3s^{-1}}} = 0.25$ at $\overline{Y} = 0.5$. The scale values of each system then decreased again as it began to approach the process end time: at the SECT, or $\overline{Y} = 0.125$, $\omega_{0.38\mathrm{m^3s^{-1}}} = 0.12$ and $\omega_{0.77\mathrm{m^3s^{-1}}} = 0.14$. The skewness over time behaviour is quantified with shape values of $\alpha_{0.38\mathrm{m^3s^{-1}}} = -4.77$ and $\alpha_{0.77\mathrm{m^3s^{-1}}} = -1.94$ near the start of the cooling process ($\overline{Y} = 0.875$); and $\alpha_{0.38\mathrm{m^3s^{-1}}} = 2.86$ and $\alpha_{0.77\mathrm{m^3s^{-1}}} = 5.27$ at the process end time ($\overline{Y} = 0.125$). This indicates that despite an elevated overall cooling rate, the second

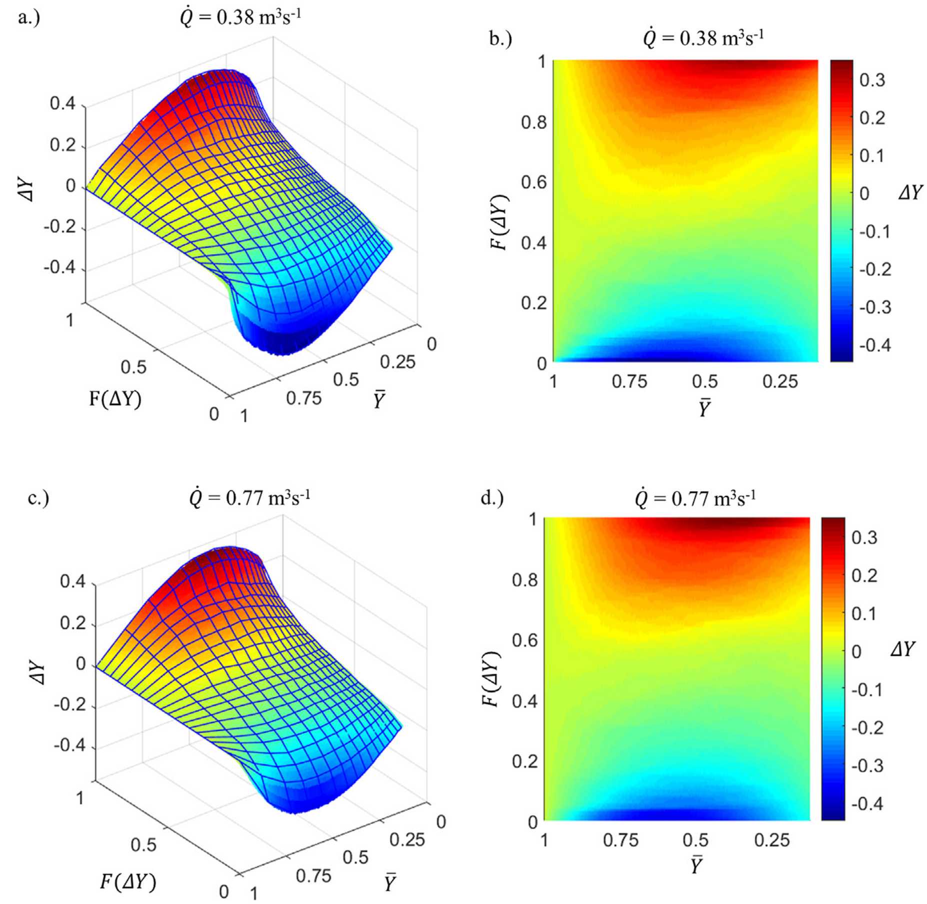

Fig. 10. Experimental heterogeneity maps for the forced-air cooling of kiwifruit, using $\overline{Y}$ as the process progression index. a.) 3-D heterogeneity map for pallet one; b.) 2-D heterogeneity map for pallet one. $OHI_{\overline{Y},0.38\mathrm{m^3s^{-1}}} = 0.0817$ was derived. c.) 3-D heterogeneity map for pallet two; d.) 2-D heterogeneity map for pallet two. $OHI_{\overline{Y},0.77\mathrm{m^3s^{-1}}} = 0.0845$ was derived.

pallet will enter the cold chain with a higher proportion of warm fruit when compared to the first pallet, despite an almost doubling of the airflow rate. Location values – the SN equivalent of the mean, μ – followed disparate trends, with the first pallet favouring positive values of ξ for a majority of the cooling process, while the second pallet favoured negative values. Although the average ΔY was always 0 (Eq. (13)), this did not necessarily mean that the distribution was centred at 0. For example, Fig. 8b shows the temperature distributions for both pallets at the same average temperature, $\overline{Y} = 0.5$. The second pallet, with its accelerated airflow rate, was shifted significantly to the left – and hence colder temperatures – compared to the first pallet. These differences at the HCT are reflected in the representative location values of $\xi_{0.38\mathrm{m^3s^{-1}}} = 0.15$ and $\xi_{0.77\mathrm{m^3s^{-1}}} = -0.17$.

Following the application of the new heterogeneity index, it would seem that the forced-air cooling of kiwifruit wrapped in polyliner bags is a highly variable process with many opportunities for optimization. The hypothesis that increasing the airflow rate would result in a more homogenous cooling profile was proven false – rather, an almost doubling of airflow resulted in a small increase in total process heterogeneity of 3.4%. $OHI_{\overline{Y}}$ values of 0.0817 and 0.0845 for the low and high airflow rates, respectively, indicates the total process heterogeneity of both systems is comparable to the theoretical system presented in Fig. 6c, which was constructed as a hypothetical example of a highly inefficient process; and both pallets are very far away from the theoretically perfect system of Fig. 6a. Increasing the airflow rate also resulted in a slightly higher degree of temperature variability at the SECT – when the pallet would normally enter cold storage – and a higher level of skewness favouring warmer than average temperatures. Thus, it was concluded that an increase in the airflow rate did not contribute toward optimization of the forced-air cooling system from a heterogeneity perspective; instead, other operational settings should be investigated. In the future, the new tools developed in this paper will be used to investigate the effects of package design (vent size and vent number) on the heterogeneity of the forced-air cooling process, as this is more likely to impact the airflow pathway to one that results in a more equitable cooling process – similar to that previously conducted by Defraeye et al., 2014. An improvement of the forced-air cooling of kiwifruit could be confirmed if an $OHI_{\overline{Y}}$ <0.0817 is achieved; and as the SECT is considered the process end time, minimising the values of representative α and ω at $\overline{Y} = 0.125$ would also be considered an optimization ($\omega < 0.12$ and $\alpha < 2.86$).

3.3. VariCool software

A MATLAB software package was developed to assist new users of the heterogeneity index, called ‘VariCool’. Designed for batch chilling operations such as forced-air cooling, VariCool is capable of quickly processing raw temperature data into all of the relevant heterogeneity metrics discussed in this paper, in an automated fashion. VariCool uses raw fruit and refrigeration air temperatures as an input, and after a short processing time, outputs the

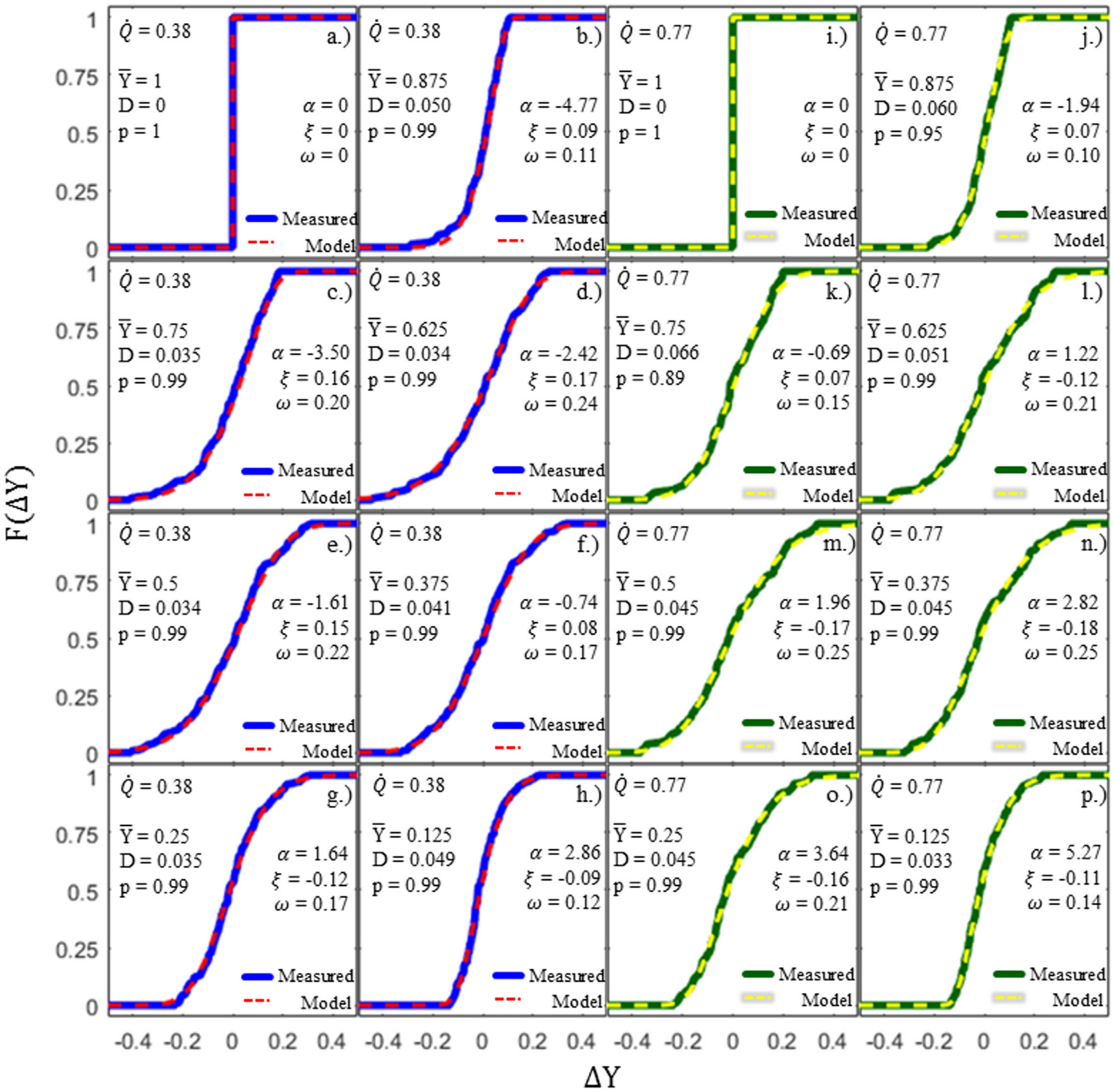

Fig. 11. Experimental cumulative distributions of ΔY for pallet one (solid blue lines) and pallet two (solid green lines) with fitted representative Skew-Normal distributions (dashed red and yellow lines, respectively) at 8 cooling stages: $\overline{Y} = 1$, 0.875, 0.75, 0.625, 0.5, 0.375, 0.25 and 0.125. $\dot{Q}$ = airflow rate (m^3. s^{-1}), D = Kolmogorov-Smirnov test statistic, p = p-value, α = shape, ξ = location and ω = scale. (For interpretation of the references to colour in this figure legend, the reader is referred to the web version of this article.)

experimental cooling curve (Fig. 7a and b), heterogeneity plot (Fig. 9a and b), heterogeneity map and *OHI* (Fig. 10). It also fits a representative SN distribution to measured distributions at specified times using non-linear regression, so that representative α, ω and ξ values can be derived (Figs. 9c and 11). Access to VariCool v1.0 can be negotiated by contacting the Centre for Postharvest and Refrigeration Research, at info.CPRR@massey.ac.nz; or alternatively, contacting the corresponding author.

4. Conclusions

New methods have been developed to robustly model, visualise and quantify the levels of heterogeneity within bulk cooling, freezing and drying operations. The new heterogeneity index describes temperature or moisture distributions at specific times as a Skew-Normal distribution; visualises heterogeneity over time through the use of the heterogeneity plot; and quantifies total process heterogeneity over time through the Overall Heterogeneity Index (*OHI*), derived from the heterogeneity map. The new methods were applied to the forced-air cooling of kiwifruit, wrapped in a polyliner bag, where the impact of increasing the air flowrate on process heterogeneity was investigated. A near doubling of the airflow rate from 0.38 to 0.77 m^3 s^{-1} resulted in a small 3.4% increase in the total process heterogeneity, where $OHI_{\overline{Y},0.38m^3s^{-1}} = 0.0817$ and $OHI_{\overline{Y},0.77m^3s^{-1}} = 0.0845$ were derived. A higher airflow rate also resulted in a slightly higher temperature variability at the process end time ($\overline{Y} = 0.125$), with a scale value of $\omega_{0.77m^3s^{-1}} = 0.14$ compared to $\omega_{0.38m^3s^{-1}} = 0.12$; and resulted in a more positive skew factor of $\alpha_{0.77m^3s^{-1}} = 5.27$ compared with $\alpha_{0.38m^3s^{-1}} = 2.86$, indicating a higher proportion of fruit will enter the cold chain with a warmer than average temperature if subjected to a higher airflow rate. The new methods developed in this paper can be applied to sequences of batch processing experiments to evaluate how operating conditions effect the heterogeneity during the process. While the new heterogeneity index was developed and applied to a cooling process, it has potential to also be applicable to other batch operations, such as drying and freezing operations. It could also be applied to heating and thawing operations, or other processes where heterogeneity of treatment to individual product units in a batch can be measured. The authors have made a software package available to assist users of the new heterogeneity index, called 'VariCool'. Access to the software can be negotiated by contacting the Centre for Postharvest and Refrigeration Research.

Acknowledgements

The authors gratefully acknowledge the New Zealand Ministry of Business, Innovation and Employment for funding this work (Fibreboard Packaging Design Project (MAUX1302)). We also acknowledge Zespri International for supplying fruit and logging equipment for experiments, and Dr. Justin O'Sullivan for his expertise. We would also like to acknowledge Alicia Tan for her assistance in collecting and processing experimental data.

References

American Society of Heating, Refrigeration and Air Conditioning Engineers, 2010. Thermal properties of food. In: ASHRAE Handbook: Refrigeration. Article 19.

Bantle, M., Petrova, I., Tolstorebrov, I., Kvalsvik, K., Nordtvedt, T., Eikevik, I., 2015. Influence of climate conditions on the energy consumption of refrigeration systems in the food processing industry. In: 5th International Congress of Refrigeration, Yokohama, Japan. Article 134.

Barbin, D.F., Neves Filho, L.C., Silveira, V., 2012. Portable forced-air tunnel evaluation for cooling products inside cold storage rooms. Int. J. Refrig. 35 (1), 202–208.

Brosnan, T., Sun, D.W., 2001. Precooling techniques and applications for horticultural products — a review. Int. J. Refrig. 24 (2), 154–170.

Chanteloup, V., Mirade, P.S., 2009. Computational fluid dynamics (CFD) modelling of local mean age of air distribution in forced-ventilation food plants. J. Food Eng. 90 (1), 90–103.

Defraeye, T., Cronjé, P., Berry, T., Opara, U.L., East, A.R., Hertog, M., Verboven, P., Nicolai, B., 2015. Towards integrated performance evaluation of future packaging for fresh produce in the cold chain. Trends Food Sci. Technol. 44 (2), 201–225.

Defraeye, T., Lambrecht, R., Delele, M.A., Tsige, A.A., Opara, U.L., Cronjé, P., Verboven, P., Nicolai, B., 2014. Forced-convective cooling of citrus fruit: cooling conditions and energy consumption in relation to package design. J. Food Eng. 121, 118–127.

Defraeye, T., Nicolai, B., Kirkman, W., Moore, S., van Niekerk, S., Verboven, P., Cronjé, P., 2016. Integral performance evaluation of the fresh-produce cold chain: a case study for ambient loading of citrus in refrigerated containers. Postharvest Biol. Technol. 112, 1–13.

Dehghannya, J., Ngadi, M., Vigneault, C., 2011. Mathematical modeling of airflow and heat transfer during forced convection cooling of produce considering various package vent areas. Food Control. 22 (8), 1393–1399.

Delele, M.A., Ngcobo, M.E.K., Getahun, S.T., Chen, L., Mellmann, J., Opara, U.L., 2013. Studying airflow and heat transfer characteristics of a horticultural produce packaging system using a 3-D CFD model. Part II: effect of package design. Postharvest Biol. Technol. 86, 546–555.

Ferrua, M.J., Singh, R.P., 2009a. Modeling the forced-air cooling process of fresh strawberry packages, Part I: numerical model. Int. J. Refrig. 32 (2), 335–348.

Ferrua, M.J., Singh, R.P., 2009b. Design guidelines for the forced-air cooling process of strawberries. Int. J. Refrig. 32 (8), 1932–1943.

Han, J.W., Zhao, C.J., Yang, X.T., Qian, J.P., Fan, B.L., 2015. Computational modeling of airflow and heat transfer in a vented box during cooling: optimal package design. Appl. Therm. Eng. 91, 883–893.

Hu, H., Argyropoulos, S.A., 1996. Mathematical modelling of solidification and melting: a review. Model. Simul. Mater. Sci. Eng. 4 (4), 371–396.

Lu, L.X., Chen, X.Q., Wang, J., 2014. Modeling and thermal analysis of tray-layered fruits inside packages during forced-air precooling process. Packag. Technol. Sci. 29 (2), 105–119.

Maguire, K.M., Banks, N.H., Opara, L.U., 2010. Factors affecting weight loss of apples. Hortic. Rev. 197–234 (John Wiley & Sons, Inc).

Morris, J.R., Brady, P.L., 2005. Temperature effects on produce degradation. In: Lamikanra, O., Imam, S.H., Ukuku, D. (Eds.), Produce Degradation: Pathways and Prevention. Taylor & Francis, Boca Raton, p. 639.

O'Hagan, A., Leonard, T., 1976. Bayes estimation subject to uncertainty about parameter constraints. Biometrika 63 (1), 201–203.

Opara, L.U., Zou, Q., 2007. Sensitivity analysis of a CFD modelling system for airflow and heat transfer of fresh food packaging: inlet air flow velocity and inside-package configurations. Int. J. Food Eng. 3 (5). Article 16.

Owen, D.B., 1956. Tables for computing bivariate normal probabilities. Ann. Math. Stat. 27 (4), 1075–1090.

O'Sullivan, J., Ferrua, M., Love, R., Verboven, P., Nicolai, B., East, A.R., 2014. Airflow measurement techniques for the improvement of forced-air cooling, refrigeration and drying operations. J. Food Eng. 143, 90–101.

O'Sullivan, J., Ferrua, M.J., Love, R.J., Verboven, P., Nicolaï, B., East, A.R., 2016. Modelling the forced-air cooling mechanisms and performance of polylined horticultural produce. Postharvest Biol. Technol. 120, 23–35.

Pathare, P.B., Opara, U.L., Vigneault, C., Delele, M.A., Al-Said, F.A.J., 2012. Design of packaging vents for cooling fresh horticultural produce. Food Bioprocess Technol. 5 (6), 2031–2045.

Petrova, I., Bantle, M., Eikevik, T.M., 2015. Manufacture of dry-cured ham: a review. Part 2. Drying kinetics, modeling and equipment. Eur. Food Res. Technol. 241 (4), 447–458.

Pons, O., 2014. Nonparametric tests for one sample. In: Pons, O. (Ed.), Statistical Tests of Nonparametric Hypotheses: Asymptotic Theory. World Scientific Publishing Company, Singapore, pp. 65–68 & 107-109.

Shapiro, S.S., Wilk, M.B., 1965. An analysis of variance test for normality (complete samples). Biometrika 52 (3/4), 591–611.

Singh, R.P., Heldman, D.R., 2009a. Food freezing. In: Singh, R.P. (Ed.), Introduction to Food Engineering. Elsevier/Academic Press, Amsterdam, pp. 521–563.

Singh, R.P., Heldman, D.R., 2009b. Heat transfer in food processing. In: Singh, R.P. (Ed.), Introduction to Food Engineering. Elsevier/Academic Press, Amsterdam, 282–280.

Terrell, D., Fomby, T.B., 2006. A multi-variate skew-garch model. In: Terrel, D. (Ed.), Econometric Analysis of Financial and Economic Time Series. Elsevier JAI, Amsterdam, pp. 36–38.

Yahia, E.M., Elansari, A., 2011. Postharvest technologies to maintain the quality of tropical and subtropical fruits. In: Yahia, E.M. (Ed.), Postharvest Biology and Technology of Tropical and Subtropical Fruits. Woodhead Pub, Oxford, p. 154.

Zhao, J.M., Bronlund, J.E., East, A.R., 2014. Effect of cooling rates on kiwifruit firmness and rot incidence in subsequent storage. In: Proceedings of the 5th Postharvest Unlimited Conference, Cyprus, pp. 313–318.

Nomenclature

C_p: specific heat capacity (J kg^{-1} K^{-1})
E: enthalpy (J kg^{-1})
$f(\Delta Y)$: frequency of ΔY
$F(\Delta Y)$: cumulative frequency of ΔY
HI: relative standard deviation, used previously as a heterogeneity metric (−)
L_{fusion}: latent heat of fusion (J kg^{-1})
m: total number of recorded temperature positions
n: individual recorded temperature position
OHI: Overall Heterogeneity Index (−)
P: partial pressure (Pa)
$\dot{Q}$: Volumetric flowrate (m^3 s^{-1})
RH: relative humidity
T: temperature (°C)
$\overline{T}$: average temperature (°C)
X: quantity: temperature, partial pressure or enthalpy
Y: fractional unaccomplished quantity change (−)
$\overline{Y}$: average unaccomplished quantity change (−)
ΔY: dimensionless quantity difference (−)

Greek symbols

α: shape (S-N)
μ: mean
ξ: location (S-N)
τ: fractional unaccomplished cooling completion time (−)
σ: standard deviation
ϕ: standard normal distribution
Φ: standard normal cumulative distribution
ω: scale (S-N)
$\mathscr{T}$: process progression index, $\overline{Y}$ or τ

Subscripts

t: absolute time (seconds)
i: initial
fl: fluid
ref: refrigeration temperature
fr: freezing temperature
cool: pre-cooling phase
fusion: latent phase
freeze: subcooling phase
N: normal distribution
SN: skew-normal distribution

ID:342

EXPLORING A NEW HETEROGENEITY INDEX TO QUANTIFY THE VARIATION OF COOLING RATES WITHIN SYSTEMS THAT UNDERGO THE FORCED-AIR COOLING PROCESS

Jamal R. OLATUNJI, Young M. SHIM, Richard J. LOVE, Maria J. FERRUA, Andrew R. EAST
Centre for Postharvest and Refrigeration Research, Massey Institute of Food Science and Technology, Massey University, New Zealand
R.J.Love@massey.ac.nz

ABSTRACT

Forced-air cooling is a commonly used pre-cooling process that forces refrigerated air through a stacked pallet of produce, rapidly removing the field heat in preparation for storage and transport. Cooling rates can vary spatially throughout the pallet due to uneven airflow distribution and the relative proximity to the inlet of refrigerated air. This heterogeneity in pre-cooling processes may result in significant differences in quality and shelf life at the end of the cold chain. Therefore in assessing pre-cooling performance, in addition to assessing average cooling rate (through $1/2$ cooling or $7/8$ cooling time), a robust heterogeneity metric is required to quantify the variability in a cooling process, and hence compare different systems. The aim of this work is to develop this heterogeneity index. The new method is illustrated through application to polylined kiwifruit inside of a modular bulk package.

1. INTRODUCTION

The forced-air cooling process is the most common and efficient method of pre-cooling used by the horticulture industry (de Castro *et al*., 2005). It is a postharvest operation that is designed to quickly and efficiently lower the temperature of freshly picked produce from their field to storage temperature. This reduces the rate at which the produce degrades, maintaining the quality of the product as it moves through the supply chain. The process operates by creating a pressure drop across a stacked pallet of produce, forcing refrigerated air to penetrate into the packaging and exchange heat with the product inside (O'Sullivan *et al*, 2015). Due to the complex airflow pattern through the pallet, the cooling rates of individual products can vary significantly with location, leading to cooling heterogeneity (Defraeye *et al.*, 2014). While the average cooling rate – measured via the half-cooling time (HCT) or seven-eighths-cooling time (SECT) – is an important measure of system performance, the uniformity of individual product temperatures must also be taken into account. For example, rates of cooling have been associated with the development of chilling injuries in kiwifruit (Zhao *et al*., 2015). Additionally, any variability that exists at the completion of commercial cooling may remain within the pallet for some time during subsequent storage and transport, resulting in product variability. The variation in temperatures or cooling can be described via a heterogeneity index. To the author's knowledge, the only heterogeneity index so far published that quantifies temperature variability during the forced-air cooling process is that provided by Dehghannya *et al.* (2011):

$$HI = \frac{\sqrt{\left(T_p - \overline{T_p}\right)^2}}{\overline{T_p}} \times 100 \tag{1}$$

Where
T_p = product temperature of a specific fruit (location within the system) at a specific time, and $\overline{T_p}$ = average product temperature at a specific time. This heterogeneity index has some significant shortcomings, including:

- being unable to describe the heterogeneity of the entire system;
- eliminating information concerning whether a temperature position is hotter or colder than the average;
- becoming mathematically unstable when the refrigeration temperature approaches 0 °C, as the heterogeneity index approaches infinity.

Therefore there is a need for a robust heterogeneity index that can be used to quantify the variation in temperatures of the entire system, either at a given time, or over the entire cooling process; and can be used to compare the performance of two or more systems with respect to cooling uniformity. In this work, the development of a new heterogeneity index is explored. The proposed new heterogeneity index is applied to the forced-air cooling of kiwifruit, with the objective of determining whether or not an increase in airflow rate had a significant effect on cooling heterogeneity.

2. METHOD

2.1. Experimental

Kiwifruit were stacked into three half-pallets, each consisting of 50 boxes (10 kg per box). The kiwifruit inside of each box was wrapped in a polyethylene polyliner to prevent moisture loss and product shrivelling (O'Sullivan *et al.*, 2013). Thermocouples were placed into the centre of kiwifruit located in a variety of locations throughout each monitored box, so that a wide spatial sample of cooling rates was collected (Figure 1). A total of 14 boxes were recorded, with each box having 12 fruit temperatures recorded. Inside of the chosen 14 boxes, the kiwifruit were stacked into an ordered arrangement to eliminate packing variability. A total of 168 positions were recorded per pallet, although the true sample size was below this due to occasional data loss. Each half pallet used the same: package design (6% total opening area; O'Sullivan *et al.*, 2013); initial temperature (20 °C); refrigeration temperature (0 °C); and processing time (cooled for 20 hours). Cooling of the pallets differed by the airflow rate through the pallet: 0.38, 0.58 or 0.77 m^3/s.

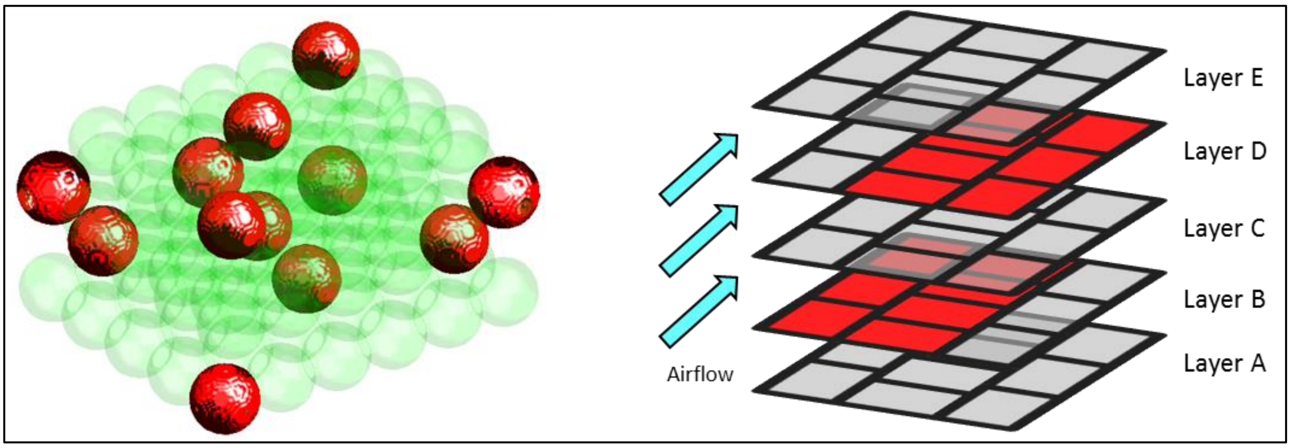

Figure 1. Experimental set up and recorded temperature positions. Locations of recorded fruit and boxes are marked in red.

2.2. Heterogeneity Index

At the beginning of the forced-air cooling process, all of the fruit has a similar initial temperature. Therefore at time = 0, the variation in temperature is low. As the process continues, there are several positions that have preferential cooling conditions (such as exposure to incoming cooling air, Defraeye *et al*, 2014), resulting in them cooling rapidly. Meanwhile, others will be in positions insulated from the effects of the cooling air, resulting in them cooling slowly. Therefore at time > 0, the variation in temperatures will be enlarged. At the completion of cooling (given infinite time), all the fruit will reach the same refrigeration temperature. Therefore at time = ∞, variation of temperature will = 0, and hence by extension, as time >> 0, the variation of temperatures will again be low. Given this expected behaviour of the variation in temperature during a bulk cooling process, the intention of this work is to develop a method to mathematically describe these changes in temperature variability over time. In doing so it is hoped that the mathematical descriptions provide a framework for the comparison of performance of two or more forced-air cooling systems, with respect to their cooling heterogeneity.

2.2.1 Dimensionless Temperature

Converting temperature data into a dimensionless form enables different systems to be directly compared (Brosnan and Sun, 2001). The dimensionless temperature used was the Fractional Unaccomplished Temperature Change, or FUTC:

$$Y_{t,n} = \frac{T_{t,n} - T_a}{T_{i,n} - T_a} \tag{2}$$

2.2.2 Dimensionless Time

In order to compare different systems at the same characteristic time scales, such as the HCT or the SECT, a dimensionless time is required. Therefore, the Average Fractional Unaccomplished Temperature Change can serve as an appropriate dimensionless time; given that it describes the proportion of cooling yet to be achieved:

$$\bar{Y}_t = \frac{\left(\sum_{n=1}^{m} Y_{t,n}\right)}{m} \tag{3}$$

Where

$\bar{Y}_t$ = average dimensionless temperature at time t; and m is the total number of fruit recorded.

Given Equations 2 and 3, every system will start at $\bar{Y} = 1$, and as cooling progresses, $\bar{Y}$ will tend towards 0. When $\bar{Y} = 0.5$ we are at the HCT; and when $\bar{Y} = 0.125$ we are at the SECT. Although we are using dimensionless time to compare systems in this work, in some situations comparison at true time points (i.e. at the decided cooling completion time) may also be appropriate.

2.2.3 Temperature Variability at a Given Time

Throughout the cooling process, a number of the fruit will cool at the same rate as the average cooling rate. However, there will be other fruit that cool quickly, and others that cool slowly, so that there is a multitude of hot and cold spots throughout the pallet structure. The number and magnitude of these spots can be expressed by taking the difference between the FUTC of individual fruits and the average FUTC:

$$\Delta Y_{t,n} = Y_{t,n} - \bar{Y}_t \tag{4}$$

ΔY can be plotted as a histogram (Figure 2), where, should the population of selected potential measurement locations be appropriate, the distribution of temperatures will form a bell curve. Since most of the fruit will be at or near to the average temperature, the ΔY bell curve will have a mean of zero. Positive numbers represent fruit that are warmer than average and hence are cooling slowly (hot spots); while negative numbers represent fruit that are cooler and hence are cooling faster (cold spots). If there is a low variation in temperatures, the ΔY bell curve will be tall and narrow, while a ΔY bell curve indicating high variability will be short and wide. In summary, we can describe the temperature variability at a given time as a population bell curve that has a mean of zero, and a standard deviation representing the standard deviation of ΔY.

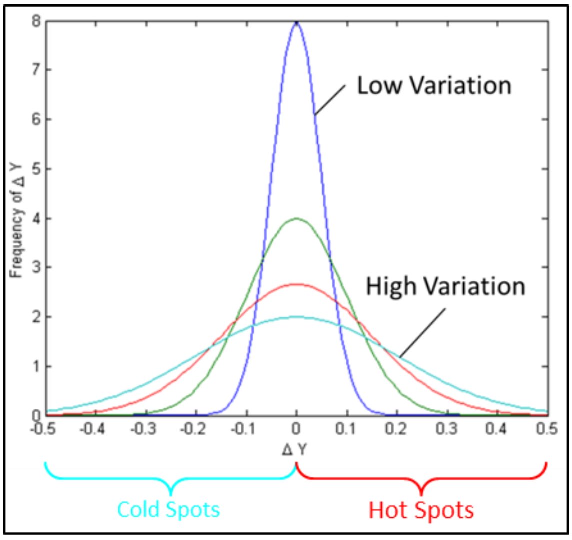

Figure 2. Frequency of ΔY histogram, showing the potential variation of temperatures within a pallet at a single point in time. Data presented is theoretical.

2.2.4 Temperature Variability Over Time

The ΔY bell curve only offers information concerning the distribution of temperatures at a given time. If ΔY across all times and fruits is plotted against $\bar{Y}$ across all times, then a variability over time plot can be created that is dimensionless in terms of both temperature and time. This offers a visual tool to compare the heterogeneity of two systems across the entire cooling process. Theoretical heterogeneity plots are illustrated in Figure 3 and 4 for two idealised systems, representing high and low heterogeneity.

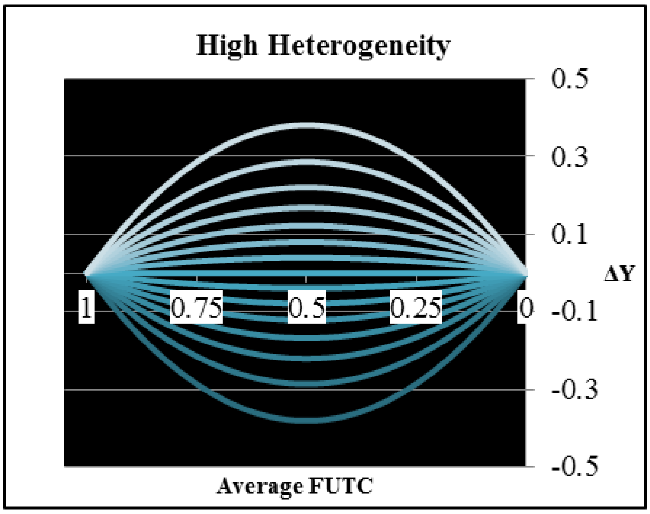

Figure 3. Idealised heterogeneity plot for a theoretical system with a high level of cooling heterogeneity.

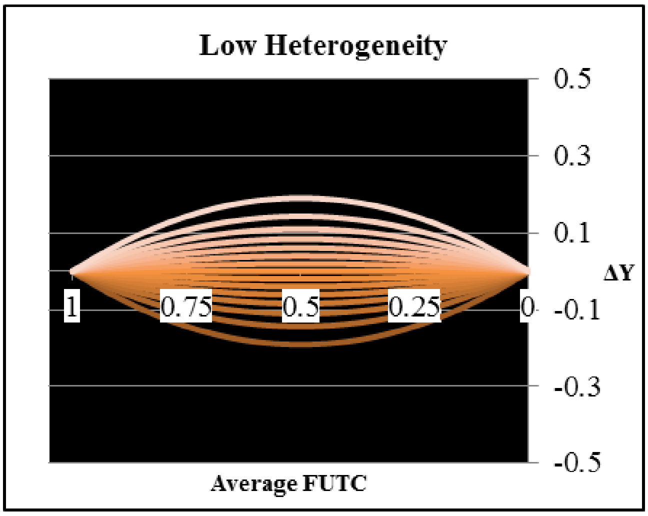

Figure 4. Idealised heterogeneity plot for a theoretical system with a low level of cooling heterogeneity.

Both systems show the same characteristic shape of being tapered on both ends, as the heterogeneity is low at the beginning and end of a cooling process. At approximately the HCT, the variation in temperatures reaches a maximum. Figure 3 represents a system with a high level of cooling heterogeneity, which is reflected in the degree at which the plot bulges (having a higher standard deviation) in the middle (at Y = 0.5). Conversely, Figure 4 represents a system with a low level of heterogeneity, with the bulge being much less pronounced. By visually comparing Figure 3 to Figure 4 it can be concluded that the system represented by Figure 4 is superior in terms of cooling uniformity (homogeneity).

2.2.5 Comparing Heterogeneity Using a Homogeneity of Variance Test

The ΔY vs $\bar{Y}$ plot offers a qualitative tool for visually comparing the heterogeneity of multiple systems. To quantitatively compare the heterogeneity, a homogeneity of variance test – such as Levene's test – can be used. The null hypothesis of the Levene's test is that the distributions have the same variation, or heterogeneity.

3. RESULTS

3.1. Comparing Cooling Rates

Pallet scale cooling curves for the three systems are given in figure 5. Box averaged cooling curves are given in Figures 6 and 7, for the two extreme airflow rates (0.38 and 0.77 m^3/s):

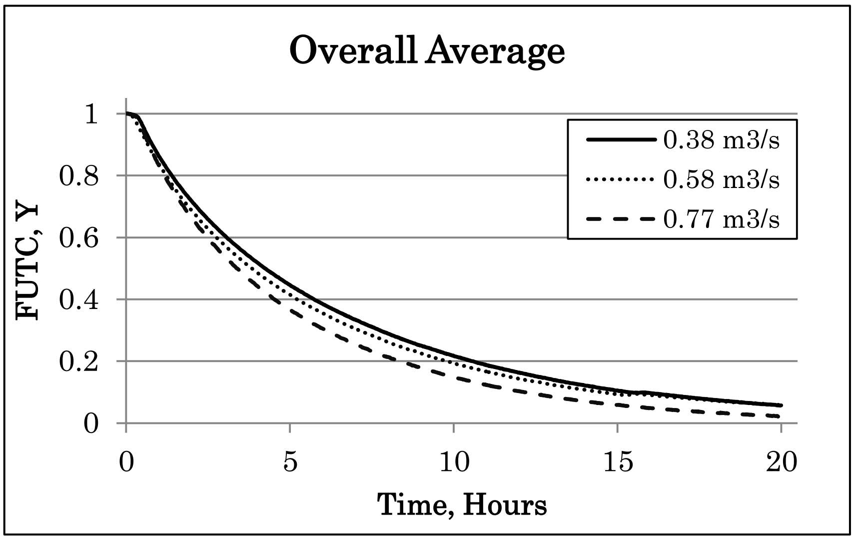

Figure 5. Average pallet cooling profile under three different airflow rates.

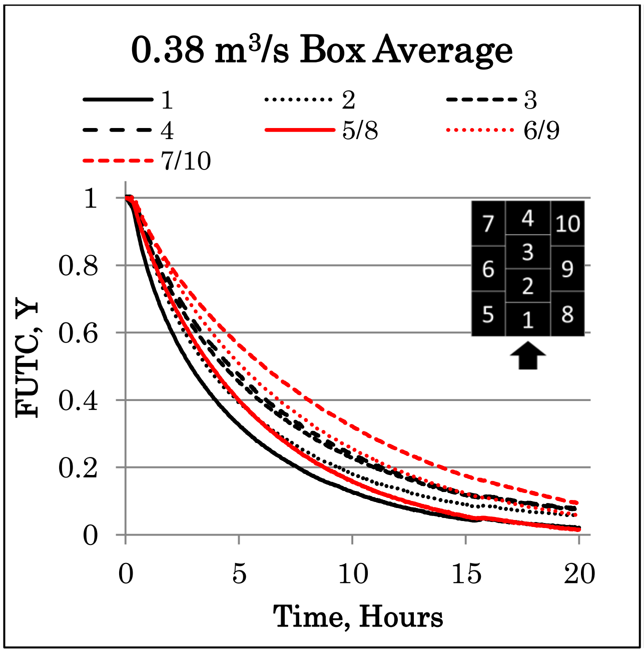

Figure 6. Average box cooling profiles, 0.38 m^3/s.

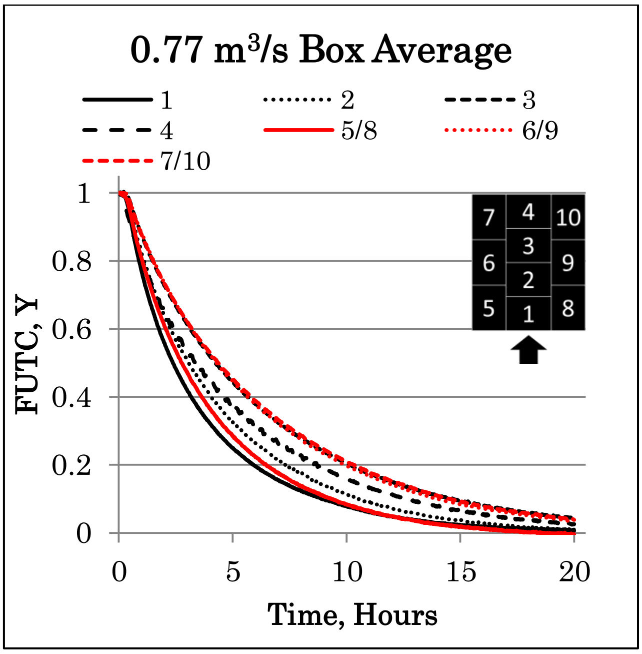

Figure 7. Average box cooling profiles, 0.77 m^3/s

As to be expected, a higher airflow rate increased the average cooling rate of the system, with half-cooling times of 4.2, 3.8 and 3.4 hours for 0.38, 0.58 and 0.77 m^3/s, respectively.

3.2. Comparing Cooling Heterogeneity Over Time

While airflow rate was positively correlated to the average cooling rate, we are concerned with the uniformity of temperatures during the process. Using the new heterogeneity index, heterogeneity plots for all three experimental systems are presented in Figures 8, 9 and 10. The heterogeneity plots show many similarities to the theoretical plots presented in Figures 3 and 4, such as having low heterogeneity at the beginning and end of the cooling process, and the bulge reaching a maximum at approximately the HCT. However some significant differences are also observed. In Figures 2, 3 and 4, it is assumed that the ΔY is normally distributed, with an equal amount of hot and cold spots. In reality, the ΔY is skewed towards the negative (cold) regions at the beginning of the cooling process, $0.5 \leq \bar{Y} < 1$; and is then skewed towards the positive (hot) regions at the end of the cooling process, $0 < \bar{Y} < 0.5$. This skewness must be incorporated into the heterogeneity index comparison in the future for it to be mathematically robust. Although a higher airflow rate improved the overall cooling rate, the heterogeneity plots reveal there are only small differences in heterogeneity with a higher airflow rate.

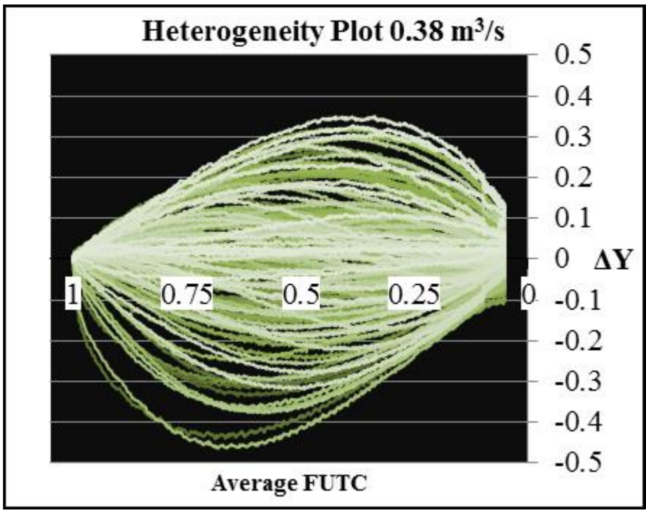

Figure 8. Experimentally determined heterogeneity plot for 0.38 m^3/s

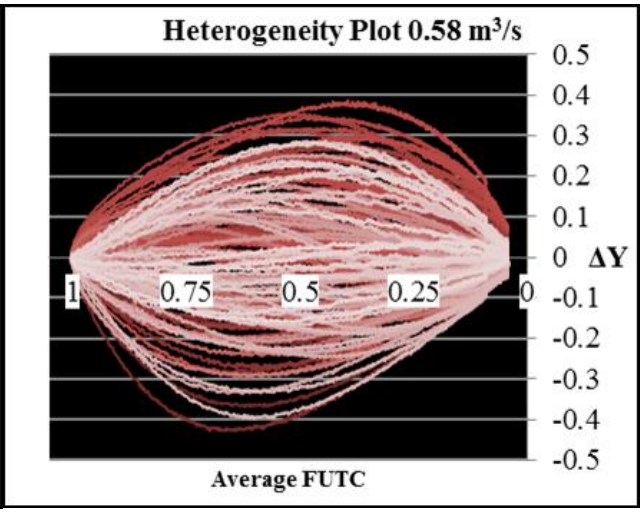

Figure 9. Experimentally determined heterogeneity plot for 0.55 m^3/s

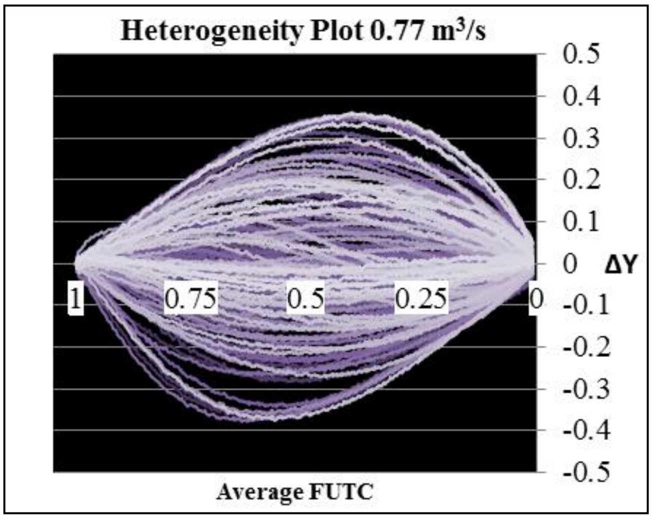

Figure 10. Experimentally determined heterogeneity plot for 0.77 m^3/s

3.3. Direct Comparison of Heterogeneity at Half-Cooling Time

The heterogeneity of the three systems was directly compared at each systems respective half-cooling time ($\bar{Y}$ = 0.5). Histograms of the ΔY are shown in Figures 11, 12 and 13. Over each histogram, a normal distribution with a mean of zero and a standard deviation equal to the standard deviation of the ΔY was plotted. Comparing the idealised curve to the bars representing the real temperature data, there was a close fit for all three cases. This was further confirmed by using Shapiro-Wilk tests. With respect to the skewness as discussed in section 3.2, this result suggests that although the distribution of temperatures is skewed at the beginning and end of the cooling process, the level of skewness is low at the half-cooling time, and can be modelled as a normal distribution. Levene's tests were used to determine if the distribution of temperatures was statistically significantly different (Table 1). In all cases the null hypothesis could not be rejected ($p > 0.05$), and hence in this case it would seem that the airflow rate did not have a significant impact on the heterogeneity of the system at the HCT.

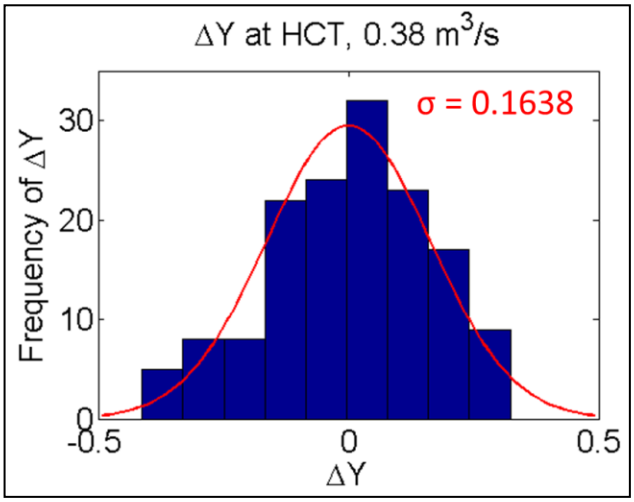

Figure 11. Frequency of ΔY plot at the HCT for 0.38 m^3/s. Shapiro-Wilk test result: W = 0.99, p-value = 0.11.

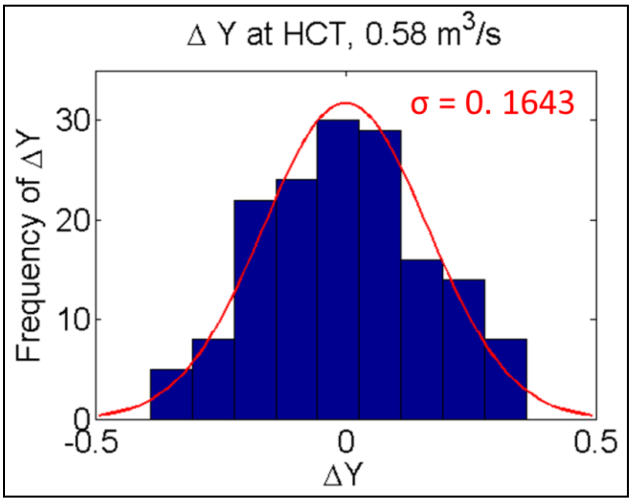

Figure 12. Frequency of ΔY plot at the HCT for 0.58 m^3/s. Shapiro-Wilk test result: W = 0.99, p-value = 0.42.

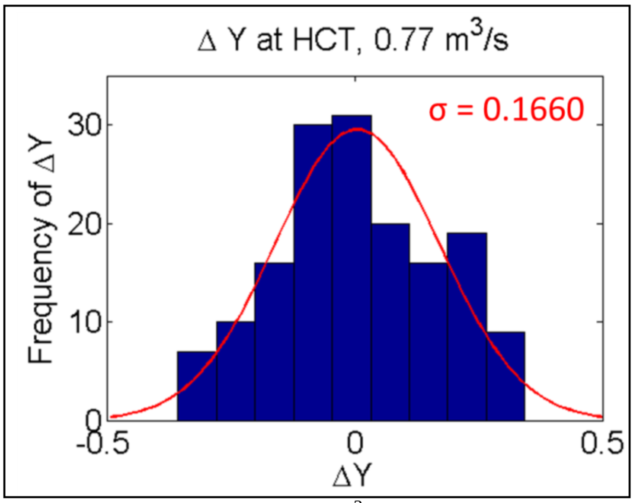

Figure 13. Frequency of ΔY plot at the HCT for 0.77 m^3/s. Shapiro-Wilk test result: W = 0.99, p-value = 0.095.

Table 1: Levene's test results comparing ΔY at HCT

Test Comparison	L-statistic	Degrees of Freedom	p-value
0.38 m^3/s ↔ 0.58 m^3/s	0.083	1, 302	0.77
0.38 m^3/s ↔ 0.77 m^3/s	0.079	1, 304	0.78
0.58 m^3/s ↔ 0.77 m^3/s	0.000018	1,312	0.99

4. CONCLUSIONS

A new method of visualising and quantifying the level of cooling heterogeneity at given points in time, or over an entire cooling process, was developed. The new heterogeneity index describes the distribution of temperatures at a given time as a bell curve, with a larger standard deviation corresponding to a higher level of heterogeneity. This new index uses dimensionless time and temperature so that the heterogeneity of two different systems can be directly compared. The new method was applied to the forced-air cooling of polylined kiwifruit stacked in a pallet, with the objective of assessing whether or not airflow rate had a significant impact on the heterogeneity of the system. The subsequent heterogeneity plots showed little difference between trials which was statistically supported with a Levene's test applied at the half-cooling time. Therefore for this system it would seem that airflow (m^3/s) did not affect cooling heterogeneity. Improvements in the method could include measures of the skewness in temperature distribution near the beginning and end of the cooling process. This new heterogeneity index has the potential to be used for a wide range of batch temperature change systems, including batch chillers and freezers or any batch heating process.

5. REFERENCES

1. Brosnan T, Sun DW. 2001, Precooling techniques and applications for horticultural products — a review, *International Journal of Refrigeration*. 24(2): 154-170.
2. de Castro LR, Vigneault C, Cortez L. 2004, Container opening design for horticultural produce cooling efficiency, *Food, Agriculture and Environment.* 2(1): 135-140.
3. Defraeye T, Lambrecht R, Delele MA, Tsige AA, Opara UL, Cronjé P, Verboven P, Nicolai B. 2014, Forced-convective cooling of citrus fruit: Cooling conditions and energy consumption in relation to package design, *Journal of Food Engineering*. 121: 118-127.
4. Dehghannya J, Ngadi M, Vigneault C. 2011, Mathematical modeling of airflow and heat transfer during forced convection cooling of produce considering various package vent areas, *Food Control.* 22(8): 1393-1399.
5. O'Sullivan J, Ferrua MJ, Love RJ, Verboven P, Nicolaï BM, East AR. 2015, Airflow measurement techniques for the improvement of forced-air cooling, refrigeration and drying operations, *Journal of Food Engineering*. 143: 90-101
6. O'Sullivan J, Ferrua MJ, Love RJ, Verboven P, Nicolaï BM, East AR. 2013, Performance of the forced-air cooling process of fruit packed in polyethylene liners as a function of pallet orientation, *Proceedings of the 2nd IIR International Conference on Sustainability and the Cold Chain*.
7. Zhao JM, Bronlund JE, East AR. 2014, Effect of cooling rates on kiwifruit firmness and rot incidence in subsequent storage. *5th Postharvest Unlimited Conference, Cyprus*. (in press)

6. NOMENCLATURE

T_p product temperature of a specific fruit at a specific time (°C)
$\overline{T_p}$ average product temperature at a specific time (°C)
T temperature (°C)
Y fractional unaccomplished temperature change (FUTC) (dimensionless)
$\bar{Y}$ average FUTC (dimensionless)
ΔY difference between individual FUTC and average FUTC (dimensionless)

Subscripts

t time (hours)
n individual fruit
m total number of measured fruit
a cooling air
i initial

7. ACKNOWLEDGEMENTS

The authors gratefully acknowledge the Ministry of Business, Innovation and Employment, New Zealand for funding this work (Fibreboard Packaging Design Project (MAUX1302)). We would also like to thank Alicia Tan for her help in the laboratory, and Justin O'Sullivan for his expertise.

TOWARD A FAST AND FLEXIBLE HEAT TRANSFER MODEL FOR HORTICULTURAL PRODUCTS PACKAGED INTO BOXES

J.R. OLATUNJI, Y.M. SHIM, M.J. FERRUA, R.J. LOVE*, A.R. EAST

Centre for Postharvest and Refrigeration Research, Massey University, Private Bag 11-222, Palmerston North 4442, New Zealand, Ph +64 6 350 4336; Fax +64 6 350 5657.
*R.J.Love@massey.ac.nz

ABSTRACT

Packaging fruit into boxes prior to pre-cooling benefits the horticultural cool chain by facilitating large-scale cooling and transport. A cooling prediction model that is applicable across many different packaging and product types would aid optimisation of packaging systems and operating conditions. This paper presents a new preliminary model, applied to a single box of kiwifruit wrapped in a polyliner. X-ray tomography was used to determine the exact bulk fruit shape; and was then divided into a small set of space averaged zones. The properties of each zone were determined in an automated fashion, based on the local porosity. The resulting cooling predictions reached unity with a resolution of just 125 zones, representing a solution time of only 42 seconds for 20 hours of simulated cooling. Being fast and flexible, the model will be validated against a real-world box of kiwifruit, being cooled in a refrigerated wind tunnel.

1. INTRODUCTION

Pre-cooling is a vital part of the cool chain for fresh fruit and vegetables. Designed to quickly and efficiently reduce produce from their field temperature to storage temperature, this unit operation is a crucial process that ensures maintenance of quality and extension of shelf life. The most common pre-cooling process employed by the horticulture industry is forced-air cooling, where fans pull refrigerated air through stacked pallets of fruit (O'Sullivan *et al*, 2014; Shim *et al*, 2016).

In industry and academia there is a focus on package design testing, where through either experimental or computational means, the performance of a given package designs efficiency is thoroughly tested (Defraeye *et al*, 2015; Dehghannya *et al*, 2010). Changes to package ventilation and the position of packages in a pallet can dramatically alter the airflow pathway, impacting cooling performance. The stacked fruit inside the package forms a convoluted shape that can be difficult to define, and will determine different airflow pathways depending on individual product shape and product stacking. In addition to the corrugated fibreboard box, the existence of other packaging materials – such as polyliners or clamshells – further complicates the problem. High fidelity models (such as Computational Fluid Dynamics (CFD) models) provide important insights into transport phenomena that otherwise cannot be measured experimentally, such as: thermal mixing of air between packaging, the magnitude of bypass air, and thermal gradients within individual products (Defraeye *et al*, 2014). However, such models can take months or years to fully construct and validate, resulting in a description of a specific cooling scenario, applied to a specific product. Additionally, depending on the computational resources available, these types of models can take many hours or days to solve. These problems limit their usefulness to aid immediate optimization of package design. Therefore, it is proposed that a mathematical model is developed that favours flexibility and computational efficiency, at the cost of detailed accuracy to ensure that the model can be applied to many different package sizes, shapes, and product types; and has fast solution times. Such a model could be integrated with an appropriate mathematical optimization strategy – such as a genetic algorithm (e.g. East and Smale, 2008) – to rapidly identify an improved package design.

In this work, the development of such a model is explored. The proposed model is based on the zonal approach (Tanner *et al*, 2002), where the package is divided into a small set of space averaged zones. This strategy significantly reduces the number of ODEs required to predict the bulk cooling rate and the uniformity of cooling, leading to fast solution times. However, defining the properties of each zone can take a great deal of thought and care for predictions to be accurate. In this paper, the zonal approach is supplemented with data provided by a CT scan, which is used to inform the properties of each zone. This allows a flexible and fast zonal model to be constructed in an automated fashion. Applied to a single box of kiwifruit, wrapped in a polyliner, the performance of the new model is demonstrated in terms of bulk cooling rate, temperature variability, and processing time, as a function of the number of zones.

2. GEOMETRY

X-ray tomography (CT scanning) was used to empirically determine the bulk shape of fruit stacked inside a box (Fig. 1a). Modular bulk packs containing 100 count 36 c.v. Hayward kiwifruit (count 36 is a size based grading category) were scanned at the maximum resolution of 0.8 mm per slice. Since the CT number (measured in Hounsfield Units (HU)) is related to the density of the material, different phases were identified and separated. Air (≈0-100 HU), packaging (≈300-500 HU) and fruit (≈900-1200 HU) were identified using MATLABs ‘multithresh’ function; and ‘imquantize’ was used to convert the raw CT scan data into a 3-D image with 3 discrete levels (Fig. 1b). The packaging was then eliminated (Fig. 1c) to give the isolated bulk fruit shape, to be used as a model input.

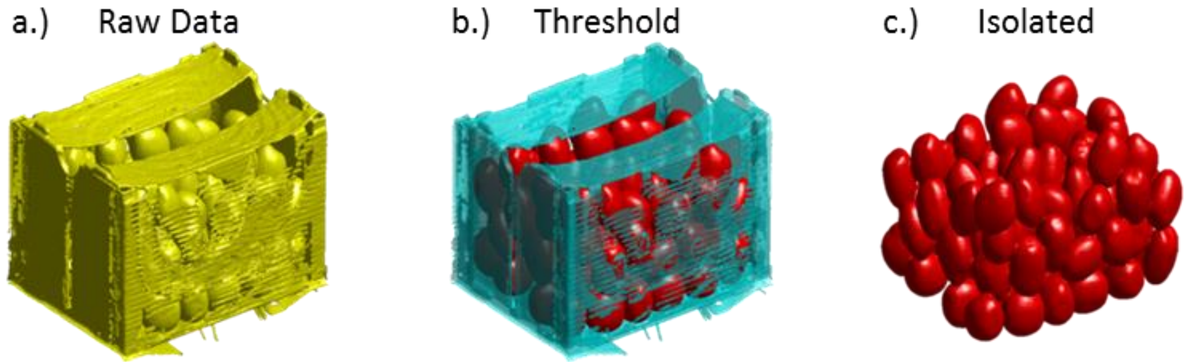

Figure 1: a.) Raw CT scan data; b.) CT scan data subjected to a threshold algorithm to separate fruit, air and packaging; c.) fruit isolated, to be used as a model input.

3. MODEL DEVELOPMENT

3.1 Model Simplification

Ferrua and Singh (2009) demonstrated that heat and momentum transfer can often be de-coupled in fruit cooling scenarios, meaning that models for airflow distribution and the consequent heat transfer can be developed independently. This paper focuses on the developments of the heat transfer model, with an airflow distribution model to be added at a later date. Kiwifruit are wrapped in a polyliner bag to prevent moisture loss as they move through the supply chain. O’Sullivan (2016) demonstrated that produce wrapped in a polyliner experiences little to no net evaporation, meaning that moisture transfer can be neglected from the model. O’Sullivan (2016) also reported that evaporation and condensation within the polyliner results in a net zero exchange of energy, so that evaporative/condensation heat transfer can also be removed. Defraeye *et al* (2014) demonstrated that thermal radiation was low compared to other more significant modes of heat transfer. Due to the existence of the polyliner bag, air was treated as stagnant, as the contribution of natural convection is considered small compared to conduction. Given these simplifications, development of an effective thermal conductivity model could be explored. This approach treats the two phases (fruit and air) as one phase with effective properties.

3.2 Model Equations

The geometry from the CT scan was divided into a small set of space averaged zones (Tanner *et al*, 2002). Air (A) and product (S) can exist within a zone. Packaging (P) occupies zones on the sides of the geometry, with the exception of the top where the polyliner is in direct contact with the refrigerated airflow.

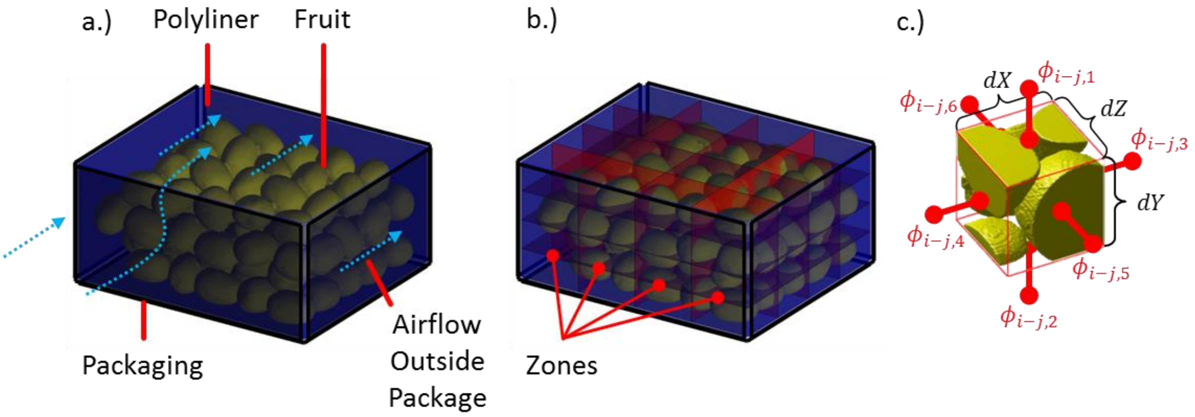

Figure 2: a.) CT scan; b.) Geometry segregated into space averaged zones; c.) An individual zone with possible directions of heat transfer

The number of ODEs that need to be solved is significantly reduced compared to the finite element approach; while still retaining the ability to predict temperature gradients within a package, allowing for cooling homogeneity prediction (Olatunji *et al*, 2015) as well as the bulk cooling rate. The generalised ODE for temperature change is Eq. 1, where an exchange of heat between the zone under study, i, and an adjacent zone, j, is $\phi_{i-j,n}$ (W). Each heat flux is determinable using Eq. 2. The effective heat transfer coefficient in a given direction is Eq.3, and resistance between zones is Eq. 4. For $\phi_{i-j,1}$ and $\phi_{i-j,2}$, $D_n = dY$ and $A_n = dX \cdot dZ$ (Fig. 2c); $\phi_{i-j,3}$ and $\phi_{i-j,4}$, $D_n = dX$ and $A_n = dY \cdot dZ$; and $\phi_{i-j,5}$ and $\phi_{i-j,6}$, $D_n = dZ$ and $A_n = dX \cdot dY$. The parallel effective thermal conductivity model was selected (Rahman and Al-Saidi, 2009; Eq. 5), as it has been used for grapes wrapped in a polyliner (Delele *et al*, 2012).

$$\frac{dT_i}{dt} = \frac{\sum_{n=1}^{N} \phi_{i-j,n}}{V_i \cdot \varepsilon_i \cdot \rho_A \cdot C_A + V_i \cdot (1-\varepsilon_i) \cdot \rho_S \cdot C_S} \quad (1)$$

$$\phi_{i-j,n} = h_{eff} \cdot A_n \cdot \left(T_{j,n} - T_i\right) \quad (2)$$

$$h_{eff} = \frac{1}{R_i + R_{j,n}} \quad (3)$$

$$R = \frac{D_n/2}{k_{eff,i}} \quad (4)$$

$$k_{eff,i} = \varepsilon_i \cdot k_A + (1-\varepsilon_i) \cdot k_S \quad (5)$$

3.3 Zone Properties

Zones were cuboid in shape, equal in size, and regularly spaced. Rather than assuming a system wide porosity (as is common in the porous medium approach (Delele *et al*, 2012). ε_i for each zone can be individually measured using the CT scan data. An automated procedure for determining ε_i was developed. It assumed a geometry presented in a voxel format, as this is the same format that CT scan information is provided. A voxel (denoted as $\mathbb{v}_n$) represents a value on a regular grid in 3-dimensional space. As long as the resolution is sufficiently high (low slice thickness during CT scanning procedure), any geometry can be represented as a collection of voxels, without the need for complex meshing. During separation (Fig. 1b), CT numbers are converted into binary, where solids are filled ($\mathbb{v}_n = 1$) and voids are empty ($\mathbb{v}_n = 0$). The volume of the solid phase of each zone is therefore the sum of all the voxels within the zone, multiplied by the volume of a single voxel (Eq. 6; Fig. 4a). For the air phase, $\sqrt{(\mathbb{v}_i - 1)^2}$ is applied to fill empty voxels, and empty filled voxels (Eq. 7). The porosity (ε_i) in zone i is therefore Eq. 8.

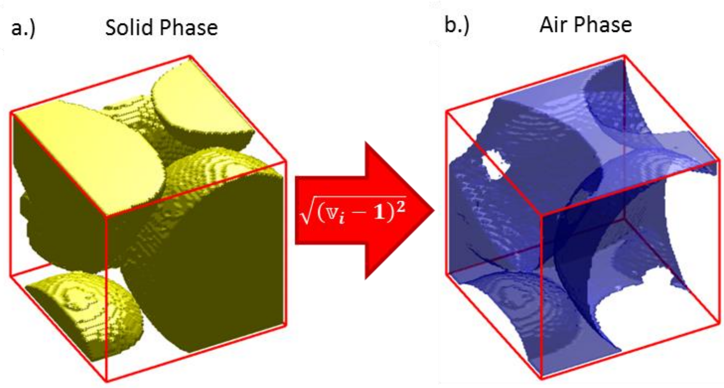

Figure 3: a.) solid phase within zone i; b.) air phase within zone i, after applying $\sqrt{(\mathbb{v}_i - 1)^2}$

$$V_{S,i} = \left(\sum \mathbb{v}_i\right) \times (dx \cdot dy \cdot dz) \tag{6}$$

$$V_{A,i} = \left(\sum \sqrt{(\mathbb{v}_i - 1)^2}\right) \times (dx \cdot dy \cdot dz) \tag{7}$$

$$\varepsilon_i = \frac{\sum \sqrt{(\mathbb{v}_i - 1)^2}}{\sum \sqrt{(\mathbb{v}_i - 1)^2} + \sum \mathbb{v}_i} \tag{8}$$

3.4 Model Set-Up

The heat transfer model was then coded in MATLAB v.R2013b. External airflow was considered to be a constant flow of 0°C over the top, sides, front and back external surfaces, resulting in a heat transfer coefficient of $h_{ext} = 10$ W.m^{-2}.K^{-1}. Packaging was considered to be an added resistance to external heat transfer of 0.6 m^2.K.W^{-1} (3mm thick, $k_P = 0.005$ W.m^{-1}.K^{-1}) on all surfaces except the top, where the polyliner is in direct contact with the airflow. The initial temperature of the fruit was 20°C. The bottom of the box was considered to have a constant temperature of 0°C, as it was resting on a refrigerated surface. Kiwifruit was considered to be a homogeneous solid with $\rho_S = 1100$ kg.m^{-3}, $C_S = 3760$ J.kg^{-1}.K^{-1} and $k_S = 0.5$ W.m^{-1}.K^{-1}; and air as $\rho_A = 1.25$ kg.m^{-3}, $C_A = 1005$ J.kg^{-1}.K^{-1} and $k_A = 0.025$ W.m^{-1}.K^{-1}. The generalised ODE for temperature change was integrated over 20 hours of cooling time using MATLABs 'ode23s' function.

4. RESULTS AND DISCUSSION

Fig. 4 shows the distribution of zone porosities (ε_i) within the domain associated with different preselected zone sizes. The bulk porosity (1 zone) was 0.5575 (blue line, Fig. 4a). Increasing the zone number to 8, the porosity of each zone was similar. However, at such a low resolution, the bulk cooling prediction time and cooling uniformity (Fig. 5a) showed a high level of discretation error. Increasing the zone number and decreasing the zone size, the range of porosities diverged significantly. This demonstrates that individual zonal porosity values have the potential to describe some of the cooling pattern differences that occur in reality.

As the number of zones increased, cooling prediction stability was reached at just 125 zones (1.45×10^{-4} m^3 per zone), representing only 42 seconds of solution time (Fig. 5b). For optimization via genetic algorithm with a typical generation size of 100, this would represent approximately one hour of simulation time per generation. In East and Smale's (2008) case, optimization ceased at 40 generations; which for this case would represent approximately two days of computation time in total. To improve the overall speed of optimization, 64 zones could be selected instead, as the difference in cooling time prediction between this zoning size and 125 zones is under 1%; but represents only 20 seconds per solution. For a slight increase in the level of error, the same optimization procedure would instead take one day.

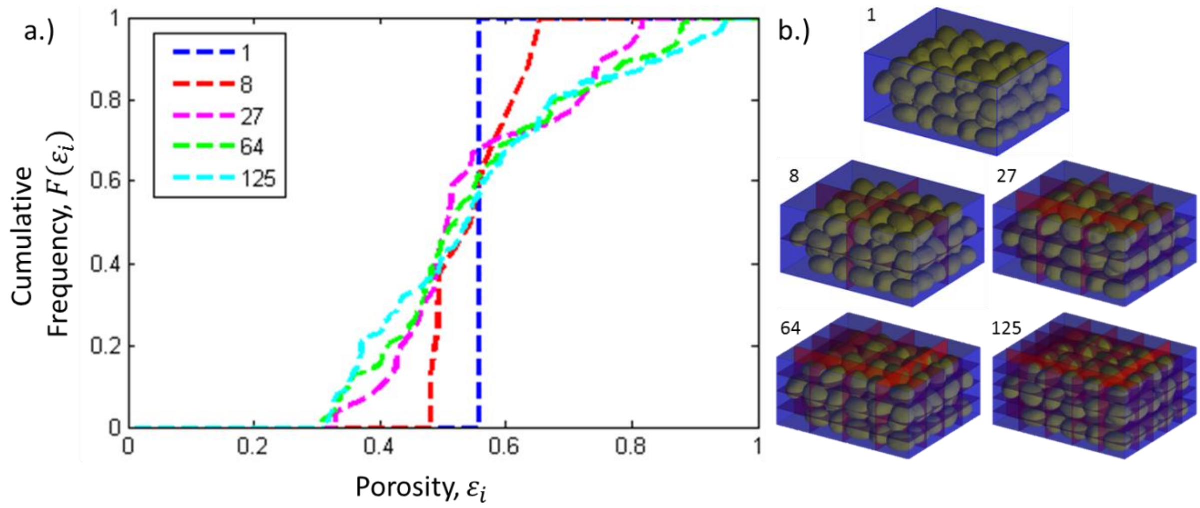

Figure 4: a.) Distribution of porosities of each zone. Legend signifies total number of zones; b.) Visual representation of each zone number, from 1 to 125 zones.

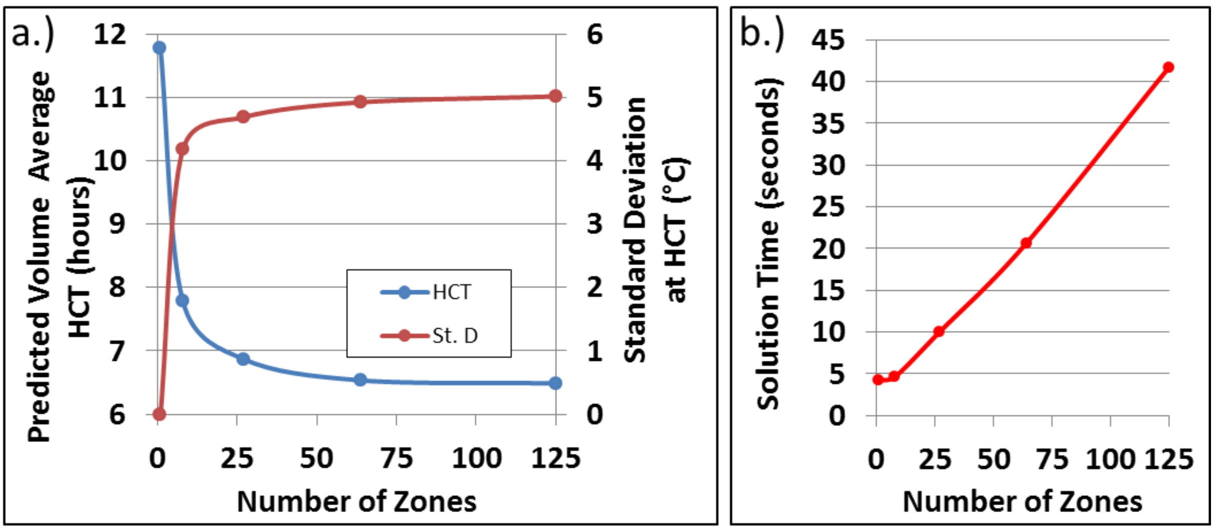

Figure 5: a.) Predicted HCT and temperature variability at the volume average half-cooling time (HCT) as a function of zone size; b.) Solution time of the MATLAB model, as a function of zone size.

Fig. 6 shows a visual result of the cooling prediction for 125 zones at various stages of the cooling process (initial stage, 1/8th cooling time, half-cooling time and 7/8th cooling time). Fruit at the top of the box cool much faster due to the polyliner being in direct contact with the external airflow. Fruit at the front, back, bottom and sides also experience an accelerated cooling rate, but to a lesser degree due to the added resistance of the packaging. Fruit in the middle of the box are insulated by the air and fruit surrounding them, so cool at a much slower rate. These trends in cooling heterogeneity were also observed experimentally by Olatunji *et al* (2015) and Shim *et al* (2015) for polylined produce.

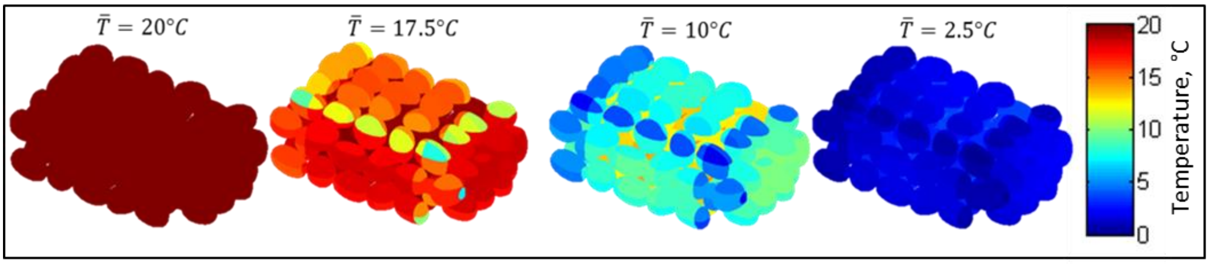

Figure 6: Visual result of the zonal approach, with 125 zones at various stages of the cooling process (initial stage, 1/8th cooling time, half-cooling time and 7/8th cooling time).

5. CONCLUSION

A preliminary cooling model for polylined packaged fruit, with a focus on flexibility and computational efficiency, has been developed. The model was based on the zonal approach, where X-ray tomography was used to automatically define the properties of each zone, reducing the amount of effort that is needed to construct the model, and significantly reducing the number of ODEs needed to solve in order to predict the bulk cooling rate and the uniformity of cooling. The model reached solution stability after the geometry was divided into just 125 zones, representing only 42 seconds of computation time to predict 20 hours of simulated cooling. Being fast and flexible, the model should be validated against a real-world box of kiwifruit, being cooled in a refrigerated wind tunnel.

ACKNOWLEDGEMENT

The authors gratefully acknowledge the New Zealand Ministry of Business, Innovation and Employment for funding this work (Fibreboard Packaging Design Project (MAUX1302)).

NOMENCLATURE

Symbols

A = heat transfer surface area (m^2)
C = specific heat capacity ($J.kg^{-1}.K^{-1}$)
dx = voxel size, x direction (m)
dX = zone size, x direction (m)
dy = voxel size, y direction (m)
dY = zone size, y direction (m)
dz = voxel size, z direction (m)
dZ = zone size, z direction (m)
D = distance, (m)
h = heat transfer coefficient ($W.m^{-2}.K^{-1}$)
k = thermal conductivity, ($W.m^{-1}.K^{-1}$)
R = resistance to heat transfer, ($m^2.K.W^{-1}$)
t = time (s)
T = temperature, (°C)
$\bar{T}$ = volume average temperature, (°C)
V = volume, (m^3)
ϕ = heat flux, (W)
ρ = density, ($kg.m^{-3}$)
$\mathbb{v}$ = voxel

Subscripts

A = air
eff = effective
ext = external airflow
i = zone under study
j = an adjacent zone to zone i
n = object out of a total number of N objects
N = the total number of objects
P = packaging
S = solid, or fruit

REFERENCES

Defraeye, T., Cronjé, P., Berry, T., Opara, U.L., East, A.R., Hertog, M., Verboven, P., Nicolai, B., 2015. Towards Integrated Performance Evaluation of Future Packaging for Fresh Produce in the Cold Chain. Trends in Food Science & Technology, 44(2), 201-225.

Defraeye, T., Lambrecht, R., Delele, M.A., Tsige, A.A., Opara, U.L., Cronjé, P., Verboven, P., Nicolai, B., 2014. Forced-Convective Cooling of Citrus Fruit: Cooling Conditions and Energy Consumption in Relation to Package Design. Journal of Food Engineering. 121, 118-127.

Dehghannya, J., Ngadi, M., Vigneault, C., 2010. Mathematical Modeling Procedures for Airflow, Heat and Mass Transfer During Forced Convection Cooling of Produce: A Review. Food Engineering Reviews, 2(4), 227-243.

Delele, M.A., Ngcobo, M.E.K., Opara, U.L., Meyer, C.J., 2012. Investigating the Effects of Table Grape Package Components and Stacking on Airflow, Heat and Mass Transfer Using 3-D CFD Modelling. Food and Bioprocess Technology, 6(9), 2571-2585.

East, A.R., Smale, N.J., 2008. Combining a Hybrid Genetic Algorithm and a Heat Transfer Model to Optimise an Insulated Box for Use in the Transport of Perishables. Vaccine. 26(10), 1322-1334.

Ferrua, M.J., Singh, R.P., 2009. Modeling the Forced-Air Cooling Process of Fresh Strawberry Packages, Part I: Numerical Model. International Journal of Refrigeration, 32(2), 335-348.

Olatunji, J.R., Shim, Y.M., Love, R.J., Ferrua, M.J., East, A.R., 2015. Exploring a New Heterogeneity Index to Quantify the Variation of Cooling Rates within Systems that Undergo the Forced-Air Cooling Process. Proceedings of the 24^{th} IIR International Congress of Refrigeration, Yokohama, Japan.

O’Sullivan, J., Ferrua, M.J., Love R.J., Verboven P., Nicolaï B., East A.R., 2014. Airflow Measurement Techniques for the Improvement of Forced-Air Cooling, Refrigeration and Drying Operations. Journal of Food Engineering 143, 90-101.

O’Sullivan, J., 2016. Significant Factors Affecting the Forced-Air Cooling Process of Polylined Horticultural Produce. PhD Thesis, Massey University, New Zealand.

Rahman, M.S., Al-Saidi, G.S., 2009. Thermal Conductivity Prediction of Foods, Food Properties Handbook, Second Edition: CRC Press.

Shim, Y.M., Olatunji, J.R., Zhou, J., Love, R.J., Ferrua, M.J., East, A.R., 2016. Industry Survey on the Pressure Drop Across Palletised Horticulture Product During Precooling. Proceedings of the 4^{th} IIR Conference on Sustainability and the Cold Chain, Auckland, New Zealand

Shim, Y.M., Tan, A., Olatunji, J.R., O’Sullivan, J., Love, R.J., Ferrua, M.J., East, A.R., 2015. A New Method to Describe the Cooling Process of Packaged Horticulture Produce. Proceedings of the 24^{th} IIR International Congress of Refrigeration, Yokohama, Japan.

Tanner, D.J., Cleland, A.C., Opara, L.U., Robertson, T.R., 2002. A Generalised Mathematical Modelling Methodology for Design of Horticultural Food Packages Exposed to Refrigerated Conditions: Part 1, Formulation. International Journal of Refrigeration, 25(1), 33-42.

Developing Cooling Models for Rapid Determination of Optimized Package Designs

Jamal R. Olatunji, Justin O'Sullivan, Young-Min Shim, Maria J. Ferrua, Richard J. Love, Andrew R. East

Centre for Postharvest and Refrigeration Research, Massey University, Private Bag 11-222, Palmerston North 4442, New Zealand, Ph +64 6 350 4336; Fax +64 6 350 5657

*R.J.Love@massey.ac.nz

Abstract: Stacking fruit boxes into pallets allows large quantities of product to be simultaneously cooled and transported, making packaging a vital component in the horticulture cool chain. Packaging features such as vent number, size and position; or the existence of a polyliner, can have significant impacts on the cooling efficiency, and hence the end-of-cool-chain product quality. A cooling prediction model that focuses on computational speed would be valuable, as optimized package designs could be rapidly identified. A preliminary model is presented in this paper, applied to a single box of polylined kiwifruit. A random stacking model was developed that applied rigid body dynamics to a collection of kiwifruit shapes that are allowed to settle naturally under simulated gravity into a box, accelerating model construction time. A zonal approach was then employed, dividing the modelling domain into a small network of zones with space averaged properties. The resulting cooling predictions reached solution stability after just 125 zones were used, representing only 89 seconds of computational time. Being fast and flexible, the model will be validated against a real-world box of kiwifruit in the future, and later allow rapid optimization of the package design.

1 INTRODUCTION

Temperature plays a crucial role in the rate of senescence and growth rate of pathogens in fresh fruits and vegetables, which in turn affect the maintenance of product quality and shelf life. Therefore, pre-cooling has become an integral part of the horticulture cool chain, a unit operation designed to quickly and efficiently reduce freshly picked produce from their field to storage temperatures. The most common pre-cooling process in the horticulture industry is forced-air cooling (Shim *et al*, 2016), where a pressure drop is created across rows of palletised produce using a large fan, forcing refrigerated air to penetrate through the packaging structure and exchange heat with the product inside (O'Sullivan *et al*, 2014) (Fig. 1a).

The design of individual packages has the potential to alter the efficiency of a pre-cooling operation – both the average cooling rate and cooling uniformity, or homogeneity (Olatunji *et al*, 2015a). The size of package ventilation, in addition to the number, shape and position of vents, combines on the pallet scale to form a convoluted airflow pathway (Fig. 1b) that can benefit the removal of energy from some fruit, while retarding the cooling rate of others. The stacked fruit inside of the pallet also forms a labyrinthine structure for the air to penetrate; a pathway that will change from box to box, as it is dependent on individual product shape and how they have naturally stacked within the packaging. Additional packaging features – such as polyliners – further complicate the system.

Experimentally, optimizing a pre-cooling system is impractical – the materials cost of manufacturing many different package designs and the purchase of tonnes of real fruit are prohibitively high; and the need to record dozens or hundreds of individual product temperatures requires an excessive amount of time and labour (Shim *et al*, 2015) and even large-scale laboratory experiments may not be truly representative of real industrial practice. It would be beneficial to both industry and academia to instead construct a mathematical model, one that can predict the airflow field as a consequence of package design; and the rate of heat transfer as a result of said airflow. Doing so would allow – depending on the solution time – many package designs to be investigated computationally.

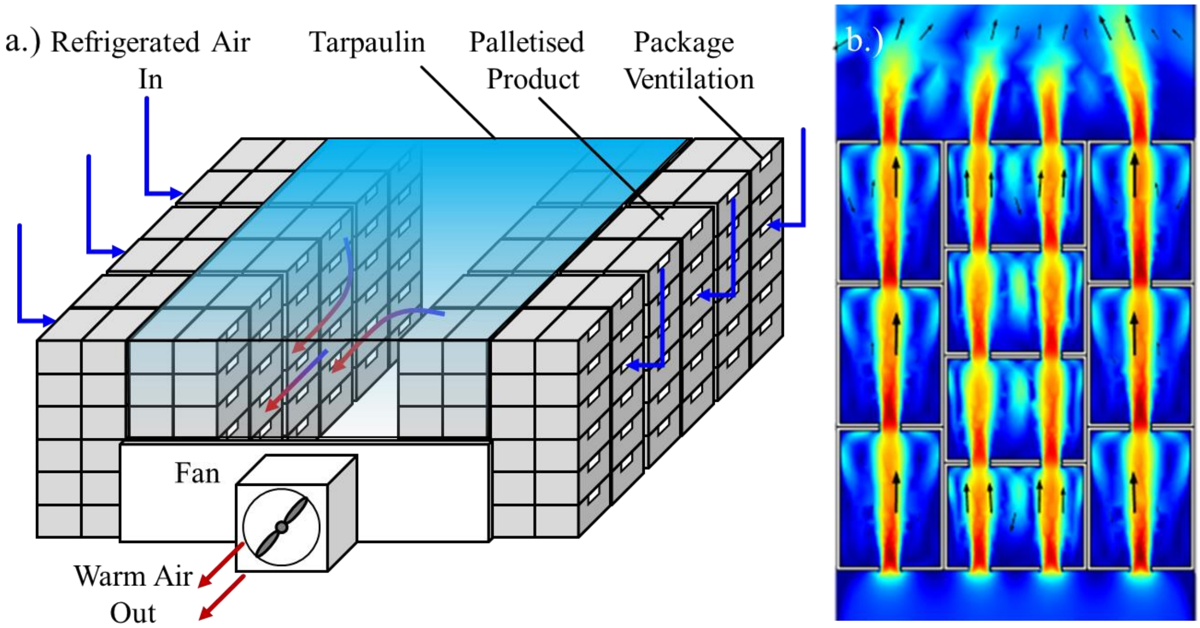

Figure 1. a.) A forced-air tunnel cooler, a commonly used setup for pre-cooling horticultural produce. b.) an illustrative 2D steady state CFD airflow solution of air being pulled through a single layer of stacked packaging, to demonstrate how the design of individual packages combines on the pallet scale to form a convoluted airflow pathway. Colours represent velocity; warmer colours are faster velocities.

Highly detailed discrete element models (such as Computational Fluid Dynamics (CFD) models) have been used recently to provide important insight into the mechanisms at play during a forced-air cooling process, such as the degree of forced and natural convection within a box, moisture transfer and evaporative cooling, thermal radiation, and temperature gradients within individual products (Defraeye *et al*, 2014; Ferrua and Singh, 2009; O'Sullivan, 2016). However, these detailed models can be difficult to construct and fully validate: due to the nature of meshing a complex geometry (Frei, 2013). These models can often only be applied to a specific cooling scenario, applied to a single product; a new scenario essentially means building a new model from scratch. Also, the large number of mesh elements required for the approach to function means high computational resources are required, and solution times of several hours or days is commonplace. These problems place limitations on their usefulness as an optimization tool.

Therefore, it is proposed that a mathematical model that favours flexibility and speed be developed. Sacrificing the high level of detail seen in CFD models for a model that can be constructed quickly and in a generalised fashion, and can be solved in a reasonable amount of time, would allow the model to be integrated with an optimization strategy, such as a genetic algorithm (East and Smale, 2008). This would allow the best package design and operational conditions for a given product to be rapidly identified.

Generalised model construction and computational efficiency are explored in this paper. The model is based on the zonal approach (Tanner *et al*, 2002), which divides the modelling domain into a small set of space averaged zones. We propose new generalised methods to automatically determine the important properties of each zone – such as the volume of solids and the resistance to heat transfer per zone. The zonal approach is supplemented with a stacking model, where a number of fruit are allowed to fall under simulated gravity and stack naturally, automatically creating a geometry to use as a model input. The new model is applied in this preliminary case to a single box of kiwifruit wrapped in a polyliner.

2 GEOMETRY

The geometry within a box of fruit poses one of the most significant challenges to model construction. Determining a computational analogue of this bulk shape is vital for an accurate cooling model to be developed. While some products can be simplified as an ordered stack of spheres – such as apples or oranges (Tanner *et al*, 2002; Defraeye *et al*, 2014) – kiwifruit are proto-ellipsoids, exported in randomly stacked bulk packages weighing approximately 10 kg. Rather than attempt to manually build such a complex shape, we have instead opted to build a computational stacking model to allow physics to inform us of the internal geometry. This was achieved by applying rigid body dynamics to a collection of kiwifruit shapes and allowing them to settle naturally under simulated gravity.

The random stacking model was built using the free and open source software package Blender™ (https://www.blender.org/). Kiwifruit shapes were created in 3D as parametric surfaces using a shape equation for kiwifruit developed previously (Olatunji *et al*, 2015b). Although the shape equation is valid for a large range of kiwifruit sizes, this preliminary case doesn't include size variability and instead models each kiwifruit as an average sized count 36 Hayward kiwifruit (count 36 is a size based grading category used by Zespri International; Fig. 2a).

102 kiwifruit shapes were created in rows of 9 above a chute with the same internal X and Y dimensions of a regular modular bulk package (372 and 292 mm, respectively). 102 were created because this is the industry standard amount of count 36 fruit exported per modular bulk package. Each fruit was created with a randomised X, Y and Z rotation to encourage random stacking, and ensure that repetition of the stacking model would result in a unique solution every time. Angled shafts were added to redirect all fruit toward the chute as they fell. Using Blender's built in physics engine, the chute and angled shafts were defined as passive objects – meaning they did not move and were impassable, rigid barriers. Fruits were defined as active objects – meaning they were subject to acceleration due to gravity, and could collide and rotate when contacting other fruit and the walls of the chute. The fruit were then allowed to settle naturally (Fig. 3a and b). Fruit that protrude above the specified Z dimension of the modular bulk pack (182 mm) were deleted from the model. A script was written to automate the construction of the chute and placement of the fruit shapes, meaning the process can be repeated easily and as many times as necessary. The resultant bulk fruit shape was then used as a model input (Fig. 3c).

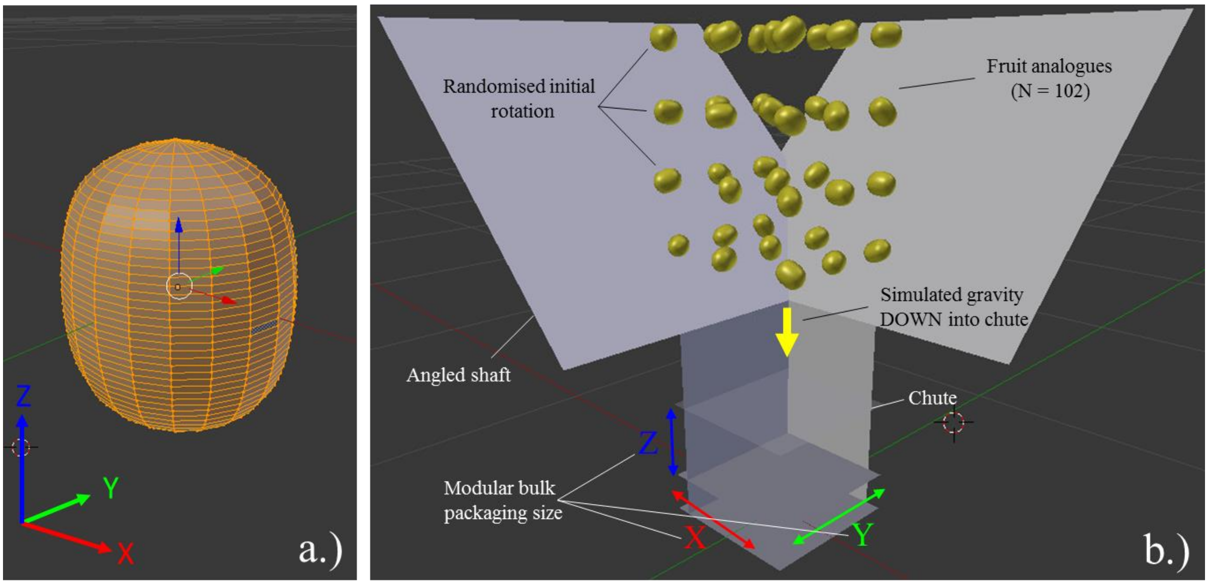

Figure 2. a.) a 3D kiwifruit shape for an average sized count 36 Hayward kiwifruit, created as a parametric surface in Blender (Olatunji *et al*, 2015b). b.) Diagram of the Blender stacking model, showing the geometry of the chute and angled shafts, as well as the starting positions of the fruit about to be stacked.

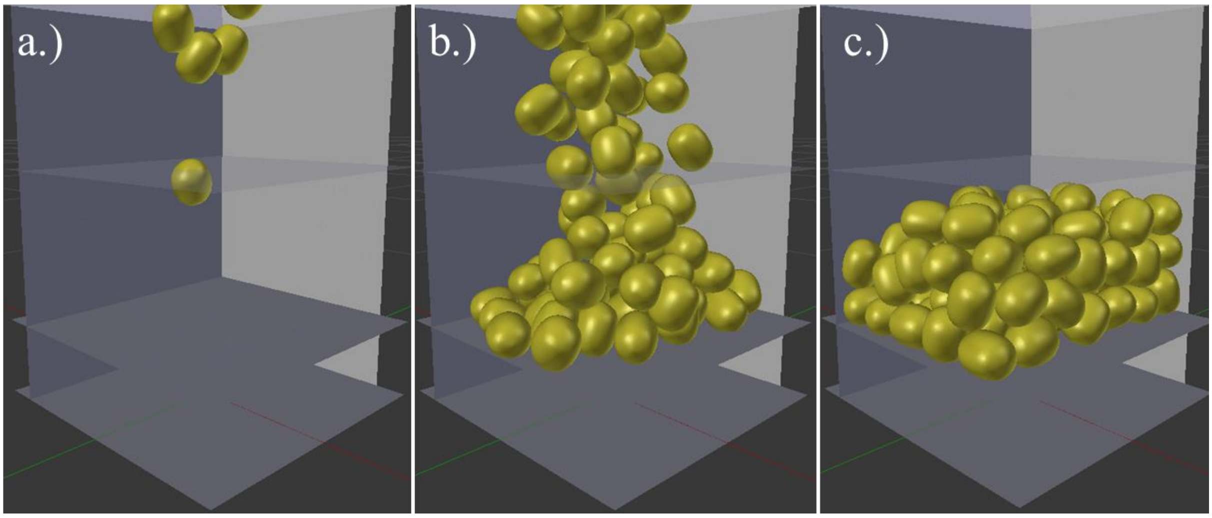

Figure 3. Time series snapshots of the stacking model for a modular bulk package, with inside X Y and Z dimensions of 372, 292 and 182 mm, respectively: t = 1, the fruit begin to fall into the chute; b.) t = 2, the fruit collide with each other and the walls of the chute as they begin to fill up the box; c.) t = final, the fruit have settled naturally under simulated gravity and have ceased motion, providing the geometry input for the cooling model.

3 COOLING MODEL DEVELOPMENT

3.1 Model Simplification

The pressure differential created by the fan during pre-cooling is much higher than any pressure differential created by thermal gradients in the air. This means that heat and momentum transfer can be de-coupled, so that separate models for airflow distribution and the consequent heat transfer can be developed independently (Ferrua and Singh, 2009; Defraeye *et al*, 2014). This paper focuses on the development of a heat transfer model, with an airflow model to be added later. The kiwifruit are wrapped in a thin polyethylene bag – called a polyliner – to prevent moisture loss and shrivelling during transport. Therefore, there is a negligible amount of moisture transfer, and by extension a negligible amount of evaporative cooling. Defraeye *et al* (2014) and O'Sullivan (2016) showed that thermal radiation was also negligible in forced-air cooling scenarios. Due to the existence of the polyliner bag, air near the fruit was considered to be stagnant, the air temperature variation within the polyliner was assumed too small to promote significant amounts of natural convection. These simplifications resulted in an effective thermal conductivity model to be explored, where two phases (fruit and air) are treated as a single phase with effective properties.

3.2 Model Equations

The geometry from the stacking model was divided into a small set of space averaged zones (Tanner *et al*, 2002). Air (A) and product (S) can exist within a zone. Packaging (P) occupies zones on the sides and bottom of the geometry, but is absent at the top where the polyliner is in direct contact with refrigerated airflow (Fig. 4a).

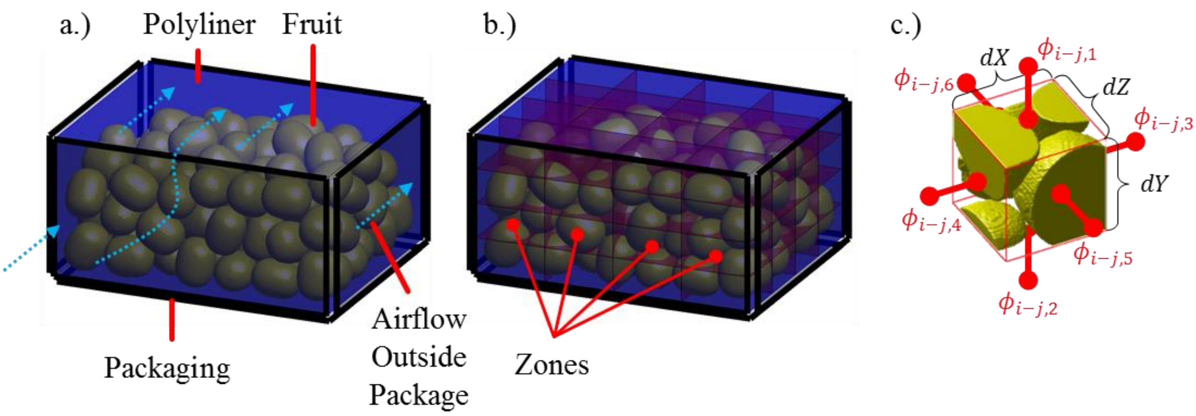

Figure 4. a.) result of the random stacking model with polyliner and packaging added; b.) geometry divided into space averaged zones (Tanner *et al*, 2002); c.) image of an individual zone with up to 6 possible directions of heat transfer.

By using the zonal, space averaged approach, the number of ODEs that need to be solved is significantly reduced compared to the finite element approach, promoting fast solution times; while retaining the ability to predict temperature gradients within the packaging so that heterogeneity analysis can be performed (Olatunji *et al*, 2015a). The generalised ODE for temperature change is Eq. 1. $\phi_{i-j,n}$ denotes an exchange of energy between zone *i* and the zones adjacent to it, *j*. These heat transfers are determined by Eq. 2. The effective heat transfer coefficient is Eq. 3, the resistance to heat transfer being Eq. 4, calculated using Eq. 5 which uses the parallel effective thermal conductivity model (Rahman and Al-Saidi, 2009; Delele *et al*, 2002).

$$\frac{dT_i}{dt} = \frac{\sum_{n=1}^{N} \phi_{i-j,n}}{V_i \cdot \varepsilon_i \cdot \rho_A \cdot C_A + V_i \cdot (1-\varepsilon_i) \cdot \rho_S \cdot C_S} \tag{1}$$

$$\phi_{i-j,n} = h_{eff} \cdot A_n \cdot (T_{j,n} - T_i) \tag{2}$$

$$h_{eff} = \frac{1}{R_i + R_{j,n}} \tag{3}$$

$$R = \frac{D_n/2}{k_{eff,i}} \tag{4}$$

$$k_{eff,i} = \varepsilon_i \cdot k_A + (1-\varepsilon_i) \cdot k_S \tag{5}$$

3.3 Zone Properties

At this preliminary stage, zones were limited to being cuboid in shape, equal in size and regularly spaced throughout the model geometry. In the case of kiwifruit – and many other fruit pre-cooling scenarios – the porous medium approach is not appropriate, as the package-to-product ratio is greater than 10; meaning a system wide porosity is not representative, even at relatively large representative elementary sizes (Verboven *et al*, 2006). Rather, ε_i is determined locally, for each individual zone.

Developing an automated process for determining ε_i requires some form of volume discretization. We have opted to avoid complex meshing strategies – such as free tetrahedral – and have instead divided the result from the random stacking model into a regular grid of equally sized cubes (voxels; Fig. 5). Individual voxels (denoted as $\mathbb{v}_n$) are assigned a value of 1 if it contains solid (i.e. fruit), or a value of 0 for air. Partially filled voxels are considered to be solids. As long as the voxel resolution is sufficiently high, any geometry can be accurately represented as a collection of voxels. Utilising voxels as a discretisation method avoids meshing errors, is repeatable for any geometry and is computationally efficient. In this case, each voxel is 1 mm³ in volume (Fig. 6); the whole box geometry contains 2E7 voxels, 9.7E6 are considered solid.

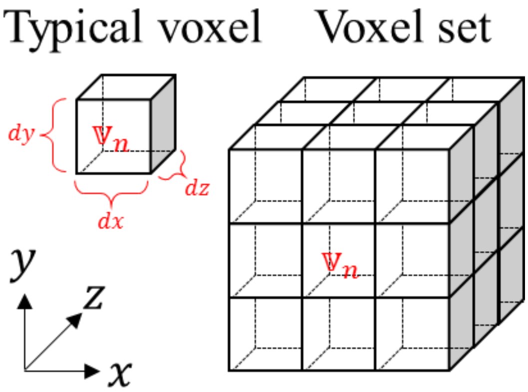

Figure 5. voxels, values represented on a regular 3D grid

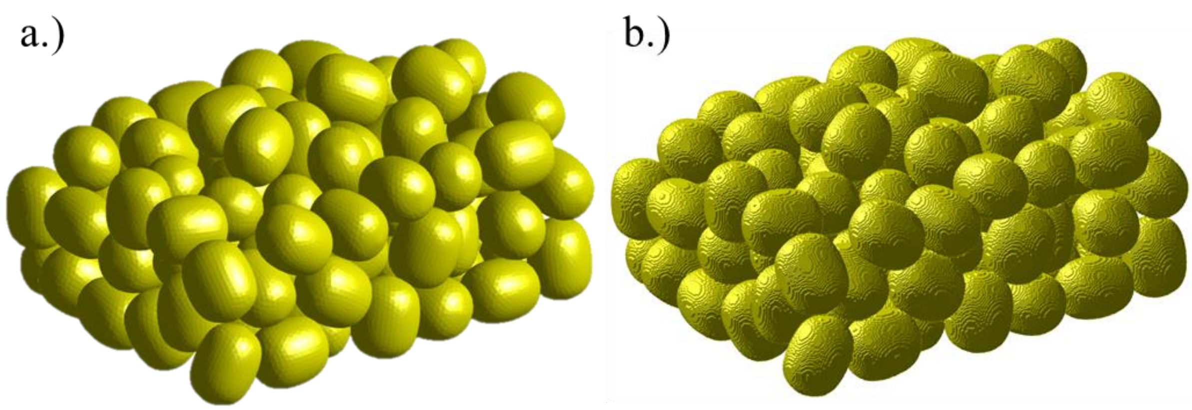

Figure 6. a.) result from the random stacking model; b.) random stacking model volume discretized into 1mm³ voxels

Within a single zone, the volume of the solids phase is therefore the sum of all voxels defined as a solid within the zone, multiplied by the volume of a single voxel (Eq. 6; Fig. 7); the remaining zone volume is air (Eq. 7). The porosity within a zone is therefore Eq. 8.

$$V_{S,i} = \left(\sum \mathbb{v}_i\right) \times (dx \cdot dy \cdot dz) \tag{6}$$

$$V_{A,i} = \left(\sum \sqrt{(\mathbb{v}_i - 1)^2}\right) \times (dx \cdot dy \cdot dz) \tag{7}$$

$$\varepsilon_i = \frac{\sum \sqrt{(\mathbb{v}_i - 1)^2}}{\sum \sqrt{(\mathbb{v}_i - 1)^2} + \sum \mathbb{v}_i} \tag{8}$$

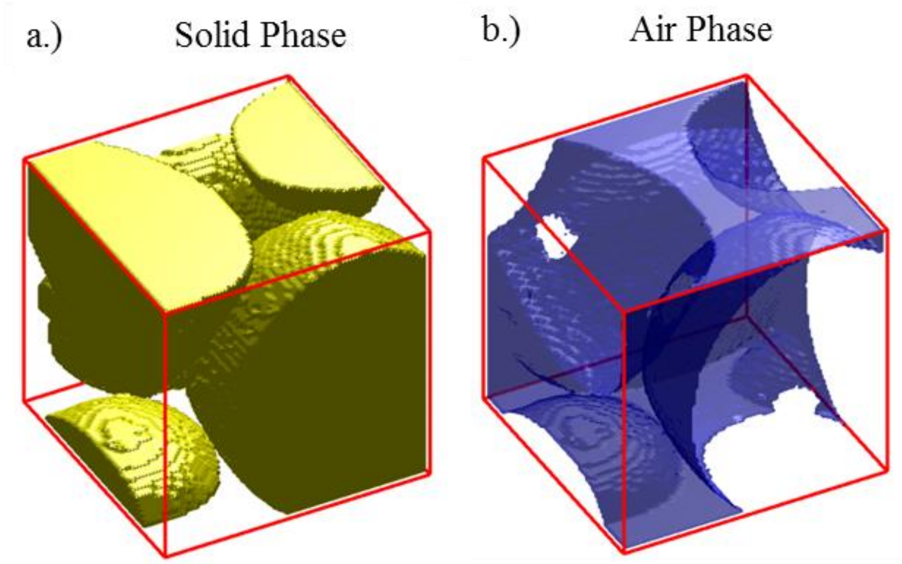

Fig. 7. a.) solid phase within a zone; b.) air phase within a zone

3.4 Model Set-Up

The model equations were coded in MATLAB R2015b. An airflow model is to be added at a later date. In this scenario there is assumed to be a constant flow of 0°C air on all outer box surfaces except the bottom, resulting in a convective heat transfer coefficient of 10 W.m^{-2}.K^{-1}. The bottom surface is resting on a refrigerated floor, so is modelled at a constant temperature of 0°C. Packaging was modelled as an extra resistance on the outer box surfaces (except the top), being 3mm thick, with a thermal conductivity of $k_P = 0.005$ W.m^{-1}.K^{-1}. No fibreboard packaging exists on the top surface, where the polyliner is in direct contact with the airflow. Kiwifruit is modelled as a homogeneous solid with thermal properties of $\rho_S = 1037$ kg.m^{-3}, $C_S = 3713$ J.kg^{-1}.K^{-1} and $k_S = 0.542$ W.m^{-1}.K^{-1} (O'Sullivan, 2016); and the air as $\rho_A = 1.25$ kg.m^{-3}, $C_A = 1005$ J.kg^{-1}.K^{-1} and $k_A = 0.025$ W.m^{-1}.K^{-1}. The initial temperature for the entire box was 20°C. The generalised ODE for temperature change (Eq. 1) was integrated numerically using MATLAB's 'ode23s' solver, over a 20-hour period.

4 RESULTS AND DISCUSSION

As mentioned previously, the porous medium approach was deemed inappropriate because the product-to-package ratio for count 36 kiwifruit inside of a modular bulk package is over 10. This was explicitly confirmed by plotting the distribution of porosities for individual zones (Fig. 8a). The bulk porosity was 0.5137. Increasing the zone number to just 8 zones, a divergence begins to occur, a problem that is exacerbated as the model is made more detailed and more zonal divisions are added. This demonstrates that a representative porosity is inappropriate. Using the local zonal porosities instead has the potential to describe some of the cooling pattern differences that occur in reality.

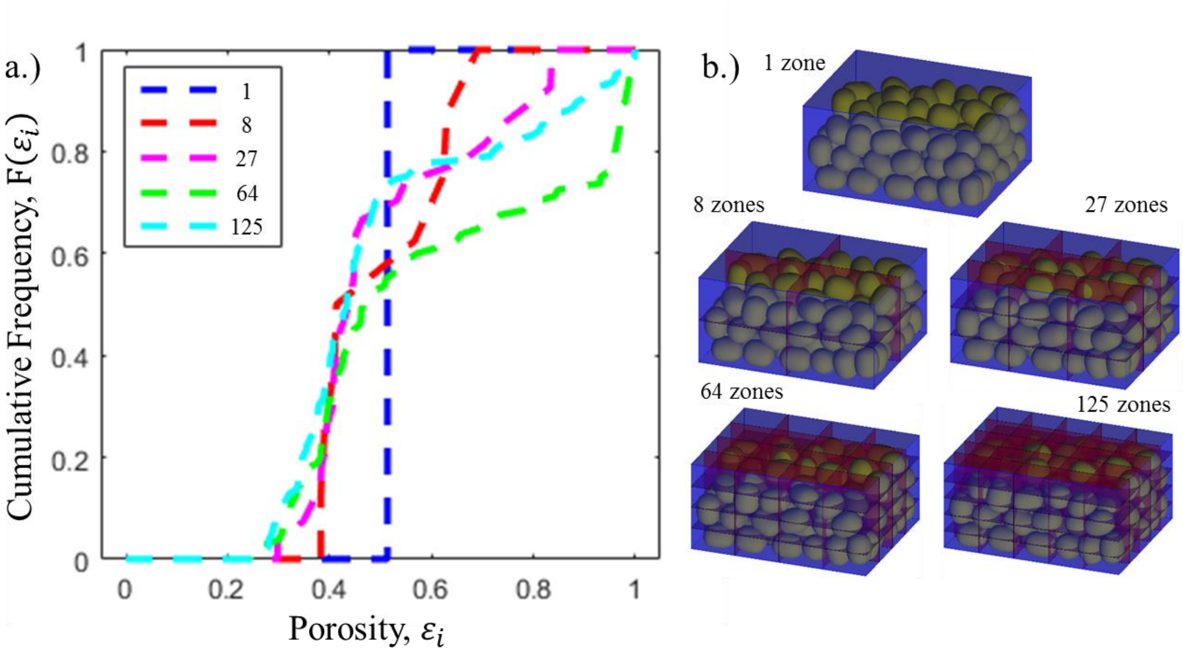

Figure 8. a.) distribution of porosities of each zone, as a function of zone number (zone size); b.) visual representation of each zone number from 1 to 125 zones.

As demonstrated in Fig. 9a, the predicted half cooling time (HCT) for the single box reaches stability at just 125 zones, giving a predicted HCT of 5.8 hours. Stability means that further increasing the number of zones does not significantly change the predicted half cooling time. Generating this value for cooling performance includes the construction of the bulk fruit geometry via the random stacking model (25 seconds), volume discretization (31 seconds), and solving the unsteady state heat transfer equations over 20 hours of cooling (34 seconds); a start to finish time of just 89 seconds (Fig. 9b).

The model is also capable of predicting representative temperature gradients within the package, so that cooling heterogeneity analysis is also possible. Fig. 10 shows the visual result for 125 zones at various stages of the cooling process (initial stage, half-cooling time and seven-eighths cooling time). Fruit on the edges cool faster as they are closest to the refrigerated airflow, however as the polyliner is in direct contact with the air at the top (with no packaging), the rate is accelerated here. Fruit in the middle of the box are shielded by the fruit and air that surrounds them, so that heat conducts more slowly from these regions.

The methods discussed in this paper demonstrate how to significantly accelerate not only model construction, but also solution times of unsteady state heat transfer problems within pre-cooling systems for horticultural products. The stacking model that was developed can construct a realistic internal bulk fruit geometry in just 25 seconds, opening this method up to a monte-carlo style investigation of the cooling performance effects of random stacking. It also allows models to be constructed for different shaped or sized packages in a similarly short period of time; as well as for kiwifruit from a larger or smaller weight range. Extending the model beyond application to kiwifruit to another non-regularly shaped fresh product would require a single change at the fruit shape creation stage to better represent the new product (and total package dimensions). This could be achieved by importing empirical produce shapes via CT scanning, or a more advanced shape equation could be developed, such as by Rogge *et al*, 2015. The discretization method (voxelisation) and determination of zonal properties would not be affected by these changes.

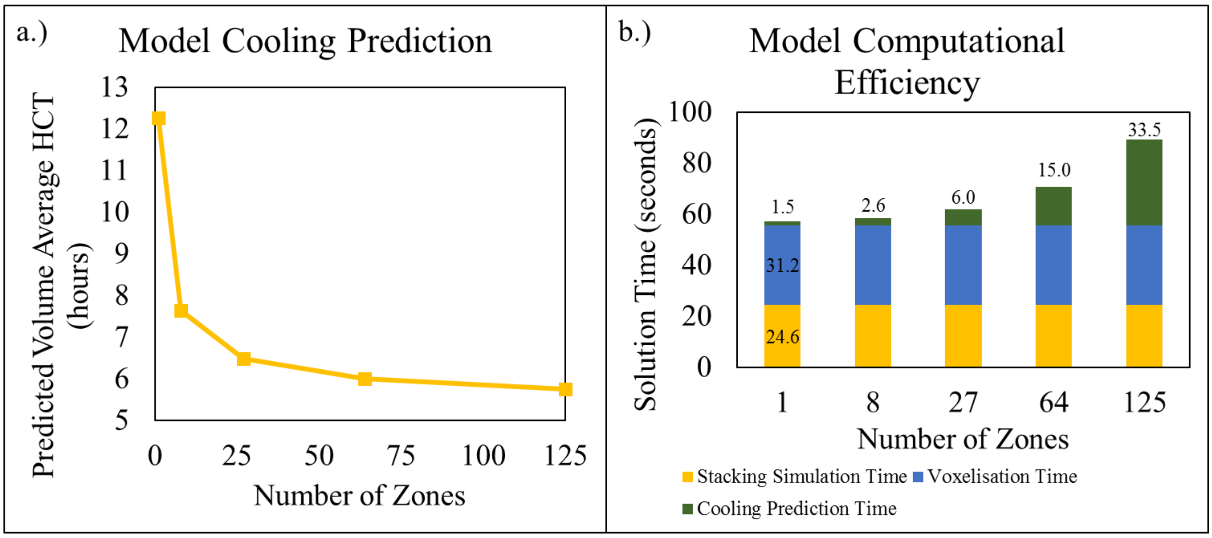

Figure 9. a.) predicted volume average HCT as a function of the number of zones used; b.) solution times for various parts of the model: blue = discretisation into voxel time; yellow = stacking simulation time; green = unsteady-state heat transfer over 20 hours of cooling solution time.

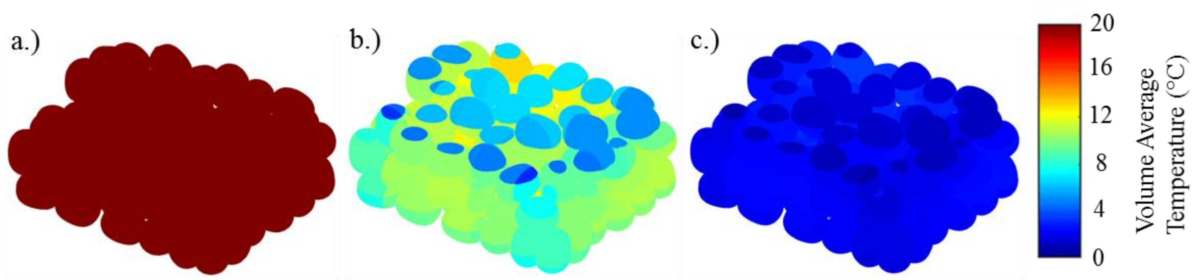

Figure 10. visual result of the zonal approach applied to a box of kiwifruit over time: a.) initial stage; b.) half-cooling time; c.) seven-eighths cooling time.

CONCLUSION

A preliminary cooling model for a single box of kiwifruit wrapped in a polyliner undergoing cooling has been developed. The model focused on accelerating model construction using a random stacking model; and on computational efficiency by employing the zonal approach, but while still producing “good enough” predictions to guide package development. The model reached solution stability after just 125 zones, representing only 89 seconds of solution time to construct the internal bulk geometry, volume discretize the geometry, and predict 20 hours of simulated cooling. The model is fast and flexible. The model predictions should now be validated against experimental data.

ACKNOWLEDGEMENTS

The authors gratefully acknowledge the New Zealand Ministry of Business, Innovation and Employment for funding this work (Fibreboard Packaging Design Project (MAUX1302)).

NOMENCLATURE

Symbols
A = heat transfer surface area (m^2)
C = specific heat capacity ($J.kg^{-1}.K^{-1}$)
dx = voxel size, x direction (m)
dX = zone size, x direction (m)
dy = voxel size, y direction (m)
dY = zone size, y direction (m)
dz = voxel size, z direction (m)
dZ = zone size, z direction (m)
D = distance, (m)
h = heat transfer coefficient ($W.m^{-2}.K^{-1}$)
k = thermal conductivity, ($W.m^{-1}.K^{-1}$)
R = resistance to heat transfer, ($m^2.K.W^{-1}$)
t = time (s)
T = temperature, (°C)
$\bar{T}$ = volume average temperature, (°C)
V = volume, (m^3)
ϕ = heat flux, (W)
ρ = density, ($kg.m^{-3}$)
$\mathbb{v}$ = voxel

Subscripts
A = air
eff = effective
ext = external airflow
i = zone under study
j = an adjacent zone to zone i
n = object out of a total number of N objects
N = the total number of objects
P = packaging
S = solid, or fruit

REFERENCES

Defraeye, T., Lambrecht, R., Delele, M.A., Tsige, A.A., Opara, U.L., Cronjé, P., Verboven, P., Nicolai, B., 2014. “Forced-Convective Cooling of Citrus Fruit: Cooling Conditions and Energy Consumption in Relation to Package Design”. Journal of Food Engineering. 121, 118-127.

Delele, M.A., Ngcobo, M.E.K., Opara, U.L., Meyer, C.J., 2012. “Investigating the Effects of Table Grape Package Components and Stacking on Airflow, Heat and Mass Transfer Using 3-D CFD Modelling”. Food and Bioprocess Technology, 6(9), 2571-2585.

East, A.R., Smale, N.J., 2008. “Combining a Hybrid Genetic Algorithm and a Heat Transfer Model to Optimise an Insulated Box for Use in the Transport of Perishables”. Vaccine. 26(10), 1322-1334.

Ferrua, M.J., Singh, R.P., 2009. “Modeling the Forced-Air Cooling Process of Fresh Strawberry Packages, Part I: Numerical Model”. International Journal of Refrigeration, 32(2), 335-348.

Frei, W. (2013). “Meshing your Geometry: When to Use the Various Element Types”. COMSOL Blog. Accessed May 2016.

Olatunji, J.R., Shim, Y.M., Love, R.J., Ferrua, M.J., East, A.R. (2015a). “Exploring a New Heterogeneity Index to Quantify the Variation of Cooling Rates within Systems that Undergo the Forced-Air Cooling Process”. Proceedings of the 24th IIR International Congress of Refrigeration, Yokohama, Japan.

Olatunji, J.R., Shim, Y.M., Love, R.J., Ferrua, M.J., East, A.R. (2015b). “Numerical Determination of Kiwifruit Shape, Volume and Surface Area”. Poster session presented at the 12th International Congress of Engineering and Food, Quebec Canada.

O’Sullivan, J., Ferrua, M.J., Love R.J., Verboven P., Nicolaï B., East A.R., 2014. “Airflow Measurement Techniques for the Improvement of Forced-Air Cooling, Refrigeration and Drying Operations”. Journal of Food Engineering 143, 90-101.

O’Sullivan, J., 2016. “Significant Factors Affecting the Forced-Air Cooling Process of Polylined Horticultural Produce”. PhD Thesis, Massey University, New Zealand.

Rahman, M.S., Al-Saidi, G.S., 2009. “Thermal Conductivity Prediction of Foods, Food Properties Handbook, Second Edition”: CRC Press.

Rogge, S., Defraeye, T., Herremans, E., Verboven, P., Nicolai, B.M. (2015). "A 3D contour based geometrical model generator for complex-shaped horticultural products". Journal of Food Engineering 157(0): 24-32.

Tanner, D.J., Cleland, A.C., Opara, L.U., Robertson, T.R., 2002. "A Generalised Mathematical Modelling Methodology for Design of Horticultural Food Packages Exposed to Refrigerated Conditions: Part 1, Formulation". International Journal of Refrigeration, 25(1), 33-42.

Shim, Y.M., Tan, Y.T., Olatunji, J.R., O'Sullivan, J.L., Love, R.J., Ferrua, M.J., East, A.R. (2015). "A New Method to Describe the Cooling Process of Packaged Horticultural Produce". Proceedings of the 24th IIR International Congress of Refrigeration, Yokohama Japan.

Shim, Y.M., Olatunji, J.R., Zhou, J., Love, R.J., Ferrua, M.J., East, A.R. (2016). "Industry Survey on the Pressure Drop Across Palletised Horticultural Produce During Pre-Cooling". Proceedings of the 4th IIR Conference on Sustainability and the Cold Chain, Auckland New Zealand.

Verboven, P., Flick, D., Nicolaï, B.M., Alvarez, G. (2006). "Modelling transport phenomena in refrigerated food bulks, packages and stacks: basics and advances". International Journal of Refrigeration, 29(6), 985-997.